The Astrophysical Journal Letters, 875:L1 (17pp), 2019 April 10 https://doi.org/10.3847/2041-8213/ab0ec7
© 2019. The American Astronomical Society.
OPEN ACCESS

First M87 Event Horizon Telescope Results. I. The Shadow of the Supermassive Black Hole

The Event Horizon Telescope Collaboration
(See the end matter for the full list of authors.)
Received 2019 March 1; revised 2019 March 12; accepted 2019 March 12; published 2019 April 10

Abstract

When surrounded by a transparent emission region, black holes are expected to reveal a dark shadow caused by gravitational light bending and photon capture at the event horizon. To image and study this phenomenon, we have assembled the Event Horizon Telescope, a global very long baseline interferometry array observing at a wavelength of 1.3 mm. This allows us to reconstruct event-horizon-scale images of the supermassive black hole candidate in the center of the giant elliptical galaxy M87. We have resolved the central compact radio source as an asymmetric bright emission ring with a diameter of $42 \pm 3\ \mu$as, which is circular and encompasses a central depression in brightness with a flux ratio $\gtrsim$10:1. The emission ring is recovered using different calibration and imaging schemes, with its diameter and width remaining stable over four different observations carried out in different days. Overall, the observed image is consistent with expectations for the shadow of a Kerr black hole as predicted by general relativity. The asymmetry in brightness in the ring can be explained in terms of relativistic beaming of the emission from a plasma rotating close to the speed of light around a black hole. We compare our images to an extensive library of ray-traced general-relativistic magnetohydrodynamic simulations of black holes and derive a central mass of $M = (6.5 \pm 0.7) \times 10^9\, M_\odot$. Our radio-wave observations thus provide powerful evidence for the presence of supermassive black holes in centers of galaxies and as the central engines of active galactic nuclei. They also present a new tool to explore gravity in its most extreme limit and on a mass scale that was so far not accessible.

Key words: accretion, accretion disks – black hole physics – galaxies: active – galaxies: individual (M87) – galaxies: jets – gravitation

1. Introduction

Black holes are a fundamental prediction of the theory of general relativity (GR; Einstein 1915). A defining feature of black holes is their event horizon, a one-way causal boundary in spacetime from which not even light can escape (Schwarzschild 1916). The production of black holes is generic in GR (Penrose 1965), and more than a century after Schwarzschild, they remain at the heart of fundamental questions in unifying GR with quantum physics (Hawking 1976; Giddings 2017).

Black holes are common in astrophysics and are found over a wide range of masses. Evidence for stellar-mass black holes comes from X-ray (Webster & Murdin 1972; Remillard & McClintock 2006) and gravitational-wave measurements (Abbott et al. 2016). Supermassive black holes, with masses from millions to tens of billions of solar masses, are thought to exist in the centers of nearly all galaxies (Lynden-Bell 1969; Kormendy & Richstone 1995; Miyoshi et al. 1995), including in the Galactic center (Eckart & Genzel 1997; Ghez et al. 1998; Gravity Collaboration et al. 2018a) and in the nucleus of the nearby elliptical galaxy M87 (Gebhardt et al. 2011; Walsh et al. 2013).

Active galactic nuclei (AGNs) are central bright regions that can outshine the entire stellar population of their host galaxy. Some of these objects, quasars, are the most luminous steady sources in the universe (Schmidt 1963; Sanders et al. 1989) and are thought to be powered by supermassive black holes accreting matter at very high rates through a geometrically thin, optically thick accretion disk (Shakura & Sunyaev 1973; Sun & Malkan 1989). In contrast, most AGNs in the local universe, including the Galactic center and M87, are associated with supermassive black holes fed by hot, tenuous accretion flows with much lower accretion rates (Ichimaru 1977; Narayan & Yi 1995; Blandford & Begelman 1999; Yuan & Narayan 2014).

In many AGNs, collimated relativistic plasma jets (Bridle & Perley 1984; Zensus 1997) launched by the central black hole contribute to the observed emission. These jets may be powered either by magnetic fields threading the event horizon, extracting the rotational energy from the black hole (Blandford & Znajek 1977), or from the accretion flow (Blandford & Payne 1982). The near-horizon emission from low-luminosity active galactic nuclei (LLAGNs; Ho 1999) is produced by synchrotron radiation that peaks from the radio through the far-infrared. This emission may be produced either in the accretion flow (Narayan et al. 1995), the jet (Falcke et al. 1993), or both (Yuan et al. 2002).

When viewed from infinity, a nonrotating Schwarzschild (1916) black hole has a photon capture radius $R_c = \sqrt{27}\ r_g$, where $r_g \equiv GM/c^2$ is the characteristic lengthscale of a black hole. The photon capture radius is larger than the Schwarzschild radius R_S that marks the event horizon of a nonrotating black hole, $R_S \equiv 2\, r_g$. Photons approaching the black hole with an impact parameter $b < R_c$ are captured and plunge into the black hole (Hilbert 1917); photons with $b > R_c$ escape to infinity; photons with $b = R_c$ are captured on an unstable circular orbit and produce what is commonly referred to as the lensed "photon ring." In the Kerr (1963) metric, which describes black holes with spin angular momentum, R_c changes with the ray's orientation relative to the angular-momentum vector, and the black hole's cross section is not necessarily circular

Original content from this work may be used under the terms of the Creative Commons Attribution 3.0 licence. Any further distribution of this work must maintain attribution to the author(s) and the title of the work, journal citation and DOI.

(Bardeen 1973). This change is small ($\lesssim$4%), but potentially detectable (Takahashi 2004; Johannsen & Psaltis 2010).

The simulations of Luminet (1979) showed that for a black hole embedded in a geometrically thin, optically thick accretion disk, the photon capture radius would appear to a distant observer as a thin emission ring inside a lensed image of the accretion disk. For accreting black holes embedded in a geometrically thick, optically thin emission region, as in LLAGNs, the combination of an event horizon and light bending leads to the appearance of a dark "shadow" together with a bright emission ring that should be detectable through very long baseline interferometery (VLBI) experiments (Falcke et al. 2000a). Its shape can appear as a "crescent" because of fast rotation and relativistic beaming (Falcke et al. 2000b; Bromley et al. 2001; Noble et al. 2007; Broderick & Loeb 2009; Kamruddin & Dexter 2013; Lu et al. 2014).

The observed projected diameter of the emission ring, which contains radiation primarily from the gravitationally lensed photon ring, is proportional to R_c and hence to the mass of the black hole, but also depends nontrivially on a number of factors: the observing resolution, the spin vector of the black hole and its inclination, as well as the size and structure of the emitting region. These factors are typically of order unity and can be calibrated using theoretical models.

Modern general-relativistic simulations of accretion flows and radiative transfer produce realistic images of black hole shadows and crescents for a wide range of near-horizon emission models (Broderick & Loeb 2006; Mościbrodzka et al. 2009; Dexter et al. 2012; Dibi et al. 2012; Chan et al. 2015; Mościbrodzka et al. 2016; Porth et al. 2017; Chael et al. 2018a; Ryan et al. 2018; Davelaar et al. 2019). These images can be used to test basic properties of black holes as predicted in GR (Johannsen & Psaltis 2010; Broderick et al. 2014; Psaltis et al. 2015), or in alternative theories of gravity (Grenzebach et al. 2014; Younsi et al. 2016; Mizuno et al. 2018). They can also be used to test alternatives to black holes (Bambi & Freese 2009; Vincent et al. 2016; Olivares et al. 2019).

VLBI at an observing wavelength of 1.3 mm (230 GHz) with Earth-diameter-scale baselines is required to resolve the shadows of the core of M87 (M87* hereafter) and of the Galactic center of Sagittarius A* (Sgr A*, Balick & Brown 1974), the two supermassive black holes with the largest apparent angular sizes (Johannsen et al. 2012). At 1.3 mm and shorter wavelengths, Earth-diameter VLBI baselines achieve an angular resolution sufficient to resolve the shadow of both sources, while the spectra of both sources become optically thin, thus revealing the structure of the innermost emission region. Early pathfinder experiments (Padin et al. 1990; Krichbaum et al. 1998) demonstrated the feasibility of VLBI techniques at $\sim$1.3 mm wavelengths. Over the following decade, a program to improve sensitivity of 1.3 mm-VLBI through development of broadband instrumentation led to the detection of event-horizon-scale structures in both Sgr A* and M87* (Doeleman et al. 2008, 2012). Building on these observations, the Event Horizon Telescope (EHT) collaboration was established to assemble a global VLBI array operating at a wavelength of 1.3 mm with the required angular resolution, sensitivity, and baseline coverage to image the shadows in M87* and Sgr A*.

In this paper, we present and discuss the first event-horizon-scale images of the supermassive black hole candidate M87* from an EHT VLBI campaign conducted in 2017 April at a wavelength of 1.3 mm. The accompanying papers give a more extensive description of the instrument (EHT Collaboration et al. 2019a, Paper II), data reduction (EHT Collaoration et al. 2019b, hereafter Paper III), imaging of the M87 shadow (EHT Collaboration et al. 2019c, hereafter Paper IV), theoretical models (EHT Collaboration et al. 2019d, hereafter Paper V), and the black hole mass estimate (EHT Collaboration et al. 2019e, hereafter Paper VI).

2. The Radio Core in M87

In Curtis (1918), Heber Curtis detected a linear feature in M87, later called a "jet" by Baade & Minkowski (1954). The jet is seen as a bright radio source, Virgo A or 3C 274 (Bolton et al. 1949; Kassim et al. 1993; Owen et al. 2000), which extends out to 65 kpc with an age estimated at about 40 Myr and a kinetic power of about 10^{42} to 10^{45} erg s^{-1} (de Gasperin et al. 2012; Broderick et al. 2015). It is also well studied in the optical (Biretta et al. 1999; Perlman et al. 2011), X-ray (Marshall et al. 2002), and gamma-ray bands (Abramowski et al. 2012). The upstream end of the jet is marked by a compact radio source (Cohen et al. 1969). Such compact radio sources are ubiquitous in LLAGNs (Wrobel & Heeschen 1984; Nagar et al. 2005) and are believed to be signatures of supermassive black holes.

The radio structures of the large-scale jet (Owen et al. 1989; de Gasperin et al. 2012) and of the core of M87 (Reid et al. 1989; Junor et al. 1999; Hada et al. 2016; Mertens et al. 2016; Kim et al. 2018b; Walker et al. 2018) have been resolved in great detail and at multiple wavelengths. Furthermore, the leveling-off of the "core-shift" effect (Blandford & Königl 1979), where the apparent position of the radio core shifts in the upstream jet direction with decreasing wavelength from increased transparency to synchrotron self-absorption, indicates that at a wavelength of 1.3 mm M87* is coincident with the supermassive black hole (Hada et al. 2011). The envelope of the jet limb maintains a quasi-parabolic shape over a wide range of distances from $\sim 10^5\, r_g$ down to $\sim 20\, r_g$ (Asada & Nakamura 2012; Hada et al. 2013; Nakamura & Asada 2013; Nakamura et al. 2018; Walker et al. 2018).

VLBI observations at 1.3 mm have revealed a diameter of the emission region of $\sim$40 μas, which is comparable to the expected horizon-scale structure (Doeleman et al. 2012; Akiyama et al. 2015). These observations, however, were not able to image the black hole shadow due to limited baseline coverage.

Based on three recent stellar population measurements, we here adopt a distance to M87 of 16.8 $\pm$ 0.8 Mpc (Blakeslee et al. 2009; Bird et al. 2010; Cantiello et al. 2018, see Paper VI). Using this distance and the modeling of surface brightness and stellar velocity dispersion at optical wavelengths (Gebhardt & Thomas 2009; Gebhardt et al. 2011), we infer the mass of M87* to be $M = 6.2^{+1.1}_{-0.6} \times 10^9\, M_\odot$ (see Table 9 in Paper VI). On the other hand, mass measurements modeling the kinematic structure of the gas disk (Harms et al. 1994; Macchetto et al. 1997) yield $M = 3.5^{+0.9}_{-0.3} \times 10^9\, M_\odot$ (Walsh et al. 2013, Paper VI). These two mass estimates, from stellar and gas dynamics, predict a theoretical shadow diameter for a Schwarzschild black hole of $37.6^{+6.2}_{-3.5}$ μas and $21.3^{+5}_{-1.7}$ μas, respectively.

3. The Event Horizon Telescope

The EHT (Paper II) is a VLBI experiment that directly measures "visibilities," or Fourier components, of the radio brightness distribution on the sky. As the Earth rotates, each telescope pair in the network samples many spatial frequencies.

The array has a nominal angular resolution of λ/L, where λ is the observing wavelength and L is the maximum projected baseline length between telescopes in the array (Thompson et al. 2017). In this way, VLBI creates a virtual telescope that spans nearly the full diameter of the Earth.

To measure interferometric visibilities, the widely separated telescopes simultaneously sample and coherently record the radiation field from the source. Synchronization using the Global Positioning System typically achieves temporal alignment of these recordings within tens of nanoseconds. Each station is equipped with a hydrogen maser frequency standard. With the atmospheric conditions during our observations the coherent integration time was typically 10 s (see Figure 2 in Paper II). Use of hydrogen maser frequency standards at all EHT sites ensures coherence across the array over this timescale. After observations, recordings are staged at a central location, aligned in time, and signals from each telescope-pair are cross-correlated.

While VLBI is well established at centimeter and millimeter wavelengths (Boccardi et al. 2017; Thompson et al. 2017) and can be used to study the immediate environments of black holes (Krichbaum et al. 1993; Doeleman et al. 2001), the extension of VLBI to a wavelength of 1.3 mm has required long-term technical developments. Challenges at shorter wavelengths include increased noise in radio receiver electronics, higher atmospheric opacity, increased phase fluctuations caused by atmospheric turbulence, and decreased efficiency and size of radio telescopes in the millimeter and submillimeter observing bands. Started in 2009 (Doeleman et al. 2009a), the EHT began a program to address these challenges by increasing array sensitivity. Development and deployment of broadband VLBI systems (Whitney et al. 2013; Vertatschitsch et al. 2015) led to data recording rates that now exceed those of typical cm-VLBI arrays by more than an order of magnitude. Parallel efforts to support infrastructure upgrades at additional VLBI sites, including the Atacama Large Millimeter/submillimeter Array (ALMA; Matthews et al. 2018; Goddi et al. 2019) and the Atacama Pathfinder Experiment telescope (APEX) in Chile (Wagner et al. 2015), the Large Millimeter Telescope Alfonso Serrano (LMT) in Mexico (Ortiz-León et al. 2016), the IRAM 30 m telescope on Pico Veleta (PV) in Spain (Greve et al. 1995), the Submillimeter Telescope Observatory in Arizona (SMT; Baars et al. 1999), the James Clerk Maxwell Telescope (JCMT) and the Submillimeter Array (SMA) in Hawai'i (Doeleman et al. 2008; Primiani et al. 2016; Young et al. 2016), and the South Pole Telescope (SPT) in Antarctica (Kim et al. 2018a), extended the range of EHT baselines and coverage, and the overall collecting area of the array. These developments increased the sensitivity of the EHT by a factor of ∼30 over early experiments that confirmed horizon-scale structures in M87* and Sgr A* (Doeleman et al. 2008, 2012; Akiyama et al. 2015; Johnson et al. 2015; Fish et al. 2016; Lu et al. 2018).

For the observations at a wavelength of 1.3 mm presented here, the EHT collaboration fielded a global VLBI array of eight stations over six geographical locations. Baseline lengths ranged from 160 m to 10,700 km toward M87*, resulting in an array with a theoretical diffraction-limit resolution of ∼25 μas (see Figures 1 and 2, and Paper II).

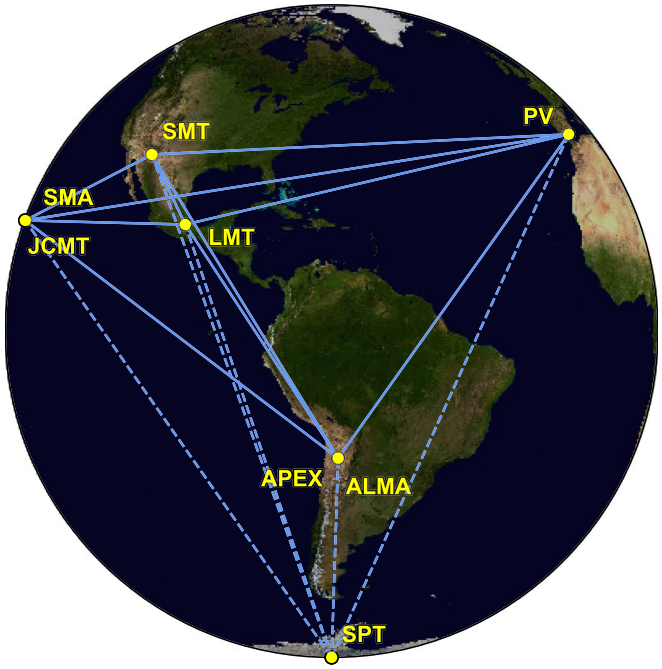

Figure 1. Eight stations of the EHT 2017 campaign over six geographic locations as viewed from the equatorial plane. Solid baselines represent mutual visibility on M87* (+12° declination). The dashed baselines were used for the calibration source 3C279 (see Papers III and IV).

4. Observations, Correlation, and Calibration

We observed M87* on 2017 April 5, 6, 10, and 11 with the EHT. Weather was uniformly good to excellent with nightly median zenith atmospheric opacities at 230 GHz ranging from 0.03 to 0.28 over the different locations. The observations were scheduled as a series of scans of three to seven minutes in duration, with M87* scans interleaved with those on the quasar 3C 279. The number of scans obtained on M87* per night ranged from 7 (April 10) to 25 (April 6) as a result of different observing schedules. A description of the M87* observations, their correlation, calibration, and validated final data products is presented in Paper III and briefly summarized here.

At each station, the astronomical signal in both polarizations and two adjacent 2 GHz wide frequency bands centered at 227.1 and 229.1 GHz were converted to baseband using standard heterodyne techniques, then digitized and recorded at a total rate of 32 Gbps. Correlation of the data was carried out using a software correlator (Deller et al. 2007) at the MIT Haystack Observatory and at the Max-Planck-Institut für Radioastronomie, each handling one of the two frequency bands. Differences between the two independent correlators were shown to be negligible through the exchange of a few identical scans for cross comparison. At correlation, signals were aligned to a common time reference using an a priori Earth geometry and clock model.

A subsequent fringe-fitting step identified detections in correlated signal power while phase calibrating the data for residual delays and atmospheric effects. Using ALMA as a highly sensitive reference station enabled critical corrections for ionospheric and tropospheric distortions at the other sites. Fringe fitting was performed with three independent automated pipelines, each tailored to the specific characteristics of the EHT observations, such as the wide bandwidth, susceptibility to atmospheric turbulence, and array heterogeneity (Blackburn et al. 2019; Janssen et al. 2019, Paper III). The pipelines made use of standard software for the processing of radio-interferometric data

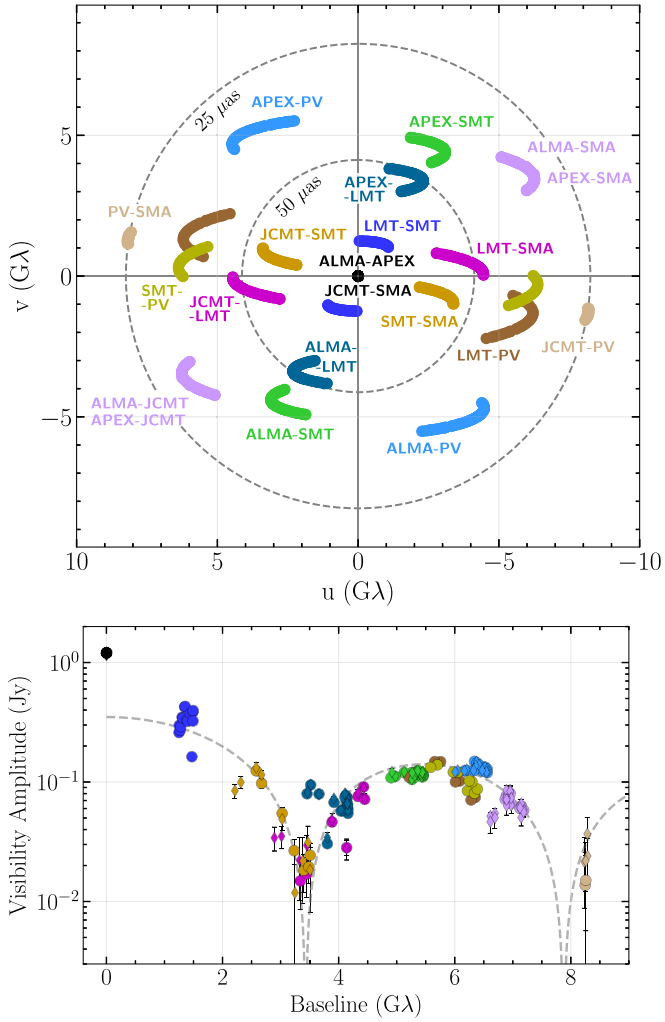

Figure 2. Top: (u, v) coverage for M87*, aggregated over all four days of the observations. (u, v) coordinates for each antenna pair are the source-projected baseline length in units of the observing wavelength λ and are given for conjugate pairs. Baselines to ALMA/APEX and to JCMT/SMA are redundant. Dotted circular lines indicate baseline lengths corresponding to fringe spacings of 50 and 25 μas. Bottom: final calibrated visibility amplitudes of M87* as a function of projected baseline length on April 11. Redundant baselines to APEX and JCMT are plotted as diamonds. Error bars correspond to thermal (statistical) uncertainties. The Fourier transform of an azimuthally symmetric thin ring model with diameter 46 μas is also shown with a dashed line for comparison.

(Greisen 2003; Whitney et al. 2004; McMullin et al. 2007, I. M. van Bemmel et al. 2019, in preparation).

Data from the fringe-fitting pipelines were scaled from correlation coefficients to a uniform physical flux density scale (in Jansky) by using an independent a priori estimate of the sensitivity of each telescope. The accuracies of the derived station sensitivities were estimated to be 5%–10% in amplitude, although certain uncharacterized losses (e.g., from poor pointing or focus) can exceed the error budget. By assuming total flux density values derived from ALMA interferometric data (Goddi et al. 2019) and utilizing array redundancy via network calibration (Paper III), we refined the absolute amplitude calibration of telescopes that are colocated and have redundant baselines, i.e., ALMA/APEX and JCMT/SMA.

The median scan-averaged signal-to-noise ratio for M87* was >10 on non-ALMA baselines and >100 on baselines to ALMA, leading to small statistical errors in visibility amplitude and phase. Comparisons between the three independent pipelines, the two polarizations, and the two frequency bands enabled estimation of systematic baseline errors of around 1° in visibility phase and 2% for visibility amplitudes. These small limiting errors remain after fitting station sensitivities and unknown station phases via self-calibration (Pearson & Readhead 1984) and affect interferometric closure quantities (Rogers et al. 1974; Readhead et al. 1980). Following data validation and pipeline comparisons, a single pipeline output was designated as the primary data set of the first EHT science data release and used for subsequent results, while the outputs of the other two pipelines offer supporting validation data sets.

The final calibrated complex visibilities $V(u, v)$ correspond to the Fourier components of the brightness distribution on the sky at spatial frequency (u, v) determined by the projected baseline expressed in units of the observing wavelength (van Cittert 1934; Thompson et al. 2017). Figure 2 shows the (u, v) coverage and calibrated visibility amplitudes of M87* for April 11. The visibility amplitudes resemble those of a thin ring (i.e., a Bessel function J_0; see Figure 10.12 in Thompson et al. 2017). Such a ring model with diameter 46 μas has a first null at 3.4 Gλ, matching the minimum in observed flux density and is consistent with a reduced flux density on the longest Hawai'i–Spain baseline (JCMT/SMA-PV) near 8 Gλ. This particular ring model, shown with a dashed line in the bottom panel of Figure 2, is only illustrative and does not fit all features in the data. First, visibility amplitudes on the shortest VLBI baselines suggest that about half of the compact flux density seen on the ~2 km ALMA–APEX baseline is resolved out by the interferometer beam (Paper IV). Second, differences in the depth of the first minimum as a function of orientation, as well as highly nonzero measured closure phases, indicate some degree of asymmetry in the source (Papers III, VI). Finally, the visibility amplitudes represent only half of the information available to us. We will next explore images and more complex geometrical models that can fit the measured visibility amplitudes and phases.

5. Images and Features

We reconstructed images from the calibrated EHT visibilities, which provide results that are independent of models (Paper IV). However, there are two major challenges in reconstructing images from EHT data. First, EHT baselines sample a limited range of spatial frequencies, corresponding to angular scales between 25 and 160 μas. Because the (u, v) plane is only sparsely sampled (Figure 2), the inverse problem is under-constrained. Second, the measured visibilities lack absolute phase calibration and can have large amplitude calibration uncertainties.

To address these challenges, imaging algorithms incorporate additional assumptions and constraints that are designed to produce images that are physically plausible (e.g., positive and compact) or conservative (e.g., smooth), while remaining consistent with the data. We explored two classes of algorithms for reconstructing images from EHT data. The first class of algorithms is the traditional CLEAN approach used in radio interferometry (e.g., Högbom 1974; Clark 1980). CLEAN is an inverse-modeling approach that deconvolves the interferometer point-spread function from the Fourier-transformed visibilities. When applying CLEAN, it is necessary to iteratively self-calibrate the data between rounds of imaging to solve for time-variable phase and amplitude errors in the data. The second class of algorithms is the so-called regularized

maximum likelihood (RML; e.g., Narayan & Nityananda 1986; Wiaux et al. 2009; Thiébaut 2013). RML is a forward-modeling approach that searches for an image that is not only consistent with the observed data but also favors specified image properties (e.g., smoothness or compactness). As with CLEAN, RML methods typically iterate between imaging and self-calibration, although they can also be used to image directly on robust closure quantities immune to station-based calibration errors. RML methods have been extensively developed for the EHT (e.g., Honma et al. 2014; Bouman et al. 2016; Akiyama et al. 2017; Chael et al. 2018b; see also Paper IV).

Every imaging algorithm has a variety of free parameters that can significantly affect the final image. We adopted a two-stage imaging approach to control and evaluate biases in the reconstructions from our choices of these parameters. In the first stage, four teams worked independently to reconstruct the first EHT images of M87* using an early engineering data release. The teams worked without interaction to minimize shared bias, yet each produced an image with a similar prominent feature: a ring of diameter ∼38–44 μas with enhanced brightness to the south (see Figure 4 in Paper IV).

In the second imaging stage, we developed three imaging pipelines, each using a different software package and associated methodology. Each pipeline surveyed a range of imaging parameters, producing between $\sim 10^3$ and 10^4 images from different parameter combinations. We determined a "Top-Set" of parameter combinations that both produced images of M87* that were consistent with the observed data and that reconstructed accurate images from synthetic data sets corresponding to four known geometric models (ring, crescent, filled disk, and asymmetric double source). For all pipelines, the Top-Set images showed an asymmetric ring with a diameter of ∼40 μas, with differences arising primarily in the effective angular resolutions achieved by different methods.

For each pipeline, we determined the single combination of fiducial imaging parameters out of the Top-Set that performed best across all the synthetic data sets and for each associated imaging methodology (see Figure 11 in Paper IV). Because the angular resolutions of the reconstructed images vary among the pipelines, we blurred each image with a circular Gaussian to a common, conservative angular resolution of 20 μas. The top part of Figure 3 shows an image of M87* on April 11 obtained by averaging the three pipelines' blurred fiducial images. The image is dominated by a ring with an asymmetric azimuthal profile that is oriented at a position angle ∼170° east of north. Although the measured position angle increases by ∼20° between the first two days and the last two days, the image features are broadly consistent across the different imaging methods and across all four observing days. This is shown in the bottom part of Figure 3, which reports the images on different days (see also Figure 15 in Paper IV). These results are also consistent with those obtained from visibility-domain fitting of geometric and general-relativistic magnetohydrodynamics (GRMHD) models (Paper VI).

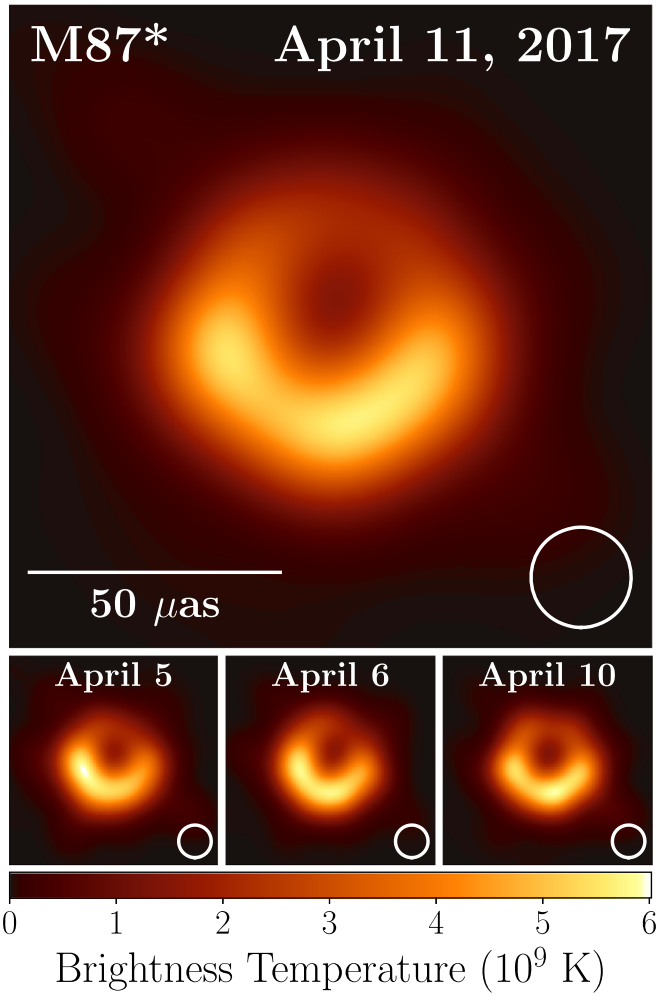

Figure 3. Top: EHT image of M87* from observations on 2017 April 11 as a representative example of the images collected in the 2017 campaign. The image is the average of three different imaging methods after convolving each with a circular Gaussian kernel to give matched resolutions. The largest of the three kernels (20 μas FWHM) is shown in the lower right. The image is shown in units of brightness temperature, $T_b = S\lambda^2/2k_B\Omega$, where S is the flux density, λ is the observing wavelength, k_B is the Boltzmann constant, and Ω is the solid angle of the resolution element. Bottom: similar images taken over different days showing the stability of the basic image structure and the equivalence among different days. North is up and east is to the left.

6. Theoretical Modeling

The appearance of M87* has been modeled successfully using GRMHD simulations, which describe a turbulent, hot, magnetized disk orbiting a Kerr black hole. They naturally produce a powerful jet and can explain the broadband spectral energy distribution observed in LLAGNs. At a wavelength of 1.3 mm, and as observed here, the simulations also predict a shadow and an asymmetric emission ring. The latter does not necessarily coincide with the innermost stable circular orbit, or ISCO, and is instead related to the lensed photon ring. To explore this scenario in great detail, we have built a library of synthetic images (Image Library) describing magnetized accretion flows onto black holes in GR[145] (Paper V). The images themselves are produced from a library of simulations (Simulation Library) collecting the results of four codes solving the equations of GRMHD (Gammie et al. 2003; Sądowski et al. 2014; Porth et al. 2017; Liska et al. 2018). The elements of the Simulation Library have been coupled to three different general-relativistic ray-tracing and radiative-transfer codes (GRRT, Bronzwaer et al. 2018; Mościbrodzka & Gammie 2018; Z. Younsi et al. 2019, in preparation). We limit ourselves to providing here a brief description of the initial setups and the physical scenarios explored in the simulations; see Paper V for details on both the GRMHD and GRRT codes, which have been cross-validated

[145] More exotic spacetimes, such as dilaton black holes, boson stars, and gravastars, have also been considered (Paper V).

for accuracy and consistency (Gold et al. 2019; Porth et al. 2019).

A typical GRMHD simulation in the library is characterized by two parameters: the dimensionless spin $a_* \equiv Jc/GM^2$, where J and M are, respectively, the spin angular momentum and mass of the black hole, and the net dimensionless magnetic flux over the event horizon $\phi \equiv \Phi/(\dot{M}R_g^2)^{1/2}$, where Φ and $\dot{M}$ are the magnetic flux and mass flux (or accretion rate) across the horizon, respectively. Since the GRMHD simulations scale with the black hole mass, M is set only at the time of producing the synthetic images with the GRRT codes. The magnetic flux is generally nonzero because magnetic field is trapped in the black hole by the accretion flow and sustained by currents in the surrounding plasma.

These two parameters allow us to describe accretion disks that are either prograde ($a_* \geqslant 0$) or retrograde ($a_* < 0$) with respect to the black hole spin axis, and whose accretion flows are either "SANE" (from "Standard and Normal Evolution," Narayan et al. 2012) with $\phi \sim 1$, or "MAD" (from "Magnetically Arrested Disk," Narayan et al. 2003) with $\phi \sim 15$.[146] In essence, SANE accretion flows are characterized by moderate dimensionless magnetic flux and result from initial magnetic fields that are smaller than those in MAD flows. Furthermore, the opening angles of the magnetic funnel in SANE flows are generically smaller than those in MAD flows. Varying a_* and ϕ, we have performed 43 high-resolution, three-dimensional and long-term simulations covering well the physical properties of magnetized accretion flows onto Kerr black holes.

All GRMHD simulations were initialized with a weakly magnetized torus orbiting around the black hole and driven into a turbulent state by instabilities, including the magnetorotational instability (Balbus & Hawley 1991), rapidly reaching a quasi-stationary state. Once a simulation was completed, the relevant flow properties at different times are collected to be employed for the further post-processing of the GRRT codes. The generation of synthetic images requires, besides the properties of the fluid (magnetic field, velocity field, and rest-mass density), also the emission and absorption coefficients, the inclination i (the angle between the accretion-flow angular-momentum vector and the line of sight), the position angle PA (the angle east of north, i.e., counter-clockwise on our images, of the projection on the sky of the accretion-flow angular momentum), the black hole mass M and distance D to the observer.

Because the photons at 1.3 mm wavelength observed by the EHT are believed to be produced by synchrotron emission, whose absorption and emission coefficients depend on the electron distribution function, we consider the plasma to be composed of electrons and ions that have the same temperature in the magnetically dominated regions of the flow (funnel), but have a substantially different temperature in the gas dominated regions (disk midplane). In particular, we consider the plasma to be composed of nonrelativistic ions with temperature T_i and relativistic electrons with temperature T_e. A simple prescription for the ratio of the temperatures of the two species can then be imposed in terms of a single parameter (Mościbrodzka et al. 2016), such that the bulk of the emission comes either from weakly magnetized (small $R_{\rm high}$, $Te \simeq Ti/R_{\rm high}$) or strongly magnetized (large $R_{\rm high}$, $Te \simeq Ti$) regions. In SANE models, the disk (jet) is weakly (strongly) magnetized, so that low (high) $R_{\rm high}$ models produce most of the emission in the disk (jet). In MAD models, there are strongly magnetized regions everywhere and the emission is mostly from the disk midplane. While this prescription is not the only one possible, it has the advantage of being simple, sufficiently generic, and robust (see Paper V for a discussion of nonthermal particles and radiative cooling).

Since each GRMHD simulation can be used to describe several different physical scenarios by changing the prescribed electron distribution function, we have used the Simulation Library to generate more than 420 different physical scenarios. Each scenario is then used to generate hundreds of snapshots at different times in the simulation leading to more than 62,000 objects in the Image Library. From the images we have created model visibilities that correspond to the EHT observing schedule and compared them to the measured VLBI visibilities as detailed in Paper VI.

As an example, the top row of Figure 4 shows three GRMHD model snapshots from the Image Library with different spins and flow type, which fitted closure phases and amplitudes of the April 11 data best. For these models we produced simulated visibilities for the April 11 schedule and weather parameters and calibrated them with a synthetic data generation and calibration pipeline (Blecher et al. 2017; Janssen et al. 2019; Roelofs et al. 2019a). The simulated data were then imaged with the same pipeline used for the observed images. The similarities between the simulated images (bottom row of Figure 4) and the observed images (Figure 3) are remarkable.

Overall, when combining all the information contained in both the Simulation Library and Image Library, the physical origin of the emission features of the image observed in M87* can be summarized as follows.

First, the observed image is consistent with the hypothesis that it is produced by a magnetized accretion flow orbiting within a few r_g of the event horizon of a Kerr black hole. The asymmetric ring is produced by a combination of strong gravitational lensing and relativistic beaming, while the central flux depression is the observational signature of the black hole shadow. Interestingly, all of the accretion models are consistent with the EHT image, except for the $a_* = -0.94$ MAD models, which fail to produce images that are sufficiently stable (i.e., the variance among snapshots is too large to be statistically consistent with the observed image).

Second, the north–south asymmetry in the emission ring is controlled by the black hole spin and can be used to deduce its orientation. In corotating disk models (where the angular momentum of the matter and of the black hole are aligned), the funnel wall, or jet sheath, rotates with the disk and the black hole; in counterrotating disk models, instead, the luminous funnel wall rotates with the black hole but against the disk. The north–south asymmetry is consistent with models in which the black hole spin is pointing away from Earth and inconsistent with models in which the spin points toward Earth.

Third, adopting an inclination of 17° between the approaching jet and the line of sight (Walker et al. 2018), the west orientation of the jet, and a corotating disk model, matter in the bottom part of the image is moving toward the observer (clockwise rotation as seen from Earth). This is consistent with the rotation of the ionized gas on scales of 20 pc, i.e., 7000 r_g (Ford et al. 1994; Walsh et al. 2013) and with the inferred sense of rotation from VLBI observations at 7 mm (Walker et al. 2018).

Finally, models with $a_* = 0$ are disfavored by the very conservative observational requirement that the jet power be $P_{\rm jet} > 10^{42}\,{\rm erg\,s^{-1}}$. Furthermore, in those models that produce a sufficiently powerful jet, it is powered by extraction of black hole

[146] We here use Heaviside units, where a factor of $\sqrt{4\pi}$ is absorbed into the definition of the magnetic field.

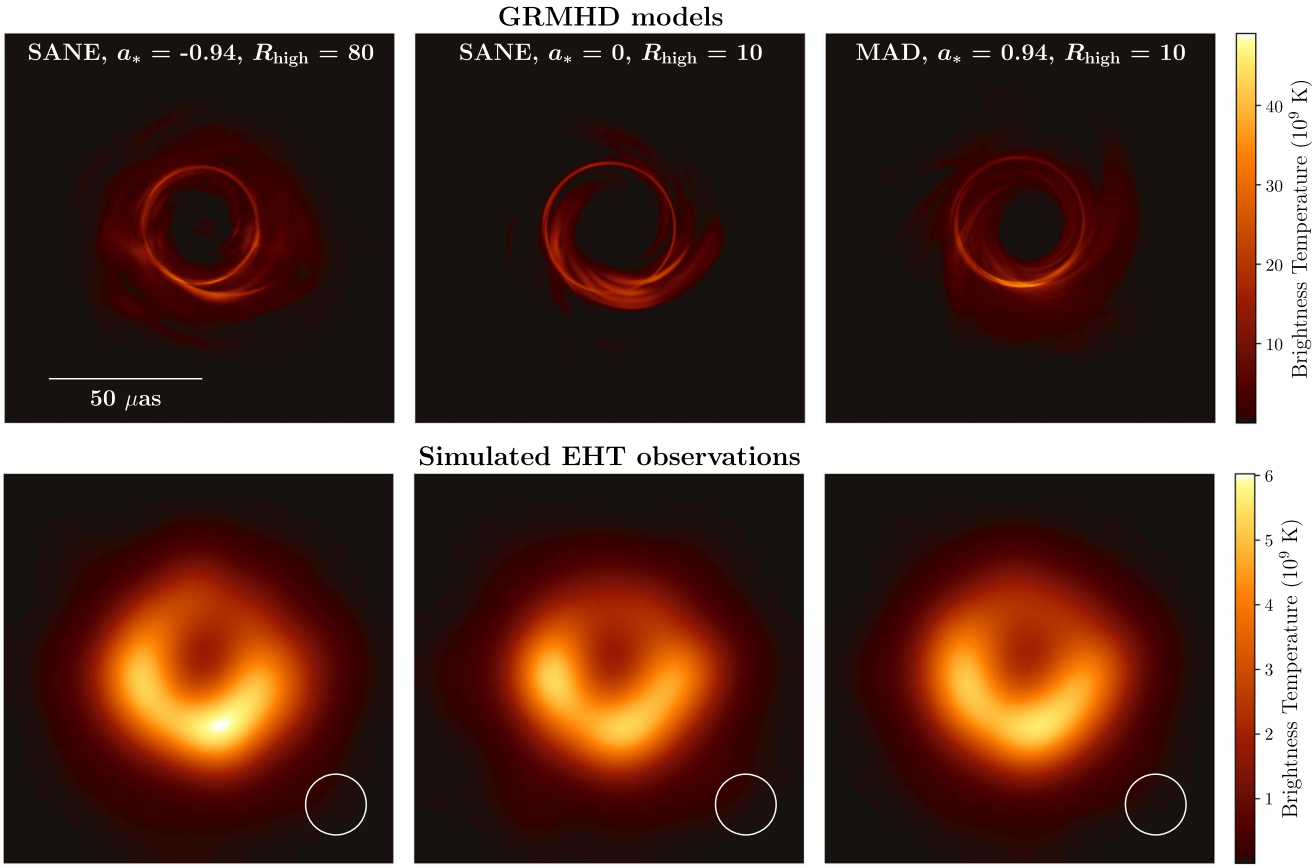

Figure 4. Top: three example models of some of the best-fitting snapshots from the image library of GRMHD simulations for April 11 corresponding to different spin parameters and accretion flows. Bottom: the same theoretical models, processed through a VLBI simulation pipeline with the same schedule, telescope characteristics, and weather parameters as in the April 11 run and imaged in the same way as Figure 3. Note that although the fit to the observations is equally good in the three cases, they refer to radically different physical scenarios; this highlights that a single good fit does not imply that a model is preferred over others (see Paper V).

spin energy through mechanisms akin to the Blandford–Znajek process.

7. Model Comparison and Parameter Estimation

In Paper VI, the black hole mass is derived from fitting to the visibility data of geometric and GRMHD models, as well as from measurements of the ring diameter in the image domain. Our measurements remain consistent across methodologies, algorithms, data representations, and observed data sets.

Motivated by the asymmetric emission ring structures seen in the reconstructed images (Section 5) and the similar emission structures seen in the images from GRMHD simulations (Section 6), we developed a family of geometric crescent models (see, e.g., Kamruddin & Dexter 2013) to compare directly to the visibility data. We used two distinct Bayesian-inference algorithms and demonstrate that such crescent models are statistically preferred over other comparably complex geometric models that we have explored. We find that the crescent models provide fits to the data that are statistically comparable to those of the reconstructed images presented in Section 5, allowing us to determine the basic parameters of the crescents. The best-fit models for the asymmetric emission ring have diameters of $43 \pm 0.9\,\mu$as and fractional widths relative to the diameter of <0.5. The emission drops sharply interior to the asymmetric emission ring with the central depression having a brightness $<10\%$ of the average brightness in the ring.

The diameters of the geometric crescent models measure the characteristic sizes of the emitting regions that surround the shadows and not the sizes of the shadows themselves (see, e.g., Psaltis et al. 2015; Johannsen et al. 2016; Kuramochi et al. 2018, for potential biases).

We model the crescent angular diameter d in terms of the gravitational radius and distance, $\theta_{\rm g} \equiv GM/c^2D$, as $d = \alpha\theta_{\rm g}$, where α is a function of spin, inclination, and $R_{\rm high}$ ($\alpha \simeq 9.6$–10.4 corresponds to emission from the lensed photon ring only). We calibrate α by fitting the geometric crescent models to a large number of visibility data generated from the Image Library. We can also fit the model visibilities generated from the Image Library to the M87* data, which allows us to measure $\theta_{\rm g}$ directly. However, such a procedure is complicated by the stochastic nature of the emission in the accretion flow (see, e.g., Kim et al. 2016). To account for this turbulent structure, we developed a formalism and multiple algorithms that estimate the statistics of the stochastic components using ensembles of images from individual GRMHD simulations. We find that the visibility data are not inconsistent with being a realization of many of the GRMHD simulations. We conclude that the recovered model parameters are consistent across algorithms.

Finally, we extract ring diameter, width, and shape directly from reconstructed images (see Section 5). The results are consistent with the parameter estimates from geometric crescent models. Following the same GRMHD calibration

Table 1
Parameters of M87*

Parameter	Estimate
Ring diameter [a] d	$42 \pm 3\ \mu$as
Ring width [a]	$<20\ \mu$as
Crescent contrast [b]	>10:1
Axial ratio [a]	<4:3
Orientation PA	150°–200° east of north
$\theta_g = GM/Dc^2$ [c]	$3.8 \pm 0.4\ \mu$as
$\alpha = d/\theta_g$ [d]	$11^{+0.5}_{-0.3}$
M [c]	$(6.5 \pm 0.7) \times 10^9\ M_\odot$
Parameter	**Prior Estimate**
D [e]	(16.8 ± 0.8) Mpc
M(stars) [e]	$6.2^{+1.1}_{-0.6} \times 10^9\ M_\odot$
M(gas) [e]	$3.5^{+0.9}_{-0.3} \times 10^9\ M_\odot$

Notes.
[a] Derived from the image domain.
[b] Derived from crescent model fitting.
[c] The mass and systematic errors are averages of the three methods (geometric models, GRMHD models, and image domain ring extraction).
[d] The exact value depends on the method used to extract d, which is reflected in the range given.
[e] Rederived from likelihood distributions (Paper VI).

procedure, we infer values of θ_g and α for regularized maximum likelihood and CLEAN reconstructed images.

Combining results from all methods, we measure emission region diameters of $42 \pm 3\ \mu$as, angular sizes of the gravitational radius $\theta_g = 3.8 \pm 0.4\ \mu$as, and scaling factors in the range $\alpha = 10.7$–11.5, with associated errors of $\sim$10%. For the distance of 16.8 ± 0.8 Mpc adopted here, the black hole mass is $M = (6.5 \pm 0.7) \times 10^9\ M_\odot$; the systematic error refers to the 68% confidence level and is much larger than the statistical error of $0.2 \times 10^9\ M_\odot$. Moreover, by tracing the peak of the emission in the ring we can determine the shape of the image and obtain a ratio between major and minor axis of the ring that is $\lesssim$4:3; this corresponds to a $\lesssim$10% deviation from circularity in terms of root-mean-square distance from an average radius.

Table 1 summarizes the measured parameters of the image features and the inferred black hole properties based on data from all bands and all days combined. The inferred black hole mass strongly favors the measurement based on stellar dynamics (Gebhardt et al. 2011). The size, asymmetry, brightness contrast, and circularity of the reconstructed images and geometric models, as well as the success of the GRMHD simulations in describing the interferometric data, are consistent with the EHT images of M87* being associated with strongly lensed emission from the vicinity of a Kerr black hole.

8. Discussion

A number of elements reinforce the robustness of our image and the conclusion that it is consistent with the shadow of a black hole as predicted by GR. First, our analysis has used multiple independent calibration and imaging techniques, as well as four independent data sets taken on four different days in two separate frequency bands. Second, the image structure matches previous predictions well (Dexter et al. 2012; Mościbrodzka et al. 2016) and is well reproduced by our extensive modeling effort presented in Section 6. Third, because our measurement of the black hole mass in M87* is not inconsistent with all of the prior mass measurements, this allows us to conclude that the null hypothesis of the Kerr metric (Psaltis et al. 2015; Johannsen et al. 2016), namely, the assumption that the black hole is described by the Kerr metric, has not been violated. Fourth, the observed emission ring reconstructed in our images is close to circular with an axial ratio $\lesssim$4:3; similarly, the time average images from our GRMHD simulations also show a circular shape. After associating to the shape of the shadow a deviation from the circularity—measured in terms of root-mean-square distance from an average radius in the image—that is $\lesssim$10%, we can set an initial limit of order four on relative deviations of the quadrupole moment from the Kerr value (Johannsen & Psaltis 2010). Stated differently, if Q is the quadrupole moment of a Kerr black hole and ΔQ the deviation as deduced from circularity, our measurement—and the fact that the inclination angle is assumed to be small—implies that $\Delta Q/Q \lesssim 4$ ($\Delta Q/Q = \varepsilon$ in Johannsen & Psaltis 2010).

Finally, when comparing the visibility amplitudes of M87* with 2009 and 2012 data (Doeleman et al. 2012; Akiyama et al. 2015), the overall radio core size at a wavelength of 1.3 mm has not changed appreciably, despite variability in total flux density. This stability is consistent with the expectation that the size of the shadow is a feature tied to the mass of the black hole and not to properties of a variable plasma flow.

It is also straightforward to reject some alternative astrophysical interpretations. For instance, the image is unlikely to be produced by a jet-feature as multi-epoch VLBI observations of the plasma jet in M87 (Walker et al. 2018) on scales outside the horizon do not show circular rings. The same is typically true for AGN jets in large VLBI surveys (Lister et al. 2018). Similarly, were the apparent ring a random alignment of emission blobs, they should also have moved away at relativistic speeds, i.e., at $\sim 5\ \mu$as day^{-1} (Kim et al. 2018b), leading to measurable structural changes and sizes. GRMHD models of hollow jet cones could show under extreme conditions stable ring features (Pu et al. 2017), but this effect is included to a certain extent in our Simulation Library for models with $R_{\rm high} > 10$. Finally, an Einstein ring formed by gravitational lensing of a bright region in the counter-jet would require a fine-tuned alignment and a size larger than that measured in 2012 and 2009.

At the same time, it is more difficult to rule out alternatives to black holes in GR, because a shadow can be produced by any compact object with a spacetime characterized by unstable circular photon orbits (Mizuno et al. 2018). Indeed, while the Kerr metric remains a solution in some alternative theories of gravity (Barausse & Sotiriou 2008; Psaltis et al. 2008), non-Kerr black hole solutions do exist in a variety of such modified theories (Berti et al. 2015). Furthermore, exotic alternatives to black holes, such as naked singularities (Shaikh et al. 2019), boson stars (Kaup 1968; Liebling & Palenzuela 2012), and gravastars (Mazur & Mottola 2004; Chirenti & Rezzolla 2007), are admissible solutions within GR and provide concrete, albeit contrived, models. Some of such exotic compact objects can already be shown to be incompatible with our observations given our maximum mass prior. For example, the shadows of naked singularities associated with Kerr spacetimes with $|a_*| > 1$ are substantially smaller and very asymmetric compared to those of Kerr black holes (Bambi & Freese 2009). Also, some commonly used types of wormholes (Bambi 2013) predict much smaller shadows than we have measured.

However, other compact-object candidates need to be analyzed with more care. Boson stars are an example of compact objects having circular photon orbits but without a surface or an event horizon. In such a spacetime, null geodesics are redirected outwards toward distant observers (Cunha et al. 2016), so that the shadow can in principle be filled with emission from lensed images of distant radio sources generating a complex mirror image of the sky. More importantly, accretion flows onto boson stars behave differently as they do not produce jets but stalled accretion tori that make them distinguishable from black holes (Olivares et al. 2019). Gravastars provide examples of compact objects having unstable photon orbits and a hard surface, but not an event horizon. In this case, while a single image of the accretion flow could in principle be very similar to that coming from a black hole, differences of the flow dynamics at the stellar surface (H. Olivares et al. 2019, in preparation), strong magnetic fields (Lobanov 2017), or excess radiation in the infrared (Broderick & Narayan 2006) would allow one to distinguish a gravastar from a black hole.

Altogether, the results derived here provide a new way to study compact-object spacetimes and are complementary to the detection of gravitational waves from coalescing stellar-mass black holes with LIGO/Virgo (Abbott et al. 2016). Our constraints on deviations from the Kerr geometry rely only on the validity of the equivalence principle and are agnostic about the underlying theory of gravity, but can be used to measure, with ever improved precision, the parameters of the background metric. On the other hand, current gravitational-wave observations of mergers probe the dynamics of the underlying theory, but cannot rely on the possibility of multiple and repeated measurements of the same source.

To underline the complementarity of gravitational-wave and electromagnetic observations of black holes, we note that a basic feature of black holes in GR is that their size scales linearly with mass. Combining our constraints on the supermassive black hole in M87 with those on the stellar-mass black holes detected via gravitational waves we can infer that this property holds over eight orders of magnitude. While this invariance is a basic prediction of GR, which is a scale-free theory, it need not be satisfied in other theories that introduce a scale to the gravitational field.

Finally, the radio core in M87 is quite typical for powerful radio jets in general. It falls on the fundamental plane of black hole activity for radio cores (Falcke et al. 2004), connecting via simple scaling laws the radio and X-ray properties of low-luminosity black hole candidates across vastly different mass and accretion rate scales. This suggests that they are powered by a scale-invariant common object. Therefore, establishing the black hole nature for M87* also supports the general paradigm that black holes are the power source for active galaxies.

9. Conclusion and Outlook

We have assembled the EHT, a global VLBI array operating at a wavelength of 1.3 mm and imaged horizon-scale structures around the supermassive black hole candidate in M87. Using multiple independent calibration, imaging, and analysis methods, we find the image to be dominated by a ring structure of $42 \pm 3\ \mu$as diameter that is brighter in the south. This structure has a central brightness depression with a contrast of >10:1, which we identify with the black hole shadow. Comparing the data with an extensive library of synthetic images obtained from GRMHD simulations covering different physical scenarios and plasma conditions reveals that the basic features of our image are relatively independent of the detailed astrophysical model. This allows us to derive an estimate for the black hole mass of $M = (6.5 \pm 0.7) \times 10^9 M_\odot$. Based on our modeling and information on the inclination angle, we derive the sense of rotation of the black hole to be in the clockwise direction, i.e., the spin of the black hole points away from us. The brightness excess in the south part of the emission ring is explained as relativistic beaming of material rotating in the clockwise direction as seen by the observer, i.e., the bottom part of the emission region is moving toward the observer.

Future observations and further analysis will test the stability, shape, and depth of the shadow more accurately. One of its key features is that it should remain largely constant with time as the mass of M87* is not expected to change measurably on human timescales. Polarimetric analysis of the images, which we will report in the future, will provide information on the accretion rate via Faraday rotation (Bower et al. 2003; Marrone et al. 2007; Kuo et al. 2014; Mościbrodzka et al. 2017) and on the magnetic flux. Higher-resolution images can be achieved by going to a shorter wavelength, i.e., 0.8 mm (345 GHz), by adding more telescopes and, in a more distant future, with space-based interferometry (Kardashev et al. 2014; Fish et al. 2019; Palumbo et al. 2019; F. Roelofs et al. 2019b, in preparation).

Another primary EHT source, Sgr A*, has a precisely measured mass three orders of magnitude smaller than that of M87*, with dynamical timescales of minutes instead of days. Observing the shadow of Sgr A* will require accounting for this variability and mitigation of scattering effects caused by the interstellar medium (Johnson 2016; Lu et al. 2016; Bouman et al. 2018). Time dependent nonimaging analysis can be used to potentially track the motion of emitting matter near the black hole, as reported recently through interferometric observations in the near-infrared (Gravity Collaboration et al. 2018b). Such observations provide separate tests and probes of GR on yet another mass scale (Broderick & Loeb 2005; Doeleman et al. 2009b; Roelofs et al. 2017; Medeiros et al. 2017).

In conclusion, we have shown that direct studies of the event horizon shadow of supermassive black hole candidates are now possible via electromagnetic waves, thus transforming this elusive boundary from a mathematical concept to a physical entity that can be studied and tested via repeated astronomical observations.

The authors of this Letter thank the following organizations and programs: the Academy of Finland (projects 274477, 284495, 312496); the Advanced European Network of E-infrastructures for Astronomy with the SKA (AENEAS) project, supported by the European Commission Framework Programme Horizon 2020 Research and Innovation action under grant agreement 731016; the Alexander von Humboldt Stiftung; the Black Hole Initiative at Harvard University, through a grant (60477) from the John Templeton Foundation; the China Scholarship Council; Comisión Nacional de Investigación Científica y Tecnológica (CONICYT, Chile, via PIA ACT172033, Fondecyt 1171506, BASAL AFB-170002, ALMA-conicyt 31140007); Consejo Nacional de Ciencia y Tecnología (CONACYT, Mexico, projects 104497, 275201, 279006, 281692); the Delaney Family via the Delaney Family John A. Wheeler Chair at Perimeter Institute; Dirección General de Asuntos del Personal Académico-Universidad Nacional

Autónoma de México (DGAPA-UNAM, project IN112417); the European Research Council (ERC) Synergy Grant "Black-HoleCam: Imaging the Event Horizon of Black Holes" (grant 610058); the Generalitat Valenciana postdoctoral grant APOSTD/2018/177; the Gordon and Betty Moore Foundation (grants GBMF-3561, GBMF-5278); the Istituto Nazionale di Fisica Nucleare (INFN) sezione di Napoli, iniziative specifiche TEONGRAV; the International Max Planck Research School for Astronomy and Astrophysics at the Universities of Bonn and Cologne; the Jansky Fellowship program of the National Radio Astronomy Observatory (NRAO); the Japanese Government (Monbukagakusho: MEXT) Scholarship; the Japan Society for the Promotion of Science (JSPS) Grant-in-Aid for JSPS Research Fellowship (JP17J08829); JSPS Overseas Research Fellowships; the Key Research Program of Frontier Sciences, Chinese Academy of Sciences (CAS, grants QYZDJ-SSW-SLH057, QYZDJ-SSW-SYS008); the Leverhulme Trust Early Career Research Fellowship; the Max-Planck-Gesellschaft (MPG); the Max Planck Partner Group of the MPG and the CAS; the MEXT/JSPS KAKENHI (grants 18KK0090, JP18K13594, JP18K03656, JP18H03721, 18K03709, 18H01245, 25120007); the MIT International Science and Technology Initiatives (MISTI) Funds; the Ministry of Science and Technology (MOST) of Taiwan (105-2112-M-001-025-MY3, 106-2112-M-001-011, 106-2119-M-001-027, 107-2119-M-001-017, 107-2119-M-001-020, and 107-2119-M-110-005); the National Aeronautics and Space Administration (NASA, Fermi Guest Investigator grant 80NSSC17K0649); the National Institute of Natural Sciences (NINS) of Japan; the National Key Research and Development Program of China (grant 2016YFA0400704, 2016YFA0400702); the National Science Foundation (NSF, grants AST-0096454, AST-0352953, AST-0521233, AST-0705062, AST-0905844, AST-0922984, AST-1126433, AST-1140030, DGE-1144085, AST-1207704, AST-1207730, AST-1207752, MRI-1228509, OPP-1248097, AST-1310896, AST-1312651, AST-1337663, AST-1440254, AST-1555365, AST-1715061, AST-1615796, AST-1614868, AST-1716327, OISE-1743747, AST-1816420); the Natural Science Foundation of China (grants 11573051, 11633006, 11650110427, 10625314, 11721303, 11725312, 11873028, 11873073, U1531245, 11473010); the Natural Sciences and Engineering Research Council of Canada (NSERC, including a Discovery Grant and the NSERC Alexander Graham Bell Canada Graduate Scholarships-Doctoral Program); the National Youth Thousand Talents Program of China; the National Research Foundation of Korea (grant 2015-R1D1A1A01056807, the Global PhD Fellowship Grant: NRF-2015H1A2A1033752, and the Korea Research Fellowship Program: NRF-2015H1D3A1066561); the Netherlands Organization for Scientific Research (NWO) VICI award (grant 639.043.513) and Spinoza Prize (SPI 78-409); the New Scientific Frontiers with Precision Radio Interferometry Fellowship awarded by the South African Radio Astronomy Observatory (SARAO), which is a facility of the National Research Foundation (NRF), an agency of the Department of Science and Technology (DST) of South Africa; the Onsala Space Observatory (OSO) national infrastructure, for the provisioning of its facilities/observational support (OSO receives funding through the Swedish Research Council under grant 2017-00648); the Perimeter Institute for Theoretical Physics (research at Perimeter Institute is supported by the Government of Canada through the Department of Innovation, Science and Economic Development Canada and by the Province of Ontario through the Ministry of Economic Development, Job Creation and Trade); the Russian Science Foundation (grant 17-12-01029); the Spanish Ministerio de Economía y Competitividad (grants AYA2015-63939-C2-1-P, AYA2016-80889-P); the State Agency for Research of the Spanish MCIU through the "Center of Excellence Severo Ochoa" award for the Instituto de Astrofísica de Andalucía (SEV-2017-0709); the Toray Science Foundation; the US Department of Energy (USDOE) through the Los Alamos National Laboratory (operated by Triad National Security, LLC, for the National Nuclear Security Administration of the USDOE (Contract 89233218CNA000001)); the Italian Ministero dell'Istruzione Università e Ricerca through the grant Progetti Premiali 2012-iALMA (CUP C52I13000140001); the European Union's Horizon 2020 research and innovation programme under grant agreement No 730562 RadioNet; ALMA North America Development Fund; Chandra TM6-17006X.

This work used the Extreme Science and Engineering Discovery Environment (XSEDE), supported by NSF grant ACI-1548562, and CyVerse, supported by NSF grants DBI-0735191, DBI-1265383, and DBI-1743442. XSEDE Stampede2 resource at TACC was allocated through TG-AST170024 and TG-AST080026N. XSEDE JetStream resource at PTI and TACC was allocated through AST170028. The simulations were performed in part on the SuperMUC cluster at the LRZ in Garching, on the LOEWE cluster in CSC in Frankfurt, and on the HazelHen cluster at the HLRS in Stuttgart. This research was enabled in part by support provided by Compute Ontario (http://computeontario.ca), Calcul Quebec (http://www.calculquebec.ca) and Compute Canada (http://www.computecanada.ca).

We thank the staff at the participating observatories, correlation centers, and institutions for their enthusiastic support.

This Letter makes use of the following ALMA data: ADS/JAO.ALMA#2016.1.01154.V. ALMA is a partnership of the European Southern Observatory (ESO; Europe, representing its member states), NSF, and National Institutes of Natural Sciences of Japan, together with National Research Council (Canada), Ministry of Science and Technology (MOST; Taiwan), Academia Sinica Institute of Astronomy and Astrophysics (ASIAA; Taiwan), and Korea Astronomy and Space Science Institute (KASI; Republic of Korea), in cooperation with the Republic of Chile. The Joint ALMA Observatory is operated by ESO, Associated Universities, Inc. (AUI)/NRAO, and the National Astronomical Observatory of Japan (NAOJ). The NRAO is a facility of the NSF operated under cooperative agreement by AUI. APEX is a collaboration between the Max-Planck-Institut für Radioastronomie (Germany), ESO, and the Onsala Space Observatory (Sweden). The SMA is a joint project between the SAO and ASIAA and is funded by the Smithsonian Institution and the Academia Sinica. The JCMT is operated by the East Asian Observatory on behalf of the NAOJ, ASIAA, and KASI, as well as the Ministry of Finance of China, Chinese Academy of Sciences, and the National Key R&D Program (No. 2017YFA0402700) of China. Additional funding support for the JCMT is provided by the Science and Technologies Facility Council (UK) and participating universities in the UK and Canada. The LMT project is a joint effort of the Instituto Nacional de Astrófisica, Óptica, y Electrónica (Mexico) and the University of Massachusetts at Amherst (USA). The IRAM 30-m telescope on Pico Veleta, Spain is operated by IRAM and supported by CNRS (Centre National de la Recherche Scientifique, France), MPG (Max-

Planck-Gesellschaft, Germany) and IGN (Instituto Geográfico Nacional, Spain).

The SMT is operated by the Arizona Radio Observatory, a part of the Steward Observatory of the University of Arizona, with financial support of operations from the State of Arizona and financial support for instrumentation development from the NSF. Partial SPT support is provided by the NSF Physics Frontier Center award (PHY-0114422) to the Kavli Institute of Cosmological Physics at the University of Chicago (USA), the Kavli Foundation, and the GBMF (GBMF-947). The SPT hydrogen maser was provided on loan from the GLT, courtesy of ASIAA. The SPT is supported by the National Science Foundation through grant PLR-1248097. Partial support is also provided by the NSF Physics Frontier Center grant PHY-1125897 to the Kavli Institute of Cosmological Physics at the University of Chicago, the Kavli Foundation and the Gordon and Betty Moore Foundation grant GBMF 947.

The EHTC has received generous donations of FPGA chips from Xilinx Inc., under the Xilinx University Program. The EHTC has benefited from technology shared under open-source license by the Collaboration for Astronomy Signal Processing and Electronics Research (CASPER). The EHT project is grateful to T4Science and Microsemi for their assistance with Hydrogen Masers. This research has made use of NASA's Astrophysics Data System. We gratefully acknowledge the support provided by the extended staff of the ALMA, both from the inception of the ALMA Phasing Project through the observational campaigns of 2017 and 2018. We would like to thank A. Deller and W. Brisken for EHT-specific support with the use of DiFX. We acknowledge the significance that Maunakea, where the SMA and JCMT EHT stations are located, has for the indigenous Hawaiian people.

ORCID iDs

Kazunori Akiyama https://orcid.org/0000-0002-9475-4254
Antxon Alberdi https://orcid.org/0000-0002-9371-1033
Rebecca Azulay https://orcid.org/0000-0002-2200-5393
Anne-Kathrin Baczko https://orcid.org/0000-0003-3090-3975
Mislav Baloković https://orcid.org/0000-0003-0476-6647
John Barrett https://orcid.org/0000-0002-9290-0764
Lindy Blackburn https://orcid.org/0000-0002-9030-642X
Katherine L. Bouman https://orcid.org/0000-0003-0077-4367
Geoffrey C. Bower https://orcid.org/0000-0003-4056-9982
Christiaan D. Brinkerink https://orcid.org/0000-0002-2322-0749
Roger Brissenden https://orcid.org/0000-0002-2556-0894
Silke Britzen https://orcid.org/0000-0001-9240-6734
Avery E. Broderick https://orcid.org/0000-0002-3351-760X
Do-Young Byun https://orcid.org/0000-0003-1157-4109
Andrew Chael https://orcid.org/0000-0003-2966-6220
Chi-kwan Chan https://orcid.org/0000-0001-6337-6126
Shami Chatterjee https://orcid.org/0000-0002-2878-1502
Ilje Cho https://orcid.org/0000-0001-6083-7521
Pierre Christian https://orcid.org/0000-0001-6820-9941
John E. Conway https://orcid.org/0000-0003-2448-9181
Geoffrey B. Crew https://orcid.org/0000-0002-2079-3189
Yuzhu Cui https://orcid.org/0000-0001-6311-4345
Jordy Davelaar https://orcid.org/0000-0002-2685-2434
Mariafelicia De Laurentis https://orcid.org/0000-0002-9945-682X
Roger Deane https://orcid.org/0000-0003-1027-5043
Jessica Dempsey https://orcid.org/0000-0003-1269-9667
Gregory Desvignes https://orcid.org/0000-0003-3922-4055
Jason Dexter https://orcid.org/0000-0003-3903-0373
Sheperd S. Doeleman https://orcid.org/0000-0002-9031-0904
Ralph P. Eatough https://orcid.org/0000-0001-6196-4135
Heino Falcke https://orcid.org/0000-0002-2526-6724
Vincent L. Fish https://orcid.org/0000-0002-7128-9345
Raquel Fraga-Encinas https://orcid.org/0000-0002-5222-1361
José L. Gómez https://orcid.org/0000-0003-4190-7613
Peter Galison https://orcid.org/0000-0002-6429-3872
Charles F. Gammie https://orcid.org/0000-0001-7451-8935
Boris Georgiev https://orcid.org/0000-0002-3586-6424
Roman Gold https://orcid.org/0000-0003-2492-1966
Minfeng Gu (顾敏峰) https://orcid.org/0000-0002-4455-6946
Mark Gurwell https://orcid.org/0000-0003-0685-3621
Kazuhiro Hada https://orcid.org/0000-0001-6906-772X
Ronald Hesper https://orcid.org/0000-0003-1918-6098
Luis C. Ho (何子山) https://orcid.org/0000-0001-6947-5846
Mareki Honma https://orcid.org/0000-0003-4058-9000
Chih-Wei L. Huang https://orcid.org/0000-0001-5641-3953
Shiro Ikeda https://orcid.org/0000-0002-2462-1448
Sara Issaoun https://orcid.org/0000-0002-5297-921X
David J. James https://orcid.org/0000-0001-5160-4486
Michael Janssen https://orcid.org/0000-0001-8685-6544
Britton Jeter https://orcid.org/0000-0003-2847-1712
Wu Jiang (江悟) https://orcid.org/0000-0001-7369-3539
Michael D. Johnson https://orcid.org/0000-0002-4120-3029
Svetlana Jorstad https://orcid.org/0000-0001-6158-1708
Taehyun Jung https://orcid.org/0000-0001-7003-8643
Mansour Karami https://orcid.org/0000-0001-7387-9333
Ramesh Karuppusamy https://orcid.org/0000-0002-5307-2919
Tomohisa Kawashima https://orcid.org/0000-0001-8527-0496
Garrett K. Keating https://orcid.org/0000-0002-3490-146X
Mark Kettenis https://orcid.org/0000-0002-6156-5617
Jae-Young Kim https://orcid.org/0000-0001-8229-7183
Junhan Kim https://orcid.org/0000-0002-4274-9373
Motoki Kino https://orcid.org/0000-0002-2709-7338
Jun Yi Koay https://orcid.org/0000-0002-7029-6658
Patrick M. Koch https://orcid.org/0000-0003-2777-5861
Shoko Koyama https://orcid.org/0000-0002-3723-3372
Michael Kramer https://orcid.org/0000-0002-4175-2271
Carsten Kramer https://orcid.org/0000-0002-4908-4925
Thomas P. Krichbaum https://orcid.org/0000-0002-4892-9586
Tod R. Lauer https://orcid.org/0000-0003-3234-7247
Sang-Sung Lee https://orcid.org/0000-0002-6269-594X
Yan-Rong Li (李彦荣) https://orcid.org/0000-0001-5841-9179
Zhiyuan Li (李志远) https://orcid.org/0000-0003-0355-6437
Michael Lindqvist https://orcid.org/0000-0002-3669-0715
Kuo Liu https://orcid.org/0000-0002-2953-7376
Elisabetta Liuzzo https://orcid.org/0000-0003-0995-5201
Laurent Loinard https://orcid.org/0000-0002-5635-3345
Ru-Sen Lu (路如森) https://orcid.org/0000-0002-7692-7967
Nicholas R. MacDonald https://orcid.org/0000-0002-6684-8691
Jirong Mao (毛基荣) https://orcid.org/0000-0002-7077-7195
Sera Markoff https://orcid.org/0000-0001-9564-0876
Daniel P. Marrone https://orcid.org/0000-0002-2367-1080

Alan P. Marscher https://orcid.org/0000-0001-7396-3332
Iván Martí-Vidal https://orcid.org/0000-0003-3708-9611
Lynn D. Matthews https://orcid.org/0000-0002-3728-8082
Lia Medeiros https://orcid.org/0000-0003-2342-6728
Karl M. Menten https://orcid.org/0000-0001-6459-0669
Yosuke Mizuno https://orcid.org/0000-0002-8131-6730
Izumi Mizuno https://orcid.org/0000-0002-7210-6264
James M. Moran https://orcid.org/0000-0002-3882-4414
Kotaro Moriyama https://orcid.org/0000-0003-1364-3761
Monika Moscibrodzka https://orcid.org/0000-0002-4661-6332
Cornelia Müller https://orcid.org/0000-0002-2739-2994
Hiroshi Nagai https://orcid.org/0000-0003-0292-3645
Neil M. Nagar https://orcid.org/0000-0001-6920-662X
Masanori Nakamura https://orcid.org/0000-0001-6081-2420
Ramesh Narayan https://orcid.org/0000-0002-1919-2730
Iniyan Natarajan https://orcid.org/0000-0001-8242-4373
Chunchong Ni https://orcid.org/0000-0003-1361-5699
Aristeidis Noutsos https://orcid.org/0000-0002-4151-3860
Héctor Olivares https://orcid.org/0000-0001-6833-7580
Gisela N. Ortiz-León https://orcid.org/0000-0002-2863-676X
Daniel C. M. Palumbo https://orcid.org/0000-0002-7179-3816
Ue-Li Pen https://orcid.org/0000-0003-2155-9578
Dominic W. Pesce https://orcid.org/0000-0002-5278-9221
Oliver Porth https://orcid.org/0000-0002-4584-2557
Ben Prather https://orcid.org/0000-0002-0393-7734
Jorge A. Preciado-López https://orcid.org/0000-0002-4146-0113
Hung-Yi Pu https://orcid.org/0000-0001-9270-8812
Venkatessh Ramakrishnan https://orcid.org/0000-0002-9248-086X
Ramprasad Rao https://orcid.org/0000-0002-1407-7944
Alexander W. Raymond https://orcid.org/0000-0002-5779-4767
Luciano Rezzolla https://orcid.org/0000-0002-1330-7103
Bart Ripperda https://orcid.org/0000-0002-7301-3908
Freek Roelofs https://orcid.org/0000-0001-5461-3687
Eduardo Ros https://orcid.org/0000-0001-9503-4892
Mel Rose https://orcid.org/0000-0002-2016-8746
Alan L. Roy https://orcid.org/0000-0002-1931-0135
Chet Ruszczyk https://orcid.org/0000-0001-7278-9707
Benjamin R. Ryan https://orcid.org/0000-0001-8939-4461
Kazi L. J. Rygl https://orcid.org/0000-0003-4146-9043
David Sánchez-Arguelles https://orcid.org/0000-0002-7344-9920
Mahito Sasada https://orcid.org/0000-0001-5946-9960
Tuomas Savolainen https://orcid.org/0000-0001-6214-1085
Lijing Shao https://orcid.org/0000-0002-1334-8853
Zhiqiang Shen (沈志强) https://orcid.org/0000-0003-3540-8746
Des Small https://orcid.org/0000-0003-3723-5404
Bong Won Sohn https://orcid.org/0000-0002-4148-8378
Jason SooHoo https://orcid.org/0000-0003-1938-0720
Fumie Tazaki https://orcid.org/0000-0003-0236-0600
Paul Tiede https://orcid.org/0000-0003-3826-5648
Remo P. J. Tilanus https://orcid.org/0000-0002-6514-553X
Michael Titus https://orcid.org/0000-0002-3423-4505
Kenji Toma https://orcid.org/0000-0002-7114-6010
Pablo Torne https://orcid.org/0000-0001-8700-6058
Sascha Trippe https://orcid.org/0000-0003-0465-1559
Ilse van Bemmel https://orcid.org/0000-0001-5473-2950
Huib Jan van Langevelde https://orcid.org/0000-0002-0230-5946
Daniel R. van Rossum https://orcid.org/0000-0001-7772-6131
John Wardle https://orcid.org/0000-0002-8960-2942
Jonathan Weintroub https://orcid.org/0000-0002-4603-5204
Norbert Wex https://orcid.org/0000-0003-4058-2837
Robert Wharton https://orcid.org/0000-0002-7416-5209
Maciek Wielgus https://orcid.org/0000-0002-8635-4242
George N. Wong https://orcid.org/0000-0001-6952-2147
Qingwen Wu (吴庆文) https://orcid.org/0000-0003-4773-4987
Ken Young https://orcid.org/0000-0002-3666-4920
André Young https://orcid.org/0000-0003-0000-2682
Ziri Younsi https://orcid.org/0000-0001-9283-1191
Feng Yuan (袁峰) https://orcid.org/0000-0003-3564-6437
J. Anton Zensus https://orcid.org/0000-0001-7470-3321
Guangyao Zhao https://orcid.org/0000-0002-4417-1659
Shan-Shan Zhao https://orcid.org/0000-0002-9774-3606
Juan-Carlos Algaba https://orcid.org/0000-0001-6993-1696
Jadyn Anczarski https://orcid.org/0000-0003-4317-3385
Uwe Bach https://orcid.org/0000-0002-7722-8412
Frederick K. Baganoff https://orcid.org/0000-0003-3852-6545
Bradford A. Benson https://orcid.org/0000-0002-5108-6823
Jay M. Blanchard https://orcid.org/0000-0002-2756-395X
Iain M. Coulson https://orcid.org/0000-0002-7316-4626
Thomas M. Crawford https://orcid.org/0000-0001-9000-5013
Sergio A. Dzib https://orcid.org/0000-0001-6010-6200
Andreas Eckart https://orcid.org/0000-0001-6049-3132
Wendeline B. Everett https://orcid.org/0000-0002-5370-6651
Joseph R. Farah https://orcid.org/0000-0003-4914-5625
Christopher H. Greer https://orcid.org/0000-0002-9590-0508
Daryl Haggard https://orcid.org/0000-0001-6803-2138
Nils W. Halverson https://orcid.org/0000-0003-2606-9340
Antonio Hernández-Gómez https://orcid.org/0000-0001-7520-4305
Rubén Herrero-Illana https://orcid.org/0000-0002-7758-8717
Atish Kamble https://orcid.org/0000-0003-0861-5168
Ryan Keisler https://orcid.org/0000-0002-5922-1137
Yusuke Kono https://orcid.org/0000-0002-4187-8747
Erik M. Leitch https://orcid.org/0000-0001-8553-9336
Kyle D. Massingill https://orcid.org/0000-0002-0830-2033
Hugo Messias https://orcid.org/0000-0002-2985-7994
Daniel Michalik https://orcid.org/0000-0002-7618-6556
Andrew Nadolski https://orcid.org/0000-0001-9479-9957
Joseph Neilsen https://orcid.org/0000-0002-8247-786X
Chi H. Nguyen https://orcid.org/0000-0001-9368-3186
Michael A. Nowak https://orcid.org/0000-0001-6923-1315
Harriet Parsons https://orcid.org/0000-0002-6327-3423
Scott N. Paine https://orcid.org/0000-0003-4622-5857
Rurik A. Primiani https://orcid.org/0000-0003-3910-7529
Alexandra S. Rahlin https://orcid.org/0000-0003-3953-1776

Pim Schellart https://orcid.org/0000-0002-8324-0880
Hotaka Shiokawa https://orcid.org/0000-0002-8847-5275
David R. Smith https://orcid.org/0000-0003-0692-8582
Anthony A. Stark https://orcid.org/0000-0002-2718-9996
Sjoerd T. Timmer https://orcid.org/0000-0003-0223-9368
Nathan Whitehorn https://orcid.org/0000-0002-3157-0407
Jan G. A. Wouterloot https://orcid.org/0000-0002-4694-6905
Melvin Wright https://orcid.org/0000-0002-9154-2440
Paul Yamaguchi https://orcid.org/0000-0002-6017-8199
Shuo Zhang https://orcid.org/0000-0002-2967-790X
Lucy Ziurys https://orcid.org/0000-0002-1805-3886

References

Abbott, B. P., Abbott, R., Abbott, T. D., et al. 2016, PhRvL, 116, 061102
Abramowski, A., Acero, F., Aharonian, F., et al. 2012, ApJ, 746, 151
Akiyama, K., Kuramochi, K., Ikeda, S., et al. 2017, ApJ, 838, 1
Akiyama, K., Lu, R.-S., Fish, V. L., et al. 2015, ApJ, 807, 150
Asada, K., & Nakamura, M. 2012, ApJL, 745, L28
Baade, W., & Minkowski, R. 1954, ApJ, 119, 215
Baars, J. W. M., Martin, R. N., Mangum, J. G., McMullin, J. P., & Peters, W. L. 1999, PASP, 111, 627
Balbus, S. A., & Hawley, J. F. 1991, ApJ, 376, 214
Balick, B., & Brown, R. L. 1974, ApJ, 194, 265
Bambi, C. 2013, PhRvD, 87, 107501
Bambi, C., & Freese, K. 2009, PhRvD, 79, 043002
Barausse, E., & Sotiriou, T. P. 2008, PhRvL, 101, 099001
Bardeen, J. M. 1973, in Black Holes, ed. C. DeWitt & B. S. DeWitt (New York: Gordon and Breach), 215
Berti, E., Barausse, E., Cardoso, V., et al. 2015, CQGra, 32, 243001
Bird, S., Harris, W. E., Blakeslee, J. P., & Flynn, C. 2010, A&A, 524, A71
Biretta, J. A., Sparks, W. B., & Macchetto, F. 1999, ApJ, 520, 621
Blackburn, L., Chan, C.-K., Crew, G. B., et al. 2019, arXiv:1903.08832
Blakeslee, J. P., Jordán, A., Mei, S., et al. 2009, ApJ, 694, 556
Blandford, R. D., & Begelman, M. C. 1999, MNRAS, 303, L1
Blandford, R. D., & Königl, A. 1979, ApJ, 232, 34
Blandford, R. D., & Payne, D. G. 1982, MNRAS, 199, 883
Blandford, R. D., & Znajek, R. L. 1977, MNRAS, 179, 433
Blecher, T., Deane, R., Bernardi, G., & Smirnov, O. 2017, MNRAS, 464, 143
Boccardi, B., Krichbaum, T. P., Ros, E., & Zensus, J. A. 2017, A&ARv, 25, 4
Bolton, J. G., Stanley, G. J., & Slee, O. B. 1949, Natur, 164, 101
Bouman, K. L., Johnson, M. D., Dalca, A. V., et al. 2018, IEEE Transactions on Computational Imaging, 4, 512
Bouman, K. L., Johnson, M. D., Zoran, D., et al. 2016, in The IEEE Conf. Computer Vision and Pattern Recognition (New York: IEEE), 913
Bower, G. C., Wright, M. C. H., Falcke, H., & Backer, D. C. 2003, ApJ, 588, 331
Bridle, A. H., & Perley, R. A. 1984, ARA&A, 22, 319
Broderick, A. E., Johannsen, T., Loeb, A., & Psaltis, D. 2014, ApJ, 784, 7
Broderick, A. E., & Loeb, A. 2005, MNRAS, 363, 353
Broderick, A. E., & Loeb, A. 2006, ApJL, 636, L109
Broderick, A. E., & Loeb, A. 2009, ApJ, 697, 1164
Broderick, A. E., & Narayan, R. 2006, ApJL, 638, L21
Broderick, A. E., Narayan, R., Kormendy, J., et al. 2015, ApJ, 805, 179
Bromley, B. C., Melia, F., & Liu, S. 2001, ApJL, 555, L83
Bronzwaer, T., Davelaar, J., Younsi, Z., et al. 2018, A&A, 613, A2
Cantiello, M., Blakeslee, J. P., Ferrarese, L., et al. 2018, ApJ, 856, 126
Chael, A., Narayan, R., & Johnson, M. D. 2018a, arXiv:1810.01983
Chael, A. A., Johnson, M. D., Bouman, K. L., et al. 2018b, ApJ, 857, 23
Chan, C.-K., Psaltis, D., Özel, F., Narayan, R., & Saowski, A. 2015, ApJ, 799, 1
Chirenti, C. B. M. H., & Rezzolla, L. 2007, CQGra, 24, 4191
Clark, B. G. 1980, A&A, 89, 377
Cohen, M. H., Moffet, A. T., Shaffer, D., et al. 1969, ApJL, 158, L83
Cunha, P. V. P., Grover, J., Herdeiro, C., et al. 2016, PhRvD, 94, 104023
Curtis, H. D. 1918, PLicO, 13, 9
Davelaar, J., Olivares, H., Porth, O., et al. 2019, A&A, submitted
de Gasperin, F., Orrú, E., Murgia, M., et al. 2012, A&A, 547, A56
Deller, A. T., Tingay, S. J., Bailes, M., & West, C. 2007, PASP, 119, 318
Dexter, J., McKinney, J. C., & Agol, E. 2012, MNRAS, 421, 1517
Dibi, S., Drappeau, S., Fragile, P. C., Markoff, S., & Dexter, J. 2012, MNRAS, 426, 1928
Doeleman, S., Agol, E., Dacker, D., et al. 2009a, astro2010: The Astronomy and Astrophysics Decadal Survey, Vol. 2010
Doeleman, S. S., Fish, V. L., Broderick, A. E., Loeb, A., & Rogers, A. E. E. 2009b, ApJ, 695, 59
Doeleman, S. S., Fish, V. L., Schenck, D. E., et al. 2012, Sci, 338, 355
Doeleman, S. S., Shen, Z.-Q., Rogers, A. E. E., et al. 2001, AJ, 121, 2610
Doeleman, S. S., Weintroub, J., Rogers, A. E. E., et al. 2008, Natur, 455, 78
Eckart, A., & Genzel, R. 1997, MNRAS, 284, 576
EHT Collaboration et al. 2019a, ApJL, 875, L2 (Paper II)
EHT Collaboration et al. 2019b, ApJL, 875, L3 (Paper III)
EHT Collaboration et al. 2019c, ApJL, 875, L4 (Paper IV)
EHT Collaboration et al. 2019d, ApJL, 875, L5 (Paper V)
EHT Collaboration et al. 2019e, ApJL, 875, L6 (Paper VI)
Einstein, A. 1915, Sitzungsberichte der Königlich Preußischen Akademie der Wissenschaften (Berlin: Deutsche Akademie der Wissenschaften zu Berlin)
Falcke, H., Körding, E., & Markoff, S. 2004, A&A, 414, 895
Falcke, H., Mannheim, K., & Biermann, P. L. 1993, A&A, 278, L1
Falcke, H., Melia, F., & Agol, E. 2000a, ApJL, 528, L13
Falcke, H., Melia, F., & Agol, E. 2000b, in AIP Conf. Ser. 522, Cosmic Explosions, ed. S. Holt & W. Zhang (Melville, NY: AIP), 317
Fish, V., Shea, M., & Akiyama, K. 2019, AdSpR, in press (arXiv:1903.09539)
Fish, V. L., Johnson, M. D., Doeleman, S. S., et al. 2016, ApJ, 820, 90
Ford, H. C., Harms, R. J., Tsvetanov, Z. I., et al. 1994, ApJL, 435, L27
Gammie, C. F., McKinney, J. C., & Tóth, G. 2003, ApJ, 589, 444
Gebhardt, K., Adams, J., Richstone, D., et al. 2011, ApJ, 729, 119
Gebhardt, K., & Thomas, J. 2009, ApJ, 700, 1690
Ghez, A. M., Klein, B. L., Morris, M., & Becklin, E. E. 1998, ApJ, 509, 678
Giddings, S. B. 2017, NatAs, 1, 0067
Goddi, C., Marti-Vidal, I., Messias, H., et al. 2019, PASP, in press
Gold, R., Broderick, A., Younsi, Z., et al. 2019, ApJS
Gravity Collaboration, Abuter, R., Amorim, A., et al. 2018a, A&A, 615, L15
Gravity Collaboration, Abuter, R., Amorim, A., et al. 2018b, A&A, 618, L10
Greisen, E. W. 2003, in Information Handling in Astronomy—Historical Vistas, Astrophysics and Space Science Library, Vol. 285, ed. A. Heck (Dordrecht: Kluwer), 109
Grenzebach, A., Perlick, V., & Lämmerzahl, C. 2014, PhRvD, 89, 124004
Greve, A., Torres, M., Wink, J. E., et al. 1995, A&A, 299, L33
Hada, K., Doi, A., Kino, M., et al. 2011, Natur, 477, 185
Hada, K., Kino, M., Doi, A., et al. 2013, ApJ, 775, 70
Hada, K., Kino, M., Doi, A., et al. 2016, ApJ, 817, 131
Harms, R. J., Ford, H. C., Tsvetanov, Z. I., et al. 1994, ApJL, 435, L35
Hawking, S. W. 1976, PhRvD, 14, 2460
Hilbert, D. 1917, Nachrichten von der Königlichen Gesellschaft der Wissenschaften zu Göttingen—Mathematisch-physikalische Klasse (Berlin: Weidmannsche Buchhandlung)
Ho, L. C. 1999, ApJ, 516, 672
Högbom, J. A. 1974, A&AS, 15, 417
Honma, M., Akiyama, K., Uemura, M., & Ikeda, S. 2014, PASJ, 66, 95
Ichimaru, S. 1977, ApJ, 214, 840
Janssen, M., Goddi, C., van Bemmel, I. M., et al. 2019, A&A, submitted (arXiv:1902.01749)
Johannsen, T., Broderick, A. E., Plewa, P. M., et al. 2016, PhRvL, 116, 031101
Johannsen, T., & Psaltis, D. 2010, ApJ, 718, 446
Johannsen, T., Psaltis, D., Gillessen, S., et al. 2012, ApJ, 758, 30
Johnson, M. D. 2016, ApJ, 833, 74
Johnson, M. D., Fish, V. L., Doeleman, S. S., et al. 2015, Sci, 350, 1242
Junor, W., Biretta, J. A., & Livio, M. 1999, Natur, 401, 891
Kamruddin, A. B., & Dexter, J. 2013, MNRAS, 434, 765
Kardashev, N. S., Novikov, I. D., Lukash, V. N., et al. 2014, PhyU, 57, 1199
Kassim, N. E., Perley, R. A., Erickson, W. C., & Dwarakanath, K. S. 1993, AJ, 106, 2218
Kaup, D. J. 1968, PhRv, 172, 1331
Kerr, R. P. 1963, PhRvL, 11, 237
Kim, J., Marrone, D. P., Beaudoin, C., et al. 2018a, Proc. SPIE, 10708, 107082S
Kim, J., Marrone, D. P., Chan, C.-K., et al. 2016, ApJ, 832, 156
Kim, J.-Y., Krichbaum, T. P., Lu, R.-S., et al. 2018b, A&A, 616, A188
Kormendy, J., & Richstone, D. 1995, ARA&A, 33, 581
Krichbaum, T. P., Graham, D. A., Witzel, A., et al. 1998, A&A, 335, L106
Krichbaum, T. P., Zensus, J. A., Witzel, A., et al. 1993, A&A, 274, L37
Kuo, C. Y., Asada, K., Rao, R., et al. 2014, ApJL, 783, L33
Kuramochi, K., Akiyama, K., Ikeda, S., et al. 2018, ApJ, 858, 56
Liebling, S. L., & Palenzuela, C. 2012, LRR, 15
Liska, M., Hesp, C., Tchekhovskoy, A., et al. 2018, MNRAS, 474, L81
Lister, M. L., Aller, M. F., Aller, H. D., et al. 2018, ApJS, 234, 12
Lobanov, A. 2017, NatAs, 1, 0069
Lu, R.-S., Broderick, A. E., Baron, F., et al. 2014, ApJ, 788, 120

Lu, R.-S., Krichbaum, T. P., Roy, A. L., et al. 2018, ApJ, 859, 60
Lu, R.-S., Roelofs, F., Fish, V. L., et al. 2016, ApJ, 817, 173
Luminet, J.-P. 1979, A&A, 75, 228
Lynden-Bell, D. 1969, Natur, 223, 690
Macchetto, F., Marconi, A., Axon, D. J., et al. 1997, ApJ, 489, 579
Marrone, D. P., Moran, J. M., Zhao, J.-H., & Rao, R. 2007, ApJL, 654, L57
Marshall, H. L., Miller, B. P., Davis, D. S., et al. 2002, ApJ, 564, 683
Matthews, L. D., Crew, G. B., Doeleman, S. S., et al. 2018, PASP, 130, 015002
Mazur, P. O., & Mottola, E. 2004, PNAS, 101, 9545
McMullin, J. P., Waters, B., Schiebel, D., Young, W., & Golap, K. 2007, in ASP Conf. Ser. 376, Astronomical Data Analysis Software and Systems XVI, ed. R. A. Shaw, F. Hill, & D. J. Bell (San Francisco, CA: ASP), 127
Medeiros, L., Chan, C.-k., Özel, F., et al. 2017, ApJ, 844, 35
Mertens, F., Lobanov, A. P., Walker, R. C., & Hardee, P. E. 2016, A&A, 595, A54
Miyoshi, M., Moran, J., Herrnstein, J., et al. 1995, Natur, 373, 127
Mizuno, Y., Younsi, Z., Fromm, C. M., et al. 2018, NatAs, 2, 585
Mościbrodzka, M., Dexter, J., Davelaar, J., & Falcke, H. 2017, MNRAS, 468, 2214
Mościbrodzka, M., Falcke, H., & Shiokawa, H. 2016, A&A, 586, A38
Mościbrodzka, M., & Gammie, C. F. 2018, MNRAS, 475, 43
Mościbrodzka, M., Gammie, C. F., Dolence, J. C., Shiokawa, H., & Leung, P. K. 2009, ApJ, 706, 497
Nagar, N. M., Falcke, H., & Wilson, A. S. 2005, A&A, 435, 521
Nakamura, M., & Asada, K. 2013, ApJ, 775, 118
Nakamura, M., Asada, K., Hada, K., et al. 2018, ApJ, 868, 146
Narayan, R., Igumenshchev, I. V., & Abramowicz, M. A. 2003, PASJ, 55, L69
Narayan, R., & Nityananda, R. 1986, ARA&A, 24, 127
Narayan, R., Sądowski, A., Penna, R. F., & Kulkarni, A. K. 2012, MNRAS, 426, 3241
Narayan, R., & Yi, I. 1995, ApJ, 452, 710
Narayan, R., Yi, I., & Mahadevan, R. 1995, Natur, 374, 623
Noble, S. C., Leung, P. K., Gammie, C. F., & Book, L. G. 2007, CQGra, 24, 259
Olivares, H., Younsi, Z., Fromm, C. M., et al. 2019, PhRvD, submitted (arXiv:1809.08682)
Ortiz-León, G. N., Johnson, M. D., Doeleman, S. S., et al. 2016, ApJ, 824, 40
Owen, F. N., Eilek, J. A., & Kassim, N. E. 2000, ApJ, 543, 611
Owen, F. N., Hardee, P. E., & Cornwell, T. J. 1989, ApJ, 340, 698
Padin, S., Woody, D. P., Hodges, M. W., et al. 1990, ApJL, 360, L11
Palumbo, F., Doeleman, S., Johnson, M., Bouman, K., & Chael, A. 2019, ApJ, submitted
Pearson, T. J., & Readhead, A. C. S. 1984, ARA&A, 22, 97
Penrose, R. 1965, PhRvL, 14, 57
Perlman, E. S., Adams, S. C., Cara, M., et al. 2011, ApJ, 743, 119
Porth, O., Chatterjee, K., Narayan, R., et al. 2019, ApJS
Porth, O., Olivares, H., Mizuno, Y., et al. 2017, ComAC, 4, 1
Primiani, R. A., Young, K. H., Young, A., et al. 2016, JAI, 5, 1641006
Psaltis, D., Özel, F., Chan, C.-K., & Marrone, D. P. 2015, ApJ, 814, 115
Psaltis, D., Perrodin, D., Dienes, K. R., & Mocioiu, I. 2008, PhRvL, 100, 091101
Pu, H.-Y., Wu, K., Younsi, Z., et al. 2017, ApJ, 845, 160
Readhead, A. C. S., Walker, R. C., Pearson, T. J., & Cohen, M. H. 1980, Natur, 285, 137
Reid, M. J., Biretta, J. A., Junor, W., Muxlow, T. W. B., & Spencer, R. E. 1989, ApJ, 336, 112
Remillard, R. A., & McClintock, J. E. 2006, ARA&A, 44, 49
Roelofs, F., Falcke, H., Brinkerink, C., et al. 2019a, A&A, submitted
Roelofs, F., Johnson, M. D., Shiokawa, H., Doeleman, S. S., & Falcke, H. 2017, ApJ, 847, 55
Rogers, A. E. E., Hinteregger, H. F., Whitney, A. R., et al. 1974, ApJ, 193, 293
Ryan, B. R., Ressler, S. M., Dolence, J. C., Gammie, C., & Quataert, E. 2018, ApJ, 864, 126
Sądowski, A., Narayan, R., McKinney, J. C., & Tchekhovskoy, A. 2014, MNRAS, 439, 503
Sanders, D. B., Phinney, E. S., Neugebauer, G., Soifer, B. T., & Matthews, K. 1989, ApJ, 347, 29
Schmidt, M. 1963, Natur, 197, 1040
Schwarzschild, K. 1916, Sitzungsberichte der Königlich Preußischen Akademie der Wissenschaften (Berlin: Deutsche Akademie der Wissenschaften zu Berlin)
Shaikh, R., Kocherlakota, P., Narayan, R., & Joshi, P. S. 2019, MNRAS, 482, 52
Shakura, N. I., & Sunyaev, R. A. 1973, A&A, 24, 337
Sun, W. H., & Malkan, M. A. 1989, ApJ, 346, 68
Takahashi, R. 2004, ApJ, 611, 996
Thiébaut, É 2013, in New Concepts in Imaging: Optical and Statistical Models, EAS Publications Series, Vol. 59, ed. D. Mary, C. Theys, & C. Aime (Les Ulis: EDP Sciences), 157
Thompson, A. R., Moran, J. M., & Swenson, G. W., Jr. 2017, Interferometry and Synthesis in Radio Astronomy (3rd ed.; Berlin: Spinger)
van Cittert, P. H. 1934, Phy, 1, 201
Vertatschitsch, L., Primiani, R., Young, A., et al. 2015, PASP, 127, 1226
Vincent, F. H., Meliani, Z., Grandclément, P., Gourgoulhon, E., & Straub, O. 2016, CQGra, 33, 105015
Wagner, J., Roy, A. L., Krichbaum, T. P., et al. 2015, A&A, 581, A32
Walker, R. C., Hardee, P. E., Davies, F. B., Ly, C., & Junor, W. 2018, ApJ, 855, 128
Walsh, J. L., Barth, A. J., Ho, L. C., & Sarzi, M. 2013, ApJ, 770, 86
Webster, B. L., & Murdin, P. 1972, Natur, 235, 37
Whitney, A. R., Beaudoin, C. J., Cappallo, R. J., et al. 2013, PASP, 125, 196
Whitney, A. R., Cappallo, R., Aldrich, W., et al. 2004, RaSc, 39
Wiaux, Y., Jacques, L., Puy, G., Scaife, A. M. M., & Vandergheynst, P. 2009, MNRAS, 395, 1733
Wrobel, J. M., & Heeschen, D. S. 1984, ApJ, 287, 41
Young, A., Primiani, R., Weintroub, J., et al. 2016, in IEEE Int. Symp., Phased Array Systems and Technology (ARRAY) (New York: IEEE), 1
Younsi, Z., Zhidenko, A., Rezzolla, L., Konoplya, R., & Mizuno, Y. 2016, PhRvD, 94, 084025
Yuan, F., Markoff, S., & Falcke, H. 2002, A&A, 383, 854
Yuan, F., & Narayan, R. 2014, ARA&A, 52, 529
Zensus, J. A. 1997, ARA&A, 35, 607

The Event Horizon Telescope Collaboration,
Kazunori Akiyama[1,2,3,4], Antxon Alberdi[5], Walter Alef[6], Keiichi Asada[7], Rebecca Azulay[8,9,6], Anne-Kathrin Baczko[6], David Ball[10], Mislav Baloković[4,11], John Barrett[2], Dan Bintley[12], Lindy Blackburn[4,11], Wilfred Boland[13], Katherine L. Bouman[4,11,14], Geoffrey C. Bower[15], Michael Bremer[16], Christiaan D. Brinkerink[17], Roger Brissenden[4,11], Silke Britzen[6], Avery E. Broderick[18,19,20], Dominique Broguiere[16], Thomas Bronzwaer[17], Do-Young Byun[21,22], John E. Carlstrom[23,24,25,26], Andrew Chael[4,11], Chi-kwan Chan[10,27], Shami Chatterjee[28], Koushik Chatterjee[29], Ming-Tang Chen[15], Yongjun Chen (陈永军)[30,31], Ilje Cho[21,22], Pierre Christian[10,11], John E. Conway[32], James M. Cordes[28], Geoffrey B. Crew[2], Yuzhu Cui[33,34], Jordy Davelaar[17], Mariafelicia De Laurentis[35,36,37], Roger Deane[38,39], Jessica Dempsey[12], Gregory Desvignes[6], Jason Dexter[40], Sheperd S. Doeleman[4,11], Ralph P. Eatough[6], Heino Falcke[17], Vincent L. Fish[2], Ed Fomalont[1], Raquel Fraga-Encinas[17], William T. Freeman[41,42], Per Friberg[12], Christian M. Fromm[36], José L. Gómez[5], Peter Galison[4,43,44], Charles F. Gammie[45,46], Roberto García[16], Olivier Gentaz[16], Boris Georgiev[19,20], Ciriaco Goddi[17,47], Roman Gold[36], Minfeng Gu (顾敏峰)[30,48], Mark Gurwell[11], Kazuhiro Hada[33,34], Michael H. Hecht[2], Ronald Hesper[49], Luis C. Ho (何子山)[50,51], Paul Ho[7], Mareki Honma[33,34], Chih-Wei L. Huang[7], Lei Huang (黄磊)[30,48], David H. Hughes[52], Shiro Ikeda[3,53,54,55], Makoto Inoue[7], Sara Issaoun[17],

David J. James[4,11], Buell T. Jannuzi[10], Michael Janssen[17], Britton Jeter[19,20], Wu Jiang (江悟)[30], Michael D. Johnson[4,11], Svetlana Jorstad[56,57], Taehyun Jung[21,22], Mansour Karami[18,19], Ramesh Karuppusamy[6], Tomohisa Kawashima[3], Garrett K. Keating[11], Mark Kettenis[58], Jae-Young Kim[6], Junhan Kim[10], Jongsoo Kim[21], Motoki Kino[3,59], Jun Yi Koay[7], Patrick M. Koch[7], Shoko Koyama[7], Michael Kramer[6], Carsten Kramer[16], Thomas P. Krichbaum[6], Cheng-Yu Kuo[60], Tod R. Lauer[61], Sang-Sung Lee[21], Yan-Rong Li (李彦荣)[62], Zhiyuan Li (李志远)[63,64], Michael Lindqvist[32], Kuo Liu[6], Elisabetta Liuzzo[65], Wen-Ping Lo[7,66], Andrei P. Lobanov[6], Laurent Loinard[67,68], Colin Lonsdale[2], Ru-Sen Lu (路如森)[30,6], Nicholas R. MacDonald[6], Jirong Mao (毛基荣)[69,70,71], Sera Markoff[29,72], Daniel P. Marrone[10], Alan P. Marscher[56], Iván Martí-Vidal[32,73], Satoki Matsushita[7], Lynn D. Matthews[2], Lia Medeiros[10,74], Karl M. Menten[6], Yosuke Mizuno[36], Izumi Mizuno[12], James M. Moran[4,11], Kotaro Moriyama[33,2], Monika Moscibrodzka[17], Cornelia Müller[6,17], Hiroshi Nagai[3,34], Neil M. Nagar[75], Masanori Nakamura[7], Ramesh Narayan[4,11], Gopal Narayanan[76], Iniyan Natarajan[39], Roberto Neri[16], Chunchong Ni[19,20], Aristeidis Noutsos[6], Hiroki Okino[33,77], Héctor Olivares[36], Gisela N. Ortiz-León[6], Tomoaki Oyama[33], Feryal Özel[10], Daniel C. M. Palumbo[4,11], Nimesh Patel[11], Ue-Li Pen[18,78,79,80], Dominic W. Pesce[4,11], Vincent Piétu[16], Richard Plambeck[81], Aleksandar PopStefanija[76], Oliver Porth[29,36], Ben Prather[45], Jorge A. Preciado-López[18], Dimitrios Psaltis[10], Hung-Yi Pu[18], Venkatessh Ramakrishnan[75], Ramprasad Rao[15], Mark G. Rawlings[12], Alexander W. Raymond[4,11], Luciano Rezzolla[36], Bart Ripperda[36], Freek Roelofs[17], Alan Rogers[2], Eduardo Ros[6], Mel Rose[10], Arash Roshanineshat[10], Helge Rottmann[6], Alan L. Roy[6], Chet Ruszczyk[2], Benjamin R. Ryan[82,83], Kazi L. J. Rygl[65], Salvador Sánchez[84], David Sánchez-Arguelles[52,85], Mahito Sasada[33,86], Tuomas Savolainen[6,87,88], F. Peter Schloerb[76], Karl-Friedrich Schuster[16], Lijing Shao[6,51], Zhiqiang Shen (沈志强)[30,31], Des Small[58], Bong Won Sohn[21,22,89], Jason SooHoo[2], Fumie Tazaki[33], Paul Tiede[19,20], Remo P. J. Tilanus[17,47,90], Michael Titus[2], Kenji Toma[91,92], Pablo Torne[6,84], Tyler Trent[10], Sascha Trippe[93], Shuichiro Tsuda[33], Ilse van Bemmel[58], Huib Jan van Langevelde[58,94], Daniel R. van Rossum[17], Jan Wagner[6], John Wardle[95], Jonathan Weintroub[4,11], Norbert Wex[6], Robert Wharton[6], Maciek Wielgus[4,11], George N. Wong[45], Qingwen Wu (吴庆文)[96], Ken Young[11], André Young[17], Ziri Younsi[97,36], Feng Yuan (袁峰)[30,48,98], Ye-Fei Yuan (袁业飞)[99], J. Anton Zensus[6], Guangyao Zhao[21], Shan-Shan Zhao[17,63], Ziyan Zhu[44], Juan-Carlos Algaba[7,100], Alexander Allardi[101], Rodrigo Amestica[102], Jadyn Anczarski[103], Uwe Bach[6], Frederick K. Baganoff[104], Christopher Beaudoin[2], Bradford A. Benson[26,24], Ryan Berthold[12], Jay M. Blanchard[75,58], Ray Blundell[11], Sandra Bustamente[105], Roger Cappallo[2], Edgar Castillo-Domínguez[105,106], Chih-Cheng Chang[7,107], Shu-Hao Chang[7], Song-Chu Chang[107], Chung-Chen Chen[7], Ryan Chilson[15], Tim C. Chuter[12], Rodrigo Córdova Rosado[4,11], Iain M. Coulson[12], Thomas M. Crawford[24,25], Joseph Crowley[108], John David[84], Mark Derome[2], Matthew Dexter[109], Sven Dornbusch[6], Kevin A. Dudevoir[2,144], Sergio A. Dzib[6], Andreas Eckart[6,110], Chris Eckert[2], Neal R. Erickson[76], Wendeline B. Everett[111], Aaron Faber[112], Joseph R. Farah[4,11,113], Vernon Fath[76], Thomas W. Folkers[10], David C. Forbes[10], Robert Freund[10], Arturo I. Gómez-Ruiz[105,106], David M. Gale[105], Feng Gao[30,40], Gertie Geertsema[114], David A. Graham[6], Christopher H. Greer[10], Ronald Grosslein[76], Frédéric Gueth[16], Daryl Haggard[115,116,117], Nils W. Halverson[118], Chih-Chiang Han[7], Kuo-Chang Han[107], Jinchi Hao[107], Yutaka Hasegawa[7], Jason W. Henning[23,119], Antonio Hernández-Gómez[67,120], Rubén Herrero-Illana[121], Stefan Heyminck[6], Akihiko Hirota[3,7], James Hoge[12], Yau-De Huang[7], C. M. Violette Impellizzeri[7,1], Homin Jiang[7], Atish Kamble[4,11], Ryan Keisler[25], Kimihiro Kimura[7], Yusuke Kono[3], Derek Kubo[122], John Kuroda[12], Richard Lacasse[102], Robert A. Laing[123], Erik M. Leitch[23], Chao-Te Li[7], Lupin C.-C. Lin[7,124], Ching-Tang Liu[107], Kuan-Yu Liu[7], Li-Ming Lu[107], Ralph G. Marson[125], Pierre L. Martin-Cocher[7], Kyle D. Massingill[10], Callie Matulonis[12], Martin P. McColl[10], Stephen R. McWhirter[2], Hugo Messias[121,126], Zheng Meyer-Zhao[7,127], Daniel Michalik[128,129], Alfredo Montaña[105,106], William Montgomerie[12], Matias Mora-Klein[102], Dirk Muders[6], Andrew Nadolski[46], Santiago Navarro[84], Joseph Neilsen[103], Chi H. Nguyen[10,130], Hiroaki Nishioka[7], Timothy Norton[11], Michael A. Nowak[131], George Nystrom[15], Hideo Ogawa[132], Peter Oshiro[15], Tomoaki Oyama[133], Harriet Parsons[12], Scott N. Paine[11], Juan Peñalver[84], Neil M. Phillips[121,126], Michael Poirier[2], Nicolas Pradel[7], Rurik A. Primiani[134], Philippe A. Raffin[15], Alexandra S. Rahlin[23,135], George Reiland[10], Christopher Risacher[16], Ignacio Ruiz[84], Alejandro F. Sáez-Madaín[102,126], Remi Sassella[16], Pim Schellart[17,136], Paul Shaw[7], Kevin M. Silva[12], Hotaka Shiokawa[11], David R. Smith[137,138], William Snow[15], Kamal Souccar[76], Don Sousa[2], T. K. Sridharan[11], Ranjani Srinivasan[15], William Stahm[12], Anthony A. Stark[11], Kyle Story[139], Sjoerd T. Timmer[17], Laura Vertatschitsch[11,134], Craig Walther[12], Ta-Shun Wei[7], Nathan Whitehorn[140], Alan R. Whitney[2], David P. Woody[141], Jan G. A. Wouterloot[12], Melvin Wright[142], Paul Yamaguchi[11], Chen-Yu Yu[7], Milagros Zeballos[105,143], Shuo Zhang[104], and Lucy Ziurys[10]

[1] National Radio Astronomy Observatory, 520 Edgemont Road, Charlottesville, VA 22903, USA
[2] Massachusetts Institute of Technology, Haystack Observatory, 99 Millstone Road, Westford, MA 01886, USA
[3] National Astronomical Observatory of Japan, 2-21-1 Osawa, Mitaka, Tokyo 181-8588, Japan
[4] Black Hole Initiative at Harvard University, 20 Garden Street, Cambridge, MA 02138, USA
[5] Instituto de Astrofísica de Andalucía-CSIC, Glorieta de la Astronomía s/n, E-18008 Granada, Spain
[6] Max-Planck-Institut für Radioastronomie, Auf dem Hügel 69, D-53121 Bonn, Germany

[7] Institute of Astronomy and Astrophysics, Academia Sinica, 11F of Astronomy-Mathematics Building, AS/NTU No. 1, Sec. 4, Roosevelt Rd, Taipei 10617, Taiwan, R.O.C.
[8] Departament d'Astronomia i Astrofísica, Universitat de València, C. Dr. Moliner 50, E-46100 Burjassot, València, Spain
[9] Observatori Astronòmic, Universitat de València, C. Catedrático José Beltrán 2, E-46980 Paterna, València, Spain
[10] Steward Observatory and Department of Astronomy, University of Arizona, 933 N. Cherry Ave., Tucson, AZ 85721, USA
[11] Center for Astrophysics | Harvard & Smithsonian, 60 Garden Street, Cambridge, MA 02138, USA
[12] East Asian Observatory, 660 N. A'ohoku Pl., Hilo, HI 96720, USA
[13] Nederlandse Onderzoekschool voor Astronomie (NOVA), PO Box 9513, 2300 RA Leiden, The Netherlands
[14] California Institute of Technology, 1200 East California Boulevard, Pasadena, CA 91125, USA
[15] Institute of Astronomy and Astrophysics, Academia Sinica, 645 N. A'ohoku Place, Hilo, HI 96720, USA
[16] Institut de Radioastronomie Millimétrique, 300 rue de la Piscine, F-38406 Saint Martin d'Hères, France
[17] Department of Astrophysics, Institute for Mathematics, Astrophysics and Particle Physics (IMAPP), Radboud University, P.O. Box 9010, 6500 GL Nijmegen, The Netherlands
[18] Perimeter Institute for Theoretical Physics, 31 Caroline Street North, Waterloo, ON, N2L 2Y5, Canada
[19] Department of Physics and Astronomy, University of Waterloo, 200 University Avenue West, Waterloo, ON, N2L 3G1, Canada
[20] Waterloo Centre for Astrophysics, University of Waterloo, Waterloo, ON N2L 3G1 Canada
[21] Korea Astronomy and Space Science Institute, Daedeok-daero 776, Yuseong-gu, Daejeon 34055, Republic of Korea
[22] University of Science and Technology, Gajeong-ro 217, Yuseong-gu, Daejeon 34113, Republic of Korea
[23] Kavli Institute for Cosmological Physics, University of Chicago, 5640 South Ellis Avenue, Chicago, IL 60637, USA
[24] Department of Astronomy and Astrophysics, University of Chicago, 5640 South Ellis Avenue, Chicago, IL 60637, USA
[25] Department of Physics, University of Chicago, 5720 South Ellis Avenue, Chicago, IL 60637, USA
[26] Enrico Fermi Institute, University of Chicago, 5640 South Ellis Avenue, Chicago, IL 60637, USA
[27] Data Science Institute, University of Arizona, 1230 N. Cherry Ave., Tucson, AZ 85721, USA
[28] Cornell Center for Astrophysics and Planetary Science, Cornell University, Ithaca, NY 14853, USA
[29] Anton Pannekoek Institute for Astronomy, University of Amsterdam, Science Park 904, 1098 XH, Amsterdam, The Netherlands
[30] Shanghai Astronomical Observatory, Chinese Academy of Sciences, 80 Nandan Road, Shanghai 200030, People's Republic of China
[31] Key Laboratory of Radio Astronomy, Chinese Academy of Sciences, Nanjing 210008, People's Republic of China
[32] Department of Space, Earth and Environment, Chalmers University of Technology, Onsala Space Observatory, SE-439 92 Onsala, Sweden
[33] Mizusawa VLBI Observatory, National Astronomical Observatory of Japan, 2-12 Hoshigaoka, Mizusawa, Oshu, Iwate 023-0861, Japan
[34] Department of Astronomical Science, The Graduate University for Advanced Studies (SOKENDAI), 2-21-1 Osawa, Mitaka, Tokyo 181-8588, Japan
[35] Dipartimento di Fisica "E. Pancini," Universitá di Napoli "Federico II," Compl. Univ. di Monte S. Angelo, Edificio G, Via Cinthia, I-80126, Napoli, Italy
[36] Institut für Theoretische Physik, Goethe-Universität Frankfurt, Max-von-Laue-Straße 1, D-60438 Frankfurt am Main, Germany
[37] INFN Sez. di Napoli, Compl. Univ. di Monte S. Angelo, Edificio G, Via Cinthia, I-80126, Napoli, Italy
[38] Department of Physics, University of Pretoria, Lynnwood Road, Hatfield, Pretoria 0083, South Africa
[39] Centre for Radio Astronomy Techniques and Technologies, Department of Physics and Electronics, Rhodes University, Grahamstown 6140, South Africa
[40] Max-Planck-Institut für Extraterrestrische Physik, Giessenbachstr. 1, D-85748 Garching, Germany
[41] Department of Electrical Engineering and Computer Science, Massachusetts Institute of Technology, 32-D476, 77 Massachussetts Ave., Cambridge, MA 02142, USA
[42] Google Research, 355 Main St., Cambridge, MA 02142, USA
[43] Department of History of Science, Harvard University, Cambridge, MA 02138, USA
[44] Department of Physics, Harvard University, Cambridge, MA 02138, USA
[45] Department of Physics, University of Illinois, 1110 West Green St, Urbana, IL 61801, USA
[46] Department of Astronomy, University of Illinois at Urbana-Champaign, 1002 West Green Street, Urbana, IL 61801, USA
[47] Leiden Observatory—Allegro, Leiden University, P.O. Box 9513, 2300 RA Leiden, The Netherlands
[48] Key Laboratory for Research in Galaxies and Cosmology, Chinese Academy of Sciences, Shanghai 200030, People's Republic of China
[49] NOVA Sub-mm Instrumentation Group, Kapteyn Astronomical Institute, University of Groningen, Landleven 12, 9747 AD Groningen, The Netherlands
[50] Department of Astronomy, School of Physics, Peking University, Beijing 100871, People's Republic of China
[51] Kavli Institute for Astronomy and Astrophysics, Peking University, Beijing 100871, People's Republic of China
[52] Instituto Nacional de Astrofísica, Óptica y Electrónica. Apartado Postal 51 y 216, 72000. Puebla Pue., México
[53] The Institute of Statistical Mathematics, 10-3 Midori-cho, Tachikawa, Tokyo, 190-8562, Japan
[54] Department of Statistical Science, The Graduate University for Advanced Studies (SOKENDAI), 10-3 Midori-cho, Tachikawa, Tokyo 190-8562, Japan
[55] Kavli Institute for the Physics and Mathematics of the Universe, The University of Tokyo, 5-1-5 Kashiwanoha, Kashiwa, 277-8583, Japan
[56] Institute for Astrophysical Research, Boston University, 725 Commonwealth Ave., Boston, MA 02215, USA
[57] Astronomical Institute, St. Petersburg University, Universitetskij pr., 28, Petrodvorets, 198504 St. Petersburg, Russia
[58] Joint Institute for VLBI ERIC (JIVE), Oude Hoogeveensedijk 4, 7991 PD Dwingeloo, The Netherlands
[59] Kogakuin University of Technology & Engineering, Academic Support Center, 2665-1 Nakano, Hachioji, Tokyo 192-0015, Japan
[60] Physics Department, National Sun Yat-Sen University, No. 70, Lien-Hai Rd, Kaosiung City 80424, Taiwan, R.O.C
[61] National Optical Astronomy Observatory, 950 North Cherry Ave., Tucson, AZ 85719, USA
[62] Key Laboratory for Particle Astrophysics, Institute of High Energy Physics, Chinese Academy of Sciences, 19B Yuquan Road, Shijingshan District, Beijing, People's Republic of China
[63] School of Astronomy and Space Science, Nanjing University, Nanjing 210023, People's Republic of China
[64] Key Laboratory of Modern Astronomy and Astrophysics, Nanjing University, Nanjing 210023, People's Republic of China
[65] Italian ALMA Regional Centre, INAF-Istituto di Radioastronomia, Via P. Gobetti 101, I-40129 Bologna, Italy
[66] Department of Physics, National Taiwan University, No.1, Sect.4, Roosevelt Rd., Taipei 10617, Taiwan, R.O.C
[67] Instituto de Radioastronomía y Astrofísica, Universidad Nacional Autónoma de México, Morelia 58089, México
[68] Instituto de Astronomía, Universidad Nacional Autónoma de México, CdMx 04510, México
[69] Yunnan Observatories, Chinese Academy of Sciences, 650011 Kunming, Yunnan Province, People's Republic of China
[70] Center for Astronomical Mega-Science, Chinese Academy of Sciences, 20A Datun Road, Chaoyang District, Beijing, 100012, People's Republic of China
[71] Key Laboratory for the Structure and Evolution of Celestial Objects, Chinese Academy of Sciences, 650011 Kunming, People's Republic of China
[72] Gravitation Astroparticle Physics Amsterdam (GRAPPA) Institute, University of Amsterdam, Science Park 904, 1098 XH Amsterdam, The Netherlands
[73] Centro Astronómico de Yebes (IGN), Apartado 148, E-19180 E-Yebes, Spain
[74] Department of Physics, Broida Hall, University of California Santa Barbara, Santa Barbara, CA 93106, USA
[75] Astronomy Department, Universidad de Concepción, Casilla 160-C, Concepción, Chile
[76] Department of Astronomy, University of Massachusetts, 01003, Amherst, MA, USA
[77] Department of Astronomy, Graduate School of Science, The University of Tokyo, 7-3-1 Hongo, Bunkyo-ku, Tokyo 113-0033, Japan

[78] Canadian Institute for Theoretical Astrophysics, University of Toronto, 60 St. George Street, Toronto, ON M5S 3H8, Canada
[79] Dunlap Institute for Astronomy and Astrophysics, University of Toronto, 50 St. George Street, Toronto, ON M5S 3H4, Canada
[80] Canadian Institute for Advanced Research, 180 Dundas St West, Toronto, ON M5G 1Z8, Canada
[81] Radio Astronomy Laboratory, University of California, Berkeley, CA 94720, USA
[82] CCS-2, Los Alamos National Laboratory, P.O. Box 1663, Los Alamos, NM 87545, USA
[83] Center for Theoretical Astrophysics, Los Alamos National Laboratory, Los Alamos, NM, 87545, USA
[84] Instituto de Radioastronomía Milimétrica, IRAM, Avenida Divina Pastora 7, Local 20, E-18012, Granada, Spain
[85] Consejo Nacional de Ciencia y Tecnología, Av. Insurgentes Sur 1582, 03940, Ciudad de México, México
[86] Hiroshima Astrophysical Science Center, Hiroshima University, 1-3-1 Kagamiyama, Higashi-Hiroshima, Hiroshima 739-8526, Japan
[87] Aalto University Department of Electronics and Nanoengineering, PL 15500, FI-00076 Aalto, Finland
[88] Aalto University Metsähovi Radio Observatory, Metsähovintie 114, FI-02540 Kylmälä, Finland
[89] Department of Astronomy, Yonsei University, Yonsei-ro 50, Seodaemun-gu, 03722 Seoul, Republic of Korea
[90] Netherlands Organisation for Scientific Research (NWO), Postbus 93138, 2509 AC Den Haag , The Netherlands
[91] Frontier Research Institute for Interdisciplinary Sciences, Tohoku University, Sendai 980-8578, Japan
[92] Astronomical Institute, Tohoku University, Sendai 980-8578, Japan
[93] Department of Physics and Astronomy, Seoul National University, Gwanak-gu, Seoul 08826, Republic of Korea
[94] Leiden Observatory, Leiden University, Postbus 2300, 9513 RA Leiden, The Netherlands
[95] Physics Department, Brandeis University, 415 South Street, Waltham, MA 02453, USA
[96] School of Physics, Huazhong University of Science and Technology, Wuhan, Hubei, 430074, People's Republic of China
[97] Mullard Space Science Laboratory, University College London, Holmbury St. Mary, Dorking, Surrey, RH5 6NT, UK
[98] School of Astronomy and Space Sciences, University of Chinese Academy of Sciences, No. 19A Yuquan Road, Beijing 100049, People's Republic of China
[99] Astronomy Department, University of Science and Technology of China, Hefei 230026, People's Republic of China
[100] Department of Physics, Faculty of Science, University of Malaya, 50603 Kuala Lumpur, Malaysia
[101] University of Vermont, Burlington, VT 05405, USA
[102] National Radio Astronomy Observatory, NRAO Technology Center, 1180 Boxwood Estate Road, Charlottesville, VA 22903, USA
[103] Department of Physics, Villanova University, 800 E. Lancaster Ave, Villanova, PA, 19085, USA
[104] Kavli Institute for Astrophysics and Space Research, Massachusetts Institute of Technology, Cambridge, MA 02139, USA
[105] Instituto Nacional de Astrofísica, Óptica y Electrónica, Luis Enrique Erro 1, Tonantzintla, Puebla, C.P. 72840, Mexico
[106] Consejo Nacional de Ciencia y Tecnología, Av. Insurgentes Sur 1582, Col. Crédito Constructor, CDMX, C.P. 03940, Mexico
[107] National Chung-Shan Institute of Science and Technology, No.566, Ln. 134, Longyuan Rd., Longtan Dist., Taoyuan City 325, Taiwan, R.O.C.
[108] MIT Haystack Observatory, 99 Millstone Road, Westford, MA 01886, USA
[109] Dept. of Astronomy, Univ. of California Berkeley, 501 Campbell, Berkeley, CA 94720, USA
[110] Physikalisches Institut der Universität zu Köln, Zülpicher Str. 77, D-50937 Köln, Germany
[111] CASA, Department of Astrophysical and Planetary Sciences, University of Colorado, Boulder, CO 80309, USA
[112] Western University, 1151 Richmond Street, London, Ontario, N6A 3K7, Canada
[113] University of Massachusetts Boston, 100 William T, Morrissey Blvd, Boston, MA 02125, USA
[114] Research and Development Weather and Climate Models, Royal Netherlands Meteorological Institute, Utrechtseweg 297, 3731 GA, De Bilt, The Netherlands
[115] Department of Physics, McGill University, 3600 University Street, Montréal, QC H3A 2T8, Canada
[116] McGill Space Institute, McGill University, 3550 University Street, Montréal, QC H3A 2A7, Canada
[117] CIFAR Azrieli Global Scholar, Gravity & the Extreme Universe Program, Canadian Institute for Advanced Research, 661 University Avenue, Suite 505, Toronto, ON M5G 1M1, Canada
[118] Department of Astrophysical and Planetary Sciences and Department of Physics, University of Colorado, Boulder, CO 80309, USA
[119] High Energy Physics Division, Argonne National Laboratory, 9700 S. Cass Avenue, Argonne, IL, 60439, USA
[120] IRAP, Université de Toulouse, CNRS, UPS, CNES, Toulouse, France
[121] European Southern Observatory, Alonso de Córdova 3107, Vitacura, Casilla 19001, Santiago de Chile, Chile
[122] ASIAA Hilo Office, 645 N. A'ohoku Place, University Park, Hilo, HI 96720, USA
[123] Square Kilometre Array Organisation, Jodrell Bank Observatory, Lower Withington, Macclesfield, Cheshire SK11 9DL, UK
[124] Department of Physics, Ulsan National Institute of Science and Technology, Ulsan, 44919, Republic of Korea
[125] National Radio Astronomy Observatory, P.O. Box O, Socorro, NM 87801, USA
[126] Joint ALMA Observatory, Alonso de Córdova 3107, Vitacura 763-0355, Santiago de Chile, Chile
[127] ASTRON, Oude Hoogeveensedijk 4, 7991 PD Dwingeloo, The Netherlands
[128] Science Support Office, Directorate of Science, European Space Research and Technology Centre (ESA/ESTEC), Keplerlaan 1, 2201 AZ Noordwijk, The Netherlands
[129] University of Chicago, 5640 South Ellis Avenue, Chicago, IL 60637, USA
[130] Center for Detectors, School of Physics and Astronomy, Rochester Institute of Technology, 1 Lomb Memorial Drive, Rochester, NY 14623, USA
[131] Physics Dept., CB 1105, Washington University, One Brookings Drive, St. Louis, MO 63130-4899, USA
[132] Osaka Prefecture University, Gakuencyou Sakai Osaka, Sakai 599-8531, Kinki, Japan
[133] Mizusawa VLBI Observatory, National Astronomical Observatory of Japan, Ohshu, Iwate 023-0861, Japan
[134] Systems & Technology Research, 600 West Cummings Park, Woburn, MA 01801, USA
[135] Fermi National Accelerator Laboratory, PO Box 500, Batavia, IL 60510, USA
[136] Department of Astrophysical Sciences, Princeton University, Princeton, NJ 08544, USA
[137] MERLAB, 357 S. Candler St., Decatur, GA 30030, USA
[138] GWW School of Mechanical Engineering, Georgia Institute of Technology, 771 Ferst Dr., Atlanta, GA 30332, USA
[139] Kavli Institute for Particle Astrophysics and Cosmology, Stanford University, 452 Lomita Mall, Stanford, CA 94305, USA
[140] Dept. of Physics and Astronomy, UCLA, Los Angeles, CA 90095, USA
[141] Owens Valley Radio Observatory, California Institute of Technology, Big Pine, CA 93513, USA
[142] Dept. of Astronomy, Radio Astronomy Laboratory, Univ. of California Berkeley, 601 Campbell, Berkeley, CA 94720, USA
[143] Universidad de las Américas Puebla, Sta. Catarina Mártir S/N, San Andrés Cholula, Puebla, C.P. 72810, Mexico
[144] Deceased.

The Astrophysical Journal Letters, 875:L2 (28pp), 2019 April 10 https://doi.org/10.3847/2041-8213/ab0c96
© 2019. The American Astronomical Society.
OPEN ACCESS

First M87 Event Horizon Telescope Results. II. Array and Instrumentation

The Event Horizon Telescope Collaboration
(See the end matter for the full list of authors.)
Received 2019 February 11; revised 2019 March 5; accepted 2019 March 5; published 2019 April 10

Abstract

The Event Horizon Telescope (EHT) is a very long baseline interferometry (VLBI) array that comprises millimeter- and submillimeter-wavelength telescopes separated by distances comparable to the diameter of the Earth. At a nominal operating wavelength of ∼1.3 mm, EHT angular resolution (λ/D) is ∼25 μas, which is sufficient to resolve nearby supermassive black hole candidates on spatial and temporal scales that correspond to their event horizons. With this capability, the EHT scientific goals are to probe general relativistic effects in the strong-field regime and to study accretion and relativistic jet formation near the black hole boundary. In this Letter we describe the system design of the EHT, detail the technology and instrumentation that enable observations, and provide measures of its performance. Meeting the EHT science objectives has required several key developments that have facilitated the robust extension of the VLBI technique to EHT observing wavelengths and the production of instrumentation that can be deployed on a heterogeneous array of existing telescopes and facilities. To meet sensitivity requirements, high-bandwidth digital systems were developed that process data at rates of 64 gigabit s^{-1}, exceeding those of currently operating cm-wavelength VLBI arrays by more than an order of magnitude. Associated improvements include the development of phasing systems at array facilities, new receiver installation at several sites, and the deployment of hydrogen maser frequency standards to ensure coherent data capture across the array. These efforts led to the coordination and execution of the first Global EHT observations in 2017 April, and to event-horizon-scale imaging of the supermassive black hole candidate in M87.

Key words: black hole physics – galaxies: individual (M87) – Galaxy: center – gravitational lensing: strong – instrumentation: interferometers – techniques: high angular resolution

1. Introduction

It is generally accepted that active galactic nuclei (AGNs) are powered by accretion onto supermassive black holes (SMBHs; Heckman & Best 2014). These central engines are powerful actors on the cosmic stage, with roles in galactic evolution, star formation, mergers, and particle acceleration as evidenced by relativistic jets that both dynamically influence and redistribute matter on galactic scales (Blandford et al. 2018). Inflowing material typically obscures the event horizons of these black hole candidates, but it is in this extreme environment of the black hole boundary that strong-field effects of general relativity become evident and the accretion and outflow processes that govern black hole feedback on galactic scales originate (Ho 2008). Imaging black holes on scales that resolve these effects and processes would enable new tests of general relativity and the extraordinarily detailed study of core AGN physics. Realization of this goal requires a specialized instrument that does two things. It must have the ultra-high angular resolution required to resolve the nearest SMBH candidates, and it must operate in a range of the electromagnetic spectrum where light streams unimpeded from the innermost accretion region to telescopes on Earth. Achieving these specifications is the primary objective of the Event Horizon Telescope (EHT): a very long baseline interferometry (VLBI) array of millimeter (mm) and submillimeter (submm) wavelength facilities that span the globe, creating a telescope with an effective Earth-sized aperture (Doeleman et al. 2009a).

Original content from this work may be used under the terms of the Creative Commons Attribution 3.0 licence. Any further distribution of this work must maintain attribution to the author(s) and the title of the work, journal citation and DOI.

While the EHT is uniquely designed for the imaging of SMBHs, other pioneering instruments are capable of probing similar angular scales for other purposes. Operating in the infrared, the GRAVITY interferometer delivers relative astrometry at the ∼10 micro-arcsecond (μas) level and has provided evidence for relativistic motion of material in close proximity to Sgr A* (GRAVITY Collaboration et al. 2018a). These infrared observations are an important and parallel probe of the spacetime surrounding Sgr A*, but cannot be used to make spatially resolved images of the black hole candidate because the interferometer intrinsic resolution is only 3 mas. The RadioAstron satellite, used as an orbiting element of combined Earth-Space VLBI arrays, is also capable of ∼10 μas angular resolution (Kardashev et al. 2013), but it operates at longer radio wavelengths that cannot penetrate the self-absorbed synchrotron plasma that surrounds the event horizon. In many ways the EHT is complementary to the Laser Interferometer Gravitational-Wave Observatory (LIGO) facility, which has detected the gravitational wave signatures from merging stellar-mass black holes (Abbott et al. 2016). LIGO and the EHT observe black holes that differ in mass by factors of 10^4–10^7; LIGO events are transient, while the EHT carries out long-term studies of its main targets.

This Letter is one in a sequence of manuscripts that describes the first EHT results. The full sequence includes an abstract Letter with a summary of results (EHT Collaboration et al. 2019a, hereafter Paper I), this Letter with a description of the array and instrumentation (Paper II), a description of the data pipeline and processing (EHT Collaboration et al. 2019b, hereafter Paper III), a description of imaging techniques (EHT Collaboration et al. 2019c, hereafter Paper IV), and theoretical analyses of astrophysical and physics results (EHT

Collaboration et al. 2019d, hereafter Paper V; EHT Collaboration et al. 2019e, hereafter Paper VI, respectively).

1.1. EHT Science Goals

The scientific goals of the EHT array are to resolve and detect strong general relativistic signatures expected to arise on event-horizon scales. The best-known effect is that a black hole, surrounded by an optically thin luminous plasma, should exhibit a "silhouette" or "shadow" morphology: a dim central region delineated by the lensed photon orbit (Falcke et al. 2000). The apparent size of the photon orbit, described not long after Schwarzschild's initial solution was published (Hilbert 1917; von Laue 1921), defines a bright ring or crescent shape that was calculated for arbitrary spin by Bardeen (1973), first imaged through simulations by Luminet 1979, and subsequently studied extensively (Chandrasekhar 1983; Takahashi 2004; Broderick & Loeb 2006). The size and shape of the resulting shadow depends primarily on the mass of the black hole, and only very weakly on its spin and the observing orientation. For a non-spinning black hole, the shadow diameter is equal to $\sqrt{27}$ Schwarzschild radii ($R_s = 2GM/c^2$). Over all black hole spins and orientations, the shadow diameter ranges from 4.8 to 5.2 R_s (Bardeen 1973; Johannsen & Psaltis 2010). Because any light that crosses the photon orbit from outside will eventually reach the event horizon, use of the term "horizon scale" will hereafter be understood to mean the size of the shadow and the lensed photon orbit. Detection of the shadow via lensed electromagnetic radiation would provide new evidence for the existence of SMBHs by confining the masses of EHT targets to within their expected photon orbits. A more detailed study of the precise shape of the photon orbit can be used to test the validity of general relativity on horizon scales (Johannsen & Psaltis 2010). Full polarimetric imaging can similarly be used to map magnetic field structure near the event horizon, placing important constraints on modes of accretion and the launching of relativistic jets (Broderick & Loeb 2009; Johnson et al. 2015; Chael et al. 2016; Akiyama et al. 2017; Gold et al. 2017).

Separate signatures, potentially offering a more sensitive probe of black hole spin, are the timescales of dynamical processes at horizon scales. A characteristic timescale for such processes is given by the orbital period of test particles at the innermost stable circular orbit (ISCO), which depends sensitively on the black hole spin (Bardeen et al. 1972). Monitoring VLBI observables to track the orbital dynamics of inhomogeneities in the accretion flow can thus be used to probe the spacetime, and potentially spin, of the black hole (Broderick & Loeb 2006; Doeleman et al. 2009b; Fish et al. 2009; Fraga-Encinas et al. 2016; Medeiros et al. 2017; Roelofs et al. 2017).

1.2. Target Sources and Confirmation of Horizon-scale Structure

The bright radio core of M87 and Sgr A* (Table 1) are the primary EHT targets, as the combination of their estimated mass and proximity make them the two most suitable sources for studying SMBH candidates at horizon-scale resolution (Narayan & McClintock 2008; Johannsen et al. 2012). With bolometric luminosities well below the Eddington limit (Di Matteo et al. 2000; Baganoff et al. 2003), both the nucleus of M87 and Sgr A* are representative of the broad and populous class of low-luminosity AGN (LLAGN). AGN spend most of their time in this low state after prior periods of high accretion (Ho 2008), and LLAGN share many characteristics of stellar black hole emission in X-ray binaries, which exhibit episodic emission and jet production (Narayan & McClintock 2008). Thus, the prospects for applying results from horizon-scale observations of the central region of M87 and Sgr A* across a broad range of astrophysical contexts are excellent.

Within the past decade, VLBI observations at a wavelength of 1.3 mm have confirmed the existence of structure on the scale of the shadow in both the nucleus of M87 and Sgr A*. M87 (Virgo A) is thought to harbor a black hole in the range of 3.3–6.2 $\times$ 10^9 solar mass ($M_\odot$) (Gebhardt et al. 2011; Walsh et al. 2013), when scaled to a distance of 16.8 Mpc (Paper VI). Structure in M87 measuring 40 μas in extent has been resolved with 1.3 mm VLBI, corresponding to a total extent of $\sim$5.5 Schwarzschild radii at the upper end of the mass range (Doeleman et al. 2012; Akiyama et al. 2015). For Sgr A*, the black hole candidate at the Galactic center with a presumed mass of 4 $\times$ 10^6 $M_\odot$ (Balick & Brown 1974; Ghez et al. 2008; Genzel et al. 2010; GRAVITY Collaboration et al. 2018a), the 1.3 mm emission has been measured to have a size of 3.7 R_s (Doeleman et al. 2008; Fish et al. 2011). More recently, full polarimetric VLBI observations at 1.3 mm wavelength have revealed ordered and time-variable magnetic fields within Sgr A* on horizon scales (Johnson et al. 2015), and extension to longer baselines has confirmed compact structure on $\sim$3 R_s scales (Lu et al. 2018). These results, obtained with three- and four-site VLBI arrays consisting of the former Combined Array for Research in Millimeter-wave Astronomy (CARMA) in California, the Submillimeter Telescope (SMT) in Arizona, the James Clerk Maxwell Telescope (JCMT) and Submillimeter Array (SMA) facilities on Maunakea in Hawaii, and the Atacama Pathfinder Experiment (APEX) telescope in Chile, demonstrated that direct imaging of emission structures near the event horizon of SMBH candidates is possible in principle. For comparison and perspective, the closest approach of the orbiting stars used to determine the mass of Sgr A* is $\sim$1400 R_s (Gravity Collaboration et al. 2018b).

1.3. Array Architecture and Context

To realize these fundamental science goals, our international collaboration has engineered the EHT to move beyond the detection of horizon-scale structure and achieve the required imaging and time-domain sampling capability.

One of the key enabling technologies behind the EHT observations has been the development of high-bandwidth (wideband) VLBI systems that compensate to some degree for the generally smaller telescope apertures at millimeter and submillimeter wavelengths. The first detections of horizon-scale structure followed directly from deployment of new digital VLBI backend and recording instrumentation, custom-built for mm-wavelength observations that achieved a recording rate of 4 gigabit s^{-1} (Gbps)[136] (Doeleman et al. 2008). Continued development led to an increased recording rate of 16 Gbps (Whitney et al. 2013). Adoption of industry-standard high-speed data protocols, increased hard disk storage capacity,

[136] The bandwidth of an EHT observation is typically expressed as a recording rate in gigabit-per-second, or Gbps. The recording rate in Gbps is four times the recorded bandwidth in GHz, a factor of two coming from the need to take samples at a rate of twice the bandwidth (Nyquist rate), and another factor of two because each sample is 2 bits.

Table 1
Assumed Physical Properties of Sgr A* and M87 Used to Establish Technical Goals[a]

		Sgr A*	M87
Black Hole Mass	M ($M_\odot$)	4.1×10^6 (1)	$(3.3–6.2) \times 10^9$ (5), (6)
Distance	D (pc)	8.34×10^3 (2)	16.8×10^6 (7)
Schwarzschild Radius	R_s (μas)	9.7	3.9–7.3
Shadow Diameter[b]	D_{sh} (μas)	47–50	19–38
Brightness Temperature[c]	T_B (K)	3×10^9 (3)	10^{10} (8)
Period ISCO[d]	P_{ISCO}	4–54 minutes	2.4–57.7 days
Mass Accretion Rate[e]	$\dot{M}$ ($M_\odot$ yr^{-1})	10^{-9}–10^{-7} (4)	$<10^{-3}$ (9)

Notes.
[a] Sgr A*: $\alpha_{J2000.0} = 17^h45^m40^s.0409$, $\delta_{J2000.0} = -29°00'28''.118$ (10); M87: $\alpha_{J2000.0} = 12^h30^m49^s.4234$, $\delta_{J2000.0} = 12°23'28''.044$ (11).
[b] The shadow diameter is within the range 4.8–5.2 R_s depending on black hole spin and orientation to the observer's line of sight (Johannsen & Psaltis 2010).
[c] Brightness temperatures are reported for an observing frequency of 230 GHz.
[d] P_{ISCO} range is given in the case of maximum spin for both prograde (shortest) and retrograde (longest) orbits (Bardeen et al. 1972).
[e] Mass accretion rates $\dot{M}$ are estimated from measurements of Faraday rotation imparted by material in the accretion flow around the black hole.
References. (1) GRAVITY Collaboration et al. (2018a), (2) Reid et al. (2014), (3) Lu et al. (2018), (4) Marrone et al. (2007), (5) Walsh et al. (2013), (6) Gebhardt et al. (2011), (7) Blakeslee et al. (2009), EHT Collaboration et al. (2019e), (8) Akiyama et al. (2015), (9) Kuo et al. (2014), (10) Reid & Brunthaler (2004), (11) Lambert & Gontier (2009).

and flexible field programmable gate array (FPGA) computational fabric have enabled the EHT to reach data throughputs of 64 Gbps (Vertatschitsch et al. 2015), or 32 times the maximum recording rate and corresponding bandwidth, offered by open access VLBI facilities at longer wavelengths (e.g., the NRAO Very Long Baseline Array; Napier et al. 1994).

In addition to the increased sensitivity provided by such large data recording rates, several factors, some engineered and some serendipitous, have converged to enable spatially and temporally resolved observations of black hole candidates by the EHT. By temporal resolution we mean that increased resolution, sensitivity, and baseline coverage allows the EHT to detect and spatially resolve horizon-scale time-variable structures, which would otherwise only be studied through light-curve analysis and light-crossing time assumptions. A list of the key enabling factors is as follows.

1. *Angular resolution*: the angular resolution of Earth-diameter VLBI baselines at wavelengths of ∼1.3 mm can resolve the lensed photon orbits of Sgr A* and M87 (Table 1: about 50 μas and 38 μas, respectively).
2. *Fourier coverage*: using Earth-rotation aperture synthesis, the number of existing and planned mm/submm wavelength telescopes provides a sufficient sampling of VLBI baseline lengths and orientations to produce images with horizon-scale resolution (Fish et al. 2014; Honma et al. 2014; Lu et al. 2014; Ricarte & Dexter 2015; Bouman et al. 2016; Chael et al. 2016).
3. *Atmospheric transparency*: at the required mm/submm observing wavelengths, the Earth's atmosphere at high-altitude sites is reliably transparent enough that global VLBI arrays can be formed for long-duration observations (Thompson et al. 2017).
4. *Optically thin accretion*: for both Sgr A* and M87 the spectral energy density of the accretion flow begins to turn over at mm wavelengths, allowing photons from deep within the gravitational potential well to escape, presuming a synchrotron emission mechanism (see Broderick & Loeb 2009; Genzel et al. 2010, for M87 and Sgr A*, respectively).
5. *Interstellar scattering*: radio images of Sgr A* are blurred due to interstellar scattering by free electrons (Lo et al. 1998; Shen et al. 2005; Bower et al. 2006; Lu et al. 2011; Bower et al. 2015; Johnson et al. 2018; Psaltis et al. 2018). This blurring decreases with wavelength as λ^2 and becomes sub-dominant for wavelengths of ∼1.3 mm and shorter, where observations enable direct access to intrinsic structures in close proximity to the event horizon (Doeleman et al. 2008; Issaoun et al. 2019).

1.4. Current EHT Array

Figure 1 shows a map of the EHT array. In 2017 April, the EHT carried out global observations with an array of eight telescopes (see Table 2) that included the Atacama Large Millimeter/submillimeter Array (ALMA) for the first time. A purpose-built system electronically combined the collecting area of ∼37 × 12 m diameter ALMA dishes (see Appendix A.1): the equivalent of adding a ∼70 m dish to the EHT array. Other participating telescopes were APEX, JCMT, SMA, SMT, the Large Millimeter Telescope Alfonso Serrano (LMT), the Pico Veleta 30 m telescope (PV), and the South Pole Telescope (SPT). Operating in the 1.3 mm window in full polarimetric mode and with an aggregate bandwidth of 8 GHz, the resulting increase in sensitivity above the first horizon-scale detections was nearly an order of magnitude (e.g., Section 3.8). For observations with phased-ALMA in 2018, the EHT added an additional facility (the 12 m diameter Greenland Telescope (GLT)) and doubled the aggregate bandwidth to its nominal target of 16 GHz.

The sections that follow describe the specifications and characteristics of the array (Section 2), the EHT instrumentation deployed (Section 3), the observing strategy (Section 4), correlation, calibration, and detection (Section 5), and future enhancements (Section 6).

2. EHT Specifications and Characteristics

Extending the VLBI technique to wavelengths of ∼1.3 mm presents technical challenges. Heterodyne receivers exhibit

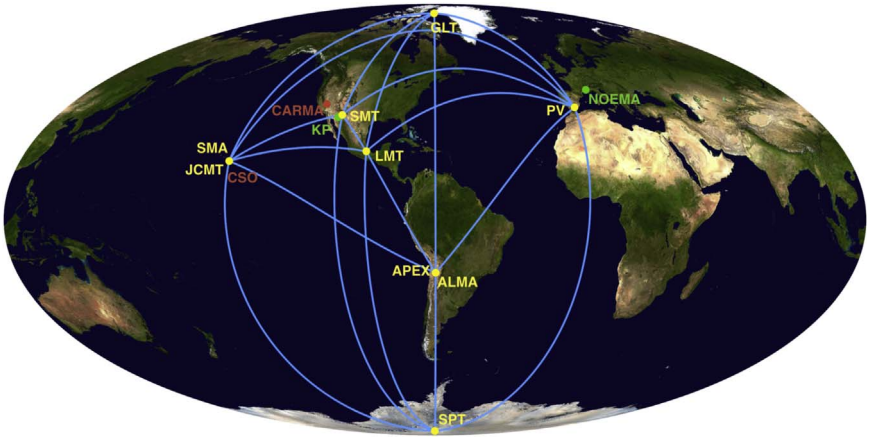

Figure 1. Map of the EHT. Stations active in 2017 and 2018 are shown with connecting lines and labeled in yellow, sites in commission are labeled in green, and legacy sites are labeled in red. Nearly redundant baselines are overlaying each other, i.e., to ALMA/APEX and SMA/JCMT. Such redundancy allows improvement in determining the amplitude calibration of the array (Paper III).

Table 2
EHT Station Information

Facility	Diameter (m)	Location	X[a] (m)	Y[a] (m)	Z[a] (m)	Latitude	Longitude	Elevation[a] (m)
Facilities that Participated in the 2017 Observations								
ALMA[b]	12 (×54) and 7 (×12)	Chile	2225061.3	−5440061.7	−2481681.2	−23°01′45.″1	−67°45′17.″1	5074.1
APEX	12	Chile	2225039.5	−5441197.6	−2479303.4	−23°00′20.″8	−67°45′32.″9	5104.5
JCMT	15	Hawaii, USA	−5464584.7	−2493001.2	2150654.0	+19°49′22.″2	−155°28′37.″3	4120.1
LMT	50	Mexico	−768715.6	−5988507.1	2063354.9	+18°59′08.″8	−97°18′53.″2	4593.3
PV 30 m	30	Spain	5088967.8	−301681.2	3825012.2	+37°03′58.″1	−3°23′33.″4	2919.5
SMA[b]	6 (×8)	Hawaii, USA	−5464555.5	−2492928.0	2150797.2	+19°49′27.″2	−155°28′39.″1	4115.1
SMT	10	Arizona, USA	−1828796.2	−5054406.8	3427865.2	+32°42′05.″8	−109°53′28.″5	3158.7
SPT[c]	10	Antarctica	809.8	−816.9	−6359568.7	−89°59′22.″9	−45°15′00.″3	2816.5
Facilities Joining EHT Observations in 2018 and Later								
GLT	12	Greenland	541547.0	−1387978.6	6180982.0	+76°32′06.″6	−68°41′08.″8	89.4
NOEMA[d]	15 (×12)	France	4524000.4	468042.1	4460309.8	+44°38′01.″2	+5°54′24.″0	2617.6
KP 12 m[d]	12	Arizona, USA	−1995954.4	−5037389.4	3357044.3	+31°57′12.″0	−111°36′53.″5	1894.5
Facilities Formerly Participating in EHT Observations								
CARMA	10.4, 6.1 (×8)	California, USA	−2397378.6	−4482048.7	3843513.2	+37°16′49.″4	−118°08′29.″9	2168.9
CSO	10	Hawaii, USA	−5464520.9	−2493145.6	2150610.6	+19°49′20.″9	−155°28′31.″9	4107.2

Notes.
[a] Geocentric coordinates with X pointing to the Greenwich meridian, Y pointing 90° away in the equatorial plane (eastern longitudes have positive Y), and positive Z pointing in the direction of the North Pole. This is a left-handed coordinate system. Elevations are relative to the GRS 80 ellipsoid (Moritz 2000).
[b] Array coordinates indicate the phasing center used in 2017.
[c] 2017 April position: the ice sheet at the South Pole moves at a rate of about 10 m yr^{-1}. Effects of this slow drift are removed during VLBI correlation.
[d] NOEMA: Northern Extended Millimeter Array; KP 12 m: Kitt Peak 12 m. These stations have not participated in global EHT observations and their coordinates are approximate.

greater noise, and the required stability of atomic frequency standards is higher than that typically specified for VLBI at longer wavelengths. Early ∼1.3 mm wavelength VLBI experiments and observations in the 1990s succeeded in making first detections of AGNs and Sgr A* on modest-length baselines (⩽1100 km; Padin et al. 1990; Greve et al. 1995; Krichbaum et al. 1998). Following this pioneering work (see Doeleman & Krichbaum 1999; Boccardi et al. 2017, for summaries), ∼1.3 mm VLBI efforts over the next decade focused on order-of-magnitude bandwidth expansion as a means to boost sensitivity. This development led to observations in 2007 with enough resolution to resolve emission on the scale of the event horizon of Sgr A* by using a three-station array with telescopes in Hawaii, California, and Arizona. Motivated by this detection, an EHT array capable of imaging strong general relativistic features was planned based on organizing coordinated observations on a network of mm-wavelength observatories (Doeleman et al. 2009a). These sites and their general characteristics are given in Table 2, which lists current and planned EHT sites as well as now-

decommissioned observatories used in prior experiments. For the most part, the EHT consists of pre-existing telescopes that perform single-dish or connected-element astronomy observations during most of the year, but which required modifications or upgrades (in some cases significant ones) to carry out VLBI. The GLT, for example, was commissioned primarily to image M87 (Inoue et al. 2014), and a heterodyne receiver for the SPT was built specifically for EHT observations (Kim et al. 2018a). Details of how each site was modified for EHT work are given in the Appendix.

Technical specifications for the EHT were adopted to unify VLBI recordings across the heterogeneous array by establishing a common frequency configuration, polarization configuration, and sampling rate (Tilanus et al. 2013; Marrone et al. 2014). When ALMA participates in EHT observations, it is by far the most sensitive site, so the overall sensitivity of the EHT array is optimized on a per-bandwidth basis when all other sites can match the recorded frequency bands at ALMA. The EHT converged on a scheme that matches ALMA specifications: two 4 GHz sidebands in each of two polarizations for the 1.3 and 0.87 mm receiver bands, which could be realized through feasible modifications and enhancements at most sites. The resulting global array geometry and sensitivity is well matched to the science goals.

2.1. Angular Resolution

Imaging a black hole shadow requires several resolution elements in each direction across the lensed innermost photon orbit, in addition to field-of-view coverage that extends beyond the feature. The longest baselines of the EHT (e.g., South Pole to Arizona, Hawaii, or Spain) provide nominal angular resolutions of $\lambda/D \simeq 25$ μas in the 1.3 mm wavelength band. Regularized maximum likelihood (RML) imaging methods (see Paper IV) typically achieve angular resolutions that are better than the nominal figure by factors of 2–3 (Narayan & Nityananda 1986). For the EHT case in particular, RML methods have been extensively tested using realistic and synthetic interferometric data to set the optimal resolution of the array (Honma et al. 2014; Bouman et al. 2016; Chael et al. 2016; Akiyama et al. 2017; Chael et al. 2018; Kuramochi et al. 2018). This results in an anticipated effective EHT angular resolution at 1.3 mm of 20 μas, yielding between about 36 resolution elements across a 120 × 120 μas field of view. For Sgr A* and M87 this field of view is expected to encompass the dim interior, bright annulus of the photon orbit, and sufficient spatial extent to extract the shadow feature (e.g., Mościbrodzka et al. 2009; Dexter et al. 2010). These considerations, and the expectation based on simulations that the EHT instrument and array could achieve such resolution, were important factors in specifying the EHT architecture. Further tests using EHT observations of quasar calibrator sources (e.g., 3C 279) obtained in the 2017 April observations demonstrate robust structural agreement between RML methods and more traditional CLEAN-based radio imaging techniques. Similar comparisons and results on M87, one of the EHT primary targets, can be found in Paper IV.

2.2. Sensitivity

Maximizing detections across sparse Fourier coverage is essential for high-fidelity image reconstruction. This is especially true for Sgr A* because its structure is scatter broadened by interstellar effects resulting in reduced VLBI visibility amplitudes on the longest baselines.

To maximize the number of interferometric detections across the array, the EHT uses a two-stage approach to fringe detection. First, detections are found on baselines from all stations to ALMA within the atmospheric coherence time. Next, these ALMA detections are used to remove the effects of phase fluctuations (due to atmospheric turbulence) above the non-ALMA stations, allowing coherent integration on non-ALMA baselines for intervals up to many minutes, thereby boosting the signal-to-noise ratio (S/N) to recover the full baseline coverage of the array (Paper III). Thus, the EHT sensitivity specification corresponds to the requirement that for baselines connecting each EHT site to ALMA, Sgr A* and M87 are detected with a typical signal-to-noise that enables this atmospheric phase correction with acceptable loss. In the usual case where the VLBI observing scan duration greatly exceeds the atmospheric coherence time, the loss due to noise in the phase-correction algorithm is $\sim e^{-(\mathrm{S/N})^2/2}$, where the S/N is the signal-to-noise on the ALMA baselines. To ensure negligible loss, we specify $\mathrm{S/N} > 3$ for EHT baselines to ALMA within an integration time, T_{int}, where T_{int} is less than the atmospheric coherence time. We note that the expected change in interferometric phase due to source structure over the imaged field of view (Section 2.1) would be less than a few degrees over typical VLBI scan lengths of a few minutes.

The S/N of a VLBI signal on a single baseline between stations is

$$\mathrm{S/N}_{(1,2)} = \frac{\eta_Q \sqrt{2\Delta\nu T_{\mathrm{int}}}\ S_{\mathrm{cor}}}{\sqrt{\mathrm{SEFD}_1\ \mathrm{SEFD}_2}} \tag{1}$$

where η_Q is the digital loss due to sampling the received signal at each antenna with finite precision ($\eta_Q = 0.88$ for 2-bit samples), $\Delta\nu$ is the bandwidth of the recording, SEFD_i is the system equivalent flux density (SEFD)[137] for station i, and S_{cor} is the expected correlated flux on the baseline between stations 1 and 2. T_{int} is the integration interval of the VLBI signal. It is typically much less than the atmospheric coherence time (T_{coh}), or the coherent integration time beyond which the VLBI visibility[138] signal decreases by 10 % due to phase fluctuations imposed by turbulence in the troposphere (typically from a few to ~20 s). On the weakest baseline involving ALMA, ALMA–SPT, with an estimated flux for Sgr A* of 0.1 Jy (see APEX-CARMA baseline in Lu et al. 2018) and with $\Delta\nu = 4$ GHz, an integration time of 3 s yields an S/N of about 12 (see Table 3 for parameters), which far exceeds the EHT S/N specification for detections on ALMA baselines. Figure 2 shows that more than 75% of scans on baselines in the 2017 array that include ALMA had T_{coh} greater than 10 s.

2.3. Fourier Coverage

An interferometer like the EHT samples the Fourier transform of the image on the sky. By correlating the data obtained from N stations, $N(N-1)/2$ spatial frequencies are measured.

[137] The SEFD of a radio telescope is the total system noise represented in units of equivalent incident flux density above the atmosphere (see Paper III, Equation (3)).

[138] The visibility is the complex two-point correlation of the electric field measured on a VLBI baseline (see Thompson et al. 2017, Chapter 1).

Table 3
EHT Station Sensitivities

Facility	Effective Diameter (m)	Aperture Efficiency (η_A)	Median Effective System Temperature (K)[a]	Median $SEFD_{1.3}$ (Jy)[a]	$\sigma_{rms-ALMA}$ (mJy)[b]
Facilities that Participated in the 2017 Observations, Showing Representative Values					
ALMA37[c]	73	0.68	76	74	⋯
APEX	12	0.61	118	4700	2.4
JCMT	15	0.52	345	10,500	3.5
LMT[d]	32.5	0.28	371	4500	2.3
PV 30 m	30	0.47	226	1900	1.5
SMA6[c]	14.7	0.75	285	6200	2.7
SMT	10	0.60	291	17,100	4.5
SPT[d]	6	0.60	118	19,300	4.8
Facilities Joining EHT Observations in 2018 and Later, Using Estimated Values					
GLT	12	0.58	120	5000	2.4
NOEMA	52	0.50	270	700	0.9
KP 12 m	12	0.59	310	13,000	3.9

Notes.
[a] $SEFD = 2kT^*_{sys}/\eta_A A_{geom}$ with T^*_{sys} the effective system temperature and A_{geom} the geometric collecting area of the telescope. The effective system temperature lists representative values for the 2017 Sgr A* and M87 observations, i.e., for median elevations of the sources and typical atmospheric opacities at each facility. It includes effects from elevation-dependent gains and phasing efficiency relevant for some of the telescopes.
[b] With $\sigma_{rms\text{-}ALMA}$ the thermal noise for the station's baseline with ALMA using Equation (1) for a bandwidth of 4 GHz and integration time of 10 s (see Figure 2).
[c] The median number of phased antennas in 2017 for the SMA was 6 × 6 m antennas and for ALMA was 37 × 12 m antennas. If all ALMA antennas are phased that would be equivalent to a single 88 m antenna.
[d] The LMT was upgraded from 32.5 m to a full 50 m diameter telescope in early 2018. At SPT the aperture was under-illuminated in 2017 with an effective diameter of 6 m.

As the Earth rotates, those spatial frequencies form tracks in the Fourier plane (i.e., the (u, v) plane) to produce a sparsely sampled Fourier transform of the sky image. With the sensitivity requirements established, one can estimate the baseline coverage that results after the two-stage detection process above (Section 2.2) is followed. Figure 3 shows that the measured spatial frequencies that satisfy the EHT signal-to-noise specification when ALMA is included in the array result in near-full coverage on all baselines in the array, thereby maximizing imaging potential. At the outset of EHT build-out, this full coverage goal served as a design goal based on imaging simulations of synthetic data (see Section 2.1). Subsequent observations in 2017 April confirm that this (u, v) coverage is sufficient to image horizon-scale features (Paper IV).

2.4. Time Resolution

Characteristic timescales that affect the evolution of structures in horizon-scale images include the light-crossing time ($T_{light} = GM/c^3$) and the period of the ISCO (P_{ISCO}), both of which scale with mass. With an assumed mass of $4.1 \times 10^6 M_\odot$ for Sgr A*, $T_{light} = 20$ s and P_{ISCO} ranges from 4 minutes for a prograde orbit around a maximally spinning black hole to 54 minutes for a retrograde orbit around a maximally spinning black hole. If a mass of $6.2 \times 10^9 M_\odot$ is assumed for M87, $T_{light} = 8.5$ h and P_{ISCO} ranges from 4.5 to 58 days for the same orbits. All of these timescales, while important for imaging and modeling time-variable structures, far exceed the coherence times of the atmosphere, which set the integration intervals and sensitivity requirements for the EHT. Hence, the EHT must already track VLBI observables on considerably finer timescales than T_{light} or P_{ISCO} for the primary cosmic targets, M87 and Sgr A*.

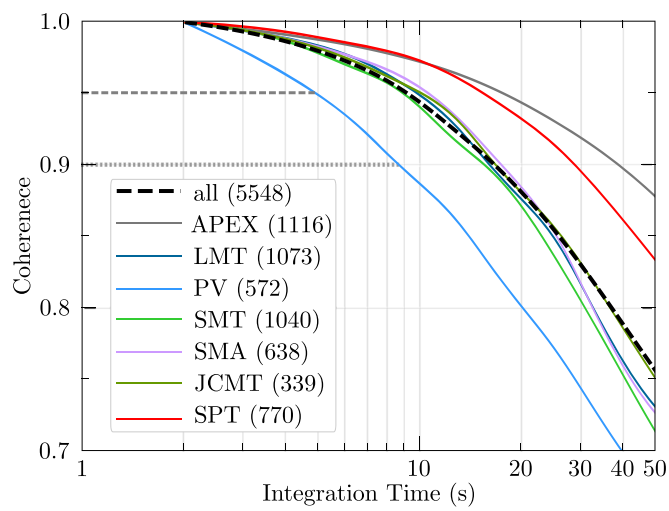

Figure 2. Atmospheric coherence time for EHT ALMA baselines. VLBI observations consist of scans, each ∼3–7 minutes long (see Figure 12). Each scan in the 2017 EHT observation campaign was divided into sequential coherent integration intervals, which were then incoherently averaged to obtain an estimate of VLBI signal amplitude per scan. As the duration of the coherent interval decreases, the loss in amplitude due to atmospheric phase fluctuations decreases. Solid lines represent the 25th percentile of the coherence distribution for each baseline: 75% of the data exhibit higher time coherence than indicated by the line. The heavy black dashed line shows the 25th percentile of the coherence distribution for all baselines. The light dashed and dotted lines show the 95 % and 90 % coherence limits for the baseline with lowest coherence, which is from PV to ALMA (largely due to low-elevation PV scans on Sgr A* during the observations). The number of scans used to compute the coherence curves are shown next to each station in parenthesis.

2.5. Frequency Configuration

The instrumentation at EHT sites is designed to match ALMA's bandwidth and intermediate frequency (IF) ranges.

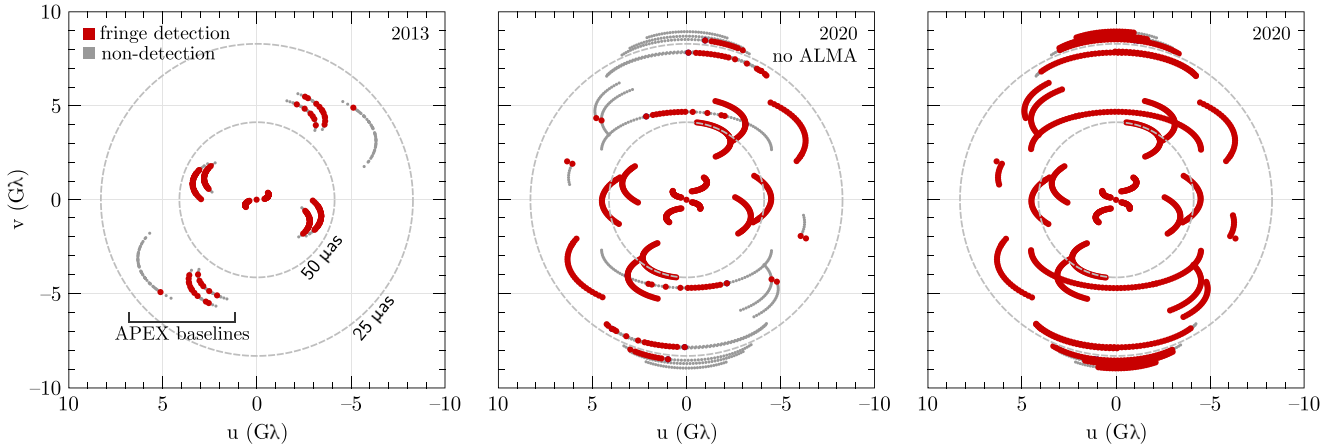

Figure 3. Expected EHT Fourier space coverage on Sgr A*. The left panel shows both detections (red) and non-detections (gray) of Sgr A* in the 2013 EHT campaign. Participating telescopes were: APEX, CARMA, JCMT, SMA, and SMT. The dashed circles mark baselines with a fringe spacing equal to 50 μas (approximately the diameter of the shadow of the SMBH candidate Sgr A*) and 25 μas. The two remaining panels show simulated EHT observations in 2020: (1) without ALMA and (2) with ALMA. Specifications to determine baseline detections shown are those detailed in Section 2.2. These figures emphasize the benefit of including ALMA in the array: its high sensitivity allows detections for SgrA* on all observed baselines. Because each EHT site requires at least one strong baseline to identify an interferometric fringe and to correct for residual delays, rates, and phase wander, ALMA significantly extends the Fourier coverage and sensitivity even for non-ALMA baselines. Coverage shown in the two right panels corresponds to an array including Chile (APEX, ALMA), Mexico (LMT), France (NOEMA), Spain (PV), Hawaii (SMA, JCMT), Arizona (SMT), and South Pole (SPT). The corresponding baseline coverage of the 2017 observations is shown in Figure 11.

Table 4
EHT Frequency Configurations

	230 GHz Band 1SB	230 GHz Band 2SB	345 GHz Band 2SB
Nominal Wavelength	1.3 mm	1.3 mm	0.87 mm
Lower-sideband Sky Freq. Range (GHz)	unused	212.1–216.1	334.6–338.6
Upper-sideband Sky Freqs. Range (GHz)	226.1–230.1	226.1–230.1	346.6–350.6
Local Oscillator (GHz)	221.1	221.1	342.6
Intermediate Frequency Range (GHz)	station dependent	5–9	4–8
Recording Rate (Gbps)	32	64	64
Year of First Use	2017	2018	>2020

ALMA antennas are equipped with dual-polarization, sideband-separating receivers with four IF outputs (Section 3.1). The total bandwidth that can be transported back from each ALMA antenna is 16 GHz, thus resulting in a maximum IF bandwidth of 4 GHz per output. The sky frequencies for both the lower- and upper-sideband must overlap perfectly from station to station, which fixes both the local oscillator (LO) frequency and IF frequency ranges at each observatory (Tilanus et al. 2013). Table 4 shows the frequency configurations of the EHT in both atmospheric transmission windows around 230 and 345 GHz.

The main considerations for selecting the chosen LO frequencies are (Marrone et al. 2014) as follows.

1. The tuning range of the receivers at participating facilities.
2. Atmospheric transmission.
3. The avoidance of Galactic ^{12}CO: $\nu \sim$ 230.3–230.8 GHz and $\nu \sim$ 345.4–346.1 GHz within the VLBI observing bands.
4. To a lesser degree: avoidance of Galactic ^{13}CO: $\nu \sim$ 220.2–220.6 GHz and $\nu \sim$ 330.3–330.9 GHz within the VLBI observing bands.
5. Access to ^{12}CO spectral lines in an extended tuning range of the receivers above 9 GHz when observing in the 1.3 mm band, or below 4 GHz when observing in the 0.87 mm band.
6. Access to maser lines within the VLBI band, e.g., the SiO maser line at 215.596 GHz ($v = 1,\ J = 5 \rightarrow 4$).
7. Performance of existing quarter-wave plates used to observe circular polarization.

For ALMA's 230 GHz band, the IF band previously was restricted to a lower limit of 5 GHz (now 4.5 GHz), which resulted in a common IF range across the telescopes of 5–9 GHz, whereas the common IF range for the 345 GHz band is 4–8 GHz.

3. Instrumentation

A schematic of the EHT's VLBI signal chain at single-dish telescopes is shown in Figure 4. The front end is typically a dual-polarization sideband-separating receiver in the 1.3 mm or 0.87 mm bands, often the product of a joint development project between the EHT and the telescope facility. These efforts are described in the Appendix. A hydrogen maser provides a frequency reference standard of sufficient stability for mm-VLBI (Section 3.2), and is used to phase lock all analog systems as well as digital sampling clocks throughout the signal chain.

Dedicated block downconverters (BDCs; Section 3.3) mix IF bands coming from the receivers to baseband. Each 4 GHz wide IF band is split and downconverted into two 2 GHz wide sections at baseband. High-bandwidth digital backends (DBEs; Section 3.4) are used to sample two 2 GHz baseband signals

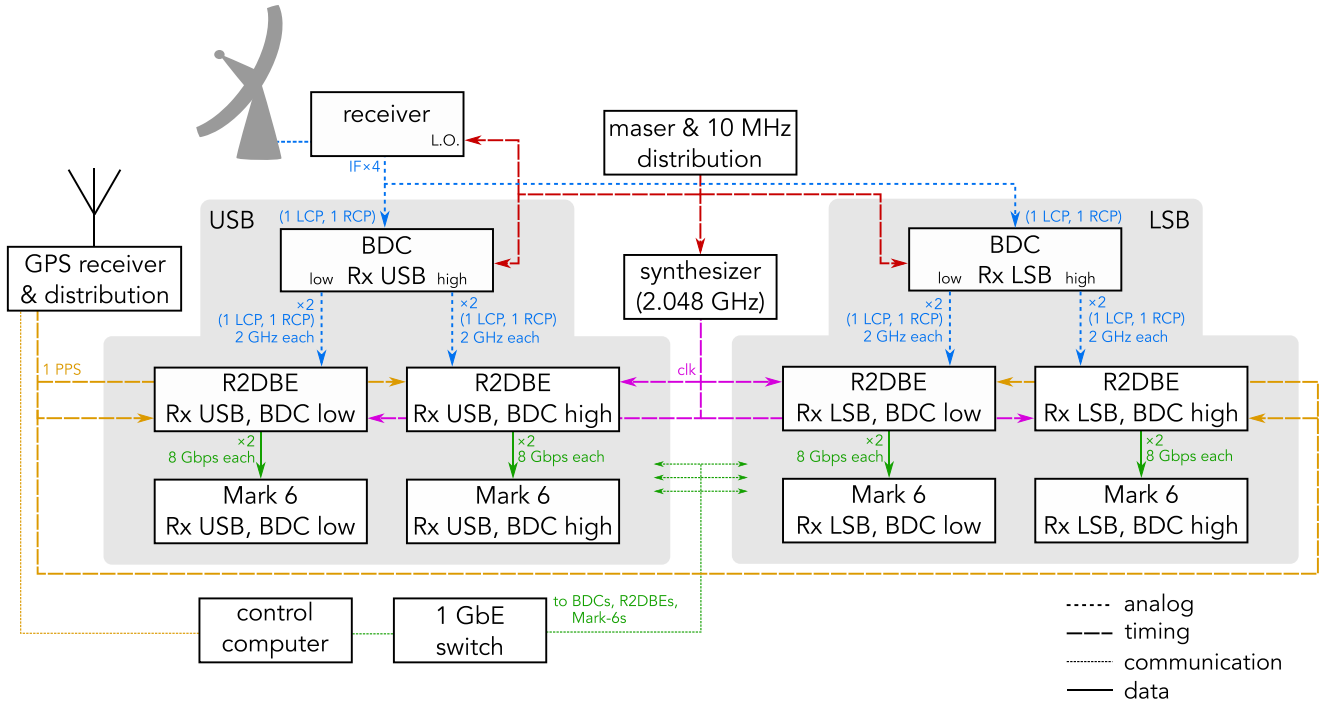

Figure 4. System diagram at a single-dish EHT site with 64 Gbps capability. Dual-polarization (left and right circular polarization (LCP and RCP)) and upper- and lower-sideband (USB and LSB) analog IF signals are sent from the receiver. The receiver local oscillator is locked to the station hydrogen maser 10 MHz reference. Block downconverters (BDCs) mix these signals to baseband. R2DBEs sample the analog signals and distribute packetized data to Mark 6 recorders over a 10 GbE network. All timing is locked to a 10 MHz maser reference and synchronized with a pulse-per-second (PPS) Global Positioning System (GPS) signal. The components are controlled through a 1 GbE network. See Figure 8 for a photograph.

each. The sampled data are put into the VLBI Data Interchange Format (VDIF; Whitney et al. 2009) and transmitted to a Mark 6 recorder (Section 3.5) via two 10 Gbps Ethernet (GbE) small form-factor pluggable (SFP+) interfaces.[139] The 16 Gbps output from each DBE matches the recording rate of a single Mark 6 VLBI recorder that records in parallel to 32 hard drives (Whitney et al. 2013). Four DBE—Mark 6 systems are used to sample and record the four 4 GHz wide IF bands coming from the two receiver sidebands and dual polarizations for an aggregate data rate of 64 Gbps.

For operations at high-altitude, helium-filled hermetically sealed hard drives are used, avoiding the need to build pressure chambers around the recorders. The hard drives collectively accumulated over 10,000 hr of recording at up to 5100 m altitude without a disk failure during the 2017 observations. The full 64 Gbps signal chain thus uses 128 hard drives in parallel, each with a capacity of 6–10 TB for a total storage capacity of about 1 PB. For the stations on the periphery of the network that cannot participate in all scans, 1 PB supports a typical VLBI observing campaign of about 6 days, while stations in the center need a double set of modules, or about 2 PB. Across the array, an EHT observing campaign involving all stations in Table 3 would require a total of about 15 PB of data storage.

Connected-element (sub)millimeter interferometers have more complex systems that use phased-array processors to sum signals from multiple telescopes into a single signal with much greater sensitivity. These processors are integrated with their digital correlators and output the summed signal as VDIF data packets to Mark 6 recorders as at single-dish stations.

[139] https://vlbi.org/vdif/

The following sections describe each subsystem in more detail.

3.1. Receivers

The past three decades have seen the development and widespread use of heterodyne receivers in the millimeter and submillimeter bands based on superconductor–insulator–superconductor (SIS) junctions (e.g., Phillips et al. 1981; Maier 2009; Carter et al. 2012; Tong et al. 2013; Kerr et al. 2014). Over this period, instantaneous bandwidths increased by more than a factor of 30, while noise temperatures decreased by an order of magnitude. Improvements in receiver and antenna reflector technology have combined with the increased recording rates to lay the foundations for a millimeter wavelength VLBI array that is capable of observing targets with a flux density below 1 Jy. In the receivers, high-frequency radiation from the sky is mixed with a pure tone (an LO signal derived from a high-stability frequency reference) and down-converted to an IF using photon-assisted tunneling to transport current across the SIS junction's energy gap. Presently installed SIS-based receivers at observatories typically support IF bandwidths of 4–12 GHz, with higher bandwidth systems becoming available at selected sites.

Heterodyne receivers have two observing bands with sky frequencies centered at $\nu_{\rm LO} - \nu_{\rm IF}$ (LSB) and $\nu_{\rm LO} + \nu_{\rm IF}$ (USB), respectively, from which the signals are folded on top of one another (double-sideband (DSB) receiver). With the use of an RF 90° hybrid, two mixers, and an IF 90° hybrid, modern millimeter receivers can separate the sidebands into two distinct IF channels (sideband-separating (2SB) receiver). The SIS mixers employed at these wavelengths use single-polarization rectangular waveguides that couple to a single polarization of

the incident radiation through planar antennas mounted in rectangular waveguides. Dual-polarization receivers employ two independent orthogonal signal chains. Polarizations are split using a wire grid or a waveguide-based orthomode transducer (OMT). The latter can be inserted in front of the mixer blocks and cryogenically cooled, resulting in reduced ohmic losses. Some of the EHT stations use OMTs with circular polarizers, but the majority use quarter-wave plates in front of the receivers. ALMA records in dual orthogonal linear polarization, which is converted to circular polarization in post-processing as described in Section 5.

3.2. Hydrogen Maser Frequency Standards

As with connected-element arrays, VLBI relies on the fundamental ability of radio band receivers to accurately preserve the phase of detected cosmic radiation. For connected-element arrays, a common LO, derived from a station frequency reference, is used for all antenna receivers. On long VLBI baselines, sharing a common frequency reference is currently not technically feasible, and each VLBI site must use its own clock. This practice imposes a strict requirement on the stability of the frequency standards used for VLBI. Generally, one requires $\omega\tau\sigma_y(\tau) \ll 1$, where ω is the observing frequency in rad s^{-1}, $\sigma_y(\tau)$ is the square root of the Allan variance (the Allan standard deviation), and τ is the integration time. This limit keeps rms phase fluctuations well below 1 rad (Rogers & Moran 1981).

Because of their excellent stability on timescales that match VLBI integrations (about 10 s, Figure 5), hydrogen masers are used almost without exception as VLBI frequency references worldwide. At $\sigma_y(10\ \mathrm{s}) = 1.5 \times 10^{-14}$, VLBI observations at wavelengths down to 0.87 mm can be carried out with coherence losses (Loss $\simeq 1 - e^{-(\omega\tau\sigma_y(\tau))^2}$) limited to <5 % on a baseline where stations at either end are equipped with similarly stable masers (Doeleman et al. 2011). The use of hydrogen masers ensures that phase fluctuations in the VLBI signal due to atmospheric turbulence are typically the dominant source of coherence loss in EHT observations (Rogers et al. 1984; see also Figure 2).

The hydrogen masers used in the EHT are monitored for stability using two tests. The first compares the stability of the 10 MHz frequency reference output of the maser with that of a high-precision quartz oscillator, known to have a similar performance as a maser on 1 s timescales. This in situ measurement confirms nominal maser operation at 1 s integration times, and extrapolation then yields an estimate of maser performance at 10 s (see Figure 5). A second test is to routinely monitor the offset between 1 PPS signals derived from the maser and a GPS receiver. GPS stability on 1 s timescales is poor due to variations induced by the ionosphere, but on longer timescales (>10^4 s) GPS precision, which is referenced to the average of many atomic clocks, will exceed that of any single maser at an EHT location. An observed linear drift (Figure 5) over month to year timescales confirms long-term maser stability and also provides an instrumental delay-rate that is required for later interferometric detection (see Section 5).

3.3. Block Downconverters

A BDC design was developed to mix selected pieces of the incoming IF band from the receiver (in the range 4–9 GHz) down to baseband (0–2 GHz) for sampling. For observing at 1.3 mm, bandpass filters select 5–7 GHz and 7–9 GHz bands that are mixed against a LO at 7 GHz to convert to baseband. Similarly, for observing at 0.87 mm, 4–6 GHz and 6–8 GHz bands are mixed against an LO at 6 GHz to convert to baseband. The LO is phase locked to a 10 MHz reference from the station frequency standard. Coaxial relays in the output stage select which set of baseband outputs is connected to the data acquisition system, and the LO of the unused set is muted to avoid interference. The downconverter has two duplicate chains of filters and mixers for processing two of the four receiver IF channels, and two such downconverters are used in a complete system. A simplified schematic of a BDC is shown in Figure 6.

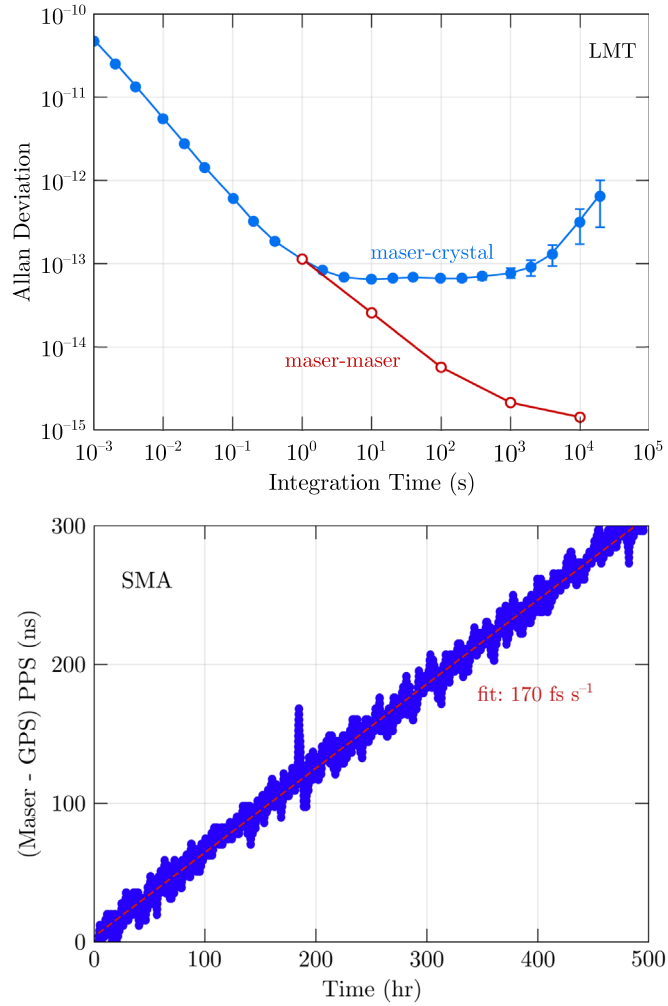

Figure 5. Top panel: measured Allan standard deviation, $\sigma_y(\tau)$, of the hydrogen maser at the LMT compared to a precision quartz oscillator. The open red points are the manufacturer specifications of the hydrogen maser when compared to another maser. At a 1 s integration time, the quartz oscillator and maser have similar stability, so the measurements indicate that the maser is meeting its specifications as installed at a coherence time of ∼1 s. The flattening of the $\sigma_y(\tau)$ curve beyond 10 s is due to the decreased stability of the quartz crystal. The extrapolation of Allan deviation from short integration times to 10 s indicates that the maser meets the stability goal of $\sigma_y(10\ \mathrm{s}) = 1.5 \times 10^{-14}$. Bottom panel: the long-term drift of the maser at the SMA compared to GPS, measured by differencing the 1 PPS ticks from the maser and local GPS receiver. The vertical width of the trace is due to variable ionospheric and tropospheric delays of the GPS signal (including the excursion near hour 200), while the long-term trend represents the frequency error of the maser. The drift measured from this plot, and its effects on the fringe visibility, are removed during VLBI correlation.

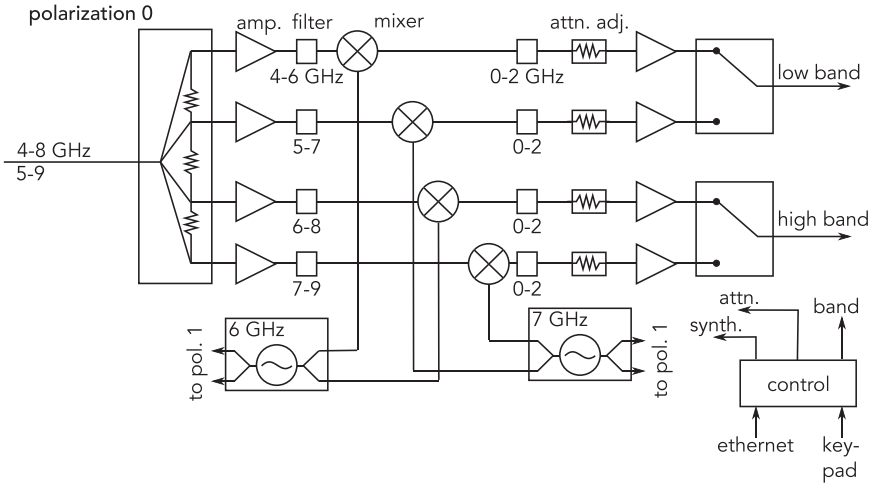

Figure 6. Simplified schematic diagram of the BDC. Only one of the two (identical) polarization channels is shown, and several intermediate amplification stages are omitted. Two local oscillators maser-locked and tuned to 6 GHz and 7 GHz are used to mix all the filtered IF bands between 4 and 9 GHz to baseband (0–2 GHz). For 230 GHz operation, a 5–9 GHz IF band is split with output of 5–7 GHz ("low-band") and 7–9 GHz ("high-band"). For 345 GHz operation, a 4–8 GHz IF band is split with an output of 4–6 GHz ("low-band") and 6–8 GHz ("high-band"). The 6 and 7 GHz local oscillator signals are also sent to the other polarization channel. The attenuation and band selection can be set using a control panel or remotely via an Ethernet connection.

The maximum conversion gain of each channel is about 23 dB, and it can be adjusted downward to about −8 dB in 0.5 dB steps to match the output power of the BDC with the input dynamic range of the digitizers. At a nominal output power of −7 dBm, the BDC operates in the linear regime over the entire programmable range of the attenuators. An 8-bit controller provides control of the synthesizers, digital attenuators, and coaxial relays, and interfaces to a keypad and display unit for manual operation, as well as to an Ethernet port for remote control.

3.4. Wideband VLBI Digital Backend

Coherent received station data in modern VLBI systems are recorded digitally. The VLBI instrument that digitizes and formats the analog received signal for recording is termed the digital backend (DBE). The high bandwidths that enhance the EHT sensitivity require proportionately fast digital sampling speeds. The timing of the samples is an implicit time stamping of the data, so the sampler clock must be timed with maser stability and precision.

For several generations of instrumentation the EHT has based its digital hardware on open-source technology shared by the Collaboration for Astronomy Signal Processing and Electronics Research (CASPER;[140] Hickish et al. 2016). The open-source hardware currently in use includes five gigasample-per-second (Gsps) analog-to-digital converter (ADC) boards, based on an integrated circuit that interleaves four cores, each with a maximum sample rate of 1.25 Gsps. The ADC circuit design and hardware testing is documented in Jiang et al. (2014). The compute hardware platform is the CASPER second-generation Reconfigurable Open Access Computing Hardware (ROACH2). The ROACH2 uses an FPGA as its digital signal processing engine.[141]

The current EHT DBE instrument was developed in 2014, and is called the ROACH2 Digital Back End (R2DBE; Vertatschitsch et al. 2015). The R2DBE samples two analog channels at 4.096 Gsps, each with 8-bit resolution, i.e., two 2.048 GHz wide bands, before re-quantizing the samples with 2-bit resolution, packing the data in VDIF format, and then transmitting it over two 10 GbE connections to the Mark 6 recorder.[142] Each R2DBE transmits two 8 Gbps data streams to a Mark 6 for recording. Accurate timing and synchronization is achieved by referencing the ROACH2 clocks to the maser via an external EHT-developed 2.048 GHz synthesizer.

The per-channel signal processing flow within the R2DBE is shown in Figure 7. Gain, offset, and sampler clock phase mismatches between the cores of the ADC produce spurious artifacts in the spectrum of the digitized signal, most prominently a spur at one quarter of the sample rate frequency that is caused by interleaving imperfection of the quad-core ADC. A calibration routine is performed at the start of each observation to tune the distribution of 8-bit samples for each core in offset, gain, and phase, removing these artifacts (Patel et al. 2014). A digital power meter is implemented in the firmware to calculate input power every millisecond, which is useful for pointing and calibration measurements.

An important design consideration is the optimal number of bits per sample recorded onto storage media at the telescopes. This is determined by trading off the sensitivity increase realized through sampling more bandwidth at higher precision (see Equation (1)) with the cost of media required to store the data (for a detailed explanation, see Thompson et al. 2017). For the EHT, a maximum aggregate bandwidth of 16 GHz is set by the characteristics of ALMA receivers. When bandwidth is limited in this way, one examines the increase in sensitivity per additional unit media. For 1-bit recording (two-level sampling), the digital efficiency (η_Q in Equation (1)) is 0.64. Moving to 2-bit recording (four-level sampling) increases η_Q to 0.88 at the expense of doubling the required recording media, for a 38 % sensitivity increase per additional unit media—this is approximately equivalent to doubling the front-end bandwidth and keeping 1-bit sampling. Tripling the media cost and recording 3

[140] For more information on CASPER, please see https://casper.berkeley.edu/.

[141] See https://www.xilinx.com/support/documentation/data_sheets/ds150.pdf.

[142] An alternative DBE that is planned to be deployed at some EHT sites is the third-generation Digital BaseBand Converter (DBBC3; Tuccari et al. 2014).

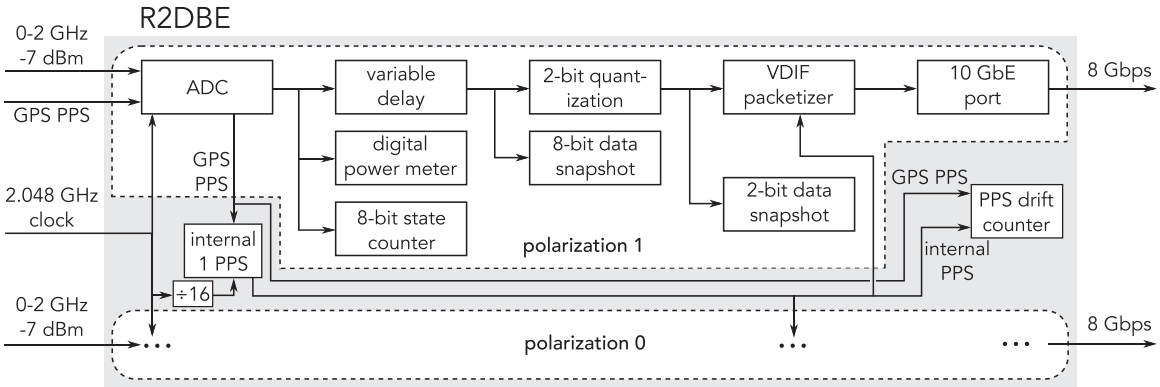

Figure 7. Functional diagram of the R2DBE. A pair of ADCs sample two channels of 2.048 GHz Nyquist bandwidth IF bands, typically representing two antenna polarizations. After requantization of the samples to 2 bits, the data are distributed in VDIF packets over a 10 GbE network to Mark 6 recorders. The maximum FPGA clock speed is too slow to process the ADC output stream rate of 4096 megasamples per second in series, so 16 ADC samples are transferred from the sampler in parallel on each FPGA clock cycle and are processed in parallel though the FPGA, which is clocked at a sixteenth of the sample clock, or 256 MHz. The FPGA and sampler clocks are locked to the maser reference frequency. In addition to the sample clock and dual IF inputs, each ADC circuit board is also equipped with a low-frequency synchronization input. On one of the ADC boards, the synchronization input is connected to GPS PPS. An internal PPS for VDIF time stamping is synthesized from the 2.048 GHz maser-referenced clock and synchronized to the GPS real-time PPS time-tick once at the beginning of an observation. The internal PPS drift relative to GPS real-time PPS (Figure 5) is measured by a counter and is available to be read from a register over Ethernet, as well as copied into the VDIF data-header, as it is a prior parameter for VLBI correlation.

bits (eight-level sampling) delivers only a 25.5 % increase in sensitivity per additional unit media. The 2-bit sampling scheme was chosen as it ensures ample margin for sensitivity requirements while minimizing recording media, which dominates the cost of VLBI correlation (Deller et al. 2011).

In a 2-bit system, the noise voltage thresholds of the four sampling levels should be properly set to maximize digital processing efficiency. A proper setting ensures that all four levels are optimally populated for a given input voltage signal from the telescope receiver system (Cooper 1970; Thompson et al. 2017). The processing efficiency is not a sensitive function of these thresholds, but the statistics of the level populations can vary significantly as elevation and weather condition changes cause fluctuations in the receiver power arriving at the sampler. For this reason, a calibration of the sampler threshold setting are performed periodically during calibration scans to maintain optimal settings.

3.5. High-speed Data Recorders

The Mark 6 VLBI Data System (Whitney et al. 2013) is a packet recording system used to store the R2DBE output streams to hard drives. The recorder captures the two 8 Gbps streams from the R2DBE using commercial 10 Gbps Ethernet network interface cards. It strips the internet packet headers and stores the payload containing VDIF data frames. For sustained recording at 16 Gbps, each Mark 6 recorder writes the data in time slices across 32 hard drives with a round-robin algorithm. The disks are mounted in groups of eight in four removable modules for ease of handling and shipping. For the EHT, four such recorders are configured in parallel to achieve an aggregate data capture rate of 64 Gbps.

Mark 6 recorders and modules are commercially available and in use in other VLBI applications. Several modifications were required for EHT use at high altitude, as hardware specifications typically state 10,000 ft as the maximum operating altitude. The low ambient air density necessitates sealed, helium-filled hard drives, both for the system disk for recorders and also in all modules onto which data are recorded. In addition, the Mark 6 interior was modified to direct a high-volume airflow onto the CPU, network, and data interface cards, which were found to be sensitive to overheating at altitude.

A photograph of the EHT VLBI backend (BDCs, R2DBEs, and Mark 6s) at the PV 30 m telescope is shown in Figure 8. Recorders used for earlier EHT campaigns included the Mark 5C system, which was capable of capturing only a 4 Gbps data stream onto two modules. The bandwidth of the EHT backend since 2004 is plotted in Figure 9 and represents a 64-fold increase, corresponding to an eight-fold improvement in sensitivity.

3.6. Phased Arrays

To use the total collecting area available at connected-element interferometers that participate as single stations in the EHT VLBI network (ALMA, SMA, and, in the future, the Northern Extended Millimeter Array (NOEMA) these arrays coherently add the signal received from the target source by each antenna and record as if from a single antenna. Practical constraints on the maximum data rate that can be recorded at each site require that this summation be performed in real time.

Forming a coherent sum requires correcting for deterministic delays, such as geometric and known instrumental delays, as well as non-deterministic delays, which at EHT frequencies are significantly affected by the distribution of water vapor in the atmosphere. The atmospheric delay varies over time, antenna location, and direction so that accurate compensation can only be achieved through the use of in situ calibration methods.

Phasing systems were developed for the SMA and ALMA (see Appendix), and these observatories participated as phased arrays since 2011 and 2017, respectively. A phasing system for NOEMA is in the process of being implemented and commissioned for VLBI. Figure 10 shows the SMA phasing efficiency, i.e., the fraction of beamformed power compared to ideal phasing, estimated using Equation (2), achieved over the course of several scans during one night of the 2017 EHT campaign. For most of the scans, the efficiency is well above 0.9 (see inset). Typical phasing performance of the ALMA array can be found in Matthews et al. (2018).

Figure 8. EHT digital VLBI backend as installed at the Institut de Radioastronomie Millimétrique (IRAM) PV 30 m telescope in Spain. The upper portion of the right-hand side rack holds the four R2DBE units. Two block downconverters are installed near the middle. The VLBI backend computer is mounted on the bottom right. The rack on the left and the lower portion of the rack on the right hold the four Mark 6 recorders with four disk modules each, providing a total of about 1 PB in data storage.

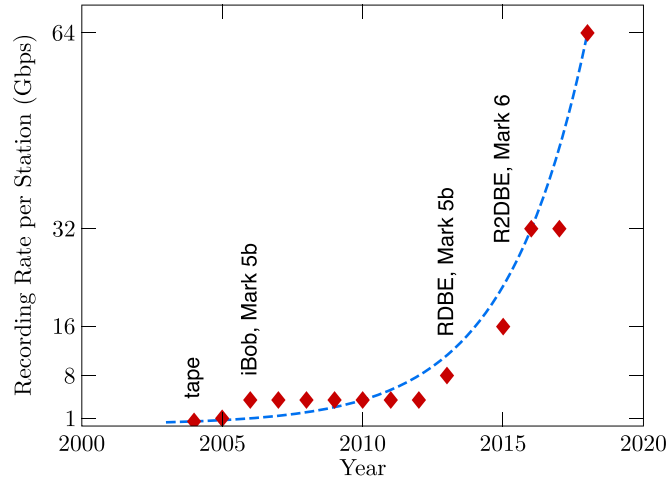

Figure 9. Recording rate of EHT observations over time. As of 2018, EHT stations record at 64 Gbps, equivalent to a doubling of recorded bandwidth every two years for over a decade (blue curve). The high bandwidth, a result of linking EHT instrumentation to industry trends and commodity electronics, is a crucial component of the EHT's sensitivity, enabling detections on long baselines, providing resilience of the network against poor weather and low-elevation targets, and allowing detections from all stations to ALMA within short atmospheric coherence times (see Section 2.2).

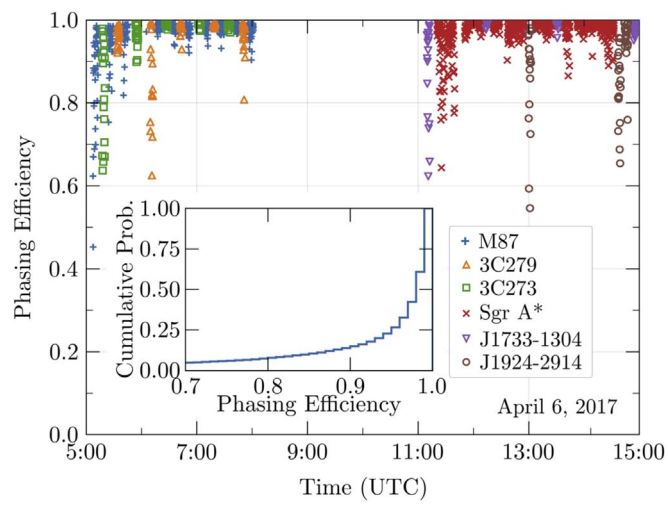

Figure 10. Phasing efficiency of the SMA on various sources over the course of one observing schedule. The inset shows the cumulative distribution of phasing efficiency of the SMA over the entire 2017 EHT observing campaign.

3.7. Setup and Verification

As part of the integration of the new VLBI systems in 2015, most station backends were configured at Haystack Observatory prior to shipment to the telescopes. New equipment still typically passes through Haystack for initial inspection, check-out, and configuration. Each site takes responsibility for the installation of the equipment and ensuring that the connections to facility hardware work to specification and are not affected by factors such as telescope motion.

Before each observing campaign, each site goes through a comprehensive setup and verification procedure, which includes the completion of a checklist by site operational staff. The procedure verifies operation of the BDC, R2DBE, and Mark 6 systems, and the exact frequency and lock status of LOs, which set the exact observed sky band, and the ADC clock that time stamps the data. The check also includes the coherence and drift of the hydrogen maser time standard as this clock rate measurement is needed during correlation for fringe-stopping.

Due to the remote nature of many of its sites and the large data volume recorded, the EHT lacks real-time verification of fringes. Shipping data from remote stations to the central correlator and processing takes several days at minimum, and many months in the worst case (from the South Pole; see Appendix A.11). If a key system fails, it is possible for a site to take data that never result in fringes, making careful testing and retesting of subsystems throughout the observation absolutely crucial. Data from brief observations (10–30 s) can be transferred from sites with fast internet connections for near real-time fringe verification. While possible, this requires robust data transfer connections.

The most complete in situ full-system check consists of the injection of a test tone at a known frequency in front of the receiver. A short data segment is recorded, and the

autocorrelations and zero-baseline cross-correlations are inspected to verify that the test tone appears at the correct frequency and with the correct profile. Further, the tone in the baseband is mixed down to 10 kHz using a third LO and compared to a 10 kHz tone derived from the maser 10 MHz reference. The two should be phase locked when examined on an oscilloscope, which verifies the phase stability of the whole system. This test is exquisitely sensitive to small disturbances in the system. At the JCMT an equivalent test is done by verification of local connected-element fringes with the SMA.

Results and logs from the setup and verification are centrally archived and available to the correlator centers for the interpretation of station issues and for fault diagnosis when data quality issues emerge.

3.8. The Array

The EHT included eight observing facilities in 2017. Three additional facilities have since joined (GLT) or will soon join (KP 12 m and NOEMA), and two facilities (CARMA and the CSO) have participated in past EHT observations but have now been decommissioned. Properties of these facilities are summarized in Tables 2 and 3, and the Appendix. The baseline Fourier coverage provided by the array in 2017 for M87 is shown in Figure 11. Table 5 shows the actual performance of the array on scans of M87 during the 2017 science observations. The scan-averaged thermal noise within one 2 GHz frequency band was significantly better than 1 mJy on most baselines to ALMA, and generally a few mJy on baselines excluding ALMA. These achieved sensitivities, combined with the realized (u, v) coverage in Figure 11, confirm that the EHT has met its essential specification in providing an array that can image features on the scale of an SMBH shadow.

4. Observing

EHT science observing campaigns are scheduled for March or April when Sgr A* and M87 are night-time sources and the weather tends to be best on average over all sites. In addition, ALMA tends to be in a more compact configuration with better prospects for including more antennas in a phased array for increased sensitivity. Test and commissioning runs are scheduled a few months prior to campaigns to ensure that VLBI equipment, which may be dormant for months at a time, is operational.

4.1. Weather

Weather is an important consideration for VLBI observations at millimeter wavelengths. Most of the EHT observatories are located in the northern hemisphere, and those stations have especially large weather variations between seasons. Opacity and turbulence are typically lowest at night and in winter and early spring. At many sites, and particularly the connected-element arrays, the reduced atmospheric turbulence during night-time hours is essentially required. To protect against inclement weather, the EHT uses flexible observing with windows that are about twice as long as the intended number of observing nights. Within the window, a few hours before the start of observing each night, weather conditions are reviewed at all sites and a decision is made whether or not to observe that night. When an EHT night is not triggered, it is often possible for the time to be used for other observing programs at an observatory.

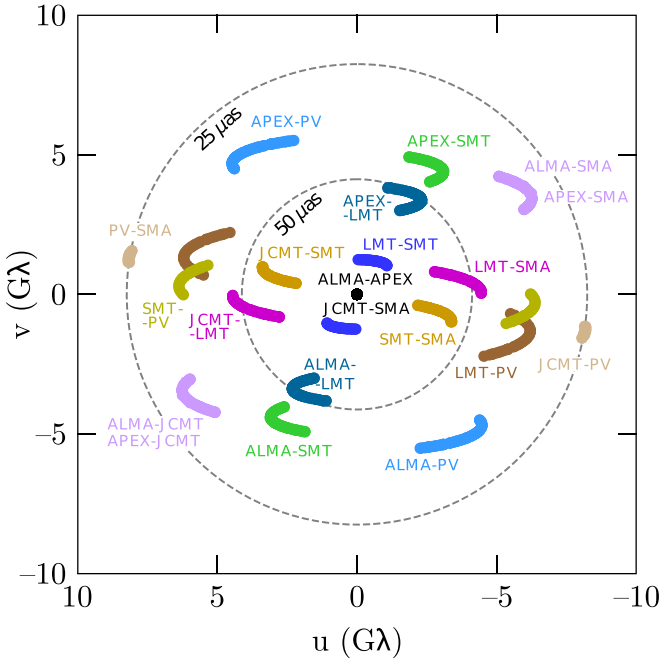

Figure 11. Aggregate EHT baseline coverage for M87 over four nights of observing with the 2017 array. Only detections are shown. The dashed circles show baseline lengths corresponding to fringe spacings of 25 and 50 μas. See Paper III for details.

Table 5
Median Thermal Noise (mJy) for Observations in 2017

	APEX	JCMT	LMT	PV	SMA6	SMT	SPT
ALMA37	0.53	0.80	0.34	0.43	0.54	0.57	1.75
APEX	⋯	9.99	4.24	4.22	6.49	6.68	14.51
JCMT	⋯	⋯	5.52	10.24	9.60	10.17	16.14
LMT	⋯	⋯	⋯	3.22	3.63	3.91	11.57
PV 30 m	⋯	⋯	⋯	⋯	7.98	6.11	14.53
SMA6	⋯	⋯	⋯	⋯	⋯	6.64	15.33
SMT	⋯	⋯	⋯	⋯	⋯	⋯	17.73

Note. Median scan-averaged thermal noise per baseline in mJy for all M87 detections in 2017 April. Entries for the SPT reflect the median thermal noise on 3C 279, since the SPT cannot observe M87 due to its geographic location. Scan durations were three to seven minutes. For more details, see Paper III.

4.2. Scheduling

The process of scheduling starts with the list of approved target sources, time allocations at EHT telescopes and ALMA, and the dates of the observing window (Section 4.1). Schedule construction has to satisfy multiple requirements:

1. a high total on-source time for each target,
2. a wide range of parallactic angles sampled for polarimetry,
3. long baseline tracks on all sources within the limited number of observing days,
4. randomized scan lengths and scan start times on Sgr A* for periodicity analysis,
5. good baseline coverage in the (u, v) plane, and
6. regular gaps for telescope pointing and calibration.

AGN sources are chosen as calibrators based on their brightness, compactness, and proximity to the target sources. The calibration sources are used for multiple purposes,

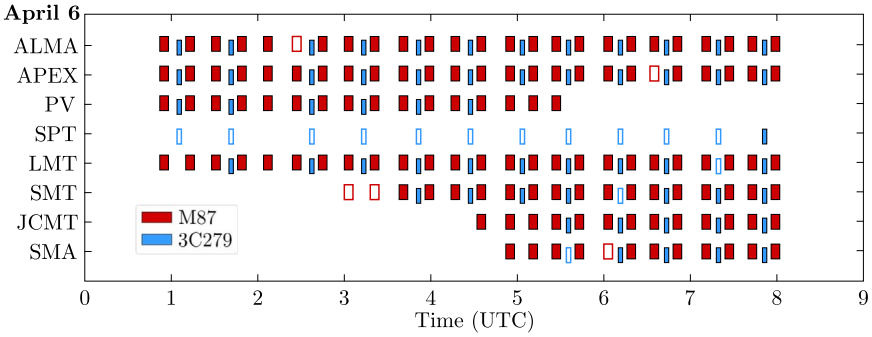

Figure 12. EHT 2017 observing schedule for M87 and 3C 279, covering one day of observations (April 6). Empty rectangles represent scans that were scheduled, but were not observed successfully due to weather, insufficient sensitivity, or technical issues. The filled rectangles represent scans corresponding to detections available in the final data set. Scan durations vary between 3 and 7 minutes, as reflected by the width of each rectangle, and scans are separated by periods of time used at each site for local pointing adjustments and calibration measurements. For this schedule, 3C 279 was the calibrator source for the primary target, M87. For information on other observing days, see Paper III.

including fringe finding, bandpass calibration, and polarization calibration.

Observing blocks are created for each of the sources, and these blocks are merged into tracks, each corresponding to a single night of observing. Depending on time allocations and Fourier-coverage needs, multiple blocks on the same source may appear in the same track or in different tracks. Each observatory has different needs for overhead because the EHT is an inhomogeneous array. Overhead accommodates time for pointing, focus, and primary and secondary flux observations at all sites, plus phase-up time and array-polarimetric calibrations at the phased arrays. A typical EHT schedule (Figure 12) records VLBI scans with a duty cycle of approximately 50%, with a substantial fraction of those scans on targets strong enough to use for array calibration.

4.3. Monitoring and VLBI Backend Control

The EHT developed a centralized monitoring tool called `VLBImonitor` to visualize observing status, collect ancillary calibration and weather data from each site, and provide real-time and predicted weather information from meteorological services. The information collected, logged, and displayed includes atmospheric and local weather conditions, observatory metadata such as telescope coordinates and on-source status, system temperature measurements, opacity measurements, digital backend and recorder state information, and comments from on-site observers and operators. Communication with the metadata server (by the software clients at each site or via a web interface) uses the JSON-RPC (remote procedure call) protocol over HTTPS. A "masterlist" defines metadata parameters that are accepted (white-listed) by the server and all their properties (e.g., data type, measurement cadence, a function that evaluates if the current value is valid or invalid, and units).

The `VLBImonitor` software[143] was introduced for the 2017 observations. In 2018, a VLBI backend computer and network were added at the sites to provide a common monitoring and control platform at each station. Both monitoring and control remain in active development. At present, the EHT deploys specialist teams at each station, which, in practice, limits the observing window to about 12 days. It is a long-term objective for the EHT to both increase the length of this window and to conduct VLBI observations without the need for on-site specialists, after an initial setup and verification by local and remote experts. A critical component toward this goal is the implementation of comprehensive remote monitoring of the stations and VLBI equipment, as well as remote control of the VLBI backend.

5. Correlation and Calibration

The recorded data modules at all sites are separated by frequency band, with the "low-band" shipped to the VLBI correlator at MIT Haystack Observatory in Westford, Massachusetts, USA, and the "high-band" to the correlator at Max-Planck-Institut für Radioastronomie (MPIfR) in Bonn, Germany. Correlation is performed using the Distributed FX (DiFX) software correlator (Deller et al. 2011) running on clusters of more than 1000 compute cores at each site, and is split between the two sites to speed processing and allow cross-checks. At least as many Mark 6 playback units are needed at each correlator as there are stations in the EHT. The Mark 6 playback units at the MIT correlator are connected via 40 Gbps data links. A 100 Gbps network switch then delivers data to the processing nodes using 25 Gbps links. At MPIfR the internode communication, which includes the Mark 6 playback units, is realized via 56 Gbps connections, exceeding the maximum playback rate of the Mark 6 units of 16 Gbps.

Each 2 GHz observing band is correlated independently, with multiple passes required to correlate the full 4 or 8 GHz in an experiment. The correlation coefficients between pairs of antennas are calculated after correcting for an a priori clock model (Earth rotation, instrumental delays, and clock offsets and drift rates). All sites except ALMA record left and right circular polarizations (L/R) producing cross-correlations in the standard circular basis (LL, LR, RL, RR). ALMA antennas, however, are natively dual-linear polarization (X/Y), so a linear-to-circular polarization conversion is performed on ALMA baselines *after* VLBI correlation. `PolConvert` (Martí-Vidal et al. 2016) is a software routine developed for this purpose as part of the program to phase the ALMA array for VLBI operation (Matthews et al. 2018; Goddi et al. 2019). This routine forms linear combinations of the cross-polarization-basis correlator products (XR, YR) and (XL, YL) with $\pm 90°$ phase shifts introduced to the visibility phase to produce complex visibilities in the circular-polarization basis, for each integration time. The input correlator products to `PolConvert` are equalized in gain and phase, and the X–Y channel phase differences are removed before polarization conversion.

[143] https://bitbucket.org/vlbi

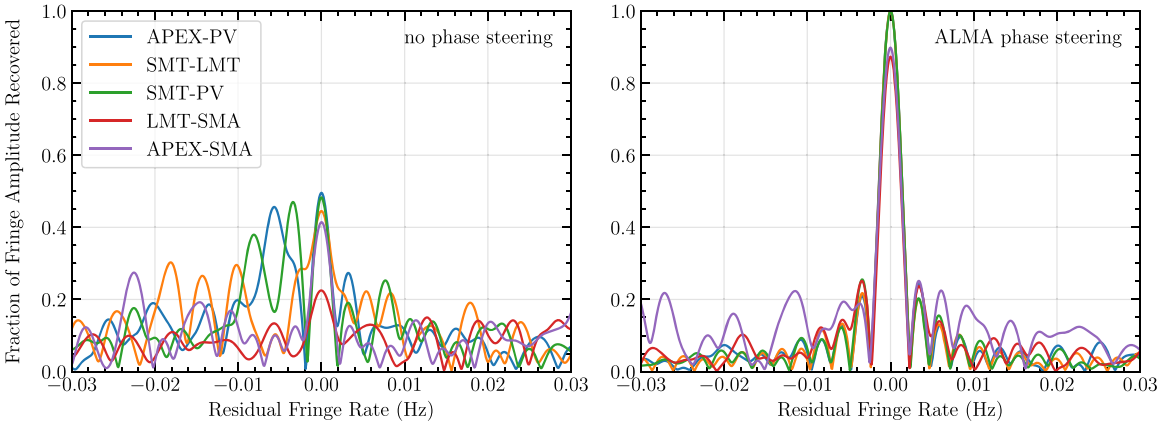

Figure 13. Fringes detected on EHT baselines before and after phase steering using the ALMA phased array as a reference station. Shown here are residual fringe-rate spectra, where the peak occurs at a single fringe-rate that is consistent with linear clock drift over the entire scan. Stochastic atmospheric phase variations result in fringe-rate variation over time, spreading the signal in the plot on the left. To recover the total fringe amplitude, baselines to ALMA are used to phase reference the array at a short timescale. Data shown are from a VLBI scan on a quasar calibrator (3C 279) obtained during EHT observations in 2017 April. The data are taken at low elevation, and at several sites during the afternoon and early evening when the atmosphere is often unstable. Baselines to ALMA are able to phase steer the remaining sites in the array at an effective timescale of 1–3 s depending on S/N. At SMA due to the mid-afternoon local observation, phasing is particularly challenging. This leads to an amplitude efficiency of about 90 % on SMA baselines, as well as increased measurement thermal noise for the APEX-SMA spectrum with a full-scan S/N of only ∼10.

This X–Y channel equalization is performed using standard calibration techniques for connected-element ALMA operation (for details see Paper III).

To reduce data volumes and increase S/N, the cross-products computed in the correlator are averaged both in time and frequency. These complex cross-products are then fitted for fringe-delay (linear change in phase versus frequency) and fringe-rate (linear change in phase versus time), which are then removed. Residual fringe-delay and fringe-rate are due to several factors. Largest among these are residual clock drifts, instrumental electronic delays, and atmospheric phase fluctuations that can result in rapidly varying fringe-rate residuals. For the compact, narrow-field EHT continuum targets, delay and rate variability due to intrinsic source structure is expected to produce much smaller residuals. The averaging time and bandwidth in the correlator is thus set to ensure that any coherence losses due to delay or rate variations are negligible, or equivalently that such variations can be tracked both in time and frequency. For EHT observations, the typical averaging bandwidth is 0.5 MHz and the averaging time is 0.4 s, allowing residual delays up to $\pm 1\ \mu$s and residual rates up to ± 2.5 Hz. These settings enable the isolation and identification of instrumental spectral features, and also the ability to track atmospheric phase variations. This averaging in both time and frequency, results in a decimation of data volumes by more than a factor of 1 million.

After the initial correlation, the data are further processed through a pipeline that results in final data products for use in imaging, time-domain analyses, and modeling (Blackburn et al. 2019; Janssen et al. 2019). During fringe detection, the excess in correlated signal power due to the source on a VLBI baseline is identified, and the complex Fourier component of source brightness distribution is measured. As outlined in Section 2.2, high signal-to-noise detections on baselines to ALMA can be used to remove atmospheric phase fluctuations on non-ALMA baselines. Phase stabilizing the array in this way allows coherent integration of the VLBI signal on non-ALMA baselines beyond the atmospheric coherence time. Figure 13 demonstrates the process on real EHT data during relatively poor weather conditions, confirming the general approach and basis for the specifications in Section 2. Precise estimates of the observed systematic errors during the 2017 April EHT campaign are detailed in Paper III.

Subsequent calibration steps convert the correlation coefficients derived from fringe detection to correlated flux density (Jy). This is accomplished through use of a priori information about station sensitivities, and by the application of self-calibration techniques to correct for variations in telescope gain over time and frequency. In cases where two EHT telescopes are in close geographical proximity (e.g., ALMA-APEX and SMA-JCMT), additional calibration constraints can be derived from the resulting baseline redundancy and using only general assumptions about the observed source (Paper III).

6. Future Developments

The EHT array is continuing to develop. With the ability to image SMBHs on horizon scales now confirmed (Papers I; III; III; V; VI), the focus of EHT development will shift to enabling observations that can refine constraints on fundamental black hole properties, processes of black hole accretion and outflow, and tests of general relativity. This depends on achieving higher angular resolution, enhancing image fidelity, and enabling dynamic imaging of time-variable phenomena. Higher resolution will allow more detailed studies and modeling of sub-horizon structures as well as sensitive tests for asymmetries in shadow features. Greater image fidelity will bring fainter emission near the horizon into focus for the study of accretion and jet processes, and it will enable a sensitive comparison across imaging epochs, which is especially germane for M87 with its dynamical timescale of days to weeks. For Sgr A*, the light-crossing time of ∼20 s requires a dynamic approach to image reconstruction, with the potential of observing the near real-time evolution of a black hole.

The planned and in-progress addition of telescope facilities at new geographic sites will improve the (u, v), or Fourier, coverage, and thus imaging fidelity. Over the course of the next two years, the EHT expects to add two more facilities: a beamformed NOEMA in France, which, once completed, will be the equivalent of an approximately 50 m dish, and a 12 m

diameter dish on Kitt Peak in Arizona. A newly realized and important consequence of designing high-bandwidth systems is that adding telescopes with modest diameters (≃6 m) creates VLBI baselines with sufficient sensitivity to detect the primary EHT targets. An expansion of the EHT can, therefore, include the possibility of deploying numerous smaller apertures, enabling not only improved image quality but also snapshot capability, which is a precursor to constructing black hole movies (Bouman et al. 2018; Johnson et al. 2018). Additional plans to enhance the data throughput of VLBI backend and phased array systems are underway, linked to new generations of wideband millimeter and submillimeter receivers and industry trends that will allow for rapid design and implementation. With the inclusion of more sites and wider bandwidths, the computational requirements for VLBI correlation will increase: linearly with bandwidth, and as the square of the number of stations. The exploration of scalable approaches to address future EHT correlation needs is underway (Gill et al. 2019). The combination of these efforts is aimed at the substantial expansion of aperture plane sampling of the EHT and improved imaging.

To significantly improve angular resolution requires development in different directions. Planned extension of the EHT to operation at 0.87 mm wavelength, a standard receiving band at many facilities, would increase the angular resolution of the array by ∼40%. VLBI tests at 0.87 mm are underway and this capability is expected at a subset of EHT sites over the next 3–5 yr (see Table 4). An alternate approach to increased angular resolution is to deploy EHT antennas in space where baseline length is not limited to the diameter of the Earth, potentially allowing horizon-scale imaging of additional SMBH candidates (Johannsen et al. 2012). Space platforms also offer the possibility of rapidly sampling the Fourier plane, thereby opening the potential for dynamical imaging of black hole accretion and outflow processes (D. Palumbo et al. 2019, in preparation; F. Roelofs et al. 2019, in preparation; M. Shea et al. 2019, in preparation).

EHT observation strategies continue to be refined. With further development of remote monitoring and control tools, the EHT can explore triggering observations during the best conditions throughout the year outside the current March–April window. One consequence of this flexibility would be that observations for Sgr A* and M87 could be optimized separately in a given observing cycle, instead of grouped together as they are currently. Distributing the observations over a larger portion of the year also increases the likelihood that the EHT would detect emission transients or flaring on intermediate timescales should they occur, and affords, in general, the opportunity to study M87 on timescales that correspond to the expected ISCO period of order one to several weeks (Table 1). Not all EHT sites may be able to participate in such flexible campaigns, but even a subset of the array, especially if augmented with many smaller dishes, could provide useful observations for variability studies.

7. Conclusion

The goal of the EHT project is to observe SMBHs with spatial and temporal resolution that permits imaging on the scale of the lensed photon orbit, and the study of dynamics on commensurate light-crossing timescales. Leading up to the detection of event-horizon-scale structure in Sgr A* in 2008, and now a decade afterward, the development of EHT instrumentation proceeded through a series of systems that supported increasingly ambitious observations. These observing campaigns led to precursor scientific results that motivated a strategy of building an imaging array: one with baselines long enough to resolve horizon-scale structure, that included enough geographical sites to sufficiently sample the Fourier plane, and had the sensitivity required to detect compact, low flux density targets. Technology maturation, fueled by industry-driven trends, was focused primarily on improving the bandwidth of observations by increasing digitization and recording rates. Over a period of 10 yr, EHT data capture rates increased from 4 to 64 Gbps, allowing for observations that take full advantage of the capabilities of modern millimeter receivers. The parallel development of phased array technologies and investment in site-specific infrastructure (see the Appendix) have now led to a global EHT array with the capability to address its science goals.

Had the EHT project needed to build a VLBI array from the ground up, the cost would have been prohibitive. By developing new systems and infrastructure that allowed for the use of existing telescopes and facilities, most of which were not originally conceived to operate as VLBI elements, the EHT has created a purpose-built array with unique capability at modest cost.

The authors of this Letter thank the following organizations and programs: the Academy of Finland (projects 274477, 284495, 312496); the Advanced European Network of E-infrastructures for Astronomy with the SKA (AENEAS) project, supported by the European Commission Framework Programme Horizon 2020 Research and Innovation action under grant agreement 731016; the Alexander von Humboldt Stiftung; the Black Hole Initiative at Harvard University, through a grant (60477) from the John Templeton Foundation; the China Scholarship Council; Comisión Nacional de Investigación Científica y Tecnológica (CONICYT, Chile, via PIA ACT172033, Fondecyt 1171506, BASAL AFB-170002, ALMA-conicyt 31140007); Consejo Nacional de Ciencia y Tecnología (CONACYT, Mexico, projects 104497, 275201, 279006, 281692); the Delaney Family via the Delaney Family John A. Wheeler Chair at Perimeter Institute; Dirección General de Asuntos del Personal Académico–Universidad Nacional Autónoma de México (DGAPA–UNAM, project IN112417); the European Research Council Synergy Grant "BlackHoleCam: Imaging the Event Horizon of Black Holes" (grant 610058); the Generalitat Valenciana postdoctoral grant APOSTD/2018/177; the Gordon and Betty Moore Foundation (grants GBMF-3561, GBMF-5278); the Istituto Nazionale di Fisica Nucleare (INFN) sezione di Napoli, iniziative specifiche TEONGRAV; the International Max Planck Research School for Astronomy and Astrophysics at the Universities of Bonn and Cologne; the Jansky Fellowship program of the National Radio Astronomy Observatory (NRAO); the Japanese Government (Monbukagakusho: MEXT) Scholarship; the Japan Society for the Promotion of Science (JSPS) Grant-in-Aid for JSPS Research Fellowship (JP17J08829); JSPS Overseas Research Fellowships; the Key Research Program of Frontier Sciences, Chinese Academy of Sciences (CAS, grants QYZDJ-SSW-SLH057, QYZDJ-SSW-SYS008); the Leverhulme Trust Early Career Research Fellowship; the Max-Planck-Gesellschaft (MPG); the Max Planck Partner Group of the MPG and the CAS; the MEXT/JSPS KAKENHI (grants

18KK0090, JP18K13594, JP18K03656, JP18H03721, 18K03709, 18H01245, 25120007); the MIT International Science and Technology Initiatives (MISTI) Funds; the Ministry of Science and Technology (MOST) of Taiwan (105-2112-M-001-025-MY3, 106-2112-M-001-011, 106-2119-M-001-027, 107-2119-M-001-017, 107-2119-M-001-020, and 107-2119-M-110-005); the National Aeronautics and Space Administration (NASA, Fermi Guest Investigator grant 80NSSC17K0649); the National Institute of Natural Sciences (NINS) of Japan; the National Key Research and Development Program of China (grant 2016YFA0400704, 2016YFA0400702); the National Science Foundation (NSF, grants AST-0096454, AST-0352953, AST-0521233, AST-0705062, AST-0905844, AST-0922984, AST-1126433, AST-1140030, DGE-1144085, AST-1207704, AST-1207730, AST-1207752, MRI-1228509, OPP-1248097, AST-1310896, AST-1312651, AST-1337663, AST-1440254, AST-1555365, AST-1715061, AST-1615796, AST-1614868, AST-1716327, OISE-1743747, AST-1816420); the Natural Science Foundation of China (grants 11573051, 11633006, 11650110427, 10625314, 11721303, 11725312, 11873028, 11873073, U1531245, 11473010); the Natural Sciences and Engineering Research Council of Canada (NSERC, including a Discovery Grant and the NSERC Alexander Graham Bell Canada Graduate Scholarships-Doctoral Program); the National Youth Thousand Talents Program of China; the National Research Foundation of Korea (grant 2015-R1D1A1A01056807, the Global PhD Fellowship Grant: NRF-2015H1A2A1033752, and the Korea Research Fellowship Program: NRF-2015H1D3A1066561); the Netherlands Organization for Scientific Research (NWO) VICI award (grant 639.043.513) and Spinoza Prize SPI 78-409; the New Scientific Frontiers with Precision Radio Interferometry Fellowship awarded by the South African Radio Astronomy Observatory (SARAO), which is a facility of the National Research Foundation (NRF), an agency of the Department of Science and Technology (DST) of South Africa; the Onsala Space Observatory (OSO) national infrastructure, for the provisioning of its facilities/observational support (OSO receives funding through the Swedish Research Council under grant 2017-00648) the Perimeter Institute for Theoretical Physics (research at Perimeter Institute is supported by the Government of Canada through the Department of Innovation, Science and Economic Development Canada and by the Province of Ontario through the Ministry of Economic Development, Job Creation and Trade); the Russian Science Foundation (grant 17-12-01029); the Spanish Ministerio de Economía y Competitividad (grants AYA2015-63939-C2-1-P, AYA2016-80889-P); the State Agency for Research of the Spanish MCIU through the "Center of Excellence Severo Ochoa" award for the Instituto de Astrofísica de Andalucía (SEV-2017-0709); the Toray Science Foundation; the US Department of Energy (USDOE) through the Los Alamos National Laboratory (operated by Triad National Security, LLC, for the National Nuclear Security Administration of the USDOE (Contract 89233218CNA000001)); the Italian Ministero dell'Istruzione Università e Ricerca through the grant Progetti Premiali 2012-iALMA (CUP C52I13000140001); the European Union's Horizon 2020 research and innovation programme under grant agreement No 730562 RadioNet; ALMA North America Development Fund Chandra TM6-17006X.

This work used the Extreme Science and Engineering Discovery Environment (XSEDE), supported by NSF grant ACI-1548562, and CyVerse, supported by NSF grants DBI-0735191, DBI-1265383, and DBI-1743442. XSEDE Stampede2 resource at TACC was allocated through TG-AST170024 and TG-AST080026N. XSEDE JetStream resource at PTI and TACC was allocated through AST170028. The simulations were performed in part on the SuperMUC cluster at the LRZ in Garching, on the LOEWE cluster in CSC in Frankfurt, and on the HazelHen cluster at the HLRS in Stuttgart. This research was enabled in part by support provided by Compute Ontario (http://computeontario.ca), Calcul Quebec (http://www.calculquebec.ca) and Compute Canada (http://www.computecanada.ca).

The EHT Collaboration is indebted to the following people for their contributions to the success of the 2017 EHT observations: Joost Adema, Claudio Agurto, Hector Alarcon, Jonathan Antognini, Juan Pablo Araneda, Oriel Arriagada, Jorge Avarias, Amit Bansod, Denis Barkats, Emilio Barrios, Alain Baudry, Alessandra Bertarini, Andy Biggs, Alan Bridger, Michel Caillat, Michael Cantzler, Patricio Caro, John Carpenter, Jorge Castillo, Miroslaw Ciechanowicz, Stuartt Corder, Antonio Cordoba, Pierre Cox, Faviola Cruzat, Mauricio Cárdenas, Itziar De Gregorio, Bill Dent, Carlos Duran, Ray Escoffier, Soledad Fuica, Enrique Garcia, Juan Carlos Gatica, Juan Pablo Gil, Brian Glendenning, Edouard Gonzales, Joe Greenberg, Rolf Güsten, Rob de Haan-Stijkel, Rüdiger Haas, Hayo Hase, Christian Herrera, Daniel Herrera, Richard Hills, Rafael Hiriart, Arturo Hoffstadt, Jorge Ibsen, Christophe Jacques, Jan Johansson, Chris Kendall, Jeff Kern, Thomas Klein, Rudiger Kneissel, Albert Koops, James Lamb, Bernhard Lopez, Cristian Lopez, Robert Lucas, Felipe MacAuliffe, Gianni Marconi, Lorenzo Martinez-Conde, Mary Mayo, Mark McKinnon, Francisco Montenegro-Montes, Rolf Märtens, Lars-Åke Nyman, Rodrigo Olivares, Hans Olofsson, Victor Pankratius, Miroslav Pantaleev, Manuel Parra, Rodrigo Parra, J Perez, Dave Pernic, Juan Pablo Pérez-Beaupuits, Jorge Ramírez, William Randolph, Anthony Remijan, Johnny Reveco, Rachel Rosen, Norman Saez, Ana Salinas, Jorge Santana, Jorge Sepulveda, Tzu-Chiang Shen, Bill Shillue, Ruben Soto, Tomas Staig, Tsuyushi Swada, Satoko Takahashi, Claudia Tapia, Karl Torstensson, Robert Treacy, Gino Tuccari, Paulina Venegas, Eric Villard, Joseph Weber, Nick Whyborn, Gundolf Wieching, Michael Wunderlich.

We thank the staff at the participating observatories, correlation centers, and institutions for their enthusiastic support.

This Letter makes use of the following ALMA data: ADS/JAO.ALMA#2016.1.01154.V. ALMA is a partnership of the European Southern Observatory (ESO; Europe, representing its member states), NSF, and National Institutes of Natural Sciences of Japan, together with National Research Council (Canada), Ministry of Science and Technology (MOST; Taiwan), Academia Sinica Institute of Astronomy and Astrophysics (ASIAA; Taiwan), and Korea Astronomy and Space Science Institute (KASI; Republic of Korea), in cooperation with the Republic of Chile. The Joint ALMA Observatory is operated by ESO, Associated Universities, Inc. (AUI)/NRAO, and the National Astronomical Observatory of Japan (NAOJ). The NRAO is a facility of the NSF operated under cooperative agreement by AUI. APEX is a collaboration between the Max-Planck-Institut für Radioastronomie (Germany), ESO, and the Onsala Space Observatory (Sweden). The GLT is supported by

the Academia Sinica (Taiwan), the MOST (Taiwan) grants (99-2119-M-001-002-MY4, 103-2119-M-001-010-MY2, 106-2119-M-001-013, 106-2923-M-001-005, and 107-2923-M-001-002), and the Smithsonian Institution. The GLT project thanks the National Chun-Shan Institute of Science and Technology (Taiwan) for their strong support, NAOJ for their support in receiver instrumentation, the NSF Office of Polar Programs for effective support in logistics, and the United States Air Force, 821st Air Base Group, Thule Air Base, Greenland for use of the site and access to the base and logistics chain. The GLT project appreciates the development work done by Vertex Antennentechnik GmbH and ADS international, and also thanks Atunas, an outdoor wear company in Taiwan, for the arctic clothing. NRAO and the Massachusetts Institute of Technology Haystack Observatory supported the acquisition of the ALMA–North America prototype antenna and its repurposing for deployment in Greenland. The NOEMA observatory at the Plateau de Bure, France, and the IRAM 30-m telescope on Pico Veleta, Spain, are operated by IRAM and supported by CNRS (Centre National de la Recherche Scientifique, France), MPG (Max-Planck-Gesellschaft, Germany) and IGN (Instituto Geográfico, Nacional, Spain). The SMA is a joint project between the SAO and ASIAA and is funded by the Smithsonian Institution and the Academia Sinica. The JCMT is operated by the East Asian Observatory on behalf of the NAOJ, ASIAA, and KASI, as well as the Ministry of Finance of China, Chinese Academy of Sciences, and the National Key R&D Program (No. 2017YFA0402700) of China. Additional funding support for the JCMT is provided by the Science and Technologies Facility Council (UK) and participating universities in the UK and Canada. The LMT project is a joint effort of the Instituto Nacional de Astrófisica, Óptica, y Electrónica (Mexico) and the University of Massachusetts at Amherst (USA).

The SMT and KP are operated by the Arizona Radio Observatory, a part of the Steward Observatory of the University of Arizona, with financial support of operations from the State of Arizona and financial support for instrumentation development from the NSF. Partial SPT support is provided by the NSF Physics Frontier Center award (PHY-0114422) to the Kavli Institute of Cosmological Physics at the University of Chicago (USA), the Kavli Foundation, and the GBMF (GBMF-947). The SPT hydrogen maser was provided on loan from the GLT, courtesy of ASIAA. The SPT is supported by the National Science Foundation through grant PLR-1248097. Partial support is also provided by the NSF Physics Frontier Center grant PHY-1125897 to the Kavli Institute of Cosmological Physics at the University of Chicago, the Kavli Foundation and the Gordon and Betty Moore Foundation grant GBMF 947.

The EHTC has received generous donations of FPGA chips from Xilinx Inc., under the Xilinx University Program. The EHTC has benefited from technology shared under open-source license by the Collaboration for Astronomy Signal Processing and Electronics Research (CASPER). The EHT project is grateful to T4Science and Microsemi for their assistance with Hydrogen Masers. This research has made use of NASA's Astrophysics Data System. We gratefully acknowledge the support provided by the extended staff of the ALMA, both from the inception of the ALMA Phasing Project through the observational campaigns of 2017 and 2018. We would like to thank A. Deller and W. Brisken for EHT-specific support with the use of DiFX. We acknowledge the significance that Maunakea, where the SMA and JCMT EHT stations are located, has for the indigenous Hawaiian people.

Appendix
Specific Details of Participating Facilities in EHT Observations

One of the technical challanges of the EHT array is that it is assembled from existing telescope facilities that differ to a greater or lesser extent in their technical characteristics and readiness for VLBI operations. As a result, EHT instrumentation installed at each site requires customization. This appendix provides information on the specifics of each site in turn, not general to the array overall.

A.1. ALMA (5100 m Altitude)

The ALMA, located on the Chajnantor plain in Chile, is an international partnership between Europe, the United States, Canada, Japan, South Korea, Taiwan, and Chile (Wootten & Thompson 2009). The connected-element interferometer consists of fifty 12 m and twelve 7 m antennas, and is supplemented with four 12 m total-power antennas. Reflector surface accuracy is better than 25 μm rms.

The ALMA Phasing Project (APP) was an international effort to produce an antenna phasing system leveraging the superb (sub)millimeter capabilities and large collecting area of ALMA for VLBI applications (Doeleman 2010; Matthews et al. 2018). The APP added to the hardware and software already available at the ALMA site for connected-element interferometry the additional components necessary for coherently summing the ALMA antennas and recording VLBI data products. The rubidium clock that was formerly used to generate the reference 5 MHz LO tone was replaced with a hydrogen maser. Phasing interface cards were added to the ALMA Baseline Correlator to serve as the VLBI backend. A fiber link system was built and deployed to transport the phased-sum signal from the ALMA high-elevation site to the ALMA Operations Support Facility at an elevation of about 2900 m, where a set of Mark 6 VLBI recorders was installed. Numerous software enhancements were also required, including the implementation of an ALMA VLBI Observing Mode (VOM) and a phase solver to calculate the phases needed to adjust each of the ALMA antennas to allow coherent summation of their signals. The ALMA phasing system treats the phased sum as another input to the Baseline Correlator, so the phased-sum signal can be correlated with individual antenna signals. Standard ALMA single-field interferometric data are generated as a matter of course during VOM operation, and ALMA-only data products are archived as usual. When all antennas are included in the phased sum, ALMA is equivalent to an effective $\sim$88 m diameter aperture for VLBI operations. Details are described in Matthews et al. (2018) and Goddi et al. (2019).

A.2. APEX (5100 m Altitude)

APEX is a 12 m antenna located on the Chajnantor plain in Chile about 2 km from the ALMA site (Güsten et al. 2006). It was built by VERTEX Antennentechnik from the ALMA prototype development and inaugurated in 2005. It was outfitted and operated by the Max-Planck-Institut für Radioastronomie in Bonn (50%), the Onsala Space Observatory

(23%), and the European Southern Observatory (27%) as the first telescope on the Chajnantor plain. The first VLBI fringes were obtained with APEX in 2012 at 230 GHz (Wagner et al. 2015).

The reflector surface accuracy is 17 μm rms, which gives good efficiency at frequencies exceeding 1 THz, and the telescope is correspondingly equipped with receivers spanning 200 GHz–1.4 THz. The surface panels and subreflector were replaced in early 2018 to improve the surface to 10 μm rms and so further raise the efficiency at the highest frequencies. At 230 GHz the elevation gain curve is flat to about 3% due to the high structural rigidity of the antenna. Pointing accuracy is better than 2 arcsec rms, and tracking accuracy is typically below 1 arcsec rms depending on wind conditions. The beam FWHM is 27.1 arcsec at 228.1 GHz.

The maser 10 MHz reference is transported to the front-end synthesizers and backend equipment on four low temperature-coefficient, double-shielded 85 m length cables. The cables are wrapped in thermal insulation and firmly fixed to support structures in the receiver cabin to minimize phase instabilities resulting from temperature changes or telescope movement. No round-trip phase stabilization is used. The front-end synthesizers (first LO and tone generation) each have their own frequency reference cable from the maser. References for the backend equipment are supplied through a distributor because the frequencies generated are much lower than for the front-end. The R2DBE and another VLBI backend called the DBBC are located in the antenna close to the receiver (15 m cable length) for low loss transmission of the dual-polarization dual-sideband 4–12 GHz receiver IF output. The Mark 6 recorders are located in a control container about 50 m from the telescope. The backends transmit eight 8 Gbps VDIF-format data streams on fiber with short-range 10 GbE 850 nm SFP+ fiber transceivers to the recorders.

A.3. GLT (100 m Altitude Currently, 3200 m Altitude Planned)

The GLT (Inoue et al. 2014) was originally the 12 m ALMA-North America prototype antenna (Mangum et al. 2006) located at the Very Large Array (VLA) site near Socorro, New Mexico. The antenna was awarded to the Smithsonian Astrophysical Observatory (SAO) in 2011, representing the partnership of the SAO and Academia Sinica Institute of Astronomy (ASIAA). The antenna was retrofitted and rebuilt for operation in the extreme arctic conditions of northern Greenland. Presently located at a temporary site on Thule Air Base, Greenland, the telescope is equipped with a new set of submillimeter receivers operating at 86, 230, and 345 GHz. In 2018, the GLT dish surface underwent iterative adjustments to improve surface accuracy, eventually achieving better than 40 μm rms. The pointing accuracy is about 3−5 arcsec during 230 GHz observations. The telescope is planned to be relocated to Greenland Summit, where the atmosphere provides excellent transparency for submm and THz observations (Matsushita et al. 2017).

The GLT has a complete VLBI backend. In 2018 January, fringes were detected between the GLT and ALMA, and in 2018 April, the GLT participated in EHT observations (Chen et al. 2018). The maser and associated equipment are located in a dedicated trailer approximately 40 m from the telescope. The maser 10 MHz is fed through a phase-stable coaxial cable to an adjacent synthesizer that generates the first LO (18–31 GHz) reference for the receivers. This first LO reference along with a separate maser reference of 100 MHz are combined and transmitted to the antenna through a single-mode fiber and used to phase-lock all the associated instruments in the receiver cabin (Kubo et al. 2018). The BDCs and R2DBEs are located in the receiver cabin and are interconnected using short segments of phase-stable coaxial cables. The Mark 6 recorders are located in the VLBI trailer approximately 35 m from the telescope. Communications between the R2DBEs and the Mark 6 recorders are via a 10 GbE optical network. The current system supports a throughput of 64 Gbps to the recorders.

A.4. JCMT (4100 m Altitude)

The JCMT is located on Maunakea in Hawai‘i. It was dedicated in 1987 and was operated by a consortium (the United Kingdom, Canada, and the Netherlands) until 2015. Since then, the East Asia Observatory has operated the JCMT with funding from Taiwan, China, Japan, Korea, the United Kingdom, and Canada. The reflector is a 15 m Cassegrain design and has a surface accuracy of about 25 μm rms. The telescope is enclosed in a co-rotating dome and is protected by a 0.3 mm thick GoreTex^{TM} windblind that is not removed for observing. The atmospheric opacity is measured with a line-of-sight 183 GHz radiometer.

The telescope participated in the VLBI observations that in 2007 detected the horizon-scale emission in Sgr A* (Doeleman et al. 2008) and has successfully participated in all EHT observing since then. This was done in cooperation with the SMA, which generated the phase-stable frequency reference signals and recorded the IF, utilizing the extended SMA (eSMA) infrastructure that enables the JCMT to join the SMA array as a connected element. From the 2019 VLBI campaign the JCMT will use a locally installed VLBI backend for recording, and will be equipped with a new receiver outfitted with ALMA 230 and 345 GHz mixers at 1.3 and 0.87 mm built by ASIAA.

A.5. Institut de Radioastronomie Millimétrique: 30 m (PV, 2900 m Altitude)

The IRAM 30 m telescope is located on Pico Veleta in the Spanish Sierra Nevada near Granada. The telescope was built in the early 1980s (Baars et al. 1987). The first VLBI fringes at ∼1.3 mm were obtained in 1995 (Greve et al. 1995) with one antenna of the Plateau de Bure interferometer, and since 1996 the PV 30 m has participated in the regular 3 mm VLBI CMVA/GMVA biannual runs.

The telescope surface has been adjusted to an accuracy of about 55 μm rms using phase-coherent holography with geostationary satellites. This yields a 230 GHz aperture efficiency of 47% at the optimal elevation of 50°. The gain elevation curve drops to about 35 % at elevations of 20° and 80°. The blind pointing accuracy is about 3 arcsec. The tracking accuracy is better than 1 arcsec for wind speeds below about 10 m s^{-1}. Active thermal control of the telescope backstructure allows for efficient operation around the clock, and a de-icing system enables quick startup after winter storms. A 225 GHz radiometer continuously monitors the sky opacity at a fixed azimuth. Since 2018 October, the 30 m telescope is connected via a 1 Gbps fiber link to IRAM/Granada and the Spanish research network RedIRIS.

The PV 30 m is currently equipped with two heterodyne receivers. One of these, the Eight MIxer Receiver (EMIR)

installed in 2009, has eight sideband-separating (2SB) mixers. The EMIR has 8 GHz of bandwidth per sideband covering the atmospheric windows at 3, 2, 1.3, and 0.87 mm wavelengths in dual-polarization. The EHT uses the EMIR 1.3 and 0.87 mm bands. Conversion from linear to circular polarization is done by quarter-wave plates, which are installed in a carousel to quickly switch between non-VLBI and VLBI observations. The IF signal from the receiver cabin is transported to a temperature-controlled backend room over 100 m coaxial cables. A new hydrogen maser was installed in 2018 January and then used for the GMVA and EHT sessions in 2018 April. For the EHT, four R2DBEs deliver 64 Gbps (two polarizations, two sidebands) to four Mark 6 recorders (see Figure 8).

A.6. IRAM: NOEMA (2600 m Altitude)

NOEMA is located in the French Alps and is the largest millimeter-wave facility in the northern hemisphere. With twelve 15 meter antennas, 2SB receivers with 8 GHz IF per sideband and polarization, and baselines up to 1.7 km, NOEMA will operate at 10 times the sensitivity and 4 times the spatial resolution of its predecessor, the former Plateau de Bure Interferometer (Guilloteau et al. 1992).

The NOEMA Phase 1 extension program was completed in 2018 September with the delivery of four additional antennas to the existing six, each with a surface accuracy of 35 μm rms. The dual-polarization 2SB receivers operate in the 3, 2, and 1.3 mm wavelength bands, with noise temperatures of, respectively, 35 K, 40 K, and 50 K in each band. Signal processing is done using an FPGA-based FFX correlator with flexible configurations modes. Beginning in 2019, NOEMA will have a phased-array mode with an initial processing bandwidth of 2×2 GHz (16 Gbps), eventually growing to 128 Gbps. The NOEMA Phase 2 extension program (2019) includes the construction of two additional antennas, the delivery of a second correlator for dual-band operation (2×32 GHz), a receiver upgrade to perform full-array observations up to 373 GHz (0.8 mm), and a baseline extension to 1.7 km for high-fidelity imaging down to a spatial resolution of 0.1 arcsec.

A.7. Kitt Peak 12 m (KP, 1900 m Altitude)

The telescope on Kitt Peak was acquired by the University of Arizona in 2013 March. The 12 m dish was a prototype antenna (Mangum et al. 2006) made for the ALMA project by the Alcatel/European Industrial Engineering consortium. It was relocated from the VLA site in New Mexico to the enclosure of the previous NRAO 12 m telescope on Kitt Peak, Arizona, in 2013 November. The telescope is operated by the Arizona Radio Observatory (ARO), a division of the Steward Observatory of the University of Arizona. First light was observed in 2014 October. The surface was adjusted to an rms figure error of 16 μm in 2018 September using photogrammetry. A 225 GHz radiometer measures atmospheric opacity.

VLBI observations will make use of a newly developed multi-band receiver (1.3–4 mm), which incorporates ALMA Band 3 and Band 6 mixers for the 3 and 1.3 mm bands. All bands sample both polarizations, and the 1.3 mm band will be converted to circular polarizations through a quartz quarter-wave plate. The receiver is under commissioning and the telescope is scheduled to participate in the next scheduled EHT observations. The master reference for this site is located within the domed enclosure adjacent to the computer room that houses the VLBI backend electronics.

A.8. LMT (4600 m Altitude)

The LMT is situated at the summit of Volcán Sierra Negra in Central Mexico. It is jointly operated by the Instituto Nacional de Astrofísica, Óptica y Electrónica (INAOE) and the University of Massachusetts (UMass). In 2017, two additional rings of precision surface panels were installed to enlarge the LMT primary mirror from 32.5 to 50 m. The primary mirror is an active surface comprised of 180 segments steered by 720 actuators to correct thermal and mechanical distortions. The large collecting area and a central geographical location with respect to other EHT sites make the LMT particularly important for array sensitivity and imaging fidelity.

Initial technical work to develop 3 mm wavelength VLBI at the LMT was the product of a multi-year collaboration between UMass, INAOE, SAO, the Massachusetts Institute of Technology Haystack Observatory, the Universidad Nacional Autónoma de México (UNAM), and NRAO. The first 3 mm observations were carried out in 2013 April with the facility Redshift Search Receiver (Erickson et al. 2007), a broadband dual-polarization, dual-beam receiver that acted as the front end. Those observations were performed with a VLBI backend using a high-precision quartz oscillator frequency reference running at 2 Gbps recording rate. Subsequent integration of a hydrogen maser and further testing in 2014 led to first VLBI science observations at 3 mm wavelength in 2015 (Ortiz-León et al. 2016).

In 2014, an interim special-purpose VLBI 1.3 mm wavelength receiver was assembled using mixers from the CARMA observatory and resourced through a collaboration including the institutes above and the University of California, Berkeley. This receiver was a single-pixel, dual-polarization, double-sideband receiver. It was deployed in 2015 for commissioning along with a 32 Gbps VLBI system (Figure 4), both of which were used for the 2017 April EHT observations. In early 2018, a new dual-polarization, sideband-separating 230 GHz receiver, using ALMA mixers, was delivered by UMass and installed along with an upgrade of the VLBI system to 64 Gbps capability.

The hydrogen maser at the LMT is located in a temperature-stable environment deep in the apex cone. The maser reference is brought to a 10 MHz distribution system in the VLBI backend room. The backend room is located one level below the receiver cabin and houses the 2.048 GHz synthesizer, the 1 PPS distribution system, BDCs, R2DBEs, and the Mark 6 recorders.

A.9. SMA (4100 m Altitude)

The SMA is an eight-element radio interferometer located atop Maunakea operated by SAO and ASIAA (Ho et al. 2004). The 6 m dishes are configurable with baselines as long as 509 m, which produces a synthesized beam of about 1 arcsec width at 230 GHz, and sub-arcsec width at 345 GHz. The SMA has participated in EHT observations since 2006. In 2006 and 2007, the SMA provided a maser reference tuning signal to the Caltech Submillimeter Observatory and the JCMT, respectively. In 2009, the SMA contributed collecting area to the EHT through the Phased Array Recording Instrument for Galactic Event Horizon Studies (PhRInGES), a 4 Gbps phased-array system.

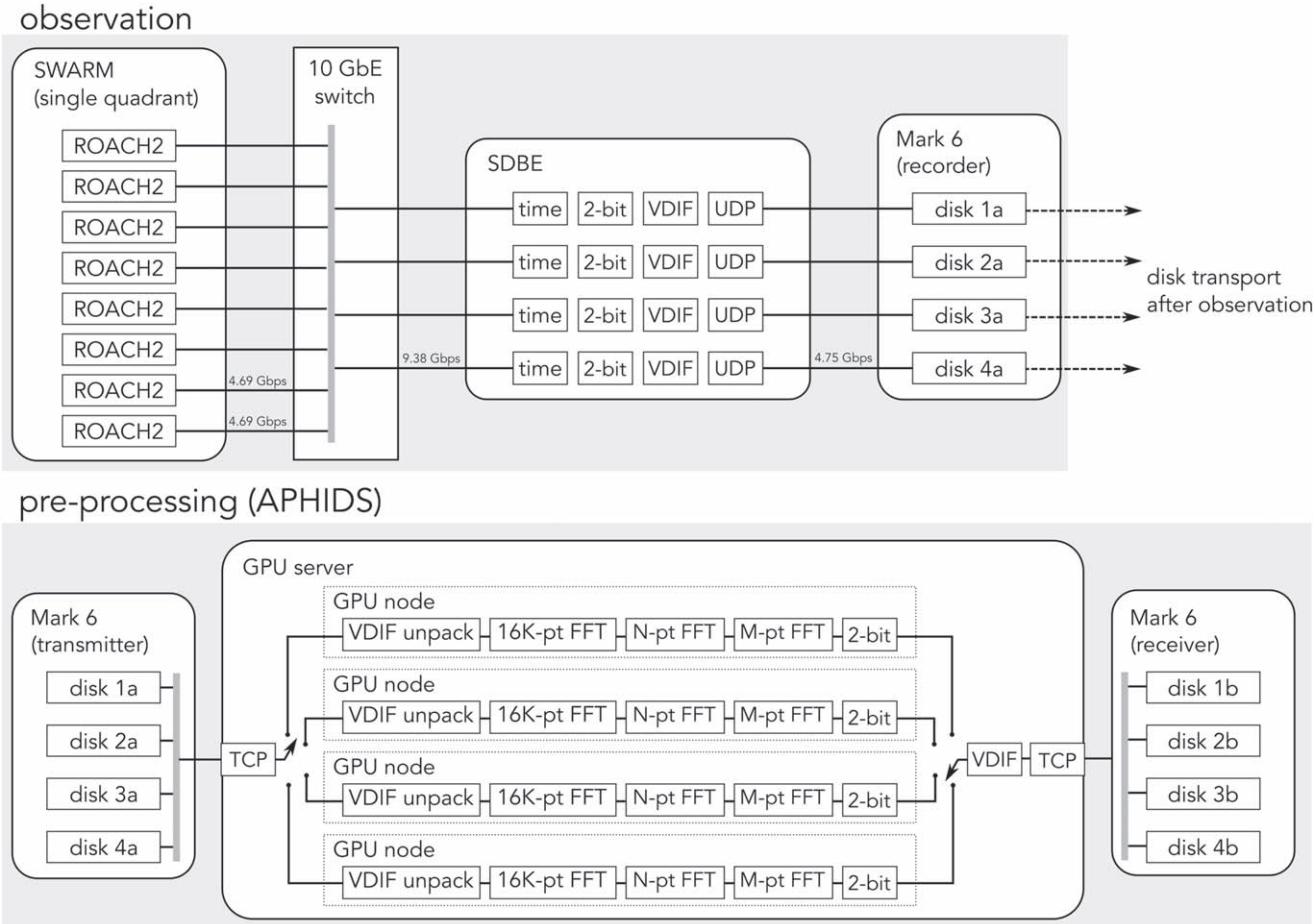

Figure 14. Block diagram demonstrating the VLBI data pipeline, from SWARM to correlatable data in VDIF format. The SDBE is integrated with SWARM and does the real-time processing necessary to interface with the on-site Mark 6 during an observation. After observing, the data is preprocessed offline in APHIDS prior to correlation with data from other sites.

During EHT observations, the SMA uses its own correlator, known as the SMA Wideband Astronomical ROACH2 Machine (SWARM), instead of the R2DBE. SWARM is a combined correlator and phased array that was initially deployed in 2014 and built out to its full 32 GHz bandwidth by 2017 (Primiani et al. 2016). SWARM supports VLBI through a built-in beamformer based on a signal-noise decomposition of the correlator output while observing the target source (Young et al. 2016). Phasing the array requires tracking all sources of delay, including fluctuations in water vapor concentration in the atmosphere. The SWARM phasing system is equipped with a real-time phasing solver that continually updates the beamforming weights over the course of the observation to compensate for these variable delays, which manifest as variable phase errors in each antenna. Because the phased array capability is used to observe sources that are unresolved on baselines within the array, the corrective beamformer weights can be computed by extracting from the correlator output that contribution associated with a point-like source. Furthermore, as the weights are applied to the signal from each antenna before computing cross-correlations between antenna pairs, the solution obtained from the correlator output for a particular integration period can also be used to calculate the average phasing efficiency over that same period. In addition to solving and applying corrective phasing in real time, the system produces an estimate of the phasing efficiency, η_ϕ,

$$\eta_\phi = \left| \sum_{\mathrm{i}} w_{\mathrm{i}} \right|^2 \Big/ \left(\sum_{\mathrm{i}} |w_{\mathrm{i}}| \right)^2, \tag{2}$$

where w_{i} is the complex-valued weight applied to antenna i. See Young et al. (2016)[144] for a more detailed discussion of the phased array and performance assessment thereof.

While the SWARM correlator architecture lends itself conveniently to phased-array processing, it also presents several challenges for integrating the instrument into a VLBI array. First, the beamformer processing of 2 GHz bands is spread across eight ROACH2 devices. These parallel data streams must be collected and formatted in real time in order to record to the Mark 6, which is done using a custom FPGA device called the SWARM Digital Backend (SDBE). The data are received on four of the eight 10 GbE ports on the SDBE. The packets are time-stamped, the frequency domain samples are quantized from 4-bit complex to 2-bit complex, the packets are formatted with VDIF headers, and then transported over Ethernet to the Mark 6. As the beamformer data packets are

[144] See also the related SMA Memo 163 at https://www.cfa.harvard.edu/sma/memos/163.pdf.

relatively small, several of these packets are bundled into each UDP packet to reduce the interrupt rate on the Mark 6 and prevent packet loss. The second complication to using SWARM in VLBI is that the data are in complex frequency domain representation as opposed to the time-domain format used by the majority of stations in the EHT, and the data are sampled at a different rate than the single-dish EHT stations: 4.576 Gsps compared to 4.096 Gsps at single-dish sites. Prior to the correlation of SWARM data with data from other sites, an offline inversion and resampling program known as the Adaptive Phased-array and Heterogeneous Interpolating Downsampler for SWARM (APHIDS) is used to preprocess the SMA data. Development of a real-time preprocessing system to be integrated into the SDBE is currently in progress. The SMA VLBI pipeline is illustrated in Figure 14.

A.10. SMT (3200 m Altitude)

The SMT, located on Mount Graham, Arizona, was built by the Max-Planck-Institut für Radioastronomie in 1993, and is now operated and maintained by the ARO (Baars et al. 1999). Work to incorporate the telescope in mm-wavelength VLBI experiments began in the late 1990s (Doeleman et al. 2002; Krichbaum et al. 2002). In 2007, the SMT participated in the observations that detected horizon-scale emission in Sgr A* (Doeleman et al. 2008). The 10 m telescope is mounted in a co-rotating enclosure that minimizes the effects of insolation and wind during observations. The telescope surface accuracy is $\sim$15 μm rms and the telescope pointing is typically accurate to better than 1.5 arcsec rms. Due to weak diurnal variations in water vapor and the protection of the telescope enclosure, the SMT can observe 24 hr per day. Atmospheric opacity is monitored at this site with a tipping 225 GHz radiometer that is mounted to the rotating dome.

The SMT is equipped with dual-polarization heterodyne receivers covering the atmospheric windows from $\sim$200 to 700 GHz. For VLBI observations, the 1.3 mm receiver system uses prototype ALMA sideband-separating mixers, with polarization splitting achieved via a room-temperature wire grid, and circular polarization induced through a quartz quarter-wave plate. The SMT also has a double-sideband receiver for observations at 0.87 mm; a replacement sideband-separating receiver for this band is in development at the University of Arizona. The 64 Gbps EHT backend hardware is mounted in the receiver cabin. The master reference for the SMT is a hydrogen maser mounted at the base of the telescope pier in a temperature-stabilized closet.

A.11. SPT (2800 m Altitude)

The SPT is a 10 m diameter mm-wavelength telescope located at the geographic South Pole (Carlstrom et al. 2011) and is operated by a collaboration led by the University of Chicago. The off-axis Gregorian design is optimized for observations of the cosmic microwave background with wide-field, multi-color bolometer cameras. The primary reflector surface accuracy is 20 μm rms.

EHT observations with the SPT are managed by the University of Arizona. The standard observing campaigns occur during the austral fall when the South Pole is inaccessible. VLBI setup and testing is performed by a two-person SPT winter-over team, with remote supervision from Arizona. EHT observing at the SPT employs a dual-frequency 230/345 GHz VLBI receiver (Kim et al. 2018a), which was constructed at the University of Arizona. The receiver was first installed in late 2014 and first operated in 2015 January (Kim et al. 2018b). The receiver was reinstalled in an upgraded receiver cabin in 2016 in preparation for the 2017 EHT campaign. To illuminate the VLBI receiver, an alternate secondary mirror is installed ahead of prime focus to form a Cassegrain telescope, which relays the light to an ellipsoidal tertiary mirror atop the receiver. The full VLBI signal chain includes a hydrogen maser and coherence monitoring loops to account for the unusual range of environmental temperatures at the site. Mark 6 data modules are shipped after flights resume in the austral spring season, around November 1.

ORCID iDs

Kazunori Akiyama https://orcid.org/0000-0002-9475-4254
Antxon Alberdi https://orcid.org/0000-0002-9371-1033
Rebecca Azulay https://orcid.org/0000-0002-2200-5393
Anne-Kathrin Baczko https://orcid.org/0000-0003-3090-3975
Mislav Baloković https://orcid.org/0000-0003-0476-6647
John Barrett https://orcid.org/0000-0002-9290-0764
Lindy Blackburn https://orcid.org/0000-0002-9030-642X
Katherine L. Bouman https://orcid.org/0000-0003-0077-4367
Geoffrey C. Bower https://orcid.org/0000-0003-4056-9982
Christiaan D. Brinkerink https://orcid.org/0000-0002-2322-0749
Roger Brissenden https://orcid.org/0000-0002-2556-0894
Silke Britzen https://orcid.org/0000-0001-9240-6734
Avery E. Broderick https://orcid.org/0000-0002-3351-760X
Do-Young Byun https://orcid.org/0000-0003-1157-4109
Andrew Chael https://orcid.org/0000-0003-2966-6220
Chi-kwan Chan https://orcid.org/0000-0001-6337-6126
Shami Chatterjee https://orcid.org/0000-0002-2878-1502
Ilje Cho https://orcid.org/0000-0001-6083-7521
Pierre Christian https://orcid.org/0000-0001-6820-9941
John E. Conway https://orcid.org/0000-0003-2448-9181
Geoffrey B. Crew https://orcid.org/0000-0002-2079-3189
Yuzhu Cui https://orcid.org/0000-0001-6311-4345
Jordy Davelaar https://orcid.org/0000-0002-2685-2434
Mariafelicia De Laurentis https://orcid.org/0000-0002-9945-682X
Roger Deane https://orcid.org/0000-0003-1027-5043
Jessica Dempsey https://orcid.org/0000-0003-1269-9667
Gregory Desvignes https://orcid.org/0000-0003-3922-4055
Jason Dexter https://orcid.org/0000-0003-3903-0373
Sheperd S. Doeleman https://orcid.org/0000-0002-9031-0904
Ralph P. Eatough https://orcid.org/0000-0001-6196-4135
Heino Falcke https://orcid.org/0000-0002-2526-6724
Vincent L. Fish https://orcid.org/0000-0002-7128-9345
Raquel Fraga-Encinas https://orcid.org/0000-0002-5222-1361
José L. Gómez https://orcid.org/0000-0003-4190-7613
Peter Galison https://orcid.org/0000-0002-6429-3872
Charles F. Gammie https://orcid.org/0000-0001-7451-8935
Boris Georgiev https://orcid.org/0000-0002-3586-6424
Roman Gold https://orcid.org/0000-0003-2492-1966
Minfeng Gu (顾敏峰) https://orcid.org/0000-0002-4455-6946

Mark Gurwell https://orcid.org/0000-0003-0685-3621
Kazuhiro Hada https://orcid.org/0000-0001-6906-772X
Ronald Hesper https://orcid.org/0000-0003-1918-6098
Luis C. Ho (何子山) https://orcid.org/0000-0001-6947-5846
Mareki Honma https://orcid.org/0000-0003-4058-9000
Chih-Wei L. Huang https://orcid.org/0000-0001-5641-3953
Shiro Ikeda https://orcid.org/0000-0002-2462-1448
Sara Issaoun https://orcid.org/0000-0002-5297-921X
David J. James https://orcid.org/0000-0001-5160-4486
Michael Janssen https://orcid.org/0000-0001-8685-6544
Britton Jeter https://orcid.org/0000-0003-2847-1712
Wu Jiang (江悟) https://orcid.org/0000-0001-7369-3539
Michael D. Johnson https://orcid.org/0000-0002-4120-3029
Svetlana Jorstad https://orcid.org/0000-0001-6158-1708
Taehyun Jung https://orcid.org/0000-0001-7003-8643
Mansour Karami https://orcid.org/0000-0001-7387-9333
Ramesh Karuppusamy https://orcid.org/0000-0002-5307-2919
Tomohisa Kawashima https://orcid.org/0000-0001-8527-0496
Garrett K. Keating https://orcid.org/0000-0002-3490-146X
Mark Kettenis https://orcid.org/0000-0002-6156-5617
Jae-Young Kim https://orcid.org/0000-0001-8229-7183
Junhan Kim https://orcid.org/0000-0002-4274-9373
Motoki Kino https://orcid.org/0000-0002-2709-7338
Jun Yi Koay https://orcid.org/0000-0002-7029-6658
Patrick M. Koch https://orcid.org/0000-0003-2777-5861
Shoko Koyama https://orcid.org/0000-0002-3723-3372
Michael Kramer https://orcid.org/0000-0002-4175-2271
Carsten Kramer https://orcid.org/0000-0002-4908-4925
Thomas P. Krichbaum https://orcid.org/0000-0002-4892-9586
Tod R. Lauer https://orcid.org/0000-0003-3234-7247
Sang-Sung Lee https://orcid.org/0000-0002-6269-594X
Yan-Rong Li (李彦荣) https://orcid.org/0000-0001-5841-9179
Zhiyuan Li (李志远) https://orcid.org/0000-0003-0355-6437
Michael Lindqvist https://orcid.org/0000-0002-3669-0715
Kuo Liu https://orcid.org/0000-0002-2953-7376
Elisabetta Liuzzo https://orcid.org/0000-0003-0995-5201
Laurent Loinard https://orcid.org/0000-0002-5635-3345
Ru-Sen Lu (路如森) https://orcid.org/0000-0002-7692-7967
Nicholas R. MacDonald https://orcid.org/0000-0002-6684-8691
Jirong Mao (毛基荣) https://orcid.org/0000-0002-7077-7195
Sera Markoff https://orcid.org/0000-0001-9564-0876
Daniel P. Marrone https://orcid.org/0000-0002-2367-1080
Alan P. Marscher https://orcid.org/0000-0001-7396-3332
Iván Martí-Vidal https://orcid.org/0000-0003-3708-9611
Lynn D. Matthews https://orcid.org/0000-0002-3728-8082
Lia Medeiros https://orcid.org/0000-0003-2342-6728
Karl M. Menten https://orcid.org/0000-0001-6459-0669
Yosuke Mizuno https://orcid.org/0000-0002-8131-6730
Izumi Mizuno https://orcid.org/0000-0002-7210-6264
James M. Moran https://orcid.org/0000-0002-3882-4414
Kotaro Moriyama https://orcid.org/0000-0003-1364-3761
Monika Moscibrodzka https://orcid.org/0000-0002-4661-6332
Cornelia Müller https://orcid.org/0000-0002-2739-2994
Hiroshi Nagai https://orcid.org/0000-0003-0292-3645
Neil M. Nagar https://orcid.org/0000-0001-6920-662X
Masanori Nakamura https://orcid.org/0000-0001-6081-2420
Ramesh Narayan https://orcid.org/0000-0002-1919-2730
Iniyan Natarajan https://orcid.org/0000-0001-8242-4373
Chunchong Ni https://orcid.org/0000-0003-1361-5699
Aristeidis Noutsos https://orcid.org/0000-0002-4151-3860
Héctor Olivares https://orcid.org/0000-0001-6833-7580
Gisela N. Ortiz-León https://orcid.org/0000-0002-2863-676X
Daniel C. M. Palumbo https://orcid.org/0000-0002-7179-3816
Ue-Li Pen https://orcid.org/0000-0003-2155-9578
Dominic W. Pesce https://orcid.org/0000-0002-5278-9221
Oliver Porth https://orcid.org/0000-0002-4584-2557
Ben Prather https://orcid.org/0000-0002-0393-7734
Jorge A. Preciado-López https://orcid.org/0000-0002-4146-0113
Hung-Yi Pu https://orcid.org/0000-0001-9270-8812
Venkatessh Ramakrishnan https://orcid.org/0000-0002-9248-086X
Ramprasad Rao https://orcid.org/0000-0002-1407-7944
Alexander W. Raymond https://orcid.org/0000-0002-5779-4767
Luciano Rezzolla https://orcid.org/0000-0002-1330-7103
Bart Ripperda https://orcid.org/0000-0002-7301-3908
Freek Roelofs https://orcid.org/0000-0001-5461-3687
Eduardo Ros https://orcid.org/0000-0001-9503-4892
Mel Rose https://orcid.org/0000-0002-2016-8746
Alan L. Roy https://orcid.org/0000-0002-1931-0135
Chet Ruszczyk https://orcid.org/0000-0001-7278-9707
Benjamin R. Ryan https://orcid.org/0000-0001-8939-4461
Kazi L. J. Rygl https://orcid.org/0000-0003-4146-9043
David Sánchez-Arguelles https://orcid.org/0000-0002-7344-9920
Mahito Sasada https://orcid.org/0000-0001-5946-9960
Tuomas Savolainen https://orcid.org/0000-0001-6214-1085
Lijing Shao https://orcid.org/0000-0002-1334-8853
Zhiqiang Shen (沈志强) https://orcid.org/0000-0003-3540-8746
Des Small https://orcid.org/0000-0003-3723-5404
Bong Won Sohn https://orcid.org/0000-0002-4148-8378
Jason SooHoo https://orcid.org/0000-0003-1938-0720
Fumie Tazaki https://orcid.org/0000-0003-0236-0600
Paul Tiede https://orcid.org/0000-0003-3826-5648
Remo P. J. Tilanus https://orcid.org/0000-0002-6514-553X
Michael Titus https://orcid.org/0000-0002-3423-4505
Kenji Toma https://orcid.org/0000-0002-7114-6010
Pablo Torne https://orcid.org/0000-0001-8700-6058
Sascha Trippe https://orcid.org/0000-0003-0465-1559
Ilse van Bemmel https://orcid.org/0000-0001-5473-2950
Huib Jan van Langevelde https://orcid.org/0000-0002-0230-5946
Daniel R. van Rossum https://orcid.org/0000-0001-7772-6131
John Wardle https://orcid.org/0000-0002-8960-2942
Jonathan Weintroub https://orcid.org/0000-0002-4603-5204
Norbert Wex https://orcid.org/0000-0003-4058-2837
Robert Wharton https://orcid.org/0000-0002-7416-5209

Maciek Wielgus https://orcid.org/0000-0002-8635-4242
George N. Wong https://orcid.org/0000-0001-6952-2147
Qingwen Wu
(吴庆文) https://orcid.org/0000-0003-4773-4987
André Young https://orcid.org/0000-0003-0000-2682
Ken Young https://orcid.org/0000-0002-3666-4920
Ziri Younsi https://orcid.org/0000-0001-9283-1191
Feng Yuan (袁峰) https://orcid.org/0000-0003-3564-6437
J. Anton Zensus https://orcid.org/0000-0001-7470-3321
Guangyao Zhao https://orcid.org/0000-0002-4417-1659
Shan-Shan Zhao https://orcid.org/0000-0002-9774-3606
Juan-Carlos Algaba https://orcid.org/0000-0001-6993-1696
Uwe Bach https://orcid.org/0000-0002-7722-8412
Bradford A. Benson https://orcid.org/0000-0002-5108-6823
Jay M. Blanchard https://orcid.org/0000-0002-2756-395X
Iain M. Coulson https://orcid.org/0000-0002-7316-4626
Thomas M. Crawford https://orcid.org/0000-0001-9000-5013
Sergio A. Dzib https://orcid.org/0000-0001-6010-6200
Wendeline B. Everett https://orcid.org/0000-0002-5370-6651
Joseph R. Farah https://orcid.org/0000-0003-4914-5625
Christopher H. Greer https://orcid.org/0000-0002-9590-0508
Nils W. Halverson https://orcid.org/0000-0003-2606-9340
Antonio Hernández-Gómez https://orcid.org/0000-0001-7520-4305
Rubén Herrero-Illana https://orcid.org/0000-0002-7758-8717
Atish Kamble https://orcid.org/0000-0003-0861-5168
Ryan Keisler https://orcid.org/0000-0002-5922-1137
Yusuke Kono https://orcid.org/0000-0002-4187-8747
Erik M. Leitch https://orcid.org/0000-0001-8553-9336
Kyle D. Massingill https://orcid.org/0000-0002-0830-2033
Hugo Messias https://orcid.org/0000-0002-2985-7994
Daniel Michalik https://orcid.org/0000-0002-7618-6556
Andrew Nadolski https://orcid.org/0000-0001-9479-9957
Chi H. Nguyen https://orcid.org/0000-0001-9368-3186
Harriet Parsons https://orcid.org/0000-0002-6327-3423
Scott N. Paine https://orcid.org/0000-0003-4622-5857
Rurik A. Primiani https://orcid.org/0000-0003-3910-7529
Alexandra S. Rahlin https://orcid.org/0000-0003-3953-1776
Pim Schellart https://orcid.org/0000-0002-8324-0880
Hotaka Shiokawa https://orcid.org/0000-0002-8847-5275
David R. Smith https://orcid.org/0000-0003-0692-8582
Antony A. Stark https://orcid.org/0000-0002-2718-9996
Sjoerd T. Timmer https://orcid.org/0000-0003-0223-9368
Nathan Whitehorn https://orcid.org/0000-0002-3157-0407
Jan G. A. Wouterloot https://orcid.org/0000-0002-4694-6905
Melvin Wright https://orcid.org/0000-0002-9154-2440
Paul Yamaguchi https://orcid.org/0000-0002-6017-8199
Lucy Ziurys https://orcid.org/0000-0002-1805-3886

References

Abbott, B. P., Abbott, R., Abbott, T. D., et al. 2016, PhRvL, 116, 061102
Akiyama, K., Ikeda, S., Pleau, M., et al. 2017, AJ, 153, 159
Akiyama, K., Lu, R.-S., Fish, V. L., et al. 2015, ApJ, 807, 150
Baars, J. W. M., Hooghoudt, B. G., Mezger, P. G., & de Jonge, M. J. 1987, A&A, 175, 319
Baars, J. W. M., Martin, R. N., Mangum, J. G., McMullin, J. P., & Peters, W. L. 1999, PASP, 111, 627
Baganoff, F. K., Maeda, Y., Morris, M., et al. 2003, ApJ, 591, 891
Balick, B., & Brown, R. L. 1974, ApJ, 194, 265
Bardeen, J. M., Press, W. H., & Teukolsky, S. A. 1972, ApJ, 178, 347
Bardeen, J. M. 1973, in Black Holes (Les Astres Occlus), ed. C. Dewitt & B. S. Dewitt (London: Gordon and Breach), 215
Blackburn, L., Chan, C.-K., Crew, G. B., et al. 2019, arXiv:1903.08832
Blakeslee, J. P., Jordán, A., Mei, S., et al. 2009, ApJ, 694, 556
Blandford, R., Meier, D., & Readhead, A. 2018, ARA&A, in press (arXiv:1812.06025)
Boccardi, B., Krichbaum, T. P., Ros, E., & Zensus, J. A. 2017, A&ARv, 25, 4
Bouman, K., Johnson, M., Dalca, A., et al. 2018, IEEE Transactions on Computational Imaging, 4, 512
Bouman, K. L., Johnson, M. D., Zoran, D., et al. 2016, in IEEE Conf. on Computer Vision and Pattern Recognition (CVPR) (New York: IEEE), 913
Bower, G. C., Deller, A., Demorest, P., et al. 2015, ApJ, 798, 120
Bower, G. C., Goss, W. M., Falcke, H., Backer, D. C., & Lithwick, Y. 2006, ApJL, 648, L127
Broderick, A. E., & Loeb, A. 2006, MNRAS, 367, 905
Broderick, A. E., & Loeb, A. 2009, ApJ, 697, 1164
Carlstrom, J. E., Ade, P. A. R., Aird, K. A., et al. 2011, PASP, 123, 568
Carter, M., Lazareff, B., Maier, D., et al. 2012, A&A, 538, A89
Chael, A. A., Johnson, M. D., Bouman, K. L., et al. 2018, ApJ, 857, 23
Chael, A. A., Johnson, M. D., Narayan, R., et al. 2016, ApJ, 829, 11
Chandrasekhar, S. 1983, The Mathematical Theory of Black Holes (Oxford: Clarendon, Oxford Univ. Press)
Chen, M.-T., Raffin, P., Ho, P. T. P., et al. 2018, Proc. SPIE, 10700, 107000H
Cooper, B. F. C. 1970, AuJPh, 23, 521
Deller, A. T., Brisken, W. F., Phillips, C. J., et al. 2011, PASP, 123, 275
Dexter, J., Agol, E., Fragile, P. C., & McKinney, J. C. 2010, ApJ, 717, 1092
Di Matteo, T., Quataert, E., Allen, S. W., Narayan, R., & Fabian, A. C. 2000, MNRAS, 311, 507
Doeleman, S. 2010, in Proc. 10th European VLBI Network Symp. and EVN Users Meeting: VLBI and the New Generation of Radio Arrays (Trieste: SISSA), 53
Doeleman, S., Agol, E., Backer, D., et al. 2009a, Astro2010: The Astronomy and Astrophysics Decadal Survey, Science White Papers, 68
Doeleman, S., & Krichbaum, T. P. 1999, in 2nd Millimeter-VLBI Science Workshop, ed. A. Greve & T. P. Krichbaum (St. Martin d'Heres: IRAM), 73
Doeleman, S., Mai, T., Rogers, A. E. E., et al. 2011, PASP, 123, 582
Doeleman, S. S., Fish, V. L., Broderick, A. E., Loeb, A., & Rogers, A. E. E. 2009b, ApJ, 695, 59
Doeleman, S. S., Fish, V. L., Schenck, D. E., et al. 2012, Sci, 338, 355
Doeleman, S. S., Phillips, R. B., Rogers, A. E. E., et al. 2002, in Proc. 6th EVN Symp., ed. E. Ros et al. (Bonn: Max-Planck-Institut für Radioastronomie), 223
Doeleman, S. S., Weintroub, J., Rogers, A. E. E., et al. 2008, Natur, 455, 78
EHT Collaboration et al. 2019a, ApJL, 875, L1 (Paper I)
EHT Collaboration et al. 2019b, ApJL, 875, L3 (Paper III)
EHT Collaboration et al. 2019c, ApJL, 875, L4 (Paper IV)
EHT Collaboration et al. 2019d, ApJL, 875, L5 (Paper V)
EHT Collaboration et al. 2019e, ApJL, 875, L6 (Paper VI)
Erickson, N., Narayanan, G., Goeller, R., & Grosslein, R. 2007, in ASP Conf. Ser. 375, From Z-Machines to ALMA: (Sub)Millimeter Spectroscopy of Galaxies, ed. A. J. Baker et al. (San Francisco, CA: ASP), 71
Falcke, H., Melia, F., & Agol, E. 2000, ApJL, 528, L13
Fish, V. L., Doeleman, S. S., Beaudoin, C., et al. 2011, ApJL, 727, L36
Fish, V. L., Doeleman, S. S., Broderick, A. E., Loeb, A., & Rogers, A. E. E. 2009, ApJ, 706, 1353
Fish, V. L., Johnson, M. D., Lu, R.-S., et al. 2014, ApJ, 795, 134
Fraga-Encinas, R., Mościbrodzka, M., Brinkerink, C., & Falcke, H. 2016, A&A, 588, A57
Gebhardt, K., Adams, J., Richstone, D., et al. 2011, ApJ, 729, 119
Genzel, R., Eisenhauer, F., & Gillessen, S. 2010, RvMP, 82, 3121
Ghez, A. M., Salim, S., Weinberg, N. N., et al. 2008, ApJ, 689, 1044
Gill, A., Blackburn, L., Roshanineshat, A., et al. 2019, PASP, submitted
Goddi, C., Marti-Vidal, I., Messias, H., et al. 2019, PASP, in press
Gold, R., McKinney, J. C., Johnson, M. D., & Doeleman, S. S. 2017, ApJ, 837, 180
GRAVITY Collaboration, Abuter, R., Amorim, A., et al. 2018a, A&A, 618, L10
Gravity Collaboration, Abuter, R., Amorim, A., et al. 2018b, A&A, 615, L15
Greve, A., Torres, M., Wink, J. E., et al. 1995, A&A, 299, L33
Guilloteau, S., Delannoy, J., Downes, D., et al. 1992, A&A, 262, 624
Güsten, R., Nyman, L. Å., Schilke, P., et al. 2006, A&A, 454, L13
Heckman, T. M., & Best, P. N. 2014, ARA&A, 52, 589
Hickish, J., Abdurashidova, Z., Ali, Z., et al. 2016, JAI, 5, 1641001

Hilbert, D. 1917, NWGot, 8, 53
Ho, L. C. 2008, ARA&A, 46, 475
Ho, P. T. P., Moran, J. M., & Lo, K. Y. 2004, ApJL, 616, L1
Honma, M., Akiyama, K., Uemura, M., & Ikeda, S. 2014, PASJ, 66, 95
Inoue, M., Algaba-Marcos, J. C., Asada, K., et al. 2014, RaSc, 49, 564
Issaoun, S., Johnson, M. D., Blackburn, L., et al. 2019, ApJ, 871, 30
Janssen, M., Goddi, C., van Bemmel, I. M., et al. 2019, A&A, submitted (arXiv:1902.01749)
Jiang, H., Liu, H., Guzzino, K., et al. 2014, PASP, 126, 761
Johannsen, T., & Psaltis, D. 2010, ApJ, 718, 446
Johannsen, T., Psaltis, D., Gillessen, S., et al. 2012, ApJ, 758, 30
Johnson, M. D., Fish, V. L., Doeleman, S. S., et al. 2015, Sci, 350, 1242
Johnson, M. D., Narayan, R., Psaltis, D., et al. 2018, ApJ, 865, 104
Kardashev, N. S., Khartov, V. V., Abramov, V. V., et al. 2013, ARep, 57, 153
Kerr, A. R., Pan, S.-K., Claude, S. M. X., et al. 2014, ITTST, 4, 201
Kim, J., Marrone, D. P., Beaudoin, C., et al. 2018a, Proc. SPIE, 10708, 107082S
Kim, J., Marrone, D. P., Roy, A. L., et al. 2018b, ApJ, 861, 129
Krichbaum, T. P., Graham, D. A., Alef, W., et al. 2002, in Proc. 6th EVN Symp., ed. E. Ros et al. (Bonn: Max-Planck-Institut für Radioastronomie), 125
Krichbaum, T. P., Graham, D. A., Witzel, A., et al. 1998, A&A, 335, L106
Kubo, D., Han, C.-C., Nishioka, H., et al. 2018, Proc. SPIE, 10708, 1070816
Kuo, C. Y., Asada, K., Rao, R., et al. 2014, ApJL, 783, L33
Kuramochi, K., Akiyama, K., Ikeda, S., et al. 2018, ApJ, 858, 56
Lambert, S. B., & Gontier, A.-M. 2009, A&A, 493, 317
Lo, K. Y., Shen, Z.-Q., Zhao, J.-H., & Ho, P. T. P. 1998, ApJL, 508, L61
Lu, R.-S., Broderick, A. E., Baron, F., et al. 2014, ApJ, 788, 120
Lu, R.-S., Krichbaum, T. P., Eckart, A., et al. 2011, A&A, 525, A76
Lu, R.-S., Krichbaum, T. P., Roy, A. L., et al. 2018, ApJ, 859, 60
Luminet, J.-P. 1979, A&A, 75, 228
Maier, D. 2009, EAS, 37, 49
Mangum, J. G., Baars, J. W. M., Greve, A., et al. 2006, PASP, 118, 1257
Marrone, D. P., Moran, J. M., Zhao, J.-H., & Rao, R. 2007, ApJL, 654, L57
Marrone, D. P., Tilanus, R. P. J., & Doeleman, S. S. 2014, EHT Memo Series, 2014-ETWG-01
Martí-Vidal, I., Roy, A., Conway, J., & Zensus, A. J. 2016, A&A, 587, A143
Matsushita, S., Asada, K., Martin-Cocher, P. L., et al. 2017, PASP, 129, 025001
Matthews, L. D., Crew, G. B., Doeleman, S. S., et al. 2018, PASP, 130, 015002
Medeiros, L., Chan, C.-K., Özel, F., et al. 2017, ApJ, 844, 35
Moritz, H. 2000, JGeod, 74, 128
Mościbrodzka, M., Gammie, C. F., Dolence, J. C., Shiokawa, H., & Leung, P. K. 2009, ApJ, 706, 497
Napier, P. J., Bagri, D. S., Clark, B. G., et al. 1994, IEEEP, 82, 658
Narayan, R., & McClintock, J. E. 2008, NewAR, 51, 733
Narayan, R., & Nityananda, R. 1986, ARA&A, 24, 127
Ortiz-León, G. N., Johnson, M. D., Doeleman, S. S., et al. 2016, ApJ, 824, 40
Padin, S., Woody, D. P., Hodges, M. W., et al. 1990, ApJL, 360, L11
Patel, N. A., Wilson, R. W., Primiani, R., et al. 2014, JAI, 3, 1450001
Phillips, T., Woody, D., Dolan, G. R. M., & Linke, R. 1981, ITM, 17, 684
Primiani, R. A., Young, K. H., Young, A., et al. 2016, JAI, 5, 1641006
Psaltis, D., Johnson, M., Narayan, R., et al. 2018, arXiv:1805.01242
Reid, M. J., & Brunthaler, A. 2004, ApJ, 616, 872
Reid, M. J., Menten, K. M., Brunthaler, A., et al. 2014, ApJ, 783, 130
Ricarte, A., & Dexter, J. 2015, MNRAS, 446, 1973
Roelofs, F., Johnson, M. D., Shiokawa, H., Doeleman, S. S., & Falcke, H. 2017, ApJ, 847, 55
Rogers, A. E. E., Moffet, A. T., Backer, D. C., & Moran, J. M. 1984, RaSc, 19, 1552
Rogers, A. E. E., & Moran, J. M., Jr. 1981, ITIM, 30, 283
Shen, Z.-Q., Lo, K. Y., Liang, M.-C., Ho, P. T. P., & Zhao, J.-H. 2005, Natur, 438, 62
Takahashi, R. 2004, ApJ, 611, 996
Thompson, A. R., Moran, J. M., & Swenson, G. W., Jr. 2017, Interferometry and Synthesis in Radio Astronomy (3rd ed.; Berlin: Springer)
Tilanus, R. P. J., Marrone, D. P., Fish, V. L., et al. 2013, EHT Memo Series, 2013-ETWG-01
Tong, C. E., Grimes, P., Blundell, R., Wang, M., & Noguchi, T. 2013, ITTST, 3, 428
Tuccari, G., Alef, W., Buttaccio, S., et al. 2014, in Int. VLBI Service for Geodesy and Astrometry 2014 General Meeting Proc.: "VGOS: The New VLBI Network", ed. D. Behrend, K. D. Baver, & K. L. Armstrong (Beijing: Science Press), 86
Vertatschitsch, L., Primiani, R., Young, A., et al. 2015, PASP, 127, 1226
von Laue, M. 1921, Die Relativitätstheorie. Zweiter Band: Die Allgemeine Relativitätstheorie Und Einsteins Lehre Von Der Schwerkraft (Braunsweig: F. Vieweg & Sohn)
Wagner, J., Roy, A. L., Krichbaum, T. P., et al. 2015, A&A, 581, A32
Walsh, J. L., Barth, A. J., Ho, L. C., & Sarzi, M. 2013, ApJ, 770, 86
Whitney, A., Kettenis, M., Phillips, C., & Sekido, M. 2009, in 8th Int. e-VLBI Workshop (Trieste: SISSA), 42
Whitney, A. R., Beaudoin, C. J., Cappallo, R. J., et al. 2013, PASP, 125, 196
Wootten, A., & Thompson, A. R. 2009, IEEEP, 97, 1463
Young, A., Primiani, R., Weintroub, J., et al. 2016, in 2016 IEEE Int. Symp. Phased Array Systems and Technology (PAST) (New York: IEEE), 1

The Event Horizon Telescope Collaboration,
Kazunori Akiyama[1,2,3,4], Antxon Alberdi[5], Walter Alef[6], Keiichi Asada[7], Rebecca Azulay[8,9,6], Anne-Kathrin Baczko[6], David Ball[10], Mislav Baloković[4,11], John Barrett[2], Dan Bintley[12], Lindy Blackburn[4,11], Wilfred Boland[13], Katherine L. Bouman[4,11,14], Geoffrey C. Bower[15], Michael Bremer[16], Christiaan D. Brinkerink[17], Roger Brissenden[4,11], Silke Britzen[6], Avery E. Broderick[18,19,20], Dominique Broguiere[16], Thomas Bronzwaer[17], Do-Young Byun[21,22], John E. Carlstrom[23,24,25,26], Andrew Chael[4,11], Chi-kwan Chan[10,27], Shami Chatterjee[28], Koushik Chatterjee[29], Ming-Tang Chen[15], Yongjun Chen (陈永军)[30,31], Ilje Cho[21,22], Pierre Christian[10,11], John E. Conway[32], James M. Cordes[28], Geoffrey B. Crew[2], Yuzhu Cui[33,34], Jordy Davelaar[17], Mariafelicia De Laurentis[35,36,37], Roger Deane[38,39], Jessica Dempsey[12], Gregory Desvignes[6], Jason Dexter[40], Sheperd S. Doeleman[4,11], Ralph P. Eatough[6], Heino Falcke[17], Vincent L. Fish[2], Ed Fomalont[1], Raquel Fraga-Encinas[17], Per Friberg[12], Christian M. Fromm[36], José L. Gómez[5], Peter Galison[4,41,42], Charles F. Gammie[43,44], Roberto García[16], Olivier Gentaz[16], Boris Georgiev[19,20], Ciriaco Goddi[17,45], Roman Gold[36], Minfeng Gu (顾敏峰)[30,46], Mark Gurwell[11], Kazuhiro Hada[33,34], Michael H. Hecht[2], Ronald Hesper[47], Luis C. Ho (何子山)[48,49], Paul Ho[7], Mareki Honma[33,34], Chih-Wei L. Huang[7], Lei Huang (黄磊)[30,46], David H. Hughes[50], Shiro Ikeda[3,51,52,53], Makoto Inoue[7], Sara Issaoun[17], David J. James[4,11], Buell T. Jannuzi[10], Michael Janssen[17], Britton Jeter[19,20], Wu Jiang (江悟)[30], Michael D. Johnson[4,11], Svetlana Jorstad[54,55], Taehyun Jung[21,22], Mansour Karami[18,19], Ramesh Karuppusamy[6], Tomohisa Kawashima[3], Garrett K. Keating[11], Mark Kettenis[56], Jae-Young Kim[6], Junhan Kim[10], Jongsoo Kim[21], Motoki Kino[3,57], Jun Yi Koay[7], Patrick M. Koch[7], Shoko Koyama[7], Michael Kramer[6], Carsten Kramer[16], Thomas P. Krichbaum[6], Cheng-Yu Kuo[58], Tod R. Lauer[59], Sang-Sung Lee[21], Yan-Rong Li (李彦荣)[60], Zhiyuan Li (李志远)[61,62], Michael Lindqvist[32], Kuo Liu[6], Elisabetta Liuzzo[63], Wen-Ping Lo[7,64], Andrei P. Lobanov[6], Laurent Loinard[65,66], Colin Lonsdale[2], Ru-Sen Lu (路如森)[6,30], Nicholas R. MacDonald[6], Jirong Mao (毛基荣)[67,68,69], Sera Markoff[29,70], Daniel P. Marrone[10],

Alan P. Marscher[54], Iván Martí-Vidal[32,71], Satoki Matsushita[7], Lynn D. Matthews[2], Lia Medeiros[10,72], Karl M. Menten[6], Yosuke Mizuno[36], Izumi Mizuno[12], James M. Moran[4,11], Kotaro Moriyama[2,33], Monika Moscibrodzka[17], Cornelia Müller[6,17], Hiroshi Nagai[3,34], Neil M. Nagar[73], Masanori Nakamura[7], Ramesh Narayan[4,11], Gopal Narayanan[74], Iniyan Natarajan[39], Roberto Neri[16], Chunchong Ni[19,20], Aristeidis Noutsos[6], Hiroki Okino[33,75], Héctor Olivares[36], Gisela N. Ortiz-León[6], Tomoaki Oyama[33], Feryal Özel[10], Daniel C. M. Palumbo[4,11], Nimesh Patel[11], Ue-Li Pen[18,76,77,78], Dominic W. Pesce[4,11], Vincent Piétu[16], Richard Plambeck[79], Aleksandar PopStefanija[74], Oliver Porth[29,36], Ben Prather[43], Jorge A. Preciado-López[18], Dimitrios Psaltis[10], Hung-Yi Pu[18], Venkatessh Ramakrishnan[73], Ramprasad Rao[15], Mark G. Rawlings[12], Alexander W. Raymond[4,11], Luciano Rezzolla[36], Bart Ripperda[36], Freek Roelofs[17], Alan Rogers[2], Eduardo Ros[6], Mel Rose[10], Arash Roshanineshat[10], Helge Rottmann[6], Alan L. Roy[6], Chet Ruszczyk[2], Benjamin R. Ryan[80,81], Kazi L. J. Rygl[63], Salvador Sánchez[82], David Sánchez-Arguelles[50,83], Mahito Sasada[33,84], Tuomas Savolainen[6,85,86], F. Peter Schloerb[74], Karl-Friedrich Schuster[16], Lijing Shao[6,49], Zhiqiang Shen (沈志强)[30,31], Des Small[56], Bong Won Sohn[21,22,87], Jason SooHoo[2], Fumie Tazaki[33], Paul Tiede[19,20], Remo P. J. Tilanus[17,45,88], Michael Titus[2], Kenji Toma[89,90], Pablo Torne[6,82], Tyler Trent[10], Sascha Trippe[91], Shuichiro Tsuda[33], Ilse van Bemmel[56], Huib Jan van Langevelde[56,92], Daniel R. van Rossum[17], Jan Wagner[6], John Wardle[93], Jonathan Weintroub[4,11], Norbert Wex[6], Robert Wharton[6], Maciek Wielgus[4,11], George N. Wong[43], Qingwen Wu (吴庆文)[94], André Young[17], Ken Young[11], Ziri Younsi[95,36], Feng Yuan (袁峰)[30,46,96], Ye-Fei Yuan (袁业飞)[97], J. Anton Zensus[6], Guangyao Zhao[21], Shan-Shan Zhao[17,61], Ziyan Zhu[42], Juan-Carlos Algaba[7,98], Alexander Allardi[99], Rodrigo Amestica[100], Uwe Bach[6], Christopher Beaudoin[2], Bradford A. Benson[23,24,26], Ryan Berthold[12], Jay M. Blanchard[56,73], Ray Blundell[11], Sandra Bustamente[101], Roger Cappallo[2], Edgar Castillo-Domínguez[101,102], Chih-Cheng Chang[7,103], Shu-Hao Chang[7], Song-Chu Chang[103], Chung-Chen Chen[7], Ryan Chilson[15], Tim C. Chuter[12], Rodrigo Córdova Rosado[4,11], Iain M. Coulson[12], Thomas M. Crawford[24], Joseph Crowley[104], John David[82], Mark Derome[2], Matthew Dexter[105], Sven Dornbusch[6], Kevin A. Dudevoir[135], Sergio A. Dzib[6], Chris Eckert[2], Neal R. Erickson[74], Wendeline B. Everett[106], Aaron Faber[107], Joseph R. Farah[4,11,108], Vernon Fath[74], Thomas W. Folkers[10], David C. Forbes[10], Robert Freund[10], Arturo I. Gómez-Ruiz[101,102], David M. Gale[101], Feng Gao[30,40], Gertie Geertsema[109], David A. Graham[6], Christopher H. Greer[10], Ronald Grosslein[74], Frédéric Gueth[16], Nils W. Halverson[110], Chih-Chiang Han[7], Kuo-Chang Han[103], Jinchi Hao[103], Yutaka Hasegawa[111], Jason W. Henning[112,23], Antonio Hernández-Gómez[65,113], Rubén Herrero-Illana[114], Stefan Heyminck[6], Akihiko Hirota[3,115], James Hoge[12], Yau-De Huang[7], C. M. Violette Impellizzeri[115,116], Homin Jiang[7], Atish Kamble[4,11], Ryan Keisler[25], Kimihiro Kimura[111], Yusuke Kono[3], Derek Kubo[117], John Kuroda[12], Richard Lacasse[100], Robert A. Laing[118], Erik M. Leitch[23], Chao-Te Li[7], Lupin C.-C. Lin[7,119], Ching-Tang Liu[103], Kuan-Yu Liu[7], Li-Ming Lu[103], Ralph G. Marson[120], Pierre L. Martin-Cocher[7], Kyle D. Massingill[10], Callie Matulonis[12], Martin P. McColl[10], Stephen R. McWhirter[2], Hugo Messias[114,115], Zheng Meyer-Zhao[7,121], Daniel Michalik[122,24], Alfredo Montaña[101,102], William Montgomerie[12], Matias Mora-Klein[100], Dirk Muders[6], Andrew Nadolski[44], Santiago Navarro[82], Chi H. Nguyen[10,123], Hiroaki Nishioka[7], Timothy Norton[11], George Nystrom[15], Hideo Ogawa[111], Peter Oshiro[15], Tomoaki Oyama[124], Stephen Padin[23,24], Harriet Parsons[12], Scott N. Paine[11], Juan Peñalver[82], Neil M. Phillips[114,115], Michael Poirier[2], Nicolas Pradel[7], Rurik A. Primiani[125], Philippe A. Raffin[15], Alexandra S. Rahlin[23,126], George Reiland[10], Christopher Risacher[16], Ignacio Ruiz[82], Alejandro F. Sáez-Madaín[100,115], Remi Sassella[16], Pim Schellart[17,127], Paul Shaw[7], Kevin M. Silva[12], Hotaka Shiokawa[11], David R. Smith[128,129], William Snow[15], Kamal Souccar[74], Don Sousa[2], T. K. Sridharan[11], Ranjani Srinivasan[15], William Stahm[12], Antony A. Stark[11], Kyle Story[130], Sjoerd T. Timmer[17], Laura Vertatschitsch[11,125], Craig Walther[12], Ta-Shun Wei[7], Nathan Whitehorn[131], Alan R. Whitney[2], David P. Woody[132], Jan G. A. Wouterloot[12], Melvin Wright[133], Paul Yamaguchi[11], Chen-Yu Yu[7], Milagros Zeballos[101,134], and Lucy Ziurys[10]

[1] National Radio Astronomy Observatory, 520 Edgemont Rd, Charlottesville, VA 22903, USA
[2] Massachusetts Institute of Technology Haystack Observatory, 99 Millstone Road, Westford, MA 01886, USA
[3] National Astronomical Observatory of Japan, 2-21-1 Osawa, Mitaka, Tokyo 181-8588, Japan
[4] Black Hole Initiative at Harvard University, 20 Garden Street, Cambridge, MA 02138, USA
[5] Instituto de Astrofísica de Andalucía-CSIC, Glorieta de la Astronomía s/n, E-18008 Granada, Spain
[6] Max-Planck-Institut für Radioastronomie, Auf dem Hügel 69, D-53121 Bonn, Germany
[7] Institute of Astronomy and Astrophysics, Academia Sinica, 11F of Astronomy-Mathematics Building, AS/NTU No. 1, Sec. 4, Roosevelt Rd, Taipei 10617, Taiwan, R.O.C.
[8] Departament d'Astronomia i Astrofísica, Universitat de València, C. Dr. Moliner 50, E-46100 Burjassot, València, Spain
[9] Observatori Astronòmic, Universitat de València, C. Catedrático José Beltrán 2, E-46980 Paterna, València, Spain
[10] Steward Observatory and Department of Astronomy, University of Arizona, 933 N. Cherry Ave., Tucson, AZ 85721, USA
[11] Center for Astrophysics | Harvard & Smithsonian, 60 Garden Street, Cambridge, MA 02138, USA
[12] East Asian Observatory, 660 N. A'ohoku Place, Hilo, HI 96720, USA
[13] Nederlandse Onderzoekschool voor Astronomie (NOVA), PO Box 9513, 2300 RA Leiden, The Netherlands
[14] California Institute of Technology, 1200 East California Boulevard, Pasadena, CA 91125, USA
[15] Institute of Astronomy and Astrophysics, Academia Sinica, 645 N. A'ohoku Place, Hilo, HI 96720, USA
[16] Institut de Radioastronomie Millimétrique, 300 rue de la Piscine, F-38406 Saint Martin d'Hères, France
[17] Department of Astrophysics, Institute for Mathematics, Astrophysics and Particle Physics (IMAPP), Radboud University, P.O. Box 9010, 6500 GL Nijmegen, The Netherlands

[18] Perimeter Institute for Theoretical Physics, 31 Caroline Street North, Waterloo, ON, N2L 2Y5, Canada
[19] Department of Physics and Astronomy, University of Waterloo, 200 University Avenue West, Waterloo, ON, N2L 3G1, Canada
[20] Waterloo Centre for Astrophysics, University of Waterloo, Waterloo, ON N2L 3G1 Canada
[21] Korea Astronomy and Space Science Institute, Daedeok-daero 776, Yuseong-gu, Daejeon 34055, Republic of Korea
[22] University of Science and Technology, Gajeong-ro 217, Yuseong-gu, Daejeon 34113, Republic of Korea
[23] Kavli Institute for Cosmological Physics, University of Chicago, 5640 South Ellis Avenue, Chicago, IL 60637, USA
[24] Department of Astronomy and Astrophysics, University of Chicago, 5640 South Ellis Avenue, Chicago, IL 60637, USA
[25] Department of Physics, University of Chicago, 5640 South Ellis Avenue, Chicago, IL 60637, USA
[26] Enrico Fermi Institute, University of Chicago, 5640 South Ellis Avenue, Chicago, IL 60637, USA
[27] Data Science Institute, University of Arizona, 1230 N. Cherry Ave., Tucson, AZ 85721, USA
[28] Cornell Center for Astrophysics and Planetary Science, Cornell University, Ithaca, NY 14853, USA
[29] Anton Pannekoek Institute for Astronomy, University of Amsterdam, Science Park 904, 1098 XH, Amsterdam, The Netherlands
[30] Shanghai Astronomical Observatory, Chinese Academy of Sciences, 80 Nandan Road, Shanghai 200030, People's Republic of China
[31] Key Laboratory of Radio Astronomy, Chinese Academy of Sciences, Nanjing 210008, People's Republic of China
[32] Department of Space, Earth and Environment, Chalmers University of Technology, Onsala Space Observatory, SE-43992 Onsala, Sweden
[33] Mizusawa VLBI Observatory, National Astronomical Observatory of Japan, 2-12 Hoshigaoka, Mizusawa, Oshu, Iwate 023-0861, Japan
[34] Department of Astronomical Science, The Graduate University for Advanced Studies (SOKENDAI), 2-21-1 Osawa, Mitaka, Tokyo 181-8588, Japan
[35] Dipartimento di Fisica "E. Pancini", Universitá di Napoli "Federico II", Compl. Univ. di Monte S. Angelo, Edificio G, Via Cinthia, I-80126, Napoli, Italy
[36] Institut für Theoretische Physik, Goethe-Universität Frankfurt, Max-von-Laue-Straße 1, D-60438 Frankfurt am Main, Germany
[37] INFN Sez. di Napoli, Compl. Univ. di Monte S. Angelo, Edificio G, Via Cinthia, I-80126, Napoli, Italy
[38] Department of Physics, University of Pretoria, Lynnwood Road, Hatfield, Pretoria 0083, South Africa
[39] Centre for Radio Astronomy Techniques and Technologies, Department of Physics and Electronics, Rhodes University, Grahamstown 6140, South Africa
[40] Max-Planck-Institut für Extraterrestrische Physik, Giessenbachstr. 1, D-85748 Garching, Germany
[41] Department of History of Science, Harvard University, Cambridge, MA 02138, USA
[42] Department of Physics, Harvard University, Cambridge, MA 02138, USA
[43] Department of Physics, University of Illinois, 1110 West Green St, Urbana, IL 61801, USA
[44] Department of Astronomy, University of Illinois at Urbana-Champaign, 1002 West Green Street, Urbana, IL 61801, USA
[45] Leiden Observatory—Allegro, Leiden University, P.O. Box 9513, 2300 RA Leiden, The Netherlands
[46] Key Laboratory for Research in Galaxies and Cosmology, Chinese Academy of Sciences, Shanghai 200030, People's Republic of China
[47] NOVA Sub-mm Instrumentation Group, Kapteyn Astronomical Institute, University of Groningen, Landleven 12, 9747 AD Groningen, The Netherlands
[48] Department of Astronomy, School of Physics, Peking University, Beijing 100871, People's Republic of China
[49] Kavli Institute for Astronomy and Astrophysics, Peking University, Beijing 100871, People's Republic of China
[50] Instituto Nacional de Astrofísica, Óptica y Electrónica. Apartado Postal 51 y 216, 72000. Puebla Pue., México
[51] The Institute of Statistical Mathematics, 10-3 Midori-cho, Tachikawa, Tokyo, 190-8562, Japan
[52] Department of Statistical Science, The Graduate University for Advanced Studies (SOKENDAI), 10-3 Midori-cho, Tachikawa, Tokyo 190-8562, Japan
[53] Kavli Institute for the Physics and Mathematics of the Universe, The University of Tokyo, 5-1-5 Kashiwanoha, Kashiwa, 277-8583, Japan
[54] Institute for Astrophysical Research, Boston University, 725 Commonwealth Ave., Boston, MA 02215, USA
[55] Astronomical Institute, St. Petersburg University, Universitetskij pr., 28, Petrodvorets,198504 St.Petersburg, Russia
[56] Joint Institute for VLBI ERIC (JIVE), Oude Hoogeveensedijk 4, 7991 PD Dwingeloo, The Netherlands
[57] Kogakuin University of Technology & Engineering, Academic Support Center, 2665-1 Nakano, Hachioji, Tokyo 192-0015, Japan
[58] Physics Department, National Sun Yat-Sen University, No. 70, Lien-Hai Rd, Kaosiung City 80424, Taiwan, R.O.C
[59] National Optical Astronomy Observatory, 950 North Cherry Ave., Tucson, AZ 85719, USA
[60] Key Laboratory for Particle Astrophysics, Institute of High Energy Physics, Chinese Academy of Sciences, 19B Yuquan Road, Shijingshan District, Beijing, People's Republic of China
[61] School of Astronomy and Space Science, Nanjing University, Nanjing 210023, People's Republic of China
[62] Key Laboratory of Modern Astronomy and Astrophysics, Nanjing University, Nanjing 210023, People's Republic of China
[63] Italian ALMA Regional Centre, INAF-Istituto di Radioastronomia, Via P. Gobetti 101, I-40129 Bologna, Italy
[64] Department of Physics, National Taiwan University, No.1, Sect.4, Roosevelt Rd., Taipei 10617, Taiwan, R.O.C
[65] Instituto de Radioastronomía y Astrofísica, Universidad Nacional Autónoma de México, Morelia 58089, México
[66] Instituto de Astronomía, Universidad Nacional Autónoma de México, CdMx 04510, México
[67] Yunnan Observatories, Chinese Academy of Sciences, 650011 Kunming, Yunnan Province, People's Republic of China
[68] Center for Astronomical Mega-Science, Chinese Academy of Sciences, 20A Datun Road, Chaoyang District, Beijing, 100012, People's Republic of China
[69] Key Laboratory for the Structure and Evolution of Celestial Objects, Chinese Academy of Sciences, 650011 Kunming, People's Republic of China
[70] Gravitation Astroparticle Physics Amsterdam (GRAPPA) Institute, University of Amsterdam, Science Park 904, 1098 XH Amsterdam, The Netherlands
[71] Centro Astronómico de Yebes (IGN), Apartado 148, E-19180 Yebes, Spain
[72] Department of Physics, Broida Hall, University of California Santa Barbara, Santa Barbara, CA 93106, USA
[73] Astronomy Department, Universidad de Concepción, Casilla 160-C, Concepción, Chile
[74] Department of Astronomy, University of Massachusetts, 01003, Amherst, MA, USA
[75] Department of Astronomy, Graduate School of Science, The University of Tokyo, 7-3-1 Hongo, Bunkyo-ku, Tokyo 113-0033, Japan
[76] Canadian Institute for Theoretical Astrophysics, University of Toronto, 60 St. George Street, Toronto, ON M5S 3H8, Canada
[77] Dunlap Institute for Astronomy and Astrophysics, University of Toronto, 50 St. George Street, Toronto, ON M5S 3H4, Canada
[78] Canadian Institute for Advanced Research, 180 Dundas St West, Toronto, ON M5G 1Z8, Canada
[79] Radio Astronomy Laboratory, University of California, Berkeley, CA 94720, USA
[80] CCS-2, Los Alamos National Laboratory, P.O. Box 1663, Los Alamos, NM 87545, USA
[81] Center for Theoretical Astrophysics, Los Alamos National Laboratory, Los Alamos, NM, 87545, USA
[82] Instituto de Radioastronomía Milimétrica, IRAM, Avenida Divina Pastora 7, Local 20, E-18012, Granada, Spain
[83] Consejo Nacional de Ciencia y Tecnología, Av. Insurgentes Sur 1582, 03940, Ciudad de México, México
[84] Hiroshima Astrophysical Science Center, Hiroshima University, 1-3-1 Kagamiyama, Higashi-Hiroshima, Hiroshima 739-8526, Japan
[85] Aalto University Department of Electronics and Nanoengineering, PL 15500, FI-00076 Aalto, Finland
[86] Aalto University Metsähovi Radio Observatory, Metsähovintie 114, FI-02540 Kylmälä, Finland
[87] Department of Astronomy, Yonsei University, Yonsei-ro 50, Seodaemun-gu, 03722 Seoul, Republic of Korea
[88] Netherlands Organisation for Scientific Research (NWO), Postbus 93138, 2509 AC Den Haag, The Netherlands
[89] Frontier Research Institute for Interdisciplinary Sciences, Tohoku University, Sendai 980-8578, Japan
[90] Astronomical Institute, Tohoku University, Sendai 980-8578, Japan
[91] Department of Physics and Astronomy, Seoul National University, Gwanak-gu, Seoul 08826, Republic of Korea

[92] Leiden Observatory, Leiden University, Postbus 2300, 9513 RA Leiden, The Netherlands
[93] Physics Department, Brandeis University, 415 South Street, Waltham, MA 02453, USA
[94] School of Physics, Huazhong University of Science and Technology, Wuhan, Hubei, 430074, People's Republic of China
[95] Mullard Space Science Laboratory, University College London, Holmbury St. Mary, Dorking, Surrey, RH5 6NT, UK
[96] School of Astronomy and Space Sciences, University of Chinese Academy of Sciences, No. 19A Yuquan Road, Beijing 100049, People's Republic of China
[97] Astronomy Department, University of Science and Technology of China, Hefei 230026, People's Republic of China
[98] Department of Physics, Faculty of Science, University of Malaya, 50603 Kuala Lumpur, Malaysia
[99] University of Vermont, Burlington, VT 05405, USA
[100] National Radio Astronomy Observatory, NRAO Technology Center, 1180 Boxwood Estate Road, Charlottesville, VA 22903, USA
[101] Instituto Nacional de Astrofísica, Óptica y Electrónica, Luis Enrique Erro 1, Tonantzintla, Puebla, C.P. 72840, Mexico
[102] Consejo Nacional de Ciencia y Tecnología, Av. Insurgentes Sur 1582, Col. Crédito Constructor, CDMX, C.P. 03940, Mexico
[103] National Chung-Shan Institute of Science and Technology, No.566, Ln. 134, Longyuan Rd., Longtan Dist., Taoyuan City 325, Taiwan, R.O.C.
[104] MIT Haystack Observatory, 99 Millstone Road, Westford, MA 01886, USA
[105] Dept. of Astronomy, Univ. of California Berkeley, 501 Campbell, Berkeley, CA 94720, USA
[106] CASA, Department of Astrophysical and Planetary Sciences, University of Colorado, Boulder, CO 80309, USA
[107] Western University, 1151 Richmond Street, London, Ontario, N6A 3K7, Canada
[108] University of Massachusetts Boston, 100 William T, Morrissey Blvd, Boston, MA 02125, USA
[109] Research and Development Weather and Climate Models, Royal Netherlands Meteorological Institute, Utrechtseweg 297, 3731 GA, De Bilt, The Netherlands
[110] Department of Astrophysical and Planetary Sciences and Department of Physics, University of Colorado, Boulder, CO 80309, USA
[111] Osaka Prefecture University, Gakuencyou Sakai Osaka, Sakai 599-8531, Kinki, Japan
[112] High Energy Physics Division, Argonne National Laboratory, 9700 S. Cass Avenue, Argonne, IL 60439, USA
[113] IRAP, Université de Toulouse, CNRS, UPS, CNES, Toulouse, France
[114] European Southern Observatory, Alonso de Córdova 3107, Vitacura, Casilla 19001, Santiago de Chile, Chile
[115] Joint ALMA Observatory, Alonso de Córdova 3107, Vitacura 763-0355, Santiago de Chile, Chile
[116] National Radio Astronomy Observatory, 520 Edgemont Road, Charlottesville, VA 22903, USA
[117] ASIAA Hilo Office, 645 N. A'ohoku Place, University Park, Hilo, HI 96720, USA
[118] Square Kilometre Array Organisation, Jodrell Bank Observatory, Lower Withington, Macclesfield, Cheshire SK11 9DL, UK
[119] Department of Physics, Ulsan National Institute of Science and Technology, Ulsan, 44919, Republic of Korea
[120] National Radio Astronomy Observatory, P.O. Box O, Socorro, NM 87801, USA
[121] ASTRON, Oude Hoogeveensedijk 4, 7991 PD Dwingeloo, The Netherlands
[122] Science Support Office, Directorate of Science, European Space Research and Technology Centre (ESA/ESTEC), Keplerlaan 1, 2201 AZ Noordwijk, The Netherlands
[123] Center for Detectors, School of Physics and Astronomy, Rochester Institute of Technology, 1 Lomb Memorial Drive, Rochester, NY 14623, USA
[125] Mizusawa VLBI Observatory, National Astronomical Observatory of Japan, Ohshu, Iwate 023-0861, Japan
[125] Systems & Technology Research, 600 West Cummings Park, Woburn, MA 01801, USA
[126] Fermi National Accelerator Laboratory, PO Box 500, Batavia IL 60510, USA
[127] Department of Astrophysical Sciences, Princeton University, Princeton, NJ 08544, USA
[128] MERLAB, 357 S. Candler St., Decatur, GA 30030, USA
[129] GWW School of Mechanical Engineering, Georgia Institute of Technology, 771 Ferst Dr., Atlanta, GA 30332, USA
[130] Kavli Institute for Particle Astrophysics and Cosmology, Stanford University, 452 Lomita Mall, Stanford, CA 94305, USA
[131] Dept. of Physics and Astronomy, UCLA, Los Angeles, CA 90095, USA
[132] Owens Valley Radio Observatory, California Institute of Technology, Big Pine, CA 93513, USA
[133] Dept. of Astronomy, Radio Astronomy Laboratory, Univ. of California Berkeley, 601 Campbell, Berkeley, CA 94720, USA
[134] Universidad de las Américas Puebla, Sta. Catarina Mártir S/N, San Andrés Cholula, Puebla, C.P. 72810, Mexico
[135] Deceased.

The Astrophysical Journal Letters, 875:L3 (32pp), 2019 April 10 https://doi.org/10.3847/2041-8213/ab0c57
© 2019. The American Astronomical Society.
OPEN ACCESS

First M87 Event Horizon Telescope Results. III. Data Processing and Calibration

The Event Horizon Telescope Collaboration
(See the end matter for the full list of authors.)
Received 2019 February 11; revised 2019 March 3; accepted 2019 March 3; published 2019 April 10

Abstract

We present the calibration and reduction of Event Horizon Telescope (EHT) 1.3 mm radio wavelength observations of the supermassive black hole candidate at the center of the radio galaxy M87 and the quasar 3C 279, taken during the 2017 April 5–11 observing campaign. These global very long baseline interferometric observations include for the first time the highly sensitive Atacama Large Millimeter/submillimeter Array (ALMA); reaching an angular resolution of 25 μas, with characteristic sensitivity limits of $\sim$1 mJy on baselines to ALMA and $\sim$10 mJy on other baselines. The observations present challenges for existing data processing tools, arising from the rapid atmospheric phase fluctuations, wide recording bandwidth, and highly heterogeneous array. In response, we developed three independent pipelines for phase calibration and fringe detection, each tailored to the specific needs of the EHT. The final data products include calibrated total intensity amplitude and phase information. They are validated through a series of quality assurance tests that show consistency across pipelines and set limits on baseline systematic errors of 2% in amplitude and 1° in phase. The M87 data reveal the presence of two nulls in correlated flux density at $\sim$3.4 and $\sim$8.3 Gλ and temporal evolution in closure quantities, indicating intrinsic variability of compact structure on a timescale of days, or several light-crossing times for a few billion solar-mass black hole. These measurements provide the first opportunity to image horizon-scale structure in M87.

Key words: black hole physics – galaxies: individual (M87, 3C279) – galaxies: jets – techniques: high angular resolution – techniques: interferometric

1. Introduction

The principle of very long baseline interferometry (VLBI) is to connect distant radio telescopes to create a single virtual telescope. On the ground, VLBI enables baseline lengths comparable to the size of the Earth. This significantly boosts angular resolution, at the expense of having a non-uniform filling of the aperture. In order to reconstruct the brightness distribution of an observed source, VLBI requires cross-correlation between the individual signals recorded independently at each station, brought to a common time reference using local atomic clocks paired with the Global Positioning System (GPS) for coarse synchronization. The resulting complex correlation coefficients need to be calibrated for residual clock and phase errors, and then scaled to physical flux density units using time-dependent and station-specific sensitivity estimates. Once this process is completed, further analysis in the image domain can refine the calibration using model-dependent self-calibration techniques (e.g., Pearson & Readhead 1984; Wilkinson 1989). For more details on the principles of VLBI, see, e.g., Thompson et al. (2017).

At centimeter wavelengths, the technique of VLBI is well established. Correlation and calibration have been optimized over decades, resulting in standard procedures for the processing of data obtained at national and international facility instruments, such as the Very Long Baseline Array[103] (VLBA), the Australian Long Baseline Array[104] (LBA), the East Asian VLBI Network[105] (EAVN), and the European VLBI Network[106] (EVN). At higher frequencies, the increased effects from atmospheric opacity and turbulence pose major challenges. The characteristic atmospheric coherence timescale is only a few seconds for millimeter wavelengths, and sensitivity must be sufficient to track phase variation over correspondingly short timescales. Large collecting areas and wide bandwidths prove essential when observing even the brightest continuum sources over a range of elevations and reasonable weather conditions. Furthermore, the transfer of phase solutions from a bright calibrator to a weak source, typically done at centimeter wavelengths, is not feasible at high frequencies, because differential atmospheric propagation effects are more significant, and because there are few bright, compact calibrators.

The Event Horizon Telescope (EHT) is a global VLBI array of millimeter- and submillimeter-wavelength observatories with the primary goal of studying the strong gravity, near-horizon environments of the supermassive black holes in the Galactic Center, Sagittarius A* (Sgr A*), and at the center of the nearby radio galaxy M87 (Doeleman et al. 2009; EHT Collaboration et al. 2019b, hereafter Paper II). In 2017 April, the EHT conducted science observations at a wavelength of $\lambda \simeq 1.3$ mm, corresponding to a frequency of $\nu \simeq 230$ GHz. The network was joined for the first time by the Atacama Large Millimeter/submillimeter Array (ALMA) configured as a phased array, a capability developed by the ALMA Phasing Project (APP; Doeleman 2010; Fish et al. 2013; Matthews et al. 2018). The addition of ALMA, as a highly sensitive central

[103] https://science.nrao.edu/facilities/vlba

[104] http://www.atnf.csiro.au/vlbi

[105] https://radio.kasi.re.kr/eavn

[106] http://www.evlbi.org

Original content from this work may be used under the terms of the Creative Commons Attribution 3.0 licence. Any further distribution of this work must maintain attribution to the author(s) and the title of the work, journal citation and DOI.

anchor station, drastically changes the overall characteristics and sensitivity limits of the global array (Paper II).

Although operating as a single instrument spanning the globe, the EHT remains a mixture of new and well-exercised stations, single-dish telescopes, and phased arrays with varying designs and operations. Each observing cycle over the last several years has been accompanied by the introduction of new telescopes to the array, and/or significant changes and upgrades to existing stations, data acquisition hardware, and recorded bandwidth (Paper II). EHT observations result in data spanning a wide range of signal-to-noise ratio (S/N) due to the heterogeneous nature of the array, and the high observing frequency produces data that are particularly sensitive to systematics in the signal chain. These factors, along with the typical challenges associated with VLBI, have motivated the development of specialized processing and calibration techniques.

In this Letter we describe the full data processing pathway and pipeline convergence leading to the first science release (SR1) of the EHT 2017 data. Given the uniqueness of the data set and scientific goal of the EHT observations, our processing focuses on the use of unbiased automated procedures, reproducibility, and extensive review and cross-validation. In particular, data reduction is carried out with three independent phase calibration (fringe-fitting) and reduction pipelines. The Haystack Observatory Processing System (`HOPS`; Whitney et al. 2004) has been the standard for calibrating EHT data from prior observations (e.g., Doeleman et al. 2008, 2012; Fish et al. 2011, 2016; Akiyama et al. 2015; Johnson et al. 2015; Lu et al. 2018). HOPS reduction of the 2017 data is supported by a suite of auxiliary calibration scripts to form the EHT-HOPS pipeline (Blackburn et al. 2019). The Common Astronomy Software Applications package (`CASA`; McMullin et al. 2007) is primarily aimed at processing connected-element interferometer data. The recent addition of a fringe fitter and reduction pipeline has enabled the use of CASA for high-frequency VLBI data processing (Janssen et al. 2019a, I. van Bemmel et al. 2019, in preparation). The NRAO Astronomical Image Processing System (`AIPS`; Greisen 2003) is the most commonly used reduction package for centimeter VLBI data. For this work, an automated `ParselTongue` (Kettenis et al. 2006) pipeline was constructed and tailored to the needs of EHT data reduction in AIPS.

The SR1 data consist of Stokes I complex interferometric visibilities of M87 and the quasar 3C 279, corresponding to spatial frequencies of the sky brightness distribution sampled by the interferometer. M87 data indicate the presence of a resolved compact emission structure on a spatial scale of a few tens of μas, persistent throughout the week-long observing campaign. Closure phases and closure amplitudes unambiguously reflect non-trivial brightness distributions on M87 for the first time. They display broad consistency over different days, and in certain cases show clear evolution. A detailed analysis of this near-horizon-scale structure is the subject of companion Letters (EHT Collaboration et al. 2019a, 2019c, 2019d, 2019e, hereafter Papers I, IV, V, and VI, respectively).

This Letter is organized as follows. Section 2 presents an overview of the 2017 April observations. In Section 3 we outline the data flow from observations to science-ready data sets. We describe the correlation process in Section 4, the phase calibration process via three independent fringe-fitting pipelines in Section 5, and the common flux density calibration scheme and amplitude error budget in Section 6. We give an overview of SR1 data products and a rudimentary description of their most evident, remarkable properties in Section 7. We present data set validation procedures and tests, estimates of systematic errors, and inter-pipeline comparisons in Section 8. Conclusions are given in Section 9.

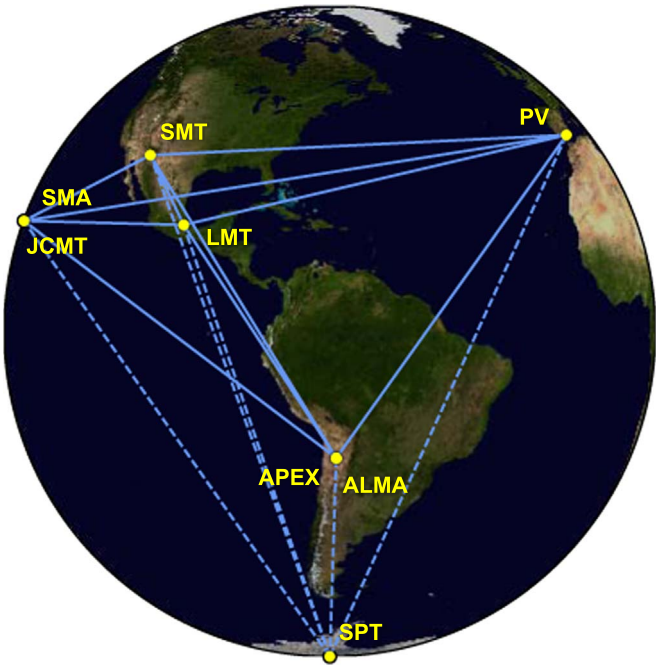

Figure 1. The eight EHT 2017 stations over six geographic locations as viewed from the equatorial plane. Solid baselines represent mutual visibility on M87 (+12° decl.), while dashed baselines to SPT are also present for 3C 279 (−6° decl.).

2. Observations

The EHT 2017 science observing run was scheduled for 5 nights during the 10-night 2017 April 5–14 (UTC) window with eight participating observatories at six distinct geographical locations, shown in Figure 1: the ALMA and the Atacama Pathfinder Experiment (APEX) in the Atacama Desert in Chile, the Large Millimeter Telescope Alfonso Serrano (LMT) on the Volcán Sierra Negra in Mexico, the South Pole Telescope (SPT) at the geographic south pole, the IRAM 30 m telescope (PV) on Pico Veleta in Spain, the Submillimeter Telescope (SMT) on Mt. Graham in Arizona, and the Submillimeter Array (SMA) and the James Clerk Maxwell Telescope (JCMT) on Maunakea in Hawai‘i. A detailed description of the EHT array is presented in Paper II. The 2017 science observing run consisted of observations of six science targets: the primary EHT targets Sgr A* and M87, and the secondary targets 3C 279, OJ 287, Centaurus A, and NGC 1052.

An array-wide go/no-go decision was made a few hours before the start of each night's schedule, based on weather conditions and technical readiness at each of the participating observatories. A dry run of the go/no-go decision making was performed on April 4 to assess triggering and readiness procedures. All sites were technically ready and with good weather on the first night of the observing window. Observations were triggered on 2017 April 5, 6, 7, 10, and 11. Table 1 shows the median zenith sky opacities for each of the triggered days. April 8 was not triggered due to thunderstorms at the LMT, SMT shutdown due to strong winds, and the need to run

Table 1
Median Zenith Sky Opacities (1.3 mm) at EHT Sites during the 2017 April Observations

Station	Median Zenith $\tau_{1.3\ \mathrm{mm}}$				
	Apr 5	Apr 6	Apr 7	Apr 10	Apr 11
ALMA/APEX	0.06	0.04	0.05	0.03	0.06
SMA/JCMT	0.10	0.07	0.09	0.05	0.08
PV	0.18	0.13	0.14	0.10	0.15
LMT	0.13	0.16	0.21	0.26	0.24
SMT	0.21	0.28	0.23	0.19	0.16
SPT	0.04	0.05	0.07	0.08	0.07

Note. Median zenith sky opacities are measured at each site and reported through station log files and the VLBImonitor as described in Paper II.

technical tests at ALMA. April 9 was not triggered due to a chance of the SMT remaining closed due to strong winds and LMT snow forecast. Weather was good to excellent for all other stations throughout the observing window.

In addition to favorable weather conditions, operations at all sites were successful and resulted in fringe detections across the entire array. A number of mild to moderate site and data issues were uncovered during the analysis, and their detailed characterization and mitigation are given in the Appendix. Notable issues affecting processing, calibration, and data interpretation are: (1) a clock frequency instability at PV resulting in ∼50% amplitude loss to that station; (2) recorder configuration issues at APEX resulting in a significant number of data gaps and low data validity at correlation; (3) pointing errors at LMT, large compared to the beam, resulting in unpredictable amplitude loss and inter- and intra-scan gain variability; and (4) a common local oscillator (LO) used at SMA and JCMT resulting in opposite sideband contamination at the level of ∼15% for short integration times, making the SMA–JCMT intra-site baseline less useful for calibration. All known issues with a significant effect on the data are addressed at various stages of processing and calibration, although some (such as residual gains at the LMT, and SMA–JCMT sideband contamination) necessitate additional care taken during data interpretation.

M87 ($\alpha_{\mathrm{J2000}} = 12^{\mathrm{h}}30^{\mathrm{m}}49\overset{\mathrm{s}}{.}42$, $\delta_{\mathrm{J2000}} = 12°23'28\overset{''}{.}04$) was observed as a target source on three nights (2017 April 5, 6, and 11). In addition, seven scans on M87 were included as a calibration source (for 3C 279) on 2017 April 10. Each of the four tracks consists of multiple scans lasting between 3 and 7 minutes. In most tracks, VLBI scans on M87 began when it rose at the LMT and ended when it set below 20° elevation at ALMA. Scans on M87 were interleaved with scans on the quasar 3C 279 ($\alpha_{\mathrm{J2000}} = 12^{\mathrm{h}}56^{\mathrm{m}}11\overset{\mathrm{s}}{.}17$, $\delta_{\mathrm{J2000}} = -05°47'21\overset{''}{.}52$), another EHT target with a similar R.A. The observed schedules for M87 and 3C 279 during the 2017 campaign are shown in Figure 2. The schedules were optimized for wide (u, v) coverage on all target sources when possible. All stations apart from the JCMT observed with full polarization. The JCMT observed a single circular polarization component per night (right circular polarization (RCP) for April 5 and 6, left circular polarization (LCP) for April 10 and 11).

The 2017 observing run recorded two 2 GHz bands, low and high, centered at sky frequencies of 227.1 and 229.1 GHz, respectively, onto Mark 6 VLBI recorders (Whitney et al. 2013) at an aggregate recording rate of 32 Gbps with 2-bit sampling. All telescopes apart from ALMA observed in circular polarization with the installation of quarter-wave plates. Single-dish sites used block downconverters to convert the intermediate frequency (IF) signal from the front-ends to a common 0–2 GHz baseband, which was digitally sampled via Reconfigurable Open Architecture Computing Hardware 2 (ROACH2) digital backends (R2DBEs; Vertatschitsch et al. 2015). The SMA observed as a phased array of six or seven antennas, for which the phased-sum signal was processed in the SMA Wideband Astronomical ROACH2 Machine (SWARM) correlator (see Primiani et al. 2016; Young et al. 2016, for more details). ALMA observed as a phased array of usually 37 dual linear polarization antennas, for which the phased-sum signal was processed in the Phasing Interface Cards installed at the ALMA baseline correlator (see Matthews et al. 2018 for more details). Instrumentation development leading up to the 2017 observations is presented in Paper II.

3. Data Flow

The EHT data flow from recording to analysis is outlined in Figure 3. Through the receiver and backend electronics at each telescope, the sky signal is mixed to baseband, digitized, and recorded directly to hard disk, resulting in petabytes of raw VLBI voltage signal data. The correlator uses an a priori Earth geometry and clock/delay model to align the signals from each telescope to a common time reference, and estimates the pair-wise complex correlation coefficient (r_{ij}) between antennas. For signals x_i and x_j between stations i and j

$$r_{ij} = \frac{\langle x_i x_j^* \rangle}{\eta_Q \sqrt{\langle x_i x_i^* \rangle \langle x_j x_j^* \rangle}}, \tag{1}$$

where η_Q represents a digital correction factor to compensate for the effects of low-bit quantization. For optimal 2-bit quantization, $\eta_Q \approx 0.88$.

The correlation coefficient may vary with both time and frequency. For FX correlators, signals from each antenna are first taken to the frequency domain using temporal Fourier transforms on short segments (F), and then pair-wise correlated (X). The expectation values in Equation (1) are calculated by averaging over time–frequency volumes where the inner products remain stable. At millimeter wavelengths, a correlator can average around 1 s × 1 MHz, or 2×10^6 samples, before clock errors such as residual delay, delay-rate (e.g., Doppler shift), and stochastic changes in atmospheric path length cause unwanted decoherence in the signal (Section 4). The post-correlation data reduction pipeline models and fits these residual clock systematics, allowing data to be further averaged by a factor of 10^3 or more, to the limits imposed by intrinsic source structure and variability (Section 5). For many EHT baselines, the astronomical signal is not detectable above the noise until phase corrections resulting from these calibration solutions are applied and the data are coherently (vector) averaged.

In addition to reducing the overall volume and complexity of the data, the calibration process attempts to relate the pair-wise correlation coefficients r_{ij}, which are in units of thermal noise of the detector, to correlated flux density in units of Jansky (Jy),

$$r_{ij} = \gamma_i \gamma_j^* V_{ij}. \tag{2}$$

The *visibility function*, V_{ij}, represents the mutual coherence of the electric field between ends of the baseline vector joining the sites, projected onto the plane of propagation. For an ideal interferometer, V_{ij} samples a Fourier component of the

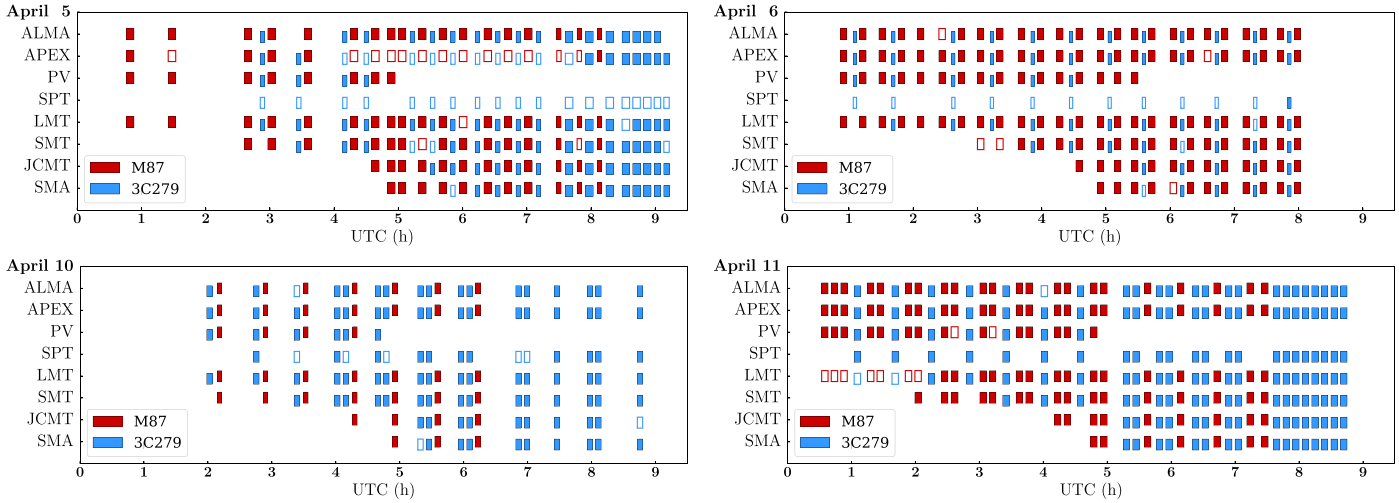

Figure 2. EHT 2017 observing schedules for M87 and 3C 279 covering the four days of observations. Empty rectangles represent scans that were scheduled, but were not observed successfully due to weather, insufficient sensitivity, or technical issues. The filled rectangles represent scans corresponding to detections available in the final data set. Scan duration varies between 3 and 7 minutes, as reflected by the width of each rectangle.

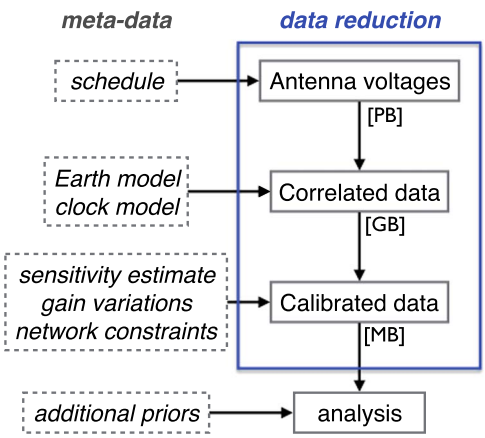

Figure 3. Data processing pathway of an EHT observation from recording to source parameter estimation (images, or other physical parameters). At the calibration stage, instrumental and environmental gain systematics are estimated and removed from the data so that a smaller and simpler data product can be used for source model fitting at a downstream analysis stage.

brightness distribution on the sky (via the van Cittert–Zernike theorem; van Cittert 1934; Zernike 1938; Thompson et al. 2017). The dimensionless spatial frequency $\boldsymbol{u} = (u, v)$ of the Fourier component is determined by the projected baseline expressed in units of the observing wavelength. Here, we have made the implicit assumption that the relationship between correlation coefficient and visibility can be factored into complex station-based forward gains γ_i and γ_j. This process of flux density calibration requires an a priori assessment of the sensitivity of each antenna in the array, captured by the *system-equivalent flux density* ($\mathrm{SEFD}_i = |1/\gamma_i|^2$) of the thermal noise power, as described in Section 6.

After the basic calibration and reduction process, the data are passed through additional post-processing tasks to further average the data to a manageable size for source imaging and model fitting, and to apply any network self-calibration constraints based on independent a priori assumptions about the source, such as large-scale (milliarcsecond and larger) structure, total flux density, and degree of total polarization (Section 6.2). The final network-calibrated data products are further averaged to a 10 s segmentation in time and across each 2 GHz band to provide smaller files for downstream analysis (Section 7.1).

4. Correlation

The recorded data from each station were split by frequency band and sent to MIT Haystack Observatory and the Max-Planck-Institut für Radioastronomie (MPIfR) for correlation, as described in Paper II. The Haystack correlator handled the low-frequency band (centered at 227.1 GHz), with MPIfR correlating the high band (centered at 229.1 GHz). Each correlator is a networked computer cluster running a standard installation of the `DiFX` software package (Deller et al. 2011). The correlators use a model (`calc11`) of the expected wavefront arrival delay as a function of time on each baseline. The delay model very precisely takes into account the geometry of the observing array at the time of observation, the direction of the source, and a model of atmospheric delay contributions (e.g., Romney 1995). Baseband data on a few high-S/N scans with good coverage were exchanged between the two sites to verify the output of each correlator against the other.

Data were correlated with an accumulation period (AP) of 0.4 s and a frequency resolution of 0.5 MHz (Figure 4). Due to the need to rationalize frequency channelization with the ALMA setup (each 1.875 GHz spectral window at ALMA is broken up into 32 spectral IFs of 62.5 MHz, separated by 58.59375 MHz and thus slightly overlapping; Matthews et al. 2018), the frequency points are grouped into IFs that are 58 MHz wide (using `DiFX` *zoom mode*), each with 116 individual channels and a small amount of bandwidth discarded between spectral IFs.

At the SMA, the original data are recorded in the frequency domain rather than the time domain, owing to the architecture of the SMA correlator. Moreover, the recorded frequency range of 2288 MHz is slightly larger and offset by 150 MHz from the frequency range at the other non-ALMA sites. An offline pre-processing pipeline, called the Adaptive Phased-array and Heterogeneous Interpolating Downsampler for SWARM (APHIDS; Primiani et al. 2016), is used to perform the

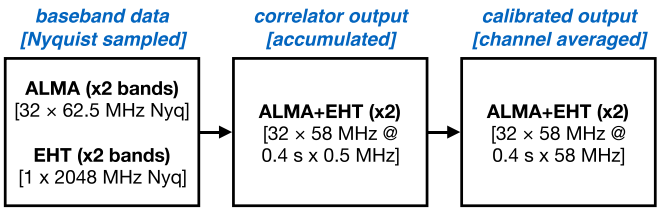

Figure 4. Time and frequency resolution of EHT 2017 data as it is recorded and processed. Correlation parameters for the EHT are chosen to be compatible with ALMA's recorded sub-bands that are 62.5 MHz wide, overlap slightly, and have starting frequencies aligned to $1/(32\ \mu s)$. The raw output after calibration and reduction maintains the original correlator accumulation of 0.4 s, but averages over each 58 MHz spectral IF, centered on each ALMA sub-band. The data are further averaged at the network amplitude self-calibration stage (not shown) for a more manageable data volume.

necessary filtering, frequency conversion, and transformation to the time domain, so that the format of the SMA data delivered to the VLBI correlator is the same as for single-dish stations. Part of the necessary offline pre-processing includes deriving clock offsets on a scan-by-scan basis for the delivered data. These offsets are determined by cross-correlating the pre-processed SMA data with separate data recorded with an R2DBE-Mark 6 pair, taking a second IF signal from the SMA reference antenna as input.

The IF from the JCMT was recorded using backend equipment installed at the SMA (Paper II). This was achieved by transporting the first IF from the JCMT to the SMA, where the second downconversion, digitization, and recording were done. Because the second downconversion at the SMA introduces a net offset of 150 MHz with respect to the nominal EHT RF band, this means that the recorded JCMT data sent to the correlator are subject to the same frequency offset. The mismatch eliminates one of the thirty-two 58 MHz spectral IFs in the final correlation for JCMT baselines.

ALMA observes linear polarization, while the rest of the EHT observes circular polarization. The software routine `PolConvert` (Martí-Vidal et al. 2016; Matthews et al. 2018) was created to convert visibilities, output from the correlator in a mixed-polarization basis, to the pure circular basis of the EHT. `PolConvert` takes auxiliary calibration input from the quality assurance stage 2 (QA2) ALMA interferometric reduction of data (Goddi et al. 2019). Execution of the `PolConvert` tool completes the correlation (circularized visibilities on baselines to ALMA) and provides final ANTAB[107] format data for flux density calibration of the ALMA phased array. The original native (Swinburne format) correlator output from `DiFX` is converted using available `DiFX` tools to a `Mark4` (Whitney et al. 2004) compatible file format for processing through HOPS, and to `FITS-IDI` (Greisen 2011) files for further processing with AIPS and CASA.

5. Fringe Detection

In the limit for which all correlator delay model parameters were known perfectly ahead of time and there were no atmospheric variations, the model delays would exactly compensate for the delay on each baseline of the data, and the correlated data could be coherently integrated in time and frequency to build up sensitivity. In practice, many of the model parameters are not known exactly at correlation. For example, the observed source may have structure and may be centered at an offset from the expected coordinates, the position of each telescope may differ from the best estimate, instrumental electronic delays may not be known, or variable water content in the atmosphere may cause the atmospheric delay to deviate from the simple model. It is therefore necessary to search in delay and delay-rate space for small corrections to the model values that maximize the fringe amplitude: in VLBI data processing this process is known as fringe-fitting (e.g., Cotton 1995). In this section, we describe three independent fringe-fitting pipelines for phase calibration, based on three different software packages for VLBI data processing: HOPS (Section 5.1), CASA (Section 5.2), and AIPS (Section 5.3).

5.1. HOPS Pipeline

HOPS[108] is a collection of software packages and data framework designed to analyze and reduce output from a Mark III, IV, or `DiFX` correlator. It has been used extensively for the processing of early EHT data (Doeleman et al. 2008, 2012; Fish et al. 2011, 2016; Akiyama et al. 2015; Johnson et al. 2015; Lu et al. 2018). For EHT 2017 observations, HOPS was augmented with a collection of auxiliary calibration scripts, and packaged into an EHT-HOPS pipeline (Blackburn et al. 2019) for automated processing of this and similar data sets. Compared to the reduction of data from previous runs, the EHT-HOPS pipeline is unique in that it finds a single self-consistent global fringe solution (station-based delays, delay-rates, and instrumental and atmospheric phase) for calibration. The pipeline also provides standard `UVFITS` formatted visibility data products for downstream analysis.

The EHT-HOPS pipeline processes output from the `DiFX` correlator that has been converted to `Mark4` format via the `DiFX` tool `difx2mark4`. This conversion process includes normalization by auto-correlation power per 58 MHz spectral IF in each AP of 0.4 s (Figure 4), as well as a 1/0.88252 amplitude correction factor for 2-bit quantization efficiency. Stages of the pipeline (Figure 5) run the HOPS fringe fitter `fourfit` several times (once per stage) while making iterative corrections to the phase calibration applied to the data before solving for delays and delay-rates. The initial setup (*default config, flags*—Figure 5) includes manual flagging (removal of bad data) in time and frequency, as well as an ALMA-specific correction for digital phase offsets between spectral IFs.

ALMA is used as a reference station for estimating stable instrumental phase (*phase bandpass*) and relative delay between right and left circular polarization (*R-L delay offsets*) for remote stations. The estimates are done using S/N-weighted averages of the strong ALMA baseline measurements. Here we make use of the fact that ALMA RCP and LCP data are already delay- and phase-calibrated during the QA2/`PolConvert` process (Goddi et al. 2019). For rapid nonlinear phase (*atmospheric phase*) that varies over seconds and that must be calibrated on-source, the strongest station (generally ALMA when it is present; see also Section 2 of Paper II) is automatically determined for each scan based on signal-to-noise, and is used as a phase reference. Baselines to the reference station are then used to phase stabilize the remaining sites.

[107] Free-format parsable text file containing flux density calibration information and keywords as defined for AIPS: http://www.aips.nrao.edu/cgi-bin/ZXHLP2.PL?ANTAB.

[108] https://www.haystack.mit.edu/tech/vlbi/hops.html

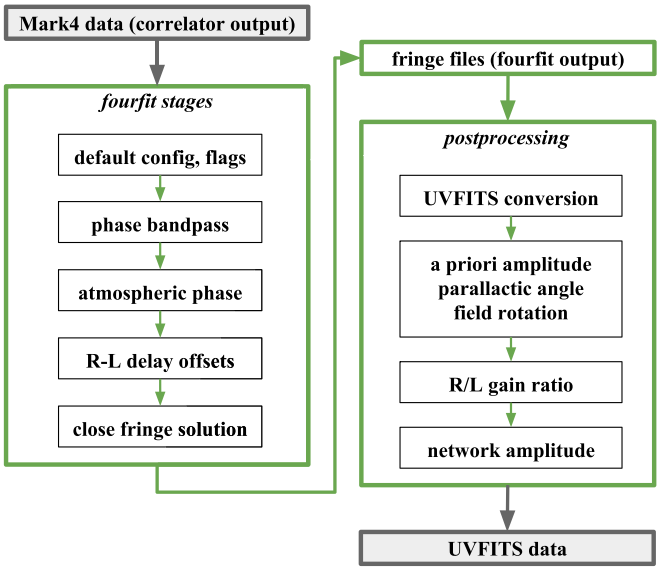

Figure 5. Stages of the EHT-HOPS pipeline and post-processing steps, as described in the text. The first five stages, shown in the left box, are iterations of HOPS fringe fitter `fourfit`. Here, a comprehensive phase calibration model is gradually built for the data. At the end of the five fourfit stages, the correlation coefficients are evaluated at a single global (station-based) set of relative delays and delay-rates. The data are then converted to `UVFITS` format, and a remaining suite of post-processing tools provide amplitude calibration and time-and-polarization-dependent phase calibration.

Due to the large number of free parameters involved in correcting for atmospheric phase, a leave-out-one cross-estimation approach is adopted for this step to avoid self-tuning. For each baseline, a smooth phase model is estimated by stacking RCP and LCP data over 31 (of 32) spectral IFs. The estimated phase from the 31-IF average is used to correct the remaining IF, and the process cycles through IFs to cover the full band. In this way, phase corrections are never estimated from the same data to which they are applied, which avoids introducing false coherence from self-tuning to random thermal noise and introducing a positive bias to amplitudes. The effective solution interval for the phase model depends on S/N, and is chosen per baseline to balance anticipated atmospheric phase drift with thermal noise in the estimate. Additional a priori corrections for small residual clock frequency offsets after correlation (Appendix) are made here as well.

During a final reduction with `fourfit` (*close fringe solution*), rather than fitting for unconstrained delays and delay-rates per baseline and polarization product, a single set of station-based delays and delay-rates is fixed corresponding to a global fringe solution. These are derived from a least-squares solution (as proposed by Alef & Porcas 1986) to relative delays and delay-rates from confident baseline detections with $S/N > 7$, and stations that remain unconstrained by this process are removed from the data set. No interpolation of these fringe solutions is performed across sources and scans; instead, precise closure of delay and delay-rate from strong baseline detections is required to report any measurement on a weak baseline. Correlation coefficients on baselines with no detectable signal are still calculated (Figure 11, where $S/N <$ few), but only when the relative clock model is constrained through other baseline detections.

The resulting complex visibility data are converted to `UVFITS` format, and amplitude calibration is done in the EHT Analysis Toolkit's (`eat`)[109] post-processing framework, shared by all pipelines and described in Section 6. For the HOPS pipeline, the calibration of complex polarization gain ratios is performed in a post-processing stage rather than during `fourfit`. Deterministic field rotation from parallactic angle and receiver mount type is corrected as a complex polarization-dependent a priori gain factor, and a smoothly varying polynomial model is fit over many sources and used to correct residual RCP−LCP phase drift for each station. Details for all steps can be found in Blackburn et al. (2019).

The EHT-HOPS pipeline was additionally used for the reduction of observations of Sgr A* and calibrators at 86 GHz, with the Global Millimeter VLBI Array[110] (GMVA) joined by ALMA. Despite the magnitude difference in bandwidth, a similar reduction to EHT data was performed on the GMVA data set. ALMA baselines were used to estimate stable instrumental phase and delay corrections. Baselines to either ALMA or the Green Bank Telescope (GBT) were used, due to their high S/N, to correct for stochastic atmospheric phase fluctuations on timescales of a few seconds. The performance of the pipeline on the GMVA data is described in Blackburn et al. (2019) while scientific results from the data set are validated against historical observations in Issaoun et al. (2019).

5.2. CASA Pipeline

The `CASA` (McMullin et al. 2007) package was developed by NRAO to process data acquired with the JVLA and ALMA connected-element interferometers and in recent years has become the standard software for the calibration and analysis of radio-interferometric data. A newly developed fringe-fitting task `fringefit` (I. van Bemmel et al. 2019, in preparation) has added the necessary delay and delay-rate calibration capabilities for VLBI. The modular, general-purpose `rPICARD` VLBI data reduction pipeline (Janssen et al. 2019a) is used for the calibration of EHT data. This section describes the incremental `rPICARD` calibration steps for EHT data, summarized in Figure 6.

The `importfitsidi` CASA task is used to import the `FITS-IDI` correlator output into CASA. Additionally, a digital correction factor for the 2-bit recorder sampling is applied when the data are loaded. Bad data are flagged based on text files compiled from station logs and known sources of radio frequency interference in stations' signal chains with the `flagdata` task before performing the incremental calibration procedures. The `accor` task is used to scale the auto-correlations to unity and adjust the cross-correlations accordingly, correcting for incorrect sampler settings from the data recording stage. This is done for each 58 MHz spectral IF individually, thereby correcting for a coarse bandpass at each station. This amplitude bandpass is refined by dividing the data by the auto-correlations at the 0.5 MHz channel resolution.

The phase calibration is done with the `fringefit` task, which solves for station-based residual post-correlation phases, delays, and rates with respect to a chosen reference station (Schwab & Cotton 1983). Unlike the HOPS pipeline, where field rotation angles are corrected a posteriori, `rPICARD` applies field rotation angle gain solutions on-the-fly, i.e., before each phase calibration correction. The most sensitive station is picked as reference in each scan. Eventually, all

[109] http://github.com/sao-eht/eat
[110] https://www3.mpifr-bonn.mpg.de/div/vlbi/globalmm

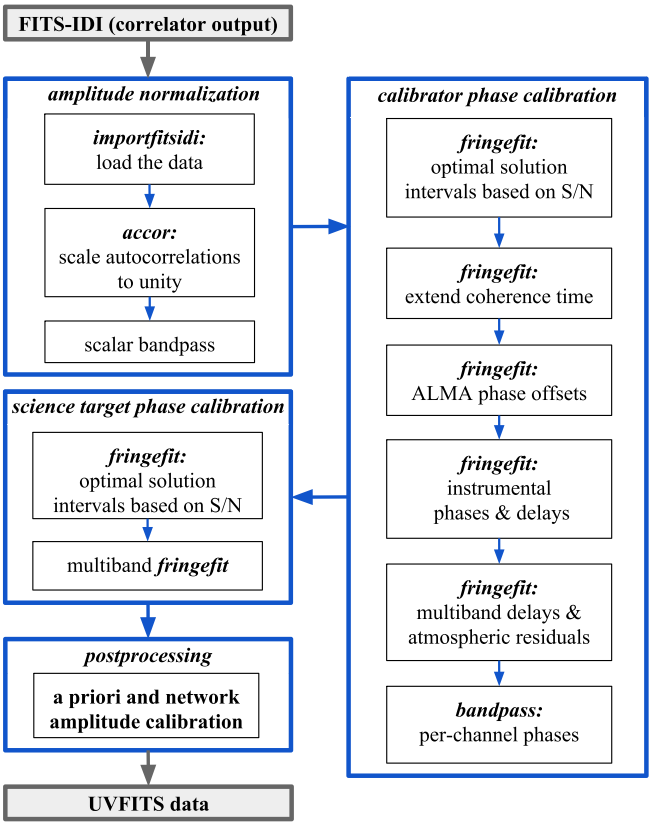

Figure 6. EHT data processing stages of `rPICARD`. Instrumental amplitude calibration effects are described in the top-left box. Phases for the calibrator sources are corrected first to solve for instrumental effects (second box) and science targets are phase-calibrated after the instrumental effects have been solved (third box). Finally, post-processing steps are done outside of CASA for amplitude calibration (fourth box).

fringe solutions are re-referenced with the CASA `rerefant` task to a common station for each observing track to ensure phase continuity across scans.

Phases are first calibrated for the high S/N calibrator sources, which are used to correct for instrumental effects. Optimal time solution intervals to calibrate atmospheric intra-scan phase fluctuations ($\mathcal{T}_{\rm sol}$) are determined automatically based on the S/N of the data. The search is done for short solution intervals, close to the coherence time, which still yield detections on all possible baselines (Janssen et al. 2019a). Typical solution intervals range from 2 to 30 s. Using these solution intervals, phases and rates are calibrated to extend the coherence time of the calibrator scans. This results in high S/N scan-based fringe solutions per 58 MHz spectral IF, which are used to obtain calibration solutions for instrumental effects. ALMA-induced phase offsets between spectral IFs are corrected with the short ALMA–APEX baseline. All baselines in the array are used by the global fringe fitter in the next step to solve for residual instrumental phase and delay offsets for all stations. After removing these instrumental data corruptions, a final `fringefit` step solves for multi-band delays on the (previously determined) solution intervals. A 60 s median window filter is used to smooth the slowly varying multi-band delays, which effectively removes potential outliers. After fringe fitting, the phases are coherent in time and frequency, and the `bandpass` task is used to solve for the frequency-dependent phase gains within each 58 MHz spectral IF for each station, using the combined data of all calibrator sources.

After all instrumental effects are calibrated out, the optimal fringe-fit solution intervals $\mathcal{T}_{\rm sol}$ are determined for the weaker science targets, and phases, delays, and rates are solved for in a single `fringefit` step. The intra-scan fringe fritting on short solution intervals flags low S/N segments where no fringes are found to a specific station, e.g., when a station arrived late on source. Finally, the `exportuvfits` task is used to export the calibrated data from internal *Measurement Set* format to `UVFITS` files, which are then flux-density and network-calibrated in the common post-processing framework.

Janssen et al. (2019a) demonstrate the `rPICARD` calibration capabilities in a close comparison with a traditional AIPS-based calibration using 43 GHz VLBA data of M87. The resultant image of the jet and counter-jet, which reveals a complex collimation profile, is in good agreement with earlier results from the literature (e.g., Walker et al. 2018). The `rPICARD` pipeline was further used for the generation of synthetic EHT data (Paper IV), where known input delay and phase offsets were recovered as a ground-truth validation.

5.3. AIPS Pipeline

AIPS (Greisen 2003) is the most widely used software package for VLBI data reduction and processing at frequencies at or below ∼86 GHz. It is commonly used in the VLBI community and was built to process low-S/N data from fairly homogeneous centimeter-wave observatories at low recording bandwidths. The EHT, however, falls in a different category: its high recording bandwidth and heterogeneous array produce data with a wide range of S/N, often dominated by systematic effects instead of thermal noise. These properties required the development of a custom pipeline based on AIPS, deviating from standard fringe-fitting procedures for lower frequency data processing as outlined in e.g., the AIPS Cookbook.[111]

The custom AIPS pipeline is an automated `Python`-based script using functions implemented in the `eat` package. It makes use of `ParselTongue` (Kettenis et al. 2006), which provides a platform to manipulate AIPS tasks and data outside of the AIPS interface. The pipeline is summarized in Figure 7 and shows individual tasks used for calibration. A suite of diagnostic plots, using tasks `VPLOT` and `POSSM`, are also generated at each calibration step within the pipeline.

The loading of EHT data into AIPS, during which digital corrections for 2-bit quantization efficiency are applied, requires a concatenation of several packaged `FITS-IDI` files and a careful handling of the JCMT, which observes with a slightly shifted IF setup of the band (Section 4). The pipeline reduces each band (low and high) in separate runs. Data inspection and flagging of spurs in the frequency domain from accumulated scalar bandpass tables (generated with `BPASS`) and dropouts or amplitude jumps in the time domain are done interactively with the AIPS tasks `BPEDT` and `EDITA`. The flags are saved in output flag tables to use in non-interactive reruns of the pipeline. Standard amplitude normalization steps are performed with the AIPS task `ACSCL`. The field rotation angle corrections are performed with an EHT-specific receiver mount correction script (`ehtutil.ehtpang`, modifying the antenna table from the `DiFX` alt-az default to the proper receiver mounts of each station) using the AIPS task `CLCOR` before fringe fitting.

[111] http://www.aips.nrao.edu/cook.html

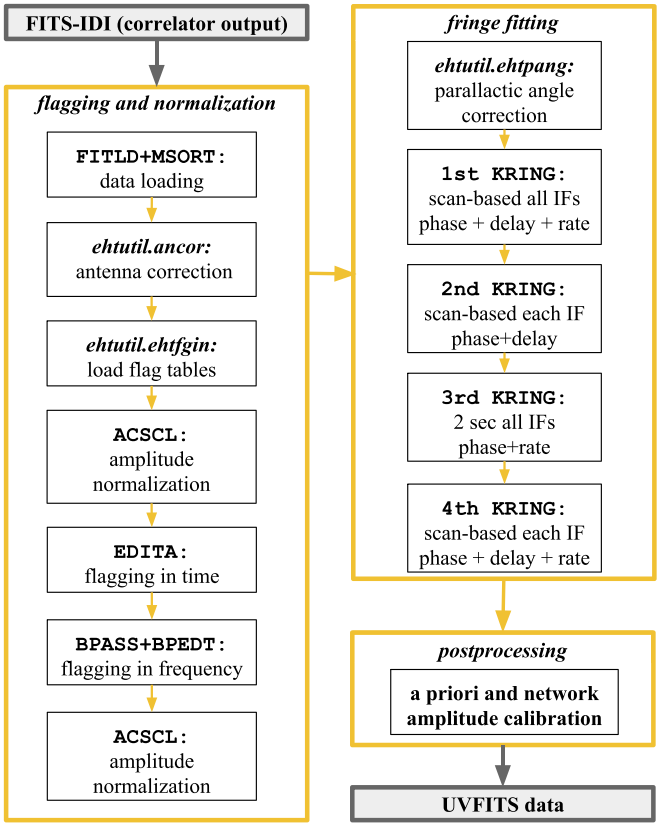

Figure 7. Stages of the AIPS fringe-fitting pipeline and post-processing steps. The pipeline begins with direct data editing (interactively or via input correction and flag tables) and amplitude normalization (first box). The phase calibration process then follows via four steps with the AIPS fringe fitter KRING to solve for phase and delay offsets and rates (second box). Finally, post-processing steps are done outside of AIPS for amplitude calibration (third box).

The fringe-fitting steps follow a similar framework to the HOPS pipeline but use KRING,[112] a station-based fringe fitter that outperforms the standard FRING in terms of computational efficiency for large data sets, while maintaining an equivalent accuracy. The first step of the fringe search, commonly known as instrumental phase calibration, consists of solving for delay and phase offsets and fringe-rates using the full scan coherence and full 2 GHz bandwidth (combining spectral IFs). The second step solves for delay and phase offset residuals per individual spectral IF, again using the full scan coherence. The third step uses a fixed solution interval of 2 s to solve for fast phase rotations in time across the full bandwidth (combining IFs). The final stage is solving for scan-based residual delays and phases per individual spectral IF.

The AIPS pipeline particularly relies on ALMA being present to accurately solve for short interval solutions, as it uses ALMA as the reference station for the initial baseline-based FFT within KRING. Without ALMA, or in certain cases of a weak baseline to ALMA, KRING is unable to accumulate enough S/N in a single spectral IF or within a two-second segment to constrain a fringe solution. After applying all calibration steps, the data are frequency-averaged and exported in UVFITS format. A priori and network calibration are performed outside of AIPS in the common post-processing framework.

[112] See AIPS MEMOS 101 and 107 for details; http://www.aips.nrao.edu/aipsmemo.html.

6. Flux Density Calibration

The flux density calibration for the EHT is done in two steps and is a common post-processing procedure for all three phase calibration pipelines, as it involves very little handling of the data themselves. In Section 6.1, we describe the a priori calibration process to calibrate visibility amplitudes to a common flux density scale across the array. In Section 6.2, we present the network calibration process, where we use array redundancy to absolutely calibrate stations with an intra-site companion.

6.1. A Priori Amplitude Calibration

A priori amplitude calibration serves to calibrate visibility amplitudes from correlation coefficients to flux density measurements, as in Equation (2). As the normalized correlation coefficients are in units of noise power, it is necessary to account for telescope sensitivities to convert to a uniform flux density scale across the array. The SEFD of a radio telescope is the total system noise represented in units of equivalent incident flux density above the atmosphere. It can be written as

$$\mathrm{SEFD} = \frac{T^*_{\mathrm{sys}}}{\mathrm{DPFU} \times \eta_{\mathrm{el}}}, \tag{3}$$

using the three measurable parameters:

1. T^*_{sys}: the *effective system noise temperature* describes the total noise characterization of the system corrected for atmospheric attenuation (Equations (4) and (5)),
2. DPFU: the *degrees per flux density unit* provides the conversion factor (K/Jy) from a temperature scale to a flux density scale, correcting for the aperture efficiency (Equation (6)),
3. η_{el}: the *gain curve* is a modeled elevation dependence of the telescope's aperture efficiency (Equation (7)), factored out of the DPFU to track gain variation as the telescope moves across the sky.

The EHT is a heterogeneous array with telescopes of various sensitivities (ranging nearly three orders of magnitude, see Figure 8), operation schemes, and designs. A clear understanding of each station's metadata measurement and delivery is required for an accurate calibration of the measured visibilities. We determine the SEFDs of the individual stations and their uncertainties under idealized conditions, assuming adequate pointing and focus (see Sections 6.1.1, 6.1.3, and 6.1.4). Further losses and uncertainty in the SEFDs, particularly those induced by focus or pointing errors, are difficult to quantify using available metadata, but are qualitatively explained in Section 6.1.5. A more quantitative assessment of station behavior can be done via derived residual station gains from self-calibration methods in imaging or model fitting (Papers IV, VI).

6.1.1. Quantifying Station Performance

In order to determine the sensitivity of a single-dish station at a given time, measurements of the effective system temperature, the DPFU, and the gain curve are required. Here we

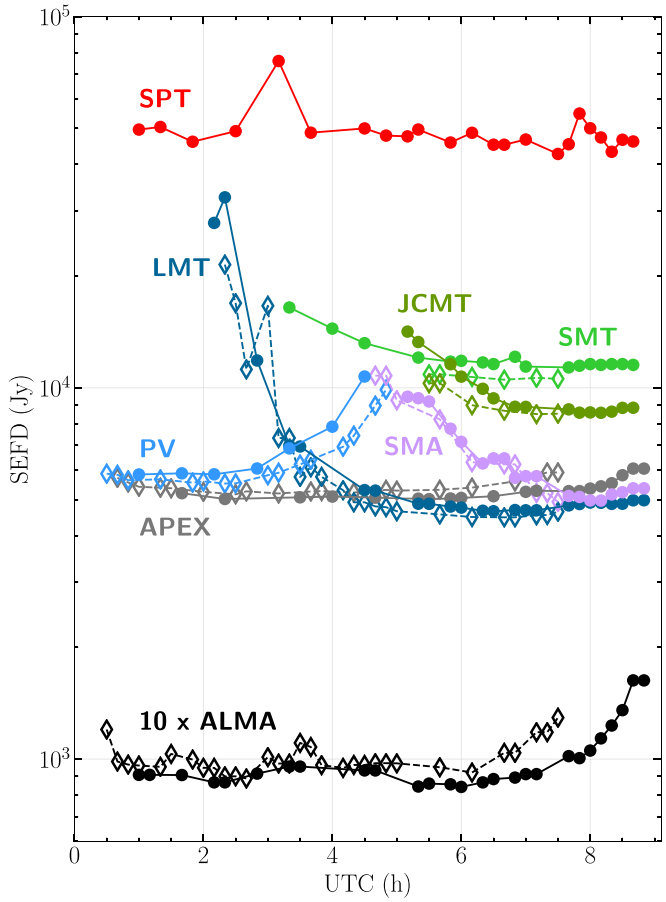

Figure 8. Example of SEFD values during a single night of the 2017 EHT observations (April 11, low-band RCP). Values for 3C 279 are marked with full circles, values for M87 are marked with empty diamonds. ALMA SEFDs have been multiplied by 10 in this plot. The SPT is observing 3C 279 at an elevation of just 5°.8, resulting in an uncharacteristically high SEFD due to the large airmass.

provide details on how these parameters are measured for the EHT array.

The EHT operates in the millimeter-wave radio regime, where observations are very sensitive to atmospheric absorption and water vapor content. In contrast with centimeter-wave interferometers (e.g., VLBA/JVLA), millimeter-wave telescopes typically measure $T^*_{\rm sys}$ via the "chopper" (or hot-load) method: an ambient temperature load $T_{\rm hot}$ with known blackbody properties is placed in front of the receiver, blocking everything but the receiver noise, and the resulting noise power is compared to the same measurement on cold sky. Assuming $T_{\rm hot} \sim T_{\rm atm}$ (the hot load is at a temperature comparable to the radiating atmosphere), this method automatically compensates for atmospheric absorption to first order, essentially transferring the incident flux density reference point to above the atmosphere (e.g., Penzias & Burrus 1973; Ulich & Haas 1976):

$$T^*_{\rm sys} \simeq e^{\tau}(T_{\rm rx} + (1 - e^{-\tau})T_{\rm atm}), \quad (4)$$

where $T_{\rm rx}$ is the receiver noise temperature, and τ is the sky opacity in the line of sight. Details on the chopper techniques adopted for the EHT are provided in a technical memo[113] (Issaoun et al. 2017a).

Three stations in the EHT array have double-sideband (DSB) receivers in 2017 (SMA, JCMT, and LMT), where both upper and lower sidebands on either side of the oscillator frequency are folded together in the recorded signal (e.g., Iguchi 2005, Paper II). Because only one 4 GHz sideband is correlated across the array, we correct $T^*_{\rm sys}$ for the excess noise contribution from the uncorrelated sideband

$$T^*_{\rm sys} = T^*_{\rm sys,DSB}(1 + r_{\rm sb}), \quad (5)$$

where the sideband ratio $r_{\rm sb}$ is the ratio of source signal power in the uncorrelated sideband to that in the correlated sideband. A sideband ratio of unity, for an ideal DSB system, is assumed for the SMA and LMT based on known receiver performance. A measured sideband ratio of 1.25 is used for the JCMT.[114] The remaining stations use sideband-separating receiver systems and do not need this adjustment. The SPT, although sideband-separating, is believed to have suffered from a degree of incomplete sideband separation in 2017, giving it some amount of (uncharacterized) effective $r_{\rm sb}$.

In addition to the noise characterization, the efficiency of the telescope must also be quantified. The DPFU relates flux density units incident onto the dish to equivalent degrees of thermal noise power through the following equation:

$$\mathrm{DPFU} = \frac{\eta_{\rm A} A_{\rm geom}}{2k_{\rm B}}, \quad (6)$$

where $k_{\rm B}$ is the Boltzmann constant ($k_{\rm B} = 1.38 \times 10^3$ Jy/K), $A_{\rm geom}$ is the geometric area of the dish, and $\eta_{\rm A}$ is the aperture efficiency of the telescope. For an idealized telescope with a uniform illumination (no blockage or surface errors), the full area would be available to collect the incoming signal and the aperture efficiency would be unity. Real radio telescopes intentionally taper their illumination to minimize spillover past the primary mirror, most have secondary mirror support legs that block part of the primary aperture, and generally the surface accuracy produces a non-negligible degradation in efficiency. To determine $\eta_{\rm A}$, well-focused and well-pointed observations are made of calibrator sources of known brightness, usually planets (e.g., Kutner & Ulich 1981; Mangum 1993; Baars 2007). The planet brightness temperature models from the GILDAS[115] software package were used for this calibration. For each single-dish EHT station, we determine a single DPFU value per polarization/band, except for JCMT, which has measurable temporal variations from solar heating during daytime observations. A more detailed overview of the methodology for $\eta_{\rm A}$ is presented in Issaoun et al. (2017a).

We separately determine the elevation-dependent efficiency factor $\eta_{\rm el}$ (or gain curve) due primarily to gravitational deformation of each parabolic dish. The characterization of the telescope's geometric gain curve is particularly important for the EHT, which often observes science targets at extreme elevations in order to maximize (u, v) coverage. The elevation-dependent gain curve is estimated by fitting a second-order polynomial to measurements of bright calibrator sources continuously tracked over a wide range of elevation (see Figure 9 and the technical memo by Issaoun et al. 2017b). In

[113] EHT Memo Series: https://eventhorizontelescope.org/for-astronomers/memos.

[114] https://www.eaobservatory.org/jcmt/instrumentation/heterodyne/rxa/

[115] http://www.iram.fr/IRAMFR/GILDAS

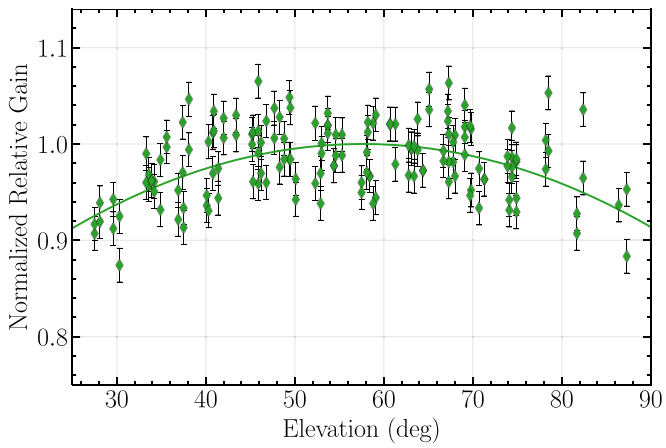

Figure 9. Example of a gain curve fit to single-dish normalized flux density measurements of calibrators at the SMT (Issaoun et al. 2017b).

the EHT array, SMT, PV, and APEX have characterized gain curves. The gain curve is parameterized as a second-order polynomial about the elevation at maximum efficiency:

$$\eta_{\rm el} = 1 - B({\rm el} - {\rm el}_{\rm max})^2 . \quad (7)$$

The JCMT has no elevation dependence at 230 GHz as it is operating at the lower end of its frequency range. The LMT has an adaptive surface that is able to actively correct for surface deformation as a function of elevation. Through observations of planets, the LMT was determined to have a flat 1.3 mm gain between 25° and 80° to within 10% uncertainty. At the SPT, the elevation of extra-solar sources is constant, and therefore possible elevation-dependent efficiency losses remain uncharacterized.

We also mitigate a number of pathological issues uncovered in the 2017 data affecting the visibility amplitudes in a priori calibration. Additional loss of coherence in the signal chain at PV due to impurities in the LO, an excess noise contribution at APEX due to the inclusion of a timing signal, and the partial SMA channel dropouts were identified during data processing. Correction factors for the visibility amplitudes on baselines to these sites were estimated, as explained in the Appendix. These correction factors translate to a square multiplicative effect on the station-based SEFDs, as shown in Table 2. In the a priori calibration metadata, the multiplicative factors were folded into the DPFUs for PV and APEX and into the $T^*_{\rm sys}$ measurements for SMA (due to its time dependence). Representative median values for the aperture efficiency, DPFU, effective system temperature, and SEFD on EHT primary targets (M87 and Sgr A*) for each station participating in the EHT 2017 observations are shown in Table 2. A site-by-site overview of the derivation of a priori calibration quantities is given in a technical memo (Janssen et al. 2019b).

6.1.2. Calibrating Visibility Amplitudes

The $T^*_{\rm sys}$, DPFU, and elevation gain data for all stations are aggregated in ANTAB format text files. They are subsequently matched with observed visibilities for a given source using linear interpolation. Visibility amplitudes are calibrated in units of flux density by multiplying the normalized visibility amplitudes by the geometric mean of the derived SEFDs of the two stations across a baseline *i–j*:

$$|V_{ij}| = \sqrt{{\rm SEFD}_i \times {\rm SEFD}_j}\ |r_{ij}|, \quad (8)$$

where $|V_{\rm ij}|$ is then the calibrated visibility amplitude in Jy on that baseline, as in Equation (2).

Figure 10 shows the scan-averaged S/N on individual baselines, which is proportional to the phase-calibrated correlated signal, as a function of the projected baseline length (top panel), and the equivalent correlated flux density after a priori calibration (center panel) for observations of M87 (left) and 3C 279 (right) on April 11. The split in the S/N distributions is due to the difference in sensitivity between the co-located sites ALMA and APEX, leading to simultaneous baselines with two levels of sensitivity. The a priori calibration process puts all points on the same flux density scale (via Equation (8)), and the resulting data variations can thus be attributed to source structure, no longer dominated by sensitivity differences between baselines.

6.1.3. Single-dish Error Budget

The SEFD error budget, assuming nominal pointing and focus, is dominated by the measurement uncertainty for the DPFU (see Table 3). Depending on the source elevation, the uncertainty contribution for the elevation gain may also be non-trivial (particularly for the LMT) and adds in quadrature to the DPFU error to give the SEFD error budget. The gain curve error budget is obtained from the propagation of errors on the polynomial fit parameters in Equation (7), and is also itself elevation-dependent. We assume that the uncertainty in $T^*_{\rm sys}$ is negligible as it is the variable measured closest to the individual VLBI scans and the accuracy of the chopper method is well studied (see Section 6.1.5, Kutner 1978; Mangum 2002). The measurement uncertainties associated with pointing or focus errors are not folded into these error budget estimates as they are not easily quantifiable a priori.

For all single-dish stations, the DPFU uncertainty is estimated by the standard deviation in $\eta_{\rm A}$ from a distribution of planet measurements added in quadrature to the uncertainty in the model brightness temperatures assumed for the planets. The scatter in planet measurements reflects changes in telescope performance with varying weather conditions, and thus it encompasses possible fluctuations in the mean value assumed during the observing window. An exception is the JCMT during daytime observing, where $\eta_{\rm A}$ has a time dependence parametrized by a fit of a Gaussian component dip as a function of local time, described in a technical memo (Issaoun et al. 2018). The uncertainty in $\eta_{\rm A}(t)$ is determined through the propagation of the errors on the fit parameters via least-squares fitting. Individual uncertainty contributions of the various components and the resulting percentage SEFD error budget for each EHT station during the 2017 April observations are listed in Table 3. Site-by-site derivations of flux density calibration uncertainties during the EHT 2017 campaign are given in Janssen et al. (2019b).

6.1.4. Phased-array Calibration

The phased arrays combine the total collecting area of all their dishes into one virtual telescope. This depends on precise phase alignment of the signals, with an accuracy that is captured by the

Table 2
Median EHT Station Sensitivities on Primary Targets during the 2017 Campaign, Assuming Nominal Pointing and Focus

Station	Diameter in 2017 (m)	Sideband Ratio	Sideband-corrected Median $T^*_{\rm sys}$ (K)	Aperture Efficiency $\eta_{\rm A}$	DPFU (K/Jy)	Multiplicative Mitigation Factor	Median SEFD (Jy)
APEX	12	⋯	118	0.61	0.025	1.020	4800
JCMT	15	1.25	345	0.52	0.033[a]	⋯	10500
LMT	32.5	1.0	371	0.28	0.083	⋯	4500
PV	30	⋯	226	0.47	0.12	3.663	6900
SMT	10	⋯	291	0.60	0.017	⋯	17100
SPT	6[b]	⋯	118	0.60	0.0061	⋯	19300
SMA6	14.7[c]	1.0	285	0.75	0.046[d]	1.138[e], 1.515[e]	6400
ALMA37	73[c]	⋯	76	0.68	1.03[d]	⋯	74

Notes.
[a] Nighttime value for the DPFU. The daytime DPFU includes a Gaussian component dip as function of local Hawai'i time.
[b] SPT has a 10 m dish diameter, with 6 m illuminated by receiver optics in 2017.
[c] The diameter for phased arrays reflects the sum total collecting area.
[d] DPFUs for phased arrays are determined for the full collecting areas.
[e] Applied when 6.25% and 18.75% of the SMA bandwidth was corrupted, respectively.

phasing efficiency $\eta_{\rm ph}$ (see Appendix in Paper II)

$$\eta_{\rm ph} = \frac{|\sum \gamma_i|^2}{(\sum |\gamma_i|)^2}. \tag{9}$$

The phasing efficiency contributes to the aperture efficiency of the phased array, and reflects the ratio of source signal power[116] observed by the phased array, versus that observed by a perfectly phased array. The complex gains γ_i (as in Equation (2)) are taken over all the dishes in the phased array, and have zero relative phase in the case of ideal phasing ($\eta_{\rm ph} = 1$).

The phasing efficiency as defined above is valid when the signals being combined are optimally weighted by the effective collecting area of each antenna, $A_{i,\rm eff} \sim 1/{\rm SEFD}_i$. Then the SEFD of the phased array is

$${\rm SEFD}_{\rm array} = \frac{1}{\eta_{\rm ph}} \left(\sum \frac{1}{{\rm SEFD}_i} \right)^{-1}. \tag{10}$$

Both SMA and ALMA use equal weights for the formation of the sum signal. Due to their homogeneity, Equations (9) and (10) are excellent approximations.

At the SMA, the phasing efficiency $\eta_{\rm ph}$ is estimated from self-calibrated phases to a point-source model (Young et al. 2016). Phases for each dish of the connected-element array are calculated online once per integration period, which varies in the range of 6–20 s depending on the observing conditions, and the same phases are fed back as corrective phases for beamforming the phased array. The DPFU for the individual antennas that comprise the SMA are well characterized at 0.0077 K/Jy, with $\eta_A = 0.75$, and the 6 m dishes have a flat gain curve at 230 GHz, which is near the lower end of their operating frequency range (Matsushita et al. 2006). An SEFD for each antenna is calculated from DSB $T^*_{\rm sys}$ measurements taken regularly at the time of observing. The overall SEFD for the SMA phased array is then estimated via Equation (10).

For ALMA, both amplitude and phase gain for each dish are solved during the offline QA2 processing of interferometric ALMA data, under an assumed point-source model with known total flux. The SEFDs of individual antennas are thus determined through amplitude self-calibration, automatically accounting for system noise and efficiency factors but sensitive to errors in the source model. Because ALMA data has the additional complication of linear-to-circular conversion, the phased-sum signal SEFD is determined via the full-Stokes Jones matrix of the phased array, as computed by PolConvert (Equation (15) of Martí-Vidal et al. 2016). By convention, QA2 sensitivity tables place all phasing-related factors into the $T^*_{\rm sys}$ component of Equation (3), allowing DPFU to assume a constant value corresponding to a single ALMA antenna. Further details are provided in Section 6.2.1 of Goddi et al. (2019).

During the EHT 2017 observations, $\eta_{\rm ph}$ was above 0.8 for ∼80% (ALMA) and ∼90% (SMA) of the time. Poorer efficiency at both sites is associated with low elevation and increased atmospheric turbulence. At ALMA, phase corrections are calculated online by the telescope calibration system and applied to the array with a loop time of ∼18 s (Goddi et al. 2019). At the SMA, integration times at the correlator can be as short as 6 s, but longer intervals are used if needed to build S/N. The corrective phases are passed through a stabilization filter before being applied, resulting in an effective loop time of ∼12–40 s for the SMA. Phasing at both sites suffers when the atmospheric coherence timescale becomes short with respect to the loop time. To minimize the impact, both arrays are arranged in tight configurations during phased array operations.

The uncertainty on the $\eta_{\rm ph}$ measurement at the SMA is estimated to be 5%–15%, and depends primarily on the S/N of the gain solutions. The SMA (usually with six 6 m dishes phased) has considerably less collecting area than ALMA (usually with 37 12 m dishes phased) to use for solving phase gains. For weaker sources, the uncertainty in estimating corrective phases at the SMA and in calculating the phasing efficiency can be considerable. The assumed flux of the point-source model used to self-calibrate ALMA during QA2 has a quoted 10% systematic uncertainty in Goddi et al. (2019). The uncertainties from self-calibration and phasing are uncharacterized, therefore the uncertainty of 10% for the derived SEFD of the ALMA phased array is considered a lower limit. Errors from the use of a point-source model for M87 and 3C 279 during gain calibration are expected to be small in comparison to these values. The

[116] It is common to see $\eta_{\rm ph}^{1/2}$ defined as the phasing efficiency (e.g., Matthews et al. 2018), which scales with signal amplitude.

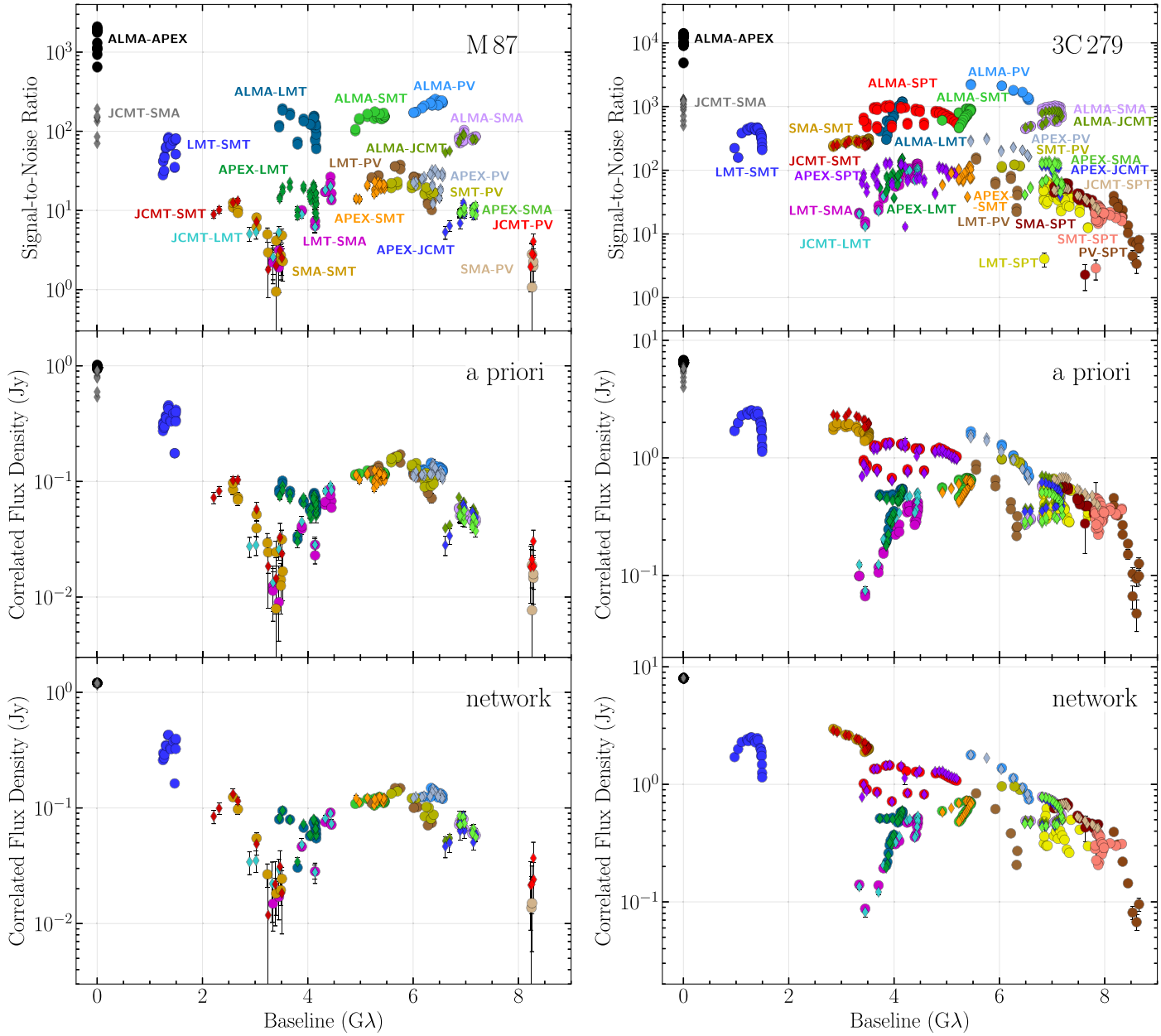

Figure 10. Stages of visibility amplitude calibration illustrated with the April 11 HOPS data set on M87 (left) and 3C 279 (right), as a function of projected baseline length. The two frequency bands are coherently scan-averaged separately and the final amplitudes are averaged incoherently across bands. Top: S/N of the correlated flux density component after phase calibration, both RCP and LCP. Middle: flux-density calibrated RCP and LCP values. Bottom: final, network-calibrated Stokes I flux densities. Error bars denote $\pm 1\sigma$ uncertainty from thermal noise.

individual uncertainties and error budget for the phased arrays are shown in Table 3.

6.1.5. Limitations of a Priori Calibration

Although the DPFU is typically represented as a single value measured under good performance conditions, a station's efficiency is expected to vary with temperature, sunlight, and quality of pointing and focus. We have attempted to characterize specific time-dependent trends such as daytime dependence for the JCMT, but other factors are very difficult to decouple from the overall station behavior and associate with individual scans. Specific efficiency losses during scans, in particular due to lack of pointing/focus accuracy, are not included in the a priori amplitude calibration information for single-dish sites and remain in the underlying correlated visibilities. Therefore, the a priori error budget in Table 3 is only representative of global station performance and cannot be estimated for individual scans. In addition to a priori calibration, a list of problematic scans, where the station performance is known to be poor and the error budget is thus assumed to be undetermined, is passed on to analysis groups. These losses can be corrected in imaging and model fitting via self-calibration methods and amplitude gain modeling (Papers IV, VI).

The uncertainty in the chopper calibration is also difficult to quantify, as we do not know the true coupling of the hot load to the receiver (including spillover and reflection) and thus its effective temperature is uncertain (Kutner 1978; Jewell 2002). One of the key assumptions of the chopper method is the

Table 3
Station-based SEFD Percentage Error Budget during the 2017 Campaign, Assuming Stable Weather Conditions and Nominal Pointing and Focus (Subdominant Effects from $T^*_{\rm sys}$ Measurements and Sideband Ratios are not Shown)

Station	DPFU Budget (%)	Gain Curve Budget (%)	$\eta_{\rm ph}$ Budget (%)	SEFD Budget (%)
APEX	11	0.3	⋯	11
JCMT	11–14[a]	⋯	⋯	11–14
LMT	20	10	⋯	22[b]
PV	10	1.5	⋯	10
SMT	7	1	⋯	7
SPT	15	⋯	⋯	15[b]
SMA6	2	⋯	5–15[c]	5–15
ALMA37	10	⋯	⋯	10[d]

Notes.
[a] The range in the budget at the JCMT is the result of a larger uncertainty in the calibration during daytime observing, due to its aperture efficiency time dependence.
[b] The error budget for SPT and LMT are lower limits due to uncharacterized losses, see Section 6.1.5.
[c] The range in the budget at the SMA is due to a larger uncertainty in the phasing for weaker sources.
[d] ALMA uncertainty is a lower limit from systematics caused by the assumed source flux density during QA2 calibration.

equivalence (to first order) of the hot load, ambient, and atmospheric temperatures, which allows for the correction of the atmospheric attenuation in the signal chain. Any deviation from this assumption in the $T^*_{\rm sys}$ measurements may introduce systematic biases. This can be partly mitigated by frequent measurements and monitoring of the DPFU under stable weather conditions and nominal telescope performance, to offset any significant scaling from temperature assumptions. The majority of stations in the EHT use a two-load (hot and cold loads) chopper method, with temperature refinement from atmospheric modeling, to measure the receiver noise temperature, and have radiometers to monitor the atmospheric opacity, which typically reduces uncertainty in the chopper calibration down to the 1% level (Jewell 2002; Mangum 2002). In contrast, the LMT and SPT used a single-load chopper method in 2017, leading to a larger error contribution estimated at the 5%–10% level minimum (Jewell 2002; Mangum 2002); with an error that grows rapidly at high line-of-sight opacity.

Limitations in accuracy of the a priori calibration may also come from the cadence of DPFU and $T^*_{\rm sys}$ measurements, typically performed between scheduled VLBI scans or outside VLBI observing altogether. The changing dish performance during the VLBI observations and intra-scan atmospheric variations are not typically captured by these measurements, although frequent pointing and focus calibration is done during the observations to keep an optimal performance. Furthermore, the time cadence varies across participating stations due to different chopper calibration setups, pointing, and focus needs, and allocated time for the EHT observing campaign. It is therefore not atypical for self-calibration corrections in downstream analysis to slightly deviate from the attributed amplitude error budget. To maximize mutual coverage, many stations are pushed past their nominal operating conditions during EHT observations, such as the LMT or the JCMT in the early evening local time due to surface heating and instability, and the SPT at extremely low elevation and high winds. For those stations and conditions, we expect residual gains to deviate significantly from the a priori amplitude error budget. A more detailed discussion of a priori calibration uncertainties and limitations is given in Issaoun et al. (2017a).

6.2. Network Calibration

Network calibration is a framework to estimate visibility amplitude corrections at some sites by utilizing array redundancy and supplemental measurements of the total flux density of a source (Fish et al. 2011; Johnson et al. 2015; Blackburn et al. 2019). It allows for absolute amplitude calibration of intra-site baselines and tightens consistency between simultaneous baselines to co-located sites when both sites are observing (see the bottom panels of Figure 10). It makes fewer assumptions than other techniques such as self-calibration and does not assume a specific compact source model.

Network calibration makes two related assumptions. The first is that redundant baselines in the EHT array (e.g., ALMA–SMA and APEX–JCMT) share the same model visibility. The second is that co-located sites provide a zero-baseline interferometer (e.g., ALMA–APEX), with a corresponding visibility that is a positive real number equal to the total flux density V_0. We express the measured visibility V_{ij} on a baseline between sites i and j as

$$V_{ij} = g_i g_j^* \mathcal{V}_{ij}, \tag{11}$$

where $\mathcal{V}_{ij}$ is the true visibility on that baseline, and g_i and g_j are the station-based residual gains assuming no thermal noise (the latter introduces uncertainty in the estimated gains).

Given two co-located sites i and j, we can solve for the amplitudes of their gains using a third remote site, using the assumptions above, $\mathcal{V}_{ik} = \mathcal{V}_{jk}$ and $\mathcal{V}_{ij} = V_0$. In the absence of thermal noise,

$$|g_i| = \sqrt{\frac{V_{ij}}{V_0} \times \frac{V_{ik}}{V_{jk}}} \quad \text{and} \quad |g_j| = \sqrt{\frac{V_{ij}}{V_0} \times \frac{V_{jk}}{V_{ik}}}. \tag{12}$$

Note that network calibration only provides gain estimates for those sites with a co-located partner.

In practice, thermal noise affects the accuracy of gains estimated using Equation (12). To optimize network calibration, we use all sets of baselines between co-located sites and distant sites and solve for the set of unknown model visibilities $\mathcal{V}_{ij}$ and station gains g_j by minimizing an associated χ^2. Specifically, for each solution interval, we minimize

$$\chi^2 = \sum_{i<j} \frac{|g_i g_j^* \mathcal{V}_{ij} - V_{ij}|^2}{\sigma_{ij}^2}, \tag{13}$$

where σ_{ij} is the thermal uncertainty on V_{ij}. We implemented network calibration via this minimization procedure within the `eht-imaging` library (Chael et al. 2016, 2018).

For the EHT 2017 April observations, network calibration is performed on frequency-averaged visibility `UVFITS` data coherently time-averaged over 10 s solution intervals. Both parallel-hand visibility components (further referred to as RCP/LCP or RR/LL) are network-calibrated with shared gain coefficients, using the total intensity measured by the ALMA array as V_0 (Goddi et al. 2019). The assumed flux density values per band on each observing day are reported in Table 4 for both M87 and 3C 279. For each source, a constant flux

Table 4
Total Flux Density Estimates used for Network Calibration

Source	Band	April 5 (Jy)	April 6 (Jy)	April 10 (Jy)	April 11 (Jy)
M87	low	1.13	1.14	1.17	1.21
	high	1.12	1.10	1.15	1.20
3C 279	low	8.61	8.57	7.99	8.01
	high	8.56	8.55	7.97	7.98

Note. The flux density values used for network calibration in SR1 come from the initial ALMA QA2 data release (2017 October), with a quoted uncertainty of 10%. Updated values are reported in Appendix B of Goddi et al. (2019) and are approximately 10% higher than shown here.

density is adopted per day, as both sources vary by <5% within an observation, well within the 10% flux density calibration error budget of ALMA measurements.

Network calibration enables absolute amplitude calibration of sites with a co-located partner (ALMA and APEX, SMA and JCMT) when both sites are operating, to the limit of thermal noise to the strongest remote stations. The remaining isolated sites (SMT, LMT, SPT, and PV) are unaffected by network calibration.

Following all calibration steps, Stokes I total intensity components correspond to

$$V_{ij,I} = \frac{1}{2}(V_{ij,\mathrm{RR}} + V_{ij,\mathrm{LL}}). \tag{14}$$

For JCMT, which is a single polarization station, we use the available RCP or LCP component as a proxy for the Stokes I value. This corresponds to assuming zero contribution from Stokes V circular polarization.

Most assumptions in the network calibration procedure are valid for all targets observed by the EHT. However, the assumption that co-located sites act as a true zero-baseline interferometer may not hold for sources with extended structure, such as M87. The distance between the SMA and the JCMT is 160 m, giving a resolution on that baseline of $\sim 1\farcs6$. The distance between ALMA (phase center) and APEX is 2.6 km, giving a resolution on that baseline of $\sim 0\farcs1$. For very compact sources, such as the quasar 3C 279, these two baselines both see point-like sources. For sources with extended structure, such as M87 and its large-scale jet, these two baselines will see slightly different structure. For example *HST*-1, a bright feature in the jet of M87 at just $0\farcs8$ from the radio core (Chang et al. 2010), produces a different response on both intra-site baselines. However, *HST*-1 has $\leqslant 1\%$ of the total core flux density of M87 as measured by ALMA (Table 4), so its effect on the network calibration gain solutions for ALMA and APEX is insignificant in comparison to the 10% uncertainty on the ALMA total flux density estimates.

7. Final Data Products

7.1. Data Release Specification

The SR1 data on M87 and 3C 279 represent a subset of a more comprehensive engineering release (ER) data production (ER5) for the EHT 2017 observations, after extensive internal validation and review. ER5 data are themselves derived from a fifth revision (Rev5) correlation data product. Information about accessing SR1 data and the software used for analysis can be found on the Event Horizon Telescope website's data portal.[117]

The sequence of correlation and engineering releases represents a year-long effort of identifying and mitigating data issues, and developing new software and procedures; first on secondary targets for ER1–ER3 and then including EHT primary science targets for ER4–ER5. Each internal engineering data release was subject to an independent review by a panel of experts not involved in the data preparation, before being made available for downstream analysis, including imaging and model fitting. The HOPS data set was present in all engineering releases, receiving the most extensive review and internal validation. AIPS data were included in ER1 for an initial comparison to HOPS on EHT 2017 secondary targets, and in ER5 for comparisons with both HOPS and the newly added CASA data set.

The final data products at the end of the calibration and reduction pipelines provide a uniform and reliable data set for scientific analysis that has been reduced and simplified by the removal of bad data (failed observations), and after compensating for non-astrophysical systematics. The data reduction process is automated and makes only minimal assumptions about the source: (1) that the target is mostly compact, and (2) that it has known a priori large-scale structure and total flux density (e.g., from ALMA observations). The calibration of systematics is therefore limited by an inability to jointly fit source parameters along with gains, but this pathway avoids introducing any strong model assumptions during the data preparation.

In addition to the raw correlator output, three levels of successive data reduction are provided, representing the assumptions made during calibration. The first level (1) includes only the phase calibration provided during fringe fitting, after which data can be averaged. At this stage, the data represent correlation coefficients and are the most fundamental data product for the formation of closure phases and closure amplitudes. This is followed by (2) data that has been brought to a physical amplitude scale (Jy) through a priori flux density calibration, and then (3) network amplitude calibrated using a priori assumptions about large-scale source structure and total flux density. The time–frequency resolutions of the various data products are presented in Table 5, and generally exceed what is needed to capture source structure. This resolution is chosen to allow for a manageable data volume while still providing flexibility for downstream time–frequency averaging as well as the fitting of any residual systematics through additional model-dependent techniques such as self-calibration.

The SR1 data release includes products of all three fringe-fitting pipelines. The HOPS pipeline data product is designated as the primary scientific EHT data set, given the degree of vetting it has received during an iterative process of five engineering releases and a current performance advantage at low S/N. The CASA and AIPS data sets are used for validation, including direct data cross-comparisons as well as validation of downstream analysis results. Each data product is provided in `UVFITS` format. The choice of format was motivated by the need for common output across all pipelines, and easy loading, inspection, and imaging in all software used in the downstream analysis efforts and via readily available `Python` modules. A suite of metadata accompany the release,

[117] https://eventhorizontelescope.org/for-astronomers/data

Table 5
Data Products Available in SR1

Stage	Δt (s)	$\Delta\nu$ (MHz)	Low Band (GB)	High Band (GB)
Corr. Data (Rev5)	0.4	0.5	665	713
Phase Cal. (SR1)	0.4	58.0	7.9	8.0
A Priori Cal. (SR1)	0.4	58.0	7.9	8.0
Network Cal. (SR1)	10.0	1875.0	0.117	0.121

Note. Integration time Δt and frequency averaging windows $\Delta\nu$ are given, as well as total data volumes for low- and high-band subsets, which have slightly different coverage.

such as the ANTAB tables used for a priori calibration, documentation and validation tests for each processing and calibration stage, assessment of derived calibration solutions, and suggested flagging information from investigations of station performance.

The first science release only provides calibrated Stokes I (total intensity) products for M87 and 3C 279. A summary of the data set content and S/N statistics is shown in Table 6, and a cumulative histogram of the Stokes I component S/N in the fully averaged data set is shown in Figure 11. A median reported thermal uncertainty is about 7 mJy on non-ALMA baselines and, remarkably, only about 0.7 mJy on baselines to ALMA for Stokes I single-band scan-averaged visibilities. In this first science release, the issue of polarimetric leakage calibration and correction is not addressed. Leakage has a relatively small influence on the total intensity and it is sufficient to parameterize the effects of leakage as a systematic source of non-closing errors (see Section 8). Future EHT results concerning polarimetry and other Stokes components will necessarily involve leakage calibration.

7.2. Closure Quantities

While the data release consists of reduced complex visibilities, derivative closure data products are particularly important for downstream data analysis, as well as for the description of data uncertainties. Unlike complex visibilities, closure quantities are robust against station-based gain errors. They are, however, susceptible to systematic non-closing errors, discussed in Section 8. For the needs of this Letter, we only provide brief definitions and description of conventions.

We define a closure phase formed from baseline visibilities on a closed triangle ijk as

$$\psi_{\mathrm{C},ijk} = \mathrm{Arg}\,(V_{ij} V_{jk} V_{ki}), \tag{15}$$

with a corresponding uncertainty

$$\sigma_{\psi_{\mathrm{C}},ijk} \approx \sqrt{S_{ij}^{-2} + S_{jk}^{-2} + S_{ki}^{-2}}, \tag{16}$$

where S_{ij} is the estimated S/N, associated with the V_{ij} visibility, that is

$$S_{ij} = \frac{|V_{ij}|}{\sigma_{ij}}. \tag{17}$$

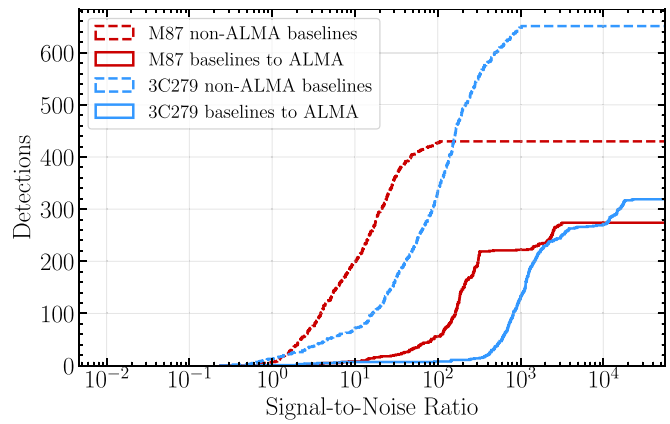

Figure 11. Cumulative histogram of Stokes I S/N in the HOPS data set for all observations of M87 and 3C 279, using fully averaged data. Solid curves represent baselines to ALMA, while the dashed curves show all other baselines.

Table 6
Content of the SR1 Data Set

		HOPS	CASA	AIPS	Shared	Max
M87	scans	72	71	71	71	72
	detections	771	753	706	702	898
	median S/N	31.4	27.3	25.9	⋯	⋯
	(shared set)	36.6	31.8	26.4	⋯	⋯
	all closure phases	912	889	790	784	1130
	(non-redundant)	482	470	432	429	579
	all closure amps	1938	1890	1569	1557	2520
	(non-redundant)	410	399	361	358	507
3C 279	scans	71	71	68	68	71
	detections	954	937	972	913	1246
	median S/N	250	219	187	⋯	⋯
	(shared set)	259	230	213	⋯	⋯
	all closure phases	1313	1285	1370	1258	1918
	(non-redundant)	631	618	646	607	864
	all closure amps	3342	3276	3591	3207	5361
	(non-redundant)	560	547	578	536	793

Note. Data products in the fully averaged SR1 data set. The shared data set is composed of only those detections that are reported by all three pipelines. The max data set is a theoretical maximum calculated assuming perfect realization of the observation schedules. The full set of all closure quantities is shown, which is used to estimate systematics in Section 8; as well as the non-redundant set, which reflects the actual number of unique phase and amplitude degrees of freedom measured by the (uncalibrated) array.

Formation of closure phase cancels the station-based gain factors that appear in Equation (2). In the case of visibility amplitudes, the gain factors can be similarly canceled by the formation of the log closure amplitude, defined as

$$\ln A_{\mathrm{C},ijk\ell} = \ln \frac{A_{ij} A_{k\ell}}{A_{ik} A_{j\ell}}, \tag{18}$$

for a quadrangle $ijk\ell$, where "ln" is a natural logarithm and A_{ij} represents debiased amplitude

$$A_{ij} = \sqrt{|V_{ij}|^2 - \sigma_{ij}^2}. \tag{19}$$

The associated uncertainty of log closure amplitude is

$$\sigma_{\ln A_C,ijk\ell} \approx \sqrt{S_{ij}^{-2} + S_{k\ell}^{-2} + S_{ik}^{-2} + S_{j\ell}^{-2}}. \quad (20)$$

Uncertainties reported in Equations (16) and (20) are calculated based on propagation of thermal visibility errors and are strictly correct in a high S/N limit, where distributions of both types of closure quantities are well approximated with a normal distribution. The number of closure quantities that can be derived from SR1 visibilities is given in Table 6. The numbers describe a fully averaged (i.e., scan and 4 GHz band-averaged) data set. We give the number of all closure quantities, corresponding to the full (or maximal) set formed from all possible loops over three or four stations in every scan. The full set has a balanced representation of baselines, and is used to estimate systematic errors in Section 8.4. Elements of a maximal set are, however, not independent (the set is highly redundant). We also provide the number of closure products in the non-redundant (or minimal) set. This is a reduced subset that captures all the available information in the closure quantities. Selection of a particular non-redundant data set is not unique and in general non-trivial (L. Blackburn et al. 2019, in preparation).

When intra-site baselines are present in the array, a special set of trivial closure quantities can be formed. Such closure phases and log closure amplitudes are zero by construction, within statistical uncertainties. While they do not carry any direct information about the source compact structure, they are useful for network calibration (Section 6.2) and the characterization of uncertainties, presented in Section 8.

7.3. Data Features

Certain properties of the reduced data can be directly observed in the behavior of visibilities and closure quantities. The data indicate remarkable persistent features in the structure of the M87 compact emission, as well as source structural variability on a timescale of days. In this section we give a rudimentary interpretation of these features. The implications of these basic features for the imaging, modeling, and scientific interpretation of the source structure are explored in companion Letters (Papers I, IV, V, VI).

Figure 12 shows the aggregate baseline coverage for EHT 2017 observations of M87 and 3C 279 via the HOPS pipeline. The coverage and data properties via the other two pipelines are comparable. Our shortest baselines are between co-located sites (SMA–JCMT and ALMA–APEX). These baselines are sensitive to arcsecond-scale structure, while our longest baselines are sensitive to microarcsecond-scale structure. For M87, the highest resolution (fringe spacing of 25 μas) is achieved in the east–west direction on baselines joining the Hawai'i stations to PV, while for 3C 279 the highest resolution (fringe spacing of 24 μas) is achieved in the north–south direction, on PV and SMT baselines to the SPT.

The 2017 observations led to detections on all baselines for M87. A longer averaging time (up to scan duration) is enabled by the atmospheric phase corrections performed by all three pipelines. Figure 10 (top-left panel) shows the S/N as a function of projected baseline length for M87 on April 11, for fully averaged data. A similar distribution is also shown for 3C 279 in Figure 10 (top-right panel), with around an order of magnitude difference due to the higher total flux density of 3C 279 compared to M87 (Table 4).

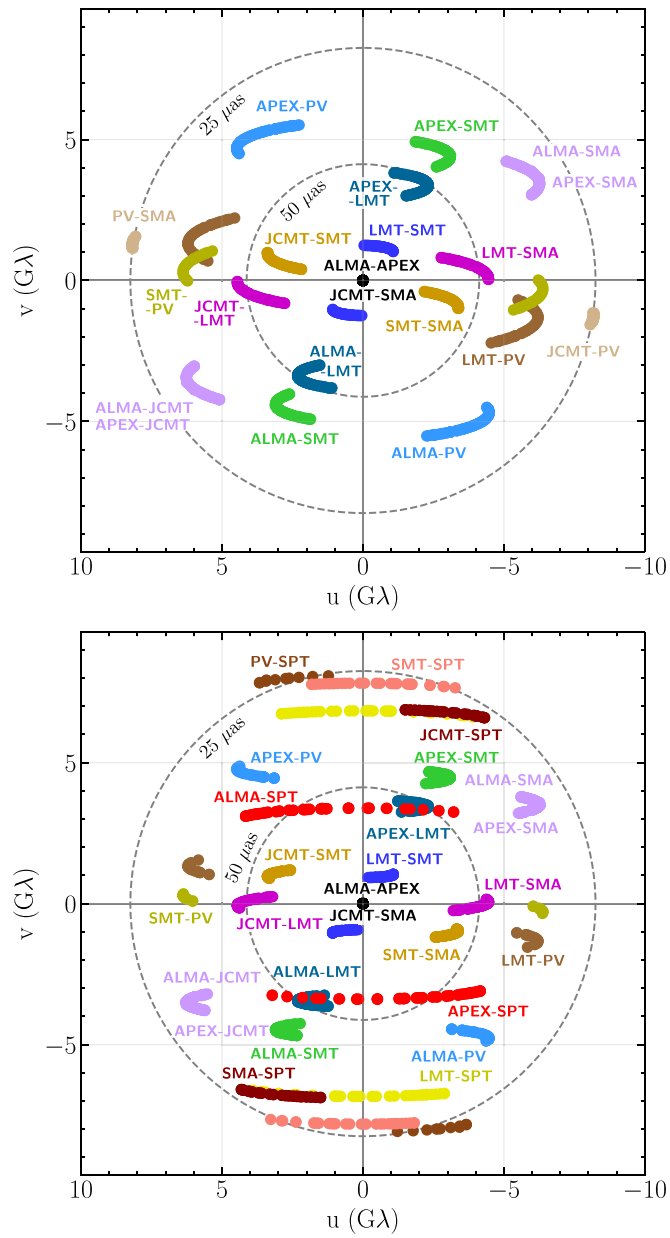

Figure 12. Aggregate (u, v) coverage for M87 (top panel) and 3C 279 (bottom panel) for the 2017 April observations, comparable for all three pipelines. Co-located sites (SMA/JCMT and ALMA/APEX) result in redundant baselines. The dashed circles show baseline lengths corresponding to fringe spacings of 25 and 50 μas.

The correlated flux density for M87 on April 11 after amplitude and network calibration is shown in Figure 10 (bottom left panel). There is a pronounced secondary peak in the visibility amplitudes with two minima on either side, interpreted as visibility nulls. The first of these nulls occurs at ~3.4 Gλ. It is steep on the east–west oriented LMT and SMT baselines to the Hawai'i stations, and shallower on the north–south oriented ALMA and APEX baselines to LMT at the same baseline length. The second null in amplitude is observed at ~8.3 Gλ, on the east–west oriented PV baselines to the Hawai'i stations. The correlated flux density for 3C 279 on

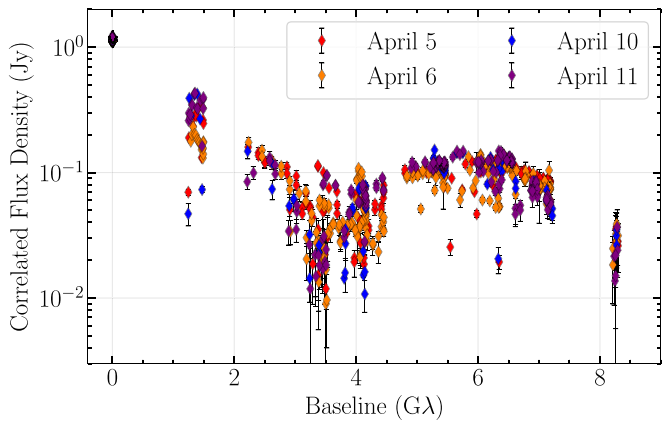

Figure 13. Correlated flux density of M87 as a function of projected baseline length for all four days of observations, from HOPS data that has been fully averaged. Outliers are due to reduced performance of the LMT or the JCMT. Error bars denote $\pm 1\sigma$ uncertainty from thermal noise.

April 11 after amplitude and network calibration is also shown in Figure 10 (bottom right panel). The trend in the visibility amplitudes is clearly different from the trend seen in M87. 3C 279 appears to have more complex structure on long baselines, and the structure varies with baseline position angle.

7.3.1. Persistent Structural Features

Figure 13 shows the correlated flux density after amplitude and network calibration as a function of baseline length for all four days of observations of M87 via the HOPS pipeline. The network-calibrated amplitudes show broad consistency over different days, and are consistent between pipelines (Section 8.5). The majority of notable low-amplitude outliers across days are due to reduced efficiency of the JCMT or the LMT on a select number of scans (caused by, e.g., telescope pointing issues or surface instability). Although the amplitudes of these data points are low, closure information remains stable and is unaffected by station gain. This is shown by comparing the erratic amplitudes on the LMT–SMT baseline in Figure 13 (cluster of points at about 1 Gλ) with the smooth trends in closure phase for the ALMA–LMT–SMT triangle (Figure 14, top left) and in closure amplitude for the ALMA–LMT–APEX–SMT quadrangle (Figure 14, top right).

The secondary peak in amplitude and the location of the two nulls are persistent for all four days. These signatures in the visibility amplitudes suggest that the source is not changing dramatically over several days, is compact with a characteristic spatial scale of $\lesssim 50\,\mu$as, and exhibits similar structure over a range of baseline position angle. Long baselines with various orientations lie in a stable trend along the second peak, and a minimum in amplitude at 3.4 Gλ is seen on both the east–west and north–south oriented baselines.

While the overall trend may indicate a compact and nearly circularly symmetric structure that is stable in time, a more detailed inspection of the data set suggests the presence of a slight anisotropy, also made evident by multiple measurements of non-zero closure phase. This can be seen comparing the ALMA/APEX–LMT and SMA/JCMT–LMT amplitudes in Figure 10 (bottom left). Both baselines probe a (u, v) distance of about 3.4 Gλ, but they have a very different, nearly perpendicular orientation (Figure 12). Flux density measured on the north–south oriented ALMA–LMT baseline is a few times larger than that for the east–west oriented SMA–LMT baseline. These properties translate to striking source features in imaging and model fitting, presented in Papers IV and VI, respectively.

7.3.2. Time Variability

M87 was observed on the two consecutive nights of April 5/6 and again four nights later for the two consecutive nights of April 10/11. We observe clear indications of modest source evolution between the two pairs of nights, and broad consistency within each pair. The evolution can be seen particularly well in the behavior of robust closure quantities.

Across the full set of closure quantities, some closure phases formed by wide and open triangles (e.g., ALMA–LMT–SMA, Figure 14, bottom left) show different closure phase trends between the first pair of days and the second pair. Additionally, the east–west oriented LMT–SMA–SMT triangle shows different closure phase trends between the two pairs of days (Figure 14, bottom center), but the equivalent triangle in the opposite orientation, LMT–PV–SMT, shows no such trend (Figure 14, top middle).

Strong night-to-night variability of closure phases is associated with baselines probing (u, v) components close to the first visibility amplitude null, where visibility phases are particularly sensitive to small structural changes. The LMT–Hawai‘i baselines are particularly affected. Rapid swings of closure phase, as large as 200° in 2 hr, are found for the LMT–SMA–SMT triangle, but exclusively for the latter pair of nights on April 10/11. Triangles that do not probe the 3.4 Gλ null location indicate less variability, e.g., ALMA–LMT–SMT or LMT–PV–SMT. Despite larger uncertainties, similar trends are seen in log closure amplitudes (right column of Figure 14). In particular, significant differences between the two pairs of nights can be seen on the ALMA–LMT–APEX–SMA quadrangle, while the ALMA–LMT–APEX–SMT quadrangle gives more consistent values.

8. Data Validation and Systematics

In this section, we summarize data set validation tests, performed using diagnostic tools developed in the `eat` library framework and focusing on the properties of the final network-calibrated data products. The section is structured as follows. In Section 8.1, we discuss internal consistency tests performed during the fringe-fitting stage. In Section 8.2, the accuracy of reported thermal uncertainties is tested. In Section 8.3 we investigate the robustness of data products against decoherence with increased coherent averaging time. Section 8.4 presents internal consistency tests in each pipeline and provides estimates for the magnitude of non-closing systematic errors, which become important considerations in the error budget for high S/N measurements. Finally, in Section 8.5, direct comparisons between the three pipelines are given. A more comprehensive discussion of these automated data validation procedures is given in a technical memo (Wielgus et al. 2019).

8.1. Fringe Validation

During fringe detection, a number of basic tests are performed on the data that check for data integrity, false fringes, and the overall self-consistency of the detected

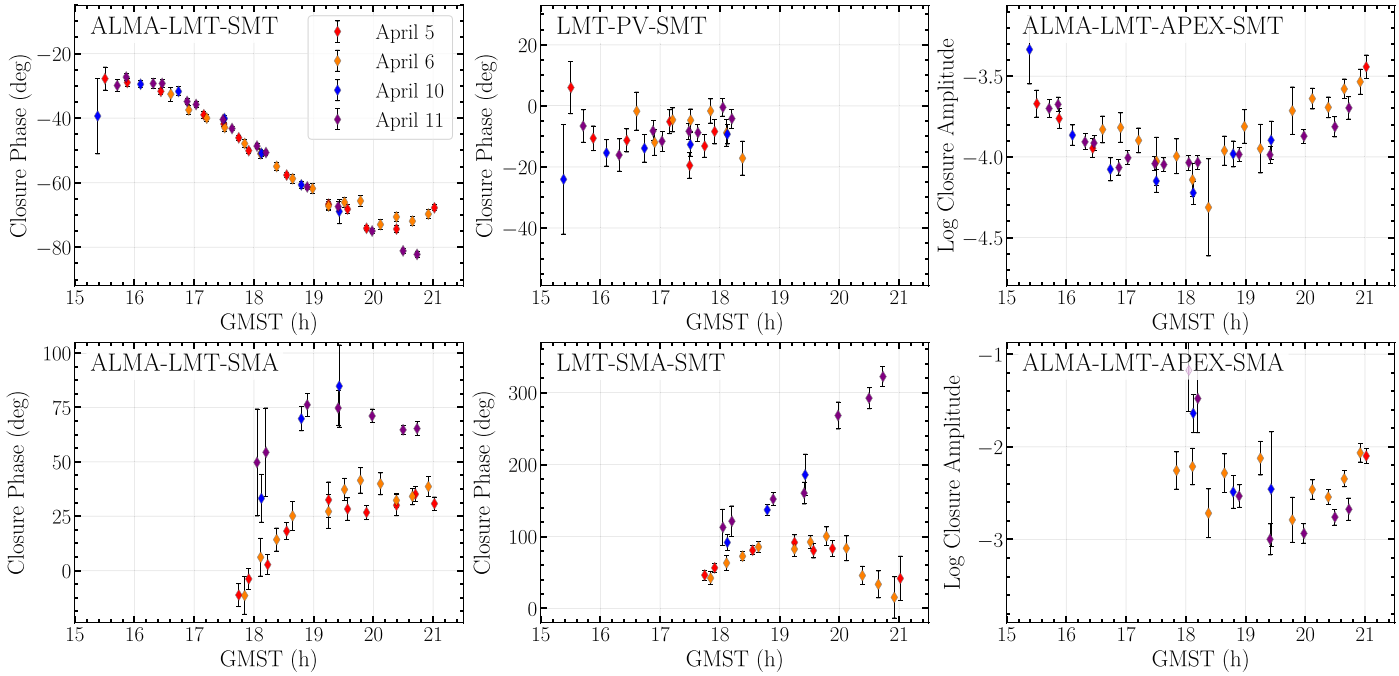

Figure 14. Selection of M87 closure phases (left and middle columns) and log closure amplitudes (right column) as a function of Greenwich Mean Sidereal Time (GMST) for all four observed nights from the HOPS data set. Plotted uncertainties denote $\pm 1\sigma$ ranges from thermal noise in the fully averaged data.

fringe solutions and measured correlation coefficients. These fringe validation tests reflect the internal validation of each pipeline, as opposed to the overall statistical validation and cross-comparisons presented in the following subsections. In addition to identifying issues with the fringe-fitting pipelines themselves, consistent review of data products throughout engineering data production played an important role in characterizing upstream issues with the data and their correlation.

Figures 15 and 16 show two fringe solution consistency tests that are run as part of an automated test suite at each stage of the HOPS pipeline (Section 5.1, with details in Blackburn et al. 2019). In Figure 16, as well as in subsequent plots of distributions, the number of 3σ outliers and the size of the tested sample for each source are provided. The dashed black curve indicates a standard normal distribution with zero mean and unity variance.

The HOPS pipeline baseline-based fringe solutions (prior to the global enforcement of fringe closure) show smooth evolution across each observing night and consistency across four polarization products, which are independently fit. Delay calibration assumes a constant RCP versus LCP delay offset per night at each station, which is verified by the stability of RR−LL delays to within thermal measurement error. Independently measured delay-rates between polarizations are also consistent to within thermal error. The lack of large-deviation outliers in these fringe solution consistency tests is a strong indication that there are no false fringes or corrupted measurements above the detection threshold.

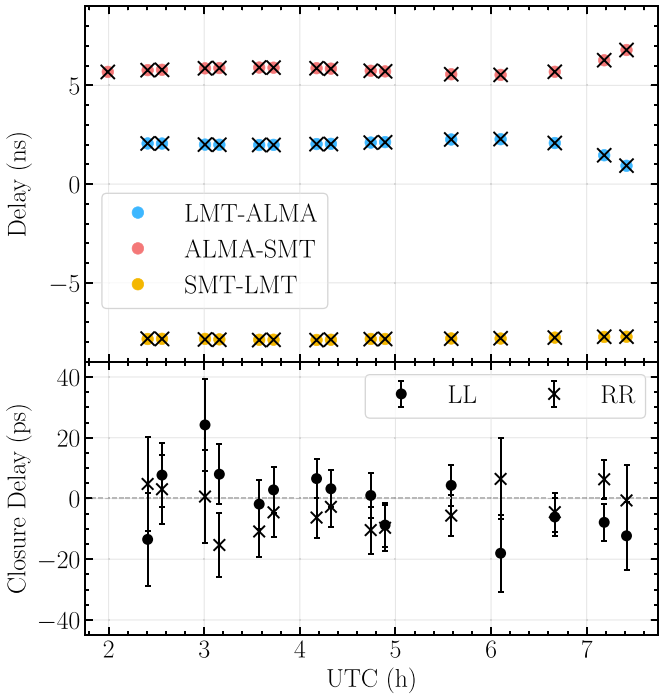

Figure 15. Measured residual relative delays for selected M87 baselines on April 11, reported by the HOPS pipeline (Section 5.1) prior to explicit fringe closure. The top panel shows smooth delay trends over the night for both parallel hands, LL (dots) and RR (crosses). The bottom panel shows the sum of the delays on this closed triangle, which is consistent with the expected value of zero to within statistical errors. After fringe closure, RR and LL are set to the same delay, and closure delay is zero by construction.

8.2. Thermal Error Consistency

Thermal error plays an essential role in the VLBI uncertainties, both for the visibilities as well as for the derivative closure quantities, for which uncertainties are simply propagated from the visibility errors (Section 7.2). An accurate accounting of thermal noise is essential for deriving faithful model-fitting uncertainties, and for correct noise debiasing in the case of incoherently averaged amplitudes (Rogers et al. 1995). Fundamentally, thermal uncertainty $\sigma_{\rm th}$ in the real and imaginary

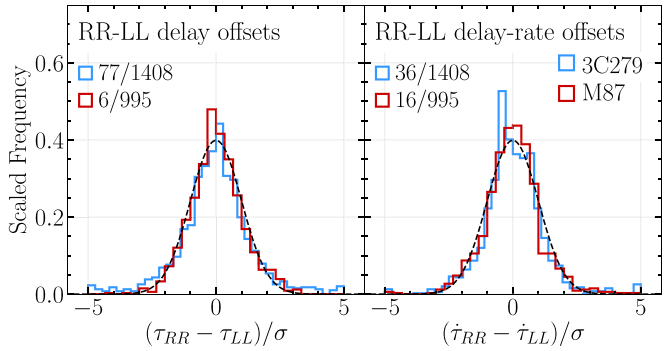

Figure 16. Delay and delay-rate differences between RR and LL parallel-hand fringe detections (S/N > 7) from the HOPS pipeline in units of thermal measurement uncertainty, along with the fraction of 3σ outliers. A small amount of systematic error is added in quadrature to delay (1 ps) and delay-rate (0.1 fs/s). The RR−LL differences are formed before fringe closure (after which they are zero by construction). These small differences demonstrate that there are no false fringes and that the relative difference between RCP and LCP feeds is stable at each site. Combined errors $\sigma^2 = \sigma_{\rm RR}^2 + \sigma_{\rm LL}^2$ are used.

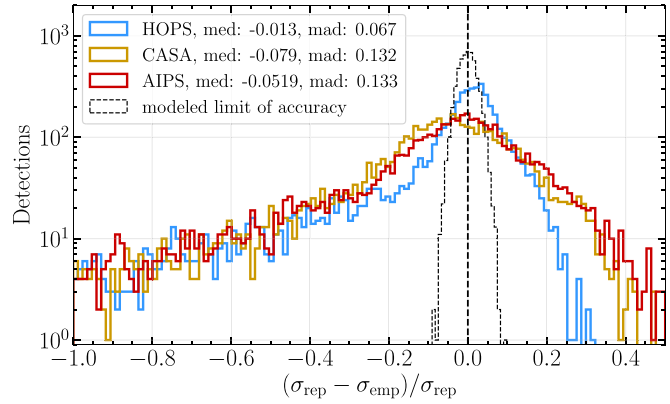

Figure 17. Joint M87 and 3C 279 histograms of differences between reported thermal uncertainties $\sigma_{\rm rep}$, and empirically estimated uncertainties $\sigma_{\rm emp}$. The dashed black histogram shows the limiting accuracy (high S/N, zero variance of $\sigma_{\rm rep}$) of the empirical estimator from the finite number of 0.4 s measurements available per scan. Median (med) and median absolute deviation (mad) of each distribution are given.

components of the dimensionless complex correlation coefficient r_{ij} (Equation (1)) can be estimated from first principles. Under the assumption of a stationary white noise process at each antenna

$$\sigma_{\rm th} = \frac{1}{\eta_Q \sqrt{2\,\Delta t\,\Delta\nu}}, \tag{21}$$

where Δt is the integration time, $\Delta\nu$ is the averaged bandwidth, and η_Q is the factor that accounts for quantization efficiency. The thermal uncertainties reported by each pipeline depend on the self-consistent tracking of scale factors through data conversion and calibration, as well as accounting for the data weights and bandpass response over the averaging windows in Equation (21).

The UVFITS file format formally associates a weight w for each visibility measurement, with associated reported uncertainty $\sigma_{\rm rep} \equiv 1/\sqrt{w}$. In the ideal case, $\sigma_{\rm rep}$ properly represents thermal uncertainties, $\sigma_{\rm rep} = \sigma_{\rm th}$. For the HOPS and CASA pipelines, the thermal uncertainty is determined from first principles. However, the weights for the AIPS pipeline require a large scaling factor to be applied for their final output to ensure that $\sigma_{\rm rep} = \sigma_{\rm th}$.[118] We derive this correction factor using the scatter from differences in adjacent high-S/N closure phases. For CASA, the direct interpretation of reported weights as $1/\sigma_{\rm th}^2$ also leads to a small bias, resulting in underestimation of $\sigma_{\rm th}$ by approximately 5%, as estimated by the closure phase-differencing technique.

We test the scan-by-scan accuracy of $\sigma_{\rm rep}$ via a comparison with an empirical estimator $\sigma_{\rm emp}$, fitting the moments of visibility amplitudes distribution. We estimate $\sigma_{\rm emp}$ for each scan, baseline, band, and polarization combination, by using moment matching of the visibility amplitude distribution over the scan duration (Wielgus et al. 2019). Each ensemble is composed of, on average, 900 individual visibility amplitude measurements. Figure 17 shows distributions of $(\sigma_{\rm rep} - \sigma_{\rm emp})/\sigma_{\rm rep}$ for all three SR1 processing pipelines, using the 5399 ensembles shared by the pipelines. The median of each distribution (med) is given in the legend of Figure 17, and shows ensemble values that are roughly consistent with the alternative closure phase differencing test. The distributions have large tails at negative values, where the empirical uncertainty exceeds the reported uncertainty. These tails are predominantly from high S/N scans with significant true intra-scan amplitude gain variation, which inflates $\sigma_{\rm emp}$ and biases the median slightly downward. The amplitude distribution test provides a scan-by-scan estimate of the thermal error and is most reliable at low S/N; while the closure phase differencing test is appropriate at high S/N, longer integrations, and under the assumption of a constant scaling factor for $\sigma_{\rm rep}/\sigma_{\rm emp}$. The median absolute deviation (mad) is given as a measure of the associated uncertainties on $\sigma_{\rm rep}$, and is fundamentally limited by the finite sample size of the estimator. From these metrics, the HOPS data set provides the most accurate accounting of thermal uncertainty.

8.3. Temporal Coherence after Calibration

All three data pipelines correct for changing visibility phase over scans, both in the correction for a linear drift via the delay-rate and in corrections for stochastic, station-dependent wander from atmospheric contributions (see Section 5). Although these corrections do not provide absolutely calibrated visibility phase, they eliminate differential wander on short timescales, allowing the visibilities to be coherently averaged for longer intervals than the atmospheric coherence time. An imperfect phase correction will lead to decoherence in the averages, which, in severe cases, may introduce non-closing amplitude errors.

To evaluate the performance of the phase correction algorithms, we compute two quantities for each scan: the amplitude $A_{\rm scan}$ resulting from coherent averaging visibilities over the full scan (3–7 minutes) and subsequent debiasing (Equation (19)), and the amplitude $A_{2\rm s}$ obtained from 2 s coherently averaged visibility segments that were subsequently incoherently averaged over the full scan (Rogers et al. 1995; Johnson et al. 2015). The ratio $A_{\rm scan}/A_{2\rm s}$ then quantifies the loss in amplitude from uncorrected phase fluctuations within scans.

Figure 18 shows cumulative histograms of $A_{\rm scan}/A_{2\rm s}$ for a common subset of 4688 ensembles (subsets of unique scan, baseline, band, and polarization) shared between pipelines, with an S/N > 7 threshold. While small errors in the estimated thermal noise have little effect on the S/N of coherent averages, they can significantly affect the outcome of incoherent averaging. Thus, only for this particular test, we applied a fixed correction factor of 1.05 to CASA thermal noise

[118] See AIPS Memo 103; http://www.aips.nrao.edu/aipsmemo.html.

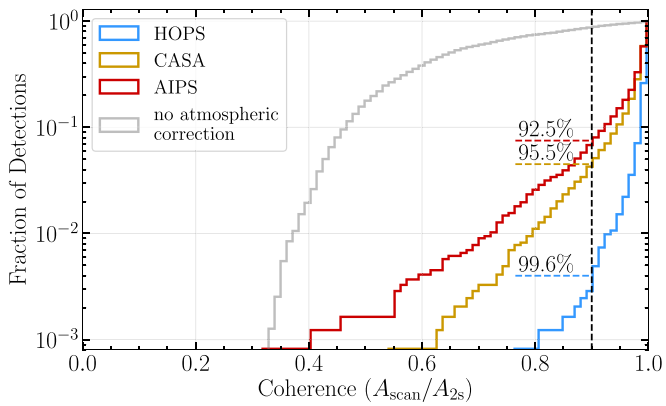

Figure 18. Joint M87 and 3C 279 cumulative histograms of amplitude ratios between coherent averaging for entire scans ($A_{\rm scan}$), and coherent averaging for 2 s before incoherent averaging over scans ($A_{2\,\rm s}$). The gray histogram shows the results from the HOPS pipeline with no atmospheric phase correction applied. For each pipeline, the fraction of data with coherence above 90% is indicated.

estimates $\sigma_{\rm rep}$ before incoherent averaging, to account for the small bias in this pipeline discussed in Section 8.2. For all three pipelines, the coherence of the phase-corrected data is significantly better than that of data with no atmospheric phase correction (the gray curve in Figure 18; see also Figure 2 of Paper II), with over 90% of the calibrated data experiencing an amplitude loss of under 10%. These results demonstrate that coherent averaging over scans is admissible for the SR1 data set, particularly in case of the HOPS data products.

8.4. Intra-pipeline Validation

In this subsection we perform internal data consistency tests for each pipeline, in order to estimate the magnitude of systematic non-closing errors, e.g., related to the uncalibrated polarimetric leakage. For that purpose, we inspect closure phases and log closure amplitudes derived from the SR1 data set and evaluate consistency between (1) RR and LL components, (2) low- and high-frequency bands, and (3) trivial closure quantities. For each test, we derive a magnitude of residual errors, in excess to the reported thermal uncertainties. These values are then used to characterize the magnitude of non-closing errors in the data set, utilized in the downstream analysis.

8.4.1. Quantifying Residual Errors

We evaluate the characteristic magnitude of systematic errors in the SR1 data set based on tests of distributions of closure quantities. In this approach we rely on the following modified median absolute deviation statistic:

$$\mathrm{mad}_0(Y) = 1.4826\ \mathrm{med}(|Y|), \tag{22}$$

where "med" denotes median, the subscript zero indicates that the raw distribution moment is estimated, and the normalization factor of 1.4826 scales the result so that it acts as a robust estimator of standard deviation for a normally distributed random variable Y with zero mean. We assume total uncertainties σ associated with closure quantities to be well approximated by

$$\sigma^2 = \sigma_{\rm th}^2 + s^2, \tag{23}$$

such that the total uncertainty consists of the known a priori thermal component $\sigma_{\rm th}$ and a constant systematic non-closing error s, of unknown magnitude, added in quadrature. We then solve for the characteristic value of s that enforces

$$\mathrm{mad}_0\left(\frac{X}{\sigma}\right) = \mathrm{mad}_0\left(\frac{X}{\sqrt{\sigma_{\rm th}^2 + s^2}}\right) = 1, \tag{24}$$

where σ is the total uncertainty associated with X. As an example, for RR–LL consistency of closure phases we have

$$\begin{aligned} X &= \psi_{\rm C,RR} - \psi_{\rm C,LL}, \\ \sigma^2 &= \sigma^2_{\psi_{\rm C},\rm RR} + \sigma^2_{\psi_{\rm C},\rm LL} + s^2. \end{aligned} \tag{25}$$

We exclude low S/N data (S/N < 7), for which the normal distribution approximation does not hold well.

8.4.2. RR–LL Consistency

Consistency of closure quantities derived from RR and LL visibilities, matched for the same scan, baseline, and band, are expected to be dominated by effects related to polarimetric leakage, which remains uncalibrated in SR1 data. Assuming that some amount of leaked polarized signal mixes randomly into the parallel-hand visibilities, the degree of systematic error can be crudely approximated as

$$\delta_{\rm leak} \approx \sqrt{2n}\ |D||\breve{m}| < 0.14\sqrt{n}\ |\breve{m}|, \tag{26}$$

where the number of baselines n is 3 for closure phases and 4 for closure amplitudes, $|D| < 0.1$ is a leakage D-term magnitude, and $|\breve{m}|$ is a typical fractional interferometric baseline polarization (i.e., fractional linearly polarized correlated flux density relative to total intensity); see Johnson et al. (2015). If a characteristic $|\breve{m}| < 0.2$ is assumed, these upper bounds translate under Equation (26) to $<2\overset{\circ}{.}8$ for the closure phase systematic uncertainty and $<5.7\%$ for the closure amplitude uncertainty. The results of the SR1 errors estimation by normalizing mad_0 are summarized in Table 7. The estimated errors are consistent with the simple upper limit given by Equation (26) and roughly consistent between all data reduction pipelines. While for the high S/N source 3C 279 the leakage related errors may dominate over the thermal errors, they remain strongly subthermal for M87.

8.4.3. Frequency Bands Consistency

Comparisons between low-/high-frequency bands may reveal the presence of band-specific systematics, including frequency-dependent polarimetric leakage. Apart from those, source spatial structure and spectral index both may add a small contribution. The estimated magnitudes of systematic errors found for closure phases and log closure amplitudes are given in Table 7. For all pipelines, the magnitude of characteristic closure phase inconsistency was found to be about 0.5 times the thermal uncertainty for M87 and about 1.5 times the thermal uncertainty for 3C 279 (scan-average, single-band/polarization). For 3C 279 systematic uncertainties strongly dominate over the thermal scatter, and this should be taken into account before the direct averaging of frequency bands.

Table 7
Systematic Errors in SR1 Data Set

Test	M87			3C 279		
	HOPS	CASA	AIPS	HOPS	CASA	AIPS
RR−LL closure phases (deg)	<1.0(0.2)	<1.0(0.2)	<1.0(0.2)	1.9(1.1)	1.9(1.1)	2.1(1.2)
RR−LL log closure amplitudes (%)	<2.0(0.2)	<3.0(0.3)	<2.0(0.2)	3.1(1.0)	3.6(1.2)	3.3(1.0)
Stokes *I* closure phase low/high (deg)	1.4(0.4)	2.5(0.6)	2.6(0.6)	2.2(1.5)	2.3(1.5)	2.0(1.3)
Stokes *I* log closure amplitude low/high (%)	5.6(0.8)	⋯	<10.0(1.3)	4.5(1.8)	5.4(2.3)	4.8(1.8)
Stokes *I* trivial closure phases (deg)	3.7(1.1)	2.6(0.8)	3.2(1.0)	1.2(1.9)	1.0(1.5)	1.0(1.4)
Stokes *I* trivial log closure amplitudes (%)	3.6(0.4)	5.6(0.7)	7.7(0.9)	3.8(2.0)	3.8(1.9)	3.3(1.6)

Note. Characteristic magnitudes of systematic errors, estimated using the subset of data shared by all three pipelines. Scan-averaged single-band data. Numbers in parentheses represent characteristic systematic errors in units of thermal noise.

8.4.4. Trivial Closure Quantities

The intra-site baselines ALMA–APEX and JCMT–SMA provide the EHT array with multiple "trivial" closure triangles and quadrangles. Ideally, these trivial closure phases and trivial log closure amplitudes should be equal to zero, but this is not precisely true in the presence of polarimetric leakage. Furthermore, the small but finite length of intra-site baselines leads to measurements that are susceptible to contamination from large-scale structure, breaking the assumptions of a trivial closure quantity. This particular aspect is a concern for M87 and its large-scale jet. The estimated characteristic magnitude of systematic errors in trivial closure phases is given in Table 7. While for 3C 279 the magnitude of about 1° can be fully explained by polarimetric leakage, M87 systematics are inconsistent with limits given by Equation (26), suggesting the presence of an additional source of error. We illustrate the systematic-error fitting procedure in Figure 19, in which 3C 279 trivial closure phase distribution is shown, before and after adding the systematics, and is estimated to be about 1° consistently for all processing pipelines.

8.4.5. Systematic Error Budget

Based on values reported in Table 7, we conclude that, for a single band, systematic errors of 3C 279 measurements are dominated by polarimetric leakage and its contribution can be approximated with characteristic values of about 1°.5 for closure phases and 0.03 for log closure amplitudes. For M87, leakage is not nearly as important, and other subtle effects like polarimetric calibration uncertainties may influence the total systematic error budget. Suggested systematics are 2° for closure phases and 0.04 for log closure amplitudes. For each test of closure phases and log closure amplitudes summarized in Table 7, we show related distributions in Figure 20. Errors in Figure 20 were inflated according to the above recommendation for systematic errors. A standard (zero mean, unit variance) normal distribution is shown with a dashed line. The match between the empirical distributions and the normal distribution indicates that the addition of the systematic uncertainties allows for the approximate capture of the total data uncertainty. Under the assumption of independent baseline errors, the closure uncertainties given in this section can be translated to 2% non-closing systematic uncertainties in visibility amplitudes and 1° of non-closing systematic uncertainties in visibility phases.

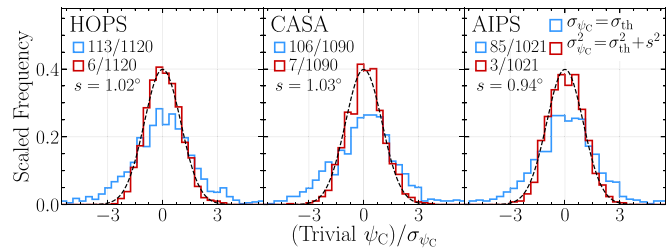

Figure 19. Normalized distributions of trivial closure phases for 3C 279 in three data reduction pipelines, before (blue) and after (red) accounting for the residual systematic uncertainties. Numbers indicate the fraction of 3σ outliers.

8.5. Inter-pipeline Consistency

Direct comparisons between corresponding data products delivered by separate pipelines allow us to quantify the degree of confidence that we may have in their properties and their dependence on specific choices in calibration procedure. Figure 21 (top) shows the distribution of visibility amplitude differences betwen the reduction pipelines, in units of their thermal uncertainty. Thermal errors represent a particular scale of interest; however, visibilities reduced by separate pipelines are not independent variables and share the same thermal noise realization. Another useful quantity is the relative absolute amplitude difference. As indicated in Table 8, the median relative difference between the most consistent pair of pipelines, HOPS–CASA, is 3.8%, well within the budget of a priori flux density calibration (Section 6). While for 3C 279 all three pairs represent a similar level of consistency, for M87 the HOPS–CASA pair is by far the most consistent one, as indicated in Table 8. This result is consistent with known difficulties in the processing of low S/N data with the AIPS pipeline, originating from the lack of S/N to constrain a fringe solution in the two-second intervals used for fringe fitting (Section 5.3). Distributions of differences between amplitude data products are unbiased; however, significant tails are present, with 10% of the M87 visibility amplitude data inconsistent by more than 22.8% for the most consistent pair, HOPS–CASA.

In Figure 22 we show HOPS–CASA and HOPS–AIPS scatter plots of correlation coefficient amplitude $|r_{ij}|$. The three pipelines demonstrate increasing levels of consistency at high S/N. AIPS shows a tendency to occasionally overestimate amplitude at low S/N, sometimes by a large factor, indicating a degree of over-tuning and acceptance of possible false fringes.

Contrary to visibility amplitudes, the distributions of closure phase and closure amplitude differences, shown in Figure 21, generally exhibit a spread at or below the level of thermal

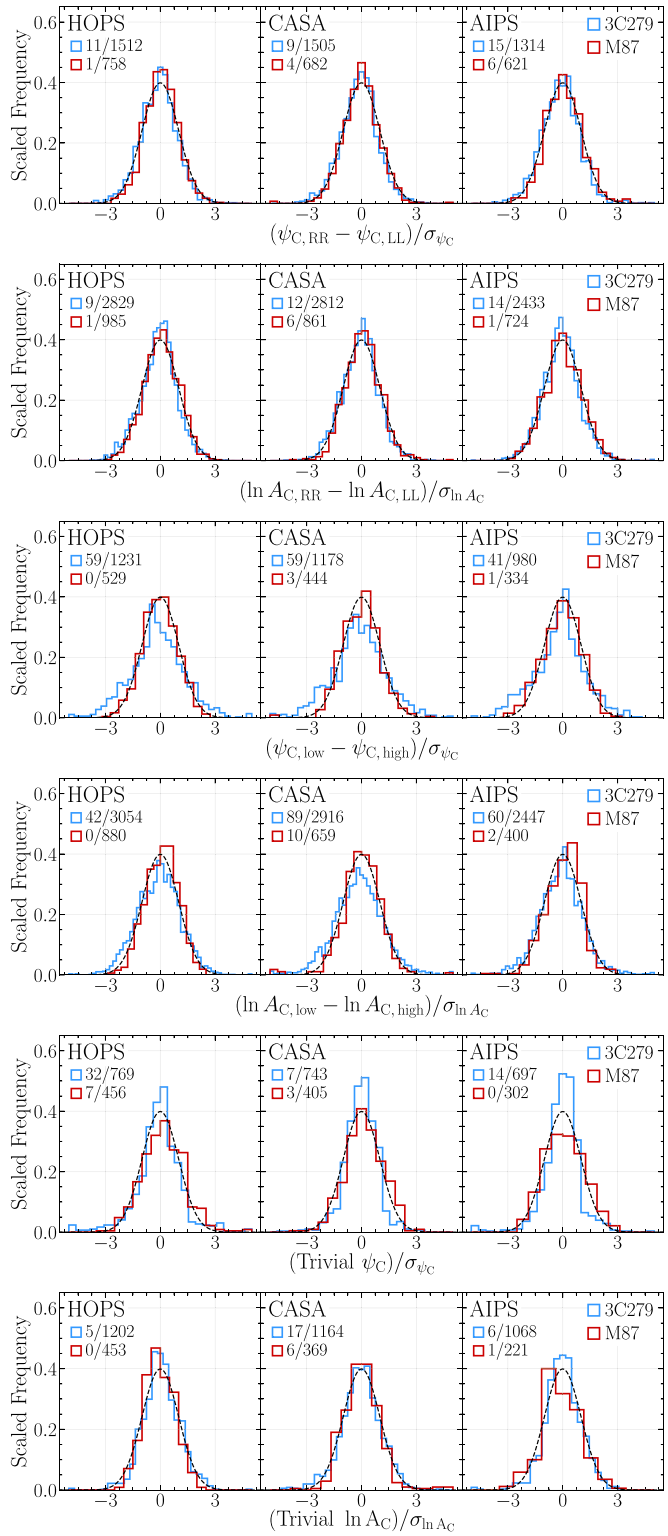

Figure 20. Closure statistics distributions after inflating errors by the amount of non-closing systematics recommended in Section 8.4.5. The plots follow the same order as the tests reported in Table 7. The dashed lines represent a standard normal distribution, and numbers show the fraction of 3σ outliers. Combined errors are used where appropriate.

uncertainty, particularly for the HOPS–CASA pair. No significant tails are present and 90% of the M87 data remain consistent to within 0.9 standard deviations of the combined thermal error budget for HOPS–CASA (Table 8). This

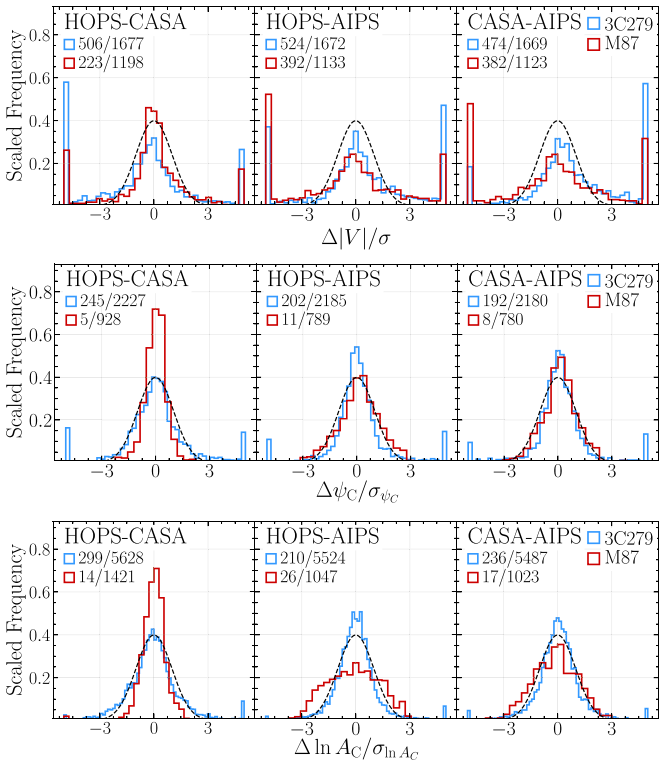

Figure 21. Consistency of visibility amplitudes (top), closure phases (middle), and log closure amplitudes (bottom) between the three reduction pipelines. Scan-averaged single-band Stokes I data are used.

highlights the robustness of the closure quantities, independent of station-based gains.

Examples of closure phases for all three pipelines, for some of the triangles discussed in Section 7, are shown in Figure 23. While there is a broad consistency, HOPS is unique in reconstructing well-behaved closure phases on triangles including the LMT–SMA baseline over the full range of observations on April 11. To corroborate smooth trends and large closure phase evolution for these data, in two panels in Figure 23 we show data from a redundant JCMT triangle (JCMT and SMA are collocated). The redundant JCMT triangles show closure phases consistent with their SMA counterparts, and are more consistently reconstructed across the pipelines.

A bias toward zero closure phase can be seen when data are averaged in time, particularly for the AIPS data set. This is due to use of a point-source model during global fringe fitting on short time intervals (2 s for AIPS). While the individual fringe solution phases are station-based and separately close, the process biases baseline phases to zero, and closure phases generated from baseline phases averaged over multiple segments will be biased toward the point-source model. This bias is not expected in HOPS products, as HOPS fringe solutions are baseline-based and assume no structure phase for the coherent stacking of data from multiple baselines. The median bias toward zero closure phase, estimated from high S/N data at least 3σ away from zero, is about 1° for AIPS and CASA with respect to unbiased HOPS. However, while 90% of CASA data are biased by less than $4^\circ.9$, 10% of AIPS data are biased by more than $8^\circ.7$. See Wielgus et al. (2019) for an additional discussion of pipeline comparisons and associated systematics.

Table 8
Inter-pipeline Consistency of the SR1 Data Set

	M87			3C 279		
	HOPS-CASA	HOPS-AIPS	CASA-AIPS	HOPS-CASA	HOPS-AIPS	CASA-AIPS
Median visibility error (%)	3.8(0.7)	7.9(1.5)	9.4(1.5)	1.1(1.2)	1.2(1.3)	1.2(1.2)
90th percentile visibility error (%)	22.8(6.0)	52.9(7.4)	58.3(9.5)	5.7(9.2)	6.7(10.0)	7.2(8.8)
Median closure phase error (deg)	3.1(0.3)	6.8(0.7)	6.2(0.6)	1.4(0.7)	1.0(0.5)	1.0(0.6)
90th percentile closure phase error (deg)	17.7(0.9)	39.4(1.9)	36.5(1.7)	6.4(3.1)	6.0(2.5)	5.8(2.5)
Median log closure amplitude error	0.1(0.3)	0.3(0.9)	0.3(0.7)	0.04(0.7)	0.03(0.6)	0.03(0.6)
90th percentile log closure amplitude error	0.5(1.0)	1.4(2.4)	1.2(2.2)	0.15(2.3)	0.13(1.7)	0.13(1.9)

Note. Results given for scan-averaged single-band Stokes I data. Numbers in parentheses are given in thermal error units. The subset of data shared by all pipelines was used.

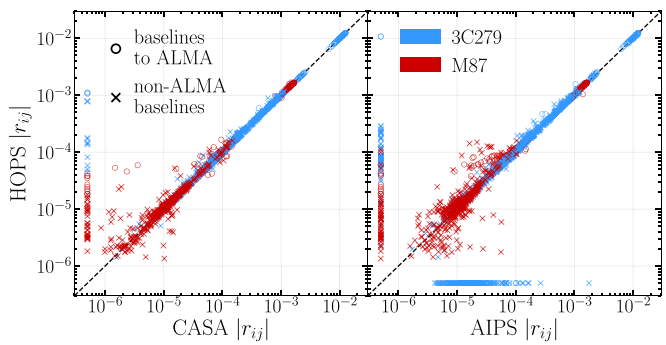

Figure 22. Scatter plots of complex correlation coefficient amplitudes for HOPS–CASA and HOPS–AIPS pairs of pipelines. Data are fully averaged, with an $S/N > 1$ threshold applied. For each detection, the mean r_{ij} of available RCP and LCP components in the low and high band is given. Detections only present in one of the pipelines are shown with a fixed value of 5×10^{-7} for the missing pipeline, and in some cases represent differences in the construction of a priori flags and fringe rejection strategies.

The HOPS pipeline benefited from a long period of development, extensive review, and internal validation through the suite of five engineering releases spanning a year-long data processing and calibration effort. In contrast, the AIPS pipeline has been used in two data releases as a secondary data set and the CASA pipeline, which is under active development, has recently been brought to maturity and included in ER5. Nonetheless, inter-pipeline comparisons of HOPS, CASA, and AIPS show a high degree of general consistency. The HOPS pipeline product was chosen as the primary scientific data set for SR1, based on the long validation history, level of calibration quality presented in this section, and to select a single data set for the preparation of scientific results. The other two pipelines are included in SR1 as supporting data sets for calibration, direct data comparisons, and as an independent pathway for validating the products of downstream analysis.

9. Conclusions

Observations from the EHT's 2017 April campaign are the first ever to have the necessary sensitivity, coverage, and resolution for horizon-scale imaging of black hole candidates M87 and Sgr A*. We have presented the complete data processing pathway that led to the first science release data set from the campaign, which includes the primary science target M87 and the secondary target 3C 279. The 2017 observations reflected a dramatic expansion of the EHT from previous years to a total of eight sites, and include for the first time ALMA as a phased array. While much more powerful, the expanded network represented a unique analysis challenge in terms of the heterogeneous nature of the array: basic telescope characteristics, weather, sensitivity, site-specific data issues, sampling rate, and channelization; and a challenge in terms of raw data volume and the needs for a homogeneous and systematized calibration strategy.

The development of processing pipelines and characterization of the data occurred over a series of five internal engineering releases, during which site-specific data issues were identified and mitigated in correlation and post-processing. SR1 is the first science release of calibrated data products arising from the mature reduction pipelines, following a series of independent internal reviews. The science data were produced without making assumptions about the detailed compact structure of the targets, and thus provide an unbiased data set for downstream imaging and modeling.

We have developed three independent processing pipelines for the initial fringe detection, phase calibration, and reduction of EHT data. The pipelines used HOPS, which has been continually developed and used for early EHT analysis over the previous decade; AIPS, the standard calibration environment for VLBI data from major facilities such as the VLBA; and CASA, a modern environment for radio interferometer calibration and analysis that has recently been augmented with VLBI capabilities. The output from each pipeline was subjected to a suite of validation tests covering self-consistency over bands and polarizations, and consistency of trivial closure quantities.

From these tests, we estimated the residual non-closing systematic errors after calibration. For M87 such errors remain smaller than Stokes I data thermal uncertainties even after full scan and frequency band averaging. Non-closing errors are no larger than 2° for closure phases and 4% for closure amplitudes. For 3C 279, systematics are small in an absolute sense, but they dominate the total uncertainties of the averaged data set due to the high S/N. Differences between pipelines, particularly for the robust closure quantities, were found to be largely within the total budget of uncertainties. The HOPS data were selected as the primary data set for the scientific conclusions presented in companion Letters (Papers I, IV, V, VI) with the remaining two data sets available for direct data comparisons and the cross-validation of downstream analysis.

At EHT frequencies, absolute flux density calibration is particularly challenging due to the large and time-varying 1.3 mm opacity from atmospheric water vapor, and difficulties maintaining pointing and surface accuracy particularly at the

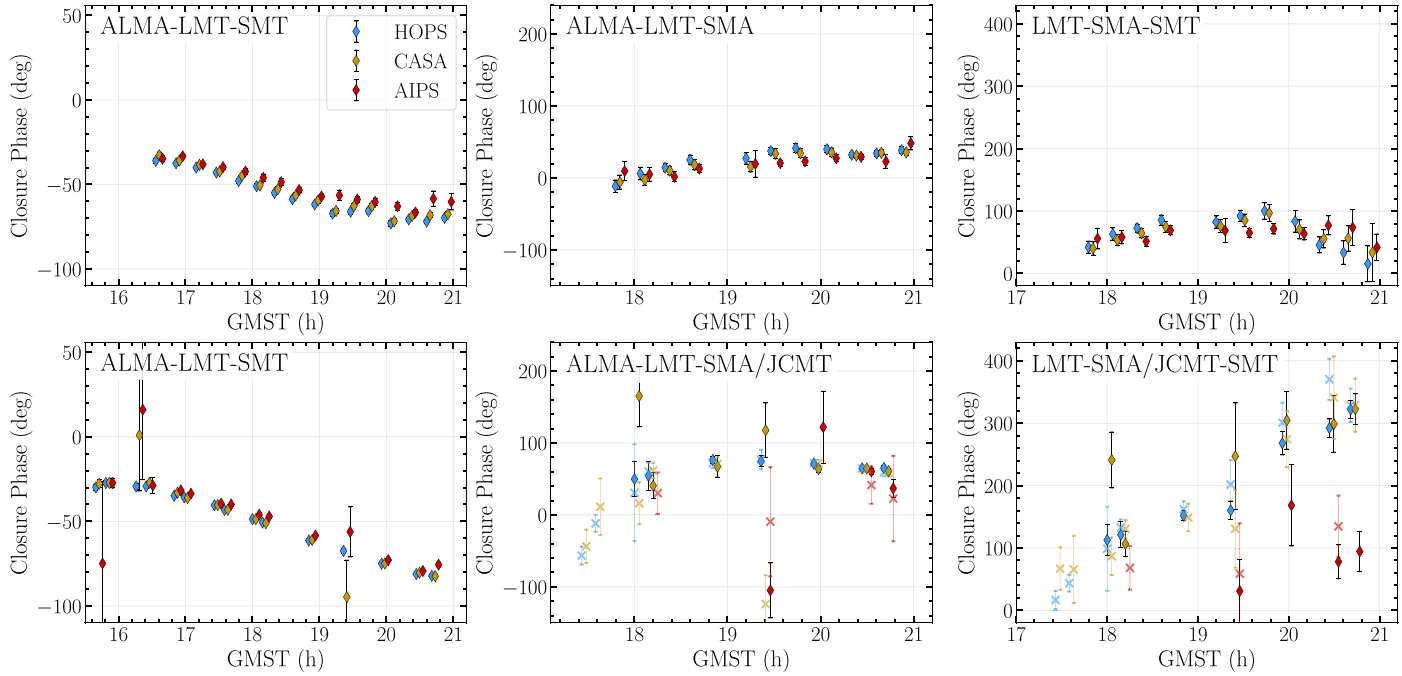

Figure 23. Comparison of M87 closure phases between the three fringe-fitting pipelines for selected triangles. April 6 is shown in the top row, April 11 in the bottom row. The pipelines are offset slightly in time for clarity (HOPS −3 minutes, CASA at the original timestamp, AIPS +3 minutes). Plotted uncertainties denote $\pm 1\sigma$ ranges from thermal noise in the fully averaged data set. For the two Hawai'i triangles that demonstrate pronounced evolution on April 11 (see also Figure 14, bottom panels), we also include the corresponding redundant triangles with JCMT (which joined the array two scans earlier) as light crosses.

larger dishes. We have outlined the gathering and unified interpretation of auxiliary calibration data from the various sites for the purposes of a priori flux density calibration, and a strategy for estimating the residual flux density error budget within the limitations of single-dish calibration. Where available, we have made use of network redundancy to further constrain flux density calibration given generic model-independent assumptions about the source.

A number of salient features became apparent in the M87 data set after processing and calibration. The visibility amplitudes as a function of projected baseline length persistently show a prominent secondary peak bracketed by two nulls, the first at $\sim$3.4 Gλ and the second at $\sim$8.3 Gλ, across all four observed days. The visibility amplitudes exhibit characteristics of a compact source with a spatial scale $\lesssim$50 μas, and broad circular symmetry broken on baselines probing the first null. This spatial scale corresponds to only a few Schwarzschild radii for a $\sim 6.5 \times 10^9\, M_\odot$ black hole (Paper VI) at the distance of M87 (Blakeslee et al. 2009; Gebhardt et al. 2011; Cantiello et al. 2018). M87 closure phases on select triangles show clear time evolution between the two pairs of days, April 5/6 and April 10/11, providing evidence for intrinsic evolution of the source. The triangles with the largest closure phase variations between the two pairs of days have a baseline probing the (u, v) plane region about the first minimum in visibility amplitude. Analysis and interpretation of these features are presented in companion Letters (Paper I, IV, V, VI).

Although previous observations of M87 from early EHT campaigns (in 2009 and 2012) probed scales of a few tens of microarcseconds, the visibility amplitude behavior on the few baselines present remained consistent with a Gaussian source, showing no apparent finer structure (Doeleman et al. 2012; Akiyama et al. 2015). The first M87 closure phases at 1.3 mm reported in Akiyama et al. (2015) were consistent with zero to within $2\,\sigma$. In addition to a first reported measurement of 1.3 mm closure amplitudes, the 2017 observations of M87 are the first to show non-Gaussian structure in the compact source and significantly non-zero closure phases.

The SR1 data provide the first opportunity for total intensity imaging of M87 (Paper IV). Efforts to characterize and remove polarization leakage are ongoing and will enable studies of the linear polarization structure of M87 and other EHT targets. Additional work to better calibrate in the presence of intrinsic source variability, as well as increased amplitude gain variability, is necessary for Sgr A* and other low-elevation targets.

For 2018, the EHT was joined by the Greenland Telescope, greatly expanding the coverage for northern sources such as M87. In the near future, the array will also be joined by the Kitt Peak 12 m telescope in Arizona and the Northern Extended Millimeter Array (NOEMA) at the Plateau de Bure observatory in France. In addition to generally improved baseline coverage, both sites provide short baselines and associated redundancy (with SMT and PV, respectively) for the array—which is particularly beneficial for amplitude calibration. The EHT doubled recorded bandwidth to a rate of 64 Gbps in 2018 as well, over four 2 GHz bands. Additional development to enable coherent fringe fitting and atmospheric phase correction across all four bands will allow the EHT to better resolve features on long baselines, short timescales, and near visibility nulls, and it will increase robustness of the array against poor weather and the potential loss of sensitive central anchor stations.

While continuous development of the instrument and the data reduction pipeline will yield future observations with improved (u, v) coverage, higher S/N, and sharper resolution, the observations carried out in 2017 already deliver data of unprecedented scientific quality. The dramatic difference between the 2017 observations and early EHT campaigns in number of participating stations, S/N, coverage, and weather

conditions make the EHT 2017 data set an exceptional opportunity for scientific discoveries via, e.g., imaging and model fitting well beyond previous EHT capabilities.

The authors of this Letter thank the following organizations and programs: the Academy of Finland (projects 274477, 284495, 312496); the Advanced European Network of E-infrastructures for Astronomy with the SKA (AENEAS) project, supported by the European Commission Framework Programme Horizon 2020 Research and Innovation action under grant agreement 731016; the Alexander von Humboldt Stiftung; the Black Hole Initiative at Harvard University, through a grant (60477) from the John Templeton Foundation; the China Scholarship Council; Comisión Nacional de Investigación Científica y Tecnológica (CONICYT, Chile, via PIA ACT172033, Fondecyt 1171506, BASAL AFB-170002, ALMA-conicyt 31140007); Consejo Nacional de Ciencia y Tecnología (CONACYT, Mexico, projects 104497, 275201, 279006, 281692); the Delaney Family via the Delaney Family John A. Wheeler Chair at Perimeter Institute; Dirección General de Asuntos del Personal Académico—Universidad Nacional Autónoma de México (DGAPA—UNAM, project IN112417); the European Research Council Synergy Grant "BlackHoleCam: Imaging the Event Horizon of Black Holes" (grant 610058); the Generalitat Valenciana postdoctoral grant APOSTD/2018/177; the Gordon and Betty Moore Foundation (grants GBMF-3561, GBMF-5278); the Istituto Nazionale di Fisica Nucleare (INFN) sezione di Napoli, iniziative specifiche TEONGRAV; the International Max Planck Research School for Astronomy and Astrophysics at the Universities of Bonn and Cologne; the Jansky Fellowship program of the National Radio Astronomy Observatory (NRAO); the Japanese Government (Monbukagakusho: MEXT) Scholarship; the Japan Society for the Promotion of Science (JSPS) Grant-in-Aid for JSPS Research Fellowship (JP17J08829); JSPS Overseas Research Fellowships; the Key Research Program of Frontier Sciences, Chinese Academy of Sciences (CAS, grants QYZDJ-SSW-SLH057, QYZDJ-SSW-SYS008); the Leverhulme Trust Early Career Research Fellowship; the Max-Planck-Gesellschaft (MPG); the Max Planck Partner Group of the MPG and the CAS; the MEXT/JSPS KAKENHI (grants 18KK0090, JP18K13594, JP18K03656, JP18H03721, 18K03709, 18H01245, 25120007); the MIT International Science and Technology Initiatives (MISTI) Funds; the Ministry of Science and Technology (MOST) of Taiwan (105-2112-M-001-025-MY3, 106-2112-M-001-011, 106-2119-M-001-027, 107-2119-M-001-017, 107-2119-M-001-020, and 107-2119-M-110-005); the National Aeronautics and Space Administration (NASA, Fermi Guest Investigator grant 80NSSC17K0649); the National Institute of Natural Sciences (NINS) of Japan; the National Key Research and Development Program of China (grant 2016YFA0400704, 2016YFA0400702); the National Science Foundation (NSF, grants AST-0096454, AST-0352953, AST-0521233, AST-0705062, AST-0905844, AST-0922984, AST-1126433, AST-1140030, DGE-1144085, AST-1207704, AST-1207730, AST-1207752, MRI-1228509, OPP-1248097, AST-1310896, AST-1312651, AST-1337663, AST-1440254, AST-1555365, AST-1715061, AST-1614868, AST-1615796, AST-1716327, OISE-1743747, AST-1816420); the Natural Science Foundation of China (grants 11573051, 11633006, 11650110427, 10625314, 11721303, 11725312, 11873028, 11873073, U1531245, 11473010); the Natural Sciences and Engineering Research Council of Canada (NSERC, including a Discovery Grant and the NSERC Alexander Graham Bell Canada Graduate Scholarships-Doctoral Program); the National Youth Thousand Talents Program of China; the National Research Foundation of Korea (grant 2015-R1D1A1A01056807, the Global PhD Fellowship Grant: NRF-2015H1A2A1033752, and the Korea Research Fellowship Program: NRF-2015H1D3A1066561); the Netherlands Organization for Scientific Research (NWO) VICI award (grant 639.043.513) and Spinoza Prize SPI 78-409; the New Scientific Frontiers with Precision Radio Interferometry Fellowship awarded by the South African Radio Astronomy Observatory (SARAO), which is a facility of the National Research Foundation (NRF), an agency of the Department of Science and Technology (DST) of South Africa; the Onsala Space Observatory (OSO) national infrastructure, for the provisioning of its facilities/observational support (OSO receives funding through the Swedish Research Council under grant 2017-00648) the Perimeter Institute for Theoretical Physics (research at Perimeter Institute is supported by the Government of Canada through the Department of Innovation, Science and Economic Development Canada and by the Province of Ontario through the Ministry of Economic Development, Job Creation and Trade); the Russian Science Foundation (grant 17-12-01029); the Spanish Ministerio de Economía y Competitividad (grants AYA2015-63939-C2-1-P, AYA2016-80889-P); the State Agency for Research of the Spanish MCIU through the "Center of Excellence Severo Ochoa" award for the Instituto de Astrofísica de Andalucía (SEV-2017-0709); the Toray Science Foundation; the US Department of Energy (USDOE) through the Los Alamos National Laboratory (operated by Triad National Security, LLC, for the National Nuclear Security Administration of the USDOE (Contract 89233218CNA000001)); the Italian Ministero dell'Istruzione Università e Ricerca through the grant Progetti Premiali 2012-iALMA (CUP C52I13000140001); ALMA North America Development Fund; the European Union's Horizon 2020 research and innovation programme under grant agreement No 730562 RadioNet; Chandra TM6-17006X. This work used the Extreme Science and Engineering Discovery Environment (XSEDE), supported by NSF grant ACI-1548562, and CyVerse, supported by NSF grants DBI-0735191, DBI-1265383, and DBI-1743442. XSEDE Stampede2 resource at TACC was allocated through TG-AST170024 and TG-AST080026N. XSEDE JetStream resource at PTI and TACC was allocated through AST170028. The simulations were performed in part on the SuperMUC cluster at the LRZ in Garching, on the LOEWE cluster in CSC in Frankfurt, and on the HazelHen cluster at the HLRS in Stuttgart. This research was enabled in part by support provided by Compute Ontario (http://computeontario.ca), Calcul Quebec (http://www.calculquebec.ca) and Compute Canada (http://www.computecanada.ca). We wish to thank Eric W. Greisen for extending the capabilities of the AIPS software package, which made it possible to handle the wide-bandwidth EHT data. We acknowledge George Moellenbrock for his invaluable contribution to the CASA VLBI upgrade. We thank the staff at the participating observatories, correlation centers, and institutions for their enthusiastic support. This Letter makes use of the following ALMA data: ADS/JAO.ALMA#2016.1.01154.V. ALMA is a partnership of the European Southern Observatory (ESO; Europe, representing its member states), NSF, and National Institutes of Natural Sciences of Japan, together with National Research Council (Canada), Ministry of Science and

Technology (MOST; Taiwan), Academia Sinica Institute of Astronomy and Astrophysics (ASIAA; Taiwan), and Korea Astronomy and Space Science Institute (KASI; Republic of Korea), in cooperation with the Republic of Chile. The Joint ALMA Observatory is operated by ESO, Associated Universities, Inc. (AUI)/NRAO, and the National Astronomical Observatory of Japan (NAOJ). The NRAO is a facility of the NSF operated under cooperative agreement by AUI. APEX is a collaboration between the Max-Planck-Institut für Radioastronomie (Germany), ESO, and the Onsala Space Observatory (Sweden). The SMA is a joint project between the SAO and ASIAA and is funded by the Smithsonian Institution and the Academia Sinica. The JCMT is operated by the East Asian Observatory on behalf of the NAOJ, ASIAA, and KASI, as well as the Ministry of Finance of China, Chinese Academy of Sciences, and the National Key R&D Program (No. 2017YFA0402700) of China. Additional funding support for the JCMT is provided by the Science and Technologies Facility Council (UK) and participating universities in the UK and Canada. The LMT project is a joint effort of the Instituto Nacional de Astrófisica, Óptica, y Electrónica (Mexico) and the University of Massachusetts at Amherst (USA). The IRAM 30-m telescope on Pico Veleta, Spain is operated by IRAM and supported by CNRS (Centre National de la Recherche Scientifique, France), MPG (Max-Planck-Gesellschaft, Germany) and IGN (Instituto Geográfico Nacional, Spain). The SMT is operated by the Arizona Radio Observatory, a part of the Steward Observatory of the University of Arizona, with financial support of operations from the State of Arizona and financial support for instrumentation development from the NSF. Partial SPT support is provided by the NSF Physics Frontier Center award (PHY-0114422) to the Kavli Institute of Cosmological Physics at the University of Chicago (USA), the Kavli Foundation, and the GBMF (GBMF-947). The SPT hydrogen maser was provided on loan from the GLT, courtesy of ASIAA. The SPT is supported by the National Science Foundation through grant PLR-1248097. Partial support is also provided by the NSF Physics Frontier Center grant PHY-1125897 to the Kavli Institute of Cosmological Physics at the University of Chicago, the Kavli Foundation and the Gordon and Betty Moore Foundation grant GBMF 947. The EHTC has received generous donations of FPGA chips from Xilinx Inc., under the Xilinx University Program. The EHTC has benefited from technology shared under open-source license by the Collaboration for Astronomy Signal Processing and Electronics Research (CASPER). The EHT project is grateful to T4Science and Microsemi for their assistance with Hydrogen Masers. This research has made use of NASA's Astrophysics Data System. We gratefully acknowledge the support provided by the extended staff of the ALMA, both from the inception of the ALMA Phasing Project through the observational campaigns of 2017 and 2018. We would like to thank A. Deller and W. Brisken for EHT-specific support with the use of DiFX. We acknowledge the significance that Maunakea, where the SMA and JCMT EHT stations are located, has for the indigenous Hawaiian people.

Facilities: EHT, ALMA, APEX, IRAM:30 m, JCMT, LMT, SMA, ARO:SMT, SPT.

Software: DiFX (Deller et al. 2011), CALC, PolConvert (Martí-Vidal et al. 2016), HOPS (Whitney et al. 2004), CASA (McMullin et al. 2007), AIPS (Greisen 2003), ParselTongue (Kettenis et al. 2006), GNU Parallel (Tange 2011), GILDAS, eht-imaging (Chael et al. 2016, 2018), Numpy (van der Walt et al. 2011), Scipy (Jones et al. 2001), Pandas (McKinney 2010), Astropy (The Astropy Collaboration et al. 2013, 2018), Jupyter (Kluyver et al. 2016), Matplotlib (Hunter 2007).

Appendix
Site and Data Issues

A.1. Issues Requiring Mitigation

The JCMT and SMA are located within hundreds of meters of each other on Maunakea. The small natural fringe rate is insufficient to wash out unwanted signals on the JCMT–SMA baselines (to phased and single-dish SMA). The JCMT and the SMA used identical frequency setups in 2017, resulting in two types of spurious correlations. For correlations between JCMT and the SMA single-dish reference antenna (not used directly for science analysis), two narrowband terrestrial signals required special handling: one from the 1024 MHz spur tone of the R2DBEs, and a second one from the YIG oscillator tone (which is part of the LO chain) locally generated at the SMA. These signals were mitigated by flagging the affected frequency channels in post-processing.

Broadband celestial signals in the lower sideband with respect to the 220.1 GHz first LO used at the JCMT and SMA also contaminated the signal in the upper-sideband data. The differential fringe rate between upper and lower sidebands is of O(Hz); thus, the lower-sideband contamination averages out to zero over sufficiently long integration times. The contamination only affects the reference antenna contribution to the phased array, as other antennas are subject to $90°/270°$ Walsh switching (Thompson et al. 2017, Section 7.5) that removes on average the lower sideband signal over a Walsh cycle of 0.65 s. Correlations between the JCMT and SMA single-dish reference antenna thus get the full lower sideband contribution, but correlations between JCMT and SMA phased array only get $1/N$ contribution, where N is the number of telescopes being phased. To avoid phase steering toward this spurious $\sim$17% contribution to the signal, neither the SMA nor the JCMT is ever used as the reference station during atmospheric phase calibration. For scans with very small fringe-rates, there may be a small residual contribution after the 10 s averages used for network calibration (Section 6.2). This adds to the intra-site baseline amplitude error budget that propagates into gain solutions for that procedure, as well as for closure amplitudes that use the baseline on comparable timescales.

Data from PV were subject to substantial amplitude loss due to instabilities in the signal chain, attributed to excess phase noise in the maser frequency reference (which has since been replaced). Examination of the data on the ALMA–PV baseline with progressively shorter APs demonstrated a pattern of frequency spikes off the main signal with evidence that the full correlated amplitude could be recovered with an AP of 2.048 ms. Further examination of a variety of scans showed that the pattern of frequency spikes was stable across scans, sources, and days, and the amplitude loss was constant. The effect was mitigated by continuing to use the data with a 0.4 s AP and multiplying the visibility amplitudes on baselines to PV by a constant derived multiplicative factor of 1.914 during a priori flux density calibration, which is equivalent to multiplying the effective SEFD for PV by 3.663.

Misconfigured Mark 6 recorders at APEX caused substantial data loss on many scans. The first 20–30 s of recording on a particular scan (sometimes much longer) were generally good,

but partial or complete data dropouts could occur thereafter. DiFX accounts for the amount of valid data and automatically corrects averaged amplitudes and data weights for partial data loss to within ∼1% accuracy. The remaining data from long-duration dropouts were manually flagged to avoid introducing bad APEX data into the processed data. The consequence is that ALMA–APEX coverage is inconsistent, and this complicates the strategy for network calibration and closure amplitude analysis, which makes use of intra-site baseline coverage. It also means that for the 2017 observations, APEX cannot be consistently used to help calibrate ALMA amplitude variation during poor weather when ALMA phasing efficiency is unstable.

A separate unrelated small correction factor is applied to APEX baselines to account for reduction in amplitude from the introduction of a 1 pulse-per-second (PPS) signal in the APEX data. The factor is estimated by measuring amplitudes with and without the PPS signal flagged. It is valid for multi-second averages of visibility amplitudes.

Isolated groups of frequency channels in the beamformer system at the SMA were occasionally corrupted, causing a small fraction of the bandwidth (in the high band) to be lost during the first three days of the observation. Processing of a single band within the SMA beamformer is divided across eight hardware units, each of which processes one-eighth of the total bandwidth, distributed across 128 channels of 2.234375 MHz each (Primiani et al. 2016), so that the exact pattern of lost channels, once identified, is predictable. The times when the data corruption occurred and the amount of bandwidth affected were identified using the strong noise correlation signal between the SMA (beamformed) phased array and the SMA single-dish reference (recorded on a standard EHT backend). The pattern of lost bandwidth is evenly distributed throughout the band, and we derive SEFD corrections to account for the effective relative signal power lost upon frequency average (Table 2).

The LMT data are contaminated by polarization leakage, which is delayed from the primary signal by ∼1.5 ns. This occurs in both polarizations, and is attributed to reflections in the optical setup of the LMT receiver used in 2017 (1.5 ns corresponds to 45 cm). The level of polarization leakage is ∼10%, but for an unpolarized source it will dominate the correlated signal power of cross-hand VLBI products, therefore causing a false fringe at the delayed location. During fringe closure with the HOPS pipeline, an additional 1.5 ns delay systematic is added in quadrature to LMT baselines, so that any such false fringes will not bias the global station delays. A future polarization leakage correction will need to accommodate leakage at non-zero delay to properly account for the contamination. For 2018 and beyond, the special-purpose interim receiver used at LMT was replaced by a dual-polarization sideband-separating 1.3 mm receiver with better stability and full 64 Gbps coverage with the rest of the EHT (Paper II).

A.2. Issues not Addressed during Processing

The failure of a hard drive in one of the JCMT modules caused one-sixteenth of the data in the low band to be lost. The lost data affects all scans on the module approximately equally, as packets are scattered onto all hard drives at record time. This issue required no special handling because DiFX automatically adjusts data weights based on the amount of data in each AP.

Due to a small glitch in the ALMA correlator, the correlation coefficients on ALMA baselines are observed to undergo a slight dip every 18.192 s. The effective amplitude loss on scan-averaged quantities, less than 0.1%, is well within the error budget and therefore unmitigated.

No corrections were made for losses due to finite fast Fourier transform (FFT) lengths, which are required to be long in order to align ALMA 32×58.59375 MHz data in the frequency domain with the wideband 2048 MHz single-channel data from most EHT stations. A small loss is introduced due to the changing delay over the 64 μs of time corresponding to the FFT length used. The loss is zero at the DC edge of the channel and increases linearly with frequency. This effect is baseline-dependent and greatest on the baselines with the greatest east–west extent, especially when the source is rising at one location and setting at the other. Across all fringes on all sources on all baselines on all five days, the median signal loss is 0.67%, with the worst case (on a scan on the Hawai'i–PV baseline) about an order of magnitude larger. FFT losses are negligible on baselines to ALMA because the delay error accumulates over a maximum of 58.59375 MHz in frequency rather than 2048 MHz.

The LMT faces significant challenges in maintaining an accurate surface for 1.3 mm as the temperature fluctuates over the course of the evening. Pointing was also a challenge for scans at low or high elevation. These issues result in large residual gain trends obtained via amplitude self-calibration beyond the nominal error budget (Paper IV). However, the station-based amplitude gain issues do not influence robust interferometric closure quantities.

The SPT, participating for the first time in the VLBI observations, suffered from pointing problems early in the campaign. 3C 279 observing time was used to diagnose and resolve these issues, resulting in missing a majority of 3C 279 scans on April 5 and 6. The pointing issues were known and captured in observing logs during the run. The non-detections do not appear in the 3C 279 data set (Figure 2), and their absence is expected.

A.3. Issues at Correlation

Two unanticipated issues with the ALMA data were discovered and fixed in a seventh revision (Rev7) correlation. First, the tuning of one of the ALMA LO generators was specified to insufficient precision, resulting in an undocumented 50 mHz LO offset. In most VLBI experiments, such a small LO offset might be transparently compensated by a small change in fitted delay-rate. However for the wide EHT bandwidths, the inability for a single delay-rate to model the effect over the entire 2 GHz band is noticed, where the result of imperfect correction is to imprint a small rate slope with frequency, or, equivalently, a small delay drift with time. For this reason, the effect is separately corrected for prior to fringe fitting when post-processing Rev5 data, which is possible for sufficiently small LO offsets.

Second, it was discovered that the ALMA delay system automatically removes the bulk atmospheric delay from above the array. By default, DiFX tries to remove the bulk atmospheric delay from above each station, resulting in a double correction for ALMA. This was most noticeable at low elevation, where the double correction imprinted a large and rapidly (but monotonically) changing delay-rate. The large residual delay-rate is not large enough to cause decoherence

over the duration of a correlation AP (0.4 s). The changing delay-rate causes substantial decoherence over a several-minute scan if only a first-order fringe solution is used. Because EHT data reduction already includes a mechanism to measure and correct for nonlinear phase due to atmospheric turbulence, it can also compensate for this drift in delay-rate imprinted on the data in the initial correlation. So long as signal-to-noise is sufficient to measure phase over short timescales, the impact on calibrated data is negligible.

Both of these issues were ultimately corrected in a final Rev7 correlation release. This included the LO adjustment for ALMA as well as special scripting for the geometric model preparation that allows the normal atmospheric correction at all sites other than ALMA to be merged with a no-atmospheric correction at ALMA. Comparison of SR1 results with comparable processing of Rev7 shows no significant difference, showing that the effects were sufficiently mitigated in post-processing for SR1.

ORCID iDs

Kazunori Akiyama https://orcid.org/0000-0002-9475-4254
Antxon Alberdi https://orcid.org/0000-0002-9371-1033
Rebecca Azulay https://orcid.org/0000-0002-2200-5393
Anne-Kathrin Baczko https://orcid.org/0000-0003-3090-3975
Mislav Baloković https://orcid.org/0000-0003-0476-6647
John Barrett https://orcid.org/0000-0002-9290-0764
Lindy Blackburn https://orcid.org/0000-0002-9030-642X
Katherine L. Bouman https://orcid.org/0000-0003-0077-4367
Geoffrey C. Bower https://orcid.org/0000-0003-4056-9982
Christiaan D. Brinkerink https://orcid.org/0000-0002-2322-0749
Roger Brissenden https://orcid.org/0000-0002-2556-0894
Silke Britzen https://orcid.org/0000-0001-9240-6734
Avery E. Broderick https://orcid.org/0000-0002-3351-760X
Do-Young Byun https://orcid.org/0000-0003-1157-4109
Andrew Chael https://orcid.org/0000-0003-2966-6220
Chi-kwan Chan https://orcid.org/0000-0001-6337-6126
Shami Chatterjee https://orcid.org/0000-0002-2878-1502
Ilje Cho https://orcid.org/0000-0001-6083-7521
Pierre Christian https://orcid.org/0000-0001-6820-9941
John E. Conway https://orcid.org/0000-0003-2448-9181
Geoffrey B. Crew https://orcid.org/0000-0002-2079-3189
Yuzhu Cui https://orcid.org/0000-0001-6311-4345
Jordy Davelaar https://orcid.org/0000-0002-2685-2434
Mariafelicia De Laurentis https://orcid.org/0000-0002-9945-682X
Roger Deane https://orcid.org/0000-0003-1027-5043
Jessica Dempsey https://orcid.org/0000-0003-1269-9667
Gregory Desvignes https://orcid.org/0000-0003-3922-4055
Jason Dexter https://orcid.org/0000-0003-3903-0373
Sheperd S. Doeleman https://orcid.org/0000-0002-9031-0904
Ralph P. Eatough https://orcid.org/0000-0001-6196-4135
Heino Falcke https://orcid.org/0000-0002-2526-6724
Vincent L. Fish https://orcid.org/0000-0002-7128-9345
Raquel Fraga-Encinas https://orcid.org/0000-0002-5222-1361
José L. Gómez https://orcid.org/0000-0003-4190-7613
Peter Galison https://orcid.org/0000-0002-6429-3872
Charles F. Gammie https://orcid.org/0000-0001-7451-8935
Boris Georgiev https://orcid.org/0000-0002-3586-6424
Roman Gold https://orcid.org/0000-0003-2492-1966
Minfeng Gu (顾敏峰) https://orcid.org/0000-0002-4455-6946
Mark Gurwell https://orcid.org/0000-0003-0685-3621
Kazuhiro Hada https://orcid.org/0000-0001-6906-772X
Ronald Hesper https://orcid.org/0000-0003-1918-6098
Luis C. Ho (何子山) https://orcid.org/0000-0001-6947-5846
Mareki Honma https://orcid.org/0000-0003-4058-9000
Chih-Wei L. Huang https://orcid.org/0000-0001-5641-3953
Shiro Ikeda https://orcid.org/0000-0002-2462-1448
Sara Issaoun https://orcid.org/0000-0002-5297-921X
David J. James https://orcid.org/0000-0001-5160-4486
Michael Janssen https://orcid.org/0000-0001-8685-6544
Britton Jeter https://orcid.org/0000-0003-2847-1712
Wu Jiang (江悟) https://orcid.org/0000-0001-7369-3539
Michael D. Johnson https://orcid.org/0000-0002-4120-3029
Svetlana Jorstad https://orcid.org/0000-0001-6158-1708
Taehyun Jung https://orcid.org/0000-0001-7003-8643
Mansour Karami https://orcid.org/0000-0001-7387-9333
Ramesh Karuppusamy https://orcid.org/0000-0002-5307-2919
Tomohisa Kawashima https://orcid.org/0000-0001-8527-0496
Garrett K. Keating https://orcid.org/0000-0002-3490-146X
Mark Kettenis https://orcid.org/0000-0002-6156-5617
Jae-Young Kim https://orcid.org/0000-0001-8229-7183
Junhan Kim https://orcid.org/0000-0002-4274-9373
Motoki Kino https://orcid.org/0000-0002-2709-7338
Jun Yi Koay https://orcid.org/0000-0002-7029-6658
Patrick M. Koch https://orcid.org/0000-0003-2777-5861
Shoko Koyama https://orcid.org/0000-0002-3723-3372
Michael Kramer https://orcid.org/0000-0002-4175-2271
Carsten Kramer https://orcid.org/0000-0002-4908-4925
Thomas P. Krichbaum https://orcid.org/0000-0002-4892-9586
Tod R. Lauer https://orcid.org/0000-0003-3234-7247
Sang-Sung Lee https://orcid.org/0000-0002-6269-594X
Yan-Rong Li (李彦荣) https://orcid.org/0000-0001-5841-9179
Zhiyuan Li (李志远) https://orcid.org/0000-0003-0355-6437
Michael Lindqvist https://orcid.org/0000-0002-3669-0715
Kuo Liu https://orcid.org/0000-0002-2953-7376
Elisabetta Liuzzo https://orcid.org/0000-0003-0995-5201
Laurent Loinard https://orcid.org/0000-0002-5635-3345
Ru-Sen Lu (路如森) https://orcid.org/0000-0002-7692-7967
Nicholas R. MacDonald https://orcid.org/0000-0002-6684-8691
Jirong Mao (毛基荣) https://orcid.org/0000-0002-7077-7195
Sera Markoff https://orcid.org/0000-0001-9564-0876
Daniel P. Marrone https://orcid.org/0000-0002-2367-1080
Alan P. Marscher https://orcid.org/0000-0001-7396-3332
Iván Martí-Vidal https://orcid.org/0000-0003-3708-9611
Lynn D. Matthews https://orcid.org/0000-0002-3728-8082
Lia Medeiros https://orcid.org/0000-0003-2342-6728
Karl M. Menten https://orcid.org/0000-0001-6459-0669
Yosuke Mizuno https://orcid.org/0000-0002-8131-6730
Izumi Mizuno https://orcid.org/0000-0002-7210-6264
James M. Moran https://orcid.org/0000-0002-3882-4414
Kotaro Moriyama https://orcid.org/0000-0003-1364-3761
Monika Moscibrodzka https://orcid.org/0000-0002-4661-6332
Cornelia Müller https://orcid.org/0000-0002-2739-2994
Hiroshi Nagai https://orcid.org/0000-0003-0292-3645
Neil M. Nagar https://orcid.org/0000-0001-6920-662X
Masanori Nakamura https://orcid.org/0000-0001-6081-2420

Ramesh Narayan https://orcid.org/0000-0002-1919-2730
Iniyan Natarajan https://orcid.org/0000-0001-8242-4373
Chunchong Ni https://orcid.org/0000-0003-1361-5699
Aristeidis Noutsos https://orcid.org/0000-0002-4151-3860
Héctor Olivares https://orcid.org/0000-0001-6833-7580
Gisela N. Ortiz-León https://orcid.org/0000-0002-2863-676X
Daniel C. M. Palumbo https://orcid.org/0000-0002-7179-3816
Ue-Li Pen https://orcid.org/0000-0003-2155-9578
Dominic W. Pesce https://orcid.org/0000-0002-5278-9221
Oliver Porth https://orcid.org/0000-0002-4584-2557
Ben Prather https://orcid.org/0000-0002-0393-7734
Jorge A. Preciado-López https://orcid.org/0000-0002-4146-0113
Hung-Yi Pu https://orcid.org/0000-0001-9270-8812
Venkatessh Ramakrishnan https://orcid.org/0000-0002-9248-086X
Ramprasad Rao https://orcid.org/0000-0002-1407-7944
Alexander W. Raymond https://orcid.org/0000-0002-5779-4767
Luciano Rezzolla https://orcid.org/0000-0002-1330-7103
Bart Ripperda https://orcid.org/0000-0002-7301-3908
Freek Roelofs https://orcid.org/0000-0001-5461-3687
Eduardo Ros https://orcid.org/0000-0001-9503-4892
Mel Rose https://orcid.org/0000-0002-2016-8746
Alan L. Roy https://orcid.org/0000-0002-1931-0135
Chet Ruszczyk https://orcid.org/0000-0001-7278-9707
Benjamin R. Ryan https://orcid.org/0000-0001-8939-4461
Kazi L. J. Rygl https://orcid.org/0000-0003-4146-9043
David Sánchez-Arguelles https://orcid.org/0000-0002-7344-9920
Mahito Sasada https://orcid.org/0000-0001-5946-9960
Tuomas Savolainen https://orcid.org/0000-0001-6214-1085
Lijing Shao https://orcid.org/0000-0002-1334-8853
Zhiqiang Shen (沈志强) https://orcid.org/0000-0003-3540-8746
Des Small https://orcid.org/0000-0003-3723-5404
Bong Won Sohn https://orcid.org/0000-0002-4148-8378
Jason SooHoo https://orcid.org/0000-0003-1938-0720
Fumie Tazaki https://orcid.org/0000-0003-0236-0600
Paul Tiede https://orcid.org/0000-0003-3826-5648
Remo P. J. Tilanus https://orcid.org/0000-0002-6514-553X
Michael Titus https://orcid.org/0000-0002-3423-4505
Kenji Toma https://orcid.org/0000-0002-7114-6010
Pablo Torne https://orcid.org/0000-0001-8700-6058
Sascha Trippe https://orcid.org/0000-0003-0465-1559
Ilse van Bemmel https://orcid.org/0000-0001-5473-2950
Huib Jan van Langevelde https://orcid.org/0000-0002-0230-5946
Daniel R. van Rossum https://orcid.org/0000-0001-7772-6131
John Wardle https://orcid.org/0000-0002-8960-2942
Jonathan Weintroub https://orcid.org/0000-0002-4603-5204
Norbert Wex https://orcid.org/0000-0003-4058-2837
Robert Wharton https://orcid.org/0000-0002-7416-5209
Maciek Wielgus https://orcid.org/0000-0002-8635-4242
George N. Wong https://orcid.org/0000-0001-6952-2147
Qingwen Wu (吴庆文) https://orcid.org/0000-0003-4773-4987
André Young https://orcid.org/0000-0003-0000-2682
Ken Young https://orcid.org/0000-0002-3666-4920
Ziri Younsi https://orcid.org/0000-0001-9283-1191
Feng Yuan (袁峰) https://orcid.org/0000-0003-3564-6437
J. Anton Zensus https://orcid.org/0000-0001-7470-3321
Guangyao Zhao https://orcid.org/0000-0002-4417-1659
Shan-Shan Zhao https://orcid.org/0000-0002-9774-3606
Joseph R. Farah https://orcid.org/0000-0003-4914-5625
Daniel Michalik https://orcid.org/0000-0002-7618-6556
Andrew Nadolski https://orcid.org/0000-0001-9479-9957
Rurik A. Primiani https://orcid.org/0000-0003-3910-7529
Paul Yamaguchi https://orcid.org/0000-0002-6017-8199

References

Akiyama, K., Lu, R.-S., Fish, V. L., et al. 2015, ApJ, 807, 150
Alef, W., & Porcas, R. W. 1986, A&A, 168, 365
Baars, J. W. M. 2007, The Paraboloidal Reflector Antenna in Radio Astronomy and Communication (Berlin: Springer)
Blackburn, L., Chan, C.-K., Crew, G. B., et al. 2019, arXiv:1903.08832
Blakeslee, J. P., Jordán, A., Mei, S., et al. 2009, ApJ, 694, 556
Cantiello, M., Blakeslee, J. P., Ferrarese, L., et al. 2018, ApJ, 856, 126
Chael, A. A., Johnson, M. D., Bouman, K. L., et al. 2018, ApJ, 857, 23
Chael, A. A., Johnson, M. D., Narayan, R., et al. 2016, ApJ, 829, 11
Chang, C. S., Ros, E., Kovalev, Y. Y., & Lister, M. L. 2010, A&A, 515, A38
Cotton, W. D. 1995, in ASP Conf. Ser. 82, Very Long Baseline Interferometry and the VLBA, ed. J. A. Zensus, P. J. Diamond, & P. J. Napier (San Francisco, CA: ASP), 189
Deller, A. T., Brisken, W. F., Phillips, C. J., et al. 2011, PASP, 123, 275
Doeleman, S. 2010, in 10th European VLBI Network Symp. and EVN Users Meeting: VLBI and the New Generation of Radio Arrays (Trieste: SISSA), 53
Doeleman, S., Agol, E., Backer, D., et al. 2009, in Astro2010: The Astronomy and Astrophysics Decadal Survey, Science White Papers, 68
Doeleman, S. S., Fish, V. L., Schenck, D. E., et al. 2012, Sci, 338, 355
Doeleman, S. S., Weintroub, J., Rogers, A. E. E., et al. 2008, Natur, 455, 78
EHT Collaboration et al. 2019a, ApJL, 875, L1 (Paper I)
EHT Collaboration et al. 2019b, ApJL, 875, L2 (Paper II)
EHT Collaboration et al. 2019c, ApJL, 875, L4 (Paper IV)
EHT Collaboration et al. 2019d, ApJL, 875, L5 (Paper V)
EHT Collaboration et al. 2019e, ApJL, 875, L6 (Paper VI)
Fish, V., Alef, W., Anderson, J., et al. 2013, arXiv:1309.3519
Fish, V. L., Doeleman, S. S., Beaudoin, C., et al. 2011, ApJL, 727, L36
Fish, V. L., Johnson, M. D., Doeleman, S. S., et al. 2016, ApJ, 820, 90
Gebhardt, K., Adams, J., Richstone, D., et al. 2011, ApJ, 729, 119
Goddi, C., Marti-Vidal, I., Messias, H., et al. 2019, PASP, in press
Greisen, E. W. 2003, in Information Handling in Astronomy—Historical Vistas, Vol. 285, ed. A. Heck (Dordrecht: Kluwer), 109
Greisen, E. W. 2011, AIPS Memo Series, 114r (New Mexico, USA: Socorro)
Hunter, J. D. 2007, CSE, 9, 90
Iguchi, S. 2005, PASJ, 57, 643
Issaoun, S., Falcke, H., Friberg, P., et al. 2018, EHT Memo Series, 2018-CE-01
Issaoun, S., Folkers, T. W., Blackburn, L., et al. 2017a, EHT Memo Series, 2017-CE-02
Issaoun, S., Folkers, T. W., Marrone, D. P., et al. 2017b, EHT Memo Series, 2017-CE-03
Issaoun, S., Johnson, M. D., Blackburn, L., et al. 2019, ApJ, 871, 30
Janssen, M., Goddi, C., van Bemmel, I. M., et al. 2019a, arXiv:1902.01749
Janssen, M., Issaoun, S., Blackburn, L., et al. 2019b, EHT Memo Series, 2019-CE-01
Jewell, P. R. 2002, in ASP Conf. Ser. 278, Single-Dish Radio Astronomy: Techniques and Applications, ed. S. Stanimirovic et al. (San Francisco, CA: ASP), 313
Johnson, M. D., Fish, V. L., Doeleman, S. S., et al. 2015, Sci, 350, 1242
Jones, E., Oliphant, T., Peterson, P., et al. 2001, SciPy: Open source scientific tools for Python
Kettenis, M., van Langevelde, H. J., Reynolds, C., & Cotton, B. 2006, in ASP Conf. Ser. 351, Astronomical Data Analysis Software and Systems XV, ed. C. Gabriel et al. (San Francisco, CA: ASP), 497
Kluyver, T., Ragan-Kelley, B., Pérez, F., et al. 2016, in Positioning and Power in Academic Publishing: Players, Agents and Agendas, ed. F. Loizides & B. Schmidt (IOS Press), 87
Kutner, M. L. 1978, ApJL, 19, 81
Kutner, M. L., & Ulich, B. L. 1981, ApJ, 250, 341
Lu, R.-S., Krichbaum, T. P., Roy, A. L., et al. 2018, ApJ, 859, 60
Mangum, J. G. 1993, PASP, 105, 117
Mangum, J. G. 2002, ALMA Memo Series, 434
Martí-Vidal, I., Roy, A., Conway, J., & Zensus, A. J. 2016, A&A, 587, A143
Matsushita, S., Saito, M., Sakamoto, K., et al. 2006, Proc. SPIE, 6275, 62751W

Matthews, L. D., Crew, G. B., Doeleman, S. S., et al. 2018, PASP, 130, 015002
McKinney, W. 2010, in Proc. 9th Python in Science Conf., ed. S. van der Walt & J. Millman (Washington, D.C.: IEEE), 51
McMullin, J. P., Waters, B., Schiebel, D., Young, W., & Golap, K. 2007, in ASP Conf. Ser. 376, Astronomical Data Analysis Software and Systems XVI, ed. R. A. Shaw, F. Hill, & D. J. Bell (San Francisco, CA: ASP), 127
Pearson, T. J., & Readhead, A. C. S. 1984, ARA&A, 22, 97
Penzias, A. A., & Burrus, C. A. 1973, ARA&A, 11, 51
Primiani, R. A., Young, K. H., Young, A., et al. 2016, JAI, 5, 1641006
Rogers, A. E. E., Doeleman, S. S., & Moran, J. M. 1995, AJ, 109, 1391
Romney, J. D. 1995, in ASP Conf. Ser. 82, Very Long Baseline Interferometry and the VLBA, ed. J. A. Zensus, P. J. Diamond, & P. J. Napier (San Francisco, CA: ASP), 17
Schwab, F. R., & Cotton, W. D. 1983, AJ, 88, 688
Tange, O. 2011, login: The USENIX Magazine, 36, 42
The Astropy Collaboration, Robitaille, T. P., Tollerud, E. J., et al. 2013, A&A, 558, A33
The Astropy Collaboration, Price-Whelan, A. M., Sipőcz, B. M., et al. 2018, AJ, 156, 123
Thompson, A. R., Moran, J. M., Jr., & , G. W. S. 2017, Interferometry and Synthesis in Radio Astronomy (3rd ed.; Berlin: Springer)
Ulich, B. L., & Haas, R. W. 1976, ApJS, 30, 247
van Cittert, P. H. 1934, Phy, 1, 201
van der Walt, S., Colbert, S. C., & Varoquaux, G. 2011, CSE, 13, 22
Vertatschitsch, L., Primiani, R., Young, A., et al. 2015, PASP, 127, 1226
Walker, R. C., Hardee, P. E., Davies, F. B., Ly, C., & Junor, W. 2018, ApJ, 855, 128
Whitney, A. R., Beaudoin, C. J., Cappallo, R. J., et al. 2013, PASP, 125, 196
Whitney, A. R., Cappallo, R., Aldrich, W., et al. 2004, RaSc, 39, RS1007
Wielgus, M., Blackburn, L., Issaoun, S., et al. 2019, EHT Memo Series, 2019-CE-02
Wilkinson, P. N. 1989, in NATO Advanced Science Institutes (ASI) Series C, Vol. 283, ed. M. Felli & R. E. Spencer (Berlin: Springer), 69
Young, A., Primiani, R., Weintroub, J., et al. 2016, in 2016 IEEE Int. Symp., Phased Array Systems and Technology (ARRAY) (New York: IEEE), 1
Zernike, F. 1938, Phy, 5, 785

The Event Horizon Telescope Collaboration,
Kazunori Akiyama[1,2,3,4], Antxon Alberdi[5], Walter Alef[6], Keiichi Asada[7], Rebecca Azulay[8,9,6], Anne-Kathrin Baczko[6], David Ball[10], Mislav Baloković[4,11], John Barrett[2], Dan Bintley[12], Lindy Blackburn[4,11], Wilfred Boland[13], Katherine L. Bouman[4,11,14], Geoffrey C. Bower[15], Michael Bremer[16], Christiaan D. Brinkerink[17], Roger Brissenden[4,11], Silke Britzen[6], Avery E. Broderick[18,19,20], Dominique Broguiere[16], Thomas Bronzwaer[17], Do-Young Byun[21,22], John E. Carlstrom[23,24,25,26], Andrew Chael[4,11], Chi-kwan Chan[10,27], Shami Chatterjee[28], Koushik Chatterjee[29], Ming-Tang Chen[15], Yongjun Chen (陈永军)[30,31], Ilje Cho[21,22], Pierre Christian[10,11], John E. Conway[32], James M. Cordes[28], Geoffrey B. Crew[2], Yuzhu Cui[33,34], Jordy Davelaar[17], Mariafelicia De Laurentis[35,36,37], Roger Deane[38,39], Jessica Dempsey[12], Gregory Desvignes[6], Jason Dexter[40], Sheperd S. Doeleman[4,11], Ralph P. Eatough[6], Heino Falcke[17], Vincent L. Fish[2], Ed Fomalont[1], Raquel Fraga-Encinas[17], Per Friberg[12], Christian M. Fromm[36], José L. Gómez[5], Peter Galison[4,41,42], Charles F. Gammie[43,44], Roberto García[16], Olivier Gentaz[16], Boris Georgiev[19], Ciriaco Goddi[17,45], Roman Gold[36], Minfeng Gu (顾敏峰)[30,46], Mark Gurwell[11], Kazuhiro Hada[33,34], Michael H. Hecht[2], Ronald Hesper[47], Luis C. Ho (何子山)[48,49], Paul Ho[7], Mareki Honma[33,34], Chih-Wei L. Huang[7], Lei Huang (黄磊)[30,46], David H. Hughes[50], Shiro Ikeda[3,51,52,53], Makoto Inoue[7], Sara Issaoun[17], David J. James[4,11], Buell T. Jannuzi[10], Michael Janssen[17], Britton Jeter[19,20], Wu Jiang (江悟)[30], Michael D. Johnson[4,11], Svetlana Jorstad[54,55], Taehyun Jung[21,22], Mansour Karami[18,19], Ramesh Karuppusamy[6], Tomohisa Kawashima[3], Garrett K. Keating[11], Mark Kettenis[56], Jae-Young Kim[6], Junhan Kim[10], Jongsoo Kim[21], Motoki Kino[3,57], Jun Yi Koay[7], Patrick M. Koch[7], Shoko Koyama[7], Michael Kramer[6], Carsten Kramer[16], Thomas P. Krichbaum[6], Cheng-Yu Kuo[58], Tod R. Lauer[59], Sang-Sung Lee[21], Yan-Rong Li (李彦荣)[60], Zhiyuan Li (李志远)[61,62], Michael Lindqvist[32], Kuo Liu[6], Elisabetta Liuzzo[63], Wen-Ping Lo[7,64], Andrei P. Lobanov[6], Laurent Loinard[65,66], Colin Lonsdale[2], Ru-Sen Lu (路如森)[30,6], Nicholas R. MacDonald[6], Jirong Mao (毛基荣)[67,68,69], Sera Markoff[29,70], Daniel P. Marrone[10], Alan P. Marscher[54], Iván Martí-Vidal[32,71], Satoki Matsushita[7], Lynn D. Matthews[2], Lia Medeiros[10,72], Karl M. Menten[6], Yosuke Mizuno[36], Izumi Mizuno[12], James M. Moran[4,11], Kotaro Moriyama[33,2], Monika Moscibrodzka[17], Cornelia Müller[6,17], Hiroshi Nagai[3,34], Neil M. Nagar[73], Masanori Nakamura[7], Ramesh Narayan[4,11], Gopal Narayanan[74], Iniyan Natarajan[39], Roberto Neri[16], Chunchong Ni[19,20], Aristeidis Noutsos[6], Hiroki Okino[33,75], Héctor Olivares[36], Gisela N. Ortiz-León[6], Tomoaki Oyama[33], Feryal Özel[10], Daniel C. M. Palumbo[4,11], Nimesh Patel[11], Ue-Li Pen[18,76,77,78], Dominic W. Pesce[4,11], Vincent Piétu[16], Richard Plambeck[79], Aleksandar PopStefanija[74], Oliver Porth[36,29], Ben Prather[43], Jorge A. Preciado-López[18], Dimitrios Psaltis[10], Hung-Yi Pu[18], Venkatessh Ramakrishnan[73], Ramprasad Rao[15], Mark G. Rawlings[12], Alexander W. Raymond[4,11], Luciano Rezzolla[36], Bart Ripperda[36], Freek Roelofs[17], Alan Rogers[2], Eduardo Ros[6], Mel Rose[10], Arash Roshanineshat[10], Helge Rottmann[6], Alan L. Roy[6], Chet Ruszczyk[2], Benjamin R. Ryan[80,81], Kazi L. J. Rygl[63], Salvador Sánchez[82], David Sánchez-Arguelles[50,83], Mahito Sasada[33,84], Tuomas Savolainen[6,85,86], F. Peter Schloerb[74], Karl-Friedrich Schuster[16], Lijing Shao[6,49], Zhiqiang Shen (沈志强)[30,31], Des Small[56], Bong Won Sohn[21,22,87], Jason SooHoo[2], Fumie Tazaki[33], Paul Tiede[18,19], Remo P. J. Tilanus[17,45,88], Michael Titus[2], Kenji Toma[89,90], Pablo Torne[6,82], Tyler Trent[10], Sascha Trippe[91], Shuichiro Tsuda[33], Ilse van Bemmel[56], Huib Jan van Langevelde[56,92], Daniel R. van Rossum[17],

Jan Wagner[6], John Wardle[93], Jonathan Weintroub[4,11], Norbert Wex[6], Robert Wharton[6], Maciek Wielgus[4,11], George N. Wong[43], Qingwen Wu (吴庆文)[94], André Young[17], Ken Young[11], Ziri Younsi[95,36], Feng Yuan (袁峰)[30,46,96], Ye-Fei Yuan (袁业飞)[97], J. Anton Zensus[6], Guangyao Zhao[21], Shan-Shan Zhao[17,61], Ziyan Zhu[42], Roger Cappallo[2], Joseph R. Farah[11,98,4], Thomas W. Folkers[10], Zheng Meyer-Zhao[7,99], Daniel Michalik[100,101], Andrew Nadolski[44], Hiroaki Nishioka[7], Nicolas Pradel[7], Rurik A. Primiani[11,102], Kamal Souccar[74], Laura Vertatschitsch[11,102], and Paul Yamaguchi[11]

[1] National Radio Astronomy Observatory, 520 Edgemont Rd, Charlottesville, VA 22903, USA
[2] Massachusetts Institute of Technology Haystack Observatory, 99 Millstone Road, Westford, MA 01886, USA
[3] National Astronomical Observatory of Japan, 2-21-1 Osawa, Mitaka, Tokyo 181-8588, Japan
[4] Black Hole Initiative at Harvard University, 20 Garden Street, Cambridge, MA 02138, USA
[5] Instituto de Astrofísica de Andalucía-CSIC, Glorieta de la Astronomía s/n, E-18008 Granada, Spain
[6] Max-Planck-Institut für Radioastronomie, Auf dem Hügel 69, D-53121 Bonn, Germany
[7] Institute of Astronomy and Astrophysics, Academia Sinica, 11F of Astronomy-Mathematics Building, AS/NTU No. 1, Sec. 4, Roosevelt Rd, Taipei 10617, Taiwan, R.O.C.
[8] Departament d'Astronomia i Astrofísica, Universitat de València, C. Dr. Moliner 50, E-46100 Burjassot, València, Spain
[9] Observatori Astronòmic, Universitat de València, C. Catedrático José Beltrán 2, E-46980 Paterna, València, Spain
[10] Steward Observatory and Department of Astronomy, University of Arizona, 933 N. Cherry Avenue, Tucson, AZ 85721, USA
[11] Center for Astrophysics | Harvard & Smithsonian, 60 Garden Street, Cambridge, MA 02138, USA
[12] East Asian Observatory, 660 N. A'ohoku Pl., Hilo, HI 96720, USA
[13] Nederlandse Onderzoekschool voor Astronomie (NOVA), PO Box 9513, 2300 RA Leiden, The Netherlands
[14] California Institute of Technology, 1200 East California Boulevard, Pasadena, CA 91125, USA
[15] Institute of Astronomy and Astrophysics, Academia Sinica, 645 N. A'ohoku Place, Hilo, HI 96720, USA
[16] Institut de Radioastronomie Millimétrique, 300 rue de la Piscine, F-38406 Saint Martin d'Hères, France
[17] Department of Astrophysics, Institute for Mathematics, Astrophysics and Particle Physics (IMAPP), Radboud University, P.O. Box 9010, 6500 GL Nijmegen, The Netherlands
[18] Perimeter Institute for Theoretical Physics, 31 Caroline Street North, Waterloo, ON, N2L 2Y5, Canada
[19] Department of Physics and Astronomy, University of Waterloo, 200 University Avenue West, Waterloo, ON, N2L 3G1, Canada
[20] Waterloo Centre for Astrophysics, University of Waterloo, Waterloo, ON N2L 3G1, Canada
[21] Korea Astronomy and Space Science Institute, Daedeok-daero 776, Yuseong-gu, Daejeon 34055, Republic of Korea
[22] University of Science and Technology, Gajeong-ro 217, Yuseong-gu, Daejeon 34113, Republic of Korea
[23] Kavli Institute for Cosmological Physics, University of Chicago, 5640 South Ellis Avenue, Chicago, IL 60637, USA
[24] Department of Astronomy and Astrophysics, University of Chicago, 5640 South Ellis Avenue, Chicago, IL 60637, USA
[25] Department of Physics, University of Chicago, 5720 South Ellis Avenue, Chicago, IL 60637, USA
[26] Enrico Fermi Institute, University of Chicago, 5640 South Ellis Avenue, Chicago, IL 60637, USA
[27] Data Science Institute, University of Arizona, 1230 N. Cherry Ave., Tucson, AZ 85721, USA
[28] Cornell Center for Astrophysics and Planetary Science, Cornell University, Ithaca, NY 14853, USA
[29] Anton Pannekoek Institute for Astronomy, University of Amsterdam, Science Park 904, 1098 XH, Amsterdam, The Netherlands
[30] Shanghai Astronomical Observatory, Chinese Academy of Sciences, 80 Nandan Road, Shanghai 200030, People's Republic of China
[31] Key Laboratory of Radio Astronomy, Chinese Academy of Sciences, Nanjing 210008, People's Republic of China
[32] Department of Space, Earth and Environment, Chalmers University of Technology, Onsala Space Observatory, SE-43992 Onsala, Sweden
[33] Mizusawa VLBI Observatory, National Astronomical Observatory of Japan, 2-12 Hoshigaoka, Mizusawa, Oshu, Iwate 023-0861, Japan
[34] Department of Astronomical Science, The Graduate University for Advanced Studies (SOKENDAI), 2-21-1 Osawa, Mitaka, Tokyo 181-8588, Japan
[35] Dipartimento di Fisica "E. Pancini", Universitá di Napoli "Federico II", Compl. Univ. di Monte S. Angelo, Edificio G, Via Cinthia, I-80126, Napoli, Italy
[36] Institut für Theoretische Physik, Goethe-Universität Frankfurt, Max-von-Laue-Straße 1, D-60438 Frankfurt am Main, Germany
[37] INFN Sez. di Napoli, Compl. Univ. di Monte S. Angelo, Edificio G, Via Cinthia, I-80126, Napoli, Italy
[38] Department of Physics, University of Pretoria, Lynnwood Road, Hatfield, Pretoria 0083, South Africa
[39] Centre for Radio Astronomy Techniques and Technologies, Department of Physics and Electronics, Rhodes University, Grahamstown 6140, South Africa
[40] Max-Planck-Institut für Extraterrestrische Physik, Giessenbachstr. 1, D-85748 Garching, Germany
[41] Department of History of Science, Harvard University, Cambridge, MA 02138, USA
[42] Department of Physics, Harvard University, Cambridge, MA 02138, USA
[43] Department of Physics, University of Illinois, 1110 West Green St, Urbana, IL 61801, USA
[44] Department of Astronomy, University of Illinois at Urbana-Champaign, 1002 West Green Street, Urbana, Illinois 61801, USA
[45] Leiden Observatory—Allegro, Leiden University, P.O. Box 9513, 2300 RA Leiden, The Netherlands
[46] Key Laboratory for Research in Galaxies and Cosmology, Chinese Academy of Sciences, Shanghai 200030, People's Republic of China
[47] NOVA Sub-mm Instrumentation Group, Kapteyn Astronomical Institute, University of Groningen, Landleven 12, 9747 AD Groningen, The Netherlands
[48] Department of Astronomy, School of Physics, Peking University, Beijing 100871, People's Republic of China
[49] Kavli Institute for Astronomy and Astrophysics, Peking University, Beijing 100871, People's Republic of China
[50] Instituto Nacional de Astrofísica, Óptica y Electrónica. Apartado Postal 51 y 216, 72000. Puebla Pue., México
[51] The Institute of Statistical Mathematics, 10-3 Midori-cho, Tachikawa, Tokyo, 190-8562, Japan
[52] Department of Statistical Science, The Graduate University for Advanced Studies (SOKENDAI), 10-3 Midori-cho, Tachikawa, Tokyo 190-8562, Japan
[53] Kavli Institute for the Physics and Mathematics of the Universe, The University of Tokyo, 5-1-5 Kashiwanoha, Kashiwa, 277-8583, Japan
[54] Institute for Astrophysical Research, Boston University, 725 Commonwealth Ave., Boston, MA 02215, USA
[55] Astronomical Institute, St. Petersburg University, Universitetskij pr., 28, Petrodvorets,198504 St.Petersburg, Russia
[56] Joint Institute for VLBI ERIC (JIVE), Oude Hoogeveensedijk 4, 7991 PD Dwingeloo, The Netherlands
[57] Kogakuin University of Technology and Engineering, Academic Support Center, 2665-1 Nakano, Hachioji, Tokyo 192-0015, Japan
[58] Physics Department, National Sun Yat-Sen University, No. 70, Lien-Hai Rd, Kaosiung City 80424, Taiwan, R.O.C
[59] National Optical Astronomy Observatory, 950 North Cherry Ave., Tucson, AZ 85719, USA
[60] Key Laboratory for Particle Astrophysics, Institute of High Energy Physics, Chinese Academy of Sciences, 19B Yuquan Road, Shijingshan District, Beijing, People's Republic of China
[61] School of Astronomy and Space Science, Nanjing University, Nanjing 210023, People's Republic of China
[62] Key Laboratory of Modern Astronomy and Astrophysics, Nanjing University, Nanjing 210023, People's Republic of China
[63] Italian ALMA Regional Centre, INAF-Istituto di Radioastronomia, Via P. Gobetti 101, I-40129 Bologna, Italy
[64] Department of Physics, National Taiwan University, No.1, Sect.4, Roosevelt Rd., Taipei 10617, Taiwan, R.O.C

[65] Instituto de Radioastronomía y Astrofísica, Universidad Nacional Autónoma de México, Morelia 58089, México
[66] Instituto de Astronomía, Universidad Nacional Autónoma de México, CdMx 04510, México
[67] Yunnan Observatories, Chinese Academy of Sciences, 650011 Kunming, Yunnan Province, People's Republic of China
[68] Center for Astronomical Mega-Science, Chinese Academy of Sciences, 20A Datun Road, Chaoyang District, Beijing, 100012, People's Republic of China
[69] Key Laboratory for the Structure and Evolution of Celestial Objects, Chinese Academy of Sciences, 650011 Kunming, People's Republic of China
[70] Gravitation Astroparticle Physics Amsterdam (GRAPPA) Institute, University of Amsterdam, Science Park 904, 1098 XH Amsterdam, The Netherlands
[71] Centro Astronómico de Yebes (IGN), Apartado 148, E-19180 Yebes, Spain
[72] Department of Physics, Broida Hall, University of California Santa Barbara, Santa Barbara, CA 93106, USA
[73] Astronomy Department, Universidad de Concepción, Casilla 160-C, Concepción, Chile
[74] Department of Astronomy, University of Massachusetts, 01003, Amherst, MA, USA
[75] Department of Astronomy, Graduate School of Science, The University of Tokyo, 7-3-1 Hongo, Bunkyo-ku, Tokyo 113-0033, Japan
[76] Canadian Institute for Theoretical Astrophysics, University of Toronto, 60 St. George Street, Toronto, ON M5S 3H8, Canada
[77] Dunlap Institute for Astronomy and Astrophysics, University of Toronto, 50 St. George Street, Toronto, ON M5S 3H4, Canada
[78] Canadian Institute for Advanced Research, 180 Dundas St West, Toronto, ON M5G 1Z8, Canada
[79] Radio Astronomy Laboratory, University of California, Berkeley, CA 94720, USA
[80] CCS-2, Los Alamos National Laboratory, P.O. Box 1663, Los Alamos, NM 87545, USA
[81] Center for Theoretical Astrophysics, Los Alamos National Laboratory, Los Alamos, NM, 87545, USA
[82] Instituto de Radioastronomía Milimétrica, IRAM, Avenida Divina Pastora 7, Local 20, E-18012, Granada, Spain
[83] Consejo Nacional de Ciencia y Tecnología, Av. Insurgentes Sur 1582, 03940, Ciudad de México, México
[84] Hiroshima Astrophysical Science Center, Hiroshima University, 1-3-1 Kagamiyama, Higashi-Hiroshima, Hiroshima 739-8526, Japan
[85] Aalto University Department of Electronics and Nanoengineering, PL 15500, FI-00076 Aalto, Finland
[86] Aalto University Metsähovi Radio Observatory, Metsähovintie 114, FI-02540 Kylmälä, Finland
[87] Department of Astronomy, Yonsei University, Yonsei-ro 50, Seodaemun-gu, 03722 Seoul, Republic of Korea
[88] Netherlands Organisation for Scientific Research (NWO), Postbus 93138, 2509 AC Den Haag, The Netherlands
[89] Frontier Research Institute for Interdisciplinary Sciences, Tohoku University, Sendai 980-8578, Japan
[90] Astronomical Institute, Tohoku University, Sendai 980-8578, Japan
[91] Department of Physics and Astronomy, Seoul National University, Gwanak-gu, Seoul 08826, Republic of Korea
[92] Leiden Observatory, Leiden University, Postbus 2300, 9513 RA Leiden, The Netherlands
[93] Physics Department, Brandeis University, 415 South Street, Waltham, MA 02453, USA
[94] School of Physics, Huazhong University of Science and Technology, Wuhan, Hubei, 430074, People's Republic of China
[95] Mullard Space Science Laboratory, University College London, Holmbury St. Mary, Dorking, Surrey, RH5 6NT, UK
[96] School of Astronomy and Space Sciences, University of Chinese Academy of Sciences, No. 19A Yuquan Road, Beijing 100049, People's Republic of China
[97] Astronomy Department, University of Science and Technology of China, Hefei 230026, People's Republic of China
[98] University of Massachusetts Boston, 100 William T, Morrissey Blvd, Boston, MA 02125, USA
[99] ASTRON, Oude Hoogeveensedijk 4, 7991 PD Dwingeloo, The Netherlands
[100] Science Support Office, Directorate of Science, European Space Research and Technology Centre (ESA/ESTEC), Keplerlaan 1, 2201 AZ Noordwijk, The Netherlands
[101] University of Chicago, 5640 South Ellis Avenue, Chicago, IL 60637, USA
[102] Systems and Technology Research, 600 West Cummings Park, Woburn, MA 01801, USA

The Astrophysical Journal Letters, 875:L4 (52pp), 2019 April 10 https://doi.org/10.3847/2041-8213/ab0e85
© 2019. The American Astronomical Society.
OPEN ACCESS

First M87 Event Horizon Telescope Results. IV. Imaging the Central Supermassive Black Hole

The Event Horizon Telescope Collaboration
(See the end matter for the full list of authors.)

Received 2019 February 11; revised 2019 March 5; accepted 2019 March 6; published 2019 April 10

Abstract

We present the first Event Horizon Telescope (EHT) images of M87, using observations from April 2017 at 1.3 mm wavelength. These images show a prominent ring with a diameter of ∼40 μas, consistent with the size and shape of the lensed photon orbit encircling the "shadow" of a supermassive black hole. The ring is persistent across four observing nights and shows enhanced brightness in the south. To assess the reliability of these results, we implemented a two-stage imaging procedure. In the first stage, four teams, each blind to the others' work, produced images of M87 using both an established method (CLEAN) and a newer technique (regularized maximum likelihood). This stage allowed us to avoid shared human bias and to assess common features among independent reconstructions. In the second stage, we reconstructed synthetic data from a large survey of imaging parameters and then compared the results with the corresponding ground truth images. This stage allowed us to select parameters objectively to use when reconstructing images of M87. Across all tests in both stages, the ring diameter and asymmetry remained stable, insensitive to the choice of imaging technique. We describe the EHT imaging procedures, the primary image features in M87, and the dependence of these features on imaging assumptions.

Key words: black hole physics – galaxies: individual (M87) – galaxies: jets – techniques: high angular resolution – techniques: image processing – techniques: interferometric

1. Introduction

Since the discovery of the first astrophysical jet apparently connected to its nucleus (Curtis 1918), the giant elliptical galaxy M87 in the Virgo cluster has been intensively studied with imaging observations. M87's nuclear gas and stellar dynamics, as traced by optical and infrared (IR) spectroscopy, suggest the presence of a nuclear supermassive black hole (SMBH) of mass $M_{\rm BH} \sim (3.3\text{–}6.2) \times 10^9\, M_\odot$ (Macchetto et al. 1997; Gebhardt & Thomas 2009; Gebhardt et al. 2011; Walsh et al. 2013). This high mass, combined with its proximity ($D = 16.8$ Mpc; Blakeslee et al. 2009; Bird et al. 2010; Cantiello et al. 2018; see also EHT Collaboration et al. 2019e, hereafter Paper VI), implies that the nuclear black hole candidate in M87 (hereafter referred to as M87) has an event horizon subtending the second-largest known angular size after Sagittarius A* (Sgr A*) in the Galactic Center.

Unlike Sgr A*, M87 hosts a powerful kpc-long jet that is bright in the radio, optical, and X-ray bands (e.g., Owen et al. 1989; Sparks et al. 1996; Perlman et al. 1999; Marshall et al. 2002). Weak emission east of the very long baseline interferometry (VLBI) core from the expected counter-jet has also been detected in high-frequency VLBI images (Walker et al. 2018). Material moves down the approaching jet with a maximum apparent speed of ∼6c (Biretta et al. 1999). On pc and sub-pc scales, VLBI observations show the jet to be edge-brightened and parabolic in shape (Reid et al. 1989; Dodson et al. 2006; Kovalev et al. 2007; Asada & Nakamura 2012; Hada et al. 2013; Nakamura & Asada 2013; Asada et al. 2016) with a characteristic progressive acceleration downstream (Asada et al. 2014; Mertens et al. 2016; Britzen et al. 2017; Hada et al. 2017; Walker et al. 2018; Kim et al. 2018a). High-frequency astrometric VLBI measurements reveal a frequency-dependent shift of the radio core (from optical depth effects), which asymptotically converges to ∼40 microarcseconds (μas) east of the 7 mm core (Hada et al. 2011); this indicates that the jet is launched in the vicinity of the central black hole (e.g., Nakamura et al. 2018) residing within the central ∼100 μas. The high mass and relative proximity of M87 provides an opportunity to image this black hole and jet-launching region on event-horizon scales; however, accessing these scales with ground-based VLBI requires observations with microarcsecond resolution at a wavelength of $\lesssim$1 mm.

To this end, we have developed the Event Horizon Telescope (EHT), a global ad hoc VLBI array operating at 1.3 mm wavelength (EHT Collaboration et al. 2019b, hereafter Paper II). With its longest baselines spanning nearly the diameter of the Earth, the synthesized beam size of the EHT array is approximately 20 μas. For M87, the EHT beam size corresponds to 3–5 $R_{\rm s}$, where the Schwarzschild radius $R_{\rm s} = 2GM_{\rm BH}/c^2$ subtends 3.9–7.3 μas for the black hole mass range and distance given above. Thus, the EHT can potentially resolve general relativistic effects associated with the SMBH in M87, most notably the "shadow" cast by the black hole on the bright surrounding emission (Bardeen 1973; Luminet 1979; Falcke et al. 2000). This shadow is expected to be encircled by a bright ring at the radius of the lensed photon sphere, with a diameter between approximately 4.8 and 5.2 $R_{\rm s}$ for a maximally spinning black hole (viewed face-on) and a non-spinning (i.e., Schwarzschild) black hole, respectively (Bardeen 1973; Johannsen & Psaltis 2010). For M87, the expected shadow diameter is 19–38 μas. Physical models and general relativistic magnetohydrodynamic (GRMHD) simulations show that Doppler-boosted emission from rapidly rotating material near the black hole can result in substantial image brightness asymmetry very near the ring (EHT Collaboration et al. 2019d, hereafter Paper V).

Original content from this work may be used under the terms of the Creative Commons Attribution 3.0 licence. Any further distribution of this work must maintain attribution to the author(s) and the title of the work, journal citation and DOI.

Early EHT observations in 2009 and 2012 detected compact emission with an FWHM size of approximately 40 μas (Doeleman et al. 2012; Akiyama et al. 2015). However, because of their limited interferometric baseline coverage, these early experiments could not synthesize an image of M87, leaving considerable uncertainty about the nature of the detected emission.

In 2017 April, the EHT conducted an observing campaign using eight stations in six geographic sites.[105] The EHT observed M87 on four days (April 5, 6, 10, and 11), interleaved with observations of other targets. Notably, these observations included 37 telescopes of the Atacama Large Millimeter/submillimeter Array (ALMA) coherently combined to act as a single 73 m diameter telescope (Matthews et al. 2018). The addition of baselines to ALMA significantly increases the sensitivity of the entire EHT array. Additional details of the EHT instrument are given in Paper II; details of the 2017 observations, correlation, and calibration are given in EHT Collaboration et al. (2019c, hereafter Paper III).

We generated images of M87 from the 2017 EHT data in two stages. In the first stage, our aim was to compare the results of four independent imaging teams. Each team used their collective judgment to produce an image, while remaining blind to the others' work. In the second stage, our aim was to minimize reliance on expert judgment, and we instead utilized three imaging pipelines to perform large searches over the imaging parameter spaces. We then selected fiducial imaging parameters for M87 from these searches based on the performance of the parameters when reconstructing images from synthetic data. In both stages, the reconstructed images were consistently dominated by a single feature: a bright ring with a $\sim$40 μas diameter and azimuthal brightness asymmetry, consistent with the shadow of a $\sim 6.5 \times 10^9\, M_\odot$ SMBH in the nucleus of M87.

This Letter presents details of this imaging procedure and analysis; our primary images of M87 are shown in Figures 11 and 15. We begin, in Section 2, by providing a brief review of interferometric measurements and imaging techniques. In Section 3, we describe the EHT observations of M87 in 2017. In Section 4, we estimate image properties for M87 such as total compact flux density and size of the emission region using a non-imaging analysis of the EHT data in combination with results from VLBI imaging of M87 at longer wavelengths. In Section 5, we present the first reconstructed EHT images, generated by four separate imaging teams working independently. In Section 6, we derive fiducial imaging parameters for three different imaging pipelines by performing large parameter surveys and testing on synthetic data. In Section 7, we show the corresponding fiducial images from each pipeline, and we assess their properties and uncertainties in the image and visibility domains. In Section 8, we perform validation tests of the fiducial images via comparisons of gain solutions with the simultaneously observed target 3C 279 and by exploring the dependence of reconstructed images on the participation and calibration of each site. In Section 9, we give a quantitative analysis of the image and ring properties. In Section 10, we summarize our results.

2. Background

Every antenna i in an interferometric array records the incoming complex electric field as a function of time, frequency, and polarization: $E_i(t, \nu, P)$. Every pair of sites (i, j) then gives an interferometric visibility, defined as the complex cross-correlation between their recorded electric fields,

$$V_{ij}(t, \nu, P_1, P_2) = \langle E_i(t, \nu, P_1) E_j^*(t, \nu, P_2) \rangle. \quad (1)$$

In practice, radio telescopes record data in dual circular feeds, right circular polarization (RCP) and left circular polarization (LCP), or in an orthogonal linear basis. The set of four possible cross-correlations among the two recorded polarizations at the two sites then provides information about the four Stokes parameters (see, e.g., Roberts et al. 1994). Because this Letter is focused on monochromatic and total intensity imaging, we will suppress the frequency and polarimetric parameters for the remainder of our discussion.

By the van Cittert–Zernike theorem (van Cittert 1934; Zernike 1938), the visibility measured with an ideal interferometer is related to the brightness distribution on the sky $I(x, y)$ via a simple Fourier transform. The interferometer samples a spatial frequency of the image given by the vector baseline $\boldsymbol{b}_{ij}$ joining the sites, projected orthogonal to the line of sight and measured in wavelengths: $\boldsymbol{u}_{ij} = \boldsymbol{b}_{\perp,ij}/\lambda$, where $\lambda = c/\nu$. For a pair of telescopes at fixed locations on the Earth, their projected baseline coordinates (u, v) trace an ellipse as the Earth rotates, sampling a range of spatial frequencies (Thompson et al. 2017). Generalizing to an arbitrary projected baseline $\boldsymbol{u} = (u, v)$, the ideal visibility $\mathcal{V}$ is given by

$$\mathcal{V}(u, v) = \iint e^{-2\pi i(ux+vy)} I(x, y)\, dx\, dy. \quad (2)$$

In this expression, x and y are angular coordinates on the sky in radians. Equation (2) assumes that the source radiation is spatially incoherent and in the far-field limit. It also assumes that the sky brightness distribution is only non-zero within both a radian and the primary beams of the individual telescopes. All of these criteria are satisfied for EHT observations.[106] In the remainder of this section, we describe the specific interferometric data products used for imaging from EHT data, and we discuss how these data products are affected by practical measurement limitations (Section 2.1). We then summarize the primary methods used to reconstruct images from interferometric data (Section 2.2). For a comprehensive discussion of the EHT data reduction pipeline, see Paper III.

2.1. VLBI Data Products and Their Uncertainties

In practice, each measured visibility is contaminated by thermal noise, station-dependent errors, and baseline-dependent errors. However, some combinations of visibilities (so-called "closure" quantities) can be used to construct data products that are independent of station-dependent errors. We now discuss these various data products and define how they will be used to assess consistency between a trial image I and the data.

2.1.1. Interferometric Visibilities

The fundamental interferometric data product is the complex visibility, V_{ij} (see Equation (1)). Each visibility is complex-valued and obeys a conjugation relationship under baseline reversal, $V_{ij} = V_{ji}^*$. Thus, an $N_{\rm el}$-element array samples at most $N_{\rm el}(N_{\rm el} - 1)/2$ different visibilities at each time.

[105] M87 (J2000 decl. of $+12°23'28''$) is not visible to one of the EHT stations, the South Pole Telescope (SPT).

[106] EHT baselines are sensitive to image structure subtending $\lesssim$100 μas $\approx 5 \times 10^{-10}$ radians (Section 4.4).

Visibility measurements have a simple thermal error budget. Neglecting errors in calibration (Section 2.1.2), the measured visibility V_{ij} on a baseline $\boldsymbol{u}_{ij}$ is given by the true visibility $\mathcal{V}_{ij} = \mathcal{V}(\boldsymbol{u}_{ij})$ plus baseline-dependent thermal noise ϵ_{ij}: $V_{ij} = \mathcal{V}_{ij} + \epsilon_{ij}$. For perfect coherent averaging, the thermal noise on measurements obeys a complex normal distribution, with equal variance on the real and imaginary parts. The thermal noise standard deviation, σ_{ij}, is related to the system equivalent flux densities (SEFDs) of the two sites, the bandwidth $\Delta\nu$, and the coherent integration time Δt:

$$\sigma_{ij} = \frac{1}{\eta_{\rm Q}}\sqrt{\frac{{\rm SEFD}_i \times {\rm SEFD}_j}{2\,\Delta\nu\,\Delta t}}, \tag{3}$$

where $\eta_{\rm Q}$ is a factor that accounts for sensitivity loss from quantization of the incident electric field. The EHT utilizes standard 2-bit recording, for which $\eta_{\rm Q} = 0.88$ (Thompson et al. 2017).

We quantify agreement between a trial image I and a set of measured visibilities using the mean squared standardized residual. Specifically, for a measured set of $N_{\rm V}$ visibilities, we define

$$\chi^2_{\rm vis}(I) = \frac{1}{2N_{\rm V}}\sum \frac{|\hat{V} - V|^2}{\sigma^2}, \tag{4}$$

where $\hat{V}$ denotes a model visibility corresponding to the trial image, and the sum ranges over all measured visibilities (which may include different baselines, times, and frequencies). The quantity $\chi^2_{\rm vis}$ does not formally correspond to a reduced χ^2, and its interpretation requires caution. For example, we do not include a correction for the effective number of image degrees of freedom, and the results can be sensitive to data processing procedures such as self-calibration. Nevertheless, we expect $\chi^2_{\rm vis} \approx 1$ for final imaging results.

We also use a mean squared standardized residual to quantify agreement between a trial image and a set of measured visibility amplitudes:

$$\chi^2_{\rm amp}(I) = \frac{1}{N_{\rm V}}\sum \frac{|\hat{A} - A|^2}{\sigma^2}, \tag{5}$$

where $\hat{A} = |\hat{V}|$ denotes a model visibility amplitude, and

$$A = \sqrt{(|V|^2 - \sigma^2)\Theta(|V| - \sigma)} \tag{6}$$

is a measured visibility amplitude after correcting for an upward bias from thermal noise. Here, the Heaviside Θ-function ensures that the debiased amplitudes are always real and positive.

2.1.2. Closure Quantities

In addition to thermal noise, measured visibilities have systematic errors on both their amplitudes and phases. These errors can often be factorized into multiplicative station-based "gains," which are complex-valued and may vary in both time and frequency. In general, these gains act as linear transformations of the incident polarized electric fields at each site; here, we focus on a simpler model using scalar electric fields. These complex systematic errors modify the relationship between a measurement V_{ij} and the corresponding ideal visibility $\mathcal{V}_{ij}$ as

$$V_{ij} \approx g_i g_j^* \mathcal{V}_{ij} + \epsilon_{ij}, \tag{7}$$

where ϵ_{ij} is the thermal noise. Equation (7) is an approximation, as it neglects cross-talk between orthogonal receivers, the non-factorizability of the station-dependent bandpass after frequency averaging, the non-factorizability of station-dependent temporal fluctuations after coherent averaging, and other imperfections. We discuss these imperfections and their implications for the EHT error budget in Section 4.2 (for a comprehensive discussion, see Paper III).[107]

The site dependence of the gains allows for the construction of data products that are insensitive to these systematic errors. Such quantities are called "closure" quantities. For instance, the sum of three visibility phases $\psi = \arg(V)$ around a directed triangle i–j–k of sites is insensitive to the phase of the complex station-based gains g_i. Namely, neglecting thermal noise,

$$\psi_{{\rm C},ijk} = \psi_{ij} + \psi_{jk} + \psi_{ki} = \Psi_{ij} + \Psi_{jk} + \Psi_{ki}, \tag{8}$$

where $\Psi = \arg(\mathcal{V})$ is the phase of the ideal visibility. This phase $\psi_{{\rm C},ijk}$ is called the closure phase of the i–j–k triangle (Jennison 1958). Because phase stability is challenging for millimeter VLBI, closure phase is a useful measurement of intrinsic source phase. For an $N_{\rm el}$-element interferometer, there are $N_{\rm el}(N_{\rm el}-1)(N_{\rm el}-2)/6$ closure phase measurements, but only $(N_{\rm el}-1)(N_{\rm el}-2)/2$ of these are non-redundant.

When the signal-to-noise ratio (S/N) of each component visibility is at least $\sim$3, closure phase errors are well approximated as Gaussian and depend only on the three component S/N values S (e.g., Rogers et al. 1995):

$$\sigma_{\psi_{\rm C},ijk} \approx \sqrt{S_{ij}^{-2} + S_{jk}^{-2} + S_{ki}^{-2}}. \tag{9}$$

In this expression, $\sigma_{\psi_{\rm C}}$ is the closure phase standard deviation in radians.

We compute $\chi^2_{\rm CP}$ statistics to quantify image-data agreement analogously to Equation (4):

$$\chi^2_{\rm CP}(I) = \frac{1}{N_{\psi_{\rm C}}}\sum \frac{|e^{i\hat{\psi}_{\rm C}} - e^{i\psi_{\rm C}}|^2}{\sigma^2_{\psi_{\rm C}}}, \tag{10}$$

where $\hat{\psi}_{\rm C}$ denotes a model closure phase from the trial image, $N_{\psi_{\rm C}}$ is the number of closure phases in the sum, and the sum ranges over all measurements (which may include different triangles, times, and frequencies).

Similar to closure phase, certain combinations of four visibility amplitudes on a quadrangle $ijk\ell$ are insensitive to gain amplitudes $|g_i|$. For example, neglecting thermal noise,

$$A_{{\rm C},ijk\ell} = \frac{A_{ij}A_{k\ell}}{A_{ik}A_{j\ell}} = \frac{\mathcal{A}_{ij}\mathcal{A}_{k\ell}}{\mathcal{A}_{ik}\mathcal{A}_{j\ell}}, \tag{11}$$

where $\mathcal{A} = |\mathcal{V}|$. Such combinations $A_{{\rm C},ijk\ell}$ are called closure amplitudes (Twiss et al. 1960). While $N_{\rm el}$ sites give at most $N_{\rm el}(N_{\rm el}-1)(N_{\rm el}-2)(N_{\rm el}-3)/8$ closure amplitudes, only $N_{\rm el}(N_{\rm el}-3)/2$ of these are non-redundant. Also, while the noise statistics of closure amplitudes are approximately Gaussian if each of the four amplitudes has high S/N, the distribution is highly non-Gaussian when any of the measurements is low S/N, especially those in the denominator (L. Blackburn et al. 2019, in preparation; A. E. Broderick et al. 2019, in preparation). To

[107] Note that the simulated data used later in this Letter do not use the simplified Equation (7) but instead employ a full Jones matrix formulation (Appendix C).

mitigate this behavior and to symmetrize the properties of numerator and denominator terms, we use the logarithm of the closure amplitudes, $\ln A_{\rm C}$, for analysis. We compute $\chi^2_{\log {\rm CA}}$ statistics as

$$\chi^2_{\log {\rm CA}}(I) = \frac{1}{N_{\ln {\rm A_C}}} \sum \frac{|\ln \hat{A}_{\rm C} - \ln A_{\rm C}|^2}{\sigma^2_{\ln {\rm A_C}}}, \tag{12}$$

where the uncertainty on the log closure amplitude is, in the high-S/N limit,

$$\sigma_{\ln A_{\rm C}, ijk\ell} \approx \sqrt{S_{ij}^{-2} + S_{k\ell}^{-2} + S_{ik}^{-2} + S_{j\ell}^{-2}}. \tag{13}$$

Note that closure quantities are generally not independent, and their uncertainties are only approximately Gaussian.

2.2. Interferometric Imaging Methods

Because an interferometer incompletely samples the visibility domain, the inverse problem of determining an image from a measured set of visibilities is ill-posed. Consequently, reconstructed images are not unique—they always require information, assumptions, or constraints beyond the interferometer measurements. One strong imaging constraint is image positivity. A second strong constraint is a restricted field of view (FOV) for the reconstructed image (i.e., the gridded FOV).[108] The choice of FOV must be made with care, as incorrect restrictions can result in false image structure. Imaging algorithms can additionally impose or favor other physically motivated properties related to the image (e.g., image smoothness) or to the instrument (e.g., a maximal resolution of reconstructed features).

Imaging algorithms can be broadly categorized into two methodologies: inverse modeling and forward modeling. The former includes deconvolution methods such as CLEAN (Högbom 1974; Clark 1980), while the latter includes regularized maximum likelihood (RML) methods such as the classical maximum entropy method (MEM; e.g., Narayan & Nityananda 1986). We now discuss each of these in more depth, with an emphasis on aspects and algorithms that are most relevant for EHT imaging.

2.2.1. Imaging via Inverse Modeling

Conventional inverse modeling approaches to imaging typically begin with an inverse Fourier transform of the sampled visibilities (giving the so-called "dirty image"). They then deconvolve the effects associated with the limited baseline coverage (giving the so-called "dirty beam"). For both VLBI and connected-element radio interferometry, the standard reconstruction algorithm in this category is CLEAN (e.g., Högbom 1974; Schwarz 1978; Clark 1980; Schwab 1984; Cornwell et al. 1999; Cornwell 2008).

The classical CLEAN algorithm (Högbom 1974; Clark 1980) models the image as a collection of point sources and determines the locations and flux densities of these point sources iteratively. After reaching a specified stopping criterion, CLEAN typically convolves the many-point-source image model with a "clean beam." This beam is obtained by matching a Gaussian to the central component of the dirty beam, and it approximates the point-spread function of the interferometric data. However, it is the *unconvolved* point-source model that is compared with the data to assess goodness of fit; the beam-convolved image displayed will not fit the measured visibility amplitudes.

Lack of absolute phase information and a priori calibration uncertainties in EHT measurements require multiple consecutive iterations of CLEAN followed by self-calibration, a routine that solves for station gains to maximize consistency with visibilities of a specified trial image (Wilkinson et al. 1977; Readhead et al. 1980; Cornwell & Wilkinson 1981; Pearson & Readhead 1984; Cornwell & Fomalont 1999). For the CLEAN imaging in this Letter, we used the `DIFMAP` software (Shepherd 1997, 2011).

2.2.2. Imaging via Forward Modeling

Forward modeling approaches to imaging usually represent the image as an array of pixels and only require a Fourier transform of this array to evaluate consistency between the image and data. These methods can easily integrate nonlinear image-data consistency measures and constraints on the reconstructed image properties, such as sparsity or smoothness. While these types of imaging algorithms have been developed for decades (e.g., Frieden 1972; Gull & Daniell 1978; Cornwell & Evans 1985; Narayan & Nityananda 1986; Briggs 1995; Wiaux et al. 2009a, 2009b) and are commonly utilized in optical interferometry (e.g., Buscher 1994; Baron et al. 2010; Thiébaut 2013; Thiébaut & Young 2017), they are used less frequently than CLEAN for radio interferometry. However, forward modeling methods have been intensively developed for the EHT (e.g., Honma et al. 2014; Bouman et al. 2016, 2018; Chael et al. 2016, 2018; Ikeda et al. 2016; Akiyama et al. 2017a, 2017b; Johnson et al. 2017; Kuramochi et al. 2018).

These methods are often derived using probabilistic arguments, although they do not typically produce results that have formal probabilistic interpretations. The general approach in this type of imaging is to find the image I that minimizes a specified objective function,

$$J(I) = \sum_{\text{data terms}} \alpha_D \chi^2_D(I) - \sum_{\text{regularizers}} \beta_R S_R(I). \tag{14}$$

In this expression, each χ^2_D is a goodness-of-fit function corresponding to the data term D (Section 2.1), and each S_R is a regularization term corresponding to the regularizer R (Appendix A). The "hyperparameters" α_D and β_R control the relative weighting of the data and regularization terms. Placing too much weight on the regularization terms will result in final reconstructed images that are not acceptably compatible with the data (i.e., the image will not achieve $\chi^2_D \sim 1$ for all data terms). Because this function is analogous to the log-likelihood of a posterior probability function, we refer to this category of imaging methods as RML methods.

Regularizers explored in VLBI include image entropy (e.g., Narayan & Nityananda 1986), smoothness (e.g., Bouman et al. 2016; Chael et al. 2016; Kuramochi et al. 2018), and sparsity in the image or its gradient domain (e.g., Wiaux et al. 2009a, 2009b; Honma et al. 2014; Akiyama et al. 2017b). Regularizing functions can be combined; e.g., simultaneously favoring both sparsity and smoothness through regularization can

[108] The $\mathrm{FOV_{arr}}$ of an interferometric array depends on the primary beams of the antennas and the averaging time and bandwidth (Thompson et al. 2017). For VLBI, $\mathrm{FOV_{arr}}$ is usually substantially larger than the FOV of reconstructed images. Throughout this Letter, we will exclusively use FOV to refer to the angular extent of reconstructed images.

mitigate limitations of using only one or the other (e.g., Akiyama et al. 2017a).

Note that while regularization is an important choice in RML methods, other decisions such as data preparation, the optimization methodology, and the FOV of the reconstructed image can be equally important in influencing the final image. Unlike CLEAN, no final restoring beam is required when using RML, and these methods often achieve a modest degree of "super resolution" (i.e., finer than the nominal diffraction limit, $\theta \sim \lambda/|\boldsymbol{u}|_{\max}$).

For the EHT, RML methods mitigate some difficulties of CLEAN reconstructions through increased flexibility in the data products used for imaging. For instance, RML methods can directly fit to robust data products such as closure quantities (e.g., Buscher 1994; Baron et al. 2010; Bouman et al. 2016; Chael et al. 2016, 2018; Akiyama et al. 2017a, 2017b). However, RML methods often introduce other difficulties, such as requiring the solution to a complex nonlinear optimization problem (minimizing Equation (14)). As with CLEAN, RML methods sometimes employ an iterative imaging loop, alternately imaging and then self-calibrating the data. For the RML reconstructions in this Letter, we used two open-source software libraries that have been developed specifically for the EHT: `eht-imaging`[109] (Chael et al. 2016, 2018, 2019) and `SMILI`[110] (Akiyama et al. 2017a, 2017b, 2019). Appendix A gives definitions of the regularizers used throughout this Letter, as implemented in these libraries.

3. Observations and Data Processing

3.1. EHT Observations and Data

The EHT observed M87 with seven stations at five geographic sites on 2017 April 5, 6, 10, and 11. The participating facilities were the phased Atacama Large Millimeter/submillimeter Array (ALMA) and Atacama Pathfinder Experiment telescope (APEX) in the Atacama Desert in Chile, the James Clerk Maxwell Telescope (JCMT) and the phased Submillimeter Array (SMA) on Maunakea in Hawai'i, the Arizona Radio Observatory Sub-Millimeter Telescope (SMT) on Mt. Graham in Arizona, the IRAM 30 m (PV) telescope on Pico Veleta in Spain, and the Large Millimeter Telescope Alfonso Serrano (LMT) on Sierra Negra in Mexico. These observations of M87 were interleaved with other targets (e.g., the quasar 3C 279), some of which were visible to an eighth EHT station, the South Pole Telescope (SPT).

Data were recorded in two polarizations and two frequency bands. All sites except ALMA and the JCMT recorded dual circular polarization (RCP and LCP). ALMA recorded dual linear polarization that was later converted to a circular basis via `PolConvert` (Martí-Vidal et al. 2016; Matthews et al. 2018; Goddi et al. 2019), and the JCMT recorded a single circular polarization (the recorded polarization varied from day to day).[111] All sites recorded two 2 GHz bands centered on 227.1 and 229.1 GHz (henceforth, low and high band, respectively). Paper II provides details on the setup, equipment, and station upgrades leading up to the 2017 observations.

Paper III outlines the correlation, calibration, and validation of these data. In particular, the data reduction utilized the sensitive baselines to ALMA to estimate and correct for stable instrumental phase offsets, RCP–LCP delays, and stochastic phase variations within scans. After these corrections, the data have sufficient phase stability to coherently average over scans. The data were also amplitude calibrated using station-specific measurements; stations with an intra-site partner (i.e., ALMA, APEX, SMA, and JCMT) were then "network calibrated" to further improve the amplitude calibration accuracy and stability via constraints among redundant baselines. The final network-calibrated data sets were frequency averaged per band and coherently averaged in 10 s intervals before being used for our imaging analysis. All data presented and analyzed in this work are Stokes I (or pseudo I) visibilities processed via the EHT–Haystack Observatory Processing System (HOPS) pipeline (Paper III; Blackburn et al. 2019). Information about accessing SR1 data and the software used for analysis can be found on the Event Horizon Telescope website's data portal.[112]

3.2. Data Properties

Figure 1 shows the baseline (u, v) coverage for EHT observations of M87. The shortest baselines in the EHT are intra-site (i.e., the SMA and JCMT are separated by 0.16 km; ALMA and APEX are separated by 2.6 km). These intra-site baselines are sensitive to arcsecond-scale structure (see Section 4.3). In contrast, our longest baselines (joining the SMA or JCMT to PV) are sensitive to microarcsecond-scale structure. Baseline coverage on individual days (bottom panels of Figure 1) is comparable for April 5, 6, and 11 (18, 25, and 22 scans, respectively). However, April 10 had significantly less coverage, with only 7 scans.

Figure 2 (left panel) shows the S/N as a function of baseline length for M87 on April 11, after coherently averaging scans. The split in S/N distributions at various baseline lengths is due to the sharp difference in sensitivity for the co-located Atacama sites ALMA and APEX. The right panel of Figure 2 shows the visibility amplitude (correlated flux density) for M87 on April 11 after amplitude and network calibration.

There is a prominent secondary peak in the network-calibrated visibility amplitudes between two deep minima ("nulls"), the first at $\sim$3.4 Gλ and the second at $\sim$8.3 Gλ. The amplitudes along the secondary peak are weakly dependent on baseline position angle, suggesting some degree of source symmetry, and their overall trends are consistent for all days (see Paper III, Figure 13). However, evidence for source anisotropy can be seen at the location of the first null, where the east–west oriented Hawai'i–LMT baseline gives significantly lower amplitudes than the north–south oriented ALMA–LMT baseline at the same projected baseline length (see also Paper VI). This anisotropy is further supported by multiple measurements of non-zero closure phase (Figure 3). The majority of notable low-amplitude outliers across days are due to reduced performance of the JCMT or the LMT on a select number of scans. Despite the amplitudes of these data being low, the derived closure quantities remain stable (Paper III).

Similarly, most closure quantities for M87 are broadly consistent across all days, although day-to-day variations are significant for some sensitive closure combinations involving

[109] https://github.com/achael/eht-imaging

[110] https://github.com/astrosmili/smili

[111] Because the JCMT recorded a single circular polarization, baselines to JCMT use Stokes "pseudo I." Namely, we use parallel-hand visibilities to approximate Stokes I under the assumption that the source is weakly circularly polarized.

[112] https://eventhorizontelescope.org/for-astronomers/data

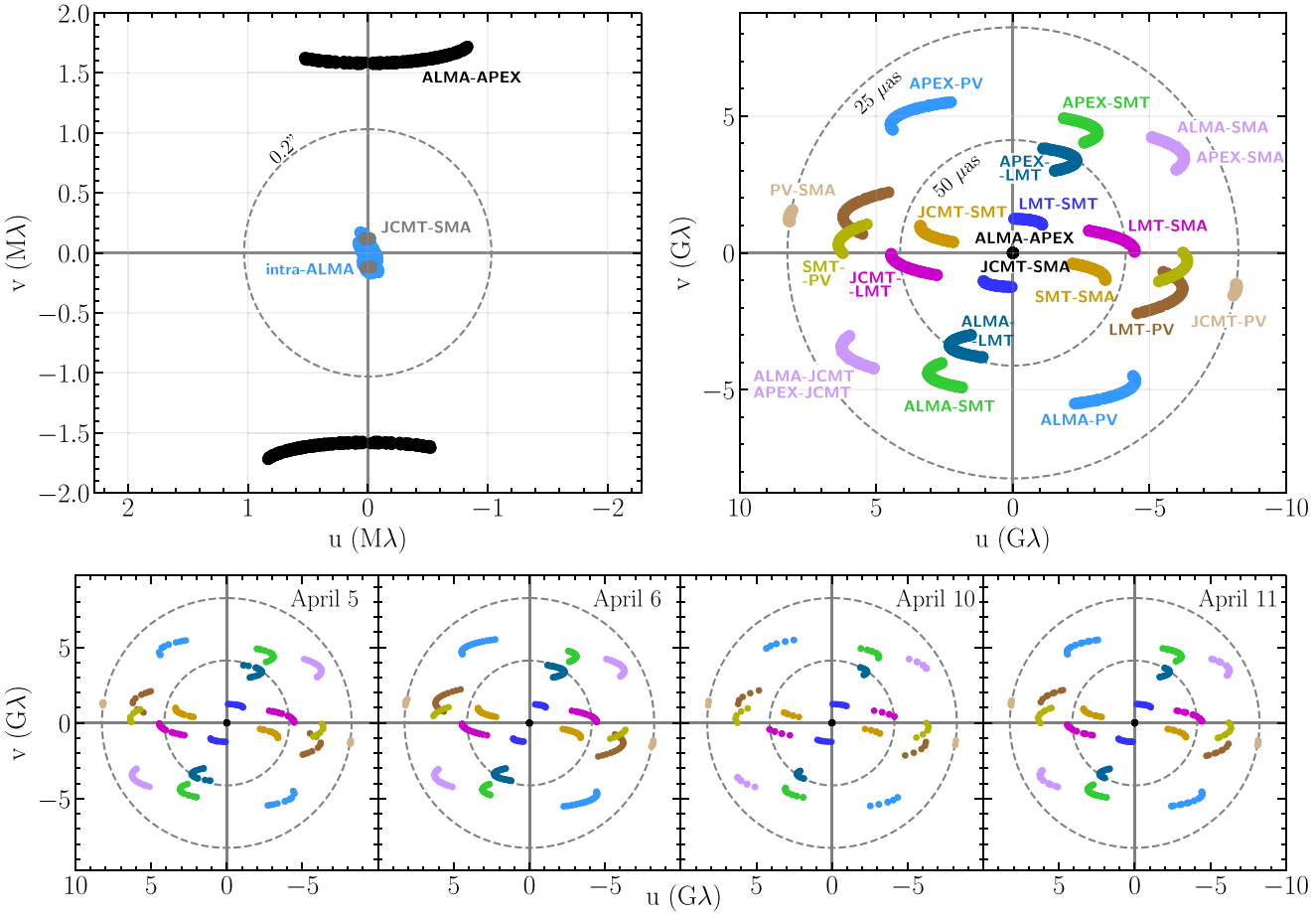

Figure 1. Top panels: aggregate baseline coverage for EHT observations of M87, combining observations on all four days. The left panel shows short-baseline coverage, comprised of ALMA interferometer baselines and intra-site EHT baselines (SMA–JCMT and ALMA–APEX). These short baselines probe angular scales larger than 0.1". The right panel shows long-baseline coverage, comprised of all inter-site EHT baselines. These long baselines span angular scales from 25 to 170 μas. Each point denotes a single scan, which range in duration from 4 to 7 minutes. Bottom panels: the full baseline coverage on M87 for each observation. In all panels, the dashed circles show baseline lengths corresponding to the indicated fringe spacings (0.2" for the upper-left panel; 25 and 50 μas for the remaining panels).

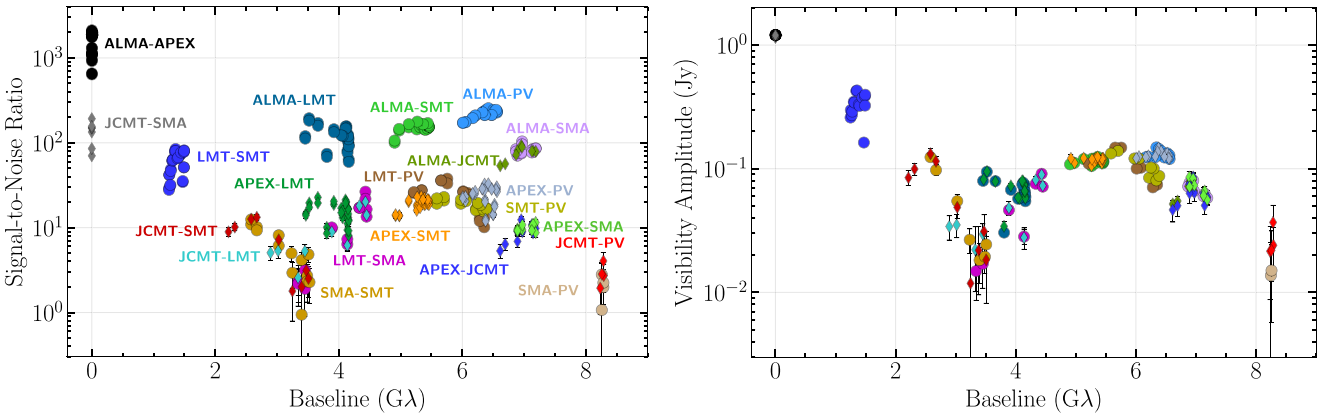

Figure 2. Left panel: S/N as a function of projected baseline length for EHT observations of M87 on April 11. Each point denotes a visibility amplitude coherently averaged over a full scan (4–7 minutes). Points are colored by baseline. Right panel: visibility amplitudes (correlated flux density) as a function of projected baseline length after a priori and network calibration. The amplitudes are corrected for upward bias from thermal noise (Equation (6)). Error bars denote $\pm 1\sigma$ uncertainty from thermal noise and do not include expected uncertainties in the a priori calibration (see Paper III and Section 4.1).

long baselines to PV or to the Hawai'i stations. Figure 3 shows examples of closure phases for various triangles and levels of variability: a "trivial" triangle including co-located sites (ALMA–APEX–SMT, left panel) that is expected to be consistent with zero, a non-trivial and mostly non-variable triangle (ALMA–LMT–SMT, center panel) with largely persistent structure across all days, and a non-trivial triangle (LMT–SMA–SMT, right panel) showing intrinsic source structure evolution in M87 between the two sets of observations on April 5, 6 and 10, 11.

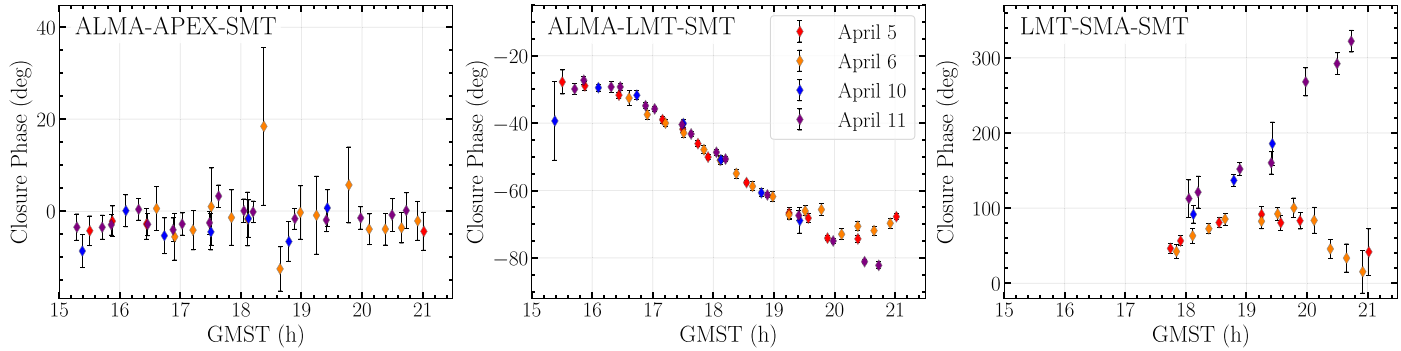

Figure 3. Selected closure phases from coherently averaged visibilities on three triangles as a function of Greenwich Mean Sidereal Time (GMST) using data from all four days. Error bars denote $\pm 1\sigma$ uncertainties from thermal noise. The trivial ALMA–APEX–SMT triangle (left panel) has closure phases near zero on all days, as expected because this triangle includes an intra-site baseline. Deviations from zero arise from a combination of thermal and systematic errors (Paper III). The ALMA–LMT–SMT triangle (middle panel) shows persistent structure across all days, while the large LMT–SMA–SMT triangle (right panel) shows source evolution between the first two days and last two days.

4. Pre-imaging Considerations

In this section, we analyze the measured M87 visibilities directly to assess what conclusions are supported by the data irrespective of choices made in the imaging procedures. This non-imaging analysis provides estimates of the quality of the a priori calibration, the level of non-closing systematic errors, and the degree of temporal variability in the source. It also guides the generation of realistic synthetic data sets (Section 6.1) and motivates the choice of imaging parameters (e.g., the FOV of reconstructed images) used to define parameter ranges in the imaging parameter surveys (Section 6.2).

4.1. Expected Amplitude Calibration Limitations

The amplitude calibration error budget is determined from uncertainties on individual measurements of station performance, as described in Paper III. The error budget is only representative of global station performance and is not specified for individual measurements. While this procedure is adequate for stations with stable performance and weather during the observing run, the error budget may be underestimated for stations with variable performance. The SMT, PV, SMA, JCMT, APEX, and ALMA stations are well characterized either through years of studies or via network calibration. More recent additions to the EHT (the LMT and the SPT) may have more variable behavior, as their observing systems are not yet well exercised and because they do not have sufficiently close sites to permit network calibration.

Specifically for M87, the LMT is the most under-characterized station. The LMT began observing M87 in the evening, when the dish is still affected by thermal gradients in the back-up structure or panel distortions from daytime heating, both of which are significant for open-air telescopes. These effects are common for sensitive millimeter-wave dishes and cause surface instability. In addition, evening conditions are inadequate for accurate pointing and focusing of the telescope (particularly on weaker sources), leading to performance that can vary substantially across scans and from day to day. A defocused dish can measure persistently low amplitudes on baselines to that station between focus attempts (typically every one to two hours). Changes in telescope pointing can cause amplitudes to fluctuate significantly from scan to scan (from the telescope moving to and from the source) and between pointing attempts (typically every half-hour). Issues in telescope focus can also lead to uncertainties in the a priori calibration for other sources observed during the same time period, such as 3C 279. However, pointing errors for 3C 279 are expected to be less severe, as it is bright enough for the LMT to point directly on-source prior to VLBI scans. Thus, the corrections needed for the LMT are expected to better match the a priori amplitude error budget during observations of 3C 279 (mostly correcting for focus errors) than during observations of M87 (correcting for both focus and pointing errors).

In Section 8.1 and Appendix F, we compare estimated residual gains for the SMT and the LMT from imaging M87 and 3C 279. In Paper VI, we compare these results with the estimated residual gains when fitting parametric models to the interferometric data.

4.2. Estimates of Non-closing Systematic Errors

Apart from the thermal errors, which are well understood and can be evaluated from first principles, there are several sources of additional systematic error present in the EHT data. These include polarimetric leakage (proportional to the magnitude of station-dependent leakage terms and the source fractional polarization), residual polarimetric-gain calibration offsets, loss of amplitude with long coherent averaging, the effects of biased S/N estimators, and the limitations of a linear error propagation model for closure quantities.

These systematic errors can affect both visibilities and closure quantities. While these effects are small, in a very high S/N regime systematic uncertainties may dominate over thermal uncertainties. In Paper III, we quantified the magnitude of systematic uncertainties in the EHT 2017 data both with a series of statistical tests on the distributions of trivial closure quantities and with cross-validation tests of data products across different frequency bands and polarizations. For M87, the characteristic magnitude of systematic errors was found to be only a fraction of the thermal errors, even for heavily averaged data. In the case of 3C 279, which has significant intrinsic polarization, systematic errors can dominate over the thermal errors. In both cases the characteristic magnitudes are small: less than 2° for closure phases, and less than 4% for closure amplitudes.

4.3. Constraints on the Total Compact Flux Density

EHT baselines sample angular scales in M87 that span nearly five orders of magnitude. The largest gap in coverage

occurs between the arcsecond scales sampled by intra-site baselines (ALMA–APEX and SMA–JCMT) and the microarcsecond scales sampled by inter-site baselines. The intra-site baselines are insensitive to detailed structure on microarcsecond scales; their measurements are consistent with an unresolved point source having ∼1.2 Jy of flux density (i.e., the "core" of M87, corresponding to the bright, upstream end of the jet) in addition to faint compact features in the large-scale jet of M87, such as "Knot A" (Owen et al. 1989). Long inter-site baselines resolve out much of this emission, and are sensitive to only the compact central source. The shortest inter-site EHT baseline is SMT–LMT, which has a fringe spacing of 139–166 μas for M87. Thus, there are two relevant estimates of the total flux density: the total flux density seen in the core on arcsecond scales, $F_{\rm tot} \approx 1.2$ Jy, and the total compact flux density, $F_{\rm cpct} \leqslant F_{\rm tot}$, which is the relevant quantity for the integrated flux density of a reconstructed image with an FOV limited to only a few hundred microarcseconds.

In Appendix B, we derive a series of constraints on $F_{\rm cpct}$ using the 2017 EHT data and quasi-simultaneous observations at longer wavelengths. These constraints depend on the effective size of the compact emission region (expressed as an equivalent Gaussian FWHM). We also compare these constraints with the estimates of source size and compact flux density reported in Doeleman et al. (2012) and Akiyama et al. (2015) from observations of M87 in 2009 and 2012, respectively. These previous results used a three-site array, which included the Combined Array for Research in Millimeter-wave Astronomy (CARMA; in California) in addition to the SMT, JCMT, and SMA. The addition of CARMA provided a short inter-site baseline (SMT–CARMA, with $|\boldsymbol{u}| \sim 0.6$ Gλ), while the two remaining baselines, SMT–JCMT/SMA and CARMA–JCMT/SMA, sampled $2.2 < |\boldsymbol{u}| < 3.5$ Gλ.

Taken together, the EHT constraints give $F_{\rm cpct} = 0.64^{+0.39}_{-0.08}$ Jy; combined with the multi-wavelength constraints, they give $F_{\rm cpct} = 0.66^{+0.16}_{-0.10}$ Jy. For both these estimates, the central value gives the maximum a posteriori estimate and the uncertainties give the 95% confidence interval after marginalizing over the source size. Because all of the EHT constraints use the SMT–LMT baseline, they correspond to the source size projected along that direction. However, because the visibility amplitudes are highly symmetric, we expect these estimates to apply at all position angles (see Section 3). We infer a value of $F_{\rm cpct}$ that is significantly lower than what was found in observations in 2009 and 2012.[113]

As there is a range of possible values for the total compact flux density, we do not enforce a common value for all reconstructed images of M87. Instead, before evaluating image-data consistency through χ^2 metrics, we add a large Gaussian component (FWHM > 500 μas) to each reconstruction, which only affects visibilities on the intra-site baselines. The integrated flux density of this Gaussian component is set so that the total flux density of the modified image matches the intra-site visibility amplitudes.

We emphasize that the constraints on the size and total flux density of the compact emission were derived by making rigid assumptions about the station gains, by combining constraints among all four observing days (over which M87 may have varied in $F_{\rm cpct}$ and size), and by imposing short-baseline approximations for the visibility function. Thus, while we will use these constraints to guide our imaging and analysis, we will not strictly enforce them.

[113] In addition to the EHT measurements in 2009, quasi-simultaneous Global mm-VLBI Array (GMVA) 86 GHz observations of M87 in 2009 May found an elevated core flux density of ∼1 Jy (Kim et al. 2018a), while in more recent epochs the total flux density decreased close to the value of $F_{\rm cpct}$ estimated for 2017 (see Hada et al. 2016; Kim et al. 2018a).

Table 1
Metrics of EHT Angular Resolution for the 2017 Observations of M87

	FWHM$_{\rm maj}$ (μas)	FWHM$_{\rm min}$ (μas)	P.A. (°)
Minimum Fringe Spacing $1/\|\boldsymbol{u}\|_{\rm max}$ (All Baselines)			
April 5–11	24.8	…	…
Minimum Fringe Spacing (ALMA Baselines)			
April 5–11	28.6	…	…
CLEAN Beam (Uniform Weighting)			
April 5	25.8	17.9	10.1
April 6	24.9	17.5	2.3
April 10	25.3	17.2	6.7
April 11	25.4	17.4	6.0
CLEAN Restoring Beam (Used in this Letter)			
April 5–11	20	20	…

Note. Because the EHT coverage is fairly symmetric, to avoid asymmetries introduced by restoring beams and to homogenize the images among epochs, we adopt a circular Gaussian restoring beam with 20 μas FWHM for all CLEAN reconstructions.

4.4. Image Resolution and Degrees of Freedom

The diffraction-limited resolution of an interferometer depends upon its finest fringe spacing: $\theta_{\rm min} = f_\theta/|\boldsymbol{u}|_{\rm max}$, where f_θ is a scaling coefficient. The resolution of reconstructed images also depends upon the baseline coverage and sensitivity and is commonly quantified using procedures to fit the central peak of the point-spread function (or "dirty beam"). Table 1 gives several common representations of the EHT resolution for observations of M87.

The maximum number of independent degrees of freedom in a reconstructed image is then $N_{\rm dof} \lesssim (\theta_{\rm fov}/\theta_{\rm min})^2$, where $\theta_{\rm fov}$ is the FOV of the image. Of course, the image may only be nonzero in a small fraction of the full FOV, reducing $N_{\rm dof}$ correspondingly. We emphasize that the number of degrees of freedom in a reconstructed image is not determined by the number of pixels in the image. Likewise, for a constrained FOV, it is not possible to arbitrarily fit (or overfit) interferometric data by making the pixel resolution increasingly fine because the baseline correlation length for measurements in the visibility domain is determined by the FOV rather than by the pixel resolution. Consequently, a reconstructed image and its effective number of degrees of freedom is sensitive to the FOV of the image, but not to the chosen pixel size.

4.5. Image Conventions

Throughout this Letter, we present images using their equivalent brightness temperatures defined by the Rayleigh–Jeans law: $T_{\rm b} = \frac{c^2}{2\nu^2 k} I_\nu$, where I_ν is the specific intensity, c is the speed of light, ν is the observing frequency, and k is the Boltzmann constant (e.g., Rybicki & Lightman 1979). We use brightness temperature rather than the standard radio convention of flux density per beam (e.g., Jy/beam) because our images are spatially resolved and because RML methods do not have a natural associated beam. However, we emphasize that brightness temperature does not necessarily correspond to any

physical temperature of the radio-emitting plasma. The radio spectrum of M87 is not a blackbody, and its 230 GHz emission is from synchrotron radiation (Paper V). Finally, for visualization of our images, we use perceptually uniform colormaps from the `ehtplot`[114] library.

Throughout this Letter, we restore CLEAN images using a circular Gaussian beam with 20 μas FWHM, which is comparable to the geometric mean of the principal axes of the CLEAN beam (see Table 1). Unless otherwise stated, any image that has been restored will include the restoring beam in the lower right. Also, for consistency with RML methods but in contrast with standard practice, our presented CLEAN images do not include the residual image, corresponding to the inverse Fourier transform of gridded residual visibilities. In Section 7.2, we describe characteristics of the residual images.

5. First M87 Images from Blind Imaging

VLBI images are sensitive to choices made in the imaging and self-calibration process. Choices required in using any imaging method include deciding which data are used (e.g., low and/or high band, flagging), specifying the self-calibration procedures, and fixing the reconstructed image FOV. In addition, imaging methods also require choices that are particular to their assumptions and methodology. For CLEAN, these choices include choosing a set of CLEAN windows and a data-weighting scheme. For RML methods, choices include the selection of which data and regularizer terms and weights to use in the objective function (Equation (14)). With this abundance of user input, it can be difficult to assess what image properties are reliable from a given imaging method.

The dangers of false confidence and collective confirmation bias are magnified for the EHT because the array has fewer sites than typical VLBI arrays, there are no previous VLBI images of any source at 1.3 mm wavelength, and there are no comparable black hole images on event-horizon scales at any wavelength. To minimize the risk of collective bias influencing our final images, in our first stage of analysis we reconstructed images of M87 in four independent imaging teams.

5.1. Imaging Procedure and Team Structure

We subdivided our first M87 imaging efforts into four separate imaging teams. The teams were blind to each others' work, prohibited from discussing their imaging results and even from discussing aspects of the data that might influence imaging (e.g., which stations or data might be of poor quality). No restrictions were imposed on the data pre-processing or imaging procedures used by each team. Teams 1 and 2 focused on RML methods, while Teams 3 and 4 primarily used CLEAN. In addition to independently imaging M87, teams also independently imaged other sources observed by the EHT in 2017 to test the blind imaging procedure.

Blind imaging procedures have long been used to reduce the risk of group bias. Prior to the 2017 observations, we organized a series of "imaging challenges" that used synthetic data to assess how conventional and newly developed imaging algorithms would perform for the EHT (Bouman 2017).[115] Reconstructing images independently in these challenges helped us identify which image features were likely intrinsic, and which were likely to be spurious. To compare EHT 2017 results among teams while keeping submissions blind, we built a website that allowed users to independently upload images and automatically compare them to the ground truth images and submissions from other users (Bouman 2017).

5.2. First M87 Imaging Results

The first M87 imaging analysis used an early-release engineering data set (ER4; Paper III). These data had a priori and network calibration applied but did not have calibrated relative RCP–LCP gains. Consequently, each team imaged the data using only parallel-hand products (i.e., RCP–RCP or LCP–LCP) to approximate total intensity. The April 11 data set was selected for the first comparison, as it had the best coverage for the M87/3C 279 pair and the most stable a priori amplitude calibration (especially for the LMT).

The imaging teams worked on the data independently, without communication, for seven weeks, after which teams submitted images to the image comparison website using LCP data (because the JCMT recorded LCP on April 11). After ensuring image consistency through a variety of blind metrics (including normalized cross-correlation, Equation (15)), we compared the independently reconstructed images from the four teams.

Figure 4 shows these first four images of M87. All four images show an asymmetric ring structure. For both RML teams and both CLEAN teams, the ring has a diameter of approximately 40 μas, with brighter emission in the south. In contrast, the ring azimuthual profile, thickness, and brightness varies substantially among the images. Some of these differences are attributable to different assumptions about the total compact flux density and systematic uncertainties (see Table 2).

The initial blind imaging stage indicated that the image of M87 is dominated by a $\sim$40 μas ring. The ring persists across the imaging methods. Next, we moved to a second, non-blind imaging stage that focused on exploring the space of acceptable images for each method. The independent team structure was only used for the first stage of imaging; the remainder of this Letter will categorize results by imaging methodology.

6. Determining Imaging Parameters via Surveys on Synthetic Data

To explore the dependence of the reconstructed images on imaging assumptions and impartially determine a combination of fiducial imaging parameters, we introduced a second stage of image production and analysis: performing scripted parameter surveys for three imaging pipelines. To objectively evaluate the fidelity of the images reconstructed by our surveys—i.e., to select imaging parameters that were independent of expert judgment—we performed these surveys on synthetic data from a suite of model images as well as on the M87 data. The synthetic data sets were designed to have properties that are similar to the EHT M87 visibility amplitudes (e.g., prominent amplitude nulls). This suite of synthetic data allowed us to test the scripted reconstructions with knowledge of the corresponding ground truth images and, thereby, select fiducial imaging parameters for each method. These fiducial parameters were selected to perform well across a variety of source

[114] https://github.com/chanchikwan/ehtplot

[115] Similar blind procedures have also been used in the optical interferometry community to evaluate and compare imaging methods (e.g., Lawson et al. 2004).

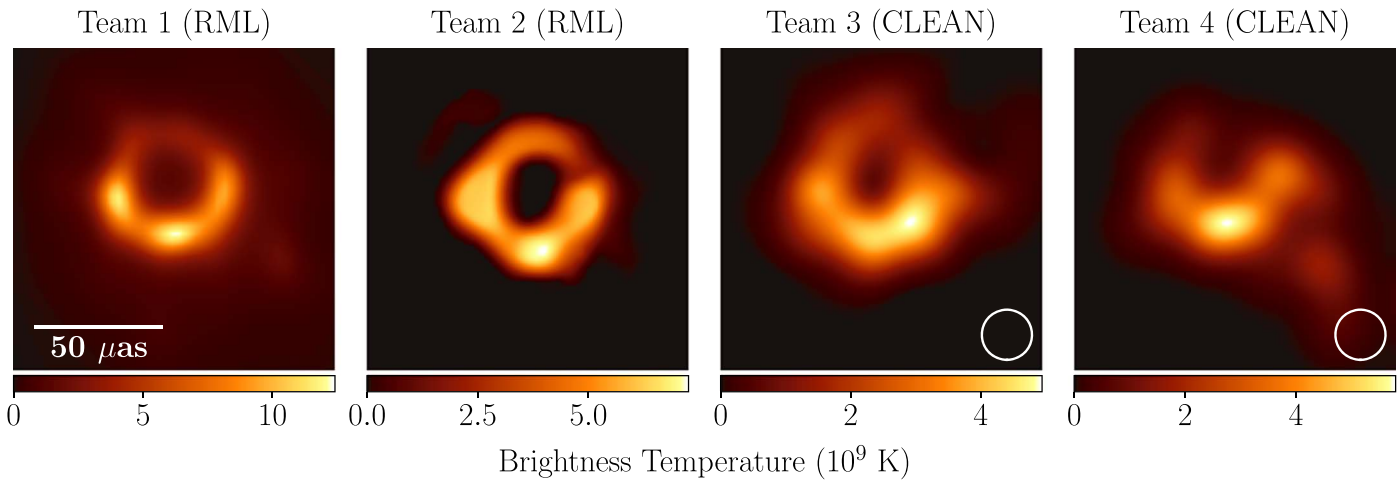

Figure 4. The first EHT images of M87, blindly reconstructed by four independent imaging teams using an early, engineering release of data from the April 11 observations. These images all used a single polarization (LCP) rather than Stokes *I*, which is used in the remainder of this Letter. Images from Teams 1 and 2 used RML methods (no restoring beam); images from Teams 3 and 4 used CLEAN (restored with a circular 20 μas beam, shown in the lower right). The images all show similar morphology, although the reconstructions show significant differences in brightness temperature because of different assumptions regarding the total compact flux density (see Table 2) and because restoring beams are applied only to CLEAN images.

Table 2
Image Properties and Data Consistency Metrics for the First M87 Images (See Figure 4)

	Team 1	Team 2	Team 3	Team 4
Image Properties				
Method	RML	RML	CLEAN	CLEAN
$F_{\rm cpct}$ (Jy)	0.94	0.43	0.42	0.42
Engineering Data (10 s avg., LCP, 0% sys. error)				
$\chi^2_{\rm CP}$	2.06	2.48	2.44	2.33
$\chi^2_{\log\,\rm CA}$	1.20	2.16	2.15	1.43
Science Release (scan-avg., Stokes *I*, 0% sys. error)				
$\chi^2_{\rm CP}$	1.13	5.40	2.28	1.89
$\chi^2_{\log\,\rm CA}$	2.12	5.41	3.90	5.32
Science Release (scan-avg., Stokes *I*, 1% sys. error)				
$\chi^2_{\rm CP}$	1.00	3.85	2.04	1.55
$\chi^2_{\log\,\rm CA}$	1.96	5.07	3.64	4.8
Science Release (scan-avg., Stokes *I*, 10% sys. error)				
$\chi^2_{\rm CP}$	0.49	0.95	1.11	0.48
$\chi^2_{\log\,\rm CA}$	0.46	1.36	0.98	0.79

Note. Data metrics are shown as originally computed on April 11 data (using 10 s averaged engineering data with LCP) and using the data from the first EHT science release (scan-averaged, Stokes *I*) when 0%, 1% and 10% systematic error has been included. Teams 2–4 chose to exclude the intra-site baselines in their imaging. However, for consistency with our later χ^2 values computed from science release data, we include these baselines when computing χ^2 after adding an extended component to these images containing the missing flux density.

structures, including sources without the prominent ring observed in our images of M87.

We emphasize that the ensemble of results from these parameter surveys do not correspond to a posterior distribution of reconstructed images. Our surveys are coarse-grained and do not completely explore the choices in the imaging process. Nonetheless, they identify regions of imaging parameter space that consistently produce faithful image reconstructions on synthetic data, and they help us identify which features of our reconstructions are consistent and which features vary with specific parameter choices.

6.1. Synthetic Source Models and Data

To create a testing suite of synthetic data, we selected simple geometric models that have corresponding visibility amplitudes that are similar to those observed in M87 (Figure 2). The primary data properties that we used to define similarity are (1) a large decrease in flux density on baselines between 0 and 1 Gλ, indicating extended structure, (2) visibility nulls at $\sim$3.4 and $\sim$8.3 Gλ, and (3) a high secondary peak between the nulls at $\sim$6 Gλ, which recovers $\sim$15% of the total compact flux density.

We selected four models with distinct compact morphologies that each reproduce these features of the M87 data. The four models are (1) a tapered ring with 44 μas ring diameter, (2) a tapered crescent of the same diameter with its brightest point oriented directly south, (3) a tapered disk with 70 μas diameter, and (4) two different circular Gaussian components separated by 32.3 μas at a position angle of 292°. To ensure rough consistency and compatibility with the M87 parameters estimated in Section 4, we adopted a total compact flux density of 0.6 Jy for all these simple geometric models. Note that none of the synthetic EHT data sets generated from these simple models reproduces all features seen in the M87 data. For example, the ring and disk models both have point symmetry, so all their closure phases are either 0° or 180°.

To simulate the effects of a large-scale jet on our data (which only significantly affects intra-site visibilities), we added a three-component Gaussian model that approximates the inner M87 jet at 3 mm (e.g., Kim et al. 2018a). The jet also has 0.6 Jy of total flux density, giving a total image flux density in each case (compact+jet) of 1.2 Jy. To produce non-closing systematic errors from polarimetric leakage, we also included linear polarization in each model. For additional details on these simulated models and data, see Appendix C.1. Figure 5 shows these model images.

We generated synthetic data from each image using the `eht-imaging` software library. The synthetic data were produced with the baseline coverage and sensitivity of the EHT on all four days of the 2017 observations. Station-based errors were added in a Jones matrix formalism (Thompson et al. 2017; see Appendix C.2). To simulate a lack of absolute phase

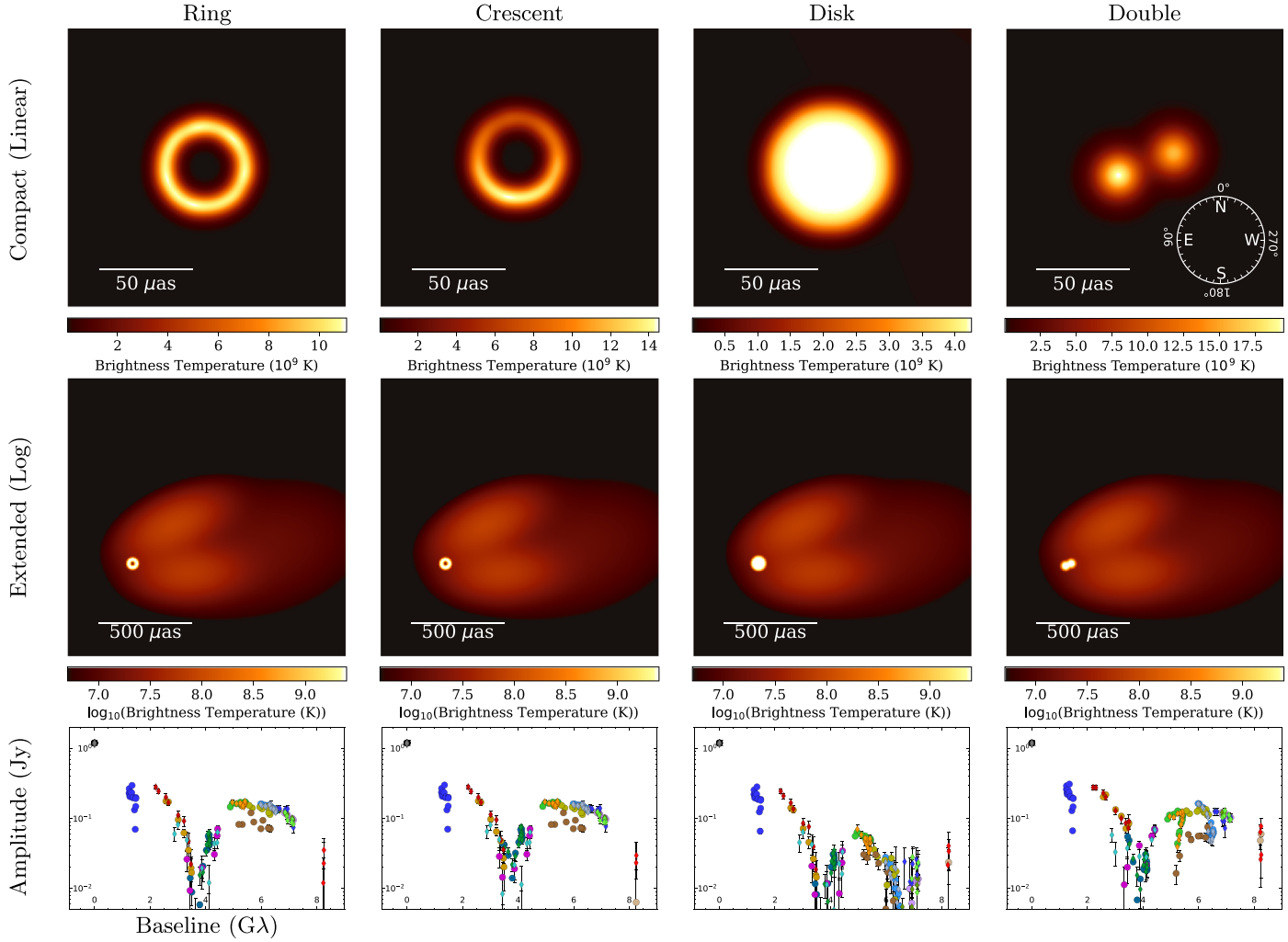

Figure 5. The four simple geometric models and synthetic data sets used in the parameter surveys (see Appendix C for details). Top: linear scale images, highlighting the compact structure of the models. Middle: logarithmic scale images, highlighting the larger-scale jet added to each model image. Bottom: one realization of simulated visibility amplitudes corresponding to the April 11 observations of M87. We indicate the conventions for cardinal direction and position angle used throughout this Letter on the upper-right panel. Note that east is oriented to the left, and position angles are defined east of north.

calibration, a random station phase is adopted for each scan. Independent station-based gains were applied to each visiblity, with two components of each gain factor drawn from normal distributions: one term that was constant over the observation, and one that varied randomly among scans. We captured the increased uncertainty and variability in station gains at the LMT (Section 4.1) by giving these gain terms larger variances. Time-independent polarimetric leakage terms were drawn from a complex Gaussian distribution with 5% standard deviation, motivated by previous estimates of the polarization leakage at EHT sites (Johnson et al. 2015). Identical gain, phase, and leakage contamination was applied to the high- and low-band data. Figure 5 shows four examples of visibility amplitudes generated using this procedure. Appendix C.2 provides full details about the synthetic data generation procedure.

Furthermore, to test whether or not our results are sensitive to specific choices made in the synthetic data generation, we compared our generated synthetic data and reconstructed images to results from another VLBI data simulator, `MeqSilhouette+rPICARD` (Blecher et al. 2017; Janssen et al. 2019). `MeqSilhouette+rPICARD` takes a more physical approach to mm-VLBI synthetic data generation (with added corruption based on, e.g., measured weather parameters and antenna pointing offsets) and it uses the full `CASA`-based EHT reduction pipeline for calibration. Despite the differences in approach, both synthetic data pipelines yield comparable results (see Appendix C.3 and Figure 31). We use `eht-imaging` for all further synthetic data in this Letter.

6.2. Imaging Pipelines and Parameter Survey Space

To survey the space of imaging parameters relevant to each imaging software package and to test their effects on reconstructions of simulated data, we designed scripted imaging pipelines in three software packages: `DIFMAP`, `eht-imaging`, and `SMILI`. Each pipeline has some choices that are fixed (e.g., the convergence criterion, the pixel size, etc.) but takes additional parameters (e.g., the regularizer weights, the total compact flux density) as arguments. We then reconstructed images from all M87 and synthetic data sets using all possible parameter combinations on a coarse grid in the space of these parameters. We chose large ranges for each parameter, deliberately including values that we expected to produce poor reconstructions.

The parameter choices and the values surveyed vary among the three pipelines, and the pipelines also differ in which frequency

bands were used. However, a consistent feature of the three pipelines is that none of them do any data flagging, even of intra-baselines.[116] We now describe each pipeline in detail.

6.2.1. DIFMAP

While CLEAN was implemented by hand in our first stage of analysis (Section 4), a scripted version of CLEAN was developed in DIFMAP to carry out the parameter search in this second stage. This script has five parameters taken as arguments: the total assumed compact component flux density, the stop condition, the relative weight correction factor for ALMA in the self-calibration process, the diameter of the cleaning region, and a parameter controlling how the (u, v) grid weights are scaled by the visibility errors. CLEAN imaging with DIFMAP was performed separately for the low- and high-band data. The DIFMAP images we present in this Letter are derived from the low-band data averaged to 10 s in time.

The DIFMAP script begins by gridding the visibilities in the (u, v) plane, after which the direct Fourier transform, or "dirty image," and the point-spread function, or "dirty beam," are computed. A uniform (u, v) density weighting function is used for gridding the visibilities. This choice gives equal weight to each gridded spatial frequency containing a measurement, irrespective of sample density. The visibility weights in (u, v) gridding can be further multiplied by σ^{κ}, where σ is the thermal noise, with our parameter survey exploring $\kappa = -2, -1$, and 0.

In addition to the (u, v) weighting, one or more antennas can be downweighted in the self-calibration process. When fitting for complex antenna gains, the self-calibration algorithm of DIFMAP uses weights that are proportional to σ^{-2}. In the case of EHT data, it is particularly helpful to downweight data on baselines to phased ALMA—which has a much higher S/N than other stations—so that these ALMA baselines do not dominate the corrections to phases and amplitudes. In the parameter survey, we have scaled the ALMA weights by a factor ranging from 0.01 to 1.0. All other station weights were kept at 1.0 (i.e., at their original values).

A disk-shaped set of CLEAN windows, or imaging mask, aligned with the previously found geometrical center of the underlying emission structure (e.g., the ring for M87) and with a specified diameter is then supplied; these windows define the area on the image where the CLEAN algorithm searches for point sources. We limited the cleaning windows to image only the compact structure ($\leqslant 100\,\mu$as) in order to prevent CLEAN from adding larger-scale emission features that are poorly constrained by the lack of short EHT baselines. The emission structure common to all early trials (Section 5) was used as a guide for setting the disk-shaped window for scripted reconstructions, but different diameters from 40 to 100 μas were tested in the parameter search.

Two main stopping criteria are implemented in the DIFMAP script to control the amount of cleaning; imaging may stop (1) when the desired total compact flux density is reached, or (2) when the relative decrease in the rms of the residual image over the image noise estimated from the visibilities dips below a given threshold. In the parameter survey, two cases were tested: (a) criterion 1 alone, and (b) a combination of criteria 1 and 2, such that cleaning will stop whenever one of the two criteria is reached first. In both cases, the assumed total compact flux density was varied from 0.5 to 0.8 Jy. The threshold for the relative decrease in the residual image rms in the criterion 2 was always fixed to 10^{-4}.

After the script finishes a round of cleaning, it introduces a large ($\gtrsim$2 mas) Gaussian component that recovers the extended missing flux density and does not affect the compact emission structure. By fitting the most extended structure, the Gaussian component also acts as an "anchor" for the intra-site baselines, minimizing the variations in the antenna gains during the amplitude self-calibration loops.

The initial image, produced by iterative cleaning and phase self-calibration, is used to amplitude self-calibrate the LMT (with a solution interval equal to the scan length), which is known to have poor a priori amplitude calibration (see Section 4.1). In this step, the gains of the other antennas in the array are fixed. The initial model is then removed and further iterations of cleaning loops are performed until a new model that recovers all the compact flux density is obtained. This round is followed by self-calibration at all sites in both phase and amplitude. The loop of cleaning and self-calibration is then repeated with progressively shorter solution intervals in the amplitude self-calibration step, from an initial solution equal to the whole duration of the observations down to a minimum solution interval of 10 s. For consistency with the outputs of the eht-imaging and SMILI pipelines, the final CLEAN image omits the large Gaussian component.

Figure 6 shows a 2D slice of the DIFMAP parameter survey results from varying the weights on ALMA data in the self-calibration step and the diameter of the circular mask of CLEAN windows on synthetic data. We show the results for synthetic data of a crescent model and for M87 data from April 11. It is important to note that although DIFMAP images are displayed using a restoring beam of 20 μas (FWHM shown on figures), as is standard in CLEAN imaging, the underlying δ-function CLEAN components are used for computing χ^2 so as to avoid modifying the reconstructed amplitudes through Gaussian convolution.

6.2.2. eht-imaging

The eht-imaging parameter survey used a template imaging script that takes seven parameters as arguments. These are the total assumed compact component flux density, the fractional systematic error on the measured visibilities, the FWHM of the circular Gaussian initial image (also used as a prior for maximum entropy regularization), and the relative weights of four regularization terms: MEM, the ℓ_1 norm (ℓ_1), total variation (TV), and total squared variation (TSV). For details on each of these regularization terms, see Appendix A.

The eht-imaging script begins by preparing the data for imaging. After scan-averaging the data and combining the high- and low-band data, it rescales the amplitude of zero baseline measurements to account for the unresolved extended components. It then performs an initial self-calibration of the LMT by using only the LMT–SMT baseline and adjusting only the LMT amplitude gains to match a Gaussian image with a total flux density of 0.6 Jy and a size of 60 μas, based on the constraints determined in Section 4.

The script also incorporates additional systematic uncertainty into the error budget during imaging. Namely, for each visibility, a specified fraction of the visibility amplitude is added in quadrature to the thermal noise; this inflated thermal noise is then used to estimate uncertainties on all data products,

[116] In the first imaging stage (Section 5), teams explored keeping or flagging the intra-site baselines and found that this choice does not significantly affect the recovered images. Although the inclusion of the intra-site baselines does not improve the (u, v) coverage, these baselines add non-trivial closure amplitudes that can improve imaging (Chael et al. 2018).

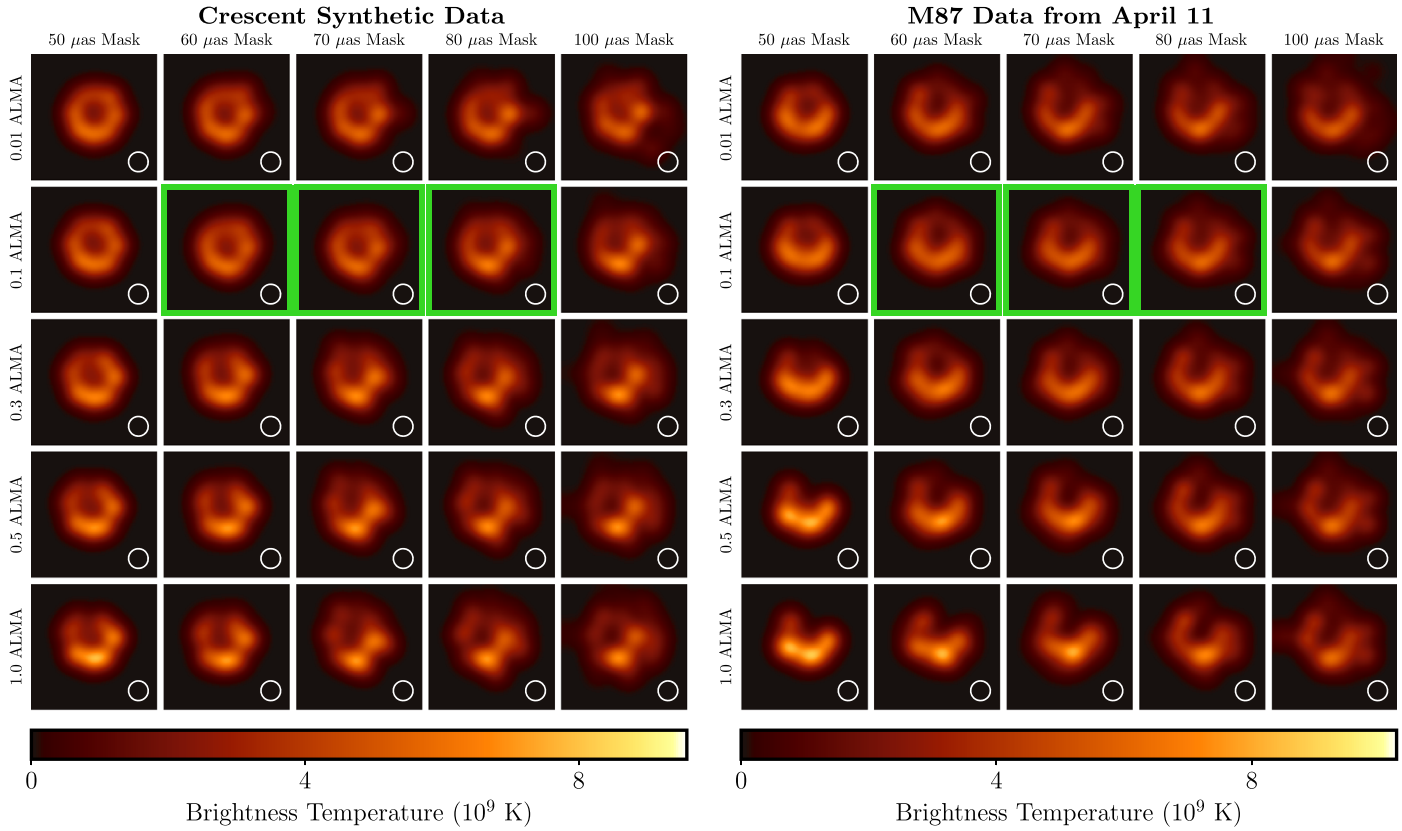

Figure 6. Selection of the DIFMAP (CLEAN) parameter survey results on real and synthetic data with April 11 EHT baseline coverage. A 2D slice of the 5D parameter space is displayed, corresponding to different diameters of the circular mask and the data weight on ALMA in self-calibration. All other parameters are kept constant (Compact Flux = 0.5 Jy, $\kappa = -1$, Stop Condition = Flux Reached). The left panel shows results of the parameter search on the Crescent synthetic data, while the right panel shows reconstructions for the same parameters on M87 data. Images that meet the threshold for the Top Set are outlined in green (see Section 6.3.1).

thereby accounting for small, non-closing systematic errors from, e.g., polarimetric leakage. We surveyed values of 0%, 1%, 2%, and 5% in computing this additional systematic uncertainty. Note that these levels of systematic uncertainty do not necessarily correspond with the estimated level of non-closing errors presented in Paper III; however, additional systematic uncertainty beyond the a priori estimate can help in avoiding overfitting to a few sensitive baselines (e.g., those to ALMA) during image optimization.

The final pre-imaging step is to *inverse* taper the visibility amplitudes. Specifically, we divide the visibility amplitudes and their estimated error by the Fourier transform of a 5 μas FWHM Gaussian, thereby raising the amplitudes on long baselines while preserving the S/N. At the end of the script, after producing an image from the inverse-tapered data, we convolve the reconstructed image with a 5 μas FWHM Gaussian to ensure that it will fit the original, untapered data. This procedure enforces a limiting angular resolution of 5 μas in the final reconstructed images.

After the data have been prepared, the `eht-imaging` script proceeds to imaging, using a 64 $\times$ 64 pixel grid with a 128 μas FOV. The script alternates between solving for the optimal image under the current data constraints and self-calibrating the complex station gains (Equation (7)). The first imaging iteration uses only visibility amplitudes and closure quantities. Because the amplitudes are uncalibrated in this iteration, systematic error tolerance is added on top of the (potentially inflated) thermal uncertainty for the visibility amplitudes, using the systematic error budget provided in Paper III for all sites except LMT, which has its budget increased by 15%. After phase self-calibration, complex visibilities are used for optimization in combination with closure quantities.

Between imaging iterations, the image is convolved with a circular Gaussian with a FWHM corresponding to the nominal array resolution, $\lambda/|\boldsymbol{u}|_{\max} \approx 25$ μas. This procedure aids convergence to a global minimum by moving intermediate images away from local minima. In each iteration, we increase the weight on data terms relative to the regularizers and reduce the systematic noise tolerance for amplitude calibration uncertainties. The final reconstructed image is convolved with the same 5 μas Gaussian that was used for the inverse taper, ensuring consistency with the original data while imposing a constraint that no features in the reconstructed image can be finer than 5 μas.

Figure 7 shows a 2D slice of the `eht-imaging` parameter survey results from varying the weights on the MEM and the TV regularizers. In this figure, we show the results for both synthetic data from a crescent model and for EHT M87 data from April 11.

6.2.3. *SMILI*

In the `SMILI` imaging pipeline, we reconstructed images using low-band EHT data and utilized weighted-ℓ_1 (ℓ_1^{w}), TV, and TSV regularizers (see Appendix A). ℓ_1^{w} favors sparsity in the image domain, using a circular Gaussian prior image as a "soft mask," which increasingly penalizes pixel intensities farther from the image center. In contrast, TV favors sparsity in the gradient domain (leading to piecewise-smooth images), and TSV favors overall image smoothness. The `SMILI` search

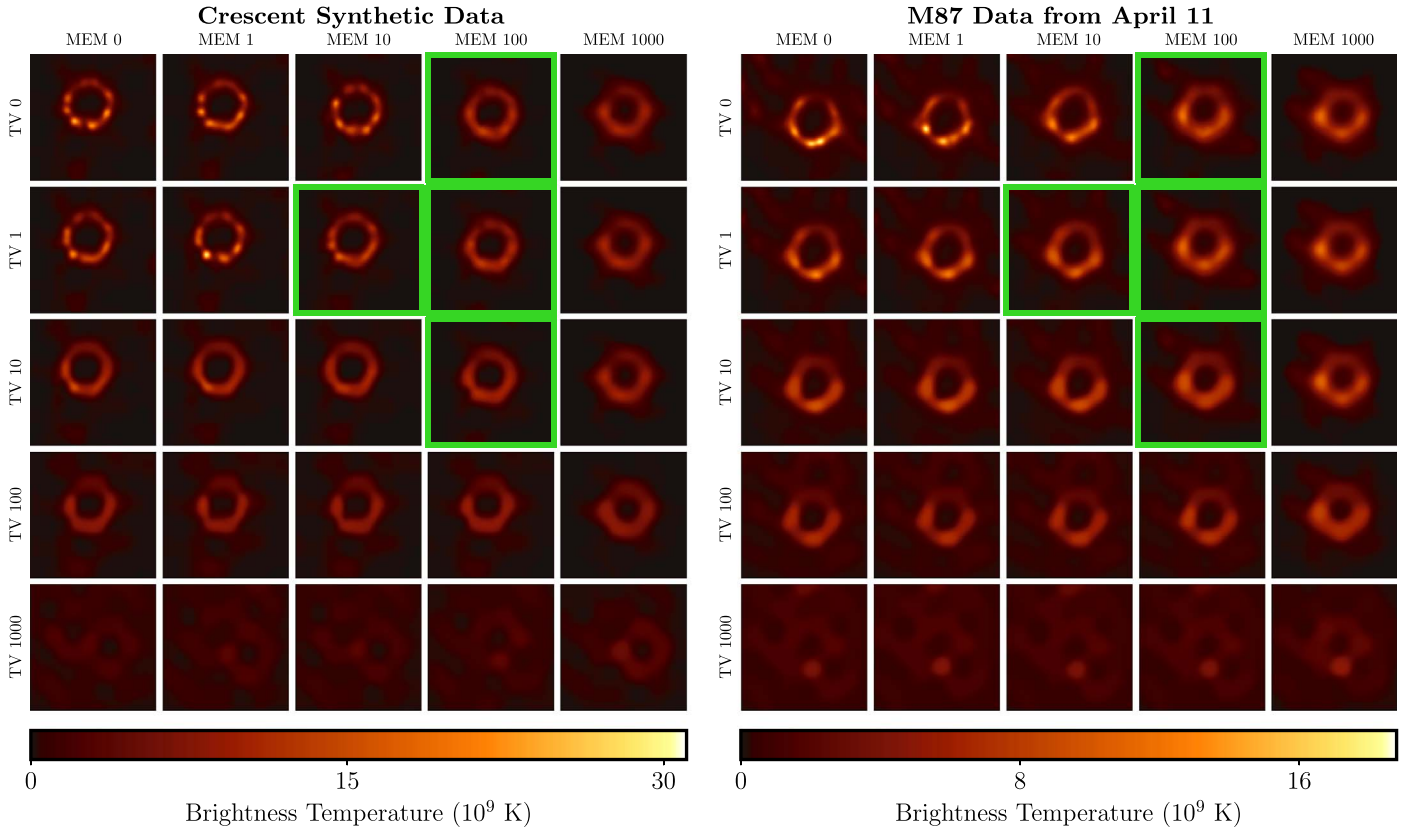

Figure 7. Selection of the `eht-imaging` (RML) parameter survey results on real and synthetic data with April 11 EHT baseline coverage. A 2D slice of the 7D parameter space is displayed, corresponding to different weights on the MEM and TV regularizers. All other parameters are kept constant (Compact Flux = 0.6 Jy, Initial/MEM FWHM = 40 μas, Systematic Error = 1%, TSV = 0, and $\ell_1 = 0$). The left panel shows results of the parameter search on the Crescent synthetic data, while the right panel shows reconstructions for the same parameters on M87 data. Images that meet the threshold for the Top Set are outlined in green. Note that the upper-left reconstruction has *no* regularization; it is produced by enforcing only image positivity and a constrained FOV.

adopts an FOV of 128 μas (matching the `eht-imaging` pipeline). The survey included five values for the FWHM of the prior image for $\ell_1^{\rm w}$, ranging from 40 to 80 μas. The pipeline also surveyed five values for the total compact flux density, between 0.4 and 0.8 Jy.

Prior to imaging, the script coherently averages the visibilities over scans and then pre-calibrates the LMT gains using an assumed Gaussian model, as in the procedure described above for the `eht-imaging` script. The script then adds systematic uncertainties in quadrature to the thermal noise of complex visibilities to account for small, non-closing errors. The survey included options for 0% (no systematic error) and 1% systematic error, which correspond to the fraction of each visibility amplitude that is added in quadrature to the reported thermal noise σ values.

Similar to the `eht-imaging` and `DIFMAP` scripts, the SMILI imaging procedure is iterative, with four stages of imaging and self-calibration. Reconstructions at each stage begin with a circular Gaussian with an FWHM of 20 μas as the initial image. After the first imaging attempt in each stage, subsequent initializations use the previously obtained image convolved with the initial Gaussian. We perform three imaging cycles for each self-calibration stage, self-calibrating only to the final reconstructed image in each of the three cycles.

In the first two self-calibration stages, the imaging step uses closure data (closure amplitudes and phases) and visibility amplitudes. To account for errors in the amplitude calibration, during these stages the visibility amplitudes have additional 5% and 30% uncertainties added in quadrature to the thermal noise (on top of the systematic error tolerance noted above) for non-LMT and LMT baselines, respectively. For the final two self-calibration stages, the imaging uses closure data and complex visibilities.

Figure 8 shows a 2D slice of the `SMILI` parameter survey results from varying the weights on the TSV regularizer and the prior radius. We show the results for synthetic data from a crescent model and for M87 data from April 11. Although the `SMILI` and `eht-imaging` pipelines have a number of similarities, these pipelines use different regularizers, calibrate and constrain data differently, and were implemented using independent software libraries.

6.3. Selecting Imaging Parameters

We derived two principal outputs from each parameter survey: a "Top Set" of parameter combinations that each produce acceptable images on the synthetic data, and a single combination of best-performing, "fiducial" parameters for each pipeline. In this section, we describe our ranking procedure to find acceptable parameter combinations, the possible limitations of this procedure, and the resulting acceptable parameter combinations for each imaging pipeline.

6.3.1. Ranking Imaging Parameters

To determine the Top Sets, we designed a two-step selection procedure. The first step requires that all reconstructions of M87

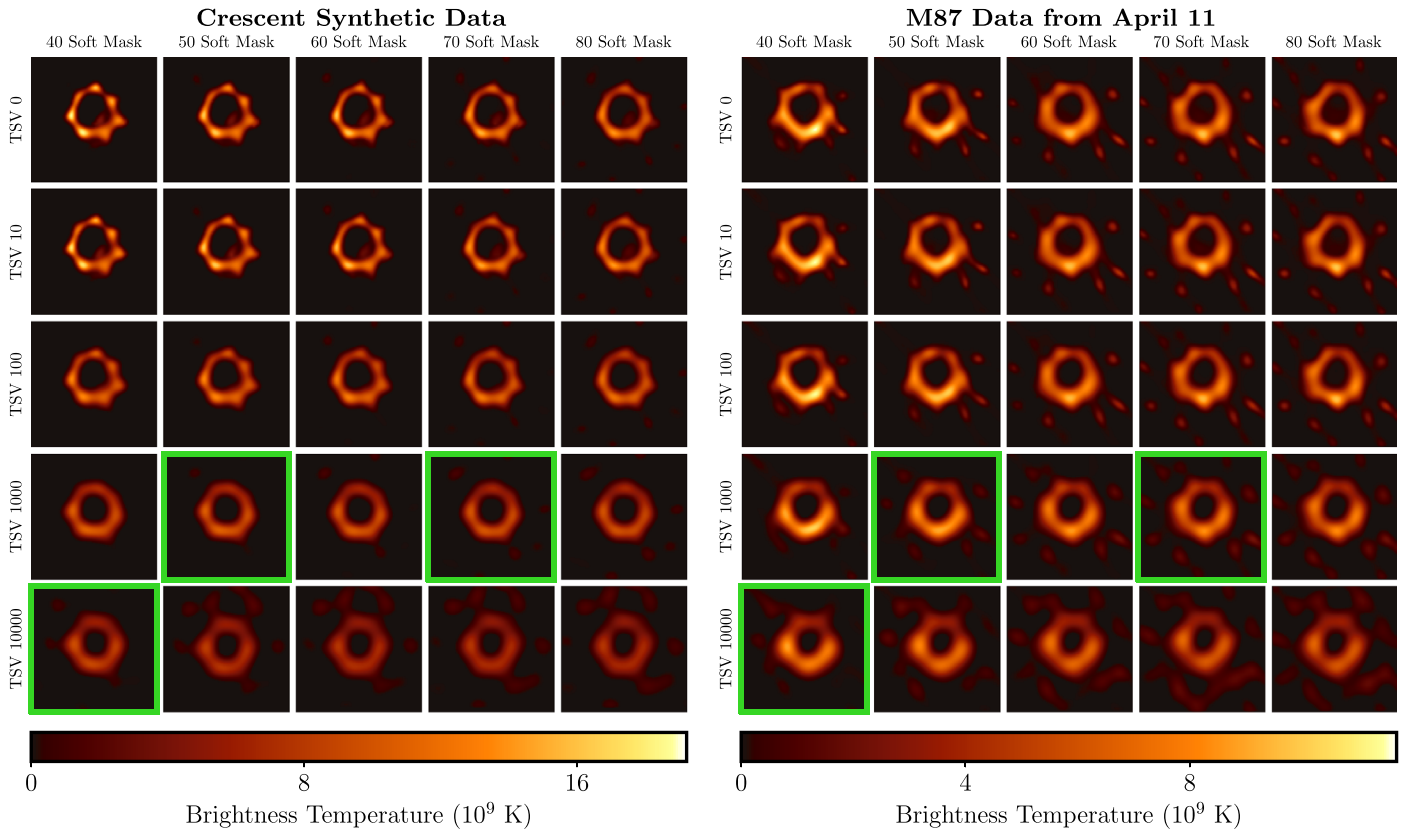

Figure 8. Selection of the SMILI (RML) parameter survey results on real and synthetic data with April 11 EHT baseline coverage. A 2D slice of the 6D parameter space is displayed, corresponding to varying the diameter of the soft mask region and the weight on the TSV regularizer. All other parameters are kept constant (Compact Flux = 0.5 Jy, Systematic Error = 0%, TV = 0, $\ell_1^{\mathrm{W}} = 1$). The left panel shows results of the parameter search on the Crescent synthetic data, while the right panel shows reconstructions for the same parameters on M87 data. Images that meet the threshold for the Top Set are outlined in green.

with a given combination of parameters are consistent with their underlying data; the second step requires that the reconstructions of simulated data are sufficiently similar to their corresponding ground truth images. Parameter combinations that meet both criteria define the Top Set, and the parameter combination in this set that gives the best performance on the simulated data is used to define the fiducial images of M87 for each day.

Each parameter survey spans a large range of parameter space, including combinations that are poorly adapted to the M87 data (e.g., very large regularizer weights in the RML methods). To filter parameter combinations that lead to final images with poor fits to the data, we calculate χ^2 values on closure phase and log closure amplitudes using scan-averaged low-band data. For the χ^2 computation, we only construct closure quantities from averaged visibilities that have synchronized start times. Any combinations with $\chi^2 \geqslant 2$ on any day of EHT observations are excluded from the Top Set. However, the DIFMAP imaging pipeline uses 10 s averages (while we estimate χ^2 values using scan averages), and the pipeline downweights the extremely high S/N baselines to ALMA during the iterative self-calibration process. Consequently, DIFMAP reconstructions tend to fail this strict χ^2 requirement unless a systematic uncertainty is included in the error budget. As a result, before performing this initial $\chi^2 < 2$ thresholding on DIFMAP reconstructions, we include 10% systematic uncertainty in quadrature to the thermal uncertainty of every visibility.

Next, to determine the fidelity of the different reconstructions on synthetic data, we compute the normalized cross-correlation ρ_{NX} between each surviving image and the corresponding ground truth image. For a given reconstruction X and its ground truth image Y, the normalized cross-correlation is

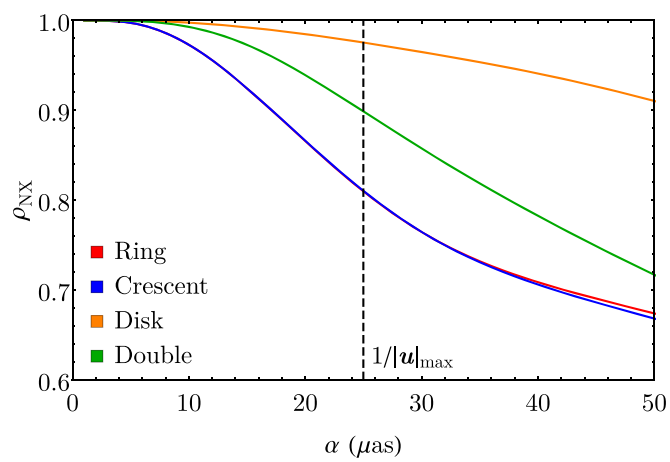

Figure 9. Normalized cross-correlation, ρ_{NX}, of the four simulated images compared before and after convolution with a circular Gaussian kernel with FWHM α. The vertical dashed line shows the nominal diffraction-limited resolution of the EHT (see Table 1). For each source, we invert these curves to obtain from a given ρ_{NX} an equivalent blurring kernel size α. The Top Set reconstructions are defined as those with this α smaller than the nominal EHT resolution.

$$\rho_{\mathrm{NX}}(X, Y) = \frac{1}{N} \sum_i \frac{(X_i - \langle X \rangle)(Y_i - \langle Y \rangle)}{\sigma_X \, \sigma_Y}, \tag{15}$$

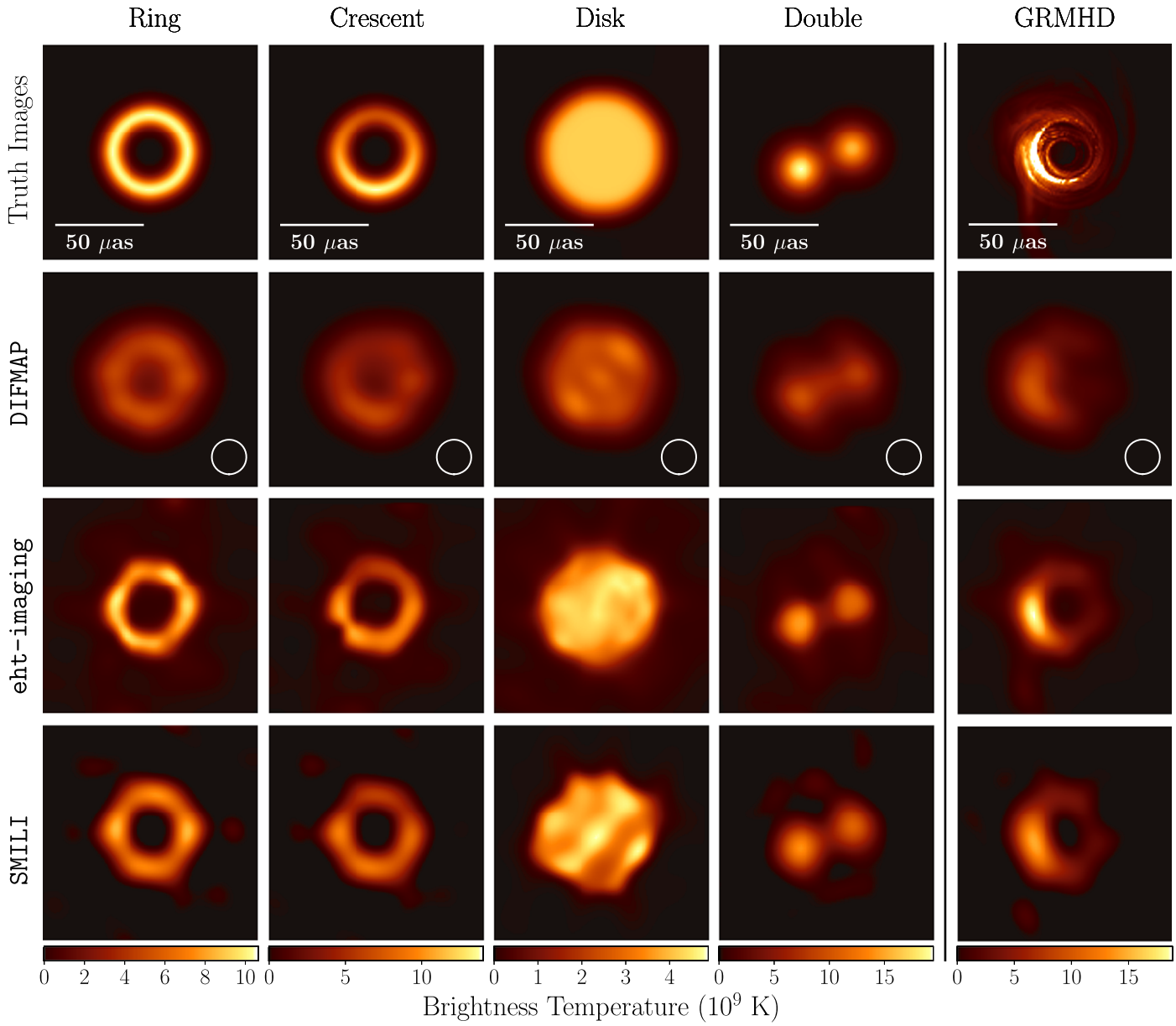

Figure 10. Cross-validation of the imaging parameter selection procedure. In each of the left four columns, we show reconstructed images for the simple geometric source models. These reconstructions do not use the fiducial imaging parameters identified by the full training set; instead, we selected the imaging parameters for each geometric source model after excluding that particular model from the parameter selection process. For example, in the disk reconstructions, the parameters were selected by assessing reconstructions of only the ring, crescent, and double source models. Thus, the selected parameters vary among these four columns, but we can verify that the training sets do not overly constrain the outcomes. In the fifth column, we show reconstructions of a GRMHD snapshot (Paper V) using the fiducial M87 parameters selected from all four geometric models. That is, the script and parameters used to produce these GRMHD image reconstructions are identical to those used to produce our fiducial M87 images (shown in Figure 11). Because the GRMHD snapshot has a substantially higher peak brightness than the reconstructions, its column has been scaled to the peak brightness of the `eht-imaging` reconstruction.

where the sum is over all N pixels in the two images, $\langle X \rangle$ and $\langle Y \rangle$ are the mean pixel values in the images, and σ_X and σ_Y are the standard deviations of the pixel values in the two images. The normalized cross-correlation quantifies image similarity, where a value of 1 implies perfect correlation between images, 0 implies no correlation, and -1 implies perfect anti-correlation. Because the absolute visibility phase is unknown and, thus, the image centroid for reconstructions is not fixed, we compute $\rho_{\rm NX}$ for each possible discrete shift between the images and select the largest value. Before computing $\rho_{\rm NX}$ for `DIFMAP` images, the CLEAN components are convolved with a restoring beam with FWHM of 20 μas.

We choose the median value of $\rho_{\rm NX}$ across all days as the representative value for a given combination of imaging parameters on a particular model. Taking the median allows us to incorporate days with different baseline coverage in the scoring procedure while preventing the poorest reconstructions (e.g., those on April 10) from dominating the outcome.

While $\rho_{\rm NX}$ is a useful measure of relative agreement among images, it does not provide an absolute score of reconstruction quality. For instance, Figure 9 shows that convolving the four geometric source models with the same circular Gaussian of FWHM α produces $\rho_{\rm NX}$ values (computed against the original image) that are different depending on the underlying model. Thus, to better standardize the interpretation of $\rho_{\rm NX}$ for

reconstructions of different underlying images, we invert the curves in Figure 9 to compute, for each value of $\rho_{\rm NX}$, an effective kernel size α. That is, we quantify the fidelity of a reconstruction in terms of an effective blurring kernel FWHM α that would give the same $\rho_{\rm NX}$ as we compute from the reconstruction.

We compute a characteristic value $\alpha_{\rm char}$ for each combination of imaging parameters by taking the mean α across the four sources, and we then rank the parameters according to this characteristic value. The top-ranked combination of parameters is then denoted as the "fiducial parameters" of that method. We also select a Top Set of parameter combinations that obtain an $\alpha_{\rm char}$ smaller than the nominal EHT resolution. That is, the Top Set includes all imaging parameter combinations with $\alpha_{\rm char} < 1/|\boldsymbol{u}|_{\rm max}$. A selection of the Top Set reconstructions is highlighted in green for the DIFMAP, eht-imaging, and SMILI parameter searches in Figures 6–8, respectively.

6.3.2. Parameter Selection Considerations

In Figure 10, we test whether or not our parameter selection procedure leads to reconstructed images that are unduly similar to the training set. In this test, we repeat the parameter selection process after withholding a specified geometric source model from the training set. For example, in Figure 10, the parameter combinations used to produce the images of the disk model were determined by selecting the best-performing parameters on only the ring, crescent, and double. Despite excluding the disk from the training set, all three pipelines produce an image with a disk morphology that does not resemble any of the other images in the training set.

A common feature of all four geometric models in the training set is that they restrict the compact emission to a region spanning $\lesssim$70 μas. One possible concern is that the resultant Top Set parameter combinations may then fail to reconstruct images of sources that have compact components extending over larger regions. However, such bright compact components would introduce variations over time in the visibilities that could not be fit with an overly restricted FOV. Thus, our requirement that Top Set reconstructions of M87 have $\chi^2 < 2$ ensures that they are not missing bright extended components.

Other common features in all our training set models are the lack of small-scale structure (the finest features in each image is $\geqslant$10 μas) and a fixed total compact flux density of 0.6. We test that our fiducial scripts produce accurate results for an image with small-scale structure using using a GRMHD snapshot image (see Figure 10), and we explore systematic uncertainties related to the total compact flux density in Appendix H.

6.3.3. Results of Parameter Selection

In Table 3, we summarize the specifications and outcomes of the three parameter surveys. In this table, for each parameter value, we list the fraction of parameter combinations in the Top Set that include that value. We also provide the total number of parameter combinations surveyed, the number of these combinations in the Top Set, and the fiducial imaging parameters for each pipeline. Table 4 quantifies the fidelity of the fiducial and Top Set images reconstructed from simulated data by reporting the equivalent blurring kernel α obtained with each method.

The distributions in Table 3 show that the parameter survey eliminates regions of parameter space from consideration based on our selection criteria. For instance, in the eht-imaging results, reconstructions using large hyperparameters (>10) on the TV and TSV regularizers or those using a large initial Gaussian (FWHM > 50 μas) perform poorly regardless of the other parameter values used. These parameters are not represented in the Top Set.

In addition, differences in the procedures for each pipeline lead to different fiducial parameters. In some cases, these are

Table 3
Parameters and Their Surveyed Values for the DIFMAP (Top), eht-imaging (Middle), and SMILI (Bottom) Pipelines

DIFMAP (1008 Param. Combinations; 30 in Top Set)							
Compact	**0.5**	**0.6**	**0.7**	**0.8**			
Flux (Jy)	$\boxed{27\%}$	27%	30%	17%			
Stop	Flux Reached			Δrms $\leqslant 10^{-4}$			
Condition		$\boxed{70\%}$		30%			
ALMA	**0.01**	**0.1**	**0.3**	**0.5**	**0.7**	**1.0**	
Weight Factor	17%	$\boxed{60\%}$	20%	3%	0%	0%	
Mask	**40**	**50**	**60**	**70**	**80**	**90**	**100**
Diam. (μas)	0%	0%	$\boxed{47\%}$	27%	23%	3%	0%
UV Weight	**0**	**−1**	**−2**				
Exponent κ	10%	$\boxed{60\%}$	30%				
eht-imaging (37500 Param. Combinations; 1572 in Top Set)							
Compact	**0.4**	**0.5**	**0.6**	**0.7**	**0.8**		
Flux (Jy)	12%	19%	$\boxed{24\%}$	23%	22%		
Init./MEM	**40**	**50**	**60**				
FWHM (μas)	$\boxed{58\%}$	42%	0%				
Systematic	**0%**	**1%**	**2%**	**5%**			
Error	26%	27%	$\boxed{26\%}$	20%			
Regularizer:	**0**	**1**	**10**	**10^2**	**10^3**		
MEM	0%	0%	8%	$\boxed{92\%}$	0%		
TV	31%	$\boxed{35\%}$	33%	0%	0%		
TSV	31%	$\boxed{34\%}$	32%	3%	0%		
ℓ_1	$\boxed{23\%}$	24%	24%	22%	7%		
SMILI (10800 Param. Combinations; 529 in Top Set)							
Compact	**0.4**	**0.5**	**0.6**	**0.7**	**0.8**		
Flux (Jy)	22%	$\boxed{31\%}$	25%	14%	8%		
$\ell_1^{\rm w}$ Soft Mask	**40**	**50**	**60**	**70**	**80**		
FWHM. (μas)	$\boxed{29\%}$	19%	21%	21%	15%		
Systematic	**0%**	**1%**					
Error	$\boxed{50\%}$	50%					
Regularizer:	**0**	**10**	**10^2**	**10^3**	**10^4**	**10^5**	
TV	9%	9%	11%	$\boxed{38\%}$	32%	0%	
TSV	13%	14%	13%	24%	$\boxed{36\%}$	0%	
	0	**10^{-2}**	**10^{-1}**	**1**	**10**	**10^2**	
$\ell_1^{\rm w}$	0%	0%	9%	$\boxed{47\%}$	44%	0%	

Note. For instance, the eht-imaging survey produced $5 \times 3 \times 4 \times 5^4 =$ 37,500 parameter combinations, and 1572 of these passed the criteria for inclusion in the Top Set. Below each parameter value we specify the fraction of the Top Set parameter combinations that include that value (see Section 6.3.1). Boxed parameters are those corresponding to the fiducial images. Note that the fiducial parameters are determined by identifying the parameter combination that jointly performs best on all the synthetic data sets; the fiducial parameters do not necessarily correspond with the parameters that have the largest share in the Top Set.

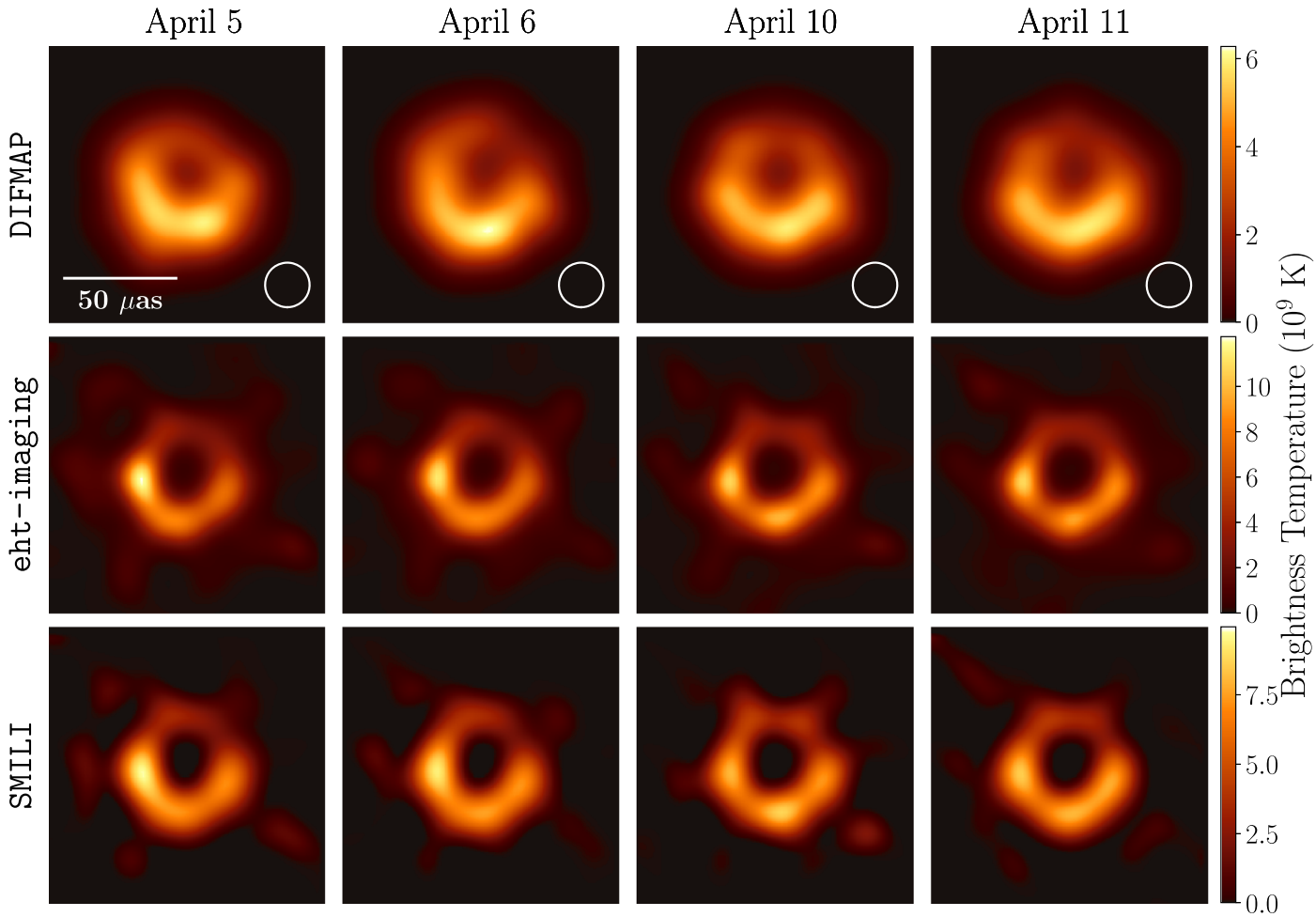

Figure 11. Fiducial images of M87 on all four observed days from each of the three imaging pipelines. CLEAN images (from DIFMAP) are shown after convolution with a 20 μas beam; eht-imaging and SMILI results have no restoring beam applied. Different selected fiducial imaging parameters (e.g., compact flux) result in different peak brightness temperatures for each method, as indicated by the unique color bars for each row.

Table 4
Equivalent Blurring Values α from the Fiducial and Top Set Images from Each Pipeline on Each of the Four Simple Geometric Models in the Training Set

	α (μas), Ring			α (μas), Crescent			α (μas), Disk			α (μas), Double		
	Fiducial	Mean	Std. Dev.	Fiducial	Mean	Std. Dev.	Fiducial	Mean	Std. Dev.	Fiducial	Mean	Std. Dev.
DIFMAP	19.4	21.2	1.5	19.0	21.6	1.5	18.5	21.2	2.1	19.8	21.6	1.5
eht-imaging	9.4	13.4	3.3	9.3	12.2	1.8	18.0	20.5	2.0	11.3	15.8	3.4
SMILI	10.6	12.2	2.8	10.6	12.2	2.3	12.3	18.7	3.1	11.3	14.8	3.4

Note. For each pipeline, we give α for the fiducial image, as well as the mean and standard deviation of α across the Top Set.

expected from differences in the underlying methods. For instance, the prior and mask sizes are treated differently in different scripts: a hard mask was used for DIFMAP, a softer mask for SMILI, and only weak constraints on compactness were used for eht-imaging. However, other choices are unexpected. For example, the top-ranked parameter combinations (i.e., the fiducial parameters) for the DIFMAP and SMILI pipelines use a total compact flux density of 0.5 Jy, favoring this value over the true total compact flux density of 0.6 Jy. However, these preferences are mild, and the Top Set from each pipeline includes images with all values of total compact flux density surveyed, from 0.4 to 0.8 Jy (see Table 3). We explore the dependence of the assumed compact flux density in Appendix H.

7. Fiducial M87 Images: Properties and Uncertainties

Having determined fiducial imaging parameters via tests on synthetic data (Section 6.3.1), we now show the corresponding fiducial M87 images from each imaging method for each day of the 2017 EHT observations. We also assess the consistency of the fiducial images with the data, discuss other visibility-domain properties of these images, and estimate image uncertainties resulting from imaging parameter choices.

7.1. Fiducial M87 Images

Figure 11 shows the fiducial images from each day of EHT observations and each imaging method. These fiducial images are broadly consistent; all twelve images have a prominent,

Table 5
Closure Quantity χ^2 Values for the Fiducial M87 Images and χ^2 Statistics (Mean and Standard Deviation) for Top Set Images

		DIFMAP			eht-imaging			SMILI		
		0%	1%	10%	0%	1%	10%	0%	1%	10%
April 5										
Fiducial:	$\chi^2_{\rm CP}$	6.03	4.55	0.85	0.98	0.94	0.32	0.98	0.94	0.32
	$\chi^2_{\log\,\rm CA}$	4.07	3.87	1.04	1.02	0.87	0.30	1.10	1.01	0.39
Top Set:	$\chi^2_{\rm CP}$	9.40 ± 3.35	6.98 ± 2.33	1.20 ± 0.33	1.00 ± 0.13	0.96 ± 0.11	0.32 ± 0.02	1.09 ± 0.21	1.04 ± 0.20	0.34 ± 0.05
	$\chi^2_{\log\,\rm CA}$	4.99 ± 1.17	4.74 ± 1.11	1.28 ± 0.29	0.97 ± 0.27	0.84 ± 0.17	0.29 ± 0.02	1.11 ± 0.28	1.02 ± 0.25	0.39 ± 0.07
April 6										
Fiducial:	$\chi^2_{\rm CP}$	2.30	2.07	0.66	1.51	1.46	0.54	1.44	1.39	0.52
	$\chi^2_{\log\,\rm CA}$	1.90	1.85	0.70	1.04	0.96	0.39	1.24	1.16	0.49
Top Set:	$\chi^2_{\rm CP}$	4.40 ± 1.45	3.96 ± 1.34	1.18 ± 0.45	1.59 ± 0.16	1.53 ± 0.15	0.55 ± 0.04	1.49 ± 0.23	1.44 ± 0.22	0.53 ± 0.07
	$\chi^2_{\log\,\rm CA}$	3.49 ± 1.51	3.38 ± 1.45	1.13 ± 0.36	1.00 ± 0.14	0.93 ± 0.11	0.38 ± 0.02	1.22 ± 0.25	1.14 ± 0.23	0.48 ± 0.07
April 10										
Fiducial:	$\chi^2_{\rm CP}$	2.22	1.95	0.56	0.77	0.75	0.37	0.68	0.66	0.35
	$\chi^2_{\log\,\rm CA}$	1.07	1.05	0.43	1.24	1.16	0.56	1.14	1.07	0.58
Top Set:	$\chi^2_{\rm CP}$	3.93 ± 2.10	3.40 ± 1.50	0.96 ± 0.26	0.83 ± 0.10	0.80 ± 0.09	0.39 ± 0.03	0.75 ± 0.14	0.73 ± 0.14	0.37 ± 0.08
	$\chi^2_{\log\,\rm CA}$	1.57 ± 0.64	1.52 ± 0.62	0.60 ± 0.21	1.30 ± 0.17	1.21 ± 0.14	0.60 ± 0.07	1.11 ± 0.32	1.05 ± 0.30	0.57 ± 0.17
April 11										
Fiducial:	$\chi^2_{\rm CP}$	1.90	1.53	0.49	0.96	0.90	0.27	1.07	1.01	0.38
	$\chi^2_{\log\,\rm CA}$	2.48	2.35	0.67	0.97	0.84	0.36	1.08	0.97	0.46
Top Set:	$\chi^2_{\rm CP}$	4.01 ± 1.67	2.87 ± 1.05	0.61 ± 0.11	0.97 ± 0.10	0.91 ± 0.09	0.27 ± 0.02	1.23 ± 0.28	1.16 ± 0.27	0.40 ± 0.06
	$\chi^2_{\log\,\rm CA}$	3.33 ± 1.01	3.16 ± 0.95	0.92 ± 0.24	0.99 ± 0.13	0.86 ± 0.09	0.36 ± 0.02	1.14 ± 0.13	1.02 ± 0.12	0.49 ± 0.07

Note. For each, values are shown after including systematic uncertainties of 0%, 1%, and 10%. Inclusion in the top set requires $\chi^2 < 2$ for both closure phases and amplitudes with 0% systematic uncertainty for eht-imaging and SMILI, and with 10% systematic uncertainty for DIFMAP. See Section 2.1 for definitions and limitations of these metrics.

asymmetric ring feature, approximately 40 μas in diameter with enhanced brightness toward the south. Each image has a prominent depression in the center of the ring and a peak brightness temperature along the ring of $\sim 10^{10}$ K. Because they are restored with a 20 μas beam, the DIFMAP images have broader structure, leading to a weaker central depression and lower peak brightness temperatures. For all pipelines, the finite resolution of the reconstructions results in brightness temperatures that are only lower limits on the maximum intrinsic brightness temperature.

As expected from tests on synthetic data (Section 6), the details of the reconstructions differ between the imaging methods. Although the RML images (eht-imaging and SMILI) are generally more similar to each other than to the DIFMAP images, SMILI reconstructions are fainter inside and outside the ring than the eht-imaging reconstructions from the strong sparsity regularization. Based on the results of the parameter survey, M87 data was reconstructed with a total compact flux density of 0.5 Jy for DIFMAP and SMILI, and with 0.6 Jy for eht-imaging. While 0.5 Jy is slightly below the range of acceptable values for $F_{\rm cpct}$ identified in Section 4, the constraints presented in Section 4 made strict assumptions about the gains that are not rigidly enforced in imaging, and our parameter surveys using synthetic data demonstrate that some imaging methods produce higher fidelity (i.e., higher $\rho_{\rm NX}$) images when reconstructing an image with less compact flux density than the true value. We explore the effects of the assumed compact flux density further in Appendix H.

In Table 5, we provide χ^2 values for the 12 fiducial images as well as χ^2 statistics across the Top Sets. We compute these values after including varying amounts of systematic uncertainty (0%, 1%, and 10% of visibility amplitudes) added in quadrature to the thermal uncertainty. This additional uncertainty accounts for possible systematic errors (e.g., from polarimetric leakage) and also ensures that the statistics quantify overall image-data consistency without being overwhelmed by the extremely sensitive ALMA baselines. For the largest value, 10%, the systematic uncertainty allows modest tolerance for source structure that is absent from the reconstructed images (e.g., from extended structure in the M87 jet outside the masked region or the FOV of the reconstructed image).

Figures 12 and 13 compare self-calibrated visibility amplitudes and closure phases on three selected triangles with the corresponding model visibility amplitudes and closure phases computed from each April 11 fiducial image. As indicated in the χ^2 values listed in Table 5, the two RML methods produce fiducial images that are consistent with the data to within roughly their thermal uncertainties, and the χ^2 values have little scatter across the Top Sets. The DIFMAP fiducial image also shows agreement with the data, but requires modest systematic tolerance for comparable image-data consistency (because of the different time averaging used in DIFMAP imaging the ALMA downweighting), and the χ^2 values show more scatter across the Top Set. All three fiducial images fit the nulls in visibility amplitudes at 3.4 and 8.3 Gλ.

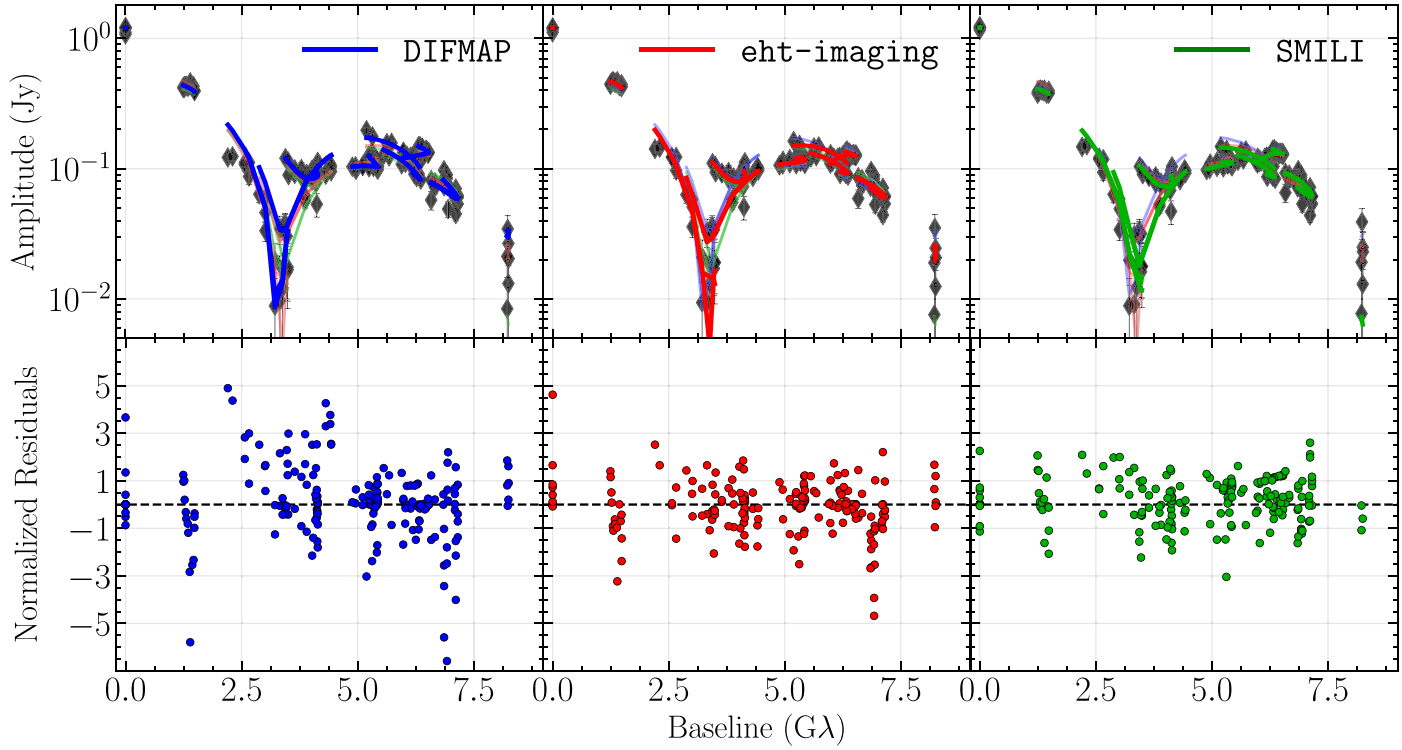

Figure 12. Top: visibility amplitudes of self-calibrated data on April 11 as a function of baseline length compared with corresponding values for the three fiducial images. In each panel, visibilities are plotted after self-calibrating the data to the indicated fiducial image; thus, the visibility amplitudes differ across the three panels. For each image, we add an additional large-scale Gaussian component before self-calibration to account for the excess flux density seen on intra-site baselines (see Section 4.3). Bottom: visibility amplitude residuals for each fiducial image, after normalizing by the thermal noise with 1% systematic uncertainty added in quadrature.

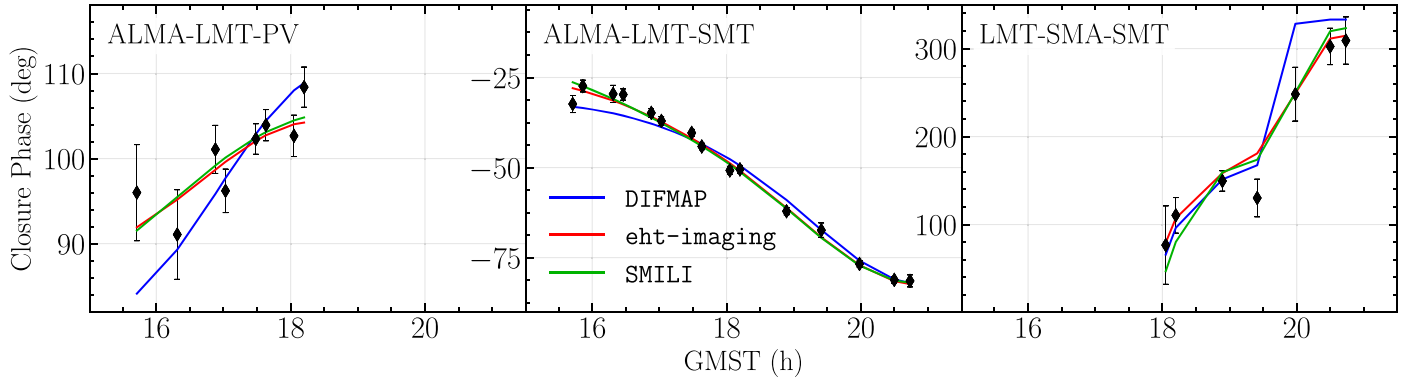

Figure 13. Closure phases plotted as function of GMST on three selected triangles from the April 11 observations. The solid lines indicate the corresponding closure phase curves from the fiducial images produced by the three pipelines.

Our images of M87 do not show extended emission outside the observed ring, although a jet is prominent in VLBI images of M87 at longer wavelengths. Likewise, while the geometric models in the training set (Section 6.1) include emission from a simple extended jet model, none of the Top Set reconstructions from simulated EHT data recover this extended component nor are their recovered compact structure affected by the missing jet components. Furthermore, our fiducial images in all three pipelines do not recover the more realistic faint jet emission in the GRMHD simulation reconstructions in Figure 10. All of these results reinforce the expectation (see Section 4.3) that the current EHT array lacks the short-baseline coverage and dynamic range necessary to recover a faint, extended jet.

In Figure 14, we show the fiducial images from the three pipelines on April 11 after blurring each of them separately to achieve a common, conservative resolution. Specifically, we restore the `DIFMAP` image with the same 20 μas beam used throughout this Letter. For `eht-imaging` and `SMILI`, we use the circular Gaussian convolution kernels that maximize the normalized cross-correlation between the restored RML image and the restored `DIFMAP` image (17.1 μas for `eht-imaging`; 18.6 μas for `SMILI`). The three blurred images have a consistent ring diameter ($\approx$40 μas) and the same overall asymmetry (oriented south). Figure 15 shows the simple average of the three equivalently blurred fiducial images for each day. We adopt the images in

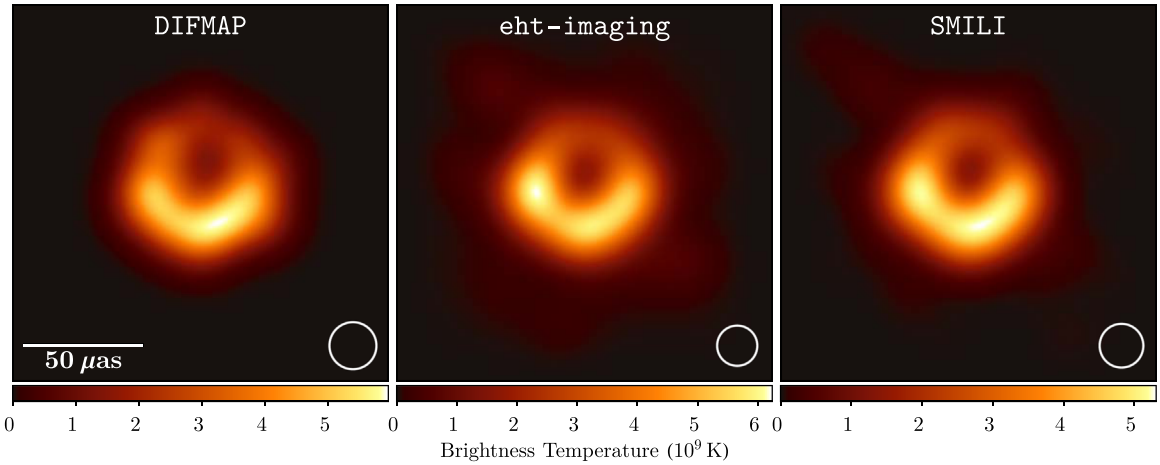

Figure 14. Fiducial images of M87 on April 11 from our three separate imaging pipelines after restoring each to an equivalent resolution. The `eht-imaging` and `SMILI` images have been restored with 17.1 and 18.6 μas FWHM Gaussian beams, respectively, to match the resolution of the `DIFMAP` reconstruction restored with a 20 μas beam.

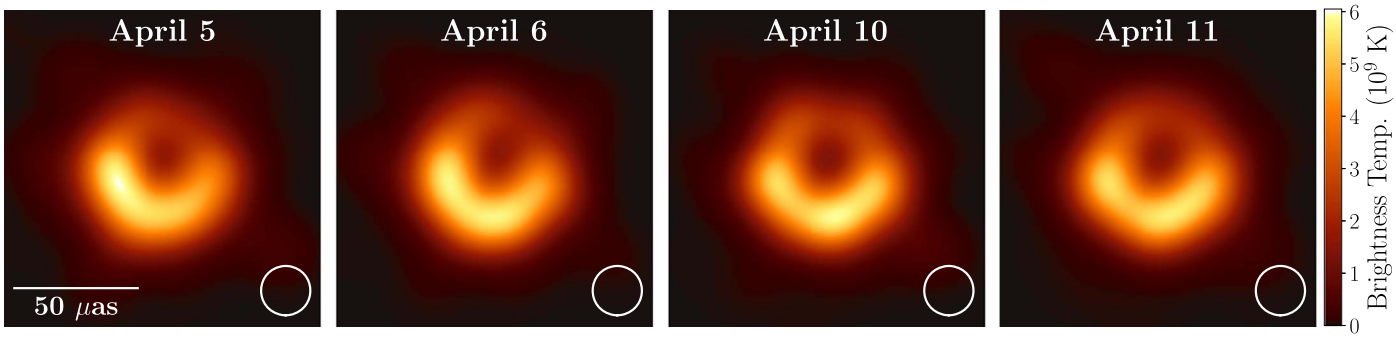

Figure 15. Averages of the three fiducial images of M87 for each of the four observed days after restoring each to an equivalent resolution, as in Figure 14. The indicated beam is 20 μas (i.e., that of `DIFMAP`, which is always the largest of the three individual beams).

Figure 15 as a conservative representation of our final M87 imaging results.

The fiducial images from each pipeline (Figure 11), as well as the conservative, blurred, pipeline-averaged images (Figure 15) provide some evidence for evolution in the ring structure between April 5, 6 and 10, 11. We discuss this evolution in more detail in Appendix E (Figure 33). Some change in the image structure between April 5, 6 and 10, 11 is necessitated by the variations seen in the underlying closure phases (Paper III). We find more variation in the image pairs that are separated by larger intervals, suggesting that these variations are intrinsic. However, we cannot unambiguously associate the observed variability with coherent evolution of a specific image feature.

Figure 16 shows the visibility amplitude and phase for each of the three April 11 fiducial images as a function of vector baseline. Note that no restoring beam is required for CLEAN in this visibility-domain analysis. Each image produces nulls in the visibility amplitude near the SMA–SMT baseline, consistent with the observed amplitudes (see Figure 2). The visibility phase shows rapid swings at these nulls. The visibilities of the images from the different pipelines are most similar near the EHT measurements, as expected. On longer baselines than those sampled by the EHT, the `DIFMAP` image produces notably higher visibility amplitudes than those of the `eht-imaging` and `SMILI` images, as expected from the fact that the `DIFMAP` image is fundamentally a collection of point sources.

7.2. Image Uncertainties

Measuring the variation in images produced in a parameter survey Top Set allows us to evaluate image uncertainties due to the explored imaging choices. Figure 17 shows uncertainties related to imaging assumptions from the largest Top Set (that of the `eht-imaging` parameter survey) on April 11 data.

Reconstructed image uncertainties are concentrated in the regions with enhanced brightness, notably in the three "knots" in the lower half of the ring (Figure 17; top panel). These are also the regions that show the most variation among different imaging methods (Appendix I compares their azimuthal profiles). Visibility-domain modeling provides another method to assess image structure. In Paper VI, we explore fitting simple crescent models to the data. For instance, a crescent with a brightness gradient and blurring reproduces the north–south asymmetry in images without additional azimuthal structure (the "blurred and slashed with LSG" crescent of Paper VI). However, this model gives $\chi^2_{\rm CP}$ between 3.2 and 11.5 and $\chi^2_{\log\,\rm CA}$ between 2.2 and 6.6 for different days and bands when assuming 0% systematic error (compare with Table 5). Adding additional degrees of freedom in the form of three elliptical Gaussian components to the crescent

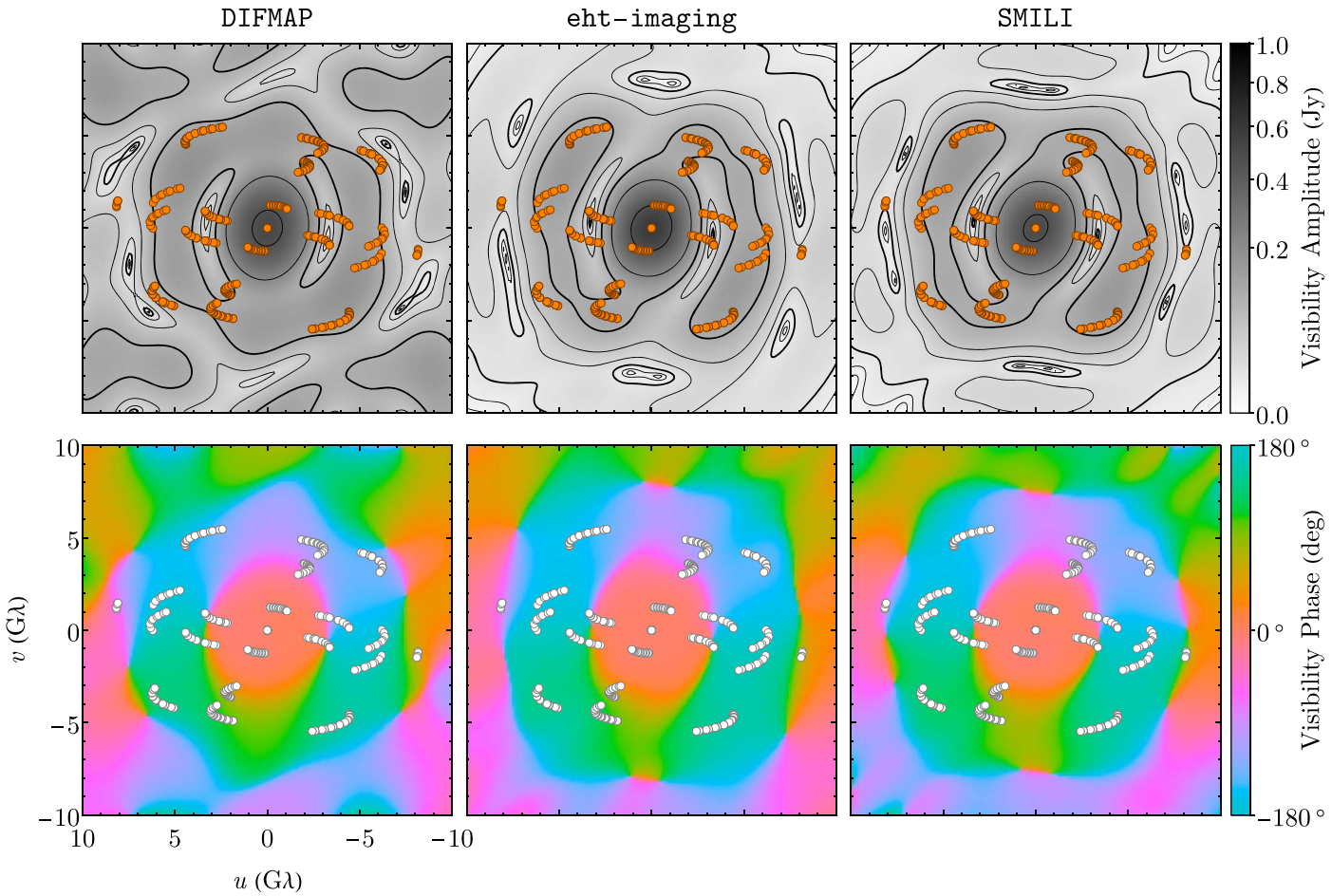

Figure 16. Visibility-domain representation of the three fiducial pipeline images for April 11. The top panels show visibility amplitude as a function of vector baseline; the bottom panels show visibility phase as a function of vector baseline. Amplitude contours are spaced logarithmically, with three contours per decade. Thicker contours correspond to 10 and 100 mJy; the lowest contour is at $10^{1/3} \approx 2.2$ mJy, although the images produce nulls in the visibility domain. Plotted points show the April 11 EHT coverage.

yields better fits, similar to those found with imaging. These Gaussian components sometimes reside near or on the crescent, affecting the azimuthal structure (see Appendix B.2.2 in Paper VI). Thus, our current image reconstructions and visibility-domain analyses are not able to confirm or reject the reality of the "knots" seen in images, and these features should be interpreted with caution.

In the visibility domain, the uncertainties are concentrated at the origin, reflecting the spread of total compact flux density choices present in the Top Set (Figure 17; bottom panel). After normalizing the total flux densities of the Top Set images, the visibility domain uncertainties at the origin are zero; the uncertainties peak on baselines at $\sim$2 Gλ, then fall gradually with increasing baseline length. The fractional uncertainties are the most straightforward to interpret, as they are low ($\lesssim$10%) in regions near EHT coverage and grow to values near or exceeding unity for baselines that are separated by more than a few Gλ from an EHT measurement.

The strong correlation between the visibility-domain fractional uncertainties and gaps in EHT coverage suggests that imaging uncertainties are dominated by imaging parameter choices rather than by thermal or systematic noise. That is, the fiducial image fidelity is primarily limited by the sparse EHT baseline coverage, rather than by sensitivity or calibration accuracy. For example, the standard deviation of visibility amplitudes across the Top Set for M87 is $\sim$50 mJy on baselines at $\sim$2 Gλ, falling to $\sim$10 mJy at $\sim$8 Gλ. In contrast, the median thermal noise of non-ALMA baselines is 7 mJy and of ALMA baselines is 0.7 mJy.

In the image domain, the median rms variation is 1.6×10^8 K for the Top Set images of M87, and 1.3×10^8 K for the normalized Top Set images. Because the peak image brightness is $\sim 10^{10}$ K, these variations indicate that our images achieve a dynamic range of $\sim$50. Across the image, the minimum fractional uncertainty from imaging parameter choices is 8.7% across the Top Set images without flux density normalization, and 7.9% with normalization. For comparison, the rms of the DIFMAP residual images is significantly smaller: $\sim 3 \times 10^7$ K across all days for the fiducial parameters. Thus, adding in the residual images would have negligible effect on our final reconstructions, especially relative to image differences between images from different imaging methods and from different parameter combinations using a single method.

8. Image Validation

Having determined fiducial images of M87 from each imaging method on each observing day, we now perform additional validation tests to assess their reliability. First, in Section 8.1, we compare the residual telescope gains estimated for M87 with those for the calibrator source 3C 279 to

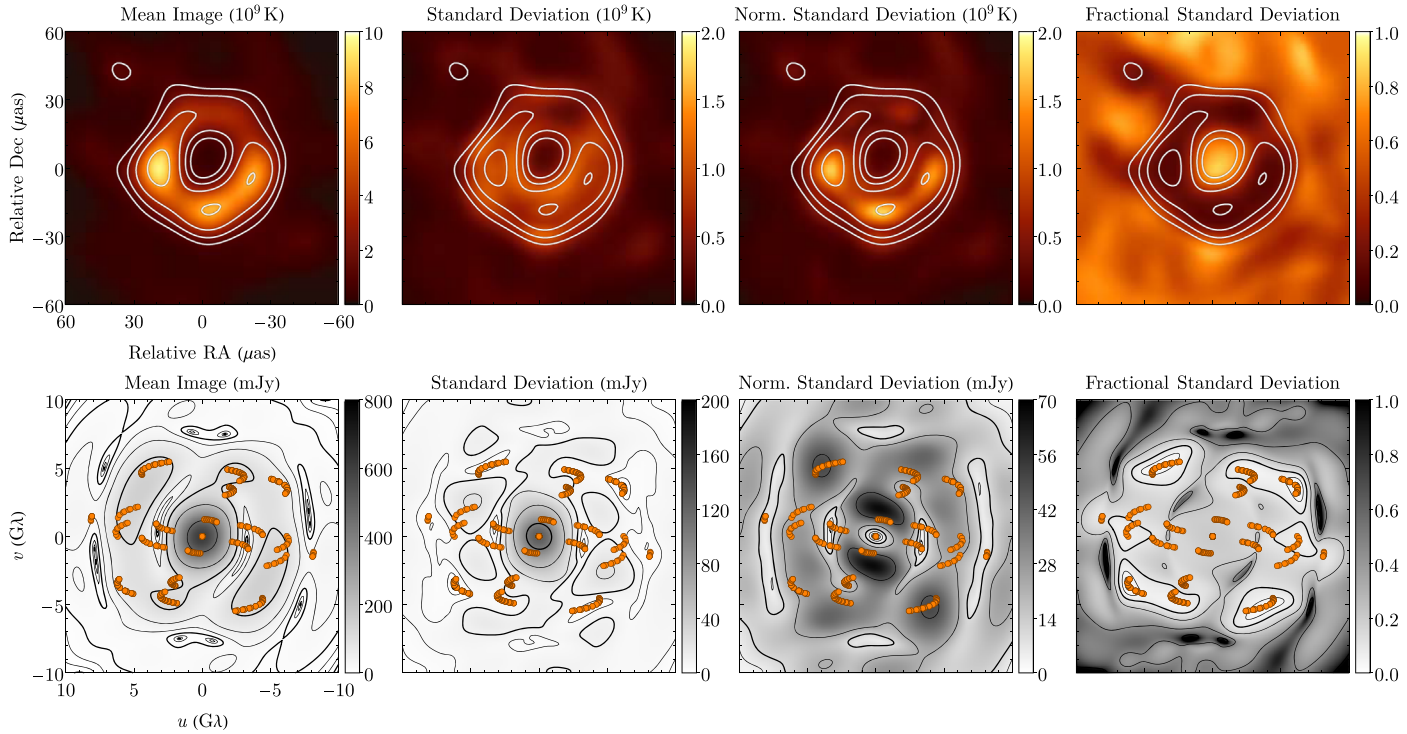

Figure 17. Uncertainties related to imaging assumptions from the `eht-imaging` parameter search on April 11 data. The top row shows the mean image and associated uncertainties in the image domain, while the bottom row shows visibility amplitudes of the mean image and their uncertainties in the visibility domain. From left to right, panels correspond to the mean Top Set image, the standard deviation of the Top Set reconstructions, the standard deviation after normalizing each reconstructed image to the total flux density of the mean image (0.62 Jy), and the standard deviation divided by the mean. In the image domain panels, contours are those of the mean image, at 10%, 20%, 40%, and 80% of the peak. In the visibility domain panels, contours are equally spaced logarithmically with three contours per decade; the thicker contours are 10 and 100 mJy (left three) and 10% (right).

determine whether or not the significant variation seen in the inferred LMT residual gains are consistent between the two sources. Next, in Section 8.2, we perform data resampling tests, using identical scripted reconstructions on data sets that exclude individual sites, to assess how sensitive the image morphology is to the loss of different combinations of data. Finally, in Section 8.3, we test whether or not the time variability seen in the fiducial images is related to differences in the sampled (u, v) coverage across the days.

8.1. Gain Validation with the Calibrator 3C 279

The 2017 EHT observations of M87 were interleaved with those of the active galactic nucleus 3C 279. We have reconstructed images of 3C 279 using the three software packages used for M87 imaging in order to assess the consistency of these 3C 279 images with the M87 reconstructions in terms of the inferred time-variable residual gains. Because the sources are nearby on the sky (separation = 19°), the inferred time-variable residual gains at each site for the same day should be similar. We do *not* use the observations of 3C 279 to derive gain corrections for M87; instead, we compare the derived gains on both sources after independent imaging as a post hoc consistency test.

Figure 18 shows the aggregate baseline coverage for the interleaved EHT observations of 3C 279 in 2017 April. While the SPT could not observe M87, it participated in the observations of 3C 279, viewing it at an elevation of ∼6° (i.e., a relative air mass of ∼10). The addition of the SPT significantly improves the north–south resolution of the array. Figure 19 shows the April 11 visibility amplitudes from 3C 279 after a priori and network calibration. From ALMA

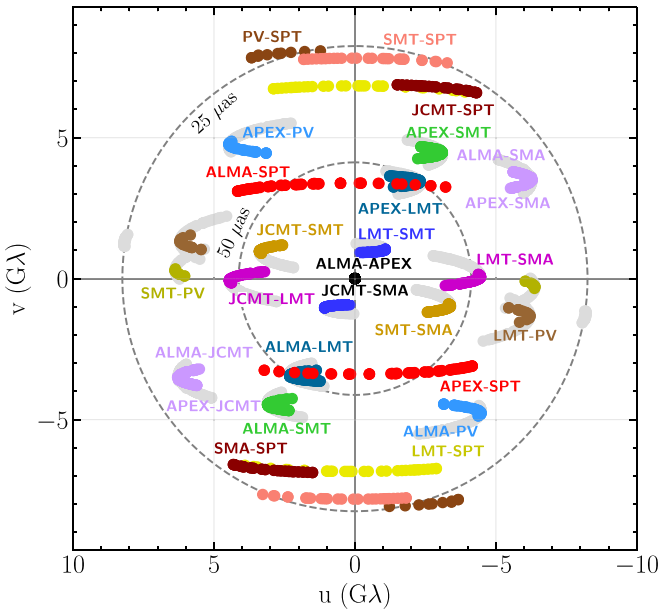

Figure 18. Aggregate baseline coverage for EHT observations of 3C 279 in 2017 April. The coverage of M87 is shown in light gray for comparison.

interferometric measurements, the total flux density for 3C 279 (8–10 Jy) is nearly an order of magnitude higher than that of M87 (Goddi et al. 2019). As expected for a source with bright, linear jet features, the 3C 279 amplitudes vary strongly with baseline position angle and have a more complex structure on long baselines than M87 (Figure 2).

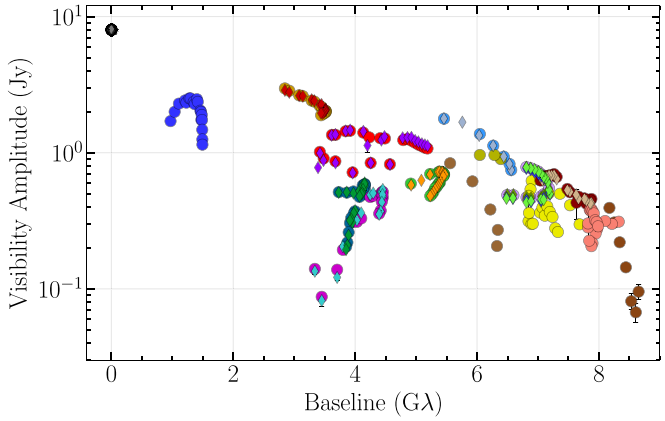

Figure 19. Visibility amplitudes of 3C 279 on April 11 as a function of projected baseline length after a priori and network calibration. The amplitudes are corrected for upward bias from thermal noise (Equation (6)). Points are colored by baseline as in Figure 18.

We imaged 3C 279 using both traditional CLEAN (`DIFMAP`) and RML (`eht-imaging` and `SMILI`) methods. Because of pronounced differences between the sources in different characteristics (total flux density, FOV, compact structure morphology), we do not use the same fiducial scripts derived for M87 on the 3C 279 data. Furthermore, as a consequence of having very few short baselines in the EHT array, we have found imaging 3C 279 to be more difficult than M87 because of its more extended structure. A full description of 3C 279 imaging procedures and results will be presented separately.

Figure 20 shows reconstructed images of 3C 279 from all three methods using data from April 11. The source exhibits two compact and bright features with a separation of $\sim$100 μas: a primary component extended in the northwest to southeast direction, and a secondary component perpendicular to the first. This secondary component extends from the core in the direction of the 3C 279 jet observed at lower frequencies (see, e.g., Lister et al. 2016; Jorstad et al. 2017).

In Figure 21, we compare the interleaved multiplicative station gains for M87 and 3C 279 on April 5. The station gains were derived via self-calibration to the fiducial images of M87 from the three imaging pipelines (Section 7) and on the three images of 3C 279 (Figure 20). In Table 6, we present the median gains for the two sources and compare them to the expected a priori visibility amplitude error budget, assuming nominal pointing and focus (Paper III).

The gains derived from images produced with the three imaging methods are consistent. For all stations except the LMT, the derived gains are time-variable, but close to unity. Issues with the performance of the LMT (Section 4, and Paper III) result in a larger median gain correction at that station, in line with the gain corrections derived directly from the visibility amplitudes via the use of crossing tracks on M87 described in Appendix B. Furthermore, the interleaved LMT gain curve has large variations with time on both sources. In particular, the M87 gains at the LMT have large, single-scan excursions not seen in the 3C 279 gain trends. These excursions are likely due to poor pointing on M87, which is nearly an order of magnitude fainter than 3C 279.

In Table 14 of Appendix F, we present the median gains for the two sources, compared to the expected a priori visibility amplitude error budget, across all days. Figure 34 in Appendix F compares the gain variations recovered from imaging M87 and 3C 279 across all days for the SMT and LMT stations. In some cases, the absolute gain is not identical across the different sources and imaging pipelines. This variation can be partly ascribed to the large uncertainty in the total flux density of 3C 279. However, in all cases the relative gain trends with time are broadly consistent, except for the occasional large excursions seen in the LMT M87 gains.

The consistency of the derived gain variations between the two sources and the different imaging methods for all stations on all days, particularly for the large corrections at LMT, provides confidence that these corrections are not the result of imaging artifacts or missing structure in M87 reconstructions. In Paper VI we show that derived gains from fitting parametric models are similar to those derived from imaging.

8.2. Image Dependence on Sites

Our comparisons of reconstructed images on different days show that the primary image features in M87 are not sensitive to small changes in baseline coverage (Figure 11). We now explore how more severe changes in baseline coverage affect imaging. In particular, we assess whether or not the image structure is closely tied to the data from any one site.

The top row of Figure 22 shows reconstructed images of M87 using the fiducial `eht-imaging` parameters after excluding all data on baselines to one of the five EHT sites that observed the source. As shown in Figure 1, removing some sites entirely from the array does not lead to a significant decrease in the length of the longest baseline in either the north–south or east–west direction. The notable exceptions are Chile (ALMA and APEX) and Pico Veleta (PV) in Spain. The Chilean sites are part of all baselines with north–south lengths $|v| > 2.5$ Gλ, while PV provides the only baselines in the northeast direction with lengths longer than 5 Gλ. Thus, the loss of either of these sites significantly elongates the synthesized beam and impedes the reconstruction of the ring feature.

The presence of a ring in our reconstructed images of M87 is resilient to several site losses, even though the fiducial imaging parameters were not chosen using a reduced (u, v) coverage. The ring is successfully reconstructed when we entirely omit both Hawai'i stations (SMA and JCMT), even though these stations are required to sample the two visibility nulls (at $\sim$3.4 and $\sim$8.3 Gλ; see Section 2.1). The fiducial scripts also reconstruct a ring when LMT data are entirely omitted, but the ring orientation is reversed. Unsurprisingly, the site losses that result in the poorest reconstructions of the ring are those that most degrade the synthesized beam, namely Chile and PV.

We also tested whether or not severe calibration errors could have affected imaging. To do so, we applied our fiducial scripts after omitting calibrated visibility amplitudes to a specified site while still retaining closure phases and closure amplitudes. The lower panels of Figure 22 show this test for M87 reconstructions using the `eht-imaging` pipeline (for similar results with `SMILI`, see Appendix D).[117] Comparing the top and bottom row of Figure 22, it is apparent that even sites with poor amplitude calibration (e.g., the LMT) can provide essential constraints through closure quantities. For this reason, we do not flag data with poor amplitude calibration before imaging. We also show an image that uses only closure quantities for the reconstruction, therefore using no calibration information for

[117] The fiducial script was minimally adapted to allow this test.

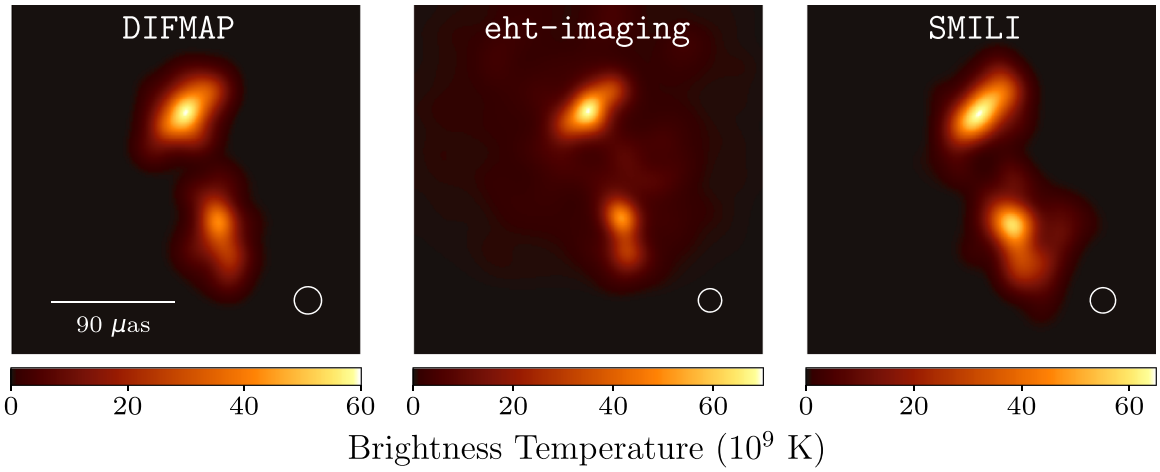

Figure 20. Representative images of 3C 279 from the April 11 EHT observations produced using `DIFMAP`, `eht-imaging`, and `SMILI`. To simplify visual comparisons and display the images at similar resolutions, the images are restored with circular Gaussian beams of 20, 17.1, and 18.6 μas FWHM, respectively.

Table 6
Median, 25th, and 75th Percentile Residual Gain Corrections for M87 and 3C 279 on April 5

Station	Fiducial M87 Median Gain			3C 279 Median Gain			A Priori Budget (%)
	DIFMAP	eht-imaging	SMILI	DIFMAP	eht-imaging	SMILI	
ALMA	$0.97^{+0.02}_{-0.03}$	$0.97^{+0.02}_{-0.01}$	$0.98^{+0.01}_{-0.01}$	$0.99^{+0.02}_{-0.09}$	$1.11^{+0.04}_{-0.02}$	$0.97^{+0.03}_{-0.01}$	5.0
APEX	$1.05^{+0.04}_{-0.02}$	$1.02^{+0.02}_{-0.01}$	$1.01^{+0.01}_{-0.01}$	$0.99^{+0.01}_{-0.00}$	$0.90^{+0.01}_{-0.00}$	$1.05^{+0.01}_{-0.02}$	5.5
SMT	$1.13^{+0.01}_{-0.06}$	$1.02^{+0.04}_{-0.01}$	$0.99^{+0.02}_{-0.01}$	$1.06^{+0.01}_{-0.02}$	$0.97^{+0.01}_{-0.02}$	$1.04^{+0.02}_{-0.01}$	3.5
JCMT	$1.00^{+0.02}_{-0.00}$	$1.00^{+0.00}_{-0.00}$	$1.00^{+0.00}_{-0.00}$	$1.00^{+0.01}_{-0.00}$	$1.02^{+0.02}_{-0.01}$	$1.00^{+0.00}_{-0.01}$	7.0
LMT	$1.46^{+0.76}_{-0.21}$	$1.55^{+0.93}_{-0.19}$	$1.47^{+0.91}_{-0.19}$	$1.08^{+0.16}_{-0.04}$	$1.21^{+0.13}_{-0.11}$	$1.35^{+0.27}_{-0.05}$	11.0
SMA	$1.00^{+0.02}_{-0.01}$	$1.00^{+0.01}_{-0.00}$	$1.00^{+0.00}_{-0.00}$	$1.01^{+0.01}_{-0.01}$	$1.04^{+0.03}_{-0.00}$	$0.99^{+0.00}_{-0.01}$	7.5
PV	$1.14^{+0.04}_{-0.04}$	$0.96^{+0.02}_{-0.07}$	$0.98^{+0.02}_{-0.07}$	$1.33^{+0.12}_{-0.04}$	$1.14^{+0.04}_{-0.05}$	$0.94^{+0.05}_{-0.02}$	5.0

Note. These gains were derived via self-calibration (with no systematic error included). The error budget on a priori calibration is derived in Paper III. Note that the median gain corrections for ALMA, APEX, SMA, and JCMT can reasonably be much smaller than this error budget because network calibration has already been applied. The variation in the recovered gains among pipelines is partly due to the large uncertainty in the total flux density (between 8 and 10 Jy) and total compact flux density of 3C 279.

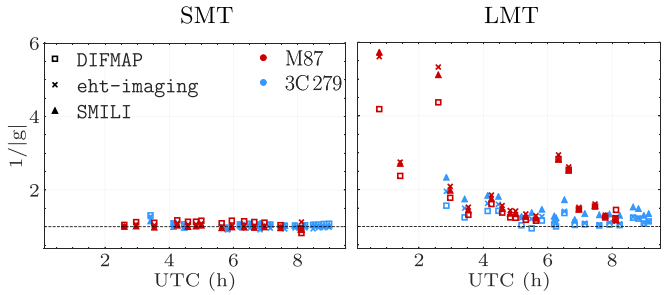

Figure 21. Multiplicative residual station gains for the SMT (left) and LMT (right) derived from the 3C 279 images (Figure 20) and fiducial M87 images (Figure 14) from the three imaging pipelines on April 5. Gains for the fiducial images of M87 are shown in red; those for 3C 279 are shown in blue. The particularly large excursions on the LMT M87 gains are likely due to poor pointing. Note that LMT could not observe 3C 279 before 2^h30 UTC.

any site. This image demonstrates that closure quantities are sufficient to recover the diameter and asymmetry of the ring in the fiducial images.

8.3. Tests of the Observed Time Variability

Our fiducial images of M87 (Figure 11) over the four observing days show an evolution in the ring structure between the two observations on April 5, 6 and the two observations on April 10, 11 (Figure 33). However, the data used to reconstruct these images do not identically sample the (u, v) plane (Figure 1). To verify whether or not the observed evolution in the fiducial M87 images is intrinsic, it is necessary to confirm that the evolution is not an artifact imprinted on the reconstructions by the changing (u, v) coverage sampled by the EHT on the different observing days.

To this end, we constructed reduced data sets from the April 6 and 11 data with "overlapping" baseline coverage. Specifically, we flag all (u, v) points along a particular baseline track that are not common to the April 6 and 11 observations (i.e., we flag points on April 6 with no measurement on April 11 within 0.01 Gλ, and vice versa). The number of (10 s averaged) visibilities is reduced from ~18,000 to ~5,000 in the overlapping data set. We then used the `eht-imaging` script with the identified fiducial parameters (Section 6.2.2) to reconstruct images on both days with these subsampled data sets.

Figure 23 compares the reconstructions made from these overlapping (u, v) data to our original images from the full data sets. The results show no significant variation in the morphology due to the changing (u, v) coverage. In particular, the enhanced southwest brightness in the April 11 image

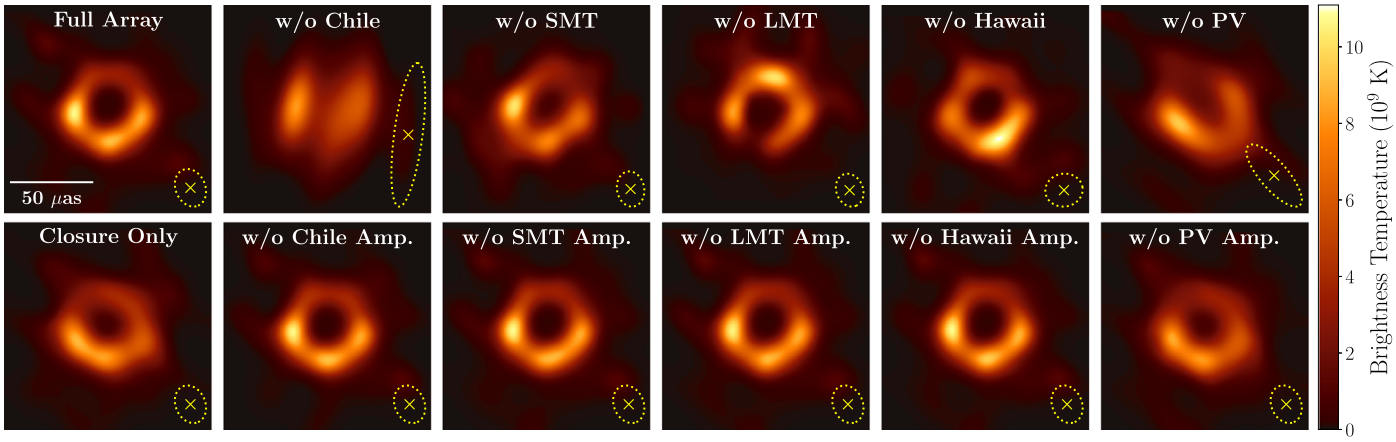

Figure 22. Example reconstructions of M87 on April 11 after omitting visibilities to each geographical site. The top row shows reconstructions that exclude all baselines to the indicated site (i.e., mimicking an observation without that site); the bottom row shows reconstructions that exclude all visibility amplitudes on baselines to the indicated site, while still including closure phases and closure amplitudes (i.e., exploring the limit of arbitrarily poor amplitude calibration). The lower-left panel shows an image reconstructed after excluding visibility amplitudes to all sites (i.e., using only closure quantities). These images were reconstructed using the `eht-imaging` pipeline with its fiducial parameters (see Section 6.3.3). The ellipse in each panel shows the corresponding synthesized beam with uniform weighting, but the image is not convolved with this beam. While the fiducial parameters used are not necessarily optimal for imaging these modified data sets, the reconstructed images of M87 are rather resilient to the loss of most sites, especially if the closure information is preserved, demonstrating that our results are insensitive to calibration assumptions. Figure 32 in Appendix D shows corresponding results for the `DIFMAP` and `SMILI` pipelines.

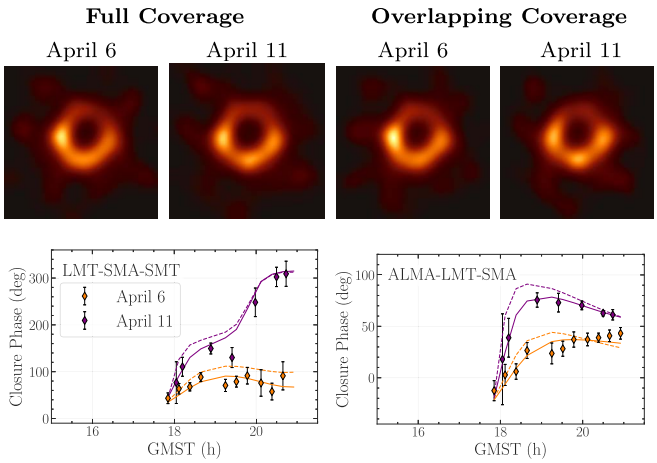

Figure 23. Validating the observed variation in the reconstructed images between April 6 and 11. Top-left panels: fiducial `eht-imaging` image reconstructions from observations on April 6 and 11 (Section 7.1). Top-right panels: reconstructions using the same fiducial script and parameters, but using data only on the (u, v) points which overlap on April 6 and 11. The reconstructions using only the overlapping (u, v) coverage show similar time evolution (a shift in brightness to the southwest; see Appendix E) to the reconstructions from the original data sets, indicating that the observed variation in images is intrinsic. Bottom panels: plots of two selected closure phases (LMT–SMA–SMT and ALMA–LMT–SMA) that clearly identify intrinsic structural evolution between April 6 and 11. The colored points identify the closure phases of the scan-averaged data, and the phases shown as solid and dotted colored lines are taken from the reconstructions of full and overlapping coverage data, respectively.

relative to the April 6 image is still prominent in the overlapping coverage reconstructions. This test shows that the reconstructed evolution is not due, at least solely, to the changes in (u, v) coverage between days, although each image is still affected by the limited (u, v) coverage. The bottom panels of Figure 23 show selected closure phases on April 6 and 11 that are significantly different; reconstructed images with both the full and overlapping data sets recover this significant evolution of closure phases. We discuss the observed time variability further in Appendix E.

9. Image Analysis

To assess the consistency of our images with each other and determine which specific image features are most reliable, we define and measure several properties that characterize asymmetric rings: the diameter d, width w, orientation angle η, azimuthal brightness asymmetry A, and fractional central brightness f_C. This approach is also motivated by GRMHD simulations of M87, which predict an image dominated by a bright and nearly circular ring morphology across a large range of parameters (Paper V). In Section 9.1, we define these quantities, explain how they are measured, and give procedures to estimate their uncertainties. In Section 9.2, we evaluate biases and systematic errors in these measurements using tests with synthetic data. In Section 9.3, we apply our results to estimate properties of the fiducial images of M87 presented in Section 7. In Paper VI, we explore model fitting in more detail, both through visibility-domain fits of geometrical models and through image-domain analysis of the reconstructions from each imaging pipeline.

9.1. Ring Parameter Definitions

To identify a ring in a given reconstructed image, we search for the central point from which radial profiles are peaked at a similar distance. From a candidate ring center position (x, y), we sample the linearly interpolated image equally in azimuthal angle θ between 0° and 360° and in radius r between 0 and 50 μas to obtain a transformed image: $I(r, \theta; x, y)$.[118] Then, for each radial profile at fixed θ, we identify the distance $r_{\rm pk}$ at which the angular profile assumes its peak brightness. We define the ring radius at a given position, $\bar{r}_{\rm pk}(x, y)$ as the mean of these peak distances:

$$r_{\rm pk}(\theta; x, y) = \mathrm{argmax}_r[I(r, \theta; x, y)],$$
$$\bar{r}_{\rm pk}(x, y) = \langle r_{\rm pk}(\theta; x, y)\rangle_{\theta\in[0,2\pi]}. \quad (16)$$

To estimate an associated uncertainty, we use the standard deviation $\sigma_{\bar{r}}(x, y)$ of the $r_{\rm pk}(\theta; x, y)$ values. For a similar

[118] We sample angles every 1° and radii every 0.5 μas between 0 and 50 μas.

method using Gaussian fits to the radial profiles, see Johannsen et al. (2016).

To find the ring center (x_0, y_0), we search over (x, y) and identify the position that minimizes the normalized radial peak dispersion:

$$(x_0, y_0) = \mathrm{argmin}\left[\frac{\sigma_{\bar{r}}(x, y)}{\bar{r}_{\mathrm{pk}}(x, y)}\right]_{(x,y)}. \tag{17}$$

The measured diameter d is then twice $\bar{r}_{\mathrm{pk}}$ measured from the identified center (x_0, y_0),

$$d = 2\bar{r}_{\mathrm{pk}}(x_0, y_0), \tag{18}$$

and the associated uncertainty σ_d in the diameter is

$$\sigma_d = 2\sigma_{\bar{r}}(x_0, y_0). \tag{19}$$

Although we have designed our analysis tools to specifically search for circular features, σ_d/d can be interpreted as a measure of the circularity of the identified feature in an individual image. See Paper VI for further discussion of the circularity of these images and model fits to the visibility data.

To avoid spurious detections when searching for the center location (Equation (17)), we first blur the image with a 2 μas FWHM Gaussian (approximately the pixel size of the original reconstructions) and threshold the search image below 5% of the peak brightness. We also restrict the range of allowed diameters to 10–100 μas. We use the original (unconvolved and unthresholded) image for all subsequent analysis. Because the remaining features are all estimated using the fixed center coordinates estimated by this procedure, we suppress the center coordinates for the remainder of our discussion, and we denote the unwrapped, centered image as $I(r, \theta)$.

After identifying the ring center and diameter, we measure the remaining characteristic features. The ring width w is determined by measuring the FWHM of each radial slice at constant θ and taking the mean. To avoid bias in the measurement from the resampled image $I(r, \theta)$ having a non-zero mean floor value outside the ring, we subtract the value $I_{\mathrm{floor}} = \langle I(r_{\mathrm{max}} = 50\ \mu\mathrm{as}, \theta)\rangle_\theta$ from each radial profile before computing the FWHM:

$$w = \langle \mathrm{FWHM}[I(r, \theta) - I_{\mathrm{floor}}]\rangle. \tag{20}$$

We estimate an uncertainty σ_w using the standard deviation of the set of FWHMs. Note that the measured width is dependent upon both the intrinsic width of the source and the finite resolution of the array. Thus, w should be viewed only as an upper limit on the intrinsic ring width, and it is upward biased by the application of a restoring beam (e.g., for DIFMAP reconstructions). We explore this bias further in Appendix G.

We define the ring orientation angle η (measured east of north) by considering the angular profiles $I(r, \theta)$ at fixed r. At each radius, we find the argument of the first angular mode $(m = 1)$ of the angular profile and then define the overall orientation angle η as the circular mean of these angles over the ring width; from $r_{\mathrm{in}} = (d - w)/2$ to $r_{\mathrm{out}} = (d + w)/2$. That is,

$$\eta = \left\langle \mathrm{Arg}\left[\int_0^{2\pi} I(\theta)e^{i\theta}d\theta\right]\right\rangle_{r\in[r_{\mathrm{in}}, r_{\mathrm{out}}]}. \tag{21}$$

Similarly, we define the associated uncertainty σ_η as the circular standard deviation of the angle measurements for $r \in [r_{\mathrm{in}}, r_{\mathrm{out}}]$.

To characterize the degree of azimuthal asymmetry in a ring, we compute the normalized amplitude of the first angular mode for radii between r_{in} and r_{out} and again take the mean. That is,

$$A = \left\langle \frac{\left|\int_0^{2\pi} I(\theta)e^{i\theta}d\theta\right|}{\int_0^{2\pi} I(\theta)d\theta}\right\rangle_{r\in[r_{\mathrm{in}}, r_{\mathrm{out}}]}. \tag{22}$$

The associated uncertainty σ_A is the standard deviation of the asymmetry at each $r \in [r_{\mathrm{in}}, r_{\mathrm{out}}]$. The asymmetry A takes values in the range from 0 to 1, with 0 corresponding to perfect azimuthal symmetry and 1 corresponding to a delta function concentrating all of the flux density at a single orientation angle. The crescent models defined in Section 6.1 have $A = 0.23$, with angular brightness profiles $I(\theta) \propto 1 + 2A\cos(\theta - \eta)$.

Finally, we define a fractional central brightness (or inverse contrast ratio) f_{C} as the ratio of the mean brightness interior to the ring to the mean brightness around the ring. To define the interior brightness, we average over a disk of radius 5 μas. That is,

$$f_{\mathrm{C}} = \frac{\langle I(r, \theta)\rangle_{\theta, r\in[0,5\ \mu\mathrm{as}]}}{\langle I(d/2, \theta)\rangle_{\theta\in[0,2\pi]}}. \tag{23}$$

We find that this statistic has an extremely large scatter across the Top Sets, primarily because the interior brightness can become arbitrarily low. Thus, our imaging methods only securely identify an upper limit on f_{C}.

9.2. Tests with Synthetic Data Reconstructions

We tested the analysis methods described in Section 9.1 on synthetic data from a crescent model with asymmetry parameter $A = 0.23$ oriented at a orientation angle $\eta = 150°$ (Appendix C), and on the GRMHD simulation image shown in Figure 10. For both sources, we measured the ring features defined in Section 9.1 for every image reconstructed with parameter combinations in the M87 Top Sets (see Section 6). While some of these images may not meet the $\chi^2 < 2$ constraint imposed for M87 images, using the M87 Top Set allows us to assess the expected variation resulting from imaging choices irrespective of image-data consistency.

The results of this analysis for the diameter (d), width (w), and orientation angle (η) are displayed in Figure 24. The points shown correspond to the measured quantities from the fiducial reconstructions. These measurements have two distinct sources of error: the intrinsic measurement uncertainty on each quantity from a single image, and the uncertainty in the quantity from varying imaging parameters across the Top Set. We combine these two sources of error in the error bars in Figure 24 by taking the quadrature sum of the measurement uncertainty from the fiducial image and the median absolute deviation of the parameter estimates across the Top Set.

In both simulated data tests, the ring diameter d is the most accurately recovered quantity; however, the diameter measurement is correlated with the ring width and is biased downward by several microarcseconds when the image is blurred (see Appendix G). In the simulated crescent, the diameter of the unblurred model is 44 μas; the value measured using our approach on the ground truth image is pushed down to 43 μas because of the Gaussian convolution (Appendix G). Taking the median across all days, the diameters extracted from the

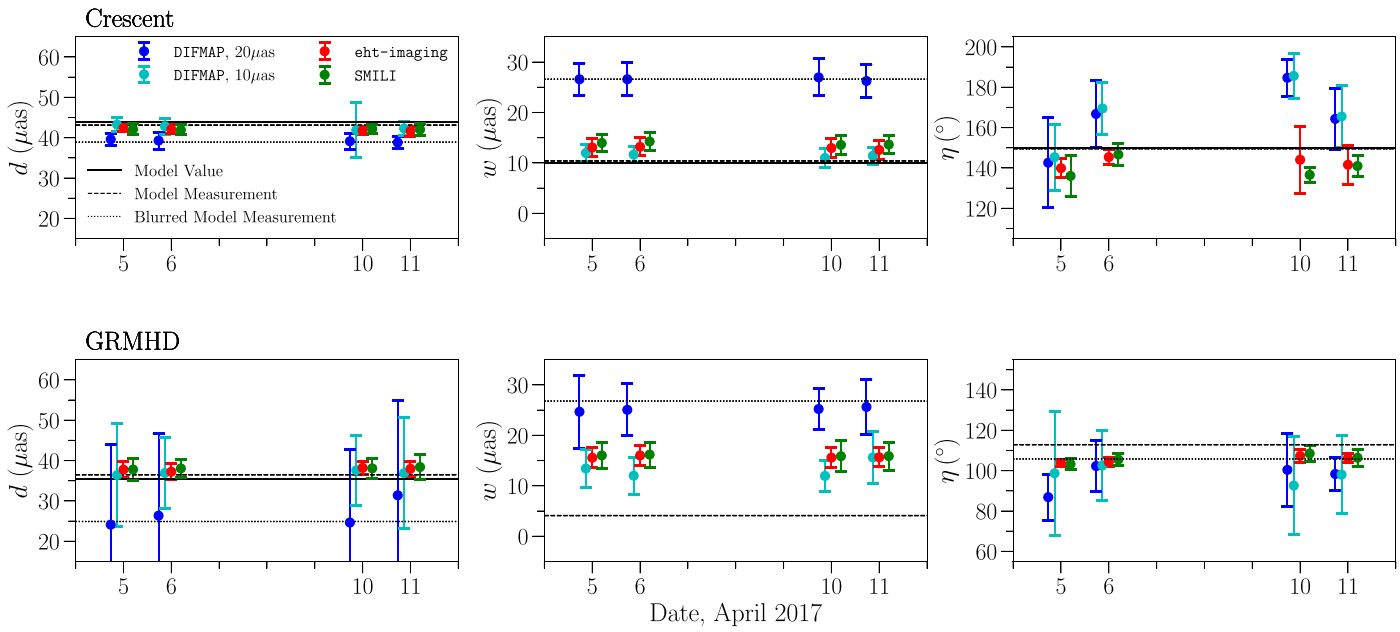

Figure 24. Measurements of ring features on fiducial reconstructions of a crescent model (top row) and a GRMHD simulation snapshot (bottom row) from images reconstructed with the fiducial parameters for three imaging pipelines. From left to right, panels show the measured ring diameter d, width w, and orientation angle η. The DIFMAP results are shown for images restored with both a 10 μas (cyan) and a 20 μas (blue) Gaussian beam. The eht-imaging (red) and SMILI (green) are shown for the unblurred images. Solid lines indicate the ground truth values of the three quantities in the crescent model, and the photon ring diameter of the GRMHD simulation. Dashed lines indicate the measured values from the ground truth images, and dotted lines indicate the measured values from the ground truth images convolved with a 20 μas FWHM circular Gaussian beam. The error bars are computed as the quadrature sum of the measurement uncertainty from the fiducial images (Section 9.1) and the median absolute deviation of the parameter estimates across the Top Set.

fiducial DIFMAP crescent model reconstructions have a median value of 40 ± 2 μas when restored with a 20 μas FWHM beam. When they are instead restored with a smaller 10 μas beam, the DIFMAP results become more accurate (compared to the model values), with a measured diameter of 43 ± 2 μas. The RML crescent model reconstructions measure a median diameter of 42 ± 1 μas.

The GRMHD image that we use (Paper V) has a lensed photon ring with a diameter of $9.79M/D \approx 35.5$ μas;[119] we recover a value of 36.5 μas from the ground truth image, indicating that even with a perfect image reconstruction, fine-scale substructure and extended flux in an image can bias the ring diameter measurement away from the photon ring value. The ring diameter measured from the eht-imaging and SMILI GRMHD fiducial reconstructions (Figure 24) has a median value of 38 ± 2 μas across all four observed days. However, for this image, the DIFMAP results are strongly dependent upon the chosen restoring beam. The DIFMAP reconstructions restored with a 20 μas beam lack prominent rings, leading to poor recovery of the ring diameter (26 ± 20 μas). When blurred with a smaller 10 μas beam, the DIFMAP results align with the RML methods but have larger uncertainties due to larger scatter across the Top Set (37 ± 11 μas).

As shown in Figure 24, the measured orientation angles from the crescent model reconstructions using the RML imaging pipelines have a median value of $141° \pm 5°$, which is moderately discrepant from the true value of 150°. The values from the DIFMAP images are even more discrepant and are unstable among days. The GRMHD image has no defined a priori orientation angle; the measured orientation angles from all pipelines are more stable than for the simple crescent model, and are consistent with the value measured from the blurred simulation image (105°). Both of these cases indicate that our procedure may underestimate uncertainties on η.

Both the crescent and GRMHD models have intrinsic widths that are much narrower than the resolution of the EHT. As expected from the 20 μas restoring beam, the DIFMAP reconstructions lead to a larger measurement of ring width than the RML reconstructions. When a 10 μas FWHM beam is used to restore the DIFMAP images, the measured width aligns with the RML results. Nonetheless, all reconstructions have widths that are systematically biased upward from the true values, and the extracted ring widths from image-domain fitting can at best be viewed as upper limits.

Similarly, the brightness depression contrast ratio f_C is highly sensitive to the image resolution and particular imaging choices. In particular, we find that the Top Sets from the RML imaging pipelines have an extremely large scatter in f_C. When blurred to the same 20 μas resolution, both RML and CLEAN methods give measurements of f_C that are consistently in the range 0.2–0.5 (Appendix G). Consequently, we can only determine an upper limit for f_C.

For all the imaging pipelines, we find that the scatter in ring diameters across the Top Set (typically $\lesssim 1$ μas) is subdominant to the intrinsic measurement uncertainty estimated from a single image (typically 1–2 μas). Thus, choices made in the imaging process do not significantly affect the measured ring diameter. In contrast, the other measured features have error budgets that are more evenly divided between intrinsic uncertainty in a single image and the scatter across the Top Set.

9.3. Results for M87

Table 7 lists the values of all ring parameters measured for the fiducial M87 reconstructions for each day from the three

[119] The simulation used an assumed black hole mass $M = 6.2 \times 10^9\ M_\odot$ and dimensionless spin $a_* = 0.9375$, observed at a distance $D = 16.9$ Mpc and 17° inclination (Paper V).

Table 7
Diameter d, Width w, Orientation Angle η, Asymmetry A, and Floor-to-ring Contrast Ratio f_C Measured from the Fiducial M87 Images for Each Day from Each Method (Section 7.1)

	d (μas)	w (μas)	η (°)	A	f_C
DIFMAP					
Apr 5	37.2 ± 2.4	28.2 ± 2.9	163.8 ± 6.5	0.21 ± 0.03	5×10^{-1}
April 6	40.1 ± 7.4	28.6 ± 3.0	162.1 ± 9.7	0.24 ± 0.08	4×10^{-1}
April 10	40.2 ± 1.7	27.5 ± 3.1	175.8 ± 9.8	0.20 ± 0.04	4×10^{-1}
April 11	40.7 ± 2.6	29.0 ± 3.0	173.3 ± 4.8	0.23 ± 0.04	5×10^{-1}
eht-imaging					
April 5	39.3 ± 1.6	16.2 ± 2.0	148.3 ± 4.8	0.25 ± 0.02	8×10^{-2}
April 6	39.6 ± 1.8	16.2 ± 1.7	151.1 ± 8.6	0.24 ± 0.02	6×10^{-2}
April 10	40.7 ± 1.6	15.7 ± 2.0	171.2 ± 6.9	0.23 ± 0.03	4×10^{-2}
April 11	41.0 ± 1.4	15.5 ± 1.8	168.0 ± 6.9	0.20 ± 0.02	4×10^{-2}
SMILI					
April 5	40.5 ± 1.9	16.1 ± 2.1	154.2 ± 7.1	0.27 ± 0.03	7×10^{-5}
April 6	40.9 ± 2.4	16.1 ± 2.1	151.7 ± 8.2	0.25 ± 0.02	2×10^{-4}
April 10	42.0 ± 1.8	15.7 ± 2.4	170.6 ± 5.5	0.21 ± 0.03	4×10^{-6}
April 11	42.3 ± 1.6	15.6 ± 2.2	167.6 ± 2.8	0.22 ± 0.03	6×10^{-6}

Note. The DIFMAP results are presented for a restoring beam of 20 μas. The estimated diameters and orientation angles are generally consistent across different imaging pipelines on all four days, but the measured width, contrast, and asymmetry differ between imaging pipelines.

parameter surveys. As in the previous section, for the fiducial images the uncertainties are computed by adding the scatter in the measured quantities across the Top Sets in quadrature to the intrinsic measurement uncertainty.

Figure 25 plots the measured diameter, width, and orientation angle from each method over all four days, and Figure 26 visualizes these parameters. Across all days, the DIFMAP reconstructions recover a median diameter of 40 ± 3 μas when restored with a 20 μas beam, and 44 ± 5 μas when restored with a 10 μas beam. The RML methods recover a median diameter of 41 ± 2 μas. For each imaging pipeline, there is slight upward trend in the diameter over time, increasing by ≈2 μas from the first to the last day of the observing campaign. However, this trend is well within the estimated uncertainty of the diameter measurements. The measured ring diameters are consistent among all imaging pipelines and largely unchanged from the first April 11 images produced from early-release engineering data (Section 5), for which we measure a median diameter of 41 ± 3 μas. The other parameters are less consistent from these first images to the final fiducial images selected by the parameter survey, indicating more sensitivity in these parameters to the data quality and the imaging method.

As in the synthetic data results presented in Figure 24, the beam-convolved DIFMAP reconstructions produce larger measured widths than the RML methods. The width measurements become consistent when the DIFMAP images are restored with a smaller 10 μas beam, but the ring width remains limited by the resolution of the EHT. Thus, from these imaging results, we can only firmly conclude that the ring width is $\leqslant$20 μas.

In the reconstructions from all three imaging methods, there is a counterclockwise trend in the orientation angle from April 5 to 11, which is consistent with the apparent shift in brightness along the ring remarked on in Section 7.1. However, we emphasize that this ≈20° change could be the result of spurious azimuthal structure, and we have seen that our orientation angle uncertainties may be underestimated (see Figure 24). Even if this shift in angle is physical, it does *not* necessarily indicate continuous motion or a flow direction associated with the black hole in M87, and it is opposite to the inferred rotation direction for the large-scale jet (Walker et al. 2018).

Identifying a ring in the fiducial images allows us to "unwrap" the brightness distribution around the ring and display the image in $I(r, \theta)$ space. Figure 27 shows these unwrapped ring profiles of the fiducial images for all pipelines and days. In Appendix I, we present more diagnostic figures to characterize the radial and azimuthal structure of the recovered rings.

Even under the assumption that the ring in our images corresponds to the lensed photon ring of an SMBH (i.e., $d \approx (5.0 \pm 0.2)\ R_s/D$; Bardeen 1973; Johannsen & Psaltis 2010), translating the estimated ring diameter to a Schwarzschild radius—or, equivalently, to a black hole mass via $R_s = GM_{BH}/c^2$—requires evaluating biases and uncertainties related to the unresolved image structure, the black hole vector spin, and the estimated distance to M87. We perform this analysis separately, in Paper VI.

10. Summary and Conclusions

We have presented imaging analysis and results for EHT observations of M87 in 2017 April. These observations achieved an angular resolution (synthesized beam size) of ∼20 μas, and they are the first EHT observations with sufficient sensitivity and baseline coverage to reconstruct images. Images can provide agnostic results, potentially identifying entirely unexpected features. However, a multitude of imaging techniques and parameters can lead to results that depend on specific imaging choices. Consequently, we adopted a staged imaging approach to control and evaluate potential biases.

We designed our first imaging stage to minimize shared bias among different groups of imaging experts and to test whether or not their independent inferences were consistent. In this stage, described in Section 5, we separately imaged M87 in four imaging teams. These imaging teams did not communicate about their methods or findings while analyzing the M87 data. Each team relied upon the judgment of its members to select strategies for data flagging, calibration, and imaging, using whatever software

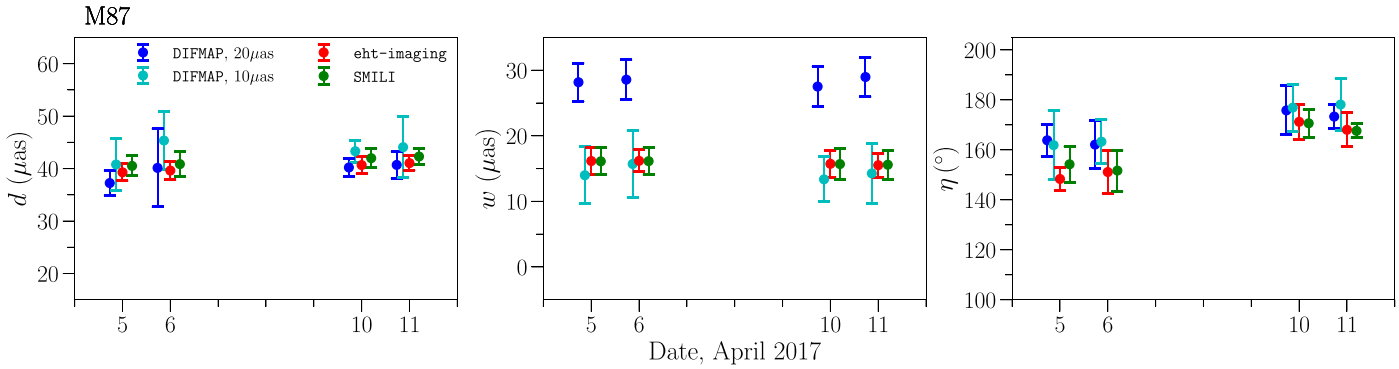

Figure 25. Measured ring properties on the fiducial images of M87 produced with all three imaging pipelines. From left to right, panels show the measured ring diameter d, width w, and orientation angle η. The `DIFMAP` results are shown for images restored with both a 10 μas (cyan) and a 20 μas (blue) Gaussian beam. The `eht-imaging` (red) and `SMILI` (green) are shown for the unblurred images. The three imaging pipelines produce consistent measurements of the ring diameter across all days. The measured orientation angles indicate a modest shift between April 5, 6 and 10, 11. The error bars are computed in the same way as in Figure 24.

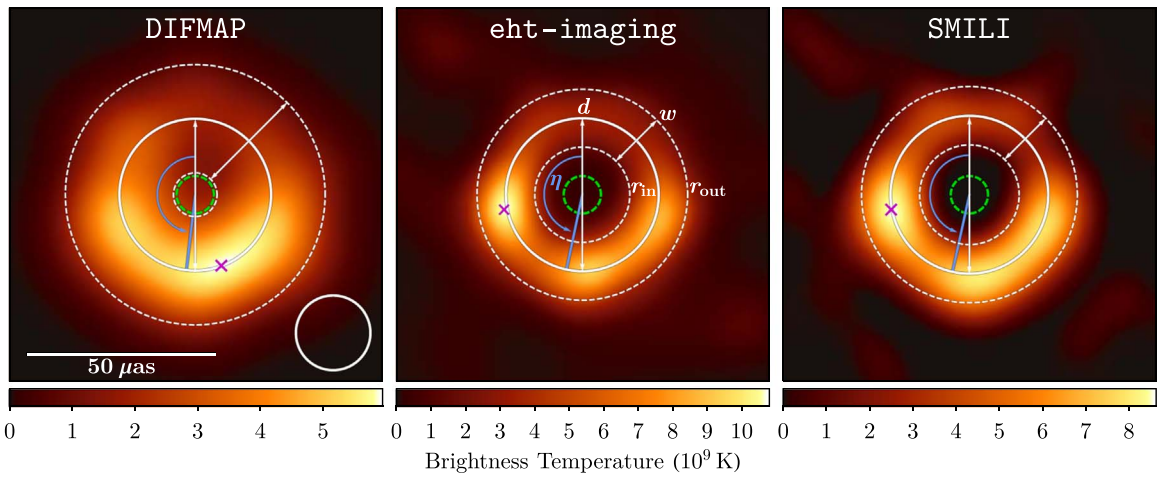

Figure 26. Summary of the estimated ring properties overlaid on the April 11 fiducial images from each imaging pipeline. Our procedure estimates the ring diameter d, width w, orientation angle η, and fractional central brightness f_C, as well as the asymmetry A (not shown). In each panel, the magenta cross indicates the location of peak ring brightness, and the dashed green circle shows the region used to define interior brightness for f_C.

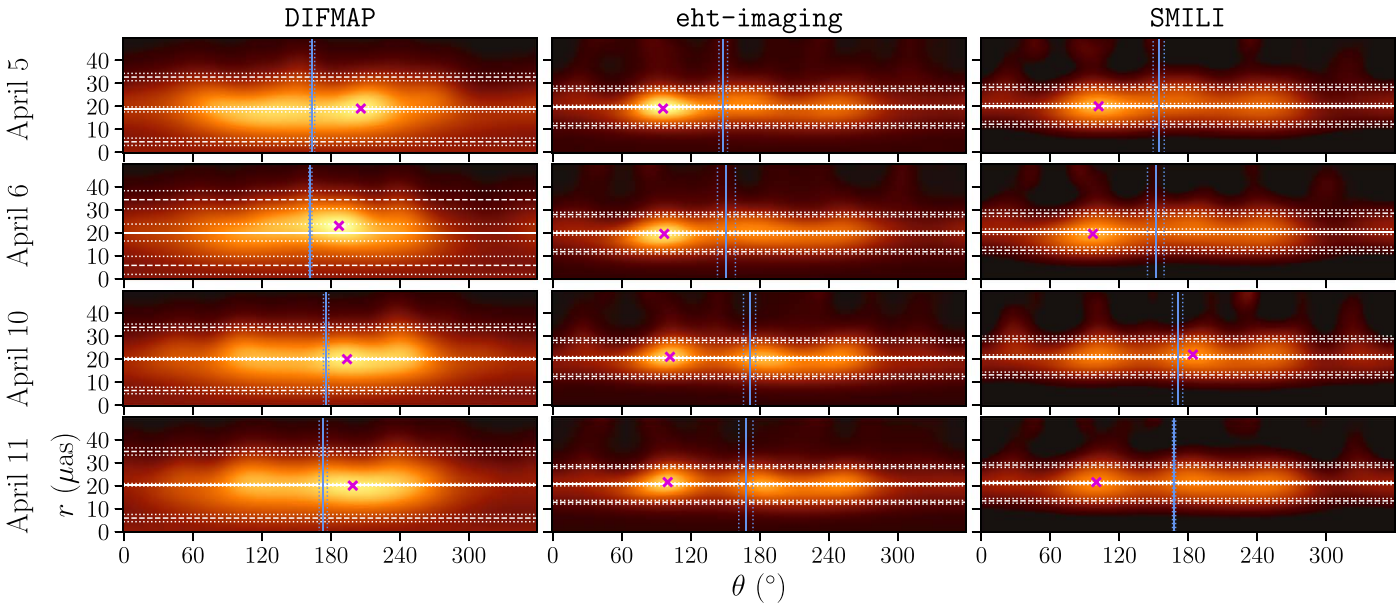

Figure 27. Unwrapped ring profiles of the fiducial images from April 5 to 11 (top to bottom) and for the three imaging pipelines (left to right). The columns are each scaled as in Figure 26. The estimated radius $d/2$ is shown with a horizontal line, with dotted lines denoting the associated uncertainty (Section 9.1). Horizontal dashed lines at $(d \pm w)/2$ show the measured ring width. Vertical blue lines give the orientation angle η and its uncertainty. The magenta cross marks the peak brightness in each reconstruction.

and techniques that they judged to be useful. The final images from the teams were blindly submitted for comparison. These first images of M87 all showed a prominent ring of ∼40 μas diameter with enhanced brightness in the south. The four teams made different assumptions about the total compact flux density of M87, varying from ∼0.4 to 0.9 Jy. The images also showed differences in the azimuthal ring structure.

We designed our second imaging stage to select imaging parameters objectively and to assess how parameter choices correspond to uncertainties in the final images. In this stage, described in Section 6, we developed scripted imaging pipelines for one established (`DIFMAP`) and two EHT-tailored imaging libraries (`eht-imaging` and `SMILI`). For each method, we conducted a parameter survey, exploring $\sim 10^3$–10^4 parameter combinations for each imaging pipeline. We then reconstructed images from synthetic data sets and compared them to the corresponding ground truth images. To determine which parameter combinations in the survey produced acceptable images, we imposed an image-data consistency requirement for reconstructions of M87, as well as an image fidelity requirement for reconstructions of synthetic data.

This procedure identified a "Top Set" of parameter choices as well as a single "fiducial" combination of parameters for each of the three surveys. When applied to M87 data, the Top Set reconstructions provide a measure of uncertainty corresponding to choices made in the imaging procedure. In addition, the fiducial image (Figure 11) acts as a single representative image from each imaging pipeline that has been identified based on objective performance, rather than expert judgment.

Our reconstructed images of M87 are consistently dominated by a ring of roughly 40 μas diameter, with enhanced brightness in the south. The ring is present in both imaging stages, across all imaging pipelines, and all observing days. The residual time-dependent station gains derived from our images are consistent between the interleaved EHT observations of M87 and the bright quasar 3C 279. Our reconstructed images of M87 show variation between the observations on April 5 and 11, as expected from the variations seen in the underlying data (Paper III). However, we cannot unambiguously associate the variability with evolution of a specific image feature.

These first images from the EHT achieve the highest angular resolution in the history of ground-based VLBI. The images reveal the central engine of M87 and are dominated by a ~ 40 μas diameter ring with pronounced azimuthal asymmetry. Such an asymmetry is expected for relativistic rotation of emitting material near a black hole. For an assumed distance of 16.8 Mpc, the ring diameter is consistent with the expected "shadow" of a $\sim 6.5 \times 10^9\, M_\odot$ black hole.

The authors of this Letter thank the following organizations and programs: the Academy of Finland (projects 274477, 284495, 312496); the Advanced European Network of E-infrastructures for Astronomy with the SKA (AENEAS) project, supported by the European Commission Framework Programme Horizon 2020 Research and Innovation action under grant agreement 731016; the Alexander von Humboldt Stiftung; the Black Hole Initiative at Harvard University, through a grant (60477) from the John Templeton Foundation; the China Scholarship Council; Comisión Nacional de Investigación Científica y Tecnológica (CONICYT, Chile, via PIA ACT172033, Fondecyt 1171506, BASAL AFB-170002, ALMA-conicyt 31140007); Consejo Nacional de Ciencia y Tecnología (CONACYT, Mexico, projects 104497, 275201, 279006, 281692); the Delaney Family via the Delaney Family John A. Wheeler Chair at Perimeter Institute; Dirección General de Asuntos del Personal Académico-Universidad Nacional Autónoma de México (DGAPA-UNAM, project IN112417); the European Research Council Synergy Grant "BlackHoleCam: Imaging the Event Horizon of Black Holes" (grant 610058); the Generalitat Valenciana postdoctoral grant APOSTD/2018/177; the Gordon and Betty Moore Foundation (grants GBMF-3561, GBMF-5278); the Istituto Nazionale di Fisica Nucleare (INFN) sezione di Napoli, iniziative specifiche TEONGRAV; the International Max Planck Research School for Astronomy and Astrophysics at the Universities of Bonn and Cologne; the Jansky Fellowship program of the National Radio Astronomy Observatory (NRAO); the Japanese Government (Monbukagakusho: MEXT) Scholarship; the Japan Society for the Promotion of Science (JSPS) Grant-in-Aid for JSPS Research Fellowship (JP17J08829); JSPS Overseas Research Fellowships; the Key Research Program of Frontier Sciences, Chinese Academy of Sciences (CAS, grants QYZDJ-SSW-SLH057, QYZDJ-SSW-SYS008); the Leverhulme Trust Early Career Research Fellowship; the Max-Planck-Gesellschaft (MPG); the Max Planck Partner Group of the MPG and the CAS; the MEXT/JSPS KAKENHI (grants 18KK0090, JP18K13594, JP18K03656, JP18H03721, 18K03709, 18H01245, 25120007); the MIT International Science and Technology Initiatives (MISTI) Funds; the Ministry of Science and Technology (MOST) of Taiwan (105-2112-M-001-025-MY3, 106-2112-M-001-011, 106-2119-M-001-027, 107-2119-M-001-017, 107-2119-M-001-020, and 107-2119-M-110-005); the National Aeronautics and Space Administration (NASA, Fermi Guest Investigator grant 80NSSC17K0649); the National Institute of Natural Sciences (NINS) of Japan; the National Key Research and Development Program of China (grant 2016YFA0400704, 2016YFA0400702); the National Science Foundation (NSF, grants AST-0096454, AST-0352953, AST-0521233, AST-0705062, AST-0905844, AST-0922984, AST-1126433, AST-1140030, DGE-1144085, AST-1207704, AST-1207730, AST-1207752, MRI-1228509, OPP-1248097, AST-1310896, AST-1312651, AST-1337663, AST-1440254, AST-1555365, AST-1715061, AST-1614868, AST-1615796, AST-1716327, OISE-1743747, AST-1816420); the Natural Science Foundation of China (grants 11573051, 11633006, 11650110427, 10625314, 11721303, 11725312, 11873028, 11873073, U1531245, 11473010); the Natural Sciences and Engineering Research Council of Canada (NSERC, including a Discovery Grant and the NSERC Alexander Graham Bell Canada Graduate Scholarships-Doctoral Program); the National Youth Thousand Talents Program of China; the National Research Foundation of Korea (grant 2015-R1D1A1A01056807, the Global PhD Fellowship Grant: NRF-2015H1A2A1033752, and the Korea Research Fellowship Program: NRF-2015H1D3A1066561); the Netherlands Organization for Scientific Research (NWO) VICI award (grant 639.043.513) and Spinoza Prize SPI 78-409; the New Scientific Frontiers with Precision Radio Interferometry Fellowship awarded by the South African Radio Astronomy Observatory (SARAO), which is a facility of the National Research Foundation (NRF), an agency of the Department of Science and Technology (DST) of South Africa; the Onsala Space Observatory (OSO) national infrastructure, for the provisioning of its facilities/observational support (OSO receives funding through the Swedish Research Council under grant 2017-00648)the Perimeter Institute for Theoretical Physics (research at Perimeter Institute is supported by the Government of Canada through the Department of

Innovation, Science and Economic Development Canada and by the Province of Ontario through the Ministry of Economic Development, Job Creation and Trade); the Russian Science Foundation (grant 17-12-01029); the Spanish Ministerio de Economía y Competitividad (grants AYA2015-63939-C2-1-P, AYA2016-80889-P); the State Agency for Research of the Spanish MCIU through the "Center of Excellence Severo Ochoa" award for the Instituto de Astrofísica de Andalucía (SEV-2017-0709); the Toray Science Foundation; the US Department of Energy (USDOE) through the Los Alamos National Laboratory (operated by Triad National Security, LLC, for the National Nuclear Security Administration of the USDOE (Contract 89233218CNA000001)); the Italian Ministero dell'Istruzione Università e Ricerca through the grant Progetti Premiali 2012-iALMA (CUP C52I13000140001); ALMA North America Development Fund; Chandra TM6-17006X. This work used the Extreme Science and Engineering Discovery Environment (XSEDE), supported by NSF grant ACI-1548562, and CyVerse, supported by NSF grants DBI-0735191, DBI-1265383, and DBI-1743442. XSEDE Stampede2 resource at TACC was allocated through TG-AST170024 and TG-AST080026N. XSEDE JetStream resource at PTI and TACC was allocated through AST170028. The simulations were performed in part on the SuperMUC cluster at the LRZ in Garching, on the LOEWE cluster in CSC in Frankfurt, and on the HazelHen cluster at the HLRS in Stuttgart. This research was enabled in part by support provided by Compute Ontario (http://computeontario.ca), Calcul Quebec (http://www.calculquebec.ca) and Compute Canada (http://www.computecanada.ca). We thank the staff at the participating observatories, correlation centers, and institutions for their enthusiastic support. This Letter makes use of the following ALMA data: ADS/JAO.ALMA#2016.1.01154.V. ALMA is a partnership of the European Southern Observatory (ESO; Europe, representing its member states), NSF, and National Institutes of Natural Sciences of Japan, together with National Research Council (Canada), Ministry of Science and Technology (MOST; Taiwan), Academia Sinica Institute of Astronomy and Astrophysics (ASIAA; Taiwan), and Korea Astronomy and Space Science Institute (KASI; Republic of Korea), in cooperation with the Republic of Chile. The Joint ALMA Observatory is operated by ESO, Associated Universities, Inc. (AUI)/NRAO, and the National Astronomical Observatory of Japan (NAOJ). The NRAO is a facility of the NSF operated under cooperative agreement by AUI. APEX is a collaboration between the Max-Planck-Institut für Radioastronomie (Germany), ESO, and the Onsala Space Observatory (Sweden). The SMA is a joint project between the SAO and ASIAA and is funded by the Smithsonian Institution and the Academia Sinica. The JCMT is operated by the East Asian Observatory on behalf of the NAOJ, ASIAA, and KASI, as well as the Ministry of Finance of China, Chinese Academy of Sciences, and the National Key R&D Program (No. 2017YFA0402700) of China. Additional funding support for the JCMT is provided by the Science and Technologies Facility Council (UK) and participating universities in the UK and Canada. The LMT project is a joint effort of the Instituto Nacional de Astrófisica, Óptica, y Electrónica (Mexico) and the Universit The IRAM 30-m telescope on Pico Veleta, Spain is operated by IRAM and supported by CNRS (Centre National de la Recherche Scientifique, France), MPG (Max-Planck-Gesellschaft, Germany) and IGN (Instituto Geográfico Nacional, Spain). The SMT is operated by the Arizona Radio Observatory, a part of the Steward Observatory of the University of Arizona, with financial support of operations from the State of Arizona and financial support for instrumentation development from the NSF. Partial SPT support is provided by the NSF Physics Frontier Center award (PHY-0114422) to the Kavli Institute of Cosmological Physics at the University of Chicago (USA), the Kavli Foundation, and the GBMF (GBMF-947). The SPT hydrogen maser was provided on loan from the GLT, courtesy of ASIAA. The SPT is supported by the National Science Foundation through grant PLR-1248097. Partial support is also provided by the NSF Physics Frontier Center grant PHY-1125897 to the Kavli Institute of Cosmological Physics at the University of Chicago, the Kavli Foundation and the Gordon and Betty Moore Foundation grant GBMF 947. This work made use of Global Millimeter VLBI Array (GMVA) data (project MM07B; PI: A. Marscher). The GMVA consists of telescopes operated by the MPIfR, IRAM, Onsala, Metsahovi, Yebes, the Korean VLBI Network, the Green Bank Observatory and the VLBA. The VLBA is an instrument of the NRAO, which is a facility of the National Science Foundation operated by Associated Universities, Inc. This research has made use of data obtained with 12 radio telescopes from the East Asian VLBI Network (EAVN): 2 stations from the Chinese VLBI Network (the Tianma radio telescope operated by Shanghai Astronomical Observatory of Chinese Academy of Sciences (CAS) and the Nanshan radio telescope operated by Xinjiang Astronomical Observatory of CAS), 2 stations from the Japanese VLBI Network (the Hitachi station operated by Ibaraki University and the Kashima station operated by the National Institute of Information and Communications Technology), the Korean VLBI Network operated by the Korea Astronomy and Space Science Institute (KASI), the VLBI Exploration of Radio Astrometry (VERA) operated by the National Astronomical Observatory of Japan (NAOJ), and the Nobeyama 45-meter radio telescope operated by NAOJ. We are grateful to KVN staff who helped to operate the array and to correlate the data for quasi-simulataneous multi-wavelength observations of M87. The KVN is a facility operated by KASI. The KVN operations are supported by KREONET (Korea Research Environment Open NETwork), which is managed and operated by KISTI (Korea Institute of Science and Technology Information). The EHTC has received generous donations of FPGA chips from Xilinx Inc., under the Xilinx University Program. The EHTC has benefited from technology shared under open-source license by the Collaboration for Astronomy Signal Processing and Electronics Research (CASPER). The EHT project is grateful to T4Science and Microsemi for their assistance with Hydrogen Masers. This research has made use of NASA's Astrophysics Data System. We gratefully acknowledge the support provided by the extended staff of the ALMA, both from the inception of the ALMA Phasing Project through the observational campaigns of 2017 and 2018. We would like to thank A. Deller and W. Brisken for EHT-specific support with the use of DiFX. We acknowledge the significance that Maunakea, where the SMA and JCMT EHT stations are located, has for the indigenous Hawaiian people.

Facility: EHT.

Software: `eht-imaging`, `DIFMAP`, `SMILI`.

Appendix A
Regularizer Definitions

Here we give definitions for the regularization terms used in the RML methods that we employ in this Letter. In particular, these terms have normalization factors applied that differ among

the imaging software libraries (`eht-imaging` and `SMILI`). The normalization factors are generally selected so that the associated regularization hyperparameter is of order unity, and to ensure that the regularization strength is independent of, e.g., the chosen pixel size and FOV of the reconstructed image.

Total Flux Density Regularizer: the total flux density regularizer favors reconstructed images that have total flux density near a specified value F:

$$S_{\text{tot flux}} = -\frac{1}{\zeta}\left(\sum_i I_i - F\right)^2. \tag{24}$$

In `eht-imaging`, the normalization factor is

$$\zeta = F^2. \tag{25}$$

In `SMILI`, the normalization factor is

$$\zeta = (f_{\rm F} F)^2, \tag{26}$$

where $f_{\rm F}$ is the target fractional error and is fixed to be 10^{-2} for imaging in this Letter.

Relative Entropy: entropy (MEM) favors pixel-to-pixel similarity to a "prior image" with pixel values P_i (in this work, the prior is always taken to be a circular Gaussian with a variable FWHM). The corresponding regularization term is

$$S_{\rm MEM} = -\frac{1}{\zeta}\sum_i I_i \log\left(\frac{I_i}{P_i}\right). \tag{27}$$

In `eht-imaging`, the normalization factor ζ for MEM is

$$\zeta = F, \tag{28}$$

where F is the user-specified target total flux density. In this Letter, `SMILI` reconstructions do not use MEM regularization.

ℓ_1 Norm: the ℓ_1 norm favors image sparsity. In `eht-imaging`, it takes the form

$$S_{\ell_1} = -\frac{1}{\zeta}\sum_i |I_i|. \tag{29}$$

where the normalization factor ζ is simply

$$\zeta = F. \tag{30}$$

In `SMILI`, a generalized weighted ℓ_1 norm ($\ell_1^{\rm w}$) is used, given by

$$S_{\ell_1^{\rm w}} = -\frac{1}{\zeta}\sum_i \frac{|I_i|}{|P_i| + \epsilon_s}, \tag{31}$$

where P_i is a specified prior image, and ϵ_s is fixed to be 10^{-12} Jy/pixel. The total scaling factor ζ is given by

$$\zeta = \sum_i \frac{|P_i|}{|P_i| + \epsilon_s}. \tag{32}$$

For the absolute value operator $|...|$, `SMILI` adopts a smoothed-approximation operator, which is differentiable everywhere, given by

$$|x| \approx \sqrt{x^2 + \epsilon_a}, \tag{33}$$

where ϵ_a is fixed to be 10^{-12} Jy/pixel. We use a circular Gaussian with a specified FWFM for the prior image.

Total Variation: TV favors piecewise-smooth images with flat regions separated by sharp edges

$$S_{\rm TV} = -\frac{1}{\zeta}\sum_{\ell,m}[(I_{\ell+1,m} - I_{\ell,m})^2 + (I_{\ell,m+1} - I_{\ell,m})^2]^{1/2}. \tag{34}$$

In this equation, the two sums are taken over the two image dimensions and the image pixels $I_{\ell,m}$ are now indexed by their position (l, m) in a 2D grid. This regularizer is not differentiable everywhere. In `eht-imaging`, the normalization factor ζ for TV is

$$\zeta = F\frac{\Delta\theta}{\Theta_{\rm beam}}, \tag{35}$$

where $\Delta\theta$ is the pixel size and $\Theta_{\rm beam}$ is the beam size.

On the other hand, `SMILI` adopts a smoothed TV that is differentiable everywhere:

$$S_{\rm TV} = -\frac{1}{\zeta}\sum_{\ell,m}[(I_{\ell+1,m} - I_{\ell,m})^2 + (I_{\ell,m+1} - I_{\ell,m})^2 + \epsilon]^{1/2}, \tag{36}$$

where ϵ is set to be 10^{-12} Jy/pixel for imaging in this Letter. The normalization factor for `SMILI` is

$$\zeta = F. \tag{37}$$

Total Squared Variation: TSV favors images with smooth edges:

$$S_{\rm TSV} = -\frac{1}{\zeta}\sum_{\ell,m}[(I_{\ell+1,m} - I_{\ell,m})^2 + (I_{\ell,m+1} - I_{\ell,m})^2]. \tag{38}$$

In `eht-imaging`, the normalization factor for TSV is

$$\zeta = F^2\left(\frac{\Delta\theta}{\Theta_{\rm beam}}\right)^4. \tag{39}$$

In `SMILI`, the normalization factor for TSV is

$$\zeta = F^2/N_{\rm pix}, \tag{40}$$

where $N_{\rm pix}$ is the total number of pixels in the reconstructed image.

Appendix B
Derivation of Constraints on the Total Compact Flux Density of M87

In this section, we use a combination of constraints directly accessible from EHT observations on long baselines (Section B.1) in combination with constraints from multi-wavelength observations (Section B.2) to constrain the compact ($\lesssim$100 μas) 230 GHz flux density of M87 during 2017 April.

B.1. Constraints from EHT Observations

As discussed in Section 4.3, there are two relevant estimates of the total flux density of M87: the total flux density seen in the core on arcsecond scales, $F_{\rm tot} \approx 1.2$ Jy, and the total compact flux density, $F_{\rm cpct} \leqslant F_{\rm tot}$, which is the integrated flux density for a reconstructed image with an FOV limited to only $\sim$100 μas. Intra-site EHT baselines are sensitive to the former, while inter-site baselines are sensitive to the latter.

The shortest inter-site EHT baseline is SMT–LMT, which has a fringe spacing of (139–166) μas for M87. However, using this baseline to estimate $F_{\rm cpct}$ requires assumptions about the compact source structure and the amplitude calibration accuracy. In particular, while SMT gains are well constrained, the use of provisional equipment at the LMT led to severe uncertainty and variability in LMT gains, as is evident by anomalously large variations in amplitudes on LMT baselines (see Figure 2 and Paper III). Nevertheless, we can still obtain useful limits that are

independent of source structure. To proceed, we will consider four separate constraints, each of which requires different assumptions about the data and image. Moreover, we will show that constraints on $F_{\rm cpct}$ are degenerate with constraints on the overall source size. For reference, the values of $F_{\rm tot}$ estimated using ALMA interferometric data are 1.13, 1.14, 1.17, and 1.21 Jy on our four observing days, April 5, 6, 10, and 11. Because of the short spacing combined with the relatively small difference in $F_{\rm tot}$ for adjacent days, we will analyze each pair of consecutive observations separately, allowing for the possibility of source evolution in the four-day observing gap.

In the following discussion, we will denote complex station gains by, e.g., $g_{\rm LMT}$, and measured complex visibilities by, e.g., $V_{\rm LMT-SMT}$. Apart from thermal noise, the measured visibilities are then related to the true visibilities $\mathcal{V}_{\rm LMT-SMT}$ via

$$V_{\rm LMT-SMT} = g_{\rm LMT} g^*_{\rm SMT} \mathcal{V}_{\rm LMT-SMT}. \tag{41}$$

In expressions using visibility amplitudes, we will assume that these are suitably debiased for the contribution of thermal noise (Equation (6)).

Constraint 1. Visibility amplitudes are maximum at zero baseline length. In addition, a priori calibration may overestimate station sensitivity (e.g., if there are unaccounted pointing errors), but it should not underestimate sensitivity; i.e., $|g_i| \leqslant 1$ for every station i, and every visibility amplitude should only underestimate the true amplitude (e.g., $|V_{\rm LMT-SMT}| \leqslant |\mathcal{V}_{\rm LMT-SMT}|$), apart from thermal noise. Combining these properties, we derive a lower limit to $F_{\rm cpct}$ by identifying the maximum LMT–SMT visibility amplitude measured for each of the four observing days: 0.34, 0.23, 0.43, and 0.43 Jy, respectively. Thus, $F_{\rm cpct} > 0.34$ Jy on the first two days and $F_{\rm cpct} > 0.43$ Jy on the latter two days.

These constraints can be strengthened under the additional assumption that the LMT–SMT baseline partially resolves the compact emission region. In this case, it is convenient to express the visibility amplitudes in terms of an equivalent Gaussian visibility function,

$$V_{\rm G}(\boldsymbol{u}; I_0, \theta) = I_0 e^{-\frac{(\pi\theta|\boldsymbol{u}|)^2}{4\ln 2}}. \tag{42}$$

In this expression, I_0 is the total flux density of the Gaussian source, and θ is its FWHM in radians. Visibility amplitudes will match this generic Gaussian form until a source is at least moderately resolved, providing a characteristic image FWHM that does not make specific assumptions about image structure.[120] Because LMT–SMT amplitudes are up to ∼20%–40% of $F_{\rm tot}$ (and $F_{\rm cpct}$ may be considerably less than $F_{\rm tot}$), we expect LMT–SMT amplitudes to lie within this regime.

Combining these properties, we obtain a modified constraint on total compact flux density that is dependent upon the compact source size, $\theta_{\rm cpct}$. For any LMT–SMT visibility amplitude on a baseline $\boldsymbol{u}$,

$$F_{\rm cpct} > |V_{\rm LMT-SMT}| e^{\frac{(\pi|\boldsymbol{u}|\theta_{\rm cpct})^2}{4\ln 2}}. \tag{43}$$

Constraint 2. Our second constraint comes from the observation that the visibility amplitudes fall steeply with baseline length on short baselines. By comparing the relative visibility amplitudes of simultaneous ALMA–LMT and SMT–LMT measurements, we obtain an estimate of the relative source visibility amplitudes that only depends on the station gains for ALMA and the SMT:

$$\frac{|V_{\rm ALMA-LMT}|}{|V_{\rm SMT-LMT}|} = \frac{|g_{\rm ALMA}|}{|g_{\rm SMT}|} \frac{|\mathcal{V}_{\rm ALMA-LMT}|}{|\mathcal{V}_{\rm SMT-LMT}|}. \tag{44}$$

Both the SMT and ALMA are stable and have well-characterized performance. Moreover, ALMA visibility amplitiudes have absolute calibration to within a few percent via "network calibration," using the short baseline to APEX. Consequently, we can make the approximation

$$\frac{|V_{\rm ALMA-LMT}|}{|V_{\rm SMT-LMT}|} \approx \frac{|\mathcal{V}_{\rm ALMA-LMT}|}{|\mathcal{V}_{\rm SMT-LMT}|}. \tag{45}$$

For M87, we find values for $|V_{\rm ALMA-LMT}|/|V_{\rm SMT-LMT}|$ ranging from 0.18 to 0.34 on the first two days, and from 0.17 to 0.28 on the last two days.

For each measurement, we can estimate a minimum image size by finding the equivalent Gaussian that achieves the same quotient on the corresponding baselines. This criterion is motivated by the property that long baselines will tend to measure more flux density than extrapolated by the equivalent Gaussian on short baselines, reflecting small-scale power from image substructure. This criterion also makes the simplifying assumption that the source has isotropic size; this assumption is both supported by our data (see Section 3.2) and is not especially problematic because the ALMA–LMT and SMT–LMT baselines sample similar orientation angles (see Figure 1).

We thereby estimate a minimum source size of $\theta \geqslant 38$ μas for the first two days, and $\theta \geqslant 41$ μas for the second two days. Note that these estimates are independent of the total (and total compact) flux density. These minimum size estimates can be applied to tighten the limits from Constraint 1, via Equation (43). Using these minimum source size estimates, we obtain $F_{\rm cpct} > 0.42$ Jy on the first two days and $F_{\rm cpct} > 0.56$ Jy on the last two days.

Constraint 3. For our third constraint, we again use the properties that LMT–SMT visibility amplitudes fall within the universal regime described via a Gaussian visibility amplitude function, and that LMT–SMT measurements will only underpredict true visibility amplitudes. Combining these properties, each measured amplitude $|V_{\rm LMT-SMT}|$ on an associated baseline $\boldsymbol{u}$ determines an upper limit on the image size $\theta_{\rm cpct}$. This upper limit occurs when the required total compact flux density must exceed $F_{\rm tot}$, giving

$$\theta_{\rm cpct} \leqslant \frac{2\sqrt{\ln 2}}{\pi|\boldsymbol{u}|} \sqrt{\ln \frac{F_{\rm tot}}{|V_{\rm LMT-SMT}|}}. \tag{46}$$

We thereby find $\theta \leqslant 82$ μas for the first two days, and $\theta \leqslant 77$ μas for the last two days.

Constraint 4. Our final constraint utilizes information from different baselines that sample nearly the same vector baseline $\boldsymbol{u}$, though not simultaneously. Specifically, the SMT–PV and LMT–PV tracks cross (see Figure 1), sampling a single baseline near $(u, v) = (5.9, 0.9)\,{\rm G}\lambda$ at times t_1 and t_2, respectively. Under the assumption of stable source structure, the true source visibility amplitudes at the crossing point must

[120] Formally, the corresponding FWHM is proportional to the second central moment of the image, projected along the baseline direction (see, e.g., Johnson et al. 2018).

Table 8
SMT–LMT Amplitudes before and after Applying a Correction Due to Crossing Baseline Tracks for Each Observing Day

	Hour UT	Baseline	u (Gλ)	v (Gλ)	$\lvert(u, v)\rvert$ (Gλ)	Amp (mJy)	σ (mJy)
April 5	4.6	SMT–PV	−6.02	−0.77	6.07	103.7	8.7
	2.6	LMT–PV	−6.24	−1.31	6.37	18.4	3.4
	2.6	SMT–LMT	−0.08	1.25	1.25	61.9	5.7
		[LMT SEFD Correction Factor: 31.7]				**348.6**	**74.5**
April 6	5.1	SMT–PV	−5.60	−0.97	5.68	140.1	10.7
	3.6	LMT–PV	−5.98	−1.69	6.22	62.6	4.2
	3.6	SMT–LMT	−0.38	1.23	1.29	174.0	6.9
		[LMT SEFD Correction Factor: 5.0]				**389.6**	**50.1**
April 10	4.3	SMT–PV	−6.03	−0.76	6.08	118.7	9.5
	2.2	LMT–PV	−6.23	−1.26	6.36	16.1	6.8
	2.2	SMT–LMT	−0.04	1.25	1.25	55.2	12.9
		[LMT SEFD Correction Factor: 54.6]				**408.2**	**164.5**
April 11	4.3	SMT–PV	−5.95	−0.81	6.00	111.7	7.1
	2.4	LMT–PV	−6.23	−1.38	6.38	71.9	7.5
	2.4	SMT–LMT	−0.14	1.25	1.26	247.1	10.6
		[LMT SEFD Correction Factor: 2.4]				**383.8**	**57.9**

Note. Non-simultaneous SMT–PV and LMT–PV visibilities at a crossing baseline location (Near 6 Gλ; see Figure 1) determine the LMT SEFD at the time of the LMT–PV measurement, yielding correction factors on a priori estimates of LMT SEFDs ranging from 2.4 to 54.6. Substituting these measurements into Equation (48) gives an estimate of the LMT–SMT visibility amplitude, shown as bold values in the table. Stated uncertainties on original measurements include only thermal noise, but those on the corrected LMT–SMT amplitudes also account for uncertainties in the LMT and SMT SEFDs. On all four days, the corrected LMT–SMT visibility amplitude is approximately 400 mJy. Note that these corrections require a substantial adjustment to the LMT SEFD. In Section 8.1 we show that these large gain corrections are consistent with those recovered through imaging.

be equal, providing an estimate of the relative station gains at their corresponding times:

$$\frac{|V^{t_1}_{\mathrm{SMT-PV}}|}{|V^{t_2}_{\mathrm{LMT-PV}}|} = \frac{|\mathcal{V}^{t_1}_{\mathrm{SMT-PV}}|}{|\mathcal{V}^{t_2}_{\mathrm{LMT-PV}}|}\left|\frac{g^{t_1}_{\mathrm{SMT}}g^{t_1}_{\mathrm{PV}}}{g^{t_2}_{\mathrm{LMT}}g^{t_2}_{\mathrm{PV}}}\right| \approx \left|\frac{g^{t_1}_{\mathrm{SMT}}}{g^{t_2}_{\mathrm{LMT}}}\right|. \tag{47}$$

The approximation makes the assumptions of stable source structure between t_1 and t_2, negligible change in the visibility function on the two baselines sampled near the crossing point, and a stable gain amplitude between t_1 and t_2 at PV.

If we further assume that the SMT gain is near unity (the a priori error budget estimates $|g_{\mathrm{SMT}}| = 1.00 \pm 0.04$), then Equation (47) provides an estimate of the LMT gain amplitude at time t_2. We can then apply this estimate to a simultaneous measurement of the SMT–LMT amplitude at time t_2 to estimate $|\mathcal{V}_{\mathrm{SMT-LMT}}|$:

$$\begin{aligned}|\mathcal{V}^{t_2}_{\mathrm{LMT-SMT}}| &= |g^{t_2}_{\mathrm{SMT}}|^{-1}|g^{t_2}_{\mathrm{LMT}}|^{-1}|V^{t_2}_{\mathrm{LMT-SMT}}| \\ &\approx \frac{|V^{t_1}_{\mathrm{SMT-PV}}|}{|g^{t_1}_{\mathrm{SMT}}||g^{t_2}_{\mathrm{SMT}}||V^{t_2}_{\mathrm{LMT-PV}}|}|V^{t_2}_{\mathrm{LMT-SMT}}| \\ &\approx \frac{|V^{t_1}_{\mathrm{SMT-PV}}||V^{t_2}_{\mathrm{LMT-SMT}}|}{|V^{t_2}_{\mathrm{LMT-PV}}|}.\end{aligned} \tag{48}$$

However, because the gain of the LMT is substantially time variable, extrapolating the gain estimated in Equation (47) to other times (even nearby times) is not reliable. To summarize, this final approximation assumes the following: that the SMT–PV measurement at time t_1 samples a baseline close to the LMT–PV measurement at t_2, that the source visibility on that baseline is stable between t_1 and t_2, that the PV gain amplitude is stable between t_1 and t_2, and that the SMT gain amplitude is near unity at both times.

We derive an uncertainty on $|\mathcal{V}^{t_2}_{\mathrm{LMT-SMT}}|$ by summing errors in quadrature from all these effects in addition to the nominal thermal noise on each of the three visibility amplitudes. We assume a conservative uncertainty in the relative PV gain amplitude between t_1 and t_2 of 10% (the a priori error budget for absolute gain calibration of PV is 5%), and we assume 3.5% uncertainty in the SMT gain amplitude (added independently for t_1 and t_2). Because we require mutual visibility of SMT and LMT at t_2, the nearest suitable points are not necessarily near the crossing point.[121] Consequently, the nearest suitable SMT–PV and LMT–PV baselines are displaced by 0.5-0.8 Gλ. Empirically, we estimate up to a 20 mJy difference from this displacement (which occurs at $|\boldsymbol{u}| \approx 6$ Gλ); the resultant uncertainty on the estimate of $|\mathcal{V}^{t_2}_{\mathrm{LMT-SMT}}|$ depends on this amplitude as a fraction of the SMT–PV and LMT–PV amplitudes.

Table 8 shows a triplet of visibility amplitudes and corresponding estimate of $|\mathcal{V}^{t_2}_{\mathrm{LMT-SMT}}|$ for each of the four observing days. With no LMT gain correction, the measurements range from 55–247 mJy, while after the LMT gain

[121] The LMT–PV baseline crosses the SMT–PV track when the elevation of M87 is only 11°.5 for the SMT. However, for the SMT, M87 rises behind the Large Binocular Telescope, so the minimum observable elevation is ∼25°. Consequently, the need for simultaneous SMT–LMT and LMT–PV visibilities necessitates using a measured LMT–PV visibility on a baseline that is slightly displaced from the crossing point.

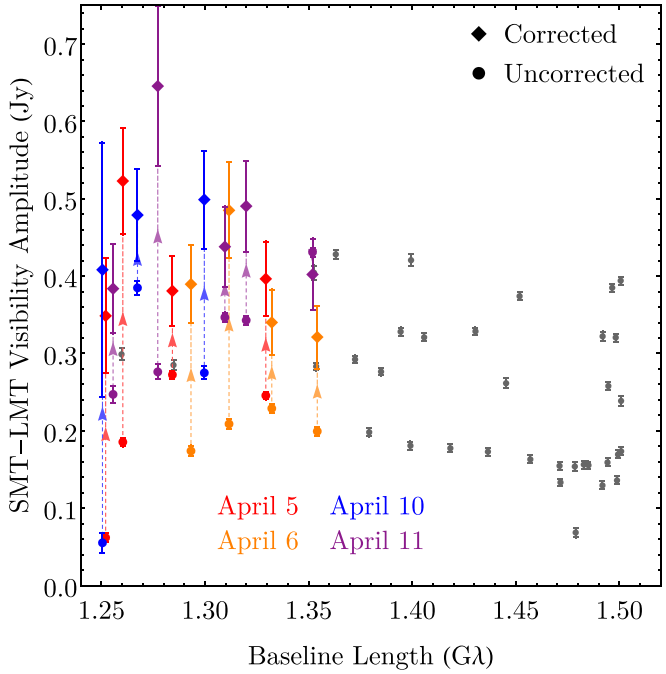

Figure 28. M87 visibility amplitudes measured on the SMT–LMT baseline, as a function of baseline length. Colored circles show measurements and their associated thermal noise ($\pm 1\sigma$) after a priori calibration; colored diamonds show the measurements after the SMT–PV/LMT–PV crossing track correction. Uncertainties in corrected amplitudes also account for propagated a priori calibration uncertainties in the derived correction factor. Correction factors are only applied if the nearest SMT–PV/LMT–PV baseline pair are located within 1 Gλ. SMT–LMT amplitudes with no associated pair meeting this criterion are colored gray and have plotted uncertainties that only account for thermal noise. All uncorrected amplitudes (circles) have scatter far exceeding their indicated thermal noise, demonstrating that amplitude calibration uncertainties are the dominant source of error.

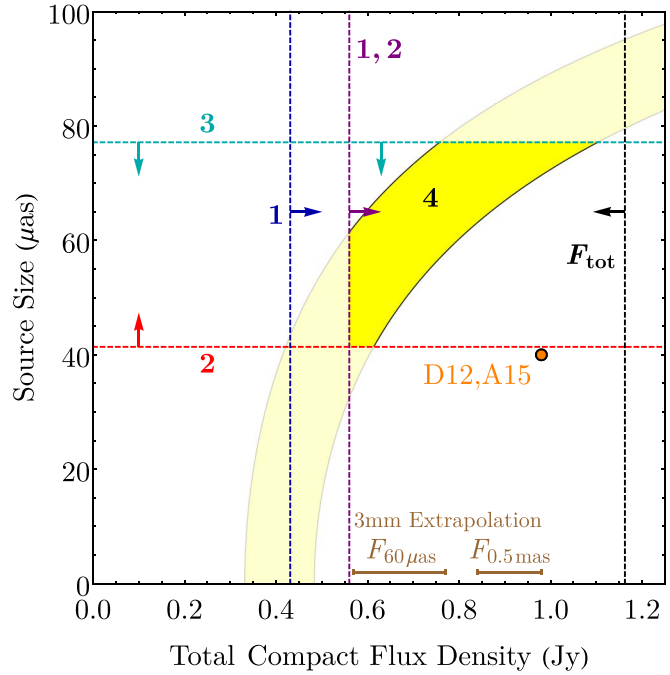

Figure 29. Joint constraints on the size and total compact flux density of 1.3 mm emission in M87. Numbered constraints (described in Appendix B.1) correspond to: (1) the maximum LMT–SMT amplitude, (2) the LMT–SMT/LMT–ALMA amplitude ratio, (3) LMT–SMT amplitudes coupled with the requirement $F_{\rm cpct} \leqslant F_{\rm tot}$, and (4) the SMT–LMT amplitude after LMT gain correction using the LMT–PV and SMT–PV crossing tracks in the (u, v) plane. Estimates on $F_{\rm cpct}$ and $F_{\rm tot}$ (with $\pm 1\sigma$ uncertainties) from extrapolating VLBI observations at 3 mm are shown in brown (see Appendix B.2). The orange circle shows the estimates from earlier EHT observations by Doeleman et al. (2012) and Akiyama et al. (2015).

correction the measurements range from 349–408 mJy. The corrections also all raise the SMT–LMT amplitude, as is expected. Some of these points represent the most significant LMT amplitude losses in the entire experiment. However, Figure 28 shows the corrected SMT–LMT amplitudes for all points with a suitable crossing track correction, demonstrating that the corrected amplitudes are broadly consistent between points with large and small derived LMT correction factors.

In summary, constraints 1–3 lead to the conclusion that $0.42 \leqslant F_{\rm cpct} \leqslant 1.14$ Jy on April 5 and 6, and that $0.56 \leqslant F_{\rm cpct} \leqslant 1.21$ Jy on April 10 and 11. We also estimate that the compact source size has an equivalent Gaussian FWHM between 38 and 82 μas on the first two days and between 41 and 77 μas on the last two days. Constraint 4 provides an absolute estimate of the LMT–SMT amplitude at a single point for each day, which allows us to provide a joint constraint on source size and $F_{\rm cpct}$. Figure 29 summarizes these constraints. Combining these constraints and marginalizing over the unknown source size, we obtain $F_{\rm cpct} = 0.64^{+0.39}_{-0.08}$ Jy.

B.2. Constraints from Quasi-simultaneous Multi-wavelength Observations

In addition to the non-imaging flux density constraints derived from EHT data (Section B.1), we can also utilize VLBI observations at longer wavelengths to estimate expected properties at 1.3 mm. Because both the compact and extended emission from M87 are variable, these observations must be quasi-simultaneous with the EHT observations to give precise constraints. Our approach assumes that the total compact emission of M87 at 230 GHz $F_{\rm tot}$ originates from the combination of (i) a compact emitter with unknown flux density $F_{\rm cpct}$ and spectral index at 230 GHz, and (ii) a larger and diffuse (milliarcsecond-scale) jet, which can be characterized by its total flux density $F_{\rm jet} = F_{\rm tot} - F_{\rm cpct}$ and a steep spectral index of $\alpha_{\rm jet} \sim -(0.7\text{–}1.0)$, as measured at cm- and mm-wavelengths (with typical errors of $\sim$0.3; see Hovatta et al. 2014; Hada et al. 2016). Then, by measuring $F_{\rm jet}$ and $F_{\rm tot}$ at lower frequencies and extrapolating them to 230 GHz using a power-law model, we can estimate the total compact flux density $F_{\rm cpct}$ at 230 GHz: $F_{\rm cpct} = F_{\rm tot} - F_{\rm jet}$.

Table 9
Quasi-simultaneous Lower-frequency VLBI Flux Density Measurements of M87 within a $0.5 \times 0.5\,\mathrm{mas}^2$ Box around the Peak Flux Density

Array	Freq. (GHz)	Flux (Jy)	Epoch
EAVN	22	1.25 ± 0.13	2017 April 3
		1.32 ± 0.13	2017 April 17
EAVN	43	1.21 ± 0.12	2017 April 4
		1.10 ± 0.11	2017 April 9
		1.18 ± 0.12	2017 April 14
		1.12 ± 0.11	2017 April 18
KVN	86	1.12 ± 0.17	2017 April 19
	129	0.91 ± 0.27	2017 April 19

In parallel with the EHT campaign, we densely monitored M87 at 22 and 43 GHz with the East Asian VLBI Network (EAVN; see Wajima et al. 2016; Hada et al. 2017; and An et al. 2018 for more details), which included 12 stations from Japan, Korea, and China (Mizusawa, Iriki, Ogasawara, Ishigaki, Hitachi, Kashima, Nobeyama, Yonsei, Ulsan, Tamna, Tianma, and Nanshan). For each epoch, a continuous 5–7 hr track was observed. The angular resolution was as fine as 0.55 mas at 22 GHz and 0.63 mas at 43 GHz. At both frequencies, the total flux densities of the nuclear region (i.e., $F_{\rm tot} = F_{\rm jet} + F_{\rm cpct}$) were measured using a large window of $0.5 \times 0.5\,\mathrm{mas}^2$ around the peak of the image and summing up the flux densities of the CLEAN components within the window. From this, we obtain total flux densities of $F_{\rm tot,22} \approx 1.3$ Jy and $F_{\rm tot,43} \approx 1.1$–$1.2$ Jy at 22 and 43 GHz, respectively.

We also make use of quasi-simultaneously obtained data sets of M87 from Korean VLBI Network (KVN) observations at 22, 43, 86, and 129 GHz on 2017 April 19 (see Lee et al. 2016 and Kim et al. 2018b for the monitoring program, details of data analysis, typical angular resolutions, and discussions about the extended jet flux). At 22 and 43 GHz, the correlated flux densities were comparable to the results of the EAVN observations. At 86 and 129 GHz, we adopted the same window of $0.5 \times 0.5\,\mathrm{mas}^2$ and obtained $F_{\rm tot,86} \approx 1.1$ Jy and $F_{\rm tot,129} \approx 0.9$ Jy, respectively. These measurements and their uncertainties are summarized in Table 9.

We fit a power-law model to the milliarcsecond-scale flux densities (i.e., $F_{\rm tot} \propto \nu^{+\alpha_{\rm tot}}$) and find $\alpha_{\rm tot} = -(0.14 \pm 0.04)$. By extrapolating this model to 230 GHz, we estimate $F_{\rm tot,230} = 0.91 \pm 0.07$ Jy. While this value is slightly lower than the ALMA interferometric measurements during the EHT observations, it only includes the total flux density within the inner $0.5 \times 0.5\,\mathrm{mas}^2$, which is nearly three orders of magnitude below the resolution limit of ALMA.

Next, we estimate the compact flux density $F_{\rm cpct,86}$ at 86 GHz using previous GMVA observations of M87 (Kim et al. 2018a). To proceed, we compute the flux densities within a much smaller window of $60 \times 60\,\mu\mathrm{as}^2$ around the peak of the GMVA images from 2004 to 2015, but excluding the 2009 epoch when the core of the jet showed exceptionally high flux densities. The values of $F_{\rm cpct,86}$ are relatively stable from epoch to epoch, and therefore we adopt a value of $F_{\rm cpct,86} = 0.55 \pm 0.06$ Jy, where the mean and uncertainty correspond to the mean and standard deviation of the measured flux densities. We can then estimate $F_{\rm jet}$ at 86 GHz in 2017 April as $F_{\rm jet,86} = F_{\rm tot,86} - F_{\rm cpct,86}$. By propagating the errors in $F_{\rm tot,86}$ and $F_{\rm cpct,86}$, we obtain $F_{\rm jet,86} = 0.57 \pm 0.18$ Jy at 86 GHz.

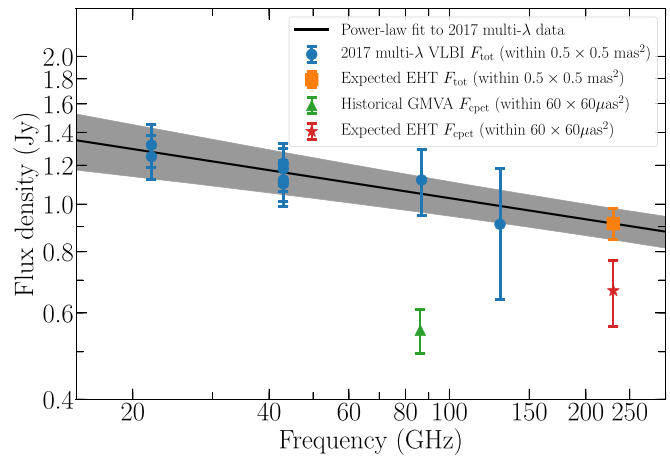

Figure 30. Multi-wavelength VLBI spectrum of M87 in 2017 and expected flux densities at 230 GHz (see Section B.2 for details). The black line and shaded region gives the model and its $\pm 1\sigma$ uncertainties for $F_{\rm tot}$.

Finally, we compute the expected $F_{\rm cpct,230}$ by estimating $F_{\rm jet,230}$ and subtracting it from the previously estimated $F_{\rm tot,230} = 0.91 \pm 0.07$ Jy. As explained above, we assume that $F_{\rm jet,230}$ follows a power law that can be extrapolated up to 230 GHz (i.e., $F_{\rm jet,230} \propto \nu^{+\alpha_{\rm jet}}$). For a range of $\alpha_{\rm jet} = -(0.7$–$1.0)$, we find $F_{\rm jet,230} = 0.25 \pm 0.08$ Jy. This value gives $F_{\rm cpct,230} = 0.67 \pm 0.10$ Jy within the central $\sim 60 \times 60\,\mu\mathrm{as}^2$. Figure 30 summarizes the spectrum of M87 at lower frequencies and the expected flux densities at 230 GHz. We emphasize that this estimate for $F_{\rm cpct,230}$ represents a characteristic value, and that the exact value may have varied slightly over the EHT observing window.

We note that this value for $F_{\rm cpct,230}$ is consistent with the constraints derived in Section B.1 using EHT measurements. Combining them, we obtain $F_{\rm cpct,230} = 0.66^{+0.16}_{-0.10}$ Jy.

Appendix C
Synthetic Data

To test and calibrate the parameters that we use in our final image reconstructions from imaging parameter surveys (Section 6), we generate synthetic data from different geometrical models and GRMHD simulations using two independent pipelines (as introduced in Section 6.1). We consider four geometric source models with parameters chosen such that their visibility data on EHT baselines match salient features of the observations, in particular the visibility nulls at $\sim$3.4 and $\sim$8.3 Gλ.

C.1. Geometric Models

We use four geometric models with different compact structure (displayed in Figure 5). The model parameters in each case were chosen such that their visibility data on EHT baselines match salient features of the observations (e.g., the visibility null at $\sim$3.4 Gλ).

All of our models have 0.6 Jy of flux density in a compact component and 0.6 Jy in an extended jet that is heavily resolved by EHT inter-site baselines. The large-scale jet model is common to all images and consists of three elliptical Gaussian components aligned to images of the M87 jet at 3 mm (e.g., Kim et al. 2018a). The jet parameters are displayed in Table 10.

We used four different models for the compact flux density. These are as follows.

Table 10
Gaussian Parameters of the Large-scale Jet Model used in Synthetic Data Generation

Flux Density (Jy)	θ_{maj} (μas)	θ_{min} (μas)	P.A. (°)	$\Delta_{R.A.}$ (μas)	$\Delta_{decl.}$ (μas)
0.3	1000	600	140	−688.77	80.86
0.2	400	200	93	−295.44	−52.09
0.1	400	200	115	−215.80	208.40

1. A delta-function ring with radius $r_0 = 22\ \mu$as, convolved with a circular Gaussian with FWHM of 10 μas.
2. A crescent composed of a delta-function ring with radius $r_0 = 22\ \mu$as and a dipolar angular intensity profile

$$I(r, \theta) = I_0[1 + 2A\cos(\theta - \eta)]\frac{\delta(r - r_0)}{2\pi r_0}, \tag{49}$$

   where $I_0 = 0.55$ Jy, the asymmetry parameter $A = 0.23$ (see Section 9.1), and η is the orientation angle east of north. The crescent is then also convolved with a 10 μas Gaussian.
3. A uniform disk with radius $r = 35\ \mu$as, convolved with a circular Gaussian with FWHM of 10 μas.
4. Two circular Gaussian components, each with a FWHM of 20 μas. The first component is located at the origin and has a total flux density of 0.27 Jy, while the second is located at $\Delta_{R.A.} = 30\ \mu$as and $\Delta_{decl.} = -12\ \mu$as and has a total flux density of 0.33 Jy.

Both the jet and compact structure are polarized in order to produce non-closing systematic errors from polarimetric leakage. The jet components all have a constant fractional polarization of 20% and a random position angle that varies across the image with a coherence length of 400 μas. The compact components all have a constant fractional polarization of 40% and a random polarization position angle with a coherence length of 5 μas.

C.2. Synthetic Data Generation with `eht-imaging`

The `eht-imaging` library produces synthetic visibilities from model images by computing their Fourier transform, adding random thermal noise (Equation (3)), and corrupting the data with systematic station-based effects using the Jones matrix formalism (Thompson et al. 2017). Off-diagonal terms in the Jones matrices mix the measured polarizations, which in the absence of noise and systematic error would correspond simply to the Fourier transform of the image polarizations by Equation (2).

We take circular polarizations as our primary basis, and consider a single baseline ij. The Fourier transform of the image gives the uncorrupted visibility of each polarization (RR'_{ij}, LL'_{ij}, LR'_{ij}, RL'_{ij}), which are assembled into a 2×2 correlation matrix:

$$V'_{ij} = \begin{pmatrix} RR'_{ij} & RL'_{ij} \\ LR'_{ij} & LL'_{ij} \end{pmatrix}. \tag{50}$$

The thermal noise standard deviation on each baseline and polarization is given by Equation (3) and assembled into a matrix $\boldsymbol{\sigma}_{ij}$ of the same form.

Table 11
Field Rotation Parameters for the EHT Stations

Station	Receiver Mount	f_{par}	f_{el}	φ_{off}
ALMA	Cassegrain	1	0	0
APEX	Nasmyth-Right	1	1	0
JCMT	Cassegrain	1	0	0
LMT	Nasmyth-Left	1	−1	0
PV	Nasmyth-Left	1	−1	0
SMA	Nasmyth-Left	1	−1	45°
SMT	Nasmyth-Right	1	1	0
SPT	Cassegrain	1	0	0

Including the effects of systematic and thermal noise, the simulated visibility matrix is $\boldsymbol{V}_{ij}$:

$$\boldsymbol{V}_{ij} = \boldsymbol{J}_i \boldsymbol{V}'_{ij} \boldsymbol{J}_j^{\dagger} + \mathcal{N}(\boldsymbol{\sigma}_{ij}), \tag{51}$$

where $\boldsymbol{J}_i$ and $\boldsymbol{J}_j$ are the station Jones matrices. Each Jones matrix has the form

$$\boldsymbol{J} = \begin{pmatrix} g_R & e^{i\varphi}\, d_R\, g_R \\ e^{-i\varphi}\, d_L\, g_L & g_L \end{pmatrix}, \tag{52}$$

where g_R, g_L are the complex gain terms, d_R and d_L are the constant station d-terms, and φ is a term from field rotation. We typically expect $g < 1$ due to losses in telescope sensitivity.

The complex gain terms include an absolute amplitude gain offset $|g|$, and a random atmospheric phase ϕ. For the purposes of this Letter, we set $g_R = g_L$ because the atmosphere is not significantly birefringent at millimeter wavelengths and because differential gains between right and left polarizations are removed in the calibration process (Paper III):

$$g_R = g_L = |g(t)|\, e^{i\phi(t)}. \tag{53}$$

The phase error ϕ is drawn from a uniform distribution once per scan; it is kept stable within scans to mimic the ad hoc phase calibration procedure. The amplitude gain of a site at each time has a time-stable component g_1 and a time-varying component $g_2(t)$:

$$g(t) = |1 - |g_1| + g_2(t)|^{1/2}. \tag{54}$$

Both g_1 and g_2 are sampled from normal distributions with zero mean: $g_1 \sim \mathcal{N}(0, \sigma_{g_1})$ and $g_2(t) \sim \mathcal{N}(0, \sigma_{g_2})$. To simulate its higher median gain error and variability, for the LMT we set $\sigma_{g_1} = 0.6$ and $\sigma_{g_2} = 0.5$. For all other sites we set $\sigma_{g_1} = 0.15$ and $\sigma_{g_2} = 0.05$. g_2. Like the atmospheric phase, we fixed the gain errors so that $g_2(t)$ changes between scans but is kept stable across scans.

The complex d terms, d_R and d_L, are stationary in time and drawn from a complex normal distribution with zero mean and a standard deviation of 0.05 in each of the real and imaginary parts (motivated by the estimates in Johnson et al. 2015). The mean amplitude of the leakage terms is then 6.3%. The field rotation phase term φ has three possible contributions depending upon the receiver mount:

$$\varphi = f_{el}\,\theta_{el} + f_{par}\,\psi_{par} + \varphi_{off}, \tag{55}$$

where θ_{el} is the elevation angle, ψ_{par} is the parallactic angle, and φ_{off} is a constant offset. Cassegrain mounts have $f_{par} = 1$ and $f_{el} = 0$. Nasmyth mounts have $f_{par} = 1$ and $f_{el} = \pm 1$, depending on the handedness. The EHT station field rotation parameters are listed in Table 11.

After being simulated with Equation (51), the synthetic data were network calibrated and converted to Stokes I, following the procedure used for the EHT data pipeline in Paper III.

C.3. Synthetic Data Generation with `MeqSilhouette` *and* `rPICARD`

An mm-VLBI synthetic data pipeline built on the synthetic data generator `MeqSilhouette` (Blecher et al. 2017) and the EHT CASA calibration pipeline `rPICARD` (Janssen et al. 2019) has been developed (F. Roelofs et al. 2019, in preparation). Like `eht-imaging`, this pipeline is able to produce synthetic data sets with statistics that closely match real VLBI data, but it is done using an a priori physics-based approach instead of an a posteriori data-based approach.

`MeqSilhouette` (Blecher et al. 2017) is a synthetic VLBI data generator that predicts visibilities from both parametric and non-parametric sky models using `MeqTrees` (Noordam & Smirnov 2010) and `WSClean` (Offringa et al. 2014), respectively, and applies physically motivated propagation and instrumental effects. Uncorrupted frequency-resolved visibilities are generated from a full-Stokes sky model, antenna locations, and a real observing schedule. Elevation-dependent mean tropospheric delays, opacity, and sky temperatures are simulated from input weather parameters (ground pressure P_g, ground temperature T_g, and precipitable water vapor) using the `ATM` software (Pardo et al. 2001). In addition, turbulent phases are simulated based on input atmospheric coherence times t_c and assuming a thin scattering screen model characterized by Kolmogorov turbulence. Station-dependent thermal noise drawn from a Gaussian distribution is included and contains contributions from both the receiver and the atmosphere. Scan-based antenna pointing errors are added using the primary beam sizes at 230 GHz and observatory-measured pointing uncertainties. Full polarization simulation of time-variable sources is also possible (as will be relevant to Sgr A* observations), with the option of introducing station-based, frequency-dependent polarization leakage and complex gain errors.

In the `MeqSilhouette+rPICARD` pipeline (F. Roelofs et al. 2019, in preparation), the full observation and calibration process is simulated by running the synthetic data generated by `MeqSilhouette` through the CASA VLBI calibration pipeline `rPICARD` (Janssen et al. 2019). In this calibration process, fringe fitting, amplitude calibration, and time and frequency averaging are done in the same way as for the real EHT data.

Figure 31 shows a comparison between synthetic data generated from the same model image using eht-imaging and

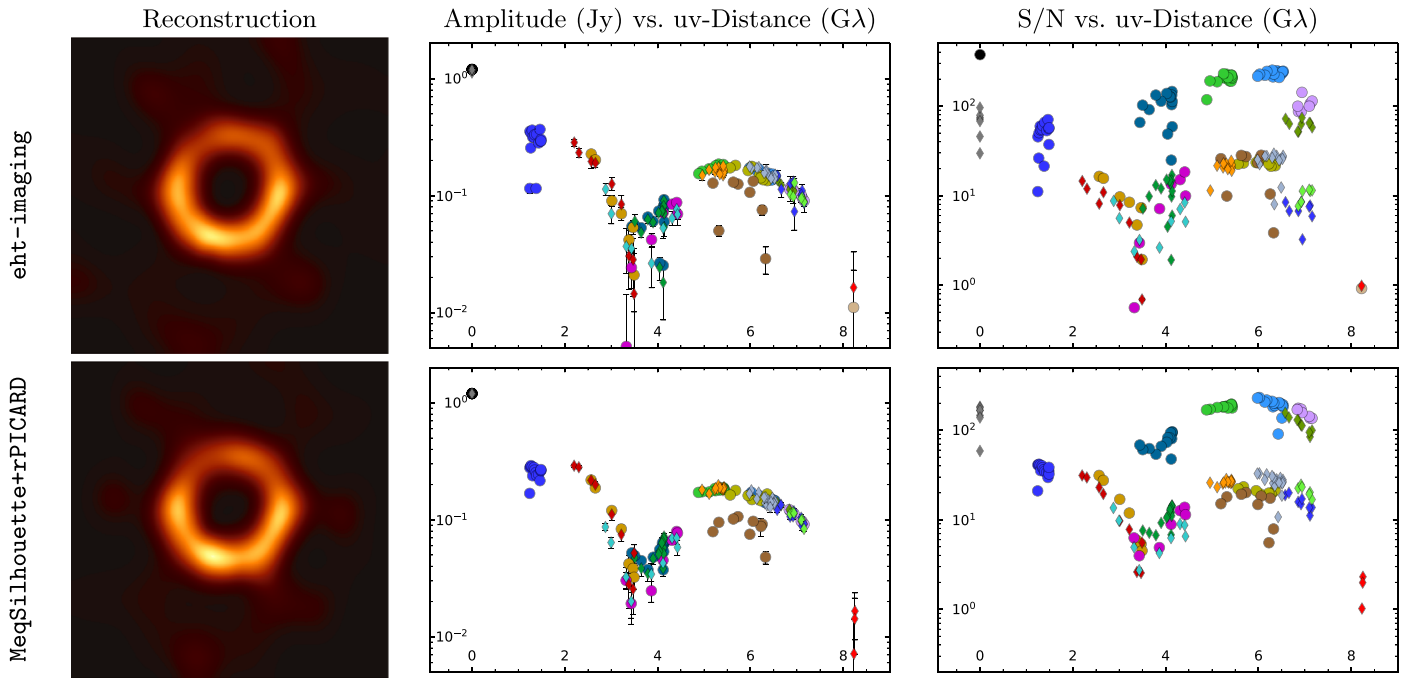

Figure 31. Comparison of the synthetic data from the `eht-imaging` and `MeqSilhouette` data generation libraries. Low-band data were generated from the same source image. The reconstructed images, visibility amplitudes, and S/Ns from the data generated with the `MeqSilhouette+rPICARD` pipeline are broadly consistent with those generated with `eht-imaging`, despite the different approaches of the software packages. Points are colored by baseline as in Figure 18. Images are reconstructed using the same script in `eht-imaging` using the fiducial parameters from Section 6.

Table 12
Weather Parameters used in the MeqSilhouette Simulations

Antenna	PWV (mm)	P_g (mb)	T_g (K)	t_c (s)
ALMA	1.6	555	271	10
APEX	1.6	555	271	10
JCMT	1.1	626	278	5
LMT	4.7	604	275	6
PV	1.5	723	270	4
SMA	1.1	626	278	5
SMT	2.7	695	276	3

Note. The parameters PWV, P_g, and T_g are median values for the EHT 2017 campaign as logged in VLBImonitor (Paper II).

the MeqSilhouette+rPICARD simulation software. For the MeqSilhouette simulations, input weather parameters (Table 12) were based on site measurements logged in VLBImonitor (Paper II) during the EHT campaign. Coherence times, SEFDs, and pointing offsets were based on measurements from individual EHT stations. A leakage of 5% was added to the visibilities with the field rotation parameters listed in Table 11, and an overall gain factor of 0.6 was set for the LMT.

The reconstructed images (generated with the M87 fiducial parameters of the eht-imaging imaging pipeline), visibility amplitudes, and S/Ns from the data generated with the MeqSilhouette and rPICARD pipeline are broadly consistent with those generated with eht-imaging, despite the different approaches used in the two software packages. Table 13 shows the normalized cross-correlation ρ_{NX} and equivalent blurring α (given in μas), for images made from the eht-imaging and MeqSilhouette+rPICARD data simulation software. Each software package was used to generate three different realizations of visibilities from the same underlying crescent geometric model (see Figure 5). The ρ_{NX} and α computed from reconstructions of this data show broad consistency. This consistency reinforces our confidence in both pipelines, particularly in corroborating that the image fidelity is primarily determined by the limited baselines coverage rather than data sensitivity or calibration limitations.

Table 13
Image Fidelity Metrics, Normalized Cross-correlation ρ_{NX}, and Equivalent Blurring α (given in μas), for Images Made from Data Simulated using eht-imaging and MeqSilhouette+rPICARD

Data Simulation Software	Sample 1		Sample 2		Sample 3	
	ρ_{NX}	α	ρ_{NX}	α	ρ_{NX}	α
eht-imaging	0.982	8.6	0.981	8.7	0.978	9.2
MeqSilhouette +rPICARD	0.980	8.9	0.980	9.0	0.983	8.4

Note. Images from three sets of visibilities of the crescent (+jet) model, with different realizations of noise (samples 1–3), were generated for each data simulation software package using the fiducial parameters from the eht-imaging imaging pipeline. The ρ_{NX} and α fidelity metrics are insensitive to both the particular noise realization and the simulation software. Thus, our selected Top Sets and fiducial parameters are insensitive to the particular noise realization and the simulation software.

Appendix D
Image Dependence on Sites for SMILI and DIFMAP Pipelines

In Section 8.2, we use the eht-imaging pipeline with fiducial parameters to show that the ring structure in reconstructed images is resilient to the loss of most sites. Figure 32 shows the corresponding reconstructions from the other two pipelines on April 11. The ring structures produced by all three pipelines are similarly sensitive to dropping most individual sites, with Chile and PV being the most critical. The image degradation due to the loss of all data to a site tends to be larger for RML approaches, as these methods use weaker constraints on the allowed FOV for image flux.

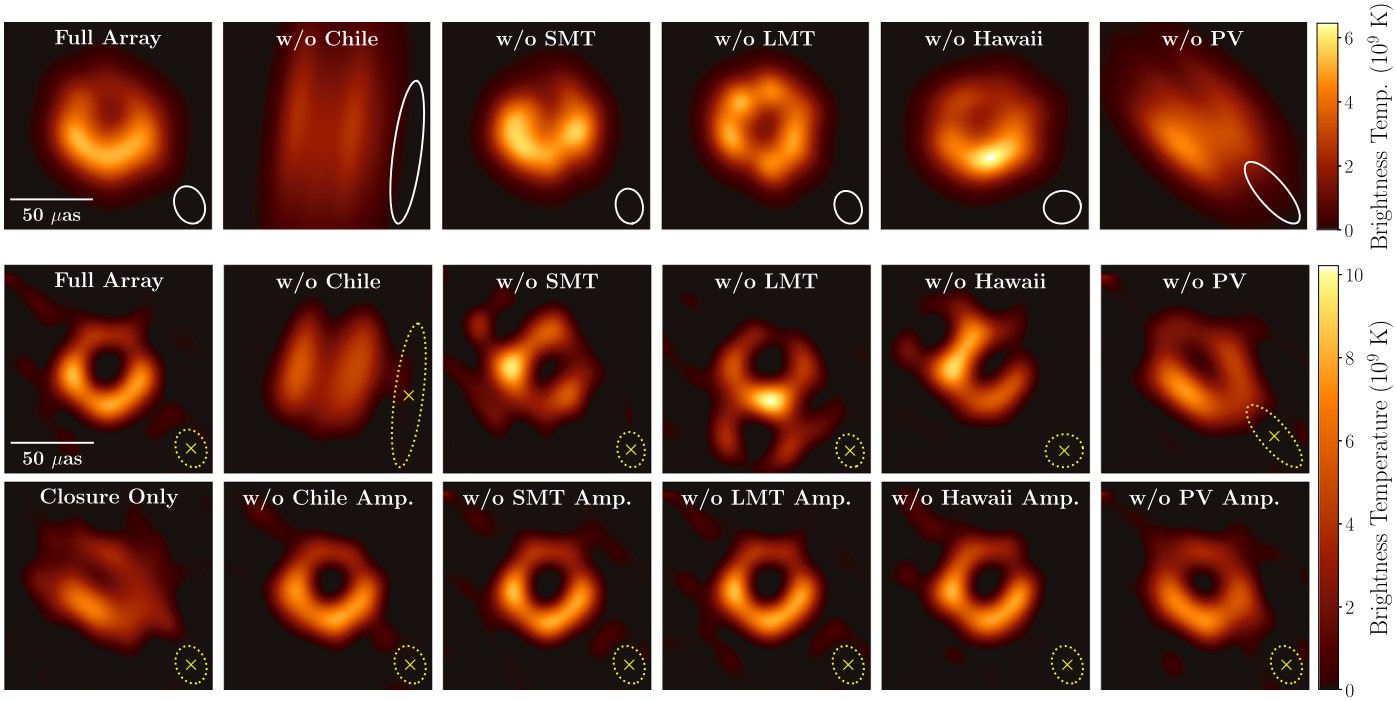

Figure 32. Example reconstructions of M87 on April 11 after omitting visibilities to each geographical site for the DIFMAP and SMILI pipelines. Following Figure 22, the top row of each pipeline shows reconstructions that exclude all baselines to the indicated site, while the bottom row shows reconstructions that exclude all visibility amplitudes on baselines to the indicated site but retain closure phases and closure amplitudes. The lower-left panel shows an image reconstructed after excluding visibility amplitudes to all sites (i.e., using only closure quantities). Because DIFMAP uses only visibilities, we only show the case of excluding baselines. The ellipse in each panel shows the corresponding synthesized beam with uniform weighting; only the DIFMAP images are restored with these beams.

Appendix E
Interday Variability in M87 Images

The closure phases of M87 show variation across the four observations (Paper III). Similarly, our fiducial images show corresponding variation in image structure between April 5, 6 and 10, 11 (Figure 11). These differences are also apparent in the averaged fiducial images restored to a common, conservative resolution (see Figure 15). In Section 8.3, we demonstrated that the image variability is not simply from changes in the baseline coverage. We now assess this image variation.

Figure 33 shows differences of reconstructed image pairs on different days. To suppress features that are specific to imaging parameter choices, we show the beam-convolved difference of two mean images, where the mean is taken over all corresponding Top Set images for the specified pipeline and day. For all pipelines, but especially for eht-imaging and SMILI, the differences are larger across the multi-day gap than across adjacent days, as expected if these differences reflect source evolution.

For both eht-imaging and SMILI, the difference images indicate a shift of the flux from the left to the right side of the ring (east to west) over the observations, which is consistent with the slight increase in η over the days (Section 9). In contrast, DIFMAP difference images are dominated by larger-scale morphology changes. For all pipelines, the beam-convolved temporal differences are nearly an order of magnitude larger than the median standard deviation of differences seen across eht-imaging Top Set images (1.6×10^8 K; see Figure 17). Nevertheless, in all cases, we cannot unambiguously associate the variability with smooth motion or evolution of a specific image feature.

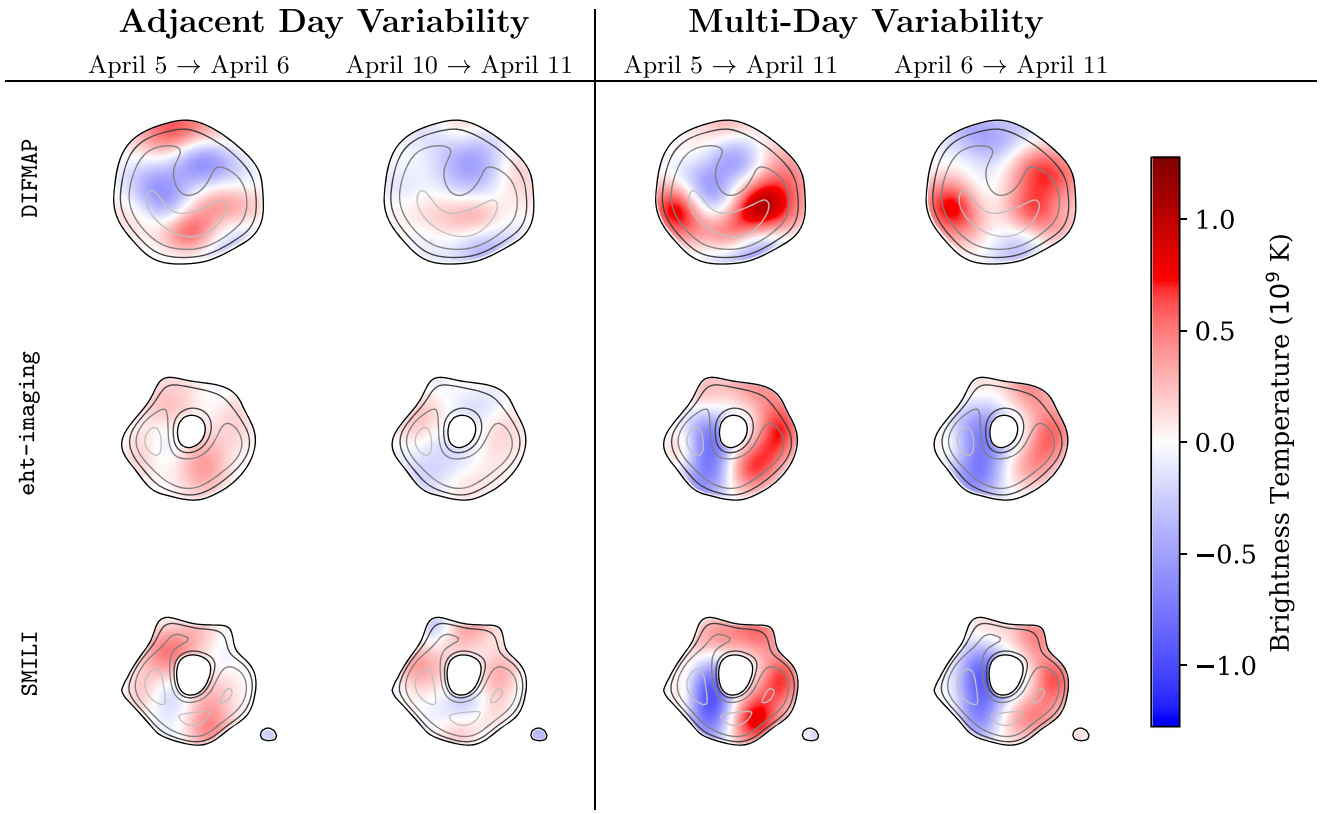

Figure 33. Variations seen in reconstructed images between days. Each row shows the beam-convolved difference of the aligned mean images from the Top Set of the corresponding parameter survey. All images are shown using the same color scale. Positive values (red) indicate an increase in brightness at the later date, and negative values (blue) indicate a decrease in brightness at the later date.

Appendix F
Multi-day Gain Comparisons with 3C 279

In Section 8, we compared the residual amplitude gains for the LMT and SMT on April 5 derived from separately imaging M87 and 3C 279. We now expand this comparison to all four days on which these sources were observed.

Figure 34 compares the interleaved multiplicative station gains for M87 and 3C 279 for each day; Table 14 presents the gain statistics for the two sources and compares them to the expected amplitude calibration error budget (Paper III). The trends of inferred residual gain amplitudes are consistent among the imaging pipelines, and those of M87 are similar to those of 3C 279. The inferred gains for M87 at the LMT have large excursions that are not seen in the 3C 279 gain trends; these excursions are likely due to poor pointing and tracking. These large LMT correction factors (up to $|g_{\rm LMT}|^{-1} \approx 6$) are also consistent with those estimated using the SMT–PV and LMT–PV crossing tracks (see Table 8 and Figure 28).

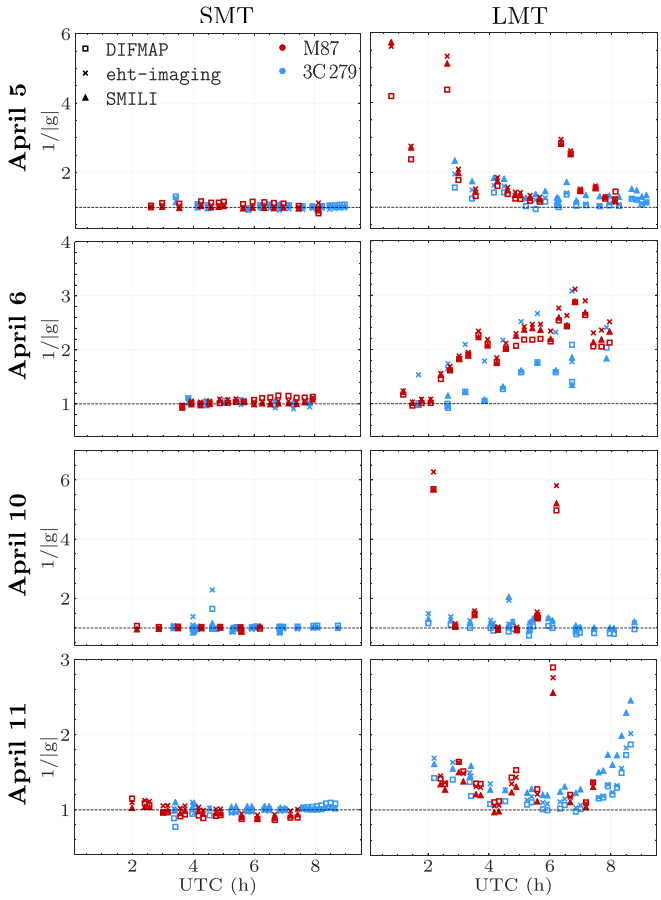

Figure 34. Derived residual gains for the SMT (left) and LMT (right) using self-calibration to images of M87 (red) and 3C 279 (blue). The M87 images are the fiducial images from each pipeline; the 3C 279 images were reconstructed separately, using adapted imaging scripts. The particularly large excursions on the LMT M87 gains are often due to poor pointing. For instance, excursions at ≈6 UTC are from difficulties tracking the source during transit (∼81° elevation). Note the different ranges shown for each observing day.

Table 14
Residual Gain Corrections Derived for M87 and 3C 279 for Observations on All Days (April 5, 6, 10, 11)

Station	Fiducial M87 Median Gain			3C 279 Median Gain			A Priori Budget (%)
April 5	DIFMAP	eht-imaging	SMILI	DIFMAP	eht-imaging	SMILI	
ALMA	$0.97^{+0.02}_{-0.03}$	$0.97^{+0.02}_{-0.01}$	$0.98^{+0.01}_{-0.01}$	$0.99^{+0.02}_{-0.09}$	$1.11^{+0.04}_{-0.02}$	$0.97^{+0.03}_{-0.01}$	5.0
APEX	$1.05^{+0.04}_{-0.02}$	$1.02^{+0.02}_{-0.01}$	$1.01^{+0.01}_{-0.01}$	$0.99^{+0.01}_{-0.00}$	$0.90^{+0.01}_{-0.00}$	$1.05^{+0.01}_{-0.02}$	5.5
SMT	$1.13^{+0.01}_{-0.06}$	$1.02^{+0.04}_{-0.01}$	$0.99^{+0.02}_{-0.01}$	$1.06^{+0.01}_{-0.02}$	$0.97^{+0.01}_{-0.02}$	$1.04^{+0.02}_{-0.01}$	3.5
JCMT	$1.00^{+0.02}_{-0.00}$	$1.00^{+0.00}_{-0.00}$	$1.00^{+0.00}_{-0.00}$	$1.00^{+0.01}_{-0.00}$	$1.02^{+0.02}_{-0.01}$	$1.00^{+0.00}_{-0.01}$	7.0
LMT	$1.46^{+0.76}_{-0.21}$	$1.55^{+0.93}_{-0.19}$	$1.47^{+0.91}_{-0.19}$	$1.08^{+0.16}_{-0.04}$	$1.21^{+0.13}_{-0.11}$	$1.35^{+0.27}_{-0.05}$	11.0
SMA	$1.00^{+0.02}_{-0.01}$	$1.00^{+0.01}_{-0.00}$	$1.00^{+0.00}_{-0.00}$	$1.01^{+0.01}_{-0.01}$	$1.04^{+0.03}_{-0.00}$	$0.99^{+0.00}_{-0.01}$	7.5
PV	$1.14^{+0.04}_{-0.04}$	$0.96^{+0.02}_{-0.07}$	$0.98^{+0.02}_{-0.07}$	$1.33^{+0.12}_{-0.04}$	$1.14^{+0.04}_{-0.05}$	$0.94^{+0.05}_{-0.02}$	5.0
SPT	…	…	…	…	…	…	7.5
April 6							
ALMA	$1.02^{+0.03}_{-0.02}$	$0.98^{+0.02}_{-0.02}$	$0.99^{+0.02}_{-0.02}$	$1.00^{+0.02}_{-0.01}$	$1.04^{+0.09}_{-0.04}$	$0.99^{+0.01}_{-0.03}$	5.0
APEX	$0.98^{+0.02}_{-0.03}$	$1.01^{+0.03}_{-0.02}$	$1.01^{+0.02}_{-0.02}$	$1.00^{+0.01}_{-0.01}$	$0.97^{+0.03}_{-0.09}$	$1.01^{+0.03}_{-0.01}$	5.5
SMT	$1.06^{+0.06}_{-0.04}$	$1.05^{+0.02}_{-0.01}$	$1.01^{+0.03}_{-0.02}$	$1.06^{+0.00}_{-0.05}$	$0.99^{+0.05}_{-0.05}$	$1.02^{+0.01}_{-0.00}$	3.5
JCMT	$1.00^{+0.00}_{-0.00}$	$1.00^{+0.00}_{-0.00}$	$1.00^{+0.00}_{-0.00}$	$1.00^{+0.00}_{-0.00}$	$1.00^{+0.01}_{-0.00}$	$1.00^{+0.01}_{-0.00}$	7.0
LMT	$2.06^{+0.12}_{-0.33}$	$2.30^{+0.16}_{-0.49}$	$2.16^{+0.20}_{-0.44}$	$1.34^{+0.29}_{-0.30}$	$2.13^{+0.30}_{-0.37}$	$1.33^{+0.32}_{-0.20}$	11.0
SMA	$1.01^{+0.01}_{-0.01}$	$1.00^{+0.00}_{-0.01}$	$1.00^{+0.00}_{-0.02}$	$1.00^{+0.01}_{-0.00}$	$1.04^{+0.00}_{-0.01}$	$0.99^{+0.00}_{-0.00}$	7.5
PV	$0.98^{+0.03}_{-0.04}$	$0.97^{+0.01}_{-0.07}$	$0.99^{+0.01}_{-0.06}$	$0.81^{+0.12}_{-0.29}$	$1.05^{+0.01}_{-0.02}$	$0.91^{+0.06}_{-0.01}$	5.0
SPT	…	…	…	…	…	…	7.5
April 10							
ALMA	$1.03^{+0.02}_{-0.03}$	$0.99^{+0.00}_{-0.01}$	$0.99^{+0.01}_{-0.02}$	$1.00^{+0.03}_{-0.00}$	$1.08^{+0.06}_{-0.08}$	$0.99^{+0.01}_{-0.02}$	5.0

Table 14
(Continued)

Station	Fiducial M87 Median Gain			3C 279 Median Gain			A Priori Budget (%)
APEX	$0.99^{+0.02}_{-0.03}$	$1.02^{+0.01}_{-0.01}$	$1.01^{+0.01}_{-0.02}$	$1.00^{+0.00}_{-0.02}$	$0.94^{+0.06}_{-0.06}$	$1.00^{+0.02}_{-0.00}$	5.5
SMT	$1.03^{+0.01}_{-0.02}$	$1.03^{+0.00}_{-0.04}$	$0.99^{+0.02}_{-0.02}$	$1.03^{+0.02}_{-0.05}$	$0.97^{+0.04}_{-0.02}$	$1.00^{+0.03}_{-0.04}$	3.5
JCMT	$1.00^{+0.01}_{-0.01}$	$1.00^{+0.00}_{-0.00}$	$1.00^{+0.00}_{-0.00}$	$1.00^{+0.00}_{-0.04}$	$0.98^{+0.01}_{-0.00}$	$1.00^{+0.00}_{-0.07}$	7.0
LMT	$1.37^{+0.98}_{-0.33}$	$1.50^{+1.13}_{-0.38}$	$1.35^{+1.02}_{-0.34}$	$0.96^{+0.04}_{-0.12}$	$1.17^{+0.09}_{-0.22}$	$1.19^{+0.07}_{-0.18}$	11.0
SMA	$1.01^{+0.04}_{-0.00}$	$1.00^{+0.02}_{-0.00}$	$1.00^{+0.02}_{-0.00}$	$1.00^{+0.01}_{-0.01}$	$1.04^{+0.02}_{-0.01}$	$1.00^{+0.01}_{-0.01}$	7.5
PV	$1.02^{+0.02}_{-0.00}$	$0.94^{+0.03}_{-0.03}$	$0.94^{+0.02}_{-0.01}$	$0.97^{+0.06}_{-0.02}$	$1.10^{+0.15}_{-0.04}$	$0.96^{+0.04}_{-0.01}$	5.0
SPT	…	…	…	$1.02^{+0.58}_{-0.09}$	$1.02^{+0.28}_{-0.08}$	$1.03^{+0.03}_{-0.10}$	7.5
April 11							
ALMA	$1.00^{+0.02}_{-0.01}$	$1.00^{+0.02}_{-0.01}$	$1.00^{+0.01}_{-0.01}$	$1.01^{+0.01}_{-0.01}$	$1.12^{+0.03}_{-0.09}$	$0.99^{+0.01}_{-0.01}$	5.0
APEX	$1.00^{+0.01}_{-0.02}$	$1.00^{+0.01}_{-0.02}$	$1.00^{+0.01}_{-0.01}$	$1.00^{+0.01}_{-0.02}$	$0.90^{+0.10}_{-0.03}$	$1.01^{+0.01}_{-0.01}$	5.5
SMT	$0.92^{+0.04}_{-0.03}$	$1.02^{+0.03}_{-0.03}$	$0.95^{+0.04}_{-0.01}$	$1.01^{+0.03}_{-0.03}$	$1.01^{+0.01}_{-0.03}$	$1.03^{+0.02}_{-0.01}$	3.5
JCMT	$1.00^{+0.01}_{-0.01}$	$1.00^{+0.01}_{-0.00}$	$1.01^{+0.01}_{-0.01}$	$1.00^{+0.00}_{-0.00}$	$1.00^{+0.01}_{-0.00}$	$1.00^{+0.00}_{-0.00}$	7.0
LMT	$1.35^{+0.16}_{-0.15}$	$1.35^{+0.10}_{-0.18}$	$1.23^{+0.11}_{-0.13}$	$1.16^{+0.20}_{-0.09}$	$1.25^{+0.25}_{-0.12}$	$1.47^{+0.14}_{-0.21}$	11.0
SMA	$1.00^{+0.01}_{-0.04}$	$0.99^{+0.01}_{-0.01}$	$1.00^{+0.02}_{-0.01}$	$1.00^{+0.01}_{-0.00}$	$1.04^{+0.00}_{-0.01}$	$1.00^{+0.00}_{-0.01}$	7.5
PV	$1.00^{+0.01}_{-0.05}$	$0.92^{+0.02}_{-0.00}$	$0.95^{+0.02}_{-0.03}$	$0.91^{+0.04}_{-0.10}$	$1.09^{+0.12}_{-0.04}$	$1.00^{+0.02}_{-0.01}$	5.0
SPT	…	…	…	$0.90^{+0.07}_{-0.03}$	$1.00^{+0.00}_{-0.05}$	$1.02^{+0.05}_{-0.06}$	7.5

Note. Numbers indicate the median of $1/|g|$, with stated uncertainties corresponding to the 25th and 75th percentiles. The multiplicative gains on the visibilities for each station are computed by self-calibrating the network-calibrated data sets to the reconstructions after rescaling the intra-site baseline amplitudes to match the total flux of the reconstructions. The percentage deviation from unity can be compared to the expectations from the station-based a priori error budget on the visibility amplitudes derived from Paper III. The SPT is omitted from gain comparisons on the first two days as it did not observe 3C 279 on April 5, and it observed only a single 3C 279 scan on April 6.

Appendix G
Finite Resolution Bias on Ring Parameters

In addition to uncertainties from thermal noise, systematic noise, and algorithmic imaging assumptions, estimated image properties are necessarily limited by the image resolution. Image structure at scales finer than the diffraction-limited resolution can bias properties such as the magnitude and location of maximum image brightness.

As a simple example, we will consider the finite resolution bias for a thin ring. Written in cylindrical coordinates (r, θ), the image of an infinitesimally thin ring of diameter d takes the form

$$I_{\rm ring}(r, \theta; d) = \frac{1}{\pi d}\delta(r - d/2), \tag{56}$$

where the image is normalized to have a total flux density of unity. Next, suppose that this image is convolved with a circular Gaussian kernel having FWHM α. The resulting blurred ring is given by

$$\begin{aligned} I_{\rm ring}(r, \theta; d, \alpha) &= \frac{4\ln 2}{\pi^2\alpha^2 d}\int r'\,dr'd\theta'\delta(r' - d/2) \\ &\quad\times \exp\left[-\frac{4\ln 2}{\alpha^2}(r^2 + r'^2 - 2rr'\cos\theta')\right] \\ &= \frac{4\ln 2}{\pi\alpha^2}\exp\left[-\frac{4\ln 2}{\alpha^2}(r^2 + d^2/4)\right] \\ &\quad\times I_0\left(4\ln 2\frac{rd}{\alpha^2}\right), \end{aligned}$$

where $I_0(x)$ in the final line is a modified Bessel function of the first kind. In the limit $\alpha \ll d$, we can simplify this expression using the identity $I_0(x) = \frac{e^x}{\sqrt{2\pi x}}\left[1 + \mathcal{O}\left(\frac{1}{x}\right)\right]$ (Abramowitz & Stegun 1972). Substituting $\Delta = r - d/2$ and only keeping terms to leading order in Δ/d and α/d, we obtain

$$I_{\rm ring}(r; d, \alpha) \approx \sqrt{\frac{4\ln 2}{\pi^3}}\frac{1}{\alpha d}\left[1 - \frac{\Delta}{d}\right]e^{-4\ln 2(\Delta/\alpha)^2}. \tag{57}$$

Thus, when $\alpha \ll d$, the FWHM of the blurred ring is approximately equal to α. More generally, convolving a ring that has a Gaussian profile of intrinsic FWHM $w_{\rm true}$ with a circular Gaussian kernel with FWHM α then gives an effective width

$$w_{\rm meas} \approx \sqrt{w_{\rm true}^2 + \alpha^2}. \tag{58}$$

Likewise, we can use Equation (57) to estimate the radius of peak brightness after blurring; to leading order in α/d, $r_{\rm pk} \approx d/2 - \frac{1}{8\ln 2}\frac{\alpha^2}{d}$. Thus, letting $d_{\rm true}$ denote the angular diameter of the unconvolved ring and $d_{\rm meas}$ denote the angular diameter of peak brightness of the convolved ring, we obtain

$$d_{\rm true} \approx \frac{d_{\rm meas}}{1 - \frac{1}{4\ln 2}\left(\frac{\alpha}{d_{\rm meas}}\right)^2}, \tag{59}$$

where the approximation is accurate to leading order in $\alpha/d_{\rm meas}$.

As a concrete example, choosing parameters that are similar to our M87 measurements in Section 9.3, an infinitesimally thin ring with true diameter $d = 44\ \mu$as and width $\alpha = 15\ \mu$as will have its measured diameter biased downward by $\approx 2\ \mu$as.

While the simple Gaussian convolution assumed in this example only crudely approximates the effects of finite resolution on reconstructed images, it indicates that for images dominated by a thin ring, estimated diameters (widths) will be biased downward (upward) by the finite resolution of an image

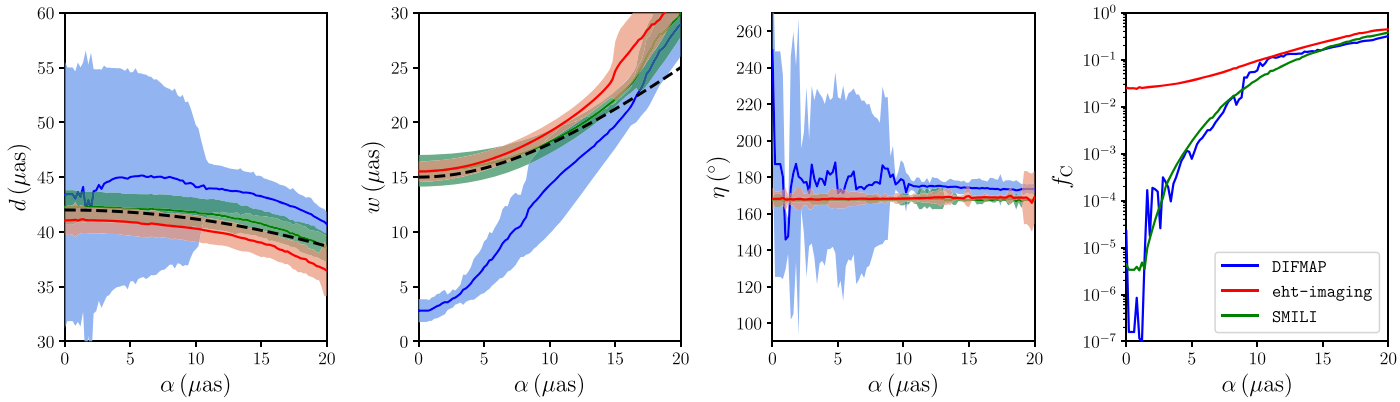

Figure 35. From left to right, measured diameter d, width w, orientation angle η, and central brightness ratio f_C measured from the April 11 fiducial images blurred with circular Gaussian kernels of increasing FWHM α. The solid lines indicate the measured value, and the shaded regions give the 1σ uncertainty as defined in Section 9.1 (these uncertainties do not include a contribution from scatter across the Top Set). The dashed line on the first panel shows the prediction of Equation (59) for the measured diameter $d_{\rm meas}$ as a function of the blur kernel assuming $d_{\rm true} = 42\ \mu$as. The dashed line in the second panel shows the FWHM of a 15 μas Gaussian convolved with the kernel of FWHM α (Equation (58)). Because the DIFMAP images are fundamentally composed of point sources, the measurements from these images become highly uncertain when $\alpha \lesssim 10\ \mu$as.

reconstruction. For the fiducial image measurements in Section 9, the diameter bias from this finite-resolution effect would be maximum in the case of an infinitesimal intrinsic ring, with α then approximately corresponding to the measured width. Thus, the finite-resolution diameter bias is at most a few μas.

In Figure 35, we explore the dependence of estimated ring parameters on the size of an applied restoring beam. Using the fiducial M87 images on April 11 from all three imaging pipelines, we show parameters computed after convolving each image with a circular Gaussian kernel having FWHM α in the range 0–20 μas. The DIFMAP images are fundamentally composed of point sources ("CLEAN" components). When these point sources are restored with $\alpha \lesssim 10\ \mu$as, the CLEAN components still appear in the convolved image as individual point sources. As a result, the feature extraction methods of Section 9, which assume a smooth ring structure, have large uncertainties when extracting parameters on these images. This uncertainty is particularly apparent in the orientation angle measurement. The RML images, by contrast, have a finite width and smooth structure even at $\alpha = 0$. As a result, their parameters vary smoothly and have similar uncertainties at all values of α.

The leftmost panel of Figure 35 shows that the dependence of the measured diameter on α closely follows Equation (59). In addition, the fiducial images have a scatter of approximately 1 μas across the different imaging methods, but an uncertainty of $\approx$3–4 μas across the varying α. Thus, when extracting physical parameters from the measured diameter, it is important to take into consideration the additional bias and uncertainty induced by this effect.

For small values of the restoring beam α, Figure 35 shows that the measured width w of the RML reconstructions follows the prediction of Equation (58). For larger $\alpha > 15\ \mu$as, the kernel size approaches the ring radius, and higher-order effects become important (i.e., contributions from the opposite side of the ring in the convolved width). Because it is intrinsically built of point sources that are *not* confined to a δ-function in radius, the DIFMAP image does not follow this simple prediction for the increase in width with blurring kernel size, and it instead increases more rapidly to converge with the RML result at $\alpha \approx 20\ \mu$as. For the RML reconstructions (and for DIFMAP with $\alpha > 10\ \mu$as), the measured orientation angle is relatively unaffected by the Gaussian convolution.

Of all the parameters defined in Section 9.1, the fractional central brightness f_C between the average ring center brightness and the rim varies the most with resolution. In the absence of a restoring beam, both SMILI and DIFMAP produce rings with practically zero brightness in the ring center; as a result of this near-zero floor, f_C is extremely small ($f_C < 10^{-5}$). As convolution with a finite Gaussian kernel fills in the center of the ring, f_C increases rapidly with α, by several orders of magnitude, for these images. By contrast, because they include inverse-tapering of the data and a final blurring with a 5 μas Gaussian, the eht-imaging fiducial reconstructions always have non-zero central brightness. All three imaging methods give $f_C \approx 0.3$ for $\alpha = 20\ \mu$as. Because f_C is sensitive to resolution and imaging methodology, we can at only securely conclude that $f_C \lesssim 0.3$ for M87.

Appendix H
Image Dependence on the Assumed Total Compact Flux Density

While all three parameter surveys explored different choices of total compact flux density from 0.4 to 0.8 Jy, they were tested against simulated images that all had $F_{\rm cpct} = 0.6$. For M87, the true value of $F_{\rm cpct}$ is unknown, adding additional uncertainty that is not explored systematically in the parameter surveys or Top Sets. In Figure 36, we explore how the estimated ring parameters of M87 from reconstructed images depend upon the assumed total compact flux density. In this analysis, we fix all other imaging parameters to their fiducial values.

Not all values of $F_{\rm cpct}$ produce acceptable images, with two primary problems. First, a reconstructed image may not be in acceptable agreement with the underlying data. Second, a reconstructed image may have corresponding station gains from self-calibration that are significantly different than a priori expectations. The SMT and LMT gains are most sensitive to $F_{\rm cpct}$ because the SMT–LMT baseline is the only inter-site EHT baseline that weakly resolves M87. To define acceptable images in this test, we require two conditions to be satisfied (similar to the requirements for the Top Sets; Section 6.3.1). First, we require that $\chi^2_{\rm CP}, \chi^2_{\log\,\rm CA} < 2$ with no systematic uncertainty for eht-

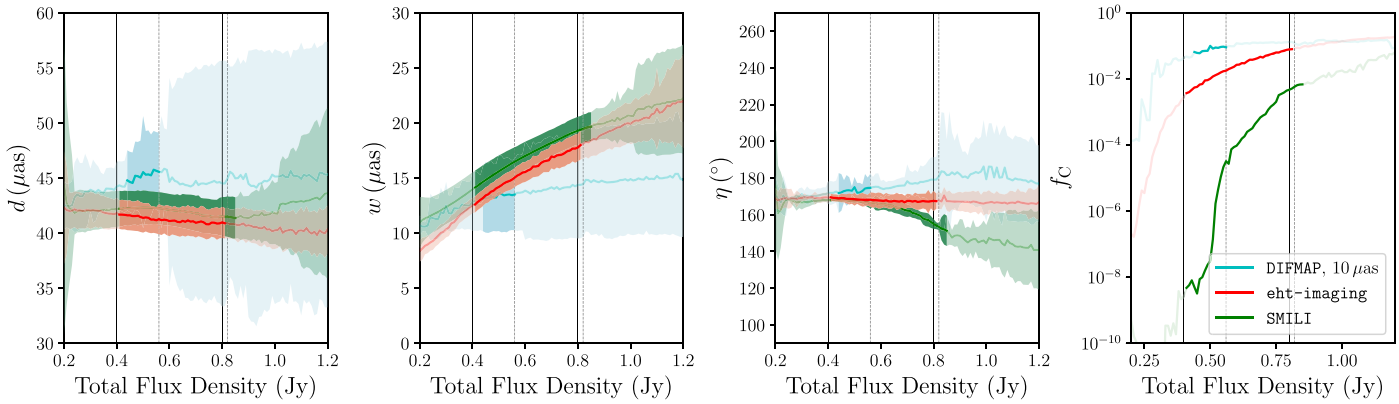

Figure 36. Measured diameter d, width w, orientation angle η, and central brightness ratio f_C of M87, measured from image reconstructions with varying total compact flux density, $F_{\rm cpct}$. All other imaging parameters were set to the fiducial parameters of the corresponding pipeline. DIFMAP values were measured after restoring with a 10 μas FWHM Gaussian beam. The solid lines indicate the measured value, and the shaded regions give the $\pm 1\sigma$ uncertainty as defined in Section 9.1 (these uncertainties do not include a contribution from scatter across the Top Set). The plotted values are dark in the range of $F_{\rm cpct}$ that produces images that have (1) $\chi^2_{\rm CP}$, $\chi^2_{\log {\rm CA}} < 2$ (with 5% systematic uncertainty for DIFMAP), and (2) a corresponding self-calibration solution with $0.9 \leqslant {\rm median}(1/|g_{\rm SMT}|) \leqslant 1.1$. The vertical dashed lines indicate the 0.56–0.82 Jy constraint on the total compact flux density from pre-imaging considerations (Section 4); the vertical solid lines indicate the 0.4–0.8 Jy range explored in the parameter surveys (Section 6).

imaging and SMILI and 5% systematic uncertainty for DIFMAP. Second, we require that the median SMT gain amplitude satisfies $0.9 \leqslant {\rm median}(1/|g_{\rm SMT}|) \leqslant 1.1$ (we only assess the images based upon $|g_{\rm SMT}|$ because the LMT a priori calibration is comparatively poor; see Appendix F). For eht-imaging and SMILI, the SMT gain constraint gives $0.40\,{\rm Jy} \leqslant F_{\rm cpct} \leqslant 0.81\,{\rm Jy}$ and $0.40\,{\rm Jy} \leqslant F_{\rm cpct} \leqslant 0.85\,{\rm Jy}$, respectively; all reconstructions across these ranges satisfy the χ^2 criterion. For DIFMAP, the SMT gain constraint gives $0.43\,{\rm Jy} \leqslant F_{\rm cpct} \leqslant 0.91\,{\rm Jy}$; however, only images with $0.18\,{\rm Jy} \leqslant F_{\rm cpct} \leqslant 0.56\,{\rm Jy}$ satisfy the χ^2 criterion. Thus, for DIFMAP, the range of images meeting both criteria is $0.43\,{\rm Jy} \leqslant F_{\rm cpct} \leqslant 0.56\,{\rm Jy}$. For all pipelines, the acceptable range of $F_{\rm cpct}$ extends lower than that derived in Section 4 because we do not strictly enforce $1/|g_{\rm SMT}| \geqslant 1$, instead enforcing the weaker constraint that the ${\rm median}(1/|g_{\rm SMT}|) \geqslant 0.9$.

For DIFMAP, the ring diameter is relatively insensitive to $F_{\rm cpct}$, although the azimuthal variations σ_d increase significantly for $F_{\rm cpct} \gtrsim 0.55$. For eht-imaging and SMILI, larger values of $F_{\rm cpct}$ lead to broader rings with slightly lower diameters, as expected from the finite resolution bias discussed in Appendix G. Across the range of $F_{\rm cpct}$ identified in Appendix B, the most significant variations are in the orientation angle η estimated with the SMILI pipeline, and in the central brightness ratio f_C, which increases steeply with $F_{\rm cpct}$ for all pipelines.

Appendix I
Image Radial and Azimuthal Profiles

In this section, we present additional radial and azimuthal profiles of the fiducial M87 images. These profiles use the ring centroids determined in Section 9.

Figure 37 shows radial profiles taken across the rings identified in the three April 11 fiducial images, with the DIFMAP image restored by the nominal 20 μas beam. For each image, we identified the orientation angle η, then divided the ring in two by the line perpendicular to the measured orientation angle. On each half-ring, we compute the median angular profile (solid lines in Figure 37), as well as the 25%–75% and 0%–100% percentile ranges of variation. Figure 37 shows that the peak-to-peak ring diameters measured from the three imaging methods are broadly consistent, as indicated by our measurements in Figure 25. The overall sense of ring asymmetry recovered from each imaging pipeline is also consistent; the ring is always brighter in the south.

However, the shape of the median radial profiles differ among the different imaging methods due to the different assumptions made in the imaging process. The DIFMAP reconstructions in Figure 37 are restored with a 20 μas beam, so they produce wider, shallower radial profiles. In contrast, the SMILI images tend to zero out low brightness regions, and the fiducial images have a near-zero brightness depression in the center of the ring. The eht-imaging results are of a higher resolution than the DIFMAP results, but they have a less dramatic brightness depression that the SMILI images as a result of the choice to include a 5 μas maximum resolution in the eht-imaging script and the use of entropy regularization.

Figure 38 shows the angular profiles along the ring from the three imaging pipelines on April 11 data. While Figure 37 showed variability in the radial profiles from the individual fiducial images, Figure 38 considers variability in the azimuthal structure across the entire Top Set of images. In each panel, the solid line represents the fiducial value of the angular profile, and the bands show variability across the entire Top Set.

The DIFMAP angular profile in Figure 38 is smooth and shallow, and it is distinct from those of the RML methods due to its 20 μas restoring beam. The dashed lines in the eht-imaging and SMILI panels show the angular profiles from the fiducial image blurred to match the DIFMAP resolution. When blurred, the angular profiles from the eht-imaging and SMILI images better match the broad DIFMAP profile, but they still differ in the measured orientation angle and the position of the brightest location on the ring.

The angular profiles for the unblurred eht-imaging and SMILI reconstructions are similar, with the 0.1 Jy difference in total flux density in these reconstructions manifesting in an overall lower profile for the SMILI reconstruction. The "knot" features in the eht-imaging and SMILI reconstructions show significant variation across the Top Sets. This suggests that these ring features are highly sensitive to imaging parameter choices, and that they are potentially artifacts of the limited (u, v) coverage. In general, the azimuthal structure

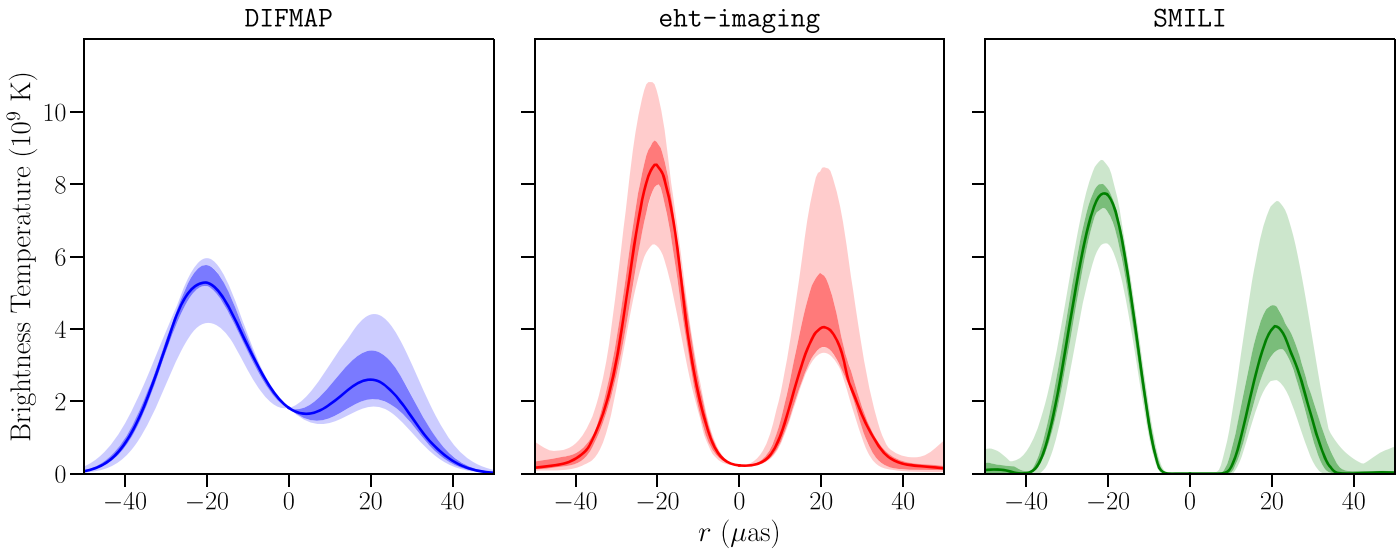

Figure 37. 1D radial brightness profiles of the three fiducial M87 images on April 11. For each image, radial profiles in the semi-circle centered on η are plotted with negative values of r, and radial profiles through the opposing semi-circle centered on $\eta + 180°$ are plotted with positive r. The solid curves show the median profile over the corresponding semi-circle, the darker band shows the 25th to 75th percentile range, and the lighter band shows the full range of profiles in the fiducial images.

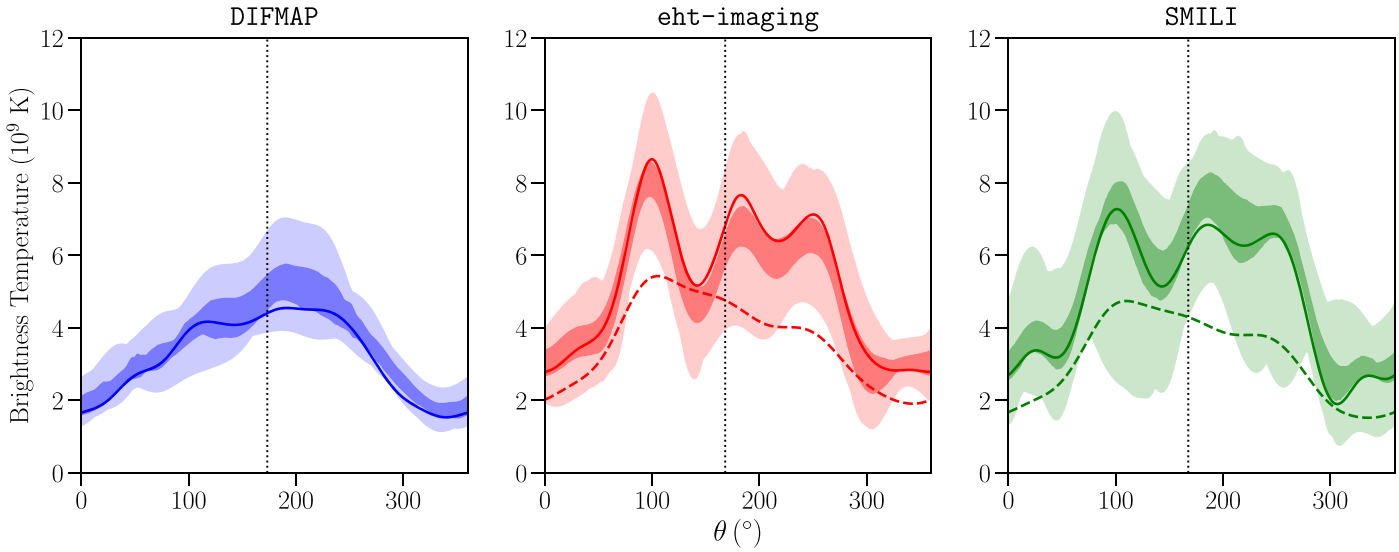

Figure 38. 1D angular profiles of M87 on April 11 from the three imaging methods. For each method, the solid line shows the angular profile obtained from the fiducial image, the darker band shows the 25th to 75th percentile range across the Top Set, and the lighter band shows the full Top Set range. For the RML methods, the dashed line shows the angular profile from the fiducial image blurred to the resolution of the `DIFMAP` image. The "knot" features in the unblurred `eht-imaging` and `SMILI` reconstructions show significant variation across the Top Set, suggesting that these features are sensitive to imaging parameter choices.

in the reconstructed images from all three imaging pipelines is more variable than the radial structure, making measurements of the orientation angle intrinsically more uncertain than measurements of the ring diameter.

ORCID iDs

Kazunori Akiyama https://orcid.org/0000-0002-9475-4254
Antxon Alberdi https://orcid.org/0000-0002-9371-1033
Rebecca Azulay https://orcid.org/0000-0002-2200-5393
Anne-Kathrin Baczko https://orcid.org/0000-0003-3090-3975
Mislav Baloković https://orcid.org/0000-0003-0476-6647
John Barrett https://orcid.org/0000-0002-9290-0764
Lindy Blackburn https://orcid.org/0000-0002-9030-642X
Katherine L. Bouman https://orcid.org/0000-0003-0077-4367
Geoffrey C. Bower https://orcid.org/0000-0003-4056-9982
Christiaan D. Brinkerink https://orcid.org/0000-0002-2322-0749
Roger Brissenden https://orcid.org/0000-0002-2556-0894
Silke Britzen https://orcid.org/0000-0001-9240-6734
Avery E. Broderick https://orcid.org/0000-0002-3351-760X
Do-Young Byun https://orcid.org/0000-0003-1157-4109
Andrew Chael https://orcid.org/0000-0003-2966-6220
Chi-kwan Chan https://orcid.org/0000-0001-6337-6126
Shami Chatterjee https://orcid.org/0000-0002-2878-1502

Ilje Cho https://orcid.org/0000-0001-6083-7521
Pierre Christian https://orcid.org/0000-0001-6820-9941
John E. Conway https://orcid.org/0000-0003-2448-9181
Geoffrey B. Crew https://orcid.org/0000-0002-2079-3189
Yuzhu Cui https://orcid.org/0000-0001-6311-4345
Jordy Davelaar https://orcid.org/0000-0002-2685-2434
Mariafelicia De Laurentis https://orcid.org/0000-0002-9945-682X
Roger Deane https://orcid.org/0000-0003-1027-5043
Jessica Dempsey https://orcid.org/0000-0003-1269-9667
Gregory Desvignes https://orcid.org/0000-0003-3922-4055
Jason Dexter https://orcid.org/0000-0003-3903-0373
Sheperd S. Doeleman https://orcid.org/0000-0002-9031-0904
Ralph P. Eatough https://orcid.org/0000-0001-6196-4135
Heino Falcke https://orcid.org/0000-0002-2526-6724
Vincent L. Fish https://orcid.org/0000-0002-7128-9345
Raquel Fraga-Encinas https://orcid.org/0000-0002-5222-1361
José L. Gómez https://orcid.org/0000-0003-4190-7613
Peter Galison https://orcid.org/0000-0002-6429-3872
Charles F. Gammie https://orcid.org/0000-0001-7451-8935
Boris Georgiev https://orcid.org/0000-0002-3586-6424
Roman Gold https://orcid.org/0000-0003-2492-1966
Minfeng Gu (顾敏峰) https://orcid.org/0000-0002-4455-6946
Mark Gurwell https://orcid.org/0000-0003-0685-3621
Kazuhiro Hada https://orcid.org/0000-0001-6906-772X
Ronald Hesper https://orcid.org/0000-0003-1918-6098
Luis C. Ho (何子山) https://orcid.org/0000-0001-6947-5846
Mareki Honma https://orcid.org/0000-0003-4058-9000
Chih-Wei L. Huang https://orcid.org/0000-0001-5641-3953
Shiro Ikeda https://orcid.org/0000-0002-2462-1448
Sara Issaoun https://orcid.org/0000-0002-5297-921X
David J. James https://orcid.org/0000-0001-5160-4486
Michael Janssen https://orcid.org/0000-0001-8685-6544
Britton Jeter https://orcid.org/0000-0003-2847-1712
Wu Jiang (江悟) https://orcid.org/0000-0001-7369-3539
Michael D. Johnson https://orcid.org/0000-0002-4120-3029
Svetlana Jorstad https://orcid.org/0000-0001-6158-1708
Taehyun Jung https://orcid.org/0000-0001-7003-8643
Mansour Karami https://orcid.org/0000-0001-7387-9333
Ramesh Karuppusamy https://orcid.org/0000-0002-5307-2919
Tomohisa Kawashima https://orcid.org/0000-0001-8527-0496
Garrett K. Keating https://orcid.org/0000-0002-3490-146X
Mark Kettenis https://orcid.org/0000-0002-6156-5617
Jae-Young Kim https://orcid.org/0000-0001-8229-7183
Junhan Kim https://orcid.org/0000-0002-4274-9373
Motoki Kino https://orcid.org/0000-0002-2709-7338
Jun Yi Koay https://orcid.org/0000-0002-7029-6658
Patrick M. Koch https://orcid.org/0000-0003-2777-5861
Shoko Koyama https://orcid.org/0000-0002-3723-3372
Michael Kramer https://orcid.org/0000-0002-4175-2271
Carsten Kramer https://orcid.org/0000-0002-4908-4925
Thomas P. Krichbaum https://orcid.org/0000-0002-4892-9586
Tod R. Lauer https://orcid.org/0000-0003-3234-7247
Sang-Sung Lee https://orcid.org/0000-0002-6269-594X
Yan-Rong Li (李彦荣) https://orcid.org/0000-0001-5841-9179
Zhiyuan Li (李志远) https://orcid.org/0000-0003-0355-6437
Michael Lindqvist https://orcid.org/0000-0002-3669-0715
Kuo Liu https://orcid.org/0000-0002-2953-7376
Elisabetta Liuzzo https://orcid.org/0000-0003-0995-5201
Laurent Loinard https://orcid.org/0000-0002-5635-3345
Ru-Sen Lu (路如森) https://orcid.org/0000-0002-7692-7967
Nicholas R. MacDonald https://orcid.org/0000-0002-6684-8691
Jirong Mao (毛基荣) https://orcid.org/0000-0002-7077-7195
Sera Markoff https://orcid.org/0000-0001-9564-0876
Daniel P. Marrone https://orcid.org/0000-0002-2367-1080
Alan P. Marscher https://orcid.org/0000-0001-7396-3332
Iván Martí-Vidal https://orcid.org/0000-0003-3708-9611
Lynn D. Matthews https://orcid.org/0000-0002-3728-8082
Lia Medeiros https://orcid.org/0000-0003-2342-6728
Karl M. Menten https://orcid.org/0000-0001-6459-0669
Yosuke Mizuno https://orcid.org/0000-0002-8131-6730
Izumi Mizuno https://orcid.org/0000-0002-7210-6264
James M. Moran https://orcid.org/0000-0002-3882-4414
Kotaro Moriyama https://orcid.org/0000-0003-1364-3761
Monika Moscibrodzka https://orcid.org/0000-0002-4661-6332
Cornelia Müller https://orcid.org/0000-0002-2739-2994
Hiroshi Nagai https://orcid.org/0000-0003-0292-3645
Neil M. Nagar https://orcid.org/0000-0001-6920-662X
Masanori Nakamura https://orcid.org/0000-0001-6081-2420
Ramesh Narayan https://orcid.org/0000-0002-1919-2730
Iniyan Natarajan https://orcid.org/0000-0001-8242-4373
Chunchong Ni https://orcid.org/0000-0003-1361-5699
Aristeidis Noutsos https://orcid.org/0000-0002-4151-3860
Héctor Olivares https://orcid.org/0000-0001-6833-7580
Daniel C. M. Palumbo https://orcid.org/0000-0002-7179-3816
Ue-Li Pen https://orcid.org/0000-0003-2155-9578
Dominic W. Pesce https://orcid.org/0000-0002-5278-9221
Oliver Porth https://orcid.org/0000-0002-4584-2557
Ben Prather https://orcid.org/0000-0002-0393-7734
Jorge A. Preciado-López https://orcid.org/0000-0002-4146-0113
Hung-Yi Pu https://orcid.org/0000-0001-9270-8812
Venkatessh Ramakrishnan https://orcid.org/0000-0002-9248-086X
Ramprasad Rao https://orcid.org/0000-0002-1407-7944
Alexander W. Raymond https://orcid.org/0000-0002-5779-4767
Bart Ripperda https://orcid.org/0000-0002-7301-3908
Freek Roelofs https://orcid.org/0000-0001-5461-3687
Eduardo Ros https://orcid.org/0000-0001-9503-4892
Mel Rose https://orcid.org/0000-0002-2016-8746
Alan L. Roy https://orcid.org/0000-0002-1931-0135
Chet Ruszczyk https://orcid.org/0000-0001-7278-9707
Benjamin R. Ryan https://orcid.org/0000-0001-8939-4461
Kazi L. J. Rygl https://orcid.org/0000-0003-4146-9043
David Sánchez-Arguelles https://orcid.org/0000-0002-7344-9920
Mahito Sasada https://orcid.org/0000-0001-5946-9960
Tuomas Savolainen https://orcid.org/0000-0001-6214-1085
Lijing Shao https://orcid.org/0000-0002-1334-8853
Zhiqiang Shen (沈志强) https://orcid.org/0000-0003-3540-8746
Des Small https://orcid.org/0000-0003-3723-5404
Bong Won Sohn https://orcid.org/0000-0002-4148-8378
Jason SooHoo https://orcid.org/0000-0003-1938-0720

Fumie Tazaki https://orcid.org/0000-0003-0236-0600
Paul Tiede https://orcid.org/0000-0003-3826-5648
Remo P. J. Tilanus https://orcid.org/0000-0002-6514-553X
Michael Titus https://orcid.org/0000-0002-3423-4505
Kenji Toma https://orcid.org/0000-0002-7114-6010
Pablo Torne https://orcid.org/0000-0001-8700-6058
Sascha Trippe https://orcid.org/0000-0003-0465-1559
Ilse van Bemmel https://orcid.org/0000-0001-5473-2950
Huib Jan van Langevelde https://orcid.org/0000-0002-0230-5946
Daniel R. van Rossum https://orcid.org/0000-0001-7772-6131
John Wardle https://orcid.org/0000-0002-8960-2942
Jonathan Weintroub https://orcid.org/0000-0002-4603-5204
Norbert Wex https://orcid.org/0000-0003-4058-2837
Robert Wharton https://orcid.org/0000-0002-7416-5209
Maciek Wielgus https://orcid.org/0000-0002-8635-4242
George N. Wong https://orcid.org/0000-0001-6952-2147
Qingwen Wu (吴庆文) https://orcid.org/0000-0003-4773-4987
André Young https://orcid.org/0000-0003-0000-2682
Ken Young https://orcid.org/0000-0002-3666-4920
Ziri Younsi https://orcid.org/0000-0001-9283-1191
Feng Yuan (袁峰) https://orcid.org/0000-0003-3564-6437
J. Anton Zensus https://orcid.org/0000-0001-7470-3321
Guangyao Zhao https://orcid.org/0000-0002-4417-1659
Shan-Shan Zhao https://orcid.org/0000-0002-9774-3606
Joseph R. Farah https://orcid.org/0000-0003-4914-5625
Daniel Michalik https://orcid.org/0000-0002-7618-6556
Andrew Nadolski https://orcid.org/0000-0001-9479-9957
Rurik A. Primiani https://orcid.org/0000-0003-3910-7529
Paul Yamaguchi https://orcid.org/0000-0002-6017-8199

References

Abramowitz, M., & Stegun, I. A. 1972, Handbook of Mathematical Functions
Akiyama, K., Ikeda, S., Pleau, M., et al. 2017a, AJ, 153, 159
Akiyama, K., Kuramochi, K., Ikeda, S., et al. 2017b, ApJ, 838, 1
Akiyama, K., Lu, R.-S., Fish, V. L., et al. 2015, ApJ, 807, 150
Akiyama, K., Tazaki, F., Moriyama, K., et al. 2019, SMILI: Sparse Modeling Imaging Library for Interferometry, Zenodo, doi:10.5281/zenodo.2616725
An, T., Sohn, B. W., & Imai, H. 2018, NatAs, 2, 118
Asada, K., & Nakamura, M. 2012, ApJL, 745, L28
Asada, K., Nakamura, M., Doi, A., Nagai, H., & Inoue, M. 2014, ApJL, 781, L2
Asada, K., Nakamura, M., & Pu, H.-Y. 2016, ApJ, 833, 56
Bardeen, J. M. 1973, in Black Holes (Les Astres Occlus), ed. C. DeWitt & B. S. DeWitt (New York: Gordon and Breach), 215
Baron, F., Monnier, J. D., & Kloppenborg, B. 2010, Proc. SPIE, 7734, 77342I
Bird, S., Harris, W. E., Blakeslee, J. P., & Flynn, C. 2010, A&A, 524, A71
Biretta, J. A., Sparks, W. B., & Macchetto, F. 1999, ApJ, 520, 621
Blackburn, L., Chan, C-K., Crew, G. B., et al. 2019, arXiv:1903.08832
Blakeslee, J. P., Jordán, A., Mei, S., et al. 2009, ApJ, 694, 556
Blecher, T., Deane, R., Bernardi, G., & Smirnov, O. 2017, MNRAS, 464, 143
Bouman, K. L. 2017, PhD thesis, Massachusetts Institute of Technology
Bouman, K. L., Johnson, M. D., Dalca, A. V., et al. 2018, IEEE Transactions on Computational Imaging, 4, 512
Bouman, K. L., Johnson, M. D., Zoran, D., et al. 2016, in The IEEE Conf. Computer Vision and Pattern Recognition (New York: IEEE), 913
Briggs, D. S. 1995, BAAS, 27, 1444
Britzen, S., Fendt, C., Eckart, A., & Karas, V. 2017, A&A, 601, A52
Buscher, D. F. 1994, in IAU Symp. 158, Very High Angular Resolution Imaging, ed. J. G. Robertson & W. J. Tango (Dordrecht: Kluwer), 91
Cantiello, M., Blakeslee, J. P., Ferrarese, L., et al. 2018, ApJ, 856, 126
Chael, A., Bouman, K., Johnson, M., et al. 2019, eht-imaging: v1.1.0: Imaging interferometric data with regularized maximum likelihood, Zenodo, doi:10.5281/zenodo.2614016
Chael, A. A., Johnson, M. D., Bouman, K. L., et al. 2018, ApJ, 857, 23
Chael, A. A., Johnson, M. D., Narayan, R., et al. 2016, ApJ, 829, 11
Clark, B. G. 1980, A&A, 89, 377
Cornwell, T., Braun, R., & Briggs, D. S. 1999, in ASP Conf. Ser. 180, Synthesis Imaging in Radio Astronomy II, ed. G. B. Taylor, C. L. Carilli, & R. A. Perley (San Francisco, CA: ASP), 151
Cornwell, T., & Fomalont, E. B. 1999, in ASP Conf. Ser. 180, Synthesis Imaging in Radio Astronomy II, ed. G. B. Taylor, C. L. Carilli, & R. A. Perley (San Francisco, CA: ASP), 187
Cornwell, T. J. 2008, ISTSP, 2, 793
Cornwell, T. J., & Evans, K. F. 1985, A&A, 143, 77
Cornwell, T. J., & Wilkinson, P. N. 1981, MNRAS, 196, 1067
Curtis, H. D. 1918, PLicO, 13, 9
Dodson, R., Edwards, P. G., & Hirabayashi, H. 2006, PASJ, 58, 243
Doeleman, S. S., Fish, V. L., Schenck, D. E., et al. 2012, Sci, 338, 355
EHT Collaboration et al. 2019a, ApJL, 875, L1 (Paper I)
EHT Collaboration et al. 2019b, ApJL, 875, L2 (Paper II)
EHT Collaboration et al. 2019c, ApJL, 875, L3 (Paper III)
EHT Collaboration et al. 2019d, ApJL, 875, L5 (Paper V)
EHT Collaboration et al. 2019e, ApJL, 875, L6 (Paper VI)
Falcke, H., Melia, F., & Agol, E. 2000, ApJL, 528, L13
Frieden, B. R. 1972, JOSA, 62, 511
Gebhardt, K., Adams, J., Richstone, D., et al. 2011, ApJ, 729, 119
Gebhardt, K., & Thomas, J. 2009, ApJ, 700, 1690
Goddi, C., Marti-Vidal, I., Messias, H., et al. 2019, PASP, in press
Gull, S. F., & Daniell, G. J. 1978, Natur, 272, 686
Hada, K., Doi, A., Kino, M., et al. 2011, Natur, 477, 185
Hada, K., Kino, M., Doi, A., et al. 2013, ApJ, 775, 70
Hada, K., Kino, M., Doi, A., et al. 2016, ApJ, 817, 131
Hada, K., Park, J. H., Kino, M., et al. 2017, PASJ, 69, 71
Högbom, J. A. 1974, A&AS, 15, 417
Honma, M., Akiyama, K., Uemura, M., & Ikeda, S. 2014, PASJ, 66, 95
Hovatta, T., Aller, M. F., Aller, H. D., et al. 2014, AJ, 147, 143
Ikeda, S., Tazaki, F., Akiyama, K., Hada, K., & Honma, M. 2016, PASJ, 68, 45
Janssen, M., Goddi, C., van Bemmel, I. M., et al. 2019, arXiv:1902.01749
Jennison, R. C. 1958, MNRAS, 118, 276
Johannsen, T., Broderick, A. E., Plewa, P. M., et al. 2016, PhRvL, 116, 031101
Johannsen, T., & Psaltis, D. 2010, ApJ, 718, 446
Johnson, M. D., Bouman, K. L., Blackburn, L., et al. 2017, ApJ, 850, 172
Johnson, M. D., Fish, V. L., Doeleman, S. S., et al. 2015, Sci, 350, 1242
Johnson, M. D., Narayan, R., Psaltis, D., et al. 2018, ApJ, 865, 104
Jorstad, S. G., Marscher, A. P., Morozova, D. A., et al. 2017, ApJ, 846, 98
Kim, J.-Y., Krichbaum, T. P., Lu, R.-S., et al. 2018a, A&A, 616, A188
Kim, J.-Y., Lee, S.-S., Hodgson, J. A., et al. 2018b, A&A, 610, L5
Kovalev, Y. Y., Lister, M. L., Homan, D. C., & Kellermann, K. I. 2007, ApJL, 668, L27
Kuramochi, K., Akiyama, K., Ikeda, S., et al. 2018, ApJ, 858, 56
Lawson, P. R., Cotton, W. D., Hummel, C. A., et al. 2004, Proc. SPIE, 5491, 886
Lee, S.-S., Wajima, K., Algaba, J.-C., et al. 2016, ApJS, 227, 8
Lister, M. L., Aller, M. F., Aller, H. D., et al. 2016, AJ, 152, 12
Luminet, J.-P. 1979, A&A, 75, 228
Macchetto, F., Marconi, A., Axon, D. J., et al. 1997, ApJ, 489, 579
Marshall, H. L., Miller, B. P., Davis, D. S., et al. 2002, ApJ, 564, 683
Martí-Vidal, I., Vlemmings, W. H. T., & Muller, S. 2016, A&A, 593, A61
Matthews, L. D., Crew, G. B., Doeleman, S. S., et al. 2018, PASP, 130, 015002
Mertens, F., Lobanov, A. P., Walker, R. C., & Hardee, P. E. 2016, A&A, 595, A54
Nakamura, M., & Asada, K. 2013, ApJ, 775, 118
Nakamura, M., Asada, K., Hada, K., et al. 2018, ApJ, 868, 146
Narayan, R., & Nityananda, R. 1986, ARA&A, 24, 127
Noordam, J. E., & Smirnov, O. M. 2010, A&A, 524, A61
Offringa, A. R., McKinley, B., Hurley-Walker, N., et al. 2014, MNRAS, 444, 606
Owen, F. N., Hardee, P. E., & Cornwell, T. J. 1989, ApJ, 340, 698
Pardo, J. R., Cernicharo, J., & Serabyn, E. 2001, ITAP, 49, 1683
Pearson, T. J., & Readhead, A. C. S. 1984, ARA&A, 22, 97
Perlman, E. S., Biretta, J. A., Zhou, F., Sparks, W. B., & Macchetto, F. D. 1999, AJ, 117, 2185
Readhead, A. C. S., Walker, R. C., Pearson, T. J., & Cohen, M. H. 1980, Natur, 285, 137
Reid, M. J., Biretta, J. A., Junor, W., Muxlow, T. W. B., & Spencer, R. E. 1989, ApJ, 336, 112
Roberts, D. H., Wardle, J. F. C., & Brown, L. F. 1994, ApJ, 427, 718
Rogers, A. E. E., Doeleman, S. S., & Moran, J. M. 1995, AJ, 109, 1391
Rybicki, G. B., & Lightman, A. P. 1979, Radiative Processes in Astrophysics (New York: Wiley)
Schwab, F. R. 1984, AJ, 89, 1076
Schwarz, U. J. 1978, A&A, 65, 345

Shepherd, M. 2011, Difmap: Synthesis Imaging of Visibility Data, Astrophysics Source Code Library, ascl:1103.001
Shepherd, M. C. 1997, in ASP Conf. Ser. 125, Astronomical Data Analysis Software and Systems VI, ed. G. Hunt & H. Payne (San Francisco, CA: ASP), 77
Sparks, W. B., Biretta, J. A., & Macchetto, F. 1996, ApJ, 473, 254
Thiébaut, É. 2013, in New Concepts in Imaging: Optical and Statistical Models, EAS Publications Ser. 59, ed. D. Mary, C. Theys, & C. Aime (Les Ulis: EDP Sciences), 157
Thompson, A. R., Moran, J. M., & Swenson, G. W., Jr. 2017, Interferometry and Synthesis in Radio Astronomy (3rd ed.; Hoboken, NJ: Wiley)
Twiss, R. Q., Carter, A. W. L., & Little, A. G. 1960, Obs, 80, 153
van Cittert, P. H. 1934, Phy, 1, 201
Wajima, K., Hagiwara, Y., An, T., et al. 2016, in Proc. Workshop Frontiers in Radio Astronomy and FAST Early Sciences Symposium 2015, ed. L. Qain & D. Li (San Francisco, CA: ASP), 81
Walker, R. C., Hardee, P. E., Davies, F. B., Ly, C., & Junor, W. 2018, ApJ, 855, 128
Walsh, J. L., Barth, A. J., Ho, L. C., & Sarzi, M. 2013, ApJ, 770, 86
Wiaux, Y., Jacques, L., Puy, G., Scaife, A. M. M., & Vandergheynst, P. 2009a, MNRAS, 395, 1733
Wiaux, Y., Puy, G., Boursier, Y., & Vandergheynst, P. 2009b, MNRAS, 400, 1029
Wilkinson, P. N., Readhead, A. C. S., Purcell, G. H., & Anderson, B. 1977, Natur, 269, 764
Thiébaut, É., & Young, J. 2017, JOSAA, 34, 904
Zernike, F. 1938, Phy, 785, 5

The Event Horizon Telescope Collaboration

Kazunori Akiyama[1,2,3,4], Antxon Alberdi[5], Walter Alef[6], Keiichi Asada[7], Rebecca Azulay[8,9,6], Anne-Kathrin Baczko[6], David Ball[10], Mislav Baloković[4,11], John Barrett[2], Dan Bintley[12], Lindy Blackburn[4,11], Wilfred Boland[13], Katherine L. Bouman[4,11,14], Geoffrey C. Bower[15], Michael Bremer[16], Christiaan D. Brinkerink[17], Roger Brissenden[4,11], Silke Britzen[6], Avery E. Broderick[18,19,20], Dominique Broguiere[16], Thomas Bronzwaer[17], Do-Young Byun[21,22], John E. Carlstrom[23,24,25,26], Andrew Chael[4,11], Chi-kwan Chan[10,27], Shami Chatterjee[28], Koushik Chatterjee[29], Ming-Tang Chen[15], Yongjun Chen (陈永军)[30,31], Ilje Cho[21,22], Pierre Christian[10,11], John E. Conway[32], James M. Cordes[28], Geoffrey B. Crew[2], Yuzhu Cui[33,34], Jordy Davelaar[17], Mariafelicia De Laurentis[35,36,37], Roger Deane[38,39], Jessica Dempsey[12], Gregory Desvignes[6], Jason Dexter[40], Sheperd S. Doeleman[4,11], Ralph P. Eatough[6], Heino Falcke[17], Vincent L. Fish[2], Ed Fomalont[1], Raquel Fraga-Encinas[17], William T. Freeman[41,42], Per Friberg[12], Christian M. Fromm[36], José L. Gómez[5], Peter Galison[4,43,44], Charles F. Gammie[45,46], Roberto García[16], Olivier Gentaz[16], Boris Georgiev[19,20], Ciriaco Goddi[17,47], Roman Gold[36], Minfeng Gu (顾敏峰)[30,48], Mark Gurwell[11], Kazuhiro Hada[33,34], Michael H. Hecht[2], Ronald Hesper[49], Luis C. Ho (何子山)[50,51], Paul Ho[7], Mareki Honma[33,34], Chih-Wei L. Huang[7], Lei Huang (黄磊)[30,48], David H. Hughes[52], Shiro Ikeda[3,53,54,55], Makoto Inoue[7], Sara Issaoun[17], David J. James[4,11], Buell T. Jannuzi[10], Michael Janssen[17], Britton Jeter[19,20], Wu Jiang (江悟)[30], Michael D. Johnson[4,11], Svetlana Jorstad[56,57], Taehyun Jung[21,22], Mansour Karami[18,19], Ramesh Karuppusamy[6], Tomohisa Kawashima[3], Garrett K. Keating[11], Mark Kettenis[58], Jae-Young Kim[6], Junhan Kim[10], Jongsoo Kim[21], Motoki Kino[3,59], Jun Yi Koay[7], Patrick M. Koch[7], Shoko Koyama[7], Michael Kramer[6], Carsten Kramer[16], Thomas P. Krichbaum[6], Cheng-Yu Kuo[60], Tod R. Lauer[61], Sang-Sung Lee[21], Yan-Rong Li (李彦荣)[62], Zhiyuan Li (李志远)[63,64], Michael Lindqvist[32], Kuo Liu[6], Elisabetta Liuzzo[65], Wen-Ping Lo[7,66], Andrei P. Lobanov[6], Laurent Loinard[67,68], Colin Lonsdale[2], Ru-Sen Lu (路如森)[30,6], Nicholas R. MacDonald[6], Jirong Mao (毛基荣)[69,70,71], Sera Markoff[29,72], Daniel P. Marrone[10], Alan P. Marscher[56], Iván Martí-Vidal[32,73], Satoki Matsushita[7], Lynn D. Matthews[2], Lia Medeiros[10,74], Karl M. Menten[6], Yosuke Mizuno[36], Izumi Mizuno[12], James M. Moran[4,11], Kotaro Moriyama[33,2], Monika Moscibrodzka[17], Cornelia Müller[6,17], Hiroshi Nagai[3,34], Neil M. Nagar[75], Masanori Nakamura[7], Ramesh Narayan[4,11], Gopal Narayanan[76], Iniyan Natarajan[39], Roberto Neri[16], Chunchong Ni[19,20], Aristeidis Noutsos[6], Hiroki Okino[33,77], Héctor Olivares[36], Tomoaki Oyama[33], Feryal Özel[10], Daniel C. M. Palumbo[4,11], Nimesh Patel[11], Ue-Li Pen[18,78,79,80], Dominic W. Pesce[4,11], Vincent Piétu[16], Richard Plambeck[81], Aleksandar PopStefanija[76], Oliver Porth[36,29], Ben Prather[45], Jorge A. Preciado-López[18], Dimitrios Psaltis[10], Hung-Yi Pu[18], Venkatessh Ramakrishnan[75], Ramprasad Rao[15], Mark G. Rawlings[12], Alexander W. Raymond[4,11], Luciano Rezzolla[36], Bart Ripperda[36], Freek Roelofs[17], Alan Rogers[2], Eduardo Ros[6], Mel Rose[10], Arash Roshanineshat[10], Helge Rottmann[6], Alan L. Roy[6], Chet Ruszczyk[2], Benjamin R. Ryan[82,83], Kazi L. J. Rygl[65], Salvador Sánchez[84], David Sánchez-Arguelles[52,85], Mahito Sasada[33,86], Tuomas Savolainen[6,87,88], F. Peter Schloerb[76], Karl-Friedrich Schuster[16], Lijing Shao[6,51], Zhiqiang Shen (沈志强)[29,30], Des Small[58], Bong Won Sohn[21,22,89], Jason SooHoo[2], Fumie Tazaki[33], Paul Tiede[18,19,20], Remo P. J. Tilanus[17,47,90], Michael Titus[2], Kenji Toma[91,92], Pablo Torne[6,84], Tyler Trent[10], Sascha Trippe[93], Shuichiro Tsuda[33], Ilse van Bemmel[58], Huib Jan van Langevelde[58,94], Daniel R. van Rossum[17], Jan Wagner[6], John Wardle[95], Jonathan Weintroub[4,11], Norbert Wex[6], Robert Wharton[6], Maciek Wielgus[4,11], George N. Wong[45], Qingwen Wu (吴庆文)[96], André Young[17], Ken Young[11], Ziri Younsi[97,36], Feng Yuan (袁峰)[30,48,98], Ye-Fei Yuan (袁业飞)[99], J. Anton Zensus[6], Guangyao Zhao[21], Shan-Shan Zhao[17,63], Ziyan Zhu[44], Joseph R. Farah[11,100,4], Zheng Meyer-Zhao[7,101], Daniel Michalik[102,103], Andrew Nadolski[46], Hiroaki Nishioka[7], Nicolas Pradel[7], Rurik A. Primiani[104], Kamal Souccar[76], Laura Vertatschitsch[11,104], and Paul Yamaguchi[11]

[1] National Radio Astronomy Observatory, 520 Edgemont Rd, Charlottesville, VA 22903, USA
[2] Massachusetts Institute of Technology Haystack Observatory, 99 Millstone Road, Westford, MA 01886, USA
[3] National Astronomical Observatory of Japan, 2-21-1 Osawa, Mitaka, Tokyo 181-8588, Japan
[4] Black Hole Initiative at Harvard University, 20 Garden Street, Cambridge, MA 02138, USA
[5] Instituto de Astrofísica de Andalucía–CSIC, Glorieta de la Astronomía s/n, E-18008 Granada, Spain
[6] Max-Planck-Institut für Radioastronomie, Auf dem Hügel 69, D-53121 Bonn, Germany
[7] Institute of Astronomy and Astrophysics, Academia Sinica, 11F of Astronomy-Mathematics Building, AS/NTU No. 1, Sec. 4, Roosevelt Rd, Taipei 10617, Taiwan, R.O.C.
[8] Departament d'Astronomia i Astrofísica, Universitat de València, C. Dr. Moliner 50, E-46100 Burjassot, València, Spain
[9] Observatori Astronòmic, Universitat de València, C. Catedrático José Beltrán 2, E-46980 Paterna, València, Spain
[10] Steward Observatory and Department of Astronomy, University of Arizona, 933 N. Cherry Ave., Tucson, AZ 85721, USA
[11] Center for Astrophysics | Harvard & Smithsonian, 60 Garden Street, Cambridge, MA 02138, USA
[12] East Asian Observatory, 660 N. A'ohoku Pl., Hilo, HI 96720, USA
[13] Nederlandse Onderzoekschool voor Astronomie (NOVA), PO Box 9513, 2300 RA Leiden, The Netherlands
[14] California Institute of Technology, 1200 East California Boulevard, Pasadena, CA 91125, USA
[15] Institute of Astronomy and Astrophysics, Academia Sinica, 645 N. A'ohoku Place, Hilo, HI 96720, USA
[16] Institut de Radioastronomie Millimétrique, 300 rue de la Piscine, F-38406 Saint Martin d'Hères, France
[17] Department of Astrophysics, Institute for Mathematics, Astrophysics and Particle Physics (IMAPP), Radboud University, P.O. Box 9010, 6500 GL Nijmegen, The Netherlands
[18] Perimeter Institute for Theoretical Physics, 31 Caroline Street North, Waterloo, ON, N2L 2Y5, Canada
[19] Department of Physics and Astronomy, University of Waterloo, 200 University Avenue West, Waterloo, ON, N2L 3G1, Canada
[20] Waterloo Centre for Astrophysics, University of Waterloo, Waterloo, ON N2L 3G1 Canada
[21] Korea Astronomy and Space Science Institute, Daedeok-daero 776, Yuseong-gu, Daejeon 34055, Republic of Korea
[22] University of Science and Technology, Gajeong-ro 217, Yuseong-gu, Daejeon 34113, Republic of Korea
[23] Kavli Institute for Cosmological Physics, University of Chicago, 5640 South Ellis Avenue, Chicago, IL 60637, USA
[24] Department of Astronomy and Astrophysics, University of Chicago, 5640 South Ellis Avenue, Chicago, IL 60637, USA
[25] Department of Physics, University of Chicago, 5720 South Ellis Avenue, Chicago, IL 60637, USA
[26] Enrico Fermi Institute, University of Chicago, 5640 South Ellis Avenue, Chicago, IL 60637, USA
[27] Data Science Institute, University of Arizona, 1230 N. Cherry Ave., Tucson, AZ 85721, USA
[28] Cornell Center for Astrophysics and Planetary Science, Cornell University, Ithaca, NY 14853, USA
[29] Anton Pannekoek Institute for Astronomy, University of Amsterdam, Science Park 904, 1098 XH, Amsterdam, The Netherlands
[30] Shanghai Astronomical Observatory, Chinese Academy of Sciences, 80 Nandan Road, Shanghai 200030, People's Republic of China
[31] Key Laboratory of Radio Astronomy, Chinese Academy of Sciences, Nanjing 210008, People's Republic of China
[32] Department of Space, Earth and Environment, Chalmers University of Technology, Onsala Space Observatory, SE-439 92 Onsala, Sweden
[33] Mizusawa VLBI Observatory, National Astronomical Observatory of Japan, 2-12 Hoshigaoka, Mizusawa, Oshu, Iwate 023-0861, Japan
[34] Department of Astronomical Science, The Graduate University for Advanced Studies (SOKENDAI), 2-21-1 Osawa, Mitaka, Tokyo 181-8588, Japan
[35] Dipartimento di Fisica "E. Pancini", Universitá di Napoli "Federico II", Compl. Univ. di Monte S. Angelo, Edificio G, Via Cinthia, I-80126, Napoli, Italy
[36] Institut für Theoretische Physik, Goethe-Universität Frankfurt, Max-von-Laue-Straße 1, D-60438 Frankfurt am Main, Germany
[37] INFN Sez. di Napoli, Compl. Univ. di Monte S. Angelo, Edificio G, Via Cinthia, I-80126, Napoli, Italy
[38] Department of Physics, University of Pretoria, Lynnwood Road, Hatfield, Pretoria 0083, South Africa
[39] Centre for Radio Astronomy Techniques and Technologies, Department of Physics and Electronics, Rhodes University, Grahamstown 6140, South Africa
[40] Max-Planck-Institut für Extraterrestrische Physik, Giessenbachstr. 1, D-85748 Garching, Germany
[41] Department of Electrical Engineering and Computer Science, Massachusetts Institute of Technology, 32-D476, 77 Massachussetts Ave., Cambridge, MA 02142, USA
[42] Google Research, 355 Main St., Cambridge, MA 02142, USA
[43] Department of History of Science, Harvard University, Cambridge, MA 02138, USA
[44] Department of Physics, Harvard University, Cambridge, MA 02138, USA
[45] Department of Physics, University of Illinois, 1110 West Green St, Urbana, IL 61801, USA
[46] Department of Astronomy, University of Illinois at Urbana-Champaign, 1002 West Green Street, Urbana, IL 61801, USA
[47] Leiden Observatory—Allegro, Leiden University, P.O. Box 9513, 2300 RA Leiden, The Netherlands
[48] Key Laboratory for Research in Galaxies and Cosmology, Chinese Academy of Sciences, Shanghai 200030, People's Republic of China
[49] NOVA Sub-mm Instrumentation Group, Kapteyn Astronomical Institute, University of Groningen, Landleven 12, 9747 AD Groningen, The Netherlands
[50] Department of Astronomy, School of Physics, Peking University, Beijing 100871, People's Republic of China
[51] Kavli Institute for Astronomy and Astrophysics, Peking University, Beijing 100871, People's Republic of China
[52] Instituto Nacional de Astrofísica, Óptica y Electrónica. Apartado Postal 51 y 216, 72000. Puebla Pue., México
[53] The Institute of Statistical Mathematics, 10-3 Midori-cho, Tachikawa, Tokyo, 190-8562, Japan
[54] Department of Statistical Science, The Graduate University for Advanced Studies (SOKENDAI), 10-3 Midori-cho, Tachikawa, Tokyo 190-8562, Japan
[55] Kavli Institute for the Physics and Mathematics of the Universe, The University of Tokyo, 5-1-5 Kashiwanoha, Kashiwa, 277-8583, Japan
[56] Institute for Astrophysical Research, Boston University, 725 Commonwealth Ave., Boston, MA 02215, USA
[57] Astronomical Institute, St. Petersburg University, Universitetskij pr., 28, Petrodvorets,198504 St. Petersburg, Russia
[58] Joint Institute for VLBI ERIC (JIVE), Oude Hoogeveensedijk 4, 7991 PD Dwingeloo, The Netherlands
[59] Kogakuin University of Technology & Engineering, Academic Support Center, 2665-1 Nakano, Hachioji, Tokyo 192-0015, Japan
[60] Physics Department, National Sun Yat-Sen University, No. 70, Lien-Hai Rd, Kaosiung City 80424, Taiwan, R.O.C
[61] National Optical Astronomy Observatory, 950 North Cherry Ave., Tucson, AZ 85719, USA
[62] Key Laboratory for Particle Astrophysics, Institute of High Energy Physics, Chinese Academy of Sciences, 19B Yuquan Road, Shijingshan District, Beijing, People's Republic of China
[63] School of Astronomy and Space Science, Nanjing University, Nanjing 210023, People's Republic of China
[64] Key Laboratory of Modern Astronomy and Astrophysics, Nanjing University, Nanjing 210023, People's Republic of China
[65] Italian ALMA Regional Centre, INAF-Istituto di Radioastronomia, Via P. Gobetti 101, 40129 Bologna, Italy
[66] Department of Physics, National Taiwan University, No.1, Sect.4, Roosevelt Rd., Taipei 10617, Taiwan, R.O.C
[67] Instituto de Radioastronomía y Astrofísica, Universidad Nacional Autónoma de México, Morelia 58089, México
[68] Instituto de Astronomía, Universidad Nacional Autónoma de México, CdMx 04510, México
[69] Yunnan Observatories, Chinese Academy of Sciences, 650011 Kunming, Yunnan Province, People's Republic of China
[70] Center for Astronomical Mega-Science, Chinese Academy of Sciences, 20A Datun Road, Chaoyang District, Beijing, 100012, People's Republic of China
[71] Key Laboratory for the Structure and Evolution of Celestial Objects, Chinese Academy of Sciences, 650011 Kunming, People's Republic of China

[72] Gravitation Astroparticle Physics Amsterdam (GRAPPA) Institute, University of Amsterdam, Science Park 904, 1098 XH Amsterdam, The Netherlands
[73] Centro Astronómico de Yebes (IGN), Apartado 148, E-19180 Yebes, Spain
[74] Department of Physics, Broida Hall, University of California Santa Barbara, Santa Barbara, CA 93106, USA
[75] Astronomy Department, Universidad de Concepción, Casilla 160-C, Concepción, Chile
[76] Department of Astronomy, University of Massachusetts, 01003, Amherst, MA, USA
[77] Department of Astronomy, Graduate School of Science, The University of Tokyo, 7-3-1 Hongo, Bunkyo-ku, Tokyo 113-0033, Japan
[78] Canadian Institute for Theoretical Astrophysics, University of Toronto, 60 St. George Street, Toronto, ON M5S 3H8, Canada
[79] Dunlap Institute for Astronomy and Astrophysics, University of Toronto, 50 St. George Street, Toronto, ON M5S 3H4, Canada
[80] Canadian Institute for Advanced Research, 180 Dundas St West, Toronto, ON M5G 1Z8, Canada
[81] Radio Astronomy Laboratory, University of California, Berkeley, CA 94720, USA
[82] CCS-2, Los Alamos National Laboratory, P.O. Box 1663, Los Alamos, NM 87545, USA
[83] Center for Theoretical Astrophysics, Los Alamos National Laboratory, Los Alamos, NM, 87545, USA
[84] Instituto de Radioastronomía Milimétrica, IRAM, Avenida Divina Pastora 7, Local 20, E-18012, Granada, Spain
[85] Consejo Nacional de Ciencia y Tecnología, Av. Insurgentes Sur 1582, 03940, Ciudad de México, México
[86] Hiroshima Astrophysical Science Center, Hiroshima University, 1-3-1 Kagamiyama, Higashi-Hiroshima, Hiroshima 739-8526, Japan
[87] Aalto University Department of Electronics and Nanoengineering, PL 15500, FI-00076 Aalto, Finland
[88] Aalto University Metsähovi Radio Observatory, Metsähovintie 114, FI-02540 Kylmälä, Finland
[89] Department of Astronomy, Yonsei University, Yonsei-ro 50, Seodaemun-gu, 03722 Seoul, Republic of Korea
[90] Netherlands Organisation for Scientific Research (NWO), Postbus 93138, 2509 AC Den Haag, The Netherlands
[91] Frontier Research Institute for Interdisciplinary Sciences, Tohoku University, Sendai 980-8578, Japan
[92] Astronomical Institute, Tohoku University, Sendai 980-8578, Japan
[93] Department of Physics and Astronomy, Seoul National University, Gwanak-gu, Seoul 08826, Republic of Korea
[94] Leiden Observatory, Leiden University, Postbus 2300, 9513 RA Leiden, The Netherlands
[95] Physics Department, Brandeis University, 415 South Street, Waltham, MA 02453, USA
[96] School of Physics, Huazhong University of Science and Technology, Wuhan, Hubei, 430074, People's Republic of China
[97] Mullard Space Science Laboratory, University College London, Holmbury St. Mary, Dorking, Surrey, RH5 6NT, UK
[98] School of Astronomy and Space Sciences, University of Chinese Academy of Sciences, No. 19A Yuquan Road, Beijing 100049, People's Republic of China
[99] Astronomy Department, University of Science and Technology of China, Hefei 230026, People's Republic of China
[100] University of Massachusetts Boston, 100 William T, Morrissey Blvd, Boston, MA 02125, USA
[101] ASTRON, Oude Hoogeveensedijk 4, 7991 PD Dwingeloo, The Netherlands
[102] Science Support Office, Directorate of Science, European Space Research and Technology Centre (ESA/ESTEC), Keplerlaan 1, 2201 AZ Noordwijk, The Netherlands
[103] University of Chicago, 5640 South Ellis Avenue, Chicago, IL 60637, USA
[104] Systems and Technology Research, 600 West Cummings Park, Woburn, MA 01801, USA

The Astrophysical Journal Letters, 875:L5 (31pp), 2019 April 10 https://doi.org/10.3847/2041-8213/ab0f43
© 2019. The American Astronomical Society.
OPEN ACCESS

First M87 Event Horizon Telescope Results. V. Physical Origin of the Asymmetric Ring

The Event Horizon Telescope Collaboration
(See the end matter for the full list of authors.)
Received 2019 March 4; revised 2019 March 12; accepted 2019 March 12; published 2019 April 10

Abstract

The Event Horizon Telescope (EHT) has mapped the central compact radio source of the elliptical galaxy M87 at 1.3 mm with unprecedented angular resolution. Here we consider the physical implications of the asymmetric ring seen in the 2017 EHT data. To this end, we construct a large library of models based on general relativistic magnetohydrodynamic (GRMHD) simulations and synthetic images produced by general relativistic ray tracing. We compare the observed visibilities with this library and confirm that the asymmetric ring is consistent with earlier predictions of strong gravitational lensing of synchrotron emission from a hot plasma orbiting near the black hole event horizon. The ring radius and ring asymmetry depend on black hole mass and spin, respectively, and both are therefore expected to be stable when observed in future EHT campaigns. Overall, the observed image is consistent with expectations for the shadow of a spinning Kerr black hole as predicted by general relativity. If the black hole spin and M87's large scale jet are aligned, then the black hole spin vector is pointed away from Earth. Models in our library of non-spinning black holes are inconsistent with the observations as they do not produce sufficiently powerful jets. At the same time, in those models that produce a sufficiently powerful jet, the latter is powered by extraction of black hole spin energy through mechanisms akin to the Blandford-Znajek process. We briefly consider alternatives to a black hole for the central compact object. Analysis of existing EHT polarization data and data taken simultaneously at other wavelengths will soon enable new tests of the GRMHD models, as will future EHT campaigns at 230 and 345 GHz.

Key words: accretion, accretion disks – black hole physics – galaxies: individual (M87) – galaxies: jets – magnetohydrodynamics (MHD) – techniques: high angular resolution

1. Introduction

In 1918 the galaxy Messier 87 (M87) was observed by Curtis and found to have "a curious straight ray ... apparently connected with the nucleus by a thin line of matter" (Curtis 1918, p. 31). Curtis's ray is now known to be a jet, extending from sub-pc to several kpc scales, and can be observed across the electromagnetic spectrum, from the radio through γ-rays. Very long baseline interferometry (VLBI) observations that zoom in on the nucleus, probing progressively smaller angular scales at progressively higher frequencies up to 86 GHz by the Global mm-VLBI Array (GMVA; e.g., Hada et al. 2016; Boccardi et al. 2017; Kim et al. 2018; Walker et al. 2018), have revealed that the jet emerges from a central core. Models of the stellar velocity distribution imply a mass for the central core $M \approx 6.2 \times 10^9\, M_\odot$ at a distance of 16.9 Mpc (Gebhardt et al. 2011); models of arcsecond-scale emission lines from ionized gas imply a mass that is lower by about a factor of two (Walsh et al. 2013).

The conventional model for the central object in M87 is a black hole surrounded by a geometrically thick, optically thin, disk accretion flow (e.g., Ichimaru 1977; Rees et al. 1982; Narayan & Yi 1994, 1995; Reynolds et al. 1996). The radiative power of the accretion flow ultimately derives from the gravitational binding energy of the inflowing plasma. There is no consensus model for jet launching, but the two main scenarios are that the jet is a magnetically dominated flow that is ultimately powered by tapping the rotational energy of the black hole (Blandford & Znajek 1977) and that the jet is a magnetically collimated wind from the surrounding accretion disk (Blandford & Payne 1982; Lynden-Bell 2006).

VLBI observations of M87 at frequencies $\gtrsim$230 GHz with the Event Horizon Telescope (EHT) can resolve angular scales of tens of μas, comparable to the scale of the event horizon (Doeleman et al. 2012; Akiyama et al. 2015; EHT Collaboration et al. 2019a, 2019b, 2019c, hereafter Paper I, II, and III). They therefore have the power to probe the nature of the central object and to test models for jet launching. In addition, EHT observations can constrain the key physical parameters of the system, including the black hole mass and spin, accretion rate, and magnetic flux trapped by accreting plasma in the black hole.

In this Letter we adopt the working hypothesis that the central object is a black hole described by the Kerr metric, with mass M and dimensionless spin a_*, $-1 < a_* < 1$. Here $a_* \equiv Jc/GM^2$, where J, G, and c are, respectively, the black hole angular momentum, gravitational constant, and speed of light. In our convention $a_* < 0$ implies that the angular momentum of the accretion flow and that of the black hole are anti-aligned. Using general relativistic magnetohydrodynamic (GRMHD) models for the accretion flow and synthetic images of these simulations produced by general relativistic radiative transfer calculations, we test whether or not the results of the 2017 EHT observing campaign (hereafter EHT2017) are consistent with the black hole hypothesis.

This Letter is organized as follows. In Section 2 we review salient features of the observations and provide order-of-magnitude estimates for the physical conditions in the source. In Section 3 we describe the numerical models. In Section 4 we outline our procedure for comparing the models to the data in a way that accounts for model variability. In Section 5 we show that many of the models cannot be rejected based on EHT data alone.

Original content from this work may be used under the terms of the Creative Commons Attribution 3.0 licence. Any further distribution of this work must maintain attribution to the author(s) and the title of the work, journal citation and DOI.

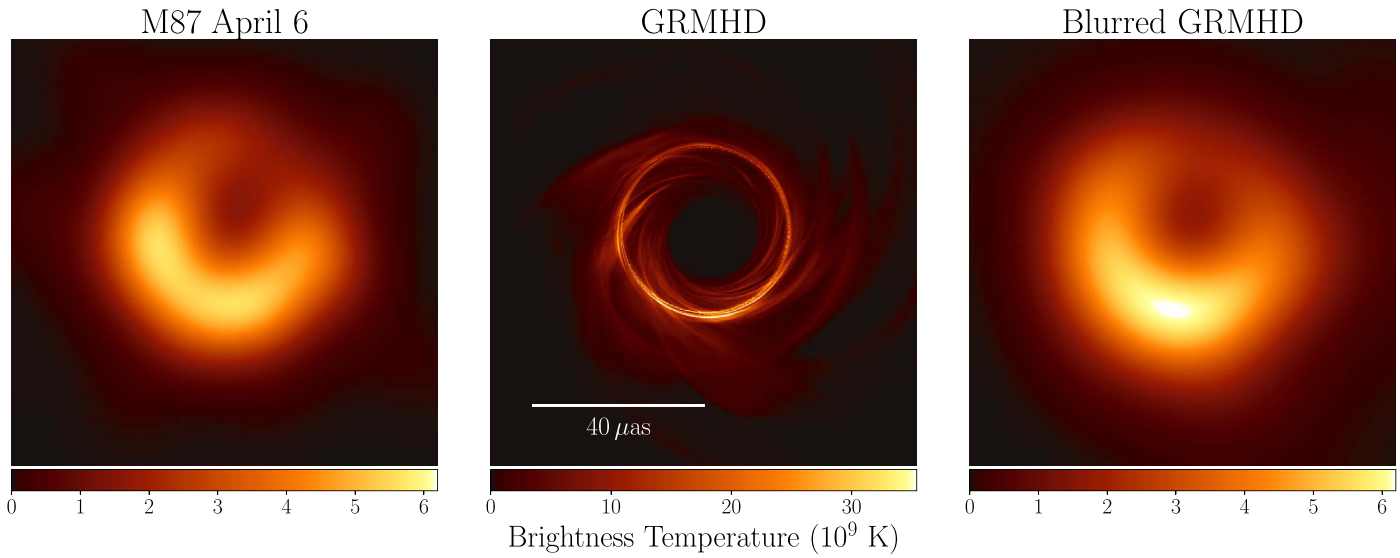

Figure 1. Left panel: an EHT2017 image of M87 from Paper IV of this series (see their Figure 15). Middle panel: a simulated image based on a GRMHD model. Right panel: the model image convolved with a 20 μas FWHM Gaussian beam. Although the most evident features of the model and data are similar, fine features in the model are not resolved by EHT.

In Section 6 we combine EHT data with other constraints on the radiative efficiency, X-ray luminosity, and jet power and show that the latter constraint eliminates all $a_* = 0$ models. In Section 7 we discuss limitations of our models and also briefly discuss alternatives to Kerr black hole models. In Section 8 we summarize our results and discuss how further analysis of existing EHT data, future EHT data, and multiwavelength companion observations will sharpen constraints on the models.

2. Review and Estimates

In EHT Collaboration et al. (2019d; hereafter Paper IV) we present images generated from EHT2017 data (for details on the array, 2017 observing campaign, correlation, and calibration, see Paper II and Paper III). A representative image is reproduced in the left panel of Figure 1.

Four features of the image in the left panel of Figure 1 play an important role in our analysis: (1) the ring-like geometry, (2) the peak brightness temperature, (3) the total flux density, and (4) the asymmetry of the ring. We now consider each in turn.

(1) The compact source shows a bright ring with a central dark area without significant extended components. This bears a remarkable similarity to the long-predicted structure for optically thin emission from a hot plasma surrounding a black hole (Falcke et al. 2000). The central hole surrounded by a bright ring arises because of strong gravitational lensing (e.g., Hilbert 1917; von Laue 1921; Bardeen 1973; Luminet 1979). The so-called "photon ring" corresponds to lines of sight that pass close to (unstable) photon orbits (see Teo 2003), linger near the photon orbit, and therefore have a long path length through the emitting plasma. These lines of sight will appear comparatively bright if the emitting plasma is optically thin. The central flux depression is the so-called black hole "shadow" (Falcke et al. 2000), and corresponds to lines of sight that terminate on the event horizon. The shadow could be seen in contrast to surrounding emission from the accretion flow or lensed counter-jet in M87 (Broderick & Loeb 2009).

The photon ring is nearly circular for all black hole spins and all inclinations of the black hole spin axis to the line of sight (e.g., Johannsen & Psaltis 2010). For an $a_* = 0$ black hole of mass M and distance D, the photon ring angular radius on the sky is

$$\theta_p \equiv \frac{\sqrt{27}\ GM}{c^2 D} = 18.8 \left(\frac{M}{6.2 \times 10^9 M_\odot}\right)\left(\frac{D}{16.9\ \mathrm{Mpc}}\right)^{-1} \mu\mathrm{as}, \quad (1)$$

where we have scaled to the most likely mass from Gebhardt et al. (2011) and a distance of 16.9 Mpc (see also EHT Collaboration et al. 2019e, (hereafter Paper VI; Blakeslee et al. 2009; Bird et al. 2010; Cantiello et al. 2018). The photon ring angular radius for other inclinations and values of a_* differs by at most 13% from Equation (1), and most of this variation occurs at $1 - |a_*| \ll 1$ (e.g., Takahashi 2004; Younsi et al. 2016). Evidently the angular radius of the observed photon ring is approximately $\sim$20 μas (Figure 1 and Paper IV), which is close to the prediction of the black hole model given in Equation (1).

(2) The observed peak brightness temperature of the ring in Figure 1 is $T_{b,pk} \sim 6 \times 10^9$ K, which is consistent with past EHT mm-VLBI measurements at 230 GHz (Doeleman et al. 2012; Akiyama et al. 2015), and GMVA 3 mm-VLBI measurements of the core region (Kim et al. 2018). Expressed in electron rest-mass (m_e) units, $\Theta_{b,pk} \equiv k_B T_{b,pk}/(m_e c^2) \simeq 1$, where k_B is Boltzmann's constant. The true peak brightness temperature of the source is higher if the ring is unresolved by EHT, as is the case for the model image in the center panel of Figure 1.

The 1.3 mm emission from M87 shown in Figure 1 is expected to be generated by the synchrotron process (see Yuan & Narayan 2014, and references therein) and thus depends on the electron distribution function (eDF). If the emitting plasma has a thermal eDF, then it is characterized by an electron temperature $T_e \geqslant T_b$, or $\Theta_e \equiv k_B T_e/(m_e c^2) > 1$, because $\Theta_e > \Theta_{b,pk}$ if the ring is unresolved or optically thin.

Is the observed brightness temperature consistent with what one would expect from phenomenological models of the source? Radiatively inefficient accretion flow models of M87

(Reynolds et al. 1996; Di Matteo et al. 2003) produce mm emission in a geometrically thick donut of plasma around the black hole. The emitting plasma is collisionless: Coulomb scattering is weak at these low densities and high temperatures. Therefore, the electron and ion temperatures need not be the same (e.g., Spitzer 1962). In radiatively inefficient accretion flow models, the ion temperature is slightly less than the ion virial temperature,

$$T_i \sim 0.3\, T_{i,\mathrm{vir}} = 0.3\, m_p c^2 r_g/(3k_B r) = 1.1 \times 10^{12} (r_g/r)\ \mathrm{K}, \quad (2)$$

where $r_g \equiv GM/c^2$ is the gravitational radius, r is the Boyer–Lindquist or Kerr–Schild radius, and m_p is the proton mass. Most models have an electron temperature $T_e < T_i$ because of electron cooling and preferential heating of the ions by turbulent dissipation (e.g., Yuan & Narayan 2014; Mościbrodzka et al. 2016). If the emission arises at $\sim 5\, r_g$, then $\Theta_e \simeq 37(T_e/T_i)$, which is then consistent with the observed $\Theta_{b,pk}$ if the source is unresolved or optically thin.

(3) The total flux density in the image at 1.3 mm is $\simeq$0.5 Jy. With a few assumptions we can use this to estimate the electron number density n_e and magnetic field strength B in the source. We adopt a simple, spherical, one-zone model for the source with radius $r \simeq 5\, r_g$, pressure $n_i k T_i + n_e k T_e = \beta_p B^2/(8\pi)$ with $\beta_p \equiv p_{gas}/p_{mag} \sim 1$, $T_i \simeq 3T_e$, and temperature $\theta_e \simeq 10\theta_{b,pk}$, which is consistent with the discussion in (2) above. Setting $n_e = n_i$ (i.e., assuming a fully ionized hydrogen plasma), the values of B and n_e required to produce the observed flux density can be found by solving a nonlinear equation (assuming an average angle between the field and line of sight, 60°). The solution can be approximated as a power law:

$$n_e = 2.9 \times 10^4 \left(\frac{r}{5\, r_g}\right)^{-1.3} \beta_p^{0.62} \times \left(\frac{T_i}{3T_e}\right)^{-0.47} \left(\frac{\theta_e}{10\theta_{b,pk}}\right)^{-2.4} \mathrm{cm}^{-3}, \quad (3)$$

$$B = 4.9 \left(\frac{r}{5\, r_g}\right)^{-0.63} \beta_p^{-0.19} \times \left(\frac{T_i}{3T_e}\right)^{0.14} \left(\frac{\theta_e}{10\theta_{b,pk}}\right)^{-0.71} \mathrm{G} \quad (4)$$

assuming that $M = 6.2 \times 10^9\, M_\odot$ and $D = 16.9$ Mpc, and using the approximate thermal emissivity of Leung et al. (2011). Then the synchrotron optical depth at 1.3 mm is $\sim$0.2. One can now estimate an accretion rate from (3) using

$$\dot{M} = 4\pi r^2 \rho v^r \sim 4\pi (5 r_g)^2\, n_e m_p\, (c/\sqrt{5}) \sim 2.7 \times 10^{-3} M_\odot\ \mathrm{yr}^{-1} \quad (5)$$

assuming spherical symmetry. The Eddington accretion rate is

$$\dot{M}_{\mathrm{Edd}} = \frac{L_{\mathrm{Edd}}}{\epsilon c^2} = \frac{2.2}{\epsilon}\left(\frac{M}{10^9\, M_\odot}\right) M_\odot\ \mathrm{yr}^{-1}, \quad (6)$$

where $L_{\mathrm{Edd}} \equiv 4\pi G M c m_p/\sigma_T$ is the Eddington luminosity (σ_T is the Thomson cross section). Setting the efficiency $\epsilon = 0.1$ and $M = 6.2 \times 10^9\, M_\odot$, $\dot{M}_{\mathrm{Edd}} = 137\, M_\odot\ \mathrm{yr}^{-1}$, and therefore $\dot{M}/\dot{M}_{\mathrm{Edd}} \sim 2.0 \times 10^{-5}$.

This estimate is similar to but slightly larger than the upper limit inferred from the 230 GHz linear polarization properties of M87 (Kuo et al. 2014).

(4) The ring is brighter in the south than the north. This can be explained by a combination of motion in the source and Doppler beaming. As a simple example we consider a luminous, optically thin ring rotating with speed v and an angular momentum vector inclined at a viewing angle $i > 0°$ to the line of sight. Then the approaching side of the ring is Doppler boosted, and the receding side is Doppler dimmed, producing a surface brightness contrast of order unity if v is relativistic. The approaching side of the large-scale jet in M87 is oriented west–northwest (position angle PA $\approx$ 288°; in Paper VI this is called $\mathrm{PA_{FJ}}$), or to the right and slightly up in the image. Walker et al. (2018) estimated that the angle between the approaching jet and the line of sight is 17°. If the emission is produced by a rotating ring with an angular momentum vector oriented along the jet axis, then the plasma in the south is approaching Earth and the plasma in the north is receding. This implies a clockwise circulation of the plasma in the source, as projected onto the plane of the sky. This sense of rotation is consistent with the sense of rotation in ionized gas at arcsecond scales (Harms et al. 1994; Walsh et al. 2013). Notice that the asymmetry of the ring is consistent with the asymmetry inferred from 43 GHz observations of the brightness ratio between the north and south sides of the jet and counter-jet (Walker et al. 2018).

All of these estimates present a picture of the source that is remarkably consistent with the expectations of the black hole model and with existing GRMHD models (e.g., Dexter et al. 2012; Mościbrodzka et al. 2016). They even suggest a sense of rotation of gas close to the black hole. A quantitative comparison with GRMHD models can reveal more.

3. Models

Consistent with the discussion in Section 2, we now adopt the working hypothesis that M87 contains a turbulent, magnetized accretion flow surrounding a Kerr black hole. To test this hypothesis quantitatively against the EHT2017 data we have generated a Simulation Library of 3D time-dependent ideal GRMHD models. To generate this computationally expensive library efficiently and with independent checks on the results, we used several different codes that evolved matching initial conditions using the equations of ideal GRMHD. The codes used include `BHAC` (Porth et al. 2017), `H-AMR` (Liska et al. 2018; K. Chatterjee et al. 2019, in preparation), `iharm` (Gammie et al. 2003), and `KORAL` (Sądowski et al. 2013b, 2014). A comparison of these and other GRMHD codes can be found in O. Porth et al. 2019 (in preparation), which shows that the differences between integrations of a standard accretion model with different codes is smaller than the fluctuations in individual simulations.

From the Simulation Library we have generated a large Image Library of synthetic images. Snapshots of the GRMHD evolutions were produced using the general relativistic ray-tracing (GRRT) schemes `ipole` (Mościbrodzka & Gammie 2018), `RAPTOR` (Bronzwaer et al. 2018), or `BHOSS` (Z. Younsi et al. 2019b, in preparation). A comparison of these and other GRRT codes can be found in Gold et al. (2019), which shows that the differences between codes is small.

In the GRMHD models the bulk of the 1.3 mm emission is produced within $\lesssim 10\, r_g$ of the black hole, where the models

can reach a statistically steady state. It is therefore possible to compute predictive radiative models for this compact component of the source without accurately representing the accretion flow at all radii.

We note that the current state-of-the-art models for M87 are radiation GRMHD models that include radiative feedback and electron-ion thermodynamics (Ryan et al. 2018; Chael et al. 2019). These models are too computationally expensive for a wide survey of parameter space, so that in this Letter we consider only nonradiative GRMHD models with a parameterized treatment of the electron thermodynamics.

3.1. Simulation Library

All GRMHD simulations are initialized with a weakly magnetized torus of plasma orbiting in the equatorial plane of the black hole (e.g., De Villiers et al. 2003; Gammie et al. 2003; McKinney & Blandford 2009; Porth et al. 2017). We do not consider tilted models, in which the accretion flow angular momentum is misaligned with the black hole spin. The limitations of this approach are discussed in Section 7.

The initial torus is driven to a turbulent state by instabilities, including the magnetorotational instability (see e.g., Balbus & Hawley 1991). In all cases the outcome contains a moderately magnetized midplane with orbital frequency comparable to the Keplerian orbital frequency, a corona with gas-to-magnetic-pressure ratio $\beta_{\rm p} \equiv p_{\rm gas}/p_{\rm mag} \sim 1$, and a strongly magnetized region over both poles of the black hole with $B^2/\rho c^2 \gg 1$. We refer to the strongly magnetized region as the funnel, and the boundary between the funnel and the corona as the funnel wall (De Villiers et al. 2005; Hawley & Krolik 2006). All models in the library are evolved from $t = 0$ to $t = 10^4\, r_{\rm g} c^{-1}$.

The simulation outcome depends on the initial magnetic field strength and geometry insofar as these affect the magnetic flux through the disk, as discussed below. Once the simulation is initiated the disk transitions to a turbulent state and loses memory of most of the details of the initial conditions. This relaxed turbulent state is found inside a characteristic radius that grows over the course of the simulation. To be confident that we are imaging only those regions that have relaxed, we draw snapshots for comparison with the data from $5 \times 10^3 \leq t/r_{\rm g} c^{-1} \leq 10^4$.

GRMHD models have two key physical parameters. The first is the black hole spin $a_*, -1 < a_* < 1$. The second parameter is the absolute magnetic flux $\Phi_{\rm BH}$ crossing one hemisphere of the event horizon (see Tchekhovskoy et al. 2011; O. Porth et al. 2019, in preparation for a definition). It is convenient to recast $\Phi_{\rm BH}$ in dimensionless form $\phi \equiv \Phi_{\rm BH}(\dot{M} r_{\rm g}^2\, c)^{-1/2}$.[110]

The magnetic flux ϕ is nonzero because magnetic field is advected into the event horizon by the accretion flow and sustained by currents in the surrounding plasma. At $\phi > \phi_{\rm max} \sim 15$,[111] numerical simulations show that the accumulated magnetic flux erupts, pushes aside the accretion flow, and escapes (Tchekhovskoy et al. 2011; McKinney et al. 2012). Models with $\phi \sim 1$ are conventionally referred to as Standard and Normal Evolution (SANE; Narayan et al. 2012; Sądowski et al (2013a)) models; models with $\phi \sim \phi_{\rm max}$ are conventionally referred to as Magnetically Arrested Disk (MAD; Igumenshchev et al. 2003; Narayan et al. 2003) models.

The Simulation Library contains SANE models with $a_* = -0.94$, -0.5, 0, 0.5, 0.75, 0.88, 0.94, 0.97, and 0.98, and MAD models with $a_* = -0.94$, -0.5, 0, 0.5, 0.75, and 0.94. The Simulation Library occupies 23 TB of disk space and contains a total of 43 GRMHD simulations, with some repeated at multiple resolutions with multiple codes, with consistent results (O. Porth et al. 2019, in preparation).

3.2. Image Library Generation

To produce model images from the simulations for comparison with EHT observations we use GRRT to generate a large number of synthetic images and derived VLBI data products. To make the synthetic images we need to specify the following: (1) the magnetic field, velocity field, and density as a function of position and time; (2) the emission and absorption coefficients as a function of position and time; and (3) the inclination angle between the accretion flow angular momentum vector and the line of sight i, the position angle PA, the black hole mass M, and the distance D to the observer. In the following we discuss each input in turn. The reader who is only interested in a high-level description of the Image Library may skip ahead to Section 3.3.

(1) GRMHD models provide the absolute velocity field of the plasma flow. Nonradiative GRMHD evolutions are invariant, however, under a rescaling of the density by a factor $\mathscr{M}$. In particular, they are invariant under $\rho \to \mathscr{M}\rho$, field strength $B \to \mathscr{M}^{1/2} B$, and internal energy $u \to \mathscr{M} u$ (the Alfvén speed $B/\rho^{1/2}$ and sound speed $\propto \sqrt{u/\rho}$ are invariant). That is, there is no intrinsic mass scale in a nonradiative model as long as the mass of the accretion flow is negligible in comparison to M.[112] We use this freedom to adjust $\mathscr{M}$ so that the average image from a GRMHD model has a 1.3 mm flux density $\approx$0.5 Jy (see Paper IV). Once $\mathscr{M}$ is set, the density, internal energy, and magnetic field are fully specified.

The mass unit $\mathscr{M}$ determines $\dot{M}$. In our ensemble of models $\dot{M}$ ranges from $2 \times 10^{-7} \dot{M}_{\rm Edd}$ to $4 \times 10^{-4} \dot{M}_{\rm Edd}$. Accretion rates vary by model category. The mean accretion rate for MAD models is $\sim 10^{-6} \dot{M}_{\rm Edd}$. For SANE models with $a_* > 0$ it is $\sim 5 \times 10^{-5} \dot{M}_{\rm Edd}$; and for $a_* < 0$ it is $\sim 2 \times 10^{-4} \dot{M}_{\rm Edd}$.

(2) The observed radio spectral energy distributions (SEDs) and the polarization characteristics of the source make clear that the 1.3 mm emission is synchrotron radiation, as is typical for active galactic nuclei (AGNs). Synchrotron absorption and emission coefficients depend on the eDF. In what follows, we adopt a relativistic, thermal model for the eDF (a Maxwell-Jüttner distribution; Jüttner 1911; Rezzolla & Zanotti 2013). We discuss the limitations of this approach in Section 7.

All of our models of M87 are in a sufficiently low-density, high-temperature regime that the plasma is collisionless (see Ryan et al. 2018, for a discussion of Coulomb coupling in M87). Therefore, T_e likely does not equal the ion temperature T_i, which is provided by the simulations. We set T_e using the GRMHD density ρ, internal energy density u, and plasma $\beta_{\rm p}$

[110] ϕ is determined by the outcome of the simulation and cannot be trivially predicted from the initial conditions, but by repeated experiment it is possible to manipulate the size of the initial torus and strength and geometry of the initial field to produce a target ϕ.

[111] In Heaviside units, where a factor of $\sqrt{4\pi}$ is absorbed into the definition of B, $\phi_{\rm max} \simeq 15$. In the Gaussian units used in some earlier papers, $\phi_{\rm max} \simeq 50$.

[112] For a black hole accreting at the Eddington rate, the ratio of the accreting mass onto a black hole mass is $\sim 10^{-22} (M/M_\odot)$; in our models mass accretion rate is far below the Eddington rate.

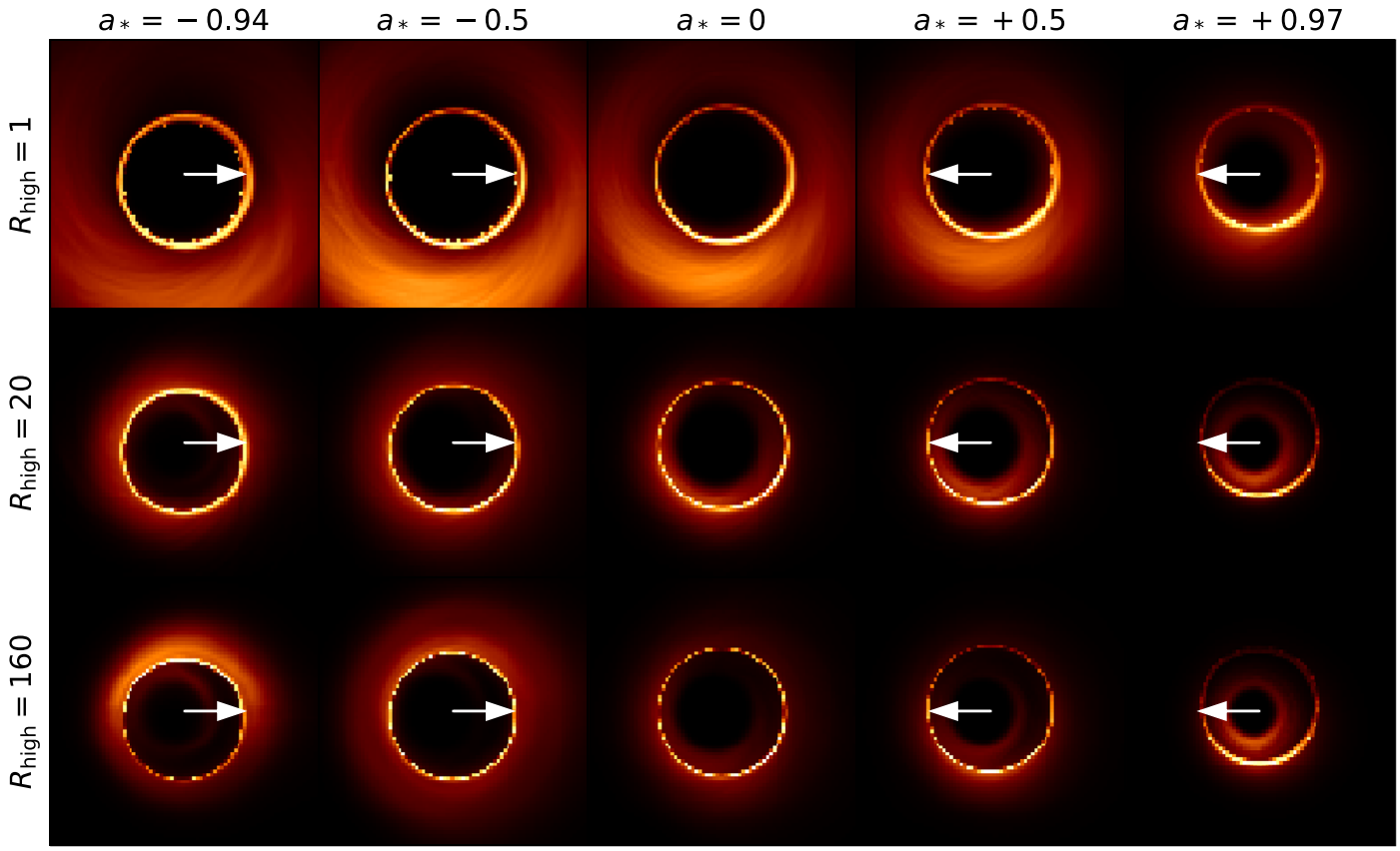

Figure 2. Time-averaged 1.3 mm images generated by five SANE GRMHD simulations with varying spin ($a_* = -0.94$ to $a_* = +0.97$ from left to right) and $R_{\rm high}$ ($R_{\rm high} = 1$ to $R_{\rm high} = 160$ from top to bottom; increasing $R_{\rm high}$ corresponds to decreasing electron temperature). The colormap is linear. All models are imaged at $i = 163°$. The jet that is approaching Earth is on the right (west) in all the images. The black hole spin vector projected onto the plane of the sky is marked with an arrow and aligned in the east–west direction. When the arrow is pointing left the black hole rotates in a clockwise direction, and when the arrow is pointing right the black hole rotates in a counterclockwise direction. The field of view for each model image is 80 μas (half of that used for the image libraries) with resolution equal to 1μas/pixel (20 times finer than the nominal resolution of EHT2017, and the same employed in the library images).

using a simple model:

$$T_e = \frac{2m_p u}{3k\rho(2+R)}, \tag{7}$$

where we have assumed that the plasma is composed of hydrogen, the ions are nonrelativistic, and the electrons are relativistic. Here $R \equiv T_i/T_e$ and

$$R = R_{\rm high}\frac{\beta_{\rm p}^2}{1+\beta_{\rm p}^2} + \frac{1}{1+\beta_{\rm p}^2}. \tag{8}$$

This prescription has one parameter, $R_{\rm high}$, and sets $T_e \simeq T_i$ in low $\beta_{\rm p}$ regions and $T_e \simeq T_i/R_{\rm high}$ in the midplane of the disk. It is adapted from Mościbrodzka et al. (2016) and motivated by models for electron heating in a turbulent, collisionless plasma that preferentially heats the ions for $\beta_{\rm p} \gtrsim 1$ (e.g., Howes 2010; Kawazura et al. 2018).

(3) We must specify the observer inclination i, the orientation of the observer through the position angle PA, the black hole mass M, and the distance D to the source. Non-EHT constraints on i, PA, and M are considered below; we have generated images at $i = 12°$, 17°, 22°, 158°, 163°, and 168° and a few at $i = 148°$. The position angle (PA) can be changed by simply rotating the image. All features of the models that we have examined, including $\dot{M}$, are insensitive to small changes in i. The image morphology does depend on whether i is greater than or less than 90°, as we will show below.

The model images are generated with a 160 × 160 μas field of view and 1μas pixels, which are small compared to the ∼20 μas nominal resolution of EHT2017. Our analysis is insensitive to changes in the field of view and the pixel scale.

For M we use the most likely value from the stellar absorption-line work, $6.2 \times 10^9 M_\odot$ (Gebhardt et al. 2011). For the distance D we use 16.9 Mpc, which is very close to that employed in Paper VI. The ratio $GM/(c^2D) = 3.62$ μas (hereafter M/D) determines the angular scale of the images. For some models we have also generated images with $M = 3.5 \times 10^9 M_\odot$ to check that the analysis results are not predetermined by the input black hole mass.

3.3. Image Library Summary

The Image Library contains of order 60,000 images. We generate images from 100 to 500 distinct output files from each of the GRMHD models at each of $R_{\rm high} = 1$, 10, 20, 40, 80, and 160. In comparing to the data we adjust the PA by rotation and the total flux and angular scale of the image by simply rescaling images from the standard parameters in the Image Library (see Figure 29 in Paper VI). Tests indicate that comparisons with the

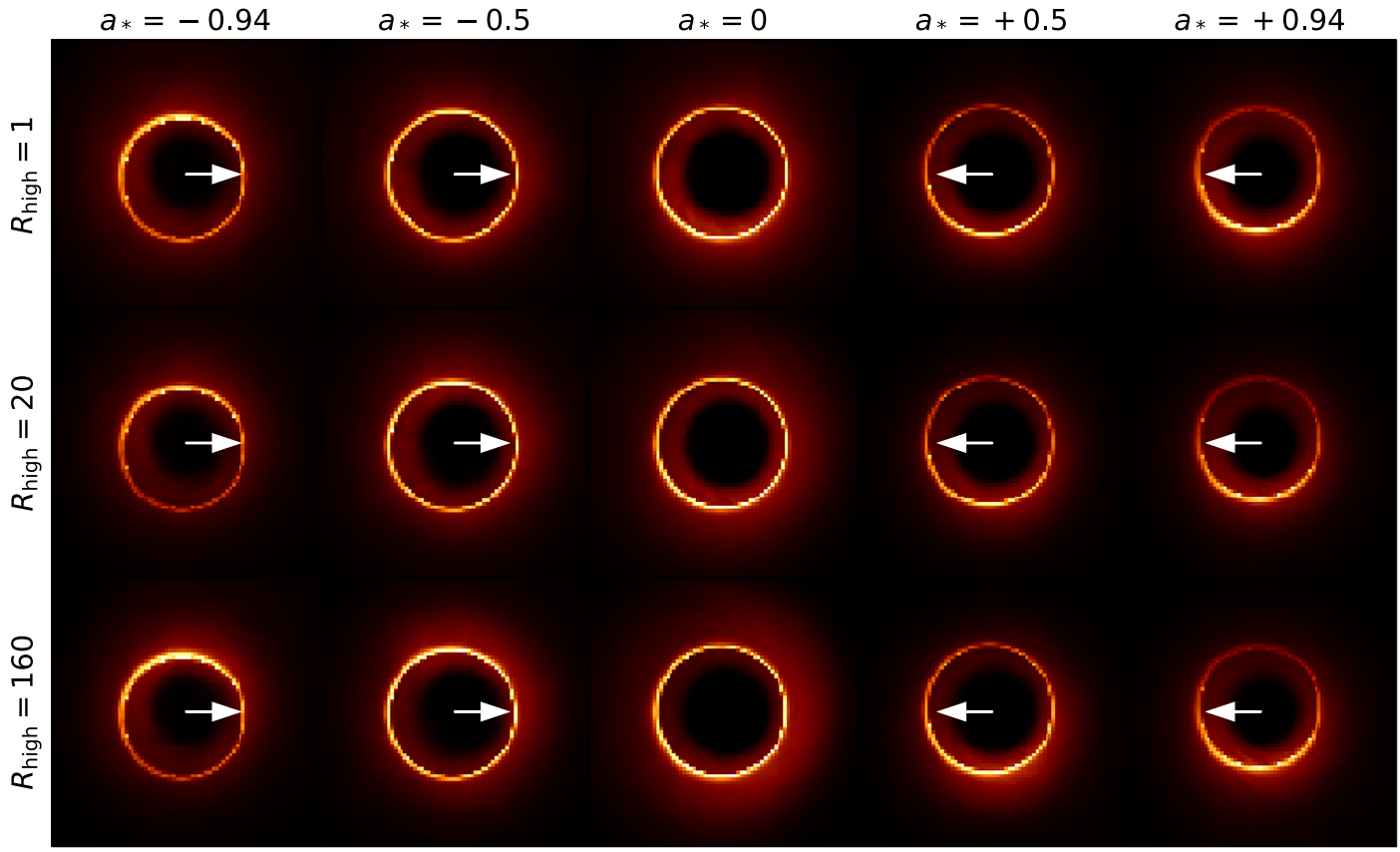

Figure 3. Same as in Figure 2 but for selected MAD models.

data are insensitive to the rescaling procedure unless the angular scaling factor or flux scaling factor is large.[113]

The comparisons with the data are also insensitive to image resolution.[114]

A representative set of time-averaged images from the Image Library are shown in Figures 2 and 3. From these figures it is clear that varying the parameters a_*, ϕ, and $R_{\rm high}$ can change the width and asymmetry of the photon ring and introduce additional structures exterior and interior to the photon ring.

The location of the emitting plasma is shown in Figure 4, which shows a map of time- and azimuth-averaged emission regions for four representative $a_* > 0$ models. For SANE models, if $R_{\rm high}$ is low (high), emission is concentrated more in the disk (funnel wall), and the bright section of the ring is dominated by the disk (funnel wall).[115] Appendix B shows images generated by considering emission only from particular regions of the flow, and the results are consistent with Figure 4.

Figures 2 and 3 show that for both MAD and SANE models the bright section of the ring, which is generated by Doppler beaming, shifts from the top for negative spin, to a nearly symmetric ring at $a_* = 0$, to the bottom for $a_* > 0$ (except the SANE $R_{\rm high} = 1$ case, where the bright section is always at the bottom when $i > 90°$). That is, the location of the peak flux in the ring is controlled by the black hole spin: it always lies roughly 90 degrees counterclockwise from the projection of the spin vector on the sky. Some of the ring emission originates in the funnel wall at $r \lesssim 8\ r_{\rm g}$. The rotation of plasma in the funnel wall is in the same sense as plasma in the funnel, which is controlled by the dragging of magnetic field lines by the black hole. The funnel wall thus rotates opposite to the accretion flow if $a_* < 0$. This effect will be studied further in a later publication (Wong et al. 2019). The resulting relationships between disk angular momentum, black hole angular momentum, and observed ring asymmetry are illustrated in Figure 5.

The time-averaged MAD images are almost independent of $R_{\rm high}$ and depend mainly on a_*. In MAD models much of the emission arises in regions with $\beta_{\rm p} \sim 1$, where $R_{\rm high}$ has little influence over the electron temperature, so the insensitivity to $R_{\rm high}$ is natural (see Figure 4). In SANE models emission arises at $\beta_{\rm p} \sim 10$, so the time-averaged SANE images, by contrast, depend strongly on $R_{\rm high}$. In low $R_{\rm high}$ SANE models, extended emission outside the photon ring, arising near the equatorial plane, is evident at $R_{\rm high} = 1$. In large $R_{\rm high}$ SANE models the inner ring emission arises from the funnel wall, and once again the image looks like a thin ring (see Figure 4).

Figure 6 and the accompanying animation show the evolution of the images, visibility amplitudes, and closure phases over a 5000 $r_{\rm g} c^{-1} \approx 5$ yr interval in a single simulation for M87. It is evident from the animation that turbulence in the simulations produces large fluctuations in the images, which

[113] In particular the distribution of best-fit M/D, which is defined in Section 4, have mean and standard deviation of $M/D = 3.552 \pm 0.605\ \mu$as when the images are made with an input $M/D = 3.62\ \mu$as, and $3.564 \pm 0.537\ \mu$as when the images are made with an input $M/D = 2.01\ \mu$as. We have also checked images made with an input 1.3 mm flux ranging from 0.1 to 1.5 Jy and find relative changes in M/D and PA of less than 1%.

[114] In particular, doubling the image resolution changes the mean best-fit M/D by 7 nano-arcsec, and the best-fit PA by $\sim 0\overset{\circ}{.}3$.

[115] In GRMHD models the jet core is effectively empty and the density is set by numerical "floors." In our radiative transfer calculations emission from regions with $B^2/\rho > 1$ is explicitly set to zero.

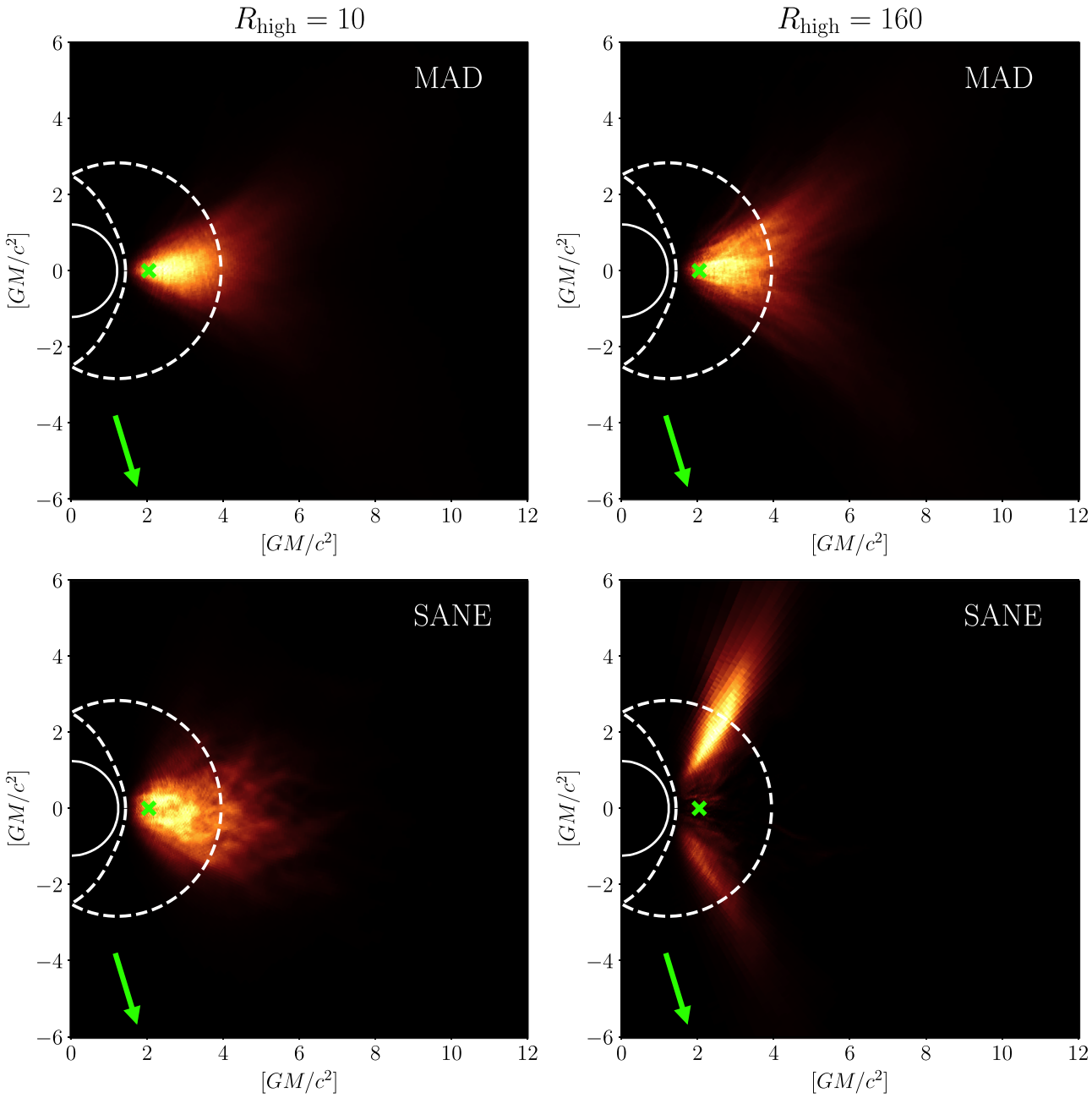

Figure 4. Binned location of the point of origin for all photons that make up an image, summed over azimuth, and averaged over all snapshots from the simulation. The colormap is linear. The event horizon is indicated by the solid white semicircle and the black hole spin axis is along the figure vertical axis. This set of four images shows MAD and SANE models with $R_{\rm high} = 10$ and 160, all with $a_* = 0.94$. The region between the dashed curves is the locus of existence of (unstable) photon orbits (Teo 2003). The green cross marks the location of the innermost stable circular orbit (ISCO) in the equatorial plane. In these images the line of sight (marked by an arrow) is located below the midplane and makes a 163° angle with the disk angular momentum, which coincides with the spin axis of the black hole.

imply changes in visibility amplitudes and closure phases that are large compared to measurement errors. The fluctuations are central to our procedure for comparing models with the data, described briefly below and in detail in Paper VI.

The timescale between frames in the animation is $50\,r_{\rm g}c^{-1} \simeq 18$ days, which is long compared to EHT2017 observing campaign. The images are highly correlated on timescales less than the innermost stable circular orbit (ISCO) orbital period, which for $a_* = 0$ is $\simeq 15\,r_{\rm g}c^{-1} \simeq 5$ days, i.e., comparable to the duration of the EHT2017 campaign. If drawn from one of our models, we would expect the EHT2017 data to look like a single snapshot (Figures 6) rather than their time averages (Figures 2 and 3).

4. Procedure for Comparison of Models with Data

As described above, each model in the Simulation Library has two dimensionless parameters: black hole spin a_* and magnetic flux ϕ. Imaging the model from each simulation adds five new parameters: $R_{\rm high}$, i, PA, M, and D, which we set to 16.9 Mpc. After fixing these parameters we draw snapshots from the time evolution at a cadence of 10 to 50 $r_{\rm g}c^{-1}$. We then compare these snapshots to the data.

The simplest comparison computes the χ^2_ν (reduced chi square) distance between the data and a snapshot. In the course of computing χ^2_ν we vary the image scale M/D, flux density F_ν, position angle PA, and the gain at each VLBI station in order to

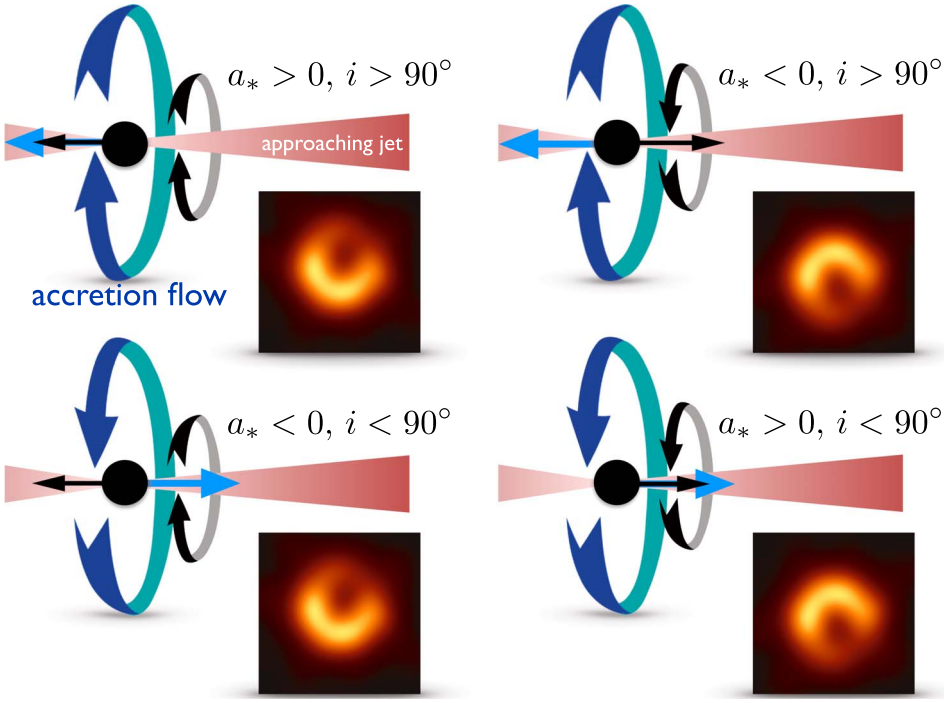

Figure 5. Illustration of the effect of black hole and disk angular momentum on ring asymmetry. The asymmetry is produced primarily by Doppler beaming: the bright region corresponds to the approaching side. In GRMHD models that fit the data comparatively well, the asymmetry arises in emission generated in the funnel wall. The sense of rotation of both the jet and funnel wall are controlled by the black hole spin. If the black hole spin axis is aligned with the large-scale jet, which points to the right, then the asymmetry implies that the black hole spin is pointing away from Earth (rotation of the black hole is clockwise as viewed from Earth). The blue ribbon arrow shows the sense of disk rotation, and the black ribbon arrow shows black hole spin. Inclination i is defined as the angle between the disk angular momentum vector and the line of sight.

give each image every opportunity to fit the data. The best-fit parameters (M/D, F_ν, PA) for each snapshot are found by two pipelines independently: the THEMIS pipeline using a Markov chain Monte Carlo method (A. E. Broderick et al. 2019a, in preparation), and the GENA pipeline using an evolutionary algorithm for multidimensional minimization (Fromm et al. 2019a; C. Fromm et al. 2019b, in preparation; see also Section 4 of Paper VI for details). The best-fit parameters contain information about the source and we use the distribution of best-fit parameters to test the model by asking whether or not they are consistent with existing measurements of M/D and estimates of the jet PA on larger scales.

The χ^2_ν comparison alone does not provide a sharp test of the models. Fluctuations in the underlying GRMHD model, combined with the high signal-to-noise ratio for EHT2017 data, imply that individual snapshots are highly unlikely to provide a formally acceptable fit with $\chi^2_\nu \simeq 1$. This is borne out in practice with the minimum $\chi^2_\nu = 1.79$ over the entire set of the more than 60,000 individual images in the Image Library. Nevertheless, it is possible to test if the χ^2_ν from the fit to the data is consistent with the underlying model, using "Average Image Scoring" with THEMIS (THEMIS-AIS), as described in detail in Appendix F of Paper VI). THEMIS-AIS measures a χ^2_ν distance (on the space of visibility amplitudes and closure phases) between a trial image and the data. In practice we use the average of the images from a given model as the trial image (hence THEMIS-AIS), but other choices are possible. We compute the χ^2_ν distance between the trial image and synthetic data produced from each snapshot. The model can then be tested by asking whether the data's χ^2_ν is likely to have been drawn from the model's distribution of χ^2_ν. In particular, we can assign a probability p that the data is drawn from a specific model's distribution.

In this Letter we focus on comparisons with a single data set, the 2017 April 6 high-band data (Paper III). The eight EHT2017 data sets, spanning four days with two bands on each day, are highly correlated. Assessing what correlation is expected in the models is a complicated task that we defer to later publications. The 2017 April 6 data set has the largest number of scans, 284 detections in 25 scans (see Paper III) and is therefore expected to be the most constraining.[116]

5. Model Constraints: EHT2017 Alone

The resolved ring-like structure obtained from the EHT2017 data provides an estimate of M/D (discussed in detail in Paper VI) and the jet PA from the immediate environment of the central black hole. As a first test of the models we can ask whether or not these are consistent with what is known from other mass measurements and from the orientation of the large-scale jet.

Figure 7 shows the distributions of best-fit values of M/D for a subset of the models for which spectra and jet power estimates are available (see below). The three lines show the M/D distribution for all snapshots (dotted lines), the best-fit 10% of snapshots (dashed lines), and the best-fit 1% of snapshots (solid lines) within each model. Evidently, as better fits are required, the distribution narrows and peaks close to $M/D \sim 3.6\ \mu$as with a width of about 0.5μas.

The distribution of M/D for the best-fit $<10\%$ of snapshots is qualitatively similar if we include only MAD or SANE models, only models produced by individual codes (BHAC,

[116] Paper I and Paper IV focus instead on the April 11 data set.

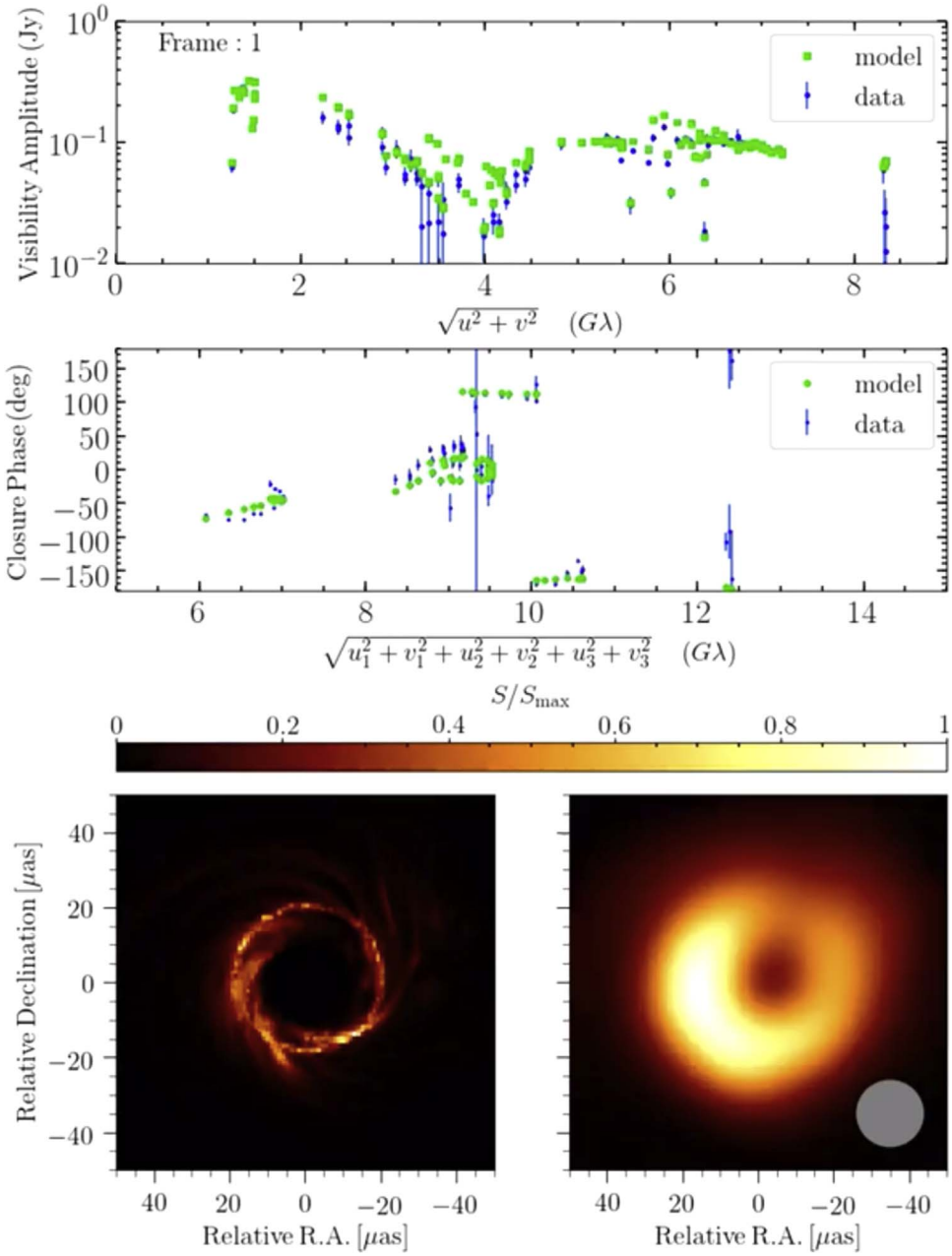

Figure 6. Single frame from the accompanying animation. This shows the visibility amplitudes (top), closure phases plotted by Euclidean distance in 6D space (middle), and associated model images at full resolution (lower left) and convolved with the EHT2017 beam (lower right). Data from 2017 April 6 high-band are also shown in the top two plots. The video shows frames 1 through 100 and has a duration of 10 s.

(An animation of this figure is available.)

H-AMR, iharm, or KORAL), or only individual spins. As the thrust of this Letter is to test the models, we simply note that Figure 7 indicates that the models are broadly consistent with earlier mass estimates (see Paper VI for a detailed discussion). This did not have to be the case: the ring radius could have been significantly larger than 3.6 μas.

We can go somewhat further and ask if any of the individual models favor large or small masses. Figure 8 shows the distributions of best-fit values of M/D for each model (different a_*, $R_{\rm high}$, and magnetic flux). Most individual models favor M/D close to 3.6 μas. The exceptions are $a_* \leqslant 0$ SANE models with $R_{\rm high} = 1$, which produce the bump in the M/D distribution near 2μas. In these models, the emission is produced at comparatively large radius in the disk (see Figure 2) because the inner edge of the disk (the ISCO) is at a large radius in a counter-rotating disk around a black hole with $|a_*| \sim 1$. For these models, the fitting procedure identifies EHT2017's ring with this outer ring, which forces the photon ring, and therefore M/D, to be small. As we will show later, these models can be rejected because they produce weak jets that are inconsistent with existing jet power estimates (see Section 6.3).

Figure 8 also shows that M/D increases with a_* for SANE models. This is due to the appearance of a secondary inner ring inside the main photon ring. The former is associated with emission produced along the wall of the approaching jet.

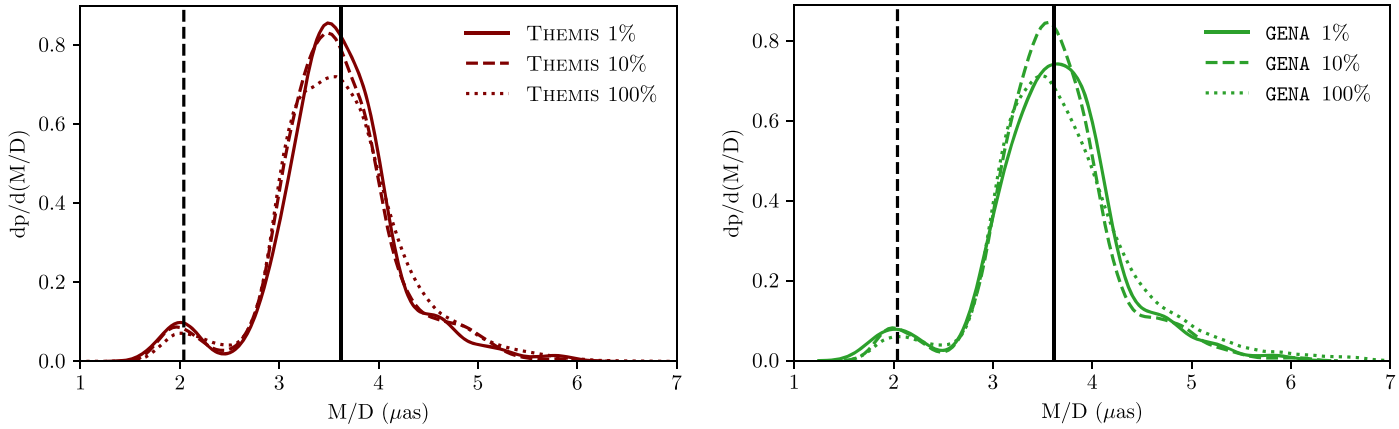

Figure 7. Distribution of M/D obtained by fitting Image Library snapshots to the 2017 April 6 data, in μas, measured independently using the (left panel) THEMIS and (right panel) GENA pipelines with qualitatively similar results. Smooth lines were drawn with a Gaussian kernel density estimator. The three lines show the best-fit 1% within each model (solid); the best-fit 10% within each model (dashed); and all model images (dotted). The vertical lines show $M/D = 2.04$ (dashed) and 3.62 μas (solid), corresponding to $M = 3.5$ and $6.2 \times 10^9\, M_\odot$. The distribution uses a subset of models for which spectra and jet power estimates are available (see Section 6). Only images with $a_* > 0$, $i > 90°$ and $a_* < 0$, $i < 90°$ (see also the left panel of Figure 5) are considered.

Because the emission is produced in front of the black hole, lensing is weak and it appears at small angular scale. The inner ring is absent in MAD models (see Figure 3), where the bulk of the emission comes from the midplane at all values of $R_{\rm high}$ (Figure 4).

We now ask whether or not the PA of the jet is consistent with the orientation of the jet measured at other wavelengths. On large (∼mas) scales the extended jet component has a PA of approximately 288° (e.g., Walker et al. 2018). On smaller (∼100 μas) scales the apparent opening angle of the jet is large (e.g., Kim et al. 2018) and the PA is therefore more difficult to measure. Also notice that the jet PA may be time dependent (e.g., Hada et al. 2016; Walker et al. 2018). In our model images the jet is relatively dim at 1.3 mm, and is not easily seen with a linear colormap. The model jet axis is, nonetheless, well defined: jets emerge perpendicular to the disk.

Figure 9 shows the distribution of best-fit PA over the same sample of snapshots from the Image Library used in Figure 7. We divide the snapshots into two groups. The first group has the black hole spin pointed away from Earth ($i > 90°$ and $a_* > 0$, or $i < 90°$ and $a_* < 0$). The spin-away model PA distributions are shown in the top two panels. The second group has the black hole spin pointed toward Earth ($i > 90$ and $a_* < 0$ or $i > 90°$ and $a_* < 0$). These spin-toward model PA distributions are shown in the bottom two panels. The large-scale jet orientation lies on the shoulder of the spin-away distribution (the distribution can be approximated as a Gaussian with, for THEMIS (GENA) mean 209 (203)° and $\sigma_{\rm PA} = 54\,(55)°$; the large-scale jet PA lies $1.5\sigma_{\rm PA}$ from the mean) and is therefore consistent with the spin-away models. On the other hand, the large-scale jet orientation lies off the shoulder of the spin-toward distribution and is inconsistent with the spin-toward models. Evidently models in which the black hole spin is pointing away from Earth are strongly favored.

The width of the spin-away and spin-toward distributions arises naturally in the models from brightness fluctuations in the ring. The distributions are relatively insensitive if split into MAD and SANE categories, although for MAD the averaged PA is $\langle {\rm PA}\rangle = 219°$, $\sigma_{\rm PA} = 46°$, while for SANE $\langle {\rm PA}\rangle = 195°$ and $\sigma_{\rm PA} = 58°$. The $a_* = 0$ and $a_* > 0$ models have similar distributions. Again, EHT2017 data strongly favor one sense of black hole spin: either $|a_*|$ is small, or the spin vector is pointed away from Earth. If the fluctuations are such that the fitted PA for each epoch of observations is drawn from a Gaussian with $\sigma_{\rm PA} \simeq 55°$, then a second epoch will be able to identify the true orientation with accuracy $\sigma_{\rm PA}/\sqrt{2} \simeq 40°$ and the Nth epoch with accuracy $\sigma_{\rm PA}/\sqrt{N}$. If the fitted PA were drawn from a Gaussian of width $\sigma_{\rm PA} = 54°$ about PA = 288°, as would be expected in a model in which the large-scale jet is aligned normal to the disk, then future epochs have a >90% chance of seeing the peak brightness counterclockwise from its position in EHT2017.

Finally, we can test the models by asking if they are consistent with the data according to THEMIS-AIS, as introduced in Section 4. THEMIS-AIS produces a probability p that the χ^2_ν distance between the data and the average of the model images is drawn from the same distribution as the χ^2_ν distance between synthetic data created from the model images, and the average of the model images. Table 1 takes these p values and categorizes them by magnetic flux and by spin, aggregating (averaging) results from different codes, $R_{\rm high}$, and i. Evidently, most of the models are formally consistent with the data by this test.

One group of models, however, is rejected by THEMIS-AIS: MAD models with $a_* = -0.94$. On average this group has $p = 0.01$, and all models within this group have $p \leqslant 0.04$. Snapshots from MAD models with $a_* = -0.94$ exhibit the highest morphological variability in our ensemble in the sense that the emission breaks up into transient bright clumps. These models are rejected by THEMIS-AIS because none of the snapshots are as similar to the average image as the data. In other words, it is unlikely that EHT2017 would have captured an $a_* = -0.94$ MAD model in a configuration as unperturbed as the data seem to be.

The remainder of the model categories contain at least some models that are consistent with the data according to the average image scoring test. That is, most models are variable and the associated snapshots lie far from the average image. These snapshots are formally inconsistent with the data, but their distance from the average image is consistent with what is expected from the models. Given the uncertainties in the model—and our lack of knowledge of the source prior to EHT2017—it is remarkable that so many of the models are acceptable. This is likely because the source structure is dominated by the photon ring, which is produced by gravitational lensing, and is therefore relatively insensitive to the details of the accretion flow and jet physics. We

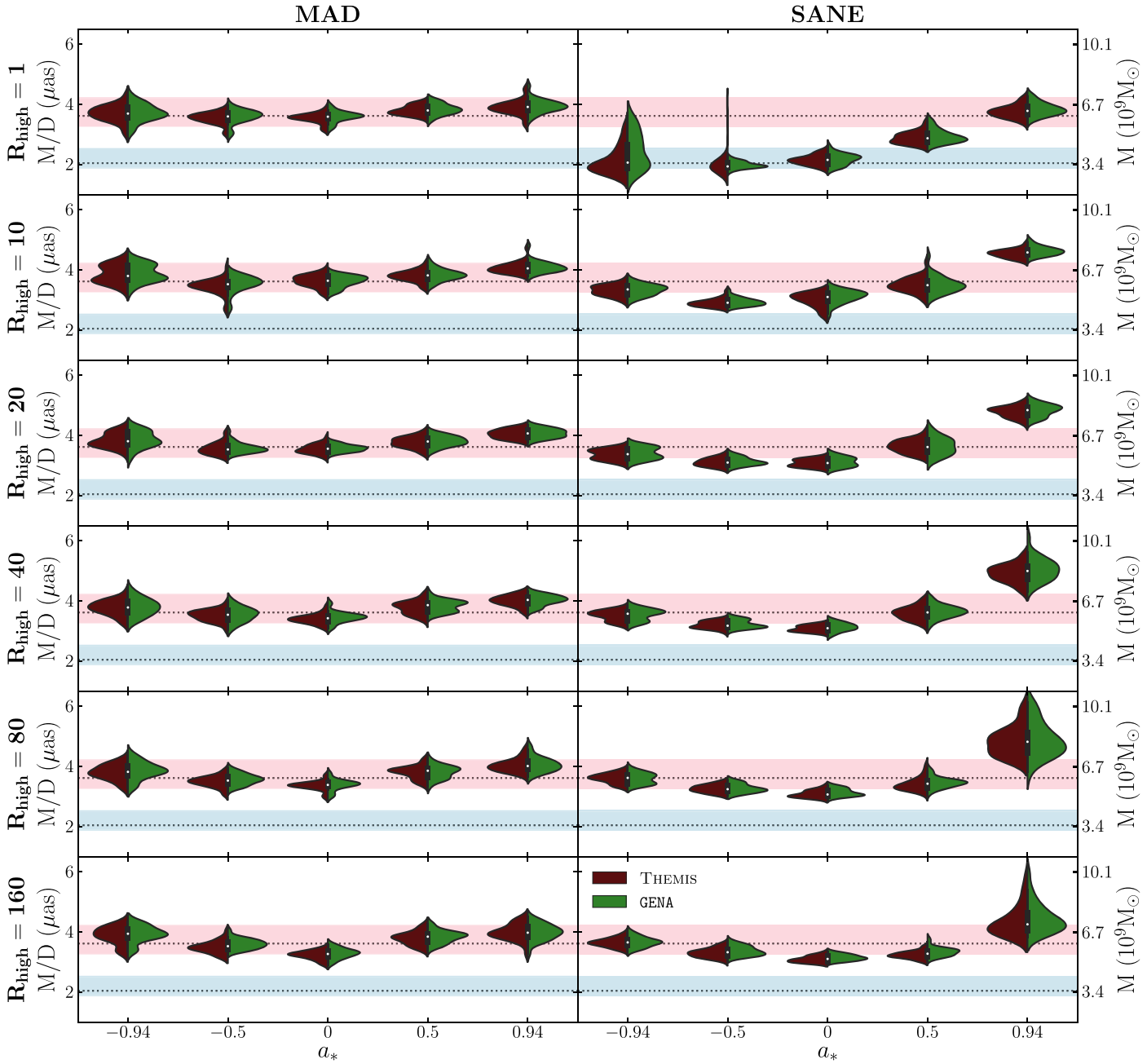

Figure 8. Distributions of M/D and black hole mass with $D = 16.9$ Mpc reconstructed from the best-fit 10% of images for MAD (left panel) and SANE (right panel) models ($i = 17°$ for $a_* \leq 0$ and 163° for $a_* > 0$) with different $R_{\rm high}$ and a_*, from the THEMIS (dark red, left), and GENA (dark green, right) pipelines. The white dot and vertical black bar correspond, respectively, to the median and region between the 25th and 75th percentiles for both pipelines combined. The blue and pink horizontal bands show the range of M/D and mass at $D = 16.9$ Mpc estimated from the gas dynamical model (Walsh et al. 2013) and stellar dynamical model (Gebhardt et al. 2011), respectively. Constraints on the models based on average image scoring (THEMIS-AIS) are discussed in Section 5. Constraints based on radiative efficiency, X-ray luminosity, and jet power are discussed in Section 6.

can further narrow the range of acceptable models, however, using additional constraints.

6. Model Constraints: EHT2017 Combined with Other Constraints

We can apply three additional arguments to further constrain the source model. (1) The model must be close to radiative equilibrium. (2) The model must be consistent with the observed broadband SED; in particular, it must not overproduce X-rays. (3) The model must produce a sufficiently powerful jet to match the measurements of the jet kinetic energy at large scales. Our discussions in this Section are based on simulation data that is provided in full detail in Appendix A.

6.1. Radiative Equilibrium

The model must be close to radiative equilibrium. The GRMHD models in the Simulation Library do not include radiative cooling, nor do they include a detailed prescription for particle energization. In nature the accretion flow and jet are expected to be cooled and heated by a combination of synchrotron and Compton cooling,

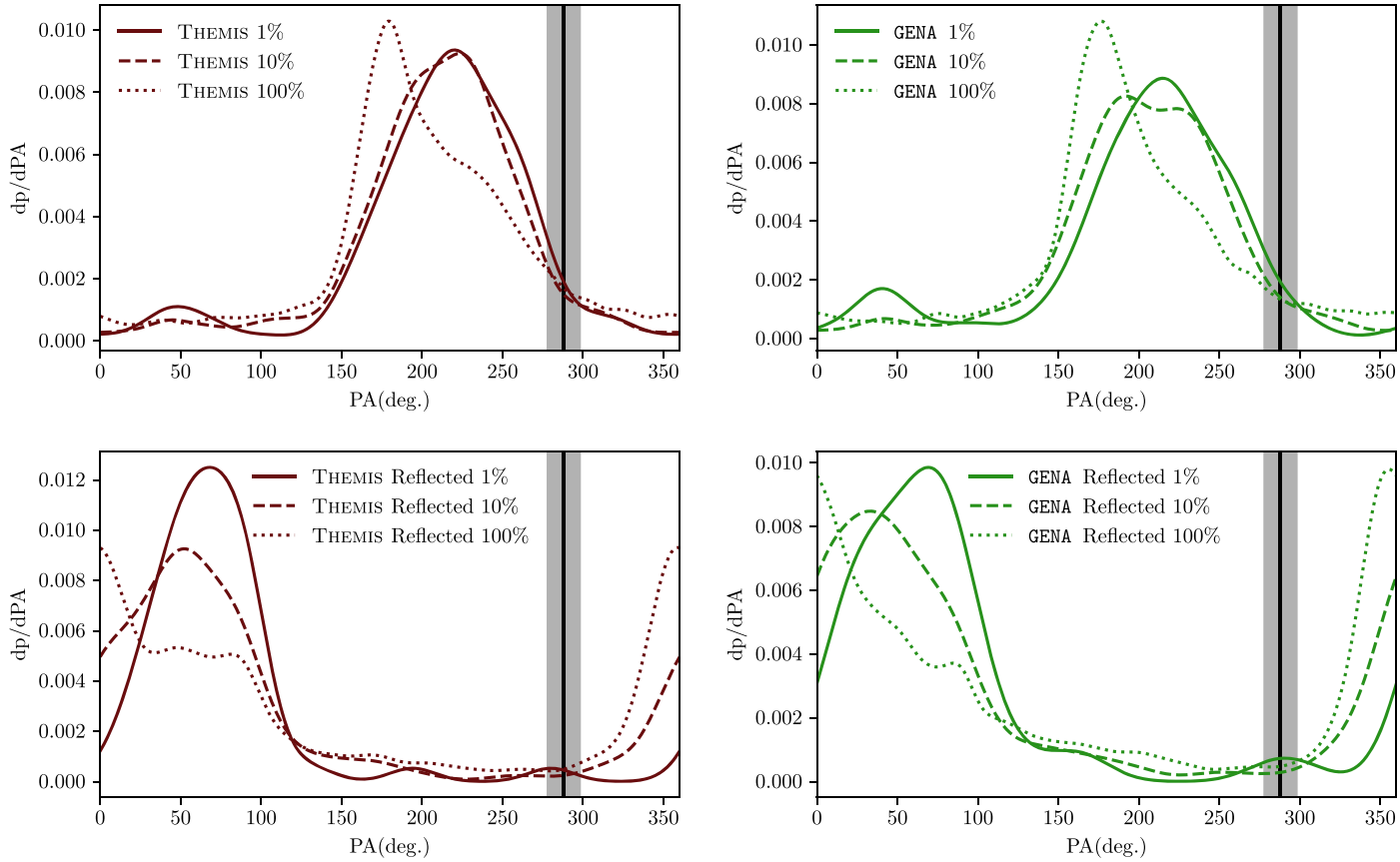

Figure 9. Top: distribution of best-fit PA (in degree) scored by the THEMIS (left) and GENA (right) pipelines for models with black hole spin vector pointing away from Earth ($i > 90°$ for $a_* > 0$ or $i < 90°$ for $a_* < 0$). Bottom: images with black hole spin vector pointing toward Earth ($i < 90°$ for $a_* > 0$ or $i > 90°$ for $a_* < 0$). Smooth lines were drawn with a wrapped Gaussian kernel density estimator. The three lines show (1) all images in the sample (dotted line); (2) the best-fit 10% of images within each model (dashed line); and (3) the best-fit 1% of images in each model (solid line). For reference, the vertical line shows the position angle PA $\sim 288°$ of the large-scale (mas) jet Walker et al. (2018), with the gray area from $(288 - 10)°$ to $(288 + 10)°$ indicating the observed PA variation.

turbulent dissipation, and Coulomb heating, which transfers energy from the hot ions to the cooler electrons. In our suite of simulations the parameter $R_{\rm high}$ can be thought of as a proxy for the sum of these processes. In a fully self-consistent treatment, some models would rapidly cool and settle to a lower electron temperature (see Mościbrodzka et al. 2011; Ryan et al. 2018; Chael et al. 2019). We crudely test for this by calculating the radiative efficiency $\epsilon \equiv L_{\rm bol}/(\dot{M}c^2)$, where $L_{\rm bol}$ is the bolometric luminosity. If it is larger than the radiative efficiency of a thin, radiatively efficient disk,[117] which depends only on a_* (Novikov & Thorne 1973), then we reject the model as physically inconsistent.

We calculate $L_{\rm bol}$ with the Monte Carlo code `grmonty` (Dolence et al. 2009), which incorporates synchrotron emission, absorption, Compton scattering at all orders, and bremsstrahlung. It assumes the same thermal eDF used in generating the Image Library. We calculate $L_{\rm bol}$ for 20% of the snapshots to minimize computational cost. We then average over snapshots to find $\langle L_{\rm bol}\rangle$. The mass accretion rate $\dot{M}$ is likewise computed for each snapshot and averaged over time. We reject models with ϵ that is larger than the classical thin disk model. (Table 3 in Appendix A lists ϵ for a large set of models.) All but two of the radiatively inconsistent models are MADs with $a_* \geqslant 0$ and $R_{\rm high} = 1$. Eliminating all MAD models with $a_* \geqslant 0$ and $R_{\rm high} = 1$ does not change any of our earlier conclusions.

6.2. X-Ray Constraints

As part of the EHT2017 campaign, we simultaneously observed M87 with the *Chandra* X-ray observatory and the *Nuclear Spectroscopic Telescope Array* (*NuSTAR*). The best fit to simultaneous *Chandra* and *NuSTAR* observations on 2017 April 12 and 14 implies a 2–10 keV luminosity of $L_{\rm X_{obs}} = 4.4 \pm 0.1 \times 10^{40}$ erg s^{-1}. We used the SEDs generated from the simulations while calculating $L_{\rm bol}$ to reject models that consistently overproduce X-rays; specifically, we reject models with $\log L_{\rm X_{obs}} < \log\langle L_{\rm X}\rangle - 2\sigma(\log L_{\rm X})$. We do not reject underluminous models because the X-rays could in principle be produced by direct synchrotron emission from nonthermal electrons or by other unresolved sources. Notice that $L_{\rm X}$ is highly variable in all models so that the X-ray observations currently reject only a few models. Table 3 in Appendix A shows $\langle L_{\rm X}\rangle$ as well as upper and lower limits for a set of models that is distributed uniformly across the parameter space.

In our models the X-ray flux is produced by inverse Compton scattering of synchrotron photons. The X-ray flux is an increasing function of $\tau_T T_e^2$ where τ_T is a characteristic Thomson optical depth ($\tau_T \sim 10^{-5}$), and the characteristic amplification factor for photon energies is $\propto T_e^2$ because the X-ray band is dominated by singly scattered photons interacting with relativistic electrons (we

[117] The thin disk radiative efficiency is 0.038 for $a_* = -1$, 0.057 for $a_* = 0$, and 0.42 for $a_* = 1$. See Equations (2.12) and (2.21) of Bardeen et al. (1972); the efficiency is $1 - E/\mu_p$, where μ_p is the rest mass of the particle. The rejected model list is identical if instead one simply rejects all models with $\epsilon > 0.2$.

include all scattering orders in the Monte Carlo calculation). Increasing $R_{\rm high}$ at fixed $F_\nu(230\ \ {\rm GHz})$ tends to increase $\dot{M}$ and therefore τ_T and decrease T_e. The increase in T_e dominates in our ensemble of models, and so models with small $R_{\rm high}$ have larger $L_{\rm X}$, while models with large $R_{\rm high}$ have smaller $L_{\rm X}$. The effect is not strictly monotonic, however, because of noise in our sampling process and the highly variable nature of the X-ray emission.

The overluminous models are mostly SANE models with $R_{\rm high} \leqslant 20$. The model with the highest $\langle L_{\rm X}\rangle = 4.2 \times 10^{42}$ erg s^{-1} is a SANE, $a_* = 0$, $R_{\rm high} = 10$ model. The corresponding model with $R_{\rm high} = 1$ has $\langle L_{\rm X}\rangle = 2.1 \times 10^{41}$ erg s^{-1}, and the difference between these two indicates the level of variability and the sensitivity of the average to the brightest snapshot. The upshot of application of the $L_{\rm X}$ constraints is that $L_{\rm X}$ is sensitive to $R_{\rm high}$. Very low values of $R_{\rm high}$ are disfavored. $L_{\rm X}$ thus most directly constrains the electron temperature model.

6.3. Jet Power

Estimates of M87's jet power ($P_{\rm jet}$) have been reviewed in Reynolds et al. (1996), Li et al. (2009), de Gasperin et al. (2012), Broderick et al. (2015), and Prieto et al. (2016). The estimates range from 10^{42} to 10^{45} erg s^{-1}. This wide range is a consequence of both physical uncertainties in the models used to estimate $P_{\rm jet}$ and the wide range in length and timescales probed by the observations. Some estimates may sample a different epoch and thus provide little information on the state of the central engine during EHT2017. Nevertheless, observations of *HST*-1 yield $P_{\rm jet} \sim 10^{44}$ erg s^{-1} (e.g., Stawarz et al. 2006). *HST*-1 is within ~70 pc of the central engine and, taking account of relativistic time foreshortening, may be sampling the central engine $P_{\rm jet}$ over the last few decades. Furthermore, the 1.3 mm light curve of M87 as observed by SMA shows $\lesssim$50% variability over decade timescales (Bower et al. 2015). Based on these considerations it seems reasonable to adopt a very conservative lower limit on jet power $\equiv P_{\rm jet,min} = 10^{42}$ erg s^{-1}.

To apply this constraint we must define and measure $P_{\rm jet}$ in our models. Our procedure is discussed in detail in Appendix A. In brief, we measure the total energy flux in outflowing regions over the polar caps of the black hole in which the energy per unit rest mass exceeds $2.2\,c^2$, which corresponds to $\beta\gamma = 1$, where $\beta \equiv v/c$ and γ is Lorentz factor. The effect of changing this cutoff is also discussed in Appendix A. Because the cutoff is somewhat arbitrary, we also calculate $P_{\rm out}$ by including the energy flux in all outflowing regions over the polar caps of the black hole; that is, it includes the energy flux in any wide-angle, low-velocity wind. $P_{\rm out}$ represents a maximal definition of jet power. Table 3 in Appendix A shows $P_{\rm jet}$ as well as a total outflow power $P_{\rm out}$.

The constraint $P_{\rm jet} > P_{\rm jet,min} = 10^{42}$ erg s^{-1} rejects all $a_* = 0$ models. This conclusion is not sensitive to the definition of $P_{\rm jet}$: all $a_* = 0$ models also have total outflow power $P_{\rm out} < 10^{42}$ erg s^{-1}. The most powerful $a_* = 0$ model is a MAD model with $R_{\rm high} = 160$, which has $P_{\rm out} = 3.7 \times 10^{41}$ erg s^{-1} and $P_{\rm jet}$ consistent with 0. We conclude that our $a_* = 0$ models are ruled out.

Can the $a_* = 0$ models be saved by changing the eDF? Probably not. There is no evidence from the GRMHD simulations that these models are capable of producing a relativistic outflow with $\beta\gamma > 1$. Suppose, however, that we are willing to identify the nonrelativistic outflow, whose power is measured by $P_{\rm out}$, with the jet. Can $P_{\rm out}$ be raised to meet our conservative threshold on jet power? Here the answer is yes, in principle, and this can be done by changing the eDF. The eDF and $P_{\rm out}$ are coupled because $P_{\rm out}$ is determined by $\dot{M}$, and $\dot{M}$ is adjusted to produce the observed compact mm flux. The relationship between $\dot{M}$ and mm flux depends upon the eDF. If the eDF is altered to produce mm photons less efficiently (for example, by lowering T_e in a thermal model), then $\dot{M}$ and therefore $P_{\rm out}$ increase. A typical nonthermal eDF, by contrast, is likely to produce mm photons with greater efficiency by shifting electrons out of the thermal core and into a nonthermal tail. It will therefore lower $\dot{M}$ and thus $P_{\rm out}$. A thermal eDF with lower T_e could have higher $P_{\rm out}$, as is evident in the large $R_{\rm high}$ SANE models in Table 3. There are observational and theoretical lower limits on T_e, however, including a lower limit provided by the observed brightness temeprature. As T_e declines, n_e and B increase and that has implications for source linear polarization (Mościbrodzka et al. 2017; Jiménez-Rosales & Dexter 2018), which will be explored in future work. As T_e declines and n_e and n_i increase there is also an increase in energy transfer from ions to electrons by Coulomb coupling, and this sets a floor on T_e.

The requirement that $P_{\rm jet} > P_{\rm jet,min}$ eliminates many models other than the $a_* = 0$ models. All SANE models with $|a_*| = 0.5$ fail to produce jets with the required minimum power. Indeed, they also fail the less restrictive condition $P_{\rm out} > P_{\rm jet,min}$, so this conclusion is insensitive to the definition of the jet. We conclude that among the SANE models, only high-spin models survive.

At this point it is worth revisiting the SANE, $R_{\rm high} = 1$, $a_* = -0.94$ model that favored a low black hole mass in Section 5. These models are not rejected by a naive application of the $P_{\rm jet} > P_{\rm jet,min}$ criterion, but they are marginal. Notice, however, that we needed to assume a mass in applying the this criterion. We have consistently assumed $M = 6.2 \times 10^9\,M_\odot$. If we use the $M \sim 3 \times 10^9\,M_\odot$ implied by the best-fit M/D, then $\dot{M}$ drops by

Table 1
Average Image Scoring[a] Summary

Flux[b]	a_*[c]	$\langle p\rangle$[d]	$N_{\rm model}$[e]	MIN(p)[f]	MAX(p)[g]
SANE	−0.94	0.33	24	0.01	0.88
SANE	−0.5	0.19	24	0.01	0.73
SANE	0	0.23	24	0.01	0.92
SANE	0.5	0.51	30	0.02	0.97
SANE	0.75	0.74	6	0.48	0.98
SANE	0.88	0.65	6	0.26	0.94
SANE	0.94	0.49	24	0.01	0.92
SANE	0.97	0.12	6	0.06	0.40
MAD	−0.94	0.01	18	0.01	0.04
MAD	−0.5	0.75	18	0.34	0.98
MAD	0	0.22	18	0.01	0.62
MAD	0.5	0.17	18	0.02	0.54
MAD	0.75	0.28	18	0.01	0.72
MAD	0.94	0.21	18	0.02	0.50

Notes.
[a] The Average Image Scoring (THEMIS-AIS) is introduced in Section 4.
[b] flux: net magnetic flux on the black hole (MAD or SANE).
[c] a_*: dimensionless black hole spin.
[d] $\langle p\rangle$: mean of the p value for the aggregated models.
[e] $N_{\rm model}$: number of aggregated models.
[f] MIN(p): minimum p value among the aggregated models.
[g] MAX(p): maximum p value among the aggregated models.

Table 2
Rejection Table

Flux[a]	a_*[b]	$R_{\rm high}$[c]	AIS[d]	ϵ[e]	L_X[f]	$P_{\rm jet}$[g]	
SANE	−0.94	1	Fail	Pass	Pass	Pass	Fail
SANE	−0.94	10	Pass	Pass	Pass	Pass	Pass
SANE	−0.94	20	Pass	Pass	Pass	Pass	Pass
SANE	−0.94	40	Pass	Pass	Pass	Pass	Pass
SANE	−0.94	80	Pass	Pass	Pass	Pass	Pass
SANE	−0.94	160	Fail	Pass	Pass	Pass	Fail
SANE	−0.5	1	Pass	Pass	Fail	Fail	Fail
SANE	−0.5	10	Pass	Pass	Fail	Fail	Fail
SANE	−0.5	20	Pass	Pass	Pass	Fail	Fail
SANE	−0.5	40	Pass	Pass	Pass	Fail	Fail
SANE	−0.5	80	Fail	Pass	Pass	Fail	Fail
SANE	−0.5	160	Pass	Pass	Pass	Fail	Fail
SANE	0	1	Pass	Pass	Pass	Fail	Fail
SANE	0	10	Pass	Pass	Pass	Fail	Fail
SANE	0	20	Pass	Pass	Fail	Fail	Fail
SANE	0	40	Pass	Pass	Pass	Fail	Fail
SANE	0	80	Pass	Pass	Pass	Fail	Fail
SANE	0	160	Pass	Pass	Pass	Fail	Fail
SANE	+0.5	1	Pass	Pass	Pass	Fail	Fail
SANE	+0.5	10	Pass	Pass	Pass	Fail	Fail
SANE	+0.5	20	Pass	Pass	Pass	Fail	Fail
SANE	+0.5	40	Pass	Pass	Pass	Fail	Fail
SANE	+0.5	80	Pass	Pass	Pass	Fail	Fail
SANE	+0.5	160	Pass	Pass	Pass	Fail	Fail
SANE	+0.94	1	Pass	Fail	Pass	Fail	Fail
SANE	+0.94	10	Pass	Fail	Pass	Fail	Fail
SANE	+0.94	20	Pass	Pass	Pass	Fail	Fail
SANE	+0.94	40	Pass	Pass	Pass	Fail	Fail
SANE	+0.94	80	Pass	Pass	Pass	Pass	Pass
SANE	+0.94	160	Pass	Pass	Pass	Pass	Pass
MAD	−0.94	1	Fail	Fail	Pass	Pass	Fail
MAD	−0.94	10	Fail	Pass	Pass	Pass	Fail
MAD	−0.94	20	Fail	Pass	Pass	Pass	Fail
MAD	−0.94	40	Fail	Pass	Pass	Pass	Fail
MAD	−0.94	80	Fail	Pass	Pass	Pass	Fail
MAD	−0.94	160	Fail	Pass	Pass	Pass	Fail
MAD	−0.5	1	Pass	Fail	Pass	Fail	Fail
MAD	−0.5	10	Pass	Pass	Pass	Fail	Fail
MAD	−0.5	20	Pass	Pass	Pass	Pass	Pass
MAD	−0.5	40	Pass	Pass	Pass	Pass	Pass
MAD	−0.5	80	Pass	Pass	Pass	Pass	Pass
MAD	−0.5	160	Pass	Pass	Pass	Pass	Pass
MAD	0	1	Pass	Fail	Pass	Fail	Fail
MAD	0	10	Pass	Pass	Pass	Fail	Fail
MAD	0	20	Pass	Pass	Pass	Fail	Fail
MAD	0	40	Pass	Pass	Pass	Fail	Fail
MAD	0	80	Pass	Pass	Pass	Fail	Fail
MAD	0	160	Pass	Pass	Pass	Fail	Fail
MAD	+0.5	1	Pass	Fail	Pass	Fail	Fail
MAD	+0.5	10	Pass	Pass	Pass	Pass	Pass
MAD	+0.5	20	Pass	Pass	Pass	Pass	Pass
MAD	+0.5	40	Pass	Pass	Pass	Pass	Pass
MAD	+0.5	80	Pass	Pass	Pass	Pass	Pass
MAD	+0.5	160	Pass	Pass	Pass	Pass	Pass
MAD	+0.94	1	Pass	Fail	Fail	Pass	Fail
MAD	+0.94	10	Pass	Fail	Pass	Pass	Fail
MAD	+0.94	20	Pass	Pass	Pass	Pass	Pass
MAD	+0.94	40	Pass	Pass	Pass	Pass	Pass
MAD	+0.94	80	Pass	Pass	Pass	Pass	Pass
MAD	+0.94	160	Pass	Pass	Pass	Pass	Pass

Notes.
[a] flux: net magnetic flux on the black hole (MAD, SANE).
[b] a_*: dimensionless black hole spin.
[c] $R_{\rm high}$: electron temperature parameter. See Equation (8).
[d] Average Image Scoring (THEMIS-AIS), models are rejected if $\langle p \rangle \leqslant 0.01$. See Section 4 and Table 1.
[e] ϵ: radiative efficiency, models are rejected if ϵ is larger than the corresponding thin disk efficiency. See Section 6.1.
[f] L_X: X-ray luminosity; models are rejected if $\langle L_X \rangle 10^{-2\sigma} > 4.4 \times 10^{40}$ erg s^{-1}. See Section 6.2.
[g] $P_{\rm jet}$: jet power, models are rejected if $P_{\rm jet} \leqslant 10^{42}$ erg s^{-1}. See Section 6.3.

a factor of two, $P_{\rm jet}$ drops below the threshold and the model is rejected.

The lower limit on jet power $P_{\rm jet,min} = 10^{42}$ erg s^{-1} is conservative and the true jet power is likely higher. If we increased $P_{\rm jet,min}$ to 3×10^{42} erg s^{-1}, the only surviving models would have $|a_*| = 0.94$ and $R_{\rm high} \geqslant 10$. This conclusion is also not sensitive to the definition of the jet power: applying the same cut to $P_{\rm out}$ adds only a single model with $|a_*| < 0.94$, the $R_{\rm high} = 160$, $a_* = 0.5$ MAD model. The remainder have $a_* = 0.94$. Interestingly, the most powerful jets in our ensemble of models are produced by SANE, $a_* = -0.94$, $R_{\rm high} = 160$ models, with $P_{\rm jet} \simeq 10^{43}$ erg s^{-1}.

Estimates for $P_{\rm jet}$ extend to 10^{45} erg s^{-1}, but in our ensemble of models the maximum $P_{\rm jet} \sim 10^{43}$ erg s^{-1}. Possible explanations include: (1) $P_{\rm jet}$ is variable and the estimates probe the central engine power at earlier epochs (discussed above); (2) the $P_{\rm jet}$ estimates are too large; or (3) the models are in error. How might our models be modified to produce a larger $P_{\rm jet}$? For a given magnetic field configuration the jet power scales with $\dot{M}c^2$. To increase $P_{\rm jet}$, then, one must reduce the mm flux per accreted nucleon so that at fixed mm flux density $\dot{M}$ increases.[118] Lowering T_e in a thermal model is unlikely to work because lower T_e implies higher synchrotron optical depth, which increases the ring width. We have done a limited series of experiments that suggest that even a modest decrease in T_e would produce a broad ring that is inconsistent with EHT2017 (Paper VI). What is required, then, is a nonthermal (or multitemperature) model with a large population of cold electrons that are invisible at mm wavelength (for a thermal subpopulation, $\Theta_{e,\rm cold} < 1$), and a population of higher-energy electrons that produces the observed mm flux (see Falcke & Biermann 1995). We have not considered such models here, but we note that they are in tension with current ideas about dissipation of turbulence because they require efficient suppression of electron heating.

The $P_{\rm jet}$ in our models is dominated by Poynting flux in the force-free region around the axis (the "funnel"), as in the Blandford & Znajek (1977) force-free magnetosphere model. The energy flux is concentrated along the walls of the funnel.[119] Tchekhovskoy et al. (2011) provided an expression for the energy flux in the funnel, the so-called Blandford–Znajek power $P_{\rm BZ}$, which becomes, in our units,

$$\begin{aligned} P_{\rm BZ} &= 2.8 f(a_*) \left(\frac{\phi}{15}\right)^2 \dot{M}c^2 \\ &= 2.2 \times 10^{43} f(a_*) \left(\frac{\phi}{15}\right)^2 \\ &\quad \times \left(\frac{\dot{M}}{10^{-6}\dot{M}_{\rm Edd}}\right)\left(\frac{M}{6.2 \times 10^9 M_\odot}\right) \text{ erg s}^{-1} \end{aligned} \tag{9}$$

where $f(a_*) \approx a_*^2(1 + \sqrt{1 - a_*^2})^{-2}$ (a good approximation for $a_* < 0.95$) and $\dot{M}_{\rm Edd} = 137\, M_\odot$ yr^{-1} for $M = 6.2 \times 10^9\, M_\odot$. This expression was developed for models with a thin disk in the equatorial plane. $P_{\rm BZ}$ is lower for models where the force-free region is excluded by a thicker disk around the equatorial plane. Clearly $P_{\rm BZ}$ is comparable to observational estimates of $P_{\rm jet}$.

[118] The compact mm flux density could be a factor of 2 larger than our assumed 0.5 Jy. That would raise $P_{\rm jet}$ by slightly less than a factor of 2.

[119] The total energy flux inside a cone of opening angle θ_0 is proportional to $\sin^4\theta_0$ in the Blandford & Znajek (1977) monopole model if the field strength is fixed, and $\sin^2\theta_0$ if the magnetic flux is fixed.

In our models (see Table 3) $P_{\rm jet}$ follows the above scaling relation but with a smaller coefficient. The ratio of coefficients is model dependent and varies from 0.15 to 0.83. This is likely because the force-free region is restricted to a cone around the poles of the black hole, and the width of the cone varies by model. Indeed, the coefficient is larger for MAD than for SANE models, which is consistent with this idea because MAD models have a wide funnel and SANE models have a narrow funnel. This also suggests that future comparison of synthetic 43 and 86 GHz images from our models with lower-frequency VLBI data may further constrain the magnetic flux on the black hole.

The connection between the Poynting flux in the funnel and black hole spin has been discussed for some time in the simulation literature, beginning with McKinney & Gammie (2004; see also McKinney 2006; McKinney & Narayan 2007). The structure of the funnel magnetic field can be time-averaged and shown to match the analytic solution of Blandford & Znajek (1977). Furthermore, the energy flux density can be time-averaged and traced back to the event horizon. Is the energy contained in black hole spin sufficient to drive the observed jet over the jet lifetime? The spindown timescale is $\tau = (M - M_{\rm irr})c^2/P_{\rm jet}$, where $M_{\rm irr} \equiv M((1+\sqrt{1-a_*^2})/2)^{1/2}$ is the irreducible mass of the black hole. For the $a_* = 0.94$ MAD model with $R_{\rm high} = 160$, $\tau = 7.3 \times 10^{12}$ yr, which is long compared to a Hubble time ($\sim 10^{10}$ yr). Indeed, the spindown time for all models is long compared to the Hubble time.

We conclude that for models that have sufficiently powerful jets and are consistent with EHT2017, $P_{\rm jet}$ is driven by extraction of black hole spin energy through the Blandford–Znajek process.

6.4. Constraint Summary

We have applied constraints from AIS, a radiative self-consistency constraint, a constraint on maximum X-ray luminosity, and a constraint on minimum jet power. Which models survive? Here we consider only models for which we have calculated $L_{\rm X}$ and $L_{\rm bol}$. Table 2 summarizes the results. Here we consider only $i = 163°$ (for $a_* \geqslant 0$) and $i = 17°$ (for $a_* < 0$). The first three columns give the model parameters. The next four columns show the result of application of each constraint: THEMIS-AIS (here broken out by individual model rather than groups of models), radiative efficiency ($\epsilon < \epsilon_{\rm thin\ \ disk}$), $L_{\rm X}$, and $P_{\rm jet}$.

The final column gives the logical AND of the previous four columns, and allows a model to pass only if it passes all tests. Evidently most of the SANE models fail, with the exception of some $a_* = -0.94$ models and a few $a_* = 0.94$ models with large $R_{\rm high}$. A much larger fraction of the MAD models pass, although $a_* = 0$ models all fail because of inadequate jet power. MAD models with small $R_{\rm high}$ also fail. It is the jet power constraint that rejects the largest number of models.

7. Discussion

We have interpreted the EHT2017 data using a limited library of models with attendant limitations. Many of the limitations stem from the GRMHD model, which treats the plasma as an ideal fluid governed by equations that encode conservation laws for particle number, momentum, and energy. The eDF, in particular, is described by a number density and temperature, rather than a full distribution function, and the electron temperature T_e is assumed to be a function of the local ion temperature and plasma $\beta_{\rm p}$. Furthermore, all models assume a Kerr black hole spacetime, but there are alternatives. Here we consider some of the model limitations and possible extensions, including to models beyond general relativity.

7.1. Radiative Effects

Post-processed GRMHD simulations that are consistent with EHT data and the flux density of 1.3 mm emission in M87 can yield unphysically large radiative efficiencies (see Section 6). This implies that the radiative cooling timescale is comparable to or less than the advection timescale. As a consequence, including radiative cooling in simulations may be necessary to recover self-consistent models (see Mościbrodzka et al. 2011; Dibi et al. 2012). In our models we use a single parameter, $R_{\rm high}$, to adjust T_e and account for all effects that might influence the electron energy density. How good is this approximation?

The importance of radiative cooling can be assessed using newly developed, state-of-the-art general relativistic radiation GRMHD ("radiation GRMHD") codes. Sądowski et al. (2013b; see also Sądowski et al. 2014, 2017; McKinney et al. 2014) applied the M1 closure (Levermore 1984), which treats the radiation as a relativistic fluid. Ryan et al. (2015) introduced a Monte Carlo radiation GRMHD method, allowing for full frequency-dependent radiation transport. Models for turbulent dissipation into the electrons and ions, as well as heating and cooling physics that sets the temperature ratio T_i/T_e, have been added to GRMHD and radiative GRMHD codes and used in simulations of Sgr A* (Ressler et al. 2015, 2017; Chael et al. 2018) and M87 (Ryan et al. 2018; Chael et al. 2019). While the radiative cooling and Coulomb coupling physics in these simulations is well understood, the particle heating process, especially the relative heating rates of ions and electrons, remains uncertain.

Radiation GRMHD models are computationally expensive per run and do not have the same scaling freedom as the GRMHD models, so they need to be repeatedly re-run with different initial conditions until they produce the correct 1.3 mm flux density. It is therefore impractical to survey the parameter space using radiation GRMHD. It is possible, however, to check individual GRMHD models against existing radiation GRMHD models of M87 (Ryan et al. 2018; Chael et al. 2019).

The SANE radiation GRMHD models of Ryan et al. (2018) with $a_* = 0.94$ and $M = 6 \times 10^9\,M_\odot$ can be compared to GRMHD SANE $a_* = 0.94$ models at various values of $R_{\rm high}$. The radiative models have $\dot{M}/\dot{M}_{\rm Edd} = 5.2 \times 10^{-6}$ and $P_{\rm jet} = 5.1 \times 10^{41}$ erg s^{-1}. The GRMHD models in this work have, for $1 \leqslant R_{\rm high} \leqslant 160$, $0.36 \times 10^{-6} \leqslant \dot{M}/\dot{M}_{\rm Edd} \leqslant 20 \times 10^{-6}$, and $0.22 \leqslant P_{\rm jet}/(10^{41}\ {\rm erg\ s^{-1}}) \leqslant 12$ (Table 3). Evidently the mass accretion rates and jet powers in the GRMHD models span a wide range that depends on $R_{\rm high}$, but when we choose $R_{\rm high} = 10 - 20$ they are similar to what is found in the radiative GRMHD model when using the turbulent electron heating model (Howes 2010).

We have also directly compared the T_e distribution in the emitting region, and the radiation GRMHD model is quite close to the $R_{\rm high} = 10$ model. The resulting images are qualitatively

similar, with an asymmetric photon ring that is brighter in the south and a weak inner ring associated with the funnel wall emission as in Figure 2. The radiation GRMHD SANE model, like all our nonradiative GRMHD SANE models (except the $R_{\rm high} = 160$ model), would be ruled out by the condition $P_{\rm jet} > 10^{42}$ erg s^{-1}.

The MAD radiation GRMHD models of Chael et al. (2019) with $a_* = 0.94$ and $M = 6.2 \times 10^9 M_\odot$ can be compared to GRMHD MAD $a_* = 0.94$ models at various values of $R_{\rm high}$. Chael et al. (2019) uses two dissipation models: the Howes (2010, hereafter H10) model of heating from a Landau-damped turbulent cascade, and the Rowan et al. (2017, hereafter R17) model of heating based on simulations of transrelativistic magnetic reconnection. The (H10, R17) models have $\dot{M}/\dot{M}_{\rm Edd} = (3.6, 2.3) \times 10^{-6}$ and $P_{\rm jet} = (6.6, 13) \times 10^{42}$ erg s^{-1}. The GRMHD models have, for $1 \leqslant R_{\rm high} \leqslant 160$, $0.13 \times 10^{-6} \leqslant \dot{M}/\dot{M}_{\rm Edd} \leqslant 1.4 \times 10^{-6}$ and $2.3 \leqslant P_{\rm jet}/(10^{42}$ erg s$^{-1}) \leqslant 8.8$ (Table 3). In the radiation GRMHD MAD models $\dot{M}$ lies in the middle of the range spanned by the nonradiative GRMHD models, and jet power lies at the upper end of the range spanned by the nonradiative GRMHD models. The T_e distributions in the radiative and nonradiative MAD models differ: the mode of the radiation GRMHD model T_e distribution is about a factor of 3 below the mode of the T_e distribution in the $R_{\rm high} = 20$ GRMHD model, and the GRMHD model has many more zones at $\Theta_e \sim 100$ that contribute to the final image than the radiation GRMHD models. This difference is a consequence of the $R_{\rm high}$ model for T_e: in MAD models almost all the emission emerges at $\beta_{\rm p} \lesssim 1$, so $R_{\rm high}$, which changes T_e in the $\beta_{\rm p} > 1$ region, offers little control over T_e in the emission region. Nevertheless, the jet power and accretion rates are similar in the radiative and nonradiative MAD models, and the time-averaged radiative and nonradiative images are qualitatively indistinguishable. This suggests that the image is determined mainly by the spacetime geometry and is insensitive to the details of the plasma evolution.

This review of radiative effects is encouraging but incomplete: it only considers a limited selection of models and a narrow set of observational constraints. Future studies of time dependence and polarization are likely to sharpen the contrast between radiative and nonradiative models.

7.2. Nonthermal Electrons

Throughout this Letter we have considered only a thermal eDF. While a thermal eDF can account for the observed emission at mm wavelengths in M87 (e.g., Mościbrodzka et al. 2016; Prieto et al. 2016; Ryan et al. 2018; Chael et al. 2019), eDFs that include a nonthermal tail can also explain the observed SED (Broderick & Loeb 2009; Yu et al. 2011; Dexter et al. 2012; Li et al. 2016; Davelaar et al. 2018; J. Davelaar et al. 2019, in preparation).

The role of nonthermal electrons (and positrons) in producing the observed compact emission is not a settled question, and cannot be settled in this first investigation of EHT2017 models, but there are constraints. The number density, mean velocity, and energy density of the eDF are fixed or limited by the GRMHD models. In addition, the eDF cannot on average sustain features that would be erased by kinetic instabilities on timescales short compared to $r_{\rm g} c^{-1}$. Some nonthermal eDFs increase $F_\nu/\dot{M}$ in comparison to a thermal eDF, implying lower values of $\dot{M}$ than quoted above (Ball et al. 2018; Davelaar et al. 2018; J. Davelaar et al. 2019, in preparation). These lower values of $\dot{M}$ can slightly change the source morphology, e.g., by decreasing the visibility of the approaching jet (e.g., Dexter et al. 2012).

One can evaluate the influence of nonthermal eDFs in several ways. For example, it is possible to study simplified, phenomenological models. Emission features due to the cooling of nonthermal electrons may then reveal how and where the nonthermal electrons are produced (Pu et al. 2017). Emission features created by the injection of nonthermal electrons within GRMHD models of the jet and their subsequent cooling will be studied separately (T. Kawashima et al. 2019, in preparation). The effect of nonthermal eDFs can also be studied by post-processing of ideal GRMHD models if one assumes that the electrons have a fixed, parameterized form such as a power-law distribution (Dexter et al. 2012) or a κ-distribution (Davelaar et al. 2018; J. Davelaar et al. 2019, in preparation). These parameterized models produce SEDs that agree with radio to near-infrared data, but they are approximations to the underlying physics and do not resolve the microscopic processes that accelerate particles. One can also include dissipative processes explicitly in the GRMHD models, including scalar resistivity (Palenzuela et al. 2009; Dionysopoulou et al. 2013; Del Zanna et al. 2016; Qian et al. 2017; Ripperda et al. 2019), heat fluxes and viscosities (pressure anisotropies; Chandra et al. 2015; Ressler et al. 2015; Foucart et al. 2017), and particle acceleration (e.g., Chael et al. 2017). Ultimately special and general relativistic particle-in-cell codes (Watson & Nishikawa 2010; Chen et al. 2018; Levinson & Cerutti 2018; Parfrey et al. 2019) will enable direct investigations of kinetic processes.

7.3. Other Models and Analysis Limitations

We have used a number of other approximations in generating our models. Among the most serious ones are as follows.

(1) Fast Light Approximation. A GRMHD simulation produces a set of dump files containing the model state at a single global (Kerr–Schild) coordinate time. Because the dynamical time is only slightly longer than the light-crossing time, in principle one needs to trace rays through a range of coordinate times, i.e., by interpolation between multiple closely spaced dump files. In practice this is difficult because a high cadence of output files is required, limiting the speed of the GRMHD simulations and requiring prohibitively large data storage. In addition, the cost of ray tracing through multiple output files is high. Because of this, we adopt the commonly used fast light approximation in which GRMHD variables are read from a single dump file and held steady during the ray tracing. Including light-travel time delays produces minor changes to the small-scale image structure and to light curves (e.g., Dexter et al. 2010; Bronzwaer et al. 2018; Z. Younsi et al. 2019b, in preparation), although it is essential for the study of variability on the light-crossing timescale.

(2) Untilted Disks. We have assumed that the disk angular momentum vector and black hole spin vector are (anti-) aligned. There is no reason for the angular momentum vector of the accretion flow on large scales to align with the black hole spin vector, and there is abundant evidence for misaligned disks in AGNs (e.g., Miyoshi et al. 1995). How might disk tilt affect our results?

Tilting the disk by as little as $\sim 15°$ is enough to set up a standing, two-armed spiral shock close to the ISCO (Fragile & Blaes 2008). This shock directly affects the morphology of mm wavelength images, especially at low inclination, in models of Sgr A* (Dexter & Fragile 2013, especially Figure 5), producing an obvious two-armed spiral pattern on the sky. If this structure were also present in images of tilted models of M87, then it is possible that even a modest tilt could be ruled out.

If a modest tilt is present in M87 it is unlikely to affect our conclusion regarding the sign of black hole spin. That conclusion depends on emission from funnel wall plasma in counter-rotating ($a_* < 0$) disks. The funnel wall plasma is loaded onto funnel plasma field lines by local instabilities at the wall and then rotates with the funnel and therefore the black hole (Wong et al. 2019). The funnel wall is already unsteady, fluctuating by tens of degrees in azimuth and in time, so a modest tilt seems unlikely to dramatically alter the funnel wall structure.

Is there observational evidence for tilt in M87? In numerical studies of tilted disks the jet emerges perpendicular to the disk (Liska et al. 2018), and tilted disks are expected to precess. One might then expect that a tilted source would produce a jet that exhibits periodic variations, or periodic changes in jet direction with distance from the source, as seen in other sources. There is little evidence of this in M87 (see Park et al. 2019 for a discussion of possible misaligned structure in the jet). Indeed, Walker et al. (2018) saw at most small displacements of the jet with time and distance from the source at mas scales. In sum, there is therefore little observational motivation for considering tilted disk models.

Tilted disk models of M87 are an interesting area for future study. It is possible that the inner disk may align with the black hole via a thick-disk variant of the Bardeen & Petterson (1975) effect. Existing tilted thick-disk GRMHD simulations (e.g., Fragile et al. 2007; McKinney et al. 2013; Shiokawa 2013; Liska et al. 2018) show some evidence for alignment and precession (McKinney et al. 2013; Shiokawa 2013; Liska et al. 2018), but understanding of the precession and alignment timescales is incomplete. It will be challenging to extend the Image Library to include a survey of tilted disk models, however, because with tilted disks there are two new parameters: the two angles that describe the orientation of the outer disk with respect to the black hole spin vector and the line of sight.

(3) Pair Production. In some models of M87 the mm emission is dominated by electron-positron pairs within the funnel, even close to the horizon scale (see Beskin et al. 1992; Levinson & Rieger 2011; Mościbrodzka et al. 2011; Broderick & Tchekhovskoy 2015; Hirotani & Pu 2016). The pairs are produced from the background radiation field or from a pair-cascade process following particle acceleration by unscreened electric fields, which we cannot evaluate using ideal GRMHD models. We leave it to future work to assess whether or not these models can plausibly suppress emission from the disk and funnel wall, and simultaneously produce a sufficiently powerful jet.

(4) Numerical Treatment of Low-density Regions. Virtually all MHD simulations, including ours, use a "floor" procedure that resets the density if it falls below a minimum value. If this is not done, then truncation error accumulates dramatically in the low-density regions and the solution is corrupted. If the volume where floors are activated contains only a small fraction of the simulation mass, momentum, and energy, then most aspects of the solution are unaffected by this procedure (e.g., McKinney & Gammie 2004).

In regions where the floors are activated the temperature of the plasma is no longer reliable. This is why we cut off emission from regions with $B^2/\rho > 1$, where floors are commonly activated. In models where floors are only activated in the funnel (e.g., most SANE models), the resulting images are insensitive to the choice of cutoff B^2/ρ. In MAD models the regions of low and high density are mixed because lightly loaded magnetic field lines that are trapped in the hole bubbles outward through the disk. In this case emission at $\nu >$ 230 GHz can be sensitive to the choice of cutoff B^2/ρ Chael et al. (2019). The sense of the effect is that greater cutoff B^2/ρ implies more emission at high frequency. Our use of a cutoff $B^2/\rho = 1$ is therefore likely to underestimate mm emission and therefore overestimate $\dot{M}$ and $P_{\rm jet}$. Accurate treatment of the dynamics and thermodynamics of low-density regions and especially sharp boundaries between low- and high-density regions is a fundamental numerical problem in black hole accretion flow modeling that merits further attention.

7.4. Alternatives to Kerr Black Holes

Although our working hypothesis has been that M87 contains a Kerr black hole, it is interesting to consider whether or not the data is also consistent with alternative models for the central object. These alternatives can be grouped into three main categories: (i) black holes within general relativity that include additional fields; (ii) black hole solutions from alternative theories of gravity or incorporating quantum effects; (iii) black hole "mimickers," i.e., compact objects, both within general relativity or in alternative theories, whose properties could be fine-tuned to resemble those of black holes.

The first category includes, for example, black holes in Einstein–Maxwell–dilaton-axion gravity (e.g., García et al. 1995; Mizuno et al. 2018), black holes with electromagnetic or Newman–Unti-Tamburino (NUT) charges (e.g., Grenzebach et al. 2014), regular black holes in nonlinear electrodynamics (e.g., Abdujabbarov et al. 2016), black hole metrics affected by a cosmological constant (e.g., Dymnikova 1992) or a dark matter halo (e.g., Hou et al. 2018), and black holes with scalar wigs (e.g., Barranco et al. 2017) or hair (e.g., Herdeiro & Radu 2014). While the shadows of this class of compact objects are expected to be similar to Kerr and therefore cannot be ruled out immediately by current observations (Mizuno et al. 2018), the most extreme examples of black holes surrounded by massive scalar field configurations should produce additional lobes in the shadow or disconnected dark regions (Cunha et al. 2015). As these features are not found in the EHT2017 image, these alternatives are not viable models for M87.

The second category comprises black hole solutions with classical modifications to general relativity, as well as effects coming from approaches to quantum gravity (see, e.g., Moffat 2015; Dastan et al. 2016; Younsi et al. 2016; Amir et al. 2018; Eiroa & Sendra 2018; Giddings & Psaltis 2018). These alternatives have shadows that are qualitatively very similar to those of Kerr black holes and are not distinguishable with present EHT capabilities. However, higher-frequency observations, together with the degree of polarization of the emitted radiation or the variability of the accretion flow, can be used to assess their viability.

Finally, the third category comprises compact objects such as spherically symmetric naked singularities (e.g., Joshi et al. 2014), superspinars (Kerr with $|a_*| > 1$, which are axisymmetric spacetime with naked singularities), and regular horizonless objects, either with or without a surface. Examples of regular surfaceless objects are: boson stars (Kaup 1968), traversable wormholes, and clumps of self-interacting dark matter (Saxton et al. 2016), while examples of black hole mimickers with a surface are gravastars (Mazur & Mottola 2004) and collapsed polymers (Brustein & Medved 2017), to cite only a few. Because the exotic genesis of these black hole mimickers is essentially unknown, their physical properties are essentially unconstrained, thus making the distinction from black holes rather challenging (see, however, Chirenti & Rezzolla 2007, 2016). Nevertheless, some conclusions can drawn already. For instance, the shadow of a superspinar is very different from that of a black hole (Bambi & Freese 2009), and the EHT2017 observations rule out any superspinar model for M87. Similarly, for certain parameter ranges, the shadows of spherically symmetric naked singularities have been found to consist of a filled disk with no dark region[120] in the center (Shaikh et al. 2019); clearly, this class of models is ruled out. In the same vein, because the shadows of wormholes can exhibit large deviations from those of black holes (see, e.g., Bambi 2013; Nedkova et al. 2013; Shaikh 2018), a large portion of the corresponding space of parameters can be constrained with the present observations.

A comparison of EHT2017 data with the boson star model, as a representative horizonless and surfaceless black hole mimicker, and a gravastar model as a representative horizonless black hole mimicker, will be presented in Olivares et al. (2019a). Both models produce images with ring-like features similar to those observed by EHT2017, which are consistent with the results of Broderick & Narayan (2006), who also consider black hole alternatives with a surface. The boson star generically requires masses that are substantially different from that expected for M87 (H. Olivares et al. 2019b, in preparation), while the gravastar has accretion variability that is considerably different from that onto a black hole.

In summary, because each of the many exotic alternatives to Kerr black holes can span an enormous space of parameters that is only poorly constrained, the comparisons carried out here must be considered preliminary. Nevertheless, they show that the EHT2017 observations are not consistent with several of the alternatives to Kerr black holes, and that some of those models that produce similar images show rather different dynamics in the accretion flow and in its variability. Future observations and more detailed theoretical modeling, combined with multiwavelength campaigns and polarimetric measurements, will further constrain alternatives to Kerr black holes.

8. Conclusion

In this Letter we have made a first attempt at understanding the physical implications of a single, high-quality EHT data set for M87. We have compared the data to a library of mock images produced from GRMHD simulations by GRRT calculations. The library covers a parameter space that is substantially larger than earlier model surveys. The results of this comparison are consistent with the hypothesis that the compact 1.3 mm emission in M87 arises within a few r_g of a Kerr black hole, and that the ring-like structure of the image is generated by strong gravitational lensing and Doppler beaming. The models predict that the asymmetry of the image depends on the sense of black hole spin. If this interpretation is accurate, then the spin vector of the black hole in M87 points away from Earth (the black hole spins clockwise on the sky). The models also predict that there is a strong energy flux directed away from the poles of the black hole, and that this energy flux is electromagnetically dominated. If the models are correct, then the central engine for the M87 jet is powered by the electromagnetic extraction of free energy associated with black hole spin via the Blandford–Znajek process.

In our models, M87's compact mm emission is generated by the synchrotron mechanism. Our ability to make physical inferences based on the models is therefore intimately tied to the quality of our understanding of the eDF. We have used a thermal model with a single free parameter that adjusts the ratio of ion to electron temperature in regions with plasma $\beta_p > 1$ (i.e., regions where magnetic pressure is less than gas pressure). This simple model does not span the range of possible plasma behavior. The theory of high temperature, collisionless plasmas must be better understood if this core physical uncertainty of sub-Eddington black hole accretion is to be eliminated. At present our understanding is inadequate, and alternative eDF models occupy a large, difficult-to-explore parameter space with the potential to surprise. Despite these uncertainties, many of the models produce images with similar morphology that is consistent with EHT2017 data. This suggests that the image shape is controlled mainly by gravitational lensing and the spacetime geometry, rather than details of the plasma physics.

Although the EHT2017 images are consistent with the vast majority of our models, parts of the parameter space can be rejected on physical grounds or by comparison with contemporaneous data at other wavelengths. We reject some models because, even though all models are variable, some models are *too variable* to be consistent with the data. We can also reject models based on a radiative efficiency cut (the models are not self-consistent and would cool quickly if radiative effects were included), an X-ray luminosity cut using contemporaneous *Chandra* and *NuSTAR* data, and on a jet-power cut. The requirement that the jet power exceed a conservative lower limit of 10^{42} erg s^{-1} turns out to eliminate many models, including all models with $a_* = 0$.

We have examined the astrophysical implications of only a subset of EHT2017 data; much remains to be done, and there are significant opportunities for further constraining the models. EHT2017 data includes tracks from four separate days of observing; each day is 2.8 $r_g c^{-1}$ (see Paper IV). This timescale is short compared to the decorrelation timescale of simulated images, which is $\sim$50 $r_g c^{-1}$, and smaller than the light-crossing time of the source plasma. Analysis techniques that use short-timescale variations in the data will need to be developed and are likely to recover new, more stringent constraints on the model from the EHT2017 data set. EHT2017 took polarized data as well. Our simulations already predict full polarization maps, albeit for our simple eDF model. Comparison of model polarization maps of the source with EHT2017 data are likely to sharply limit the space of allowed models (Mościbrodzka et al. 2017). Finally, in this Letter the only multiwavelength companion data that we consider are X-ray observations. Simultaneous data are available at many other

[120] The width of the ring, the central flux depression, and a quantitative discussion of the black hole shadow can be found in Paper VI.

wavelengths, from the radio to the gamma-rays, and is likely to further limit the range of acceptable models and guide the implementation of predictive electron physics models.

In this Letter we have focused on the time-dependent ideal GRMHD model. Physically motivated, semi-analytic models including nonthermal emission have not been applied yet and will be discussed in future papers (A. E. Broderick et al. 2019b, in preparation; T. Kawashima et al. 2019, in preparation; H.-Y. Pu et al. 2019, in preparation).

We have also not yet considered how the physical properties of the jet are constrained by lower-frequency VLBI observations, which constrain jet kinematics (Mertens et al. 2016; Britzen et al. 2017; Hada et al. 2017; Kim et al. 2018; Walker et al. 2018), the jet width profile (Asada & Nakamura 2012; Hada et al. 2013; Nakamura et al. 2018), the total jet power at kilo-parsec scale (Owen et al. 2000; Stawarz et al. 2006), the jet power (e.g., Kino et al. 2014, 2015), the core shift (Hada et al. 2011), and the symmetric limb-brightening structure (Takahashi et al. 2018; Kim et al. 2018). The jet width profile is potentially very interesting because it depends on the magnetic flux ϕ: the jet internal magnetic pressure $\propto\phi^2$. We therefore expect (and see in our numerical simulations; see Figure 4) that MAD jets are wider at the base than SANE jets. Future theoretical work will help connect the ring-like structure seen in EHT2017 to the large-scale jet (M. Nakamura et al. 2019, in preparation).

A second epoch of observations ($\gtrsim 50\, r_g c^{-1} \sim 2$ weeks after EHT2017, when the models suggest that source structure will decorrelate) will increase the power of the average image analysis to reject models. The EHT2017 data were able to reject one entire category of models with confidence: high magnetic flux (MAD), retrograde, high-spin models. Other categories of models, such as the low magnetic flux, high-spin models, are assigned comparatively low probabilities by the average image scoring scheme. Data taken later, more than a decorrelation time after EHT2017 (model decorrelation times are of order two weeks), will provide an independent realization of the source. The probabilities attached to individual models by average image scoring will then multiply. For example, a model with probability 0.05 that is assigned probability 0.05 in comparison to a second epoch of observation would then have probability $0.05^2 = 2.5 \times 10^{-3}$, and would be strongly disfavored by the average image scoring criterion (see Section 4).

Future EHT 345 GHz campaigns (Paper II) will provide excellent constraints, particularly on the width of the ring. The optical depth on every line of sight through the source is expected to decrease (the drop is model and location dependent). In our models this makes the ring narrower, better defined, easier to measure accurately from VLBI data, and less dependent on details of the source plasma model.

Certain features of the model are geometric and should be present in future EHT observations. The photon ring is a persistent feature of the model related to the mass and distance to the black hole. It should be present in the next EHT campaign unless there is a dramatic change in $\dot{M}$, which would be evident in the SED. The asymmetry in the photon ring is also a persistent feature of the model because, we have argued, it is controlled by the black hole spin. The asymmetry should therefore remain in the southern half of the ring for the next EHT campaign, unless there is a dramatic tilt of the inner accretion flow. If the small-scale and large-scale jet are aligned, then EHT2017 saw the brightest region at unusually small PA, and future campaigns are likely (but not certain) to see the peak brightness shift further to the west. Future 230 GHz EHT campaigns (Paper II) will thus sharply test the GRMHD source models.

Together with complementary studies that are presently targeting either the supermassive black hole candidate at the Galactic Center (Eckart & Genzel 1997; Ghez et al. 1998; Gravity Collaboration et al. 2018a, 2018b) or stellar-mass binary black holes whose gravitational-wave emission is recorded by the LIGO and Virgo detectors (Abbott et al. 2016), the results provided here are consistent with the existence of astrophysical black holes. More importantly, they clearly indicate that their phenomenology, despite being observed on mass scales that differ by eight orders of magnitude, follows very closely the one predicted by general relativity. This demonstrates the complementarity of experiments studying black holes on all scales, promising much imp roved tests of gravity in its most extreme regimes.

The authors of this Letter thank the following organizations and programs: the Academy of Finland (projects 274477, 284495, 312496); the Advanced European Network of E-infrastructures for Astronomy with the SKA (AENEAS) project, supported by the European Commission Framework Programme Horizon 2020 Research and Innovation action under grant agreement 731016; the Alexander von Humboldt Stiftung; the Black Hole Initiative at Harvard University, through a grant (60477) from the John Templeton Foundation; the China Scholarship Council; Comisión Nacional de Investigación Científica y Tecnológica (CONICYT, Chile, via PIA ACT172033, Fondecyt 1171506, BASAL AFB-170002, ALMA-conicyt 31140007); Consejo Nacional de Ciencia y Tecnológica (CONACYT, Mexico, projects 104497, 275201, 279006, 281692); the Delaney Family via the Delaney Family John A. Wheeler Chair at Perimeter Institute; Dirección General de Asuntos del Personal Académico—Universidad Nacional Autónoma de México (DGAPA—UNAM, project IN112417); the European Research Council Synergy Grant "BlackHoleCam: Imaging the Event Horizon of Black Holes" (grant 610058); the Generalitat Valenciana postdoctoral grant APOSTD/2018/177; the Gordon and Betty Moore Foundation (grants GBMF-3561, GBMF-5278); the Istituto Nazionale di Fisica Nucleare (INFN) sezione di Napoli, iniziative specifiche TEONGRAV; the International Max Planck Research School for Astronomy and Astrophysics at the Universities of Bonn and Cologne; the Jansky Fellowship program of the National Radio Astronomy Observatory (NRAO); the Japanese Government (Monbukagakusho: MEXT) Scholarship; the Japan Society for the Promotion of Science (JSPS) Grant-in-Aid for JSPS Research Fellowship (JP17J08829); JSPS Overseas Research Fellowships; the Key Research Program of Frontier Sciences, Chinese Academy of Sciences (CAS, grants QYZDJ-SSW-SLH057, QYZDJ-SSW-SYS008); the Leverhulme Trust Early Career Research Fellowship; the Max-Planck-Gesellschaft (MPG); the Max Planck Partner Group of the MPG and the CAS; the MEXT/JSPS KAKENHI (grants 18KK0090, JP18K13594, JP18K03656, JP18H03721, 18K03709, 18H01245, 25120007); the MIT International Science and Technology Initiatives (MISTI) Funds; the Ministry of Science and Technology (MOST) of Taiwan (105-2112-M-001-025-MY3, 106-2112-M-001-011, 106-2119-M-001-027, 107-2119-M-001-017, 107-2119-M-001-020, and 107-2119-M-110-005);

the National Aeronautics and Space Administration (NASA, Fermi Guest Investigator grant 80NSSC17K0649); the National Institute of Natural Sciences (NINS) of Japan; the National Key Research and Development Program of China (grant 2016YFA0400704, 2016YFA0400702); the National Science Foundation (NSF, grants AST-0096454, AST-0352953, AST-0521233, AST-0705062, AST-0905844, AST-0922984, AST-1126433, AST-1140030, DGE-1144085, AST-1207704, AST-1207730, AST-1207752, MRI-1228509, OPP-1248097, AST-1310896, AST-1312651, AST-1337663, AST-1440254, AST-1555365, AST-1715061, AST-1614868, AST-1615796, AST-1716327, OISE-1743747, AST-1816420); the Natural Science Foundation of China (grants 11573051, 11633006, 11650110427, 10625314, 11721303, 11725312, 11873028, 11873073, U1531245, 11473010); the Natural Sciences and Engineering Research Council of Canada (NSERC, including a Discovery Grant and the NSERC Alexander Graham Bell Canada Graduate Scholarships-Doctoral Program); the National Youth Thousand Talents Program of China; the National Research Foundation of Korea (the Global PhD Fellowship Grant: grants NRF-2015H1A2A1033752, 2015-R1D1A1A01056807, the Korea Research Fellowship Program: NRF-2015H1D3A1066561); the Netherlands Organization for Scientific Research (NWO) VICI award (grant 639.043.513) and Spinoza Prize SPI 78-409; the New Scientific Frontiers with Precision Radio Interferometry Fellowship awarded by the South African Radio Astronomy Observatory (SARAO), which is a facility of the National Research Foundation (NRF), an agency of the Department of Science and Technology (DST) of South Africa; the Onsala Space Observatory (OSO) national infrastructure, for the provisioning of its facilities/observational support (OSO receives funding through the Swedish Research Council under grant 2017-00648) the Perimeter Institute for Theoretical Physics (research at Perimeter Institute is supported by the Government of Canada through the Department of Innovation, Science and Economic Development Canada and by the Province of Ontario through the Ministry of Economic Development, Job Creation and Trade); the Russian Science Foundation (grant 17-12-01029); the Spanish Ministerio de Economía y Competitividad (grants AYA2015-63939-C2-1-P, AYA2016-80889-P); the State Agency for Research of the Spanish MCIU through the "Center of Excellence Severo Ochoa" award for the Instituto de Astrofísica de Andalucía (SEV-2017-0709); the Toray Science Foundation; the US Department of Energy (USDOE) through the Los Alamos National Laboratory (operated by Triad National Security, LLC, for the National Nuclear Security Administration of the USDOE (Contract 89233218CNA000001)); the Italian Ministero dell'Istruzione Università e Ricerca through the grant Progetti Premiali 2012-iALMA (CUP C52I13000140001); ALMA North America Development Fund; Chandra TM6-17006X and DD7-18089X; a Sprows Family VURF Fellowship; a NSERC Discovery Grant; the FRQNT Nouveaux Chercheurs program; CIFAR; the NINS program of Promoting Research by Networking among Institutions(Grant Number 01421701); MEXT as a priority issue (Elucidation of the fundamental laws and evolution of the universe) to be tackled by using post-K Computer and JICFuS; part of this work used XC50 at the Center for Computational Astrophysics, National Astronomical Observatory of Japan.This work used the Extreme Science and Engineering Discovery Environment (XSEDE), supported by NSF grant ACI-1548562, and CyVerse, supported by NSF grants DBI-0735191, DBI-1265383, and DBI-1743442. XSEDE Stampede2 resource at TACC was allocated through TG-AST170024 and TG-AST080026N. XSEDE JetStream resource at PTI and TACC was allocated through AST170028. The simulations were performed in part on the SuperMUC cluster at the LRZ in Garching, on the LOEWE cluster in CSC in Frankfurt, and on the HazelHen cluster at the HLRS in Stuttgart. This research was enabled in part by support provided by Compute Ontario (http://computeontario.ca), Calcul Quebec (http://www.calculquebec.ca) and Compute Canada (http://www.computecanada.ca). Results in this Letter are based in part on observations made by the Chandra X-ray Observatory (Observation IDs 20034, 20035, 19457, 19458, 00352, 02707, 03717) and the Nuclear Spectroscopic Telescope Array (NuSTAR; Observation IDs 90202052002, 90202052004, 60201016002, 60466002002). The authors thank Belinda Wilkes, Fiona Harrison, Pat Slane, Joshua Wing, Karl Forster, and the *Chandra* and *NuSTAR* scheduling, data processing, and archive teams for making these challenging simultaneous observations possible. We thank the staff at the participating observatories, correlation centers, and institutions for their enthusiastic support. This Letter makes use of the following ALMA data: ADS/JAO.ALMA#2016.1.01154.V. ALMA is a partnership of the European Southern Observatory (ESO; Europe, representing its member states), NSF, and National Institutes of Natural Sciences of Japan, together with National Research Council (Canada), Ministry of Science and Technology (MOST; Taiwan), Academia Sinica Institute of Astronomy and Astrophysics (ASIAA; Taiwan), and Korea Astronomy and Space Science Institute (KASI; Republic of Korea), in cooperation with the Republic of Chile. The Joint ALMA Observatory is operated by ESO, Associated Universities, Inc. (AUI)/NRAO, and the National Astronomical Observatory of Japan (NAOJ). The NRAO is a facility of the NSF operated under cooperative agreement by AUI. APEX is a collaboration between the Max-Planck-Institut für Radioastronomie (Germany), ESO, and the Onsala Space Observatory (Sweden). The SMA is a joint project between the SAO and ASIAA and is funded by the Smithsonian Institution and the Academia Sinica. The JCMT is operated by the East Asian Observatory on behalf of the NAOJ, ASIAA, and KASI, as well as the Ministry of Finance of China, Chinese Academy of Sciences, and the National Key R&D Program (No. 2017YFA0402700) of China. Additional funding support for the JCMT is provided by the Science and Technologies Facility Council (UK) and participating universities in the UK and Canada. The LMT project is a joint effort of the Instituto Nacional de Astrofísica, Óptica y Electrónica (Mexico) and the University of Massachusetts at Amherst (USA). The IRAM 30-m telescope on Pico Veleta, Spain is operated by IRAM and supported by CNRS (Centre National de la Recherche Scientifique, France), MPG (Max-Planck-Gesellschaft, Germany) and IGN (Instituto Geográfico Nacional, Spain). The SMT is operated by the Arizona Radio Observatory, a part of the Steward Observatory of the University of Arizona, with financial support of operations from the State of Arizona and financial support for instrumentation development from the NSF. Partial SPT support is provided by the NSF Physics Frontier Center award (PHY-0114422) to the Kavli Institute of Cosmological Physics at the University of Chicago (USA), the Kavli Foundation, and the

GBMF (GBMF-947). The SPT hydrogen maser was provided on loan from the GLT, courtesy of ASIAA. The SPT is supported by the National Science Foundation through grant PLR- 1248097. Partial support is also provided by the NSF Physics Frontier Center grant PHY-1125897 to the Kavli Institute of Cosmological Physics at the University of Chicago, the Kavli Foundation and the Gordon and Betty Moore Foundation grant GBMF-947.The EHTC has received generous donations of FPGA chips from Xilinx Inc., under the Xilinx University Program. The EHTC has benefited from technology shared under open-source license by the Collaboration for Astronomy Signal Processing and Electronics Research (CASPER). The EHT project is grateful to T4Science and Microsemi for their assistance with Hydrogen Masers. This research has made use of NASA's Astrophysics Data System. We gratefully acknowledge the support provided by the extended staff of the ALMA, both from the inception of the ALMA Phasing Project through the observational campaigns of 2017 and 2018. We would like to thank A. Deller and W. Brisken for EHT-specific support with the use of DiFX. We acknowledge the significance that Maunakea, where the SMA and JCMT EHT stations are located, has for the indigenous Hawai'ian people.

Appendix A
Table of Simulation Results

Below we provide a table of simulation results for models with a standard inclination of 17° between the approaching jet and the line of sight. In the notation of this Letter this corresponds to $i = 17°$ for $a_* < 0$ or $i = 163°$ for $a_* \geqslant 0$. The table shows models for which we were able to calculate $L_{\rm bol}$ and $L_{\rm X}$. When M is needed to calculate, e.g., $P_{\rm jet}$, we assume $M = 6.2 \times 10^9\, M_\odot$.

The first, third, and fourth columns in the table identify the model parameters: SANE or MAD based on dimensionless flux, a_*, and $R_{\rm high}$. Once these parameters are specified, an average value of $\dot{M}$ for the model, which is shown in last column, can be found from the requirement that the average flux density of 1.3 mm emission is ~0.5 Jy (see Paper IV). This $\dot{M}$ is shown in units of the Eddington accretion rate $\dot{M}_{\rm Edd} = 137 M_\odot\ {\rm yr}^{-1}$. The measured average dimensionless magnetic flux ϕ is shown in the second column. Notice that ϕ is determined solely from the GRMHD simulation and is independent of the mass scaling $\mathscr{M}$ and the mass M used to fix the flux density. It is also independent of the electron thermodynamics ($R_{\rm high}$).

The fifth column shows the radiative efficiency, which is the bolometric luminosity $L_{\rm bol}$ over $\dot{M}c^2$. Here $L_{\rm bol}$ was found from a relativistic Monte Carlo radiative transport model that includes synchrotron emission, Compton scattering (all orders), and bremsstrahlung. The Monte Carlo calculation makes no approximations in treating the Compton scattering (see Dolence et al. 2009). Bremsstrahlung is negligible in all models.

The sixth column shows predicted X-ray luminosity $L_{\rm X}$ in the 2–10 keV band. This was calculated using the same relativistic Monte Carlo radiative transport model as for $L_{\rm bol}$. There are three numbers in this column: the average $\langle L_{\rm X}\rangle$ (left) of the 20 sample spectra used in the calculation, and a maximum and minimum value. The maximum and minimum are obtained by taking the standard deviation $\sigma(\log_{10} L_{\rm X})$ and setting the maximum (minimum) to $10^{+2\sigma}\langle L_{\rm X}\rangle$ ($10^{-2\sigma}\langle L_{\rm X}\rangle$).

The seventh column shows the jet power

$$P_{\rm jet} \equiv \int_{\beta\gamma > (\beta\gamma)_{\rm cut}} d\theta\, \frac{1}{\Delta t} \int dt d\phi\, \sqrt{-g}\,(-T^r{}_t - \rho u^r). \quad (10)$$

The integral is evaluated at $r = 40\, r_{\rm g}$ for SANE models and $r = 100\, r_{\rm g}$ for MAD models. These radii were chosen because they are close to the outer boundary of the computational domain. Here Δt is the duration of the time-average, $-T^r{}_t$ is a component of the stress-energy tensor representing outward radial energy flux, g is the determinant of the (covariant) metric, ρ is the rest-mass density, and u^r is the radial component of the four-velocity. Here we use Kerr–Schild t, r, θ, ϕ for clarity; in practice, the integral is evaluated in simulation coordinates. The quantity in parentheses is the outward energy flux with the rest-mass energy flux subtracted off. The θ integral is done after time averaging and azimuthal integration over the region where

$$(\beta\gamma)^2 \equiv \left(\frac{-T^r{}_t}{\rho u^r}\right)^2 - 1 \quad > (\beta\gamma)^2_{\rm cut}. \quad (11)$$

Here $\beta\gamma$ would be the radial four-velocity as $r \to \infty$ if the flow were steady and all internal magnetic and internal energy were converted to kinetic energy. In Table 3 we use $(\beta\gamma)^2_{\rm cut} = 1$ to define the jet. This is equivalent to restricting the jet to regions where the total energy per unit rest-mass (including the rest-mass energy) exceeds $\sqrt{5}\,c^2 \simeq 2.2c^2$.

The ninth column shows the total outflow power $P_{\rm out}$, defined using the same integral as in Equation (10), but with the θ integral carried out over the entire region around the poles where there is steady outflow (and $\theta < 1$, although the result is insensitive to this condition). $P_{\rm out}$ thus includes both the narrow, fast, relativistic jet and any wide-angle, slow, or nonrelativistic outflow. It is the maximal $P_{\rm jet}$ under any definition of jet power.

Finally, the tenth column shows the ratio of the electromagnetic to total energy flux in the jet. In most cases this number is close to 1; i.e., the jet is Poynting dominated. This measurement is sensitive to the numerical treatment of low-density regions in the jet where the jet can be artificially loaded with plasma by numerical "floors" in the GRMHD evolution. More accurate treatment of the funnel would raise values in this column.

Our choice of $(\beta\gamma)^2_{\rm cut}$, and therefore $P_{\rm jet}$, is somewhat arbitrary. To probe the sensitivity of $P_{\rm jet}$ to $(\beta\gamma)^2_{\rm cut}$, Figure 10 shows the ratio $P_{\rm jet}/P_{\rm out}$ (which is determined by the GRMHD model and is thus independent of the electron thermodynamics, i.e., $R_{\rm high}$) as a function of $(\beta\gamma)^2_{\rm cut}$.

The eighth and tenth columns show the jet and outflow efficiency. This is determined by the GRMHD evolution, i.e., it is independent of electron thermodynamics ($R_{\rm high}$). It is >0.1 only for MAD models with $a_* \geqslant 0.5$.

The eleventh column shows the fraction of $P_{\rm jet}$ in Poynting flux. This fraction is large for all models, and meaningless for the $a_* = 0$ models, which have $P_{\rm jet}$ that is so small that it is difficult to measure accurately.

The problem of defining $P_{\rm jet}$ and $P_{\rm out}$ has been discussed extensively in the literature (e.g., Narayan et al. 2012; Yuan et al. 2015; Mościbrodzka et al. 2016), where alternative definitions of unbound regions and of the jet have been used, some based on a fluid Bernoulli parameter $B_e \equiv$

Table 3
Model Table

Flux	ϕ	Spin	$R_{\rm high}$	$L_{\rm bol}/(\dot{M}\ c^2)$	$L_{\rm X}$ (cgs)	$P_{\rm jet}$ (cgs)	$P_{\rm jet}/(\dot{M}\ c^2)$	$P_{\rm out}$ (cgs)	$P_{\rm out}/(\dot{M}\ c^2)$	$P_{\rm jet,em}/P_{\rm jet}$	$\dot{M}/\dot{M}_{\rm Edd}$
SANE	1.02	−0.94	1	1.27×10^{-2}	$3.18^{<49.55}_{>0.20} \times 10^{41}$	1.16×10^{42}	5.34×10^{-3}	1.19×10^{42}	5.48×10^{-3}	0.84	2.77×10^{-5}
SANE	1.02	−0.94	10	1.6×10^{-3}	$9.62^{<64.42}_{>1.44} \times 10^{40}$	4.94×10^{42}	5.34×10^{-3}	5.07×10^{42}	5.48×10^{-3}	0.84	1.19×10^{-4}
SANE	1.02	−0.94	20	6.09×10^{-4}	$3.26^{<11.86}_{>0.90} \times 10^{40}$	5.8×10^{42}	5.34×10^{-3}	5.96×10^{42}	5.48×10^{-3}	0.84	1.39×10^{-4}
SANE	1.02	−0.94	40	2.45×10^{-4}	$8.89^{<50.53}_{>1.56} \times 10^{39}$	7.02×10^{42}	5.34×10^{-3}	7.21×10^{42}	5.48×10^{-3}	0.84	1.69×10^{-4}
SANE	1.02	−0.94	80	1.33×10^{-4}	$2.65^{<18.26}_{>0.39} \times 10^{39}$	8.89×10^{42}	5.34×10^{-3}	9.13×10^{42}	5.48×10^{-3}	0.84	2.13×10^{-4}
SANE	1.02	−0.94	160	7.12×10^{-5}	$6.36^{<55.27}_{>0.73} \times 10^{38}$	1.2×10^{43}	5.34×10^{-3}	1.23×10^{43}	5.48×10^{-3}	0.84	2.87×10^{-4}
SANE	1.11	−0.5	1	1.62×10^{-2}	$1.97^{<3.94}_{>0.98} \times 10^{41}$	2.62×10^{40}	1.86×10^{-4}	3.84×10^{40}	2.72×10^{-4}	0.88	1.81×10^{-5}
SANE	1.11	−0.5	10	2.17×10^{-3}	$1.94^{<5.40}_{>0.69} \times 10^{41}$	1.95×10^{41}	1.86×10^{-4}	2.85×10^{41}	2.72×10^{-4}	0.88	1.34×10^{-4}
SANE	1.11	−0.5	20	6.69×10^{-4}	$3.72^{<7.72}_{>1.80} \times 10^{40}$	2.26×10^{41}	1.86×10^{-4}	3.31×10^{41}	2.72×10^{-4}	0.88	1.56×10^{-4}
SANE	1.11	−0.5	40	2.47×10^{-4}	$9.44^{<13.37}_{>6.67} \times 10^{39}$	2.62×10^{41}	1.86×10^{-4}	3.83×10^{41}	2.72×10^{-4}	0.88	1.81×10^{-4}
SANE	1.11	−0.5	80	1.26×10^{-4}	$1.23^{<4.58}_{>0.33} \times 10^{39}$	3.2×10^{41}	1.86×10^{-4}	4.68×10^{41}	2.72×10^{-4}	0.88	2.21×10^{-4}
SANE	1.11	−0.5	160	7.86×10^{-5}	$3.72^{<16.68}_{>0.83} \times 10^{38}$	4.21×10^{41}	1.86×10^{-4}	6.16×10^{41}	2.72×10^{-4}	0.88	2.9×10^{-4}
SANE	0.99	0	1	3.17×10^{-2}	$2.08^{<194.22}_{>0.02} \times 10^{41}$	2.24×10^{36}	4.4×10^{-8}	5.22×10^{39}	1.03×10^{-4}	1.01	6.5×10^{-6}
SANE	0.99	0	10	1.88×10^{-2}	$4.2^{<425.40}_{>0.04} \times 10^{42}$	4.38×10^{37}	4.4×10^{-8}	1.02×10^{41}	1.03×10^{-4}	1.01	1.27×10^{-4}
SANE	0.99	0	20	5.83×10^{-3}	$1.57^{<39.69}_{>0.06} \times 10^{42}$	8.02×10^{37}	4.4×10^{-8}	1.87×10^{41}	1.03×10^{-4}	1.01	2.33×10^{-4}
SANE	0.99	0	40	7.8×10^{-4}	$8.92^{<41.45}_{>1.92} \times 10^{40}$	9.16×10^{37}	4.4×10^{-8}	2.14×10^{41}	1.03×10^{-4}	1.01	2.66×10^{-4}
SANE	0.99	0	80	1.69×10^{-4}	$2.5^{<19.17}_{>0.33} \times 10^{39}$	1.03×10^{38}	4.4×10^{-8}	2.41×10^{41}	1.03×10^{-4}	1.01	3×10^{-4}
SANE	0.99	0	160	1.08×10^{-4}	$3.44^{<13.32}_{>0.89} \times 10^{38}$	1.23×10^{38}	4.4×10^{-8}	2.87×10^{41}	1.03×10^{-4}	1.01	3.57×10^{-4}
SANE	1.10	0.5	1	4.97×10^{-2}	$5.5^{<34.41}_{>0.88} \times 10^{40}$	2.57×10^{39}	1.63×10^{-4}	9.19×10^{39}	5.86×10^{-4}	0.88	2.01×10^{-6}
SANE	1.10	0.5	10	5.98×10^{-3}	$4.73^{<88.59}_{>0.25} \times 10^{40}$	1.91×10^{40}	1.64×10^{-4}	6.84×10^{40}	5.86×10^{-4}	0.88	1.5×10^{-5}
SANE	1.10	0.5	20	3.33×10^{-3}	$3.83^{<49.18}_{>0.30} \times 10^{40}$	4.09×10^{40}	1.64×10^{-4}	1.47×10^{41}	5.86×10^{-4}	0.88	3.2×10^{-5}
SANE	1.10	0.5	40	1.74×10^{-3}	$2.52^{<22.73}_{>0.28} \times 10^{40}$	8.02×10^{40}	1.64×10^{-4}	2.87×10^{41}	5.86×10^{-4}	0.88	6.28×10^{-5}
SANE	1.10	0.5	80	6.95×10^{-4}	$7.84^{<91.92}_{>0.67} \times 10^{39}$	1.27×10^{41}	1.64×10^{-4}	4.55×10^{41}	5.86×10^{-4}	0.88	9.95×10^{-5}
SANE	1.10	0.5	160	2.78×10^{-4}	$1.37^{<22.85}_{>0.08} \times 10^{39}$	1.69×10^{41}	1.63×10^{-4}	6.06×10^{41}	5.86×10^{-4}	0.88	1.33×10^{-4}
SANE	1.64	0.94	1	1.4	$2.38^{<359.03}_{>0.02} \times 10^{41}$	2.2×10^{40}	7.76×10^{-3}	3.38×10^{40}	1.19×10^{-2}	0.82	3.63×10^{-7}
SANE	1.64	0.94	10	2.7×10^{-1}	$2.79^{<508.99}_{>0.02} \times 10^{41}$	1.4×10^{41}	7.76×10^{-3}	2.15×10^{41}	1.19×10^{-2}	0.82	2.31×10^{-6}
SANE	1.64	0.94	20	1.74×10^{-1}	$5.75^{<1685.98}_{>0.02} \times 10^{41}$	3.22×10^{41}	7.76×10^{-3}	4.94×10^{41}	1.19×10^{-2}	0.82	5.31×10^{-6}
SANE	1.64	0.94	40	7.2×10^{-2}	$4.71^{<2490.36}_{>0.01} \times 10^{41}$	5.97×10^{41}	7.76×10^{-3}	9.17×10^{41}	1.19×10^{-2}	0.82	9.84×10^{-6}
SANE	1.64	0.94	80	2.38×10^{-2}	$1.42^{<860.83}_{>0.00} \times 10^{41}$	8.87×10^{41}	7.76×10^{-3}	1.36×10^{42}	1.19×10^{-2}	0.82	1.46×10^{-5}
SANE	1.64	0.94	160	8.45×10^{-3}	$3.22^{<1687.88}_{>0.01} \times 10^{40}$	1.23×10^{42}	7.76×10^{-3}	1.89×10^{42}	1.19×10^{-2}	0.82	2.03×10^{-5}
MAD	8.04	−0.94	1	7.61×10^{-1}	$2.12^{<17.74}_{>0.25} \times 10^{41}$	1.36×10^{42}	2.09×10^{-1}	1.6×10^{42}	2.46×10^{-1}	0.75	8.32×10^{-7}
MAD	8.04	−0.94	10	7.54×10^{-2}	$5.76^{<68.06}_{>0.49} \times 10^{40}$	1.97×10^{42}	2.09×10^{-1}	2.32×10^{42}	2.46×10^{-1}	0.75	1.21×10^{-6}
MAD	8.04	−0.94	20	3.76×10^{-2}	$2.27^{<29.09}_{>0.18} \times 10^{40}$	2.38×10^{42}	2.09×10^{-1}	2.8×10^{42}	2.46×10^{-1}	0.75	1.46×10^{-6}
MAD	8.04	−0.94	40	2.07×10^{-2}	$6.18^{<77.36}_{>0.49} \times 10^{39}$	3×10^{42}	2.09×10^{-1}	3.54×10^{42}	2.46×10^{-1}	0.75	1.84×10^{-6}
MAD	8.04	−0.94	80	1.17×10^{-2}	$1.32^{<26.36}_{>0.07} \times 10^{39}$	3.99×10^{42}	2.09×10^{-1}	4.71×10^{42}	2.46×10^{-1}	0.75	2.45×10^{-6}
MAD	8.04	−0.94	160	6.52×10^{-3}	$2.57^{<46.76}_{>0.14} \times 10^{38}$	5.7×10^{42}	2.09×10^{-1}	6.73×10^{42}	2.46×10^{-1}	0.75	3.5×10^{-6}
MAD	12.25	−0.5	1	2.96×10^{-1}	$1.39^{<11.56}_{>0.17} \times 10^{41}$	3.43×10^{41}	4.91×10^{-2}	6.04×10^{41}	8.64×10^{-2}	0.82	8.95×10^{-7}
MAD	12.25	−0.5	10	4.53×10^{-2}	$2.43^{<19.86}_{>0.30} \times 10^{40}$	5.31×10^{41}	4.92×10^{-2}	9.33×10^{41}	8.64×10^{-2}	0.82	1.38×10^{-6}
MAD	12.25	−0.5	20	2.67×10^{-2}	$8.18^{<77.51}_{>0.86} \times 10^{39}$	6.45×10^{41}	4.92×10^{-2}	1.13×10^{42}	8.64×10^{-2}	0.82	1.68×10^{-6}
MAD	12.25	−0.5	40	1.69×10^{-2}	$2.17^{<22.33}_{>0.21} \times 10^{39}$	8.07×10^{41}	4.92×10^{-2}	1.42×10^{42}	8.64×10^{-2}	0.82	2.1×10^{-6}
MAD	12.25	−0.5	80	1.07×10^{-2}	$4.87^{<50.76}_{>0.47} \times 10^{38}$	1.05×10^{42}	4.92×10^{-2}	1.85×10^{42}	8.64×10^{-2}	0.82	2.74×10^{-6}
MAD	12.25	−0.5	160	6.43×10^{-3}	$1.09^{<7.06}_{>0.17} \times 10^{38}$	1.46×10^{42}	4.92×10^{-2}	2.57×10^{42}	8.64×10^{-2}	0.82	3.81×10^{-6}
MAD	15.44	0	1	2.67×10^{-1}	$1.22^{<14.60}_{>0.10} \times 10^{41}$	0.0	0.0	8.39×10^{40}	1.51×10^{-2}	0.00	7.12×10^{-7}

Table 3
(Continued)

Flux	ϕ	Spin	$R_{\rm high}$	$L_{\rm bol}/(\dot{M}\ c^2)$	$L_{\rm X}$ (cgs)	$P_{\rm jet}$ (cgs)	$P_{\rm jet}/(\dot{M}\ c^2)$	$P_{\rm out}$ (cgs)	$P_{\rm out}/(\dot{M}\ c^2)$	$P_{\rm jet,em}/P_{\rm jet}$	$\dot{M}/\dot{M}_{\rm Edd}$
MAD	15.44	0	10	4.53×10^{-2}	$1.86^{<31.55}_{>0.11} \times 10^{40}$	0.0	0.0	1.39×10^{41}	1.51×10^{-2}	0.00	1.18×10^{-6}
MAD	15.44	0	20	2.81×10^{-2}	$5.98^{<101.81}_{>0.35} \times 10^{39}$	0.0	0.0	1.71×10^{41}	1.51×10^{-2}	0.00	1.46×10^{-6}
MAD	15.44	0	40	1.85×10^{-2}	$1.63^{<27.75}_{>0.10} \times 10^{39}$	0.0	0.0	2.15×10^{41}	1.51×10^{-2}	0.00	1.82×10^{-6}
MAD	15.44	0	80	1.21×10^{-2}	$3.51^{<61.34}_{>0.20} \times 10^{38}$	0.0	0.0	2.77×10^{41}	1.51×10^{-2}	0.00	2.35×10^{-6}
MAD	15.44	0	160	7.63×10^{-3}	$8.06^{<80.62}_{>0.81} \times 10^{37}$	0.0	0.0	3.73×10^{41}	1.51×10^{-2}	0.00	3.17×10^{-6}
MAD	15.95	0.5	1	5.45×10^{-1}	$1.57^{<11.98}_{>0.21} \times 10^{41}$	4.64×10^{41}	1.16×10^{-1}	6.74×10^{41}	1.69×10^{-1}	0.85	5.11×10^{-7}
MAD	15.95	0.5	10	9.45×10^{-2}	$2.71^{<36.30}_{>0.20} \times 10^{40}$	8.07×10^{41}	1.16×10^{-1}	1.17×10^{42}	1.69×10^{-1}	0.85	8.89×10^{-7}
MAD	15.95	0.5	20	5.54×10^{-2}	$9.67^{<126.69}_{>0.74} \times 10^{39}$	1.02×10^{42}	1.16×10^{-1}	1.49×10^{42}	1.69×10^{-1}	0.85	1.13×10^{-6}
MAD	15.95	0.5	40	3.5×10^{-2}	$3.3^{<39.01}_{>0.28} \times 10^{39}$	1.32×10^{42}	1.16×10^{-1}	1.92×10^{42}	1.69×10^{-1}	0.85	1.45×10^{-6}
MAD	15.95	0.5	80	2.22×10^{-2}	$8^{<91.84}_{>0.70} \times 10^{38}$	1.74×10^{42}	1.16×10^{-1}	2.52×10^{42}	1.69×10^{-1}	0.85	1.92×10^{-6}
MAD	15.95	0.5	160	1.35×10^{-2}	$1.79^{<8.44}_{>0.38} \times 10^{38}$	2.38×10^{42}	1.16×10^{-1}	3.46×10^{42}	1.69×10^{-1}	0.85	2.62×10^{-6}
MAD	12.78	0.94	1	3.65	$5.19^{<43.60}_{>0.62} \times 10^{41}$	1.97×10^{42}	8.23×10^{-1}	2.29×10^{42}	9.55×10^{-1}	0.80	3.07×10^{-7}
MAD	12.78	0.94	10	3.68×10^{-1}	$1.3^{<13.22}_{>0.13} \times 10^{41}$	3.04×10^{42}	8.23×10^{-1}	3.52×10^{42}	9.55×10^{-1}	0.80	4.73×10^{-7}
MAD	12.78	0.94	20	1.79×10^{-1}	$5^{<56.22}_{>0.44} \times 10^{40}$	3.73×10^{42}	8.23×10^{-1}	4.33×10^{42}	9.55×10^{-1}	0.80	5.81×10^{-7}
MAD	12.78	0.94	40	9.43×10^{-2}	$1.54^{<22.13}_{>0.11} \times 10^{40}$	4.74×10^{42}	8.23×10^{-1}	5.5×10^{42}	9.55×10^{-1}	0.80	7.38×10^{-7}
MAD	12.78	0.94	80	5.19×10^{-2}	$3.74^{<80.85}_{>0.17} \times 10^{39}$	6.26×10^{42}	8.23×10^{-1}	7.27×10^{42}	9.55×10^{-1}	0.80	9.75×10^{-7}
MAD	12.78	0.94	160	2.82×10^{-2}	$6.97^{<186.48}_{>0.26} \times 10^{38}$	8.75×10^{42}	8.23×10^{-1}	1.02×10^{43}	9.55×10^{-1}	0.80	1.36×10^{-6}

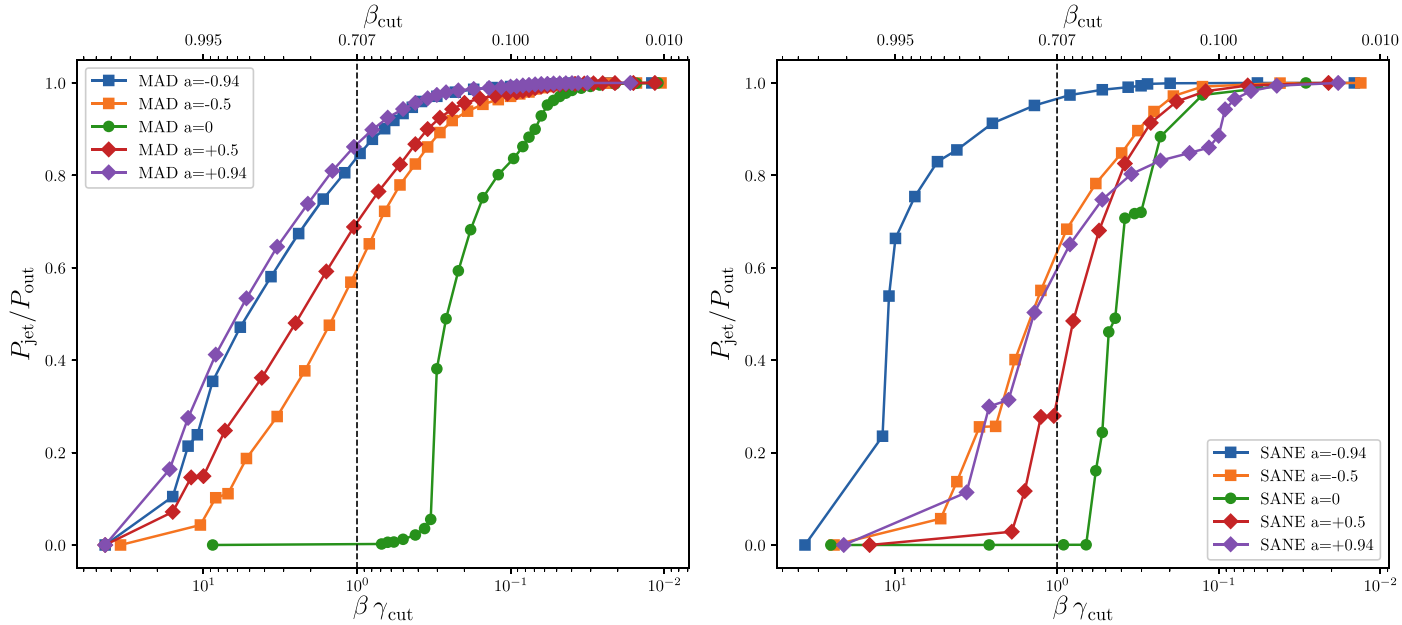

Figure 10. Ratio $P_{\rm jet}/P_{\rm out}$ as a function of the outflow velocity cutoff parameter $\beta\gamma_{\rm cut}$. Evidently, as the cut is decreased, so that the maximum asymptotic speed of the jet flow is decreased, an increasing fraction of $P_{\rm out}$ is classified as $P_{\rm jet}$. Our nominal cutoff is $\beta\gamma = 1$, which corresponds to $\beta \equiv v^r/c = 1/\sqrt{2}$. Using this definition, $P_{\rm jet}$ for $a_* = 0$ models is small because the energy flux in the relativistic outflow is small.

$-u_t(\rho + u + p)/\rho - 1$, while others use μ (the ratio of energy flux to rest mass flux), which is directly related to our $\beta\gamma$.

Appendix B
Image Decomposition into Midplane, Nearside, and Farside Components

In Section 3.3 we presented representative images from the Image Library spanning a broad range of values in both a_* and $R_{\rm high}$. It was noted that for SANEs with low values of $R_{\rm high}$ the emission is concentrated more in the midplane, whereas for larger values of $R_{\rm high}$ this emission is concentrated in the funnel wall. In particular, Figure 4 presented temporal- and azimuthal-averaged images of the point of origin of photons comprising images from $a_* = 0.94$ MAD and SANE simulations with $R_{\rm high} = 10$ and 160.

Figure 11 presents the decomposition of the four images in Figure 4 into components that we refer to as: midplane (material within $32\overset{\circ}{.}7$ of the midplane), nearside (material within 1 radian, or $57\overset{\circ}{.}3$, of the polar axis nearest to the observer), and farside (material within 1 radian of the polar axis furthest from the observer). From inspection of the first three models (rows) in Figure 11, the ratio of nearside to farside flux in the simulations is small (compared to the midplane) and of order unity and the midplane emission is dominant, as in Figure 4.

However, for the SANE, $R_{\rm high} = 160$ model the farside emission contributes a flux that exceeds that produced from the midplane, and is significantly brighter than the nearside emission. This is in agreement with what is seen in the bottom-right panel of Figures 4, and can be understood to arise from the SANE model possessing an optically thin disk and bright funnel wall in the $R_{\rm high} = 160$ case, compared to SANE, $R_{\rm high} = 10$, as also seen in Figures 2 and 3. Due to the reduced opacity along the line of sight in this case, mm photons can pass through both the intervening nearside material and the midplane without significant attenuation, before reaching the photospheric boundary in the farside component (where $\tau \sim 1$), where they originate. The image decomposition and its application to M87's image structure will be explored further in Z. Younsi et al. 2019a (in preparation).

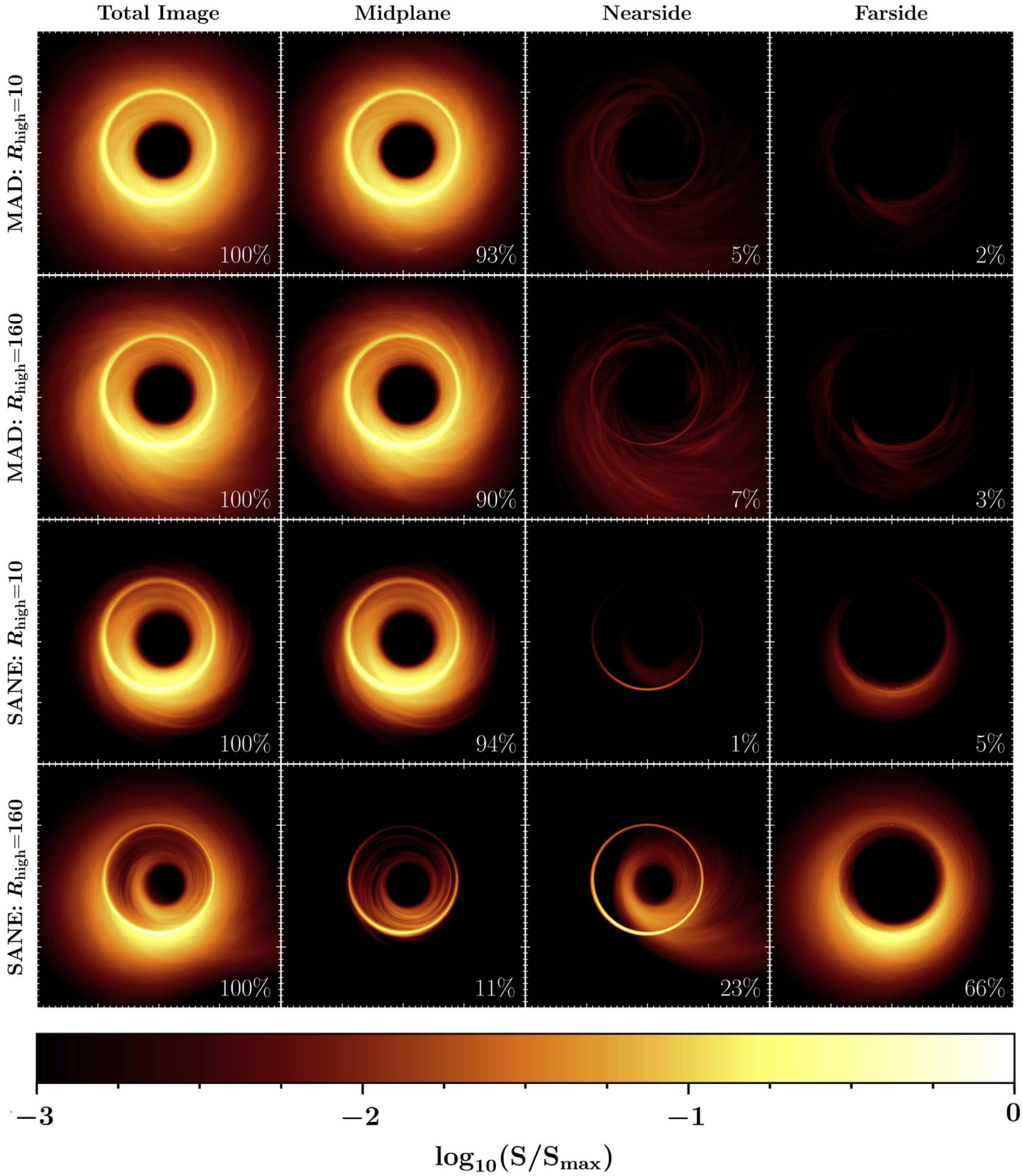

Figure 11. Decomposition of time-averaged 1.3 mm images from Figure 4 into midplane, nearside, and farside components (MAD and SANE models with $a_* = 0.94$). Each model (row) of the figure corresponds to a simulation in Figure 4. The percentage of the total image flux from each component is indicated in the bottom right of each panel. The color scale is logarithmic and spans three decades in total flux with respect to the total image from each model, chosen in order to emphasize both nearside and farside components, which are nearly invisible when shown in a linear scale. The field of view is 80 μas.

ORCID iDs

Kazunori Akiyama https://orcid.org/0000-0002-9475-4254
Antxon Alberdi https://orcid.org/0000-0002-9371-1033
Rebecca Azulay https://orcid.org/0000-0002-2200-5393
Anne-Kathrin Baczko https://orcid.org/0000-0003-3090-3975
Mislav Baloković https://orcid.org/0000-0003-0476-6647
John Barrett https://orcid.org/0000-0002-9290-0764
Lindy Blackburn https://orcid.org/0000-0002-9030-642X
Katherine L. Bouman https://orcid.org/0000-0003-0077-4367
Geoffrey C. Bower https://orcid.org/0000-0003-4056-9982
Christiaan D. Brinkerink https://orcid.org/0000-0002-2322-0749
Roger Brissenden https://orcid.org/0000-0002-2556-0894
Silke Britzen https://orcid.org/0000-0001-9240-6734
Avery E. Broderick https://orcid.org/0000-0002-3351-760X
Do-Young Byun https://orcid.org/0000-0003-1157-4109
Andrew Chael https://orcid.org/0000-0003-2966-6220
Chi-kwan Chan https://orcid.org/0000-0001-6337-6126
Shami Chatterjee https://orcid.org/0000-0002-2878-1502
Ilje Cho https://orcid.org/0000-0001-6083-7521
Pierre Christian https://orcid.org/0000-0001-6820-9941
John E. Conway https://orcid.org/0000-0003-2448-9181
Geoffrey B. Crew https://orcid.org/0000-0002-2079-3189
Yuzhu Cui https://orcid.org/0000-0001-6311-4345
Jordy Davelaar https://orcid.org/0000-0002-2685-2434
Mariafelicia De Laurentis https://orcid.org/0000-0002-9945-682X
Roger Deane https://orcid.org/0000-0003-1027-5043
Jessica Dempsey https://orcid.org/0000-0003-1269-9667
Gregory Desvignes https://orcid.org/0000-0003-3922-4055
Jason Dexter https://orcid.org/0000-0003-3903-0373
Sheperd S. Doeleman https://orcid.org/0000-0002-9031-0904
Ralph P. Eatough https://orcid.org/0000-0001-6196-4135
Heino Falcke https://orcid.org/0000-0002-2526-6724
Vincent L. Fish https://orcid.org/0000-0002-7128-9345
Raquel Fraga-Encinas https://orcid.org/0000-0002-5222-1361
José L. Gómez https://orcid.org/0000-0003-4190-7613
Peter Galison https://orcid.org/0000-0002-6429-3872
Charles F. Gammie https://orcid.org/0000-0001-7451-8935
Boris Georgiev https://orcid.org/0000-0002-3586-6424
Roman Gold https://orcid.org/0000-0003-2492-1966
Minfeng Gu (顾敏峰) https://orcid.org/0000-0002-4455-6946
Mark Gurwell https://orcid.org/0000-0003-0685-3621
Kazuhiro Hada https://orcid.org/0000-0001-6906-772X
Ronald Hesper https://orcid.org/0000-0003-1918-6098
Luis C. Ho (何子山) https://orcid.org/0000-0001-6947-5846
Mareki Honma https://orcid.org/0000-0003-4058-9000
Chih-Wei L. Huang https://orcid.org/0000-0001-5641-3953
Shiro Ikeda https://orcid.org/0000-0002-2462-1448
Sara Issaoun https://orcid.org/0000-0002-5297-921X
David J. James https://orcid.org/0000-0001-5160-4486
Michael Janssen https://orcid.org/0000-0001-8685-6544
Britton Jeter https://orcid.org/0000-0003-2847-1712
Wu Jiang (江悟) https://orcid.org/0000-0001-7369-3539
Michael D. Johnson https://orcid.org/0000-0002-4120-3029
Svetlana Jorstad https://orcid.org/0000-0001-6158-1708
Taehyun Jung https://orcid.org/0000-0001-7003-8643
Mansour Karami https://orcid.org/0000-0001-7387-9333
Ramesh Karuppusamy https://orcid.org/0000-0002-5307-2919
Tomohisa Kawashima https://orcid.org/0000-0001-8527-0496
Garrett K. Keating https://orcid.org/0000-0002-3490-146X
Mark Kettenis https://orcid.org/0000-0002-6156-5617
Jae-Young Kim https://orcid.org/0000-0001-8229-7183
Junhan Kim https://orcid.org/0000-0002-4274-9373
Motoki Kino https://orcid.org/0000-0002-2709-7338
Jun Yi Koay https://orcid.org/0000-0002-7029-6658
Patrick M. Koch https://orcid.org/0000-0003-2777-5861
Shoko Koyama https://orcid.org/0000-0002-3723-3372
Michael Kramer https://orcid.org/0000-0002-4175-2271
Carsten Kramer https://orcid.org/0000-0002-4908-4925
Thomas P. Krichbaum https://orcid.org/0000-0002-4892-9586
Tod R. Lauer https://orcid.org/0000-0003-3234-7247
Sang-Sung Lee https://orcid.org/0000-0002-6269-594X
Yan-Rong Li (李彦荣) https://orcid.org/0000-0001-5841-9179
Zhiyuan Li (李志远) https://orcid.org/0000-0003-0355-6437
Michael Lindqvist https://orcid.org/0000-0002-3669-0715
Kuo Liu https://orcid.org/0000-0002-2953-7376
Elisabetta Liuzzo https://orcid.org/0000-0003-0995-5201
Laurent Loinard https://orcid.org/0000-0002-5635-3345
Ru-Sen Lu (路如森) https://orcid.org/0000-0002-7692-7967
Nicholas R. MacDonald https://orcid.org/0000-0002-6684-8691
Jirong Mao (毛基荣) https://orcid.org/0000-0002-7077-7195
Sera Markoff https://orcid.org/0000-0001-9564-0876
Daniel P. Marrone https://orcid.org/0000-0002-2367-1080
Alan P. Marscher https://orcid.org/0000-0001-7396-3332
Iván Martí-Vidal https://orcid.org/0000-0003-3708-9611
Lynn D. Matthews https://orcid.org/0000-0002-3728-8082
Lia Medeiros https://orcid.org/0000-0003-2342-6728
Karl M. Menten https://orcid.org/0000-0001-6459-0669
Yosuke Mizuno https://orcid.org/0000-0002-8131-6730
Izumi Mizuno https://orcid.org/0000-0002-7210-6264
James M. Moran https://orcid.org/0000-0002-3882-4414
Kotaro Moriyama https://orcid.org/0000-0003-1364-3761
Monika Moscibrodzka https://orcid.org/0000-0002-4661-6332
Cornelia Müller https://orcid.org/0000-0002-2739-2994
Hiroshi Nagai https://orcid.org/0000-0003-0292-3645
Neil M. Nagar https://orcid.org/0000-0001-6920-662X
Masanori Nakamura https://orcid.org/0000-0001-6081-2420
Ramesh Narayan https://orcid.org/0000-0002-1919-2730
Iniyan Natarajan https://orcid.org/0000-0001-8242-4373
Chunchong Ni https://orcid.org/0000-0003-1361-5699
Aristeidis Noutsos https://orcid.org/0000-0002-4151-3860
Héctor Olivares https://orcid.org/0000-0001-6833-7580
Daniel C. M. Palumbo https://orcid.org/0000-0002-7179-3816
Ue-Li Pen https://orcid.org/0000-0003-2155-9578
Dominic W. Pesce https://orcid.org/0000-0002-5278-9221
Oliver Porth https://orcid.org/0000-0002-4584-2557
Ben Prather https://orcid.org/0000-0002-0393-7734
Jorge A. Preciado-López https://orcid.org/0000-0002-4146-0113
Hung-Yi Pu https://orcid.org/0000-0001-9270-8812
Venkatessh Ramakrishnan https://orcid.org/0000-0002-9248-086X

Ramprasad Rao https://orcid.org/0000-0002-1407-7944
Alexander W. Raymond https://orcid.org/0000-0002-5779-4767
Bart Ripperda https://orcid.org/0000-0002-7301-3908
Freek Roelofs https://orcid.org/0000-0001-5461-3687
Eduardo Ros https://orcid.org/0000-0001-9503-4892
Mel Rose https://orcid.org/0000-0002-2016-8746
Alan L. Roy https://orcid.org/0000-0002-1931-0135
Chet Ruszczyk https://orcid.org/0000-0001-7278-9707
Benjamin R. Ryan https://orcid.org/0000-0001-8939-4461
Kazi L. J. Rygl https://orcid.org/0000-0003-4146-9043
David Sánchez-Arguelles https://orcid.org/0000-0002-7344-9920
Mahito Sasada https://orcid.org/0000-0001-5946-9960
Tuomas Savolainen https://orcid.org/0000-0001-6214-1085
Lijing Shao https://orcid.org/0000-0002-1334-8853
Zhiqiang Shen (沈志强) https://orcid.org/0000-0003-3540-8746
Des Small https://orcid.org/0000-0003-3723-5404
Bong Won Sohn https://orcid.org/0000-0002-4148-8378
Jason SooHoo https://orcid.org/0000-0003-1938-0720
Fumie Tazaki https://orcid.org/0000-0003-0236-0600
Paul Tiede https://orcid.org/0000-0003-3826-5648
Remo P. J. Tilanus https://orcid.org/0000-0002-6514-553X
Michael Titus https://orcid.org/0000-0002-3423-4505
Kenji Toma https://orcid.org/0000-0002-7114-6010
Pablo Torne https://orcid.org/0000-0001-8700-6058
Sascha Trippe https://orcid.org/0000-0003-0465-1559
Ilse van Bemmel https://orcid.org/0000-0001-5473-2950
Huib Jan van Langevelde https://orcid.org/0000-0002-0230-5946
Daniel R. van Rossum https://orcid.org/0000-0001-7772-6131
John Wardle https://orcid.org/0000-0002-8960-2942
Jonathan Weintroub https://orcid.org/0000-0002-4603-5204
Norbert Wex https://orcid.org/0000-0003-4058-2837
Robert Wharton https://orcid.org/0000-0002-7416-5209
Maciek Wielgus https://orcid.org/0000-0002-8635-4242
George N. Wong https://orcid.org/0000-0001-6952-2147
Qingwen Wu (吴庆文) https://orcid.org/0000-0003-4773-4987
André Young https://orcid.org/0000-0003-0000-2682
Ken Young https://orcid.org/0000-0002-3666-4920
Ziri Younsi https://orcid.org/0000-0001-9283-1191
Feng Yuan (袁峰) https://orcid.org/0000-0003-3564-6437
J. Anton Zensus https://orcid.org/0000-0001-7470-3321
Guangyao Zhao https://orcid.org/0000-0002-4417-1659
Shan-Shan Zhao https://orcid.org/0000-0002-9774-3606
Jadyn Anczarski https://orcid.org/0000-0003-4317-3385
Frederick K. Baganoff https://orcid.org/0000-0003-3852-6545
Andreas Eckart https://orcid.org/0000-0001-6049-3132
Joseph R. Farah https://orcid.org/0000-0003-4914-5625
Daryl Haggard https://orcid.org/0000-0001-6803-2138
Daniel Michalik https://orcid.org/0000-0002-7618-6556
Andrew Nadolski https://orcid.org/0000-0001-9479-9957
Joseph Neilsen https://orcid.org/0000-0002-8247-786X
Michael A. Nowak https://orcid.org/0000-0001-6923-1315
Rurik A. Primiani https://orcid.org/0000-0003-3910-7529
Paul Yamaguchi https://orcid.org/0000-0002-6017-8199
Shuo Zhang https://orcid.org/0000-0002-2967-790X

References

Abbott, B. P., Abbott, R., Abbott, T. D., et al. 2016, PhRvL, 116, 061102
Abdujabbarov, A., Amir, M., Ahmedov, B., & Ghosh, S. G. 2016, PhRvD, 93, 104004
Akiyama, K., Lu, R.-S., Fish, V. L., et al. 2015, ApJ, 807, 150
Amir, M., Singh, B. P., & Ghosh, S. G. 2018, EPJC, 78, 399
Asada, K., & Nakamura, M. 2012, ApJL, 745, L28
Balbus, S. A., & Hawley, J. F. 1991, ApJ, 376, 214
Ball, D., Özel, F., Psaltis, D., Chan, C.-K., & Sironi, L. 2018, ApJ, 853, 184
Bambi, C. 2013, PhRvD, 87, 107501
Bambi, C., & Freese, K. 2009, PhRvD, 79, 043002
Bardeen, J. M. 1973, in Black Holes (Les Astres Occlus), ed. C. Dewitt & B. S. Dewitt (New York: Gordon and Breach), 215
Bardeen, J. M., & Petterson, J. A. 1975, ApJL, 195, L65
Bardeen, J. M., Press, W. H., & Teukolsky, S. A. 1972, ApJ, 178, 347
Barranco, J., Bernal, A., Degollado, J. C., et al. 2017, PhRvD, 96, 024049
Beskin, V. S., Istomin, Y. N., & Parev, V. I. 1992, SvA, 36, 642
Bird, S., Harris, W. E., Blakeslee, J. P., & Flynn, C. 2010, A&A, 524, A71
Blakeslee, J. P., Jordán, A., Mei, S., et al. 2009, ApJ, 694, 556
Blandford, R. D., & Payne, D. G. 1982, MNRAS, 199, 883
Blandford, R. D., & Znajek, R. L. 1977, MNRAS, 179, 433
Boccardi, B., Krichbaum, T. P., Ros, E., & Zensus, J. A. 2017, A&ARv, 25, 4
Bower, G. C., Dexter, J., Markoff, S., et al. 2015, ApJL, 811, L6
Britzen, S., Fendt, C., Eckart, A., & Karas, V. 2017, A&A, 601, A52
Broderick, A. E., & Loeb, A. 2009, ApJ, 697, 1164
Broderick, A. E., & Narayan, R. 2006, ApJL, 638, L21
Broderick, A. E., Narayan, R., Kormendy, J., et al. 2015, ApJ, 805, 179
Broderick, A. E., & Tchekhovskoy, A. 2015, ApJ, 809, 97
Bronzwaer, T., Davelaar, J., Younsi, Z., et al. 2018, A&A, 613, A2
Brustein, R., & Medved, A. 2017, ForPh, 65, 1600114
Cantiello, M., Blakeslee, J. P., Ferrarese, L., et al. 2018, ApJ, 856, 126
Chael, A., Narayan, R., & Johnson, M. D. 2019, arXiv:1810.01983
Chael, A., Rowan, M., Narayan, R., Johnson, M., & Sironi, L. 2018, MNRAS, 478, 5209
Chael, A. A., Narayan, R., & Sądowski, A. 2017, MNRAS, 470, 2367
Chandra, M., Gammie, C. F., Foucart, F., & Quataert, E. 2015, ApJ, 810, 162
Chen, A. Y., Yuan, Y., & Yang, H. 2018, ApJL, 863, L31
Chirenti, C., & Rezzolla, L. 2016, PhRvD, 94, 084016
Chirenti, C. B. M. H., & Rezzolla, L. 2007, CQGra, 24, 4191
Cunha, P. V. P., Herdeiro, C. A. R., Radu, E., & Rúnarsson, H. F. 2015, PhRvL, 115, 211102
Curtis, H. D. 1918, PLicO, 13, 9
Dastan, S., Saffari, R., & Soroushfar, S. 2016, arXiv:1606.06994
Davelaar, J., Mościbrodzka, M., Bronzwaer, T., & Falcke, H. 2018, A&A, 612, A34
de Gasperin, F., Orrú, E., Murgia, M., et al. 2012, A&A, 547, A56
De Villiers, J.-P., Hawley, J. F., & Krolik, J. H. 2003, ApJ, 599, 1238
De Villiers, J.-P., Hawley, J. F., Krolik, J. H., & Hirose, S. 2005, ApJ, 620, 878
Del Zanna, L., Papini, E., Landi, S., Bugli, M., & Bucciantini, N. 2016, MNRAS, 460, 3753
Dexter, J., Agol, E., Fragile, P. C., & McKinney, J. C. 2010, ApJ, 717, 1092
Dexter, J., & Fragile, P. C. 2013, MNRAS, 432, 2252
Dexter, J., McKinney, J. C., & Agol, E. 2012, MNRAS, 421, 1517
Di Matteo, T., Allen, S. W., Fabian, A. C., Wilson, A. S., & Young, A. J. 2003, ApJ, 582, 133
Dibi, S., Drappeau, S., Fragile, P. C., Markoff, S., & Dexter, J. 2012, MNRAS, 426, 1928
Dionysopoulou, K., Alic, D., Palenzuela, C., Rezzolla, L., & Giacomazzo, B. 2013, PhRvD, 88, 044020
Doeleman, S. S., Fish, V. L., Schenck, D. E., et al. 2012, Sci, 338, 355
Dolence, J. C., Gammie, C. F., Mościbrodzka, M., & Leung, P. K. 2009, ApJS, 184, 387
Dymnikova, I. 1992, GReGr, 24, 235
Eckart, A., & Genzel, R. 1997, MNRAS, 284, 576
EHT Collaboration et al. 2019a, ApJL, 875, L1 (Paper I)
EHT Collaboration et al. 2019b, ApJL, 875, L2 (Paper II)
EHT Collaboration et al. 2019c, ApJL, 875, L3 (Paper III)
EHT Collaboration et al. 2019d, ApJL, 875, L4 (Paper IV)
EHT Collaboration et al. 2019e, ApJL, 875, L6 (Paper VI)
Eiroa, E. F., & Sendra, C. M. 2018, EPJC, 78, 91
Falcke, H., & Biermann, P. L. 1995, A&A, 293, 665
Falcke, H., Melia, F., & Agol, E. 2000, ApJL, 528, L13

Foucart, F., Chandra, M., Gammie, C. F., Quataert, E., & Tchekhovskoy, A. 2017, MNRAS, 470, 2240
Fragile, P. C., & Blaes, O. M. 2008, ApJ, 687, 757
Fragile, P. C., Blaes, O. M., Anninos, P., & Salmonson, J. D. 2007, ApJ, 668, 417
Fromm, C. M., Younsi, Z., Bazcko, A., et al. 2019a, A&A, submitted (arXiv:1904.00106)
Gravity Collaboration, Abuter, R., Amorim, A., et al. 2018a, A&A, 615, L15
Gravity Collaboration, Abuter, R., Amorim, A., et al. 2018b, A&A, 618, L10
Gammie, C. F., McKinney, J. C., & Tóth, G. 2003, ApJ, 589, 444
García, A., Galtsov, D., & Kechkin, O. 1995, PhRvL, 74, 1276
Gebhardt, K., Adams, J., Richstone, D., et al. 2011, ApJ, 729, 119
Ghez, A. M., Klein, B. L., Morris, M., & Becklin, E. E. 1998, ApJ, 509, 678
Giddings, S. B., & Psaltis, D. 2018, PhRvD, 97, 084035
Gold, R., Broderick, A., Younsi, Z., et al. 2019, ApJ, submitted
Grenzebach, A., Perlick, V., & Lämmerzahl, C. 2014, PhRvD, 89, 124004
Hada, K., Doi, A., Kino, M., et al. 2011, Natur, 477, 185
Hada, K., Kino, M., Doi, A., et al. 2013, ApJ, 775, 70
Hada, K., Kino, M., Doi, A., et al. 2016, ApJ, 817, 131
Hada, K., Park, J. H., Kino, M., et al. 2017, PASJ, 69, 71
Harms, R. J., Ford, H. C., Tsvetanov, Z. I., et al. 1994, ApJL, 435, L35
Hawley, J. F., & Krolik, J. H. 2006, ApJ, 641, 103
Herdeiro, C. A. R., & Radu, E. 2014, PhRvL, 112, 221101
Hilbert, D. 1917, Nachrichten von der Königlichen Gesellschaft der Wissenschaften zu Göttingen—Mathematisch-physikalische Klasse (Berlin: Weidmannsche Buchhandlung), 53
Hirotani, K., & Pu, H.-Y. 2016, ApJ, 818, 50
Hou, X., Xu, Z., Zhou, M., & Wang, J. 2018, JCAP, 7, 015
Howes, G. G. 2010, MNRAS, 409, L104
Ichimaru, S. 1977, ApJ, 214, 840
Igumenshchev, I. V., Narayan, R., & Abramowicz, M. A. 2003, ApJ, 592, 1042
Jiménez-Rosales, A., & Dexter, J. 2018, MNRAS, 478, 1875
Johannsen, T., & Psaltis, D. 2010, ApJ, 718, 446
Joshi, P. S., Malafarina, D., & Narayan, R. 2014, CQGra, 31, 015002
Jüttner, F. 1911, AnPh, 339, 856
Kaup, D. J. 1968, PhRv, 172, 1331
Kawazura, Y., Barnes, M., & Schekochihin, A. A. 2018, arXiv:1807.07702
Kim, J.-Y., Krichbaum, T. P., Lu, R.-S., et al. 2018, A&A, 616, A188
Kino, M., Takahara, F., Hada, K., et al. 2015, ApJ, 803, 30
Kino, M., Takahara, F., Hada, K., & Doi, A. 2014, ApJ, 786, 5
Kuo, C. Y., Asada, K., Rao, R., et al. 2014, ApJL, 783, L33
Leung, P. K., Gammie, C. F., & Noble, S. C. 2011, ApJ, 737, 21
Levermore, C. D. 1984, JQSRT, 31, 149
Levinson, A., & Cerutti, B. 2018, A&A, 616, A184
Levinson, A., & Rieger, F. 2011, ApJ, 730, 123
Li, Y.-P., Yuan, F., & Xie, F.-G. 2016, ApJ, 830, 78
Li, Y.-R., Yuan, Y.-F., Wang, J.-M., Wang, J.-C., & Zhang, S. 2009, ApJ, 699, 513
Liska, M., Hesp, C., Tchekhovskoy, A., et al. 2018, MNRAS, 474, L81
Luminet, J.-P. 1979, A&A, 75, 228
Lynden-Bell, D. 2006, MNRAS, 369, 1167
Mazur, P. O., & Mottola, E. 2004, PNAS, 101, 9545
McKinney, J. C. 2006, MNRAS, 368, 1561
McKinney, J. C., & Blandford, R. D. 2009, MNRAS, 394, L126
McKinney, J. C., & Gammie, C. F. 2004, ApJ, 611, 977
McKinney, J. C., & Narayan, R. 2007, MNRAS, 375, 513
McKinney, J. C., Tchekhovskoy, A., & Blandford, R. D. 2012, MNRAS, 423, 3083
McKinney, J. C., Tchekhovskoy, A., & Blandford, R. D. 2013, Sci, 339, 49
McKinney, J. C., Tchekhovskoy, A., Sadowski, A., & Narayan, R. 2014, MNRAS, 441, 3177
Mertens, F., Lobanov, A. P., Walker, R. C., & Hardee, P. E. 2016, A&A, 595, A54
Miyoshi, M., Moran, J., Herrnstein, J., et al. 1995, Natur, 373, 127
Mizuno, Y., Younsi, Z., Fromm, C. M., et al. 2018, NatAs, 2, 585
Moffat, J. W. 2015, EPJC, 75, 175
Mościbrodzka, M., Dexter, J., Davelaar, J., & Falcke, H. 2017, MNRAS, 468, 2214
Mościbrodzka, M., Falcke, H., & Shiokawa, H. 2016, A&A, 586, A38
Mościbrodzka, M., & Gammie, C. F. 2018, MNRAS, 475, 43
Mościbrodzka, M., Gammie, C. F., Dolence, J. C., & Shiokawa, H. 2011, ApJ, 735, 9
Nakamura, M., Asada, K., Hada, K., et al. 2018, ApJ, 868, 146
Narayan, R., Igumenshchev, I. V., & Abramowicz, M. A. 2003, PASJ, 55, L69
Narayan, R., Sądowski, A., Penna, R. F., & Kulkarni, A. K. 2012, MNRAS, 426, 3241
Narayan, R., & Yi, I. 1994, ApJL, 428, L13
Narayan, R., & Yi, I. 1995, ApJ, 452, 710
Nedkova, P. G., Tinchev, V. K., & Yazadjiev, S. S. 2013, PhRvD, 88, 124019
Novikov, I. D., & Thorne, K. S. 1973, in Black Holes (Les Astres Occlus), ed. C. Dewitt & B. S. Dewitt (New York: Gordon & Breach), 343
Olivares, H., Younsi, Z., Fromm, C. M., et al. 2019a, PhRvD, arXiv:1809.08682
Owen, F. N., Eilek, J. A., & Kassim, N. E. 2000, ApJ, 543, 611
Palenzuela, C., Lehner, L., Reula, O., & Rezzolla, L. 2009, MNRAS, 394, 1727
Parfrey, K., Philippov, A., & Cerutti, B. 2019, PhRvL, 122, 035101
Park, J., Hada, K., Kino, M., et al. 2019, ApJ, 871, 257
Porth, O., Olivares, H., Mizuno, Y., et al. 2017, ComAC, 4, 1
Prieto, M. A., Fernández-Ontiveros, J. A., Markoff, S., Espada, D., & González-Martín, O. 2016, MNRAS, 457, 3801
Pu, H.-Y., Wu, K., Younsi, Z., et al. 2017, ApJ, 845, 160
Qian, Q., Fendt, C., Noble, S., & Bugli, M. 2017, ApJ, 834, 29
Rees, M. J., Begelman, M. C., Blandford, R. D., & Phinney, E. S. 1982, Natur, 295, 17
Ressler, S. M., Tchekhovskoy, A., Quataert, E., & Gammie, C. F. 2017, MNRAS, 467, 3604
Ressler, S. M., Tchekhovskoy, A., Quataert, E., Chandra, M., & Gammie, C. F. 2015, MNRAS, 454, 1848
Reynolds, C. S., Di Matteo, T., Fabian, A. C., Hwang, U., & Canizares, C. R. 1996, MNRAS, 283, L111
Rezzolla, L., & Zanotti, O. 2013, Relativistic Hydrodynamics (Oxford: Oxford Univ. Press)
Ripperda, B., Porth, O., Sironi, L., & Keppens, R. 2019, MNRAS, 485, 299
Rowan, M. E., Sironi, L., & Narayan, R. 2017, ApJ, 850, 29
Ryan, B. R., Dolence, J. C., & Gammie, C. F. 2015, ApJ, 807, 31
Ryan, B. R., Ressler, S. M., Dolence, J. C., Gammie, C., & Quataert, E. 2018, ApJ, 864, 126
Saxton, C. J., Younsi, Z., & Wu, K. 2016, MNRAS, 461, 4295
Sądowski, A., Narayan, R., McKinney, J. C., & Tchekhovskoy, A. 2014, MNRAS, 439, 503
Sądowski, A., Narayan, R., Penna, R., & Zhu, Y. 2013a, MNRAS, 436, 3856
Sądowski, A., Narayan, R., Tchekhovskoy, A., & Zhu, Y. 2013b, MNRAS, 429, 3533
Sądowski, A., Wielgus, M., Narayan, R., et al. 2017, MNRAS, 466, 705
Shaikh, R. 2018, PhRvD, 98, 024044
Shaikh, R., Kocherlakota, P., Narayan, R., & Joshi, P. S. 2019, MNRAS, 482, 52
Shiokawa, H. 2013, PhD thesis, Univ. Illinois at Urbana-Champaign
Spitzer, L. 1962, Physics of Fully Ionized Gases (2nd ed.; New York: Interscience)
Stawarz, Ł., Aharonian, F., Kataoka, J., et al. 2006, MNRAS, 370, 981
Takahashi, K., Toma, K., Kino, M., Nakamura, M., & Hada, K. 2018, ApJ, 868, 82
Takahashi, R. 2004, ApJ, 611, 996
Tchekhovskoy, A., Narayan, R., & McKinney, J. C. 2011, MNRAS, 418, L79
Teo, E. 2003, GReGr, 35, 1909
von Laue, M. 1921, Relativitätstheorie, Vol. 1 (Braunschweig: Friedrich Vieweg & Sohn) Das Relativitätsprinzip der Lorentztransformation - Vol. 2. Die allgemeine Relativitätstheorie und Einsteins Lehre von der Schwerkraft
Walker, R. C., Hardee, P. E., Davies, F. B., Ly, C., & Junor, W. 2018, ApJ, 855, 128
Walsh, J. L., Barth, A. J., Ho, L. C., & Sarzi, M. 2013, ApJ, 770, 86
Watson, M., & Nishikawa, K.-I. 2010, CoPhC, 181, 1750
Wong, G. N., Prather, B., & Gammie, C. F. 2019, ApJ, submitted
Younsi, Z., Zhidenko, A., Rezzolla, L., Konoplya, R., & Mizuno, Y. 2016, PhRvD, 94, 084025
Yu, Z., Yuan, F., & Ho, L. C. 2011, ApJ, 726, 87
Yuan, F., Gan, Z., Narayan, R., et al. 2015, ApJ, 804, 101
Yuan, F., & Narayan, R. 2014, ARA&A, 52, 529

The Event Horizon Telescope Collaboration

Kazunori Akiyama[1,2,3,4], Antxon Alberdi[5], Walter Alef[6], Keiichi Asada[7], Rebecca Azulay[8,9,6], Anne-Kathrin Baczko[6], David Ball[10], Mislav Baloković[4,11], John Barrett[2], Dan Bintley[12], Lindy Blackburn[4,11], Wilfred Boland[13], Katherine L. Bouman[4,11,14], Geoffrey C. Bower[15], Michael Bremer[16], Christiaan D. Brinkerink[17], Roger Brissenden[4,11], Silke Britzen[6], Avery E. Broderick[18,19,20], Dominique Broguiere[16], Thomas Bronzwaer[17], Do-Young Byun[21,22], John E. Carlstrom[23,24,25,26], Andrew Chael[4,11], Chi-kwan Chan[10,27], Shami Chatterjee[28], Koushik Chatterjee[29], Ming-Tang Chen[15], Yongjun Chen (陈永军)[30,31], Ilje Cho[21,22], Pierre Christian[10,11], John E. Conway[32], James M. Cordes[28], Geoffrey B. Crew[2], Yuzhu Cui[33,34], Jordy Davelaar[17], Mariafelicia De Laurentis[35,36,37], Roger Deane[38,39], Jessica Dempsey[12], Gregory Desvignes[6], Jason Dexter[40], Sheperd S. Doeleman[4,11], Ralph P. Eatough[6], Heino Falcke[17], Vincent L. Fish[2], Ed Fomalont[1], Raquel Fraga-Encinas[17], Per Friberg[12], Christian M. Fromm[36], José L. Gómez[5], Peter Galison[1,41,42], Charles F. Gammie[43,44], Roberto García[16], Olivier Gentaz[16], Boris Georgiev[19,20], Ciriaco Goddi[17,45], Roman Gold[36], Minfeng Gu (顾敏峰)[30,46], Mark Gurwell[11], Kazuhiro Hada[33,34], Michael H. Hecht[2], Ronald Hesper[47], Luis C. Ho (何子山)[48,49], Paul Ho[7], Mareki Honma[33,34], Chih-Wei L. Huang[7], Lei Huang (黄磊)[30,46], David H. Hughes[50], Shiro Ikeda[3,51,52,53], Makoto Inoue[7], Sara Issaoun[17], David J. James[4,11], Buell T. Jannuzi[10], Michael Janssen[17], Britton Jeter[19,20], Wu Jiang (江悟)[30], Michael D. Johnson[4,11], Svetlana Jorstad[54,55], Taehyun Jung[21,22], Mansour Karami[18,19], Ramesh Karuppusamy[6], Tomohisa Kawashima[3], Garrett K. Keating[11], Mark Kettenis[56], Jae-Young Kim[6], Junhan Kim[10], Jongsoo Kim[21], Motoki Kino[3,57], Jun Yi Koay[7], Patrick M. Koch[7], Shoko Koyama[7], Michael Kramer[6], Carsten Kramer[16], Thomas P. Krichbaum[6], Cheng-Yu Kuo[58], Tod R. Lauer[59], Sang-Sung Lee[21], Yan-Rong Li (李彦荣)[60], Zhiyuan Li (李志远)[61,62], Michael Lindqvist[32], Kuo Liu[6], Elisabetta Liuzzo[63], Wen-Ping Lo[7,64], Andrei P. Lobanov[6], Laurent Loinard[65,66], Colin Lonsdale[2], Ru-Sen Lu (路如森)[30,6], Nicholas R. MacDonald[6], Jirong Mao (毛基荣)[67,68,69], Sera Markoff[29,70], Daniel P. Marrone[10], Alan P. Marscher[54], Iván Martí-Vidal[32,71], Satoki Matsushita[7], Lynn D. Matthews[2], Lia Medeiros[10,72], Karl M. Menten[6], Yosuke Mizuno[36], Izumi Mizuno[12], James M. Moran[4,11], Kotaro Moriyama[33,2], Monika Moscibrodzka[17], Cornelia Müller[6,17], Hiroshi Nagai[3,34], Neil M. Nagar[73], Masanori Nakamura[7], Ramesh Narayan[4,11], Gopal Narayanan[74], Iniyan Natarajan[39], Roberto Neri[16], Chunchong Ni[19,20], Aristeidis Noutsos[6], Hiroki Okino[33,75], Héctor Olivares[36], Tomoaki Oyama[33], Feryal Özel[10], Daniel C. M. Palumbo[4,11], Nimesh Patel[11], Ue-Li Pen[76,77,78,18], Dominic W. Pesce[4,11], Vincent Piétu[16], Richard Plambeck[79], Aleksandar PopStefanija[74], Oliver Porth[36,29], Ben Prather[43], Jorge A. Preciado-López[18], Dimitrios Psaltis[10], Hung-Yi Pu[18], Venkatessh Ramakrishnan[73], Ramprasad Rao[15], Mark G. Rawlings[12], Alexander W. Raymond[4,11], Luciano Rezzolla[36], Bart Ripperda[36], Freek Roelofs[17], Alan Rogers[2], Eduardo Ros[6], Mel Rose[10], Arash Roshanineshat[10], Helge Rottmann[6], Alan L. Roy[6], Chet Ruszczyk[2], Benjamin R. Ryan[80,81], Kazi L. J. Rygl[63], Salvador Sánchez[82], David Sánchez-Arguelles[50,83], Mahito Sasada[33,84], Tuomas Savolainen[6,85,86], F. Peter Schloerb[74], Karl-Friedrich Schuster[16], Lijing Shao[6,49], Zhiqiang Shen (沈志强)[30,31], Des Small[56], Bong Won Sohn[21,22,87], Jason SooHoo[2], Fumie Tazaki[33], Paul Tiede[19,20], Remo P. J. Tilanus[17,45,88], Michael Titus[2], Kenji Toma[89,90], Pablo Torne[6,82], Tyler Trent[10], Sascha Trippe[91], Shuichiro Tsuda[33], Ilse van Bemmel[56], Huib Jan van Langevelde[56,92], Daniel R. van Rossum[17], Jan Wagner[6], John Wardle[93], Jonathan Weintroub[4,11], Norbert Wex[6], Robert Wharton[6], Maciek Wielgus[4,11], George N. Wong[43], Qingwen Wu (吴庆文)[94], André Young[17], Ken Young[11], Ziri Younsi[95,36], Feng Yuan (袁峰)[30,46,96], Ye-Fei Yuan (袁业飞)[97], J. Anton Zensus[6], Guangyao Zhao[21], Shan-Shan Zhao[17,61], Ziyan Zhu[42], Jadyn Anczarski[98], Frederick K. Baganoff[99], Andreas Eckart[6,100], Joseph R. Farah[11,101,4], Daryl Haggard[102,103,104], Zheng Meyer-Zhao[7,105], Daniel Michalik[106,107], Andrew Nadolski[44], Joseph Neilsen[98], Hiroaki Nishioka[7], Michael A. Nowak[108], Nicolas Pradel[7], Rurik A. Primiani[109], Kamal Souccar[74], Laura Vertatschitsch[11,109], Paul Yamaguchi[11], and Shuo Zhang[99]

[1] National Radio Astronomy Observatory, 520 Edgemont Rd, Charlottesville, VA 22903, USA
[2] Massachusetts Institute of Technology Haystack Observatory, 99 Millstone Road, Westford, MA 01886, USA
[3] National Astronomical Observatory of Japan, 2-21-1 Osawa, Mitaka, Tokyo 181-8588, Japan
[4] Black Hole Initiative at Harvard University, 20 Garden Street, Cambridge, MA 02138, USA
[5] Instituto de Astrofísica de Andalucía-CSIC, Glorieta de la Astronomía s/n, E-18008 Granada, Spain
[6] Max-Planck-Institut für Radioastronomie, Auf dem Hügel 69, D-53121 Bonn, Germany
[7] Institute of Astronomy and Astrophysics, Academia Sinica, 11F of Astronomy-Mathematics Building, AS/NTU No. 1, Sec. 4, Roosevelt Rd, Taipei 10617, Taiwan, R.O.C.
[8] Departament d'Astronomia i Astrofísica, Universitat de València, C. Dr. Moliner 50, E-46100 Burjassot, València, Spain
[9] Observatori Astronòmic, Universitat de València, C. Catedrático José Beltrán 2, E-46980 Paterna, València, Spain
[10] Steward Observatory and Department of Astronomy, University of Arizona, 933 N. Cherry Ave., Tucson, AZ 85721, USA
[11] Center for Astrophysics | Harvard & Smithsonian, 60 Garden Street, Cambridge, MA 02138, USA
[12] East Asian Observatory, 660 N. A'ohoku Pl., Hilo, HI 96720, USA
[13] Nederlandse Onderzoekschool voor Astronomie (NOVA), PO Box 9513, 2300 RA Leiden, The Netherlands
[14] California Institute of Technology, 1200 East California Boulevard, Pasadena, CA 91125, USA
[15] Institute of Astronomy and Astrophysics, Academia Sinica, 645 N. A'ohoku Place, Hilo, HI 96720, USA
[16] Institut de Radioastronomie Millimétrique, 300 rue de la Piscine, 38406 Saint Martin d'Hères, France

[17] Department of Astrophysics, Institute for Mathematics, Astrophysics and Particle Physics (IMAPP), Radboud University, P.O. Box 9010, 6500 GL Nijmegen, The Netherlands
[18] Perimeter Institute for Theoretical Physics, 31 Caroline Street North, Waterloo, ON, N2L 2Y5, Canada
[19] Department of Physics and Astronomy, University of Waterloo, 200 University Avenue West, Waterloo, ON, N2L 3G1, Canada
[20] Waterloo Centre for Astrophysics, University of Waterloo, Waterloo, ON N2L 3G1 Canada
[21] Korea Astronomy and Space Science Institute, Daedeok-daero 776, Yuseong-gu, Daejeon 34055, Republic of Korea
[22] University of Science and Technology, Gajeong-ro 217, Yuseong-gu, Daejeon 34113, Republic of Korea
[23] Kavli Institute for Cosmological Physics, University of Chicago, Chicago, IL 60637, USA
[24] Department of Astronomy and Astrophysics, University of Chicago, 5640 South Ellis Avenue, Chicago, IL 60637, USA
[25] Department of Physics, University of Chicago, 5720 South Ellis Avenue, Chicago, IL 60637, USA
[26] Enrico Fermi Institute, University of Chicago, 5640 South Ellis Avenue, Chicago, IL 60637, USA
[27] Data Science Institute, University of Arizona, 1230 N. Cherry Ave., Tucson, AZ 85721, USA
[28] Cornell Center for Astrophysics and Planetary Science, Cornell University, Ithaca, NY 14853, USA
[29] Anton Pannekoek Institute for Astronomy, University of Amsterdam, Science Park 904, 1098 XH, Amsterdam, The Netherlands
[30] Shanghai Astronomical Observatory, Chinese Academy of Sciences, 80 Nandan Road, Shanghai 200030, People's Republic of China
[31] Key Laboratory of Radio Astronomy, Chinese Academy of Sciences, Nanjing 210008, People's Republic of China
[32] Department of Space, Earth and Environment, Chalmers University of Technology, Onsala Space Observatory, SE-439 92 Onsala, Sweden
[33] Mizusawa VLBI Observatory, National Astronomical Observatory of Japan, 2-12 Hoshigaoka, Mizusawa, Oshu, Iwate 023-0861, Japan
[34] Department of Astronomical Science, The Graduate University for Advanced Studies (SOKENDAI), 2-21-1 Osawa, Mitaka, Tokyo 181-8588, Japan
[35] Dipartimento di Fisica "E. Pancini", Universitá di Napoli "Federico II", Compl. Univ. di Monte S. Angelo, Edificio G, Via Cinthia, I-80126, Napoli, Italy
[36] Institut für Theoretische Physik, Goethe-Universität Frankfurt, Max-von-Laue-Straße 1, D-60438 Frankfurt am Main, Germany
[37] INFN Sez. di Napoli, Compl. Univ. di Monte S. Angelo, Edificio G, Via Cinthia, I-80126, Napoli, Italy
[38] Department of Physics, University of Pretoria, Lynnwood Road, Hatfield, Pretoria 0083, South Africa
[39] Centre for Radio Astronomy Techniques and Technologies, Department of Physics and Electronics, Rhodes University, Grahamstown 6140, South Africa
[40] Max-Planck-Institut für Extraterrestrische Physik, Giessenbachstr. 1, D-85748 Garching, Germany
[41] Department of History of Science, Harvard University, Cambridge, MA 02138, USA
[42] Department of Physics, Harvard University, Cambridge, MA 02138, USA
[43] Department of Physics, University of Illinois, 1110 West Green St, Urbana, IL 61801, USA
[44] Department of Astronomy, University of Illinois at Urbana-Champaign, 1002 West Green Street, Urbana, Illinois 61801, USA
[45] Leiden Observatory—Allegro, Leiden University, P.O. Box 9513, 2300 RA Leiden, The Netherlands
[46] Key Laboratory for Research in Galaxies and Cosmology, Chinese Academy of Sciences, Shanghai 200030, People's Republic of China
[47] NOVA Sub-mm Instrumentation Group, Kapteyn Astronomical Institute, University of Groningen, Landleven 12, 9747 AD Groningen, The Netherlands
[48] Department of Astronomy, School of Physics, Peking University, Beijing 100871, People's Republic of China
[49] Kavli Institute for Astronomy and Astrophysics, Peking University, Beijing 100871, People's Republic of China
[50] Instituto Nacional de Astrofísica, Óptica y Electrónica. Apartado Postal 51 y 216, 72000. Puebla Pue., México
[51] The Institute of Statistical Mathematics, 10-3 Midori-cho, Tachikawa, Tokyo, 190-8562, Japan
[52] Department of Statistical Science, The Graduate University for Advanced Studies (SOKENDAI), 10-3 Midori-cho, Tachikawa, Tokyo 190-8562, Japan
[53] Kavli Institute for the Physics and Mathematics of the Universe, The University of Tokyo, 5-1-5 Kashiwanoha, Kashiwa, 277-8583, Japan
[54] Institute for Astrophysical Research, Boston University, 725 Commonwealth Ave., Boston, MA 02215, USA
[55] Astronomical Institute, St. Petersburg University, Universitetskij pr., 28, Petrodvorets,198504 St.Petersburg, Russia
[56] Joint Institute for VLBI ERIC (JIVE), Oude Hoogeveensedijk 4, 7991 PD Dwingeloo, The Netherlands
[57] Kogakuin University of Technology and Engineering, Academic Support Center, 2665-1 Nakano, Hachioji, Tokyo 192-0015, Japan
[58] Physics Department, National Sun Yat-Sen University, No. 70, Lien-Hai Rd, Kaosiung City 80424, Taiwan, R.O.C
[59] National Optical Astronomy Observatory, 950 North Cherry Ave., Tucson, AZ 85719, USA
[60] Key Laboratory for Particle Astrophysics, Institute of High Energy Physics, Chinese Academy of Sciences, 19B Yuquan Road, Shijingshan District, Beijing, People's Republic of China
[61] School of Astronomy and Space Science, Nanjing University, Nanjing 210023, People's Republic of China
[62] Key Laboratory of Modern Astronomy and Astrophysics, Nanjing University, Nanjing 210023, People's Republic of China
[63] Italian ALMA Regional Centre, INAF-Istituto di Radioastronomia, Via P. Gobetti 101, 40129 Bologna, Italy
[64] Department of Physics, National Taiwan University, No.1, Sect.4, Roosevelt Rd., Taipei 10617, Taiwan, R.O.C
[65] Instituto de Radioastronomía y Astrofísica, Universidad Nacional Autónoma de México, Morelia 58089, México
[66] Instituto de Astronomía, Universidad Nacional Autónoma de México, CdMx 04510, México
[67] Yunnan Observatories, Chinese Academy of Sciences, 650011 Kunming, Yunnan Province, People's Republic of China
[68] Center for Astronomical Mega-Science, Chinese Academy of Sciences, 20A Datun Road, Chaoyang District, Beijing, 100012, People's Republic of China
[69] Key Laboratory for the Structure and Evolution of Celestial Objects, Chinese Academy of Sciences, 650011 Kunming, People's Republic of China
[70] Gravitation Astroparticle Physics Amsterdam (GRAPPA) Institute, University of Amsterdam, Science Park 904, 1098 XH Amsterdam, The Netherlands
[71] Centro Astronómico de Yebes (IGN), Apartado 148, 19180 Yebes, Spain
[72] Department of Physics, Broida Hall, University of California Santa Barbara, Santa Barbara, CA 93106, USA
[73] Astronomy Department, Universidad de Concepción, Casilla 160-C, Concepción, Chile
[74] Department of Astronomy, University of Massachusetts, 01003, Amherst, MA, USA
[75] Department of Astronomy, Graduate School of Science, The University of Tokyo, 7-3-1 Hongo, Bunkyo-ku, Tokyo 113-0033, Japan
[76] Canadian Institute for Theoretical Astrophysics, University of Toronto, 60 St. George Street, Toronto, ON M5S 3H8, Canada
[77] Dunlap Institute for Astronomy and Astrophysics, University of Toronto, 50 St. George Street, Toronto, ON M5S 3H4, Canada
[78] Canadian Institute for Advanced Research, 180 Dundas St West, Toronto, ON M5G 1Z8, Canada
[79] Radio Astronomy Laboratory, University of California, Berkeley, CA 94720, USA
[80] CCS-2, Los Alamos National Laboratory, P.O. Box 1663, Los Alamos, NM 87545, USA
[81] Center for Theoretical Astrophysics, Los Alamos National Laboratory, Los Alamos, NM, 87545, USA
[82] Instituto de Radioastronomía Milimétrica, IRAM, Avenida Divina Pastora 7, Local 20, 18012, Granada, Spain
[83] Consejo Nacional de Ciencia y Tecnología, Av. Insurgentes Sur 1582, 03940, Ciudad de México, México
[84] Hiroshima Astrophysical Science Center, Hiroshima University, 1-3-1 Kagamiyama, Higashi-Hiroshima, Hiroshima 739-8526, Japan
[85] Aalto University Department of Electronics and Nanoengineering, PL 15500, 00076 Aalto, Finland
[86] Aalto University Metsähovi Radio Observatory, Metsähovintie 114, 02540 Kylmälä, Finland
[87] Department of Astronomy, Yonsei University, Yonsei-ro 50, Seodaemun-gu, 03722 Seoul, Republic of Korea
[88] Netherlands Organisation for Scientific Research (NWO), Postbus 93138, 2509 AC Den Haag, The Netherlands

[89] Frontier Research Institute for Interdisciplinary Sciences, Tohoku University, Sendai 980-8578, Japan
[90] Astronomical Institute, Tohoku University, Sendai 980-8578, Japan
[91] Department of Physics and Astronomy, Seoul National University, Gwanak-gu, Seoul 08826, Republic of Korea
[92] Leiden Observatory, Leiden University, Postbus 2300, 9513 RA Leiden, The Netherlands
[93] Physics Department, Brandeis University, 415 South Street, Waltham, MA 02453, USA
[94] School of Physics, Huazhong University of Science and Technology, Wuhan, Hubei, 430074, People's Republic of China
[95] Mullard Space Science Laboratory, University College London, Holmbury St. Mary, Dorking, Surrey, RH5 6NT, UK
[96] School of Astronomy and Space Sciences, University of Chinese Academy of Sciences, No. 19A Yuquan Road, Beijing 100049, People's Republic of China
[97] Astronomy Department, University of Science and Technology of China, Hefei 230026, People's Republic of China
[98] Department of Physics,Villanova University, 800 E. Lancaster Ave, Villanova, PA, 19085, USA
[99] Kavli Institute for Astrophysics and Space Research, Massachusetts Institute of Technology, Cambridge, MA 02139, USA
[100] Physikalisches Institut der Universität zu Köln, Zülpicher Str. 77, D-50937 Köln, Germany
[101] University of Massachusetts Boston, 100 William T, Morrissey Blvd, Boston, MA 02125, USA
[102] Department of Physics, McGill University, 3600 University Street, Montréal, QC H3A 2T8, Canada
[103] McGill Space Institute, McGill University, 3550 University Street, Montréal, QC H3A 2A7, Canada
[104] CIFAR Azrieli Global Scholar, Gravity and the Extreme Universe Program, Canadian Institute for Advanced Research, 661 University Avenue, Suite 505, Toronto, ON M5G 1M1, Canada
[105] ASTRON, Oude Hoogeveensedijk 4, 7991 PD Dwingeloo, The Netherlands
[106] Science Support Office, Directorate of Science, European Space Research and Technology Centre (ESA/ESTEC), Keplerlaan 1, 2201 AZ Noordwijk, The Netherlands
[107] University of Chicago, 5640 South Ellis Avenue, Chicago, IL 60637, USA
[108] Physics Dept., CB 1105, Washington University, One Brookings Drive, St. Louis, MO 63130-4899, USA
[109] Systems and Technology Research, 600 West Cummings Park, Woburn, MA 01801, USA

The Astrophysical Journal Letters, 875:L6 (44pp), 2019 April 10 https://doi.org/10.3847/2041-8213/ab1141
© 2019. The American Astronomical Society.
OPEN ACCESS

First M87 Event Horizon Telescope Results. VI. The Shadow and Mass of the Central Black Hole

The Event Horizon Telescope Collaboration
(See the end matter for the full list of authors.)
Received 2019 March 8; revised 2019 March 18; accepted 2019 March 20; published 2019 April 10

Abstract

We present measurements of the properties of the central radio source in M87 using Event Horizon Telescope data obtained during the 2017 campaign. We develop and fit geometric crescent models (asymmetric rings with interior brightness depressions) using two independent sampling algorithms that consider distinct representations of the visibility data. We show that the crescent family of models is statistically preferred over other comparably complex geometric models that we explore. We calibrate the geometric model parameters using general relativistic magnetohydrodynamic (GRMHD) models of the emission region and estimate physical properties of the source. We further fit images generated from GRMHD models directly to the data. We compare the derived emission region and black hole parameters from these analyses with those recovered from reconstructed images. There is a remarkable consistency among all methods and data sets. We find that >50% of the total flux at arcsecond scales comes from near the horizon, and that the emission is dramatically suppressed interior to this region by a factor >10, providing direct evidence of the predicted shadow of a black hole. Across all methods, we measure a crescent diameter of $42 \pm 3\,\mu$as and constrain its fractional width to be <0.5. Associating the crescent feature with the emission surrounding the black hole shadow, we infer an angular gravitational radius of $GM/Dc^2 = 3.8 \pm 0.4\,\mu$as. Folding in a distance measurement of $16.8^{+0.8}_{-0.7}$ Mpc gives a black hole mass of $M = 6.5 \pm 0.2|_{\rm stat} \pm 0.7|_{\rm sys} \times 10^9\,M_\odot$. This measurement from lensed emission near the event horizon is consistent with the presence of a central Kerr black hole, as predicted by the general theory of relativity.

Key words: black hole physics – galaxies: individual (M87) – gravitation – techniques: high angular resolution – techniques: interferometric

1. Introduction

Einstein's general theory of relativity not only predicts the existence of black holes, but also provides a means to directly observe them. Photons can escape from near the event horizon via an unstable circular orbit (von Laue 1921; Bardeen 1973), whose observational manifestation would be a bright ring of emission surrounding a dark interior black hole "shadow" (Luminet 1979; Falcke et al. 2000). The diameter of the shadow for a black hole of mass M as seen by a distant observer is predicted to be $\simeq$9.6–10.4 GM/c^2, which is larger than twice the coordinate radius of the event horizon due to light-bending effects (Takahashi 2004; Johannsen & Psaltis 2010). The range results from different values of black hole spin and observer inclination angle. The black hole shadow can only be seen if (i) there are a sufficient number of emitted photons to illuminate the black hole, (ii) the emission comes from close enough to the black hole to be gravitationally lensed around it, and (iii) the surrounding plasma is sufficiently transparent at the observed wavelength. For nearby low-luminosity black holes accreting via a radiatively inefficient flow, these conditions can be met at millimeter wavelengths (e.g., Özel et al. 2000; Ho 2008; Yuan & Narayan 2014).

The nearby massive elliptical galaxy M87 provides an ideal laboratory to search for such a black hole shadow. It is relatively nearby ($D \simeq 16.8$ Mpc) and has long been known to host a bright, compact radio source at its center (Cohen et al. 1969). Starting with Young et al. (1978) and Sargent et al. (1978), several attempts have been made to "weigh" the supermassive black hole (SMBH) hypothesized to power the radio source. Recent stellar-dynamics observations by Gebhardt et al. (2011) found $M = (6.6 \pm 0.4) \times 10^9 M_\odot$, while the latest gas dynamics observations by Walsh et al. (2013) yielded a more modest $M = (3.5^{+0.9}_{-0.7}) \times 10^9 M_\odot$. Both values assumed a distance $D = 17.9$ Mpc. Strictly interpreted within the predictions of the general theory of relativity, these measurements make a strong case that M87 does harbor some sort of compact massive dark object at its center, but they have insufficient resolution to formally demonstrate that it is indeed an SMBH. For M87 the expected shadow angular diameter is $\simeq 20$ or $\simeq 38\mu$ as, which is now accessible using global very long baseline interferometry (VLBI) at millimeter wavelengths (EHT Collaboration et al. 2019a, hereafter Paper II).

Accreting black holes are powered by matter flowing in via an accretion disk that in many cases launches a powerful jet of magnetized, relativistic plasma (e.g., Blandford & Znajek 1977; Blandford & Payne 1982). M87 exhibits the characteristic flat-to-inverted radio/millimeter (mm) synchrotron spectrum considered to be a hallmark of the compact innermost jet core in low-luminosity active galactic nuclei (AGNs; e.g., Blandford & Königl 1979; Ho 1999). In this picture, the jet photosphere moves inward with increasing frequency up to the spectral break, at which point the entire jet becomes optically thin. The average broadband spectrum of M87 (Reynolds et al. 1996; Di Matteo et al. 2003; Prieto et al. 2016) indicates that the mm-band should straddle this transition. While images at longer radio wavelengths reveal extended jet structure (e.g., Asada & Nakamura 2012; Hada et al. 2016; Mertens et al. 2016; Kim et al. 2018; Walker et al. 2018), both the observed core shift (Hada et al. 2011) and compact size of $\simeq$40 μas from past mm-VLBI (Doeleman et al. 2012;

Original content from this work may be used under the terms of the Creative Commons Attribution 3.0 licence. Any further distribution of this work must maintain attribution to the author(s) and the title of the work, journal citation and DOI.

Akiyama et al. 2015) are consistent with an origin of the mm-band emission near the event horizon of the central black hole.

Although the photon ring and shadow predictions are clear, the image morphology will depend on the physical origin of the surrounding emission and spacetime of the black hole. If the observed synchrotron radiation at 1.3 mm originates far from the black hole, the forward jet will dominate the observed emission and the lensed emission and shadow feature should be weak (Broderick & Loeb 2009). If instead the emission comes from near the event horizon, either the counter-jet or the accretion flow can produce a compact ring- or crescent-like image surrounding the shadow (Dexter et al. 2012). This type of image is now known to be commonly produced in radiative models of M87 based on general relativistic magnetohydrodynamic (GRMHD) simulations (Dexter et al. 2012; Mościbrodzka et al. 2016; Ryan et al. 2018; Chael et al. 2019b; see EHT Collaboration et al. 2019d, hereafter Paper V).

The outline of the shadow is expected to be nearly circular, if the central object in M87 is a black hole described by the Kerr metric (Bardeen 1973; Takahashi 2004). Violations of the no-hair theorem generically change the shadow shape and size (e.g., Bambi & Freese 2009; Johannsen & Psaltis 2010; Falcke & Markoff 2013; Broderick et al. 2014; Cunha & Herdeiro 2018). Therefore, detecting a shadow and extracting its characteristic properties, such as size and degree of asymmetry, offers a chance to constrain the spacetime metric.

The high resolution necessary to resolve horizon scales for M87 has been achieved for the first time by the Event Horizon Telescope (EHT) in April 2017, with an array that spanned eight stations in six sites across the globe (Paper II). The EHT observed M87 on four days (April 5, 6, 10, and 11) at 1.3 mm (EHT Collaboration et al. 2019b, hereafter Paper III), and imaging techniques applied to this data set reveal the presence of an asymmetric ring structure (EHT Collaboration et al. 2019c, hereafter Paper IV). A large library of model images generated from GRMHD simulations generically finds such features to arise from emission produced near the black hole (Paper V) which is strongly lensed around the shadow.

In this Letter we use three different methods to measure properties of the M87 230 GHz emission region using EHT 2017 observations. In Section 2, we describe the EHT data set used. We present in Section 3 a pedagogical description showing how within compact ring models the emission diameter and central flux depression (shadow) can be inferred directly from salient features of the visibility data. In Section 4 we describe the three analysis codes used to infer parameters from the data, and in Section 5 and Section 6 we fit both geometric and GRMHD-based models. In Section 7 we extract properties of the reconstructed images from Paper IV.

We show that asymmetric ring ("crescent") geometric source models with a substantial central brightness depression provide a better statistical description of the data than other comparably complex models (e.g., double Gaussians). We use Bayesian inference techniques to constrain the size and width of this crescent feature on the sky, as well as the brightness contrast of the depression at its center compared to the rim. We show that all measurements support a source structure dominated by lensed emission surrounding the black hole shadow.

To extract the physical scale of the black hole at the distance of M87, GM/Dc^2, from the observed ring structure in geometric models and image reconstructions, we do not simply assume that the measured emission diameter is that of the photon ring itself. We instead directly calibrate to the emission diameter found in model images from GRMHD simulations. The structure and extent of the emission preferentially from outside the photon ring leads to a $\lesssim$10% offset between the measured emission diameter in the model images and the size of the photon ring. The scatter over a large number of images, which constitutes a systematic uncertainty, is found to be of the same magnitude.

We use independent calibration factors obtained for the geometric models and reconstructed images (Paper IV), providing two estimates of GM/Dc^2. We also fit the library of GRMHD images described in Paper V directly to the EHT data, which provides a third. All three methods are found to be in remarkable agreement. We consider prior dynamical measurements of M/D and D for M87 in Section 8. In Sections 9 and 10, we discuss the evidence for the detection of lensed emission surrounding the shadow of a black hole in EHT 2017 data. We use the prior distance information to convert the physical scale to a black hole mass and show that our result is consistent with prior stellar, but not gas, dynamical measurements. We further discuss the implications for the presence of an event horizon in the central object of M87. Further technical detail supporting the analyses presented here has been included as Appendices.

2. Observations and Data

Operating as an interferometer, the EHT measures complex visibilities on a variety of baselines b_{ij} between stations i and j. A complex visibility is a Fourier component of the source brightness distribution $I(x, y)$,

$$\mathcal{V}(u, v) = \iint e^{-2\pi i(ux+vy)} I(x, y)\,dx\,dy, \tag{1}$$

where (x, y) are angular coordinates on the sky, and (u, v) are projected baseline coordinates measured in units of wavelengths (Thompson et al. 2017; hereafter TMS).

The 2017 EHT observations of M87 and their subsequent correlation, calibration, and validation are described in detail in Paper III. On each of the four days—April 5, 6, 10, and 11—the EHT observed M87 in two 2 GHz frequency bands centered on 227.1 GHz (low-band; LO) and 229.1 GHz (high-band; HI); the baseline coverage for April 11 is shown in Figure 1. For the modeling results presented in this Letter we analyze all four observing days and both bands. We use Stokes I visibility data reduced via the EHT-Haystack Observatory Processing System (HOPS) pipeline (Blackburn et al. 2019), coherently averaged in time by scan. Scan averaging decreases the data volume with negligible coherence losses (see Paper III) and it further serves to increase the signal-to-noise ratio (S/N) of the data. Fewer timestamps correspond to fewer gain terms (see Section 2.1) and higher S/N improves the validity of our Gaussian likelihood functions (see Section 4.1).

2.1. Data Products

Visibility measurements are affected by a combination of thermal noise and systematic errors. The thermal noise ϵ_{ij} is distributed as a zero-mean complex Gaussian random variable with variance determined by the radiometer equation (TMS), while the dominant systematic noise components are associated with station-based complex gains g_i. The measured visibilities can thus be expressed as

$$V_{ij} = g_i g_j^* \mathcal{V}_{ij} + \epsilon_{ij} = |V_{ij}| e^{i\phi_{ij}}, \tag{2}$$

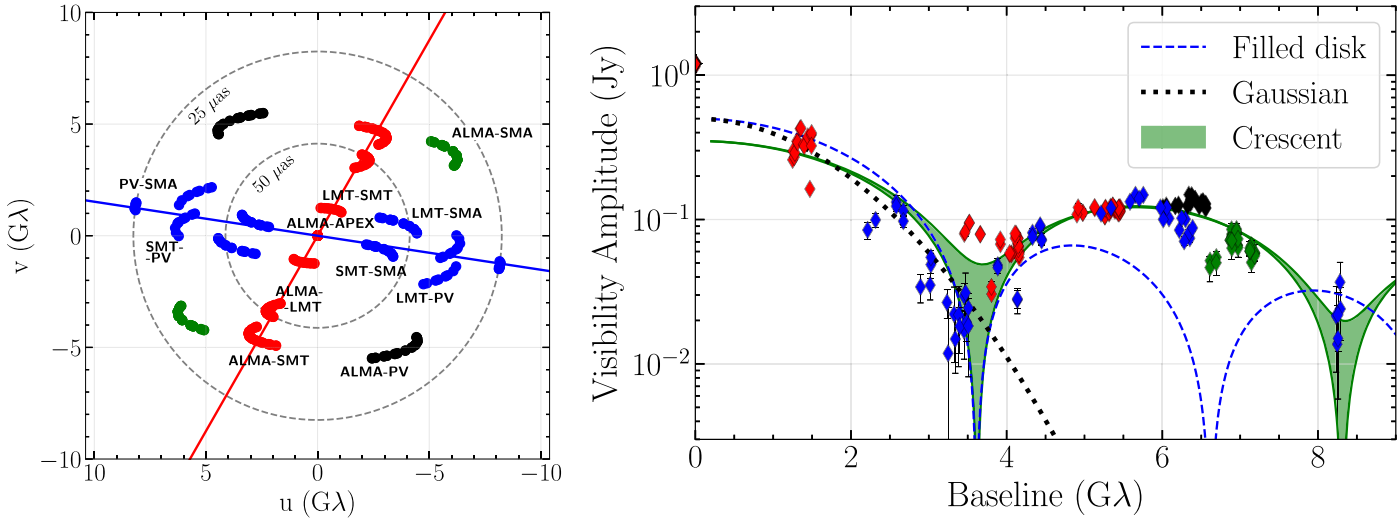

Figure 1. (u, v)-coverage (left panel) and visibility amplitudes (right panel) of M87 for the high-band April 11 data. The (u, v)-coverage has two primary orientations, east–west in blue and north–south in red, with two diagonal fillers at large baselines in green and black. Note that the Large Millimeter Telescope (LMT) and the Submillimeter Telescope (SMT) participate in both orientations, and that the LMT amplitudes are subject to significant gain errors. There is evidence for substantial depressions in the visibility amplitudes at ∼3.4 Gλ and ∼8.3 Gλ. The various lines in the right panel show the expected behavior of (dotted line) a Gaussian, (dashed line) a filled disk, and (green area) a crescent shape along different orientations. The image of M87 does not appear to be consistent with a filled disk or a Gaussian.

where $|V_{ij}|$ and $\phi_{ij} = \arg(V_{ij})$ are the measured visibility amplitude and phase. Measured visibility amplitudes are biased upward by thermal noise, so we use A_{ij} to denote debiased visibility amplitude measurements (see TMS).

All noise sources in Equation (2) are functions of time and frequency, but the gain phase variations are particularly important for EHT data. Characteristic atmospheric timescales at 230 GHz are on the order of seconds, rendering visibility phase calibration unfeasible (Paper II; Paper III). We instead recover source phase information via the construction of closure phases $\psi_{\rm C}$, given by the argument of a product of visibilities around a triangle of baselines,

$$\psi_{{\rm C},ijk} = \arg(V_{ij} V_{jk} V_{ki}) = \phi_{ij} + \phi_{jk} + \phi_{ki}. \quad (3)$$

Because each gain term in the triple product gets multiplied by its complex conjugate, closure phases are immune to gain phase corruptions (Rogers et al. 1974).

Visibility amplitudes suffer less severely than visibility phases from station gain noise but the use of gain-free amplitude quantities can still aid modeling efforts. Closure amplitudes $A_{\rm C}$ are constructed from four visibilities on a quadrangle of baselines,

$$A_{{\rm C},ijk\ell} = \frac{A_{ij} A_{k\ell}}{A_{ik} A_{j\ell}}. \quad (4)$$

The appearance of each station in both the numerator and denominator of this expression causes the station gain amplitudes to cancel out. Because the closure amplitude is constructed from products and ratios of visibility amplitudes, it is often convenient to work instead with the logarithm of the closure amplitude,

$$\ln A_{{\rm C},ijk\ell} = \ln A_{ij} + \ln A_{k\ell} - \ln A_{ik} - \ln A_{j\ell}. \quad (5)$$

2.2. Data Selection and Preparation

From the scan-averaged visibility data, we increase the uncertainty associated with the debiased visibility amplitudes, A, by adding a 1% systematic uncertainty component in quadrature to the thermal noise (Paper III; Paper IV); we refer to this increased uncertainty as the "observational error." These debiased visibility amplitudes are then used to construct a set of logarithmic closure amplitudes, $\ln A_{\rm C}$, per Equation (5). Closure amplitude measurements are generally not independent because a pair of quadrangles may have up to two baselines in common, and a choice must be made regarding which minimal (or "non-redundant") subset of closure amplitudes to use. We select the elements of our minimal set by starting with a maximal (i.e., redundant) set, from which we systematically remove the lowest-S/N quadrangles until the size of the reduced set is equal to the rank of the covariance matrix of the full set (see L. Blackburn et al. 2019, in preparation). This construction procedure serves to maximize the final S/N of the resulting closure amplitudes.

We construct closure phases, $\psi_{\rm C}$, from the visibilities using Equation (3), after first removing visibilities on the short intra-site baselines (James Clerk Maxwell Telescope–Submillimeter Array (JCMT–SMA), Atacama Large Millimeter/submillimeter Array–Atacama Pathfinder Experiment (ALMA–APEX)) which produce only "trivial" closure phases ≃0° (Paper III; Paper IV). As with closure amplitudes, closure phase measurements are in general not independent of one another because a pair of triangles may share a baseline. However, a suitable choice of non-redundant closure phase subset can minimize the covariance between measurements. We select our subset such that the highest-S/N baselines are the most frequently shared across triangles. Such a subset can be obtained by selecting one station to be the reference and then choosing all triangles containing that station (TMS). Because ALMA is so much more sensitive than the other stations in the EHT 2017 array, this construction procedure using ALMA as a reference station ensures the near-diagonality of the closure phase covariance matrix (see Section 4.1).

We list the number of data products in each class, along with the number of station gains, in Table 1 for each observing day and band. Information about accessing SR1 data and the

Table 1
The Number of Data Product and Gain Terms

Day	Band	Including Intra-site N_A	Including Intra-site N_g	Excluding Intra-site N_A	Excluding Intra-site N_g	N_{ψ_C}	$N_{\ln A_C}$
April 5	HI	168	89	152	88	81	78
	LO	168	89	152	88	81	78
April 6	HI	284	134	250	133	141	150
	LO	274	125	242	125	141	149
April 10	HI	96	40	86	40	53	56
	LO	91	43	82	42	47	48
April 11	HI	223	106	194	100	110	117
	LO	216	103	189	98	107	113

Note. N_A is the number of visibility amplitudes, N_g is the number of gain terms, N_{ψ_C} is the number of closure phases, and $N_{\ln A_C}$ is the number of logarithmic closure amplitudes. We show counts for the visibility amplitudes both with and without the inclusion of short intra-site baselines (ALMA–APEX and JCMT–SMA); the visibility amplitudes including intra-site baselines are used in Section 5, while those without are used in Section 6. The closure phase count always excludes triangles containing intra-site baselines, while the logarithmic closure amplitude count always includes quadrangles containing intra-site baselines. Both closure phase and logarithmic closure amplitude counts are for minimal (non-redundant) sets.

software used for analysis can be found on the Event Horizon Telescope website's data portal.[107]

3. Descriptive Features of the Visibility Data

In Paper IV, different image reconstruction methods all obtained similar looking images of M87 from the 2017 EHT observations, namely, a nearly circular ring with a dark center and azimuthally varying intensity. In this Letter, we consider a range of source models and calculate the corresponding visibilities as a function of the model parameters. We then employ statistical tools to select between models and to estimate model parameters by comparing the model visibilities to the observed ones. Because imaging and visibility domain analysis rely on the entire complex visibility data set and/or closure quantities, it is useful as a pedagogical guide to show first how some of the simple image characteristics are imprinted on the visibility data. We emphasize that a complete and accurate description of the source requires imaging analysis and visibility modeling, which we perform in Paper IV and in later sections of this Letter.

Here we show that the data are consistent with the presence of a ring structure with a characteristic emission diameter of $\sim$45 μas. These aspects also match the predictions for an image dominated by lensed emission near the photon ring surrounding the black hole shadow of M87 (Paper V).

The 2017 EHT observations of M87 have good (u, v)-coverage, primarily along an east–west (blue) and a north–south (red) orientation, with additional diagonal long baselines (green and black; see Figure 1 and also Paper III). The right panel of this figure shows the visibility amplitudes observed on April 11 color coded by the orientation of the baselines.

There is evidence for a minimum of the visibility amplitudes at baseline lengths of $\sim$3.4 Gλ, followed by a second peak around $\sim$6 Gλ. Such minima are often associated with edges or gaps in the image domain.

Further, the visibility amplitudes are similar in the north–south and east–west directions, suggestive of a similar characteristic image size and shape in both directions (Figure 1). This is naturally accomplished if the image possesses a large degree of azimuthal symmetry, such as in a ring or disk. Differences in the visibilities as a function of baseline length for different orientations do exist, however, particularly in the depth of the first null, indicating that the source is not perfectly symmetric.

Next, we consider the presence of the central flux depression. For the case of a uniform disk model, the second visibility amplitude minimum occurs at 1.8 times the location of the first minimum, i.e., at $\sim$6.3–7 Gλ, which is not seen in the visibility amplitudes. For a ring or annular model, however, the second minimum moves to longer baseline lengths, consistent with what is seen in the visibility amplitudes.

Indeed, the Fourier transform of an infinitesimally thin ring structure shows the first minimum in visibility amplitude at a baseline length b_1 for which the zeroth-order Bessel function is zero (see TMS). This allows us to estimate the source size for a ring model as

$$d_0 \simeq 45\left(\frac{b_1}{3.5\ \mathrm{G}\lambda}\right)^{-1} \mu\mathrm{as}. \tag{6}$$

In subsequent sections, we quantify our characterization of this model through fitting in the visibility and image domains.

4. Model Fitting to Interferometric Data

We utilize three independent algorithms for parameter space exploration to quantify the size, shape, and orientation of this asymmetric ring structure. We fit both geometric and GRMHD models to the 2017 EHT interferometric data. In this section we outline the modeling framework used to extract parameter values from the M87 data. We first detail the construction of the corresponding likelihood functions in Section 4.1, and we then describe in Section 4.2 the three different codes we have used to estimate model parameters.

4.1. Likelihood Construction

Our quantitative modeling approach seeks to estimate the posterior distribution $P(\boldsymbol{\Theta}|\boldsymbol{D})$ of some parameters $\boldsymbol{\Theta}$ within the context of a model and conditioned on some data $\boldsymbol{D}$,

$$P(\boldsymbol{\Theta}|\boldsymbol{D}) = \frac{P(\boldsymbol{D}|\boldsymbol{\Theta})P(\boldsymbol{\Theta})}{P(\boldsymbol{D})} \equiv \frac{\mathcal{L}(\boldsymbol{\Theta})\pi(\boldsymbol{\Theta})}{\mathcal{Z}}. \tag{7}$$

Here, $\mathcal{L}(\boldsymbol{\Theta}) \equiv P(\boldsymbol{D}|\boldsymbol{\Theta})$ is the likelihood of the data given the model parameters, $\pi(\boldsymbol{\Theta}) \equiv P(\boldsymbol{\Theta})$ is the prior probability of the model parameters, and

$$\mathcal{Z} \equiv P(\boldsymbol{D}) = \int \mathcal{L}(\boldsymbol{\Theta})\pi(\boldsymbol{\Theta})d\boldsymbol{\Theta} \tag{8}$$

is the Bayesian evidence. In this section we define our likelihood functions $\mathcal{L}(\boldsymbol{\Theta})$, which we note differ in detail from those adopted for the regularized maximum likelihood (RML) imaging procedures presented in Paper IV.

For each scan, the measured visibility amplitude, A, corresponds to the magnitude of a random variable distributed according to a symmetric bivariate normal distribution (TMS). This magnitude follows a Rice distribution, which in the

[107] https://eventhorizontelescope.org/for-astronomers/data

high-S/N limit reduces to a Gaussian near the mode,

$$\mathcal{L}_{A,ij} = \frac{1}{\sqrt{2\pi\sigma_{ij}^2}} \exp\left[-\frac{(A_{ij} - |g_i||g_j|\hat{A}_{ij})^2}{2\sigma_{ij}^2}\right]. \quad (9)$$

Here, σ_{ij}^2 is the variance of the visibility measurement, $\hat{A}_{ij}$ is the model visibility amplitude of the source, and $|g_i|$ and $|g_j|$ are the gain amplitudes for stations i and j. Both the mean and standard deviation of Equation (9) are biased with respect to the true visibility amplitude distribution, but for $A/\sigma \gtrsim 2.0$ these biases are below 10%; at least 94% of our visibility amplitude data for any day and band meet this criterion.

For scan-averaged EHT 2017 data, the gain amplitudes constitute on the order of 100 additional nuisance parameters per data set (see Table 1). These numerous additional parameters may be efficiently addressed by directly marginalizing the likelihood in Equation (9), a procedure detailed in Appendix A and A. E. Broderick et al. (2019, in preparation). Once the gain amplitudes have been reconstructed, the joint likelihood function for all visibility amplitude measurements within a data set is then given by the product over the individual likelihoods,

$$\mathcal{L}_A = \prod \mathcal{L}_{A,ij}, \quad (10)$$

where this product is taken over all baselines and scans.

The logarithm of the visibility amplitudes also follows a Gaussian distribution in the high-S/N limit, with an effective logarithmic uncertainty of

$$\sigma_{\ln A} = \frac{\sigma}{A}. \quad (11)$$

The Gaussianity of the logarithmic visibility amplitudes implies that the logarithm of the closure amplitudes will similarly be Gaussian distributed in the same limit, with variances given by

$$\sigma_{\ln A_{\rm C},ijk\ell}^2 = \sigma_{\ln A,ij}^2 + \sigma_{\ln A,k\ell}^2 + \sigma_{\ln A,ik}^2 + \sigma_{\ln A,j\ell}^2. \quad (12)$$

This Gaussian approximation for logarithmic closure amplitudes holds well (i.e., the mean and standard deviation are biased by less than 10%) for $\sigma_{\ln A_{\rm C}} \lesssim 2.0$; at least 87% of our logarithmic closure amplitude data for any day and band meet this criterion.

The likelihood function for a set of logarithmic closure amplitudes also depends on the covariances between individual measurements, which in general are not independent. We can construct a covariance matrix $\mathbf{\Sigma}_A$ that captures the combined likelihood via

$$\mathcal{L}_{\ln A_{\rm C}} = \frac{1}{\sqrt{(2\pi)^q \det(\mathbf{\Sigma}_A)}} \exp\left(-\frac{1}{2}\boldsymbol{A}^\top \mathbf{\Sigma}_A^{-1}\boldsymbol{A}\right), \quad (13)$$

where $\boldsymbol{A}$ is an ordered list of logarithmic closure amplitude residuals, and q is the number of non-redundant closure amplitudes; for a fully connected array with $N_{\rm el}$ elements, $q = N_{\rm el}(N_{\rm el} - 3)/2$ (TMS). The covariance between logarithmic closure amplitude measurements $\ln A_{\rm C,1234}$ and $\ln A_{\rm C,1235}$ is (Lannes 1990a; L. Blackburn et al. 2019, in preparation)

$$\mathrm{Cov}(\ln A_{\rm C,1234}, \ln A_{\rm C,1235}) = \sigma_{\ln A,12}^2 + \sigma_{\ln A,13}^2 \quad (14)$$

in the Gaussian limit; here, we have used the fact that $\sigma_{ij} = \sigma_{ji}$ to simplify notation.

The distribution of measured visibility phases, ϕ, corresponds to the projection of a symmetric bivariate normal random variable onto the unit circle, which once again reduces to a Gaussian distribution in the high-S/N limit. Closure phases, $\psi_{\rm C}$, in this limit will also be Gaussian distributed with variances given by

$$\sigma_{\psi_{\rm C},ijk}^2 = \sigma_{\phi,ij}^2 + \sigma_{\phi,jk}^2 + \sigma_{\phi,ki}^2, \quad (15)$$

where $\sigma_{\phi,ij}^2$ is the variance in the visibility phase measurement, ϕ_{ij}. The Gaussian approximation for closure phases is unbiased in the mean with respect to the true closure phase distribution, and the standard deviation is biased by less than 10% for $\sigma_{\psi_{\rm C}} \lesssim 1.5$; this criterion is satisfied for at least 92% of our closure phase data on any day and band.

Closure phase measurements are also generally covariant, and for a covariance matrix $\mathbf{\Sigma}_\psi$ the joint likelihood is given by

$$\mathcal{L}_{\psi_{\rm C}} = \frac{1}{\sqrt{(2\pi)^t \det(\mathbf{\Sigma}_\psi)}} \exp\left(-\frac{1}{2}\boldsymbol{\psi}^\top \mathbf{\Sigma}_\psi^{-1}\boldsymbol{\psi}\right), \quad (16)$$

where $\boldsymbol{\psi}$ is an ordered list of closure phase residuals, and t is the number of non-redundant closure phases; for a fully connected array containing $N_{\rm el}$ elements, $t = (N_{\rm el} - 1)(N_{\rm el} - 2)/2$ (TMS). The covariance between two closure phase measurements, $\psi_{\rm C,123}$ and $\psi_{\rm C,124}$, is given by (Kulkarni 1989; Lannes 1990b; L. Blackburn et al. 2019, in preparation)

$$\mathrm{Cov}(\psi_{\rm C,123}, \psi_{\rm C,124}) = \sigma_{\phi,12}^2. \quad (17)$$

As described in Section 2.2, a non-redundant subset of closure phases can be selected to maximize independence and thus ensure the near-diagonality of $\mathbf{\Sigma}_\psi$. In this case the closure phase measurements can be treated as individually Gaussian,

$$\mathcal{L}_{\psi_{\rm C},ijk} = \frac{1}{\sqrt{2\pi\sigma_{\psi_{\rm C},ijk}^2}} \exp\left[-\frac{(\psi_{\rm C,ijk} - \hat{\psi}_{\rm C,ijk})^2}{2\sigma_{\psi_{\rm C},ijk}^2}\right], \quad (18)$$

where $\hat{\psi}_{\rm C,ijk}$ is the modeled closure phase. The joint likelihood is then

$$\mathcal{L}_{\psi_{\rm C}} = \prod \mathcal{L}_{\psi_{\rm C},ijk}, \quad (19)$$

where the product is taken over all closure phases in the selected minimal subset. Because closure phases wrap around the unit circle, we always select the branch of $\psi_{\rm C} - \hat{\psi}_{\rm C}$ such that the difference lies between $-180°$ and $180°$.

4.2. Parameter Space Exploration Techniques

We utilize three independent algorithms for parameter space exploration. For the geometric crescent model fitting presented in Section 5, we use both Markov chain Monte Carlo (MCMC) and nested sampling (NS) algorithms. The MCMC modeling scheme explores model fits to the visibility amplitude and closure phase data, while the NS scheme fits to the closure phase and logarithmic closure amplitude data. For the GRMHD model fitting in Section 6, we use both MCMC and a genetic algorithm to fit the visibility amplitude and closure phase data.

4.2.1. THEMIS

THEMIS is an EHT-specific analysis framework for generating and comparing models to both EHT and ancillary data.

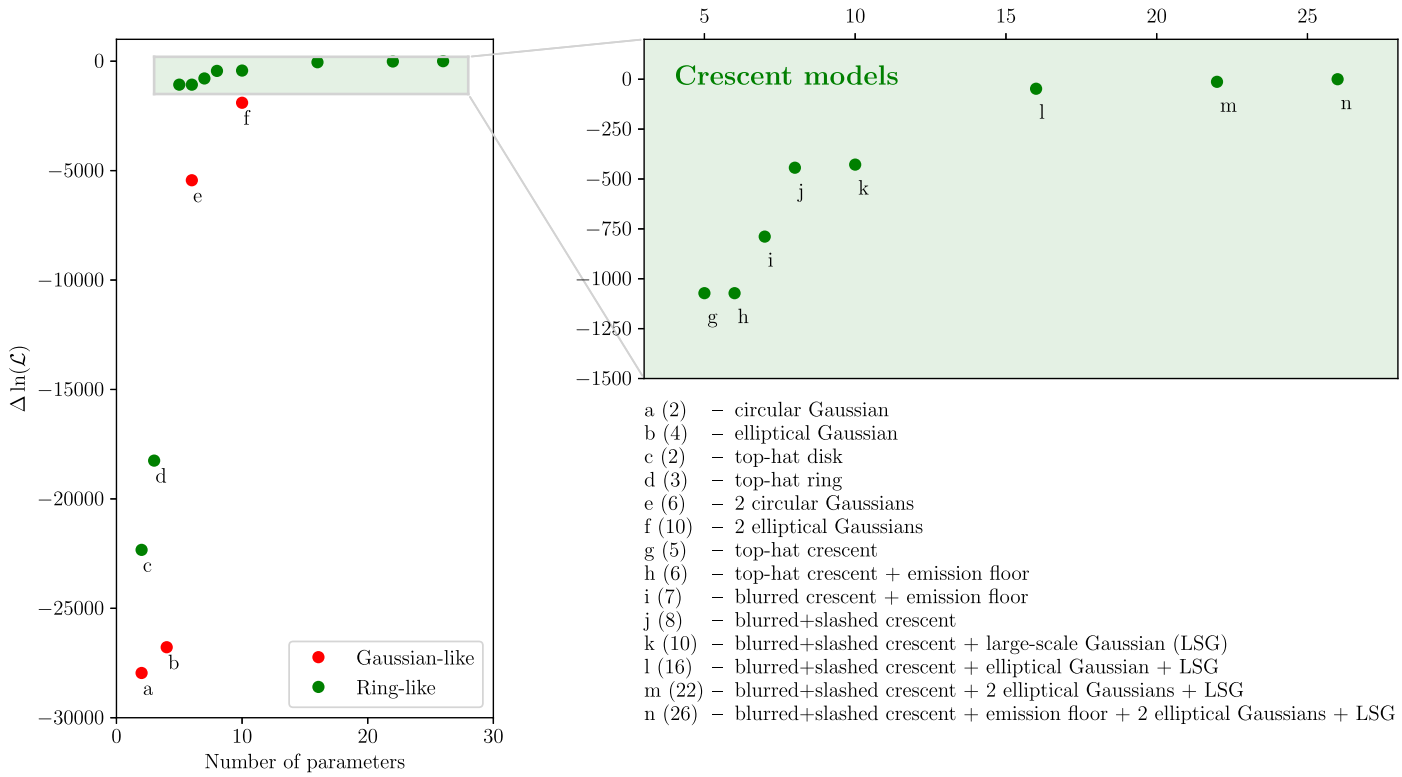

Figure 2. Relative log-likelihood values for different geometric models fit to the M87 data as a function of nominal model complexity; the number of parameters is given in parenthesis for each model. April 5 is shown here, and all days and bands show the same trend. The models shown in this figure are strict subsets of the "generalized crescent model" (labeled here as model "n"; see Section 5.1), and they have been normalized such that the generalized crescent model has a value of $\mathcal{L} = 1$; the reduced-χ^2 for the generalized crescent fit is 1.24 (see Table 2). We find that the data overwhelmingly prefer crescent models over, e.g., symmetric disk and ring models, and that additional Gaussian components lead to further substantial improvement. Note that a difference of ∼5 on the vertical axis in this plot is statistically significant.

THEMIS is written in C++ and parallelized via the Message Passing Interface (MPI) standard. THEMIS implements a differential evolution MCMC algorithm, and it utilizes parallel tempering based on the algorithm described in Nelson et al. (2014) and Braak (2006). In particular, THEMIS uses the adaptive temperature ladder prescription from Vousden et al. (2016). All sampling techniques, validation tests, and implementation details for THEMIS are described in detail in A. E. Broderick et al. (2019, in preparation).

In Sections 5 and 6, we use THEMIS to model the visibility amplitude and closure phase data, using the corresponding likelihood functions given in Equations (10) and (19), respectively. Gain amplitude terms are incorporated as model parameters (see Equation (9)) and are marginalized as described in Appendix A.

4.2.2. *dynesty*

In Section 5, we also use an NS technique, developed by Skilling (2006) primarily to evaluate Bayesian evidence integrals. We use the Python code dynesty (Speagle & Barbary 2018) as a sampler for the NS analyses presented in this Letter. The NS algorithm estimates the Bayesian evidence, $\mathcal{Z}$, by replacing the multidimensional integral over $\boldsymbol{\Theta}$ (see Equation (8)) with a 1D integral over the prior mass contained within nested isolikelihood contours. We permit dynesty to run until it estimates that less than 1% of the evidence is left unaccounted for.

Our NS analyses employ a likelihood function constructed exclusively from closure quantities; we account for data covariances in the likelihood function using Equation (16) for closure phases and Equation (13) for logarithmic closure amplitudes. Additionally, the use of logarithmic closure amplitudes in our NS fits removes information about the total flux density.

4.2.3. *GENA*

In addition to the above sampling algorithms, which seek to reconstruct a posterior distribution, we also employ an optimization procedure for comparing GRMHD simulations to data in Section 6. The optimization code, GENA (Fromm et al. 2019), is a genetic algorithm written in Python and parallelized using MPI. GENA minimizes a χ^2 statistic on visibility amplitudes and closure phases, using the gain calibration procedures in the eht-imaging (Chael et al. 2016, 2018, 2019a) Python package to solve for the gain amplitudes. GENA implements the Non-dominated Sorting Genetic Algorithm II (NSGA-II; Deb et al. 2002) for parameter exploration and the differential evolution algorithm from Storn & Price (1997) for constrained optimization.

5. Geometric Modeling

As detailed in Paper IV, images reconstructed from the M87 data show a prominent and asymmetric ring ("crescent") structure. In this section we use the techniques described in Section 4 to fit the M87 data sets with a specific class of geometric crescent models.

We first quantify the preference for crescent structure in Figure 2, which summarizes the results of fitting a series of increasingly complex geometric models to the M87 data. We

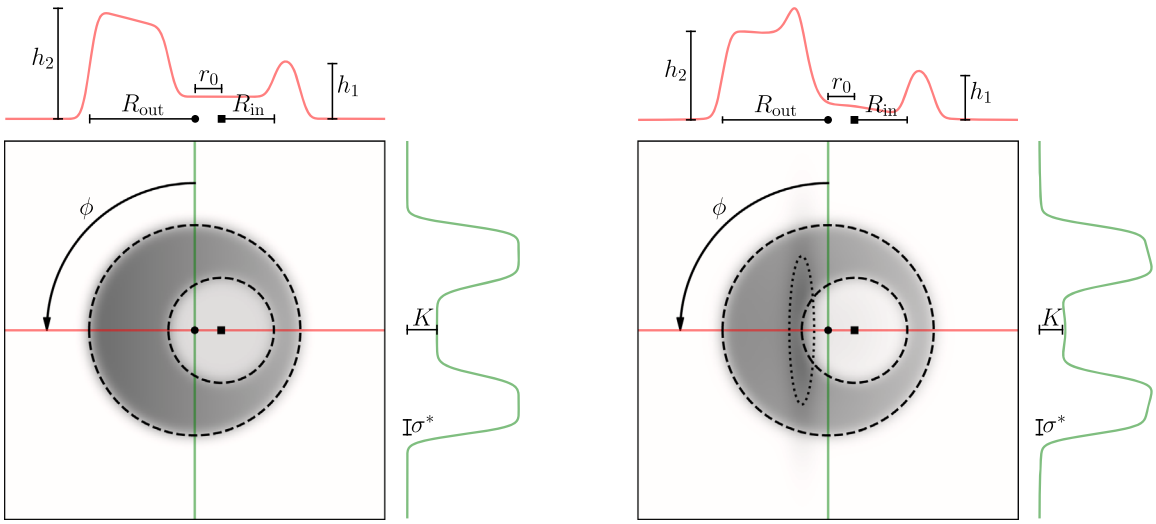

Figure 3. Schematic diagrams illustrating the crescent components of the xs-ring (left panel) and xs-ringauss (right panel) models. Dashed lines outline the inner and outer circular disk components that are differenced to produce the crescent models, and for the xs-ringauss model the FWHM of the fixed Gaussian component is additionally traced as a dotted line. The red and green curves above and to the right of each panel show cross-sectional plots of the intensity through the corresponding horizontal and vertical slices overlaid on the images. The circular and square markers indicate the centers of the outer and inner disks, respectively. The labeled parameters correspond to those described in Section 5.1. Both crescents are shown at an orientation of $\phi = \hat{\phi} = 90°$.

see that simple azimuthally symmetric models (e.g., uniform disks, rings) do a poor job of fitting the data; indeed, the strong detection of nonzero closure phases alone precludes such models. Models that allow for a central flux depression and a degree of asymmetry (e.g., double Gaussians or crescents) show significantly better performance. The most substantial gain in fit quality occurs for the crescent family of models. A top-hat crescent model (the difference of two uniform disks with the inner disk shifted, described by five parameters; see Kamruddin & Dexter 2013, Appendix B) performs vastly better than a top-hat ring model (three parameters). It also significantly outperforms the sum of two circular Gaussians (six parameters) and even the sum of two elliptical Gaussians (10 parameters). Adding parameters to the simplest crescent model continues to result in statistically significant, but comparatively modest, improvements.

5.1. Generalized Crescent Models

Among the large number of potential crescent-like models, we aim for one having the simplest geometry that is capable of both adequately fitting the M87 data and constraining several key observables. The geometric parameters of interest are the crescent diameter, its width and orientation, the sharpness of the inner edge, and the depth of any flux depression interior to the crescent.

With these key features in mind, we use an augmented version of the "slashed crescent" construction from Benkevitch et al. (2016) to provide the basis for a family of "generalized crescent" (GC) models. We refer to the two variants of the GC model that we use to fit the M87 data as xs-ring and xs-ringauss. Both GC models can be constructed in the image domain using the following procedure (see Figure 3).

1. Starting with a uniform circular disk of emission with radius $R_{\rm out}$, we subtract a smaller uniform disk with radius $R_{\rm in}$ that is offset from the first by an amount r_0. The resulting geometry is that of a "top-hat crescent."
2. We apply a "slash" operation to the top-hat crescent, which imposes a linear brightness gradient along the symmetry axis. The brightness reaches a minimum of h_1 and a maximum of h_2.
3. We add a "floor" of brightness K to the central region of the crescent. For the xs-ring model this floor takes the form of a circular disk, while for the xs-ringauss model we use a circular Gaussian with flux density V_F and width σ_F. The total flux density of the crescent plus floor component for the xs-ring model is denoted as V_0.
4. For the xs-ringauss model, we add an elliptical Gaussian component with flux density V_1 whose center is fixed to the inner edge of the crescent at the point where its width is largest (see the right panel of Figure 3), and whose orientation is set to align with that of the crescent. This fixed Gaussian component is inspired by the "xringaus" model from Benkevitch et al. (2016), which in turn sought to reproduce image structure seen in simulations from Broderick et al. (2014).
5. The image is smoothed by a Gaussian kernel of FWHM σ^*.
6. The image is rotated such that the widest section of the crescent is oriented at an angle ϕ in the counterclockwise direction (i.e., east of north).

The xs-ring model is described by eight parameters, while the xs-ringauss model is described by 11 parameters.

Though it is useful to conceptualize the GC models via their image domain construction, in practice we fit the models using their analytic Fourier domain representations. The Fourier domain construction of both models is described in Appendix B, along with a table of priors used for the model parameters. Throughout this Letter we fit the xs-ring model using the `dynesty` sampling code, while the xs-ringauss model is implemented as part of THEMIS. Below, we define the various desired key quantities within the context of this GC model parameterization.

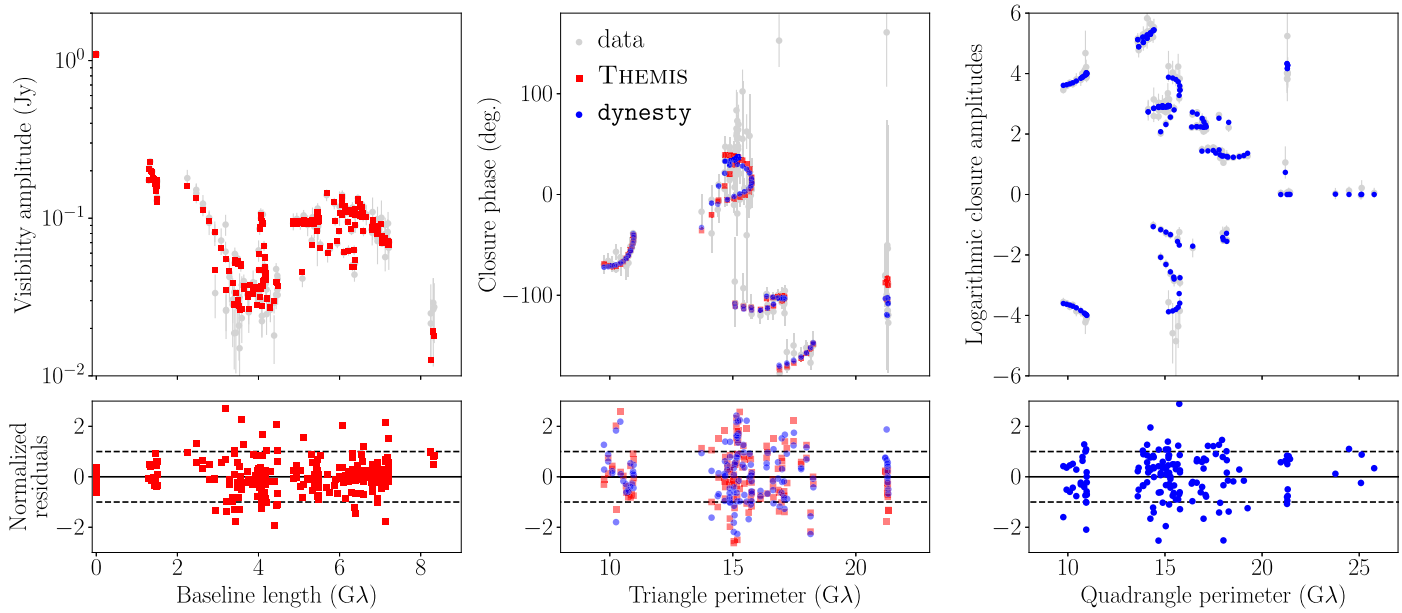

Figure 4. Modeled data (top panels) and residuals (bottom panels) for GC model fits to the April 6 high-band data set, with the data plotted in gray; we show results for the median posterior fit. The panels show visibility amplitude (left panels), closure phase (middle panels), and logarithmic closure amplitude (right panels) data. The xs-ringauss model, shown in red, is fit to the visibility amplitudes and closure phases using THEMIS; the `dynesty`-based xs-ring model, plotted in blue, comes from a fit to closure phases and logarithmic closure amplitude. Because both models fit to closure phases, the center panel shows two sets of models and residuals. All residuals are normalized by the associated observational noise values.

We define the crescent diameter $\hat{d}$ to be twice the average of the inner and outer crescent radii,

$$\hat{d} \equiv R_{\rm out} + R_{\rm in}. \tag{20}$$

The fractional crescent width $\hat{f}_{\rm w}$ is defined in a similar manner, as the mean difference between the outer and inner radii (normalized to the diameter) plus a term to account for the FWHM, $\sigma^* \equiv 2\sigma\sqrt{2\ln(2)}$, of the smoothing kernel:

$$\hat{f}_{\rm w} \equiv \frac{R_{\rm out} - R_{\rm in} + \sigma^*}{\hat{d}}. \tag{21}$$

The sharpness $\hat{s}$ is the ratio of the FWHM of the smoothing kernel to the crescent diameter, i.e.,

$$\hat{s} \equiv \frac{\sigma^*}{\hat{d}}. \tag{22}$$

The fourth quantity of interest is the ratio, $\hat{f}_{\rm c}$, between the brightness of the emission floor (interior to the crescent) and the mean brightness of the crescent,

$$\hat{f}_{\rm c} \equiv \frac{\text{brightness of emission floor}}{\text{mean brightness of crescent}}. \tag{23}$$

The different specifications for the xs-ring and xs-ringauss models (see Appendix B) means that these brightness ratios must be computed differently,

$$\hat{f}_{\rm c} = \begin{cases} \dfrac{V_F[(2R_{\rm out} + \sigma^*)^2 - (2R_{\rm in} - \sigma^*)^2]}{8\sigma_F^2(V_0 + V_1)}, & \text{xs-ringauss} \\ \dfrac{\pi K[(2R_{\rm out} + \sigma^*)^2 - (2R_{\rm in} - \sigma^*)^2]}{8V_0}, & \text{xs-ring.} \end{cases} \tag{24}$$

Finally, we determine the orientation of the crescent directly from the ϕ parameter, such that $\hat{\phi} = \phi$.

In addition to the crescent component of the GC model, we also include a small number (two to three) of additional "nuisance" elliptical Gaussian components intended to capture extraneous emission around the primary ring and to mitigate other unmodeled systematics; the parameterization and behavior of these additional Gaussian components are described in Appendix B.2. GRMHD simulations of M87 often exhibit spiral emission structures in the region immediately interior and exterior to the photon ring (see Paper V), and M87 is known to have a prominent jet that extends down to scales of several Schwarzschild radii (e.g., Hada et al. 2016, Kim et al. 2018). Such extra emission is unlikely to be adequately captured by the crescent component alone, and the nuisance Gaussian components serve as a flexible way to model generic emission structures. We define the total compact flux density, $\hat{\rm CF}$, of the model to be equal to the summed contributions from the crescent and nuisance Gaussian components,

$$\hat{\rm CF} \equiv V_0 + V_1 + V_F + \sum_i V_{g,i}, \tag{25}$$

where V_0 is the crescent flux density, V_1 is the flux density of the fixed Gaussian component, V_F is the flux density of the central emission floor, and $V_{g,i}$ are the flux densities of the nuisance Gaussian components.

5.2. M87 Fit Results

We carry out independent fits to all days and bands using both the THEMIS- and `dynesty`-based codes. We show example GC model fits to the April 6 high-band data in Figure 4, with their corresponding image domain representations shown in Figure 5. There are no apparent systematic trends in the normalized residuals for either model, and we see similar behavior in the residuals from fits across all data sets. The corresponding THEMIS gain reconstructions are described in Appendix A.

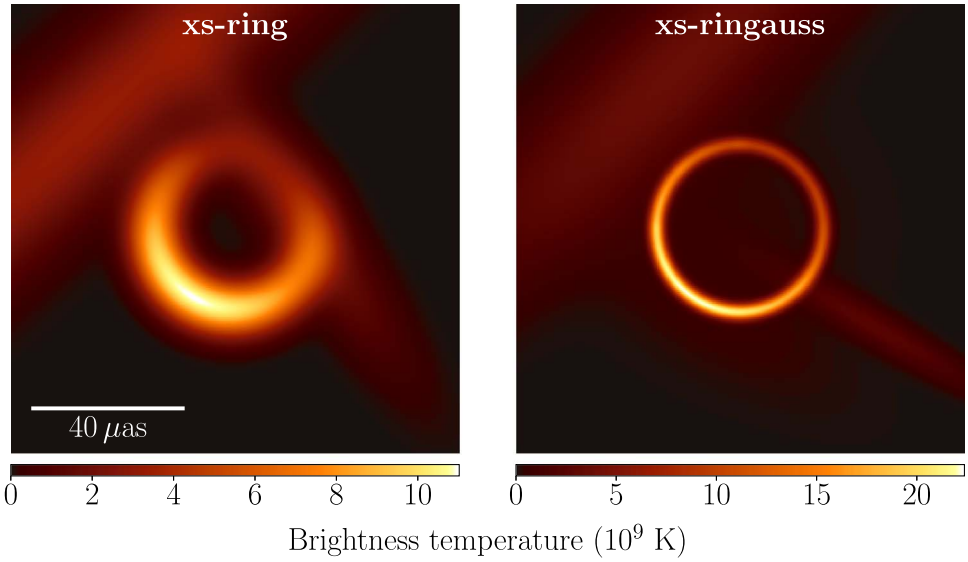

Figure 5. Image domain representations of a random posterior sample from the xs-ring (left panel) and xs-ringauss (right panel) model fits to the April 6 high-band data set; note that these are representative images drawn from the posteriors, and thus do not represent maximum likelihood or other "best-fit" equivalents. The xs-ring model fit uses only closure quantities, so we have scaled the total flux density to be equal to the 1.0 Jy flux density of the xs-ringauss model fit.

Table 2
Reduced-chi2 Statistics for the GC Model Fits

Data Set		Model					
		xs-ringauss			xs-ring		
Day	Band	χ^2_A	$\chi^2_{\psi_C}$	$\chi^2_{A+\psi_C}$	$\chi^2_{\psi_C}$	$\chi^2_{\ln A_C}$	$\chi^2_{\psi_C+\ln A_C}$
April 5	HI	1.66	1.48	1.24	1.30	1.30	1.02
	LO	1.33	1.32	1.05	1.43	1.35	1.10
	HI+LO	1.16	1.07	1.01	⋯	⋯	⋯
April 6	HI	1.02	1.46	1.12	1.44	0.96	1.06
	LO	1.57	1.36	1.32	1.37	1.52	1.29
	HI+LO	1.16	1.35	1.19	⋯	⋯	⋯
April 10	HI	1.57	1.52	1.05	1.44	1.08	0.82
	LO	2.23	2.74	1.53	1.95	1.50	1.28
	HI+LO	1.11	1.32	1.04	⋯	⋯	⋯
April 11	HI	1.40	1.37	1.20	1.37	1.02	1.02
	LO	1.34	1.16	1.07	1.18	0.92	0.89
	HI+LO	1.32	1.14	1.15	⋯	⋯	⋯

Note. Reduced-χ^2 values corresponding to the maximum likelihood posterior sample for individual M87 data sets from both fitting codes, split by data type and calculated as described in Appendix C. The xs-ringauss values are from fits to visibility amplitudes (reduced-χ^2 given by χ^2_A) and closure phases (reduced-χ^2 given by $\chi^2_{\psi_C}$), with the joint visibility amplitude and closure phase reduced-χ^2 denoted as $\chi^2_{A+\psi_C}$. The xs-ring values are from fits to closure phases and logarithmic closure amplitudes (reduced-χ^2 given by $\chi^2_{\ln A_C}$), with the joint closure phases and logarithmic closure amplitude reduced-χ^2 denoted as $\chi^2_{\psi_C+\ln A_C}$.

While our model-fitting procedures formally optimize a likelihood function modified by a prior (see Section 4.1), reduced-χ^2 values serve as general-purpose distance metrics between model and data. In our case, reduced-χ^2 values have the added benefit of enabling cross-comparisons with the images produced in Paper IV. The reduced-χ^2 expressions we use are detailed in Appendix C, and Table 2 lists their values for all M87 fits.

In general we find joint reduced-χ^2 values for the fits of ∼0.9–1.5. The number of degrees of freedom in the data ranges from ∼20 to 120, corresponding to an expected reduced-χ^2 deviation from unity of ∼0.06–0.16 if our likelihoods follow a χ^2-distribution. The implication is that while we see little evidence for overfitting, there are instances in which the residual values are distributed more broadly than the data error budget would nominally permit. The fact that such models sometimes underfit the data then indicates that we need to empirically determine our uncertainties, as posterior widths alone may not be reliable in the face of a statistically poor fit. We describe the empirical determination of the "observational uncertainties" in Appendix D.3, and we list the derived values in Table 3.

An illustrative pairwise parameter correlation diagram for both the xs-ring and xs-ringauss GC model fits to the April 5 high-band data set is shown in Figure 6, with single-parameter posteriors plotted along the diagonal. Figure 7 shows constraints on the GC model crescent component parameters, split up by data set. We also list the best-fit crescent parameters, as defined in Section 5.1, in Table 3.

Despite the differences in data products, sampling procedures, and model specifications, we find broad agreement between the derived posteriors from the two fitting codes. We note that the systematically wider posteriors from the xs-ring fits (by anywhere from a few to several tens of percent) are seen across all data sets and are an expected consequence of the use of closure amplitudes rather than visibility amplitudes.

Our primary parameter of interest is the diameter of the crescent, $\hat{d}$. The weighted mean xs-ringauss value of 43.4 μas is in excellent agreement with the corresponding xs-ring value of 43.2 μas, with an rms scatter in the measurements of 0.64 μas and 0.69 μas, respectively, across all days and bands. This remarkable consistency provides evidence for the diameter measurement being robustly recoverable. The posterior widths of diameter measurements for individual data sets are typically at the ∼1% level, but our empirically determined uncertainties associated with the changing (u, v)-coverage and other

Table 3

Best-fit GC Model Parameters for All Data Sets and Both Models, as Defined in Section 5.1; Median Posterior Values are Quoted with 68% Confidence Intervals

Data Set				Parameter					
Day	Band	Code	Model	$\hat{d}$ (μas)	$\hat{f}_w$	$\log_{10}(\hat{s})$	$\log_{10}(\hat{f}_c)$	$\hat{\phi}$ (deg.)	$\hat{\mathrm{CF}}$ (Jy)
April 5	HI	THEMIS	xs-ringauss	$43.1^{+0.35}_{-0.36}$	$0.12^{+0.07}_{-0.06}$	$-1.35^{+0.30}_{-0.54}$	$-1.60^{+0.26}_{-0.37}$	$160.6^{+2.3}_{-1.6}$	$0.75^{+0.16}_{-0.17}$
		dynesty	xs-ring	$42.9^{+0.59}_{-0.54}$	$0.39^{+0.06}_{-0.07}$	$-1.07^{+0.23}_{-0.48}$	$-1.97^{+0.40}_{-0.50}$	$160.5^{+3.4}_{-3.1}$	⋯
	LO	THEMIS	xs-ringauss	$43.5^{+0.27}_{-0.28}$	$0.09^{+0.06}_{-0.04}$	$-1.41^{+0.29}_{-0.51}$	$-1.76^{+0.29}_{-0.37}$	$160.9^{+1.5}_{-2.5}$	$0.72^{+0.17}_{-0.15}$
		dynesty	xs-ring	$43.5^{+0.44}_{-0.41}$	0.20 ± 0.06	$-1.23^{+0.26}_{-0.50}$	$-2.15^{+0.29}_{-0.48}$	$157.9^{+1.7}_{-1.8}$	⋯
	HI+LO	THEMIS	xs-ringauss	$43.3^{+0.22}_{-0.23}$	$0.09^{+0.05}_{-0.04}$	$-1.62^{+0.33}_{-0.55}$	$-1.74^{+0.24}_{-0.31}$	$160.7^{+0.8}_{-0.9}$	0.75 ± 0.15
April 6	HI	THEMIS	xs-ringauss	$44.1^{+0.23}_{-0.20}$	$0.16^{+0.04}_{-0.05}$	$-0.94^{+0.12}_{-0.30}$	$-1.96^{+0.39}_{-0.58}$	$146.4^{+2.6}_{-3.2}$	0.99 ± 0.04
		dynesty	xs-ring	$43.3^{+0.44}_{-0.43}$	$0.34^{+0.05}_{-0.06}$	$-0.70^{+0.07}_{-0.11}$	$-2.23^{+0.36}_{-0.56}$	149.1 ± 1.5	⋯
	LO	THEMIS	xs-ringauss	43.5 ± 0.14	$0.18^{+0.03}_{-0.04}$	$-0.87^{+0.09}_{-0.20}$	$-2.14^{+0.43}_{-0.62}$	$153.0^{+2.0}_{-2.4}$	$1.07^{+0.05}_{-0.04}$
		dynesty	xs-ring	$43.4^{+0.27}_{-0.26}$	$0.20^{+0.07}_{-0.06}$	$-1.31^{+0.31}_{-0.52}$	$-2.63^{+0.41}_{-0.60}$	$148.5^{+1.4}_{-1.2}$	⋯
	HI+LO	THEMIS	xs-ringauss	$43.7^{+0.10}_{-0.11}$	$0.19^{+0.03}_{-0.02}$	$-0.88^{+0.05}_{-0.07}$	$-2.28^{+0.48}_{-0.61}$	$151.8^{+1.6}_{-1.7}$	1.03 ± 0.03
April 10	HI	THEMIS	xs-ringauss	$42.9^{+1.09}_{-0.86}$	0.46 ± 0.06	$-1.03^{+0.28}_{-0.51}$	$-1.12^{+0.32}_{-0.52}$	$199.8^{+4.1}_{-4.5}$	$0.78^{+0.18}_{-0.17}$
		dynesty	xs-ring	$43.3^{+0.79}_{-0.65}$	0.50 ± 0.06	$-0.97^{+0.26}_{-0.50}$	$-1.89^{+0.47}_{-0.53}$	$194.3^{+4.1}_{-4.6}$	⋯
	LO	THEMIS	xs-ringauss	$43.6^{+1.50}_{-1.92}$	0.41 ± 0.06	$-0.98^{+0.32}_{-0.60}$	$-1.57^{+0.42}_{-0.57}$	$204.2^{+4.4}_{-4.5}$	$0.71^{+0.20}_{-0.15}$
		dynesty	xs-ring	$44.4^{+0.84}_{-0.87}$	$0.41^{+0.08}_{-0.07}$	$-1.02^{+0.26}_{-0.51}$	$-1.87^{+0.42}_{-0.52}$	$204.0^{+3.9}_{-4.2}$	⋯
	HI+LO	THEMIS	xs-ringauss	$43.9^{+0.69}_{-0.86}$	0.42 ± 0.05	$-1.16^{+0.29}_{-0.54}$	$-1.52^{+0.40}_{-0.60}$	$203.1^{+3.0}_{-3.4}$	$0.69^{+0.17}_{-0.14}$
April 11	HI	THEMIS	xs-ringauss	$41.8^{+0.46}_{-0.43}$	0.35 ± 0.04	$-1.41^{+0.31}_{-0.52}$	$-1.38^{+0.32}_{-0.52}$	$207.4^{+1.8}_{-1.9}$	0.50 ± 0.03
		dynesty	xs-ring	$43.4^{+0.74}_{-0.48}$	$0.44^{+0.05}_{-0.06}$	$-1.00^{+0.22}_{-0.48}$	$-1.69^{+0.37}_{-0.57}$	$180.1^{+2.3}_{-1.8}$	⋯
	LO	THEMIS	xs-ringauss	$42.2^{+0.43}_{-0.41}$	$0.35^{+0.05}_{-0.04}$	$-1.27^{+0.26}_{-0.51}$	$-1.69^{+0.41}_{-0.61}$	$201.1^{+2.6}_{-2.3}$	$0.50^{+0.04}_{-0.03}$
		dynesty	xs-ring	$41.6^{+0.51}_{-0.46}$	$0.50^{+0.04}_{-0.05}$	$-0.95^{+0.17}_{-0.42}$	$-1.69^{+0.36}_{-0.59}$	$175.9^{+2.1}_{-2.0}$	⋯
	HI+LO	THEMIS	xs-ringauss	$42.4^{+0.34}_{-0.33}$	0.34 ± 0.04	$-1.35^{+0.27}_{-0.48}$	$-1.80^{+0.47}_{-0.62}$	$198.1^{+1.9}_{-1.8}$	0.49 ± 0.03
Observational uncertainty		THEMIS	xs-ringauss	$^{+2.51\%}_{-1.66\%}$	$^{+30.1\%}_{-47.1\%}$	$^{+0.41}_{-0.57}$	$^{+0.47}_{-0.71}$	$^{+24.8}_{-25.9}$	$^{+57.9\%}_{-35.2\%}$
		dynesty	xs-ring	$^{+1.75\%}_{-1.69\%}$	$^{+21.3\%}_{-22.1\%}$	$^{+0.21}_{-0.46}$	$^{+0.46}_{-0.58}$	$^{+21.9}_{-11.4}$	⋯

Note. Observational uncertainties are listed at the bottom of the table and have been determined as described in Appendix D.3. Note that recovery of the total compact flux density $\hat{\mathrm{CF}}$ is not possible for the dynesty-based fits, which only make use of closure quantities.

observational systematics (see Appendix D.3) place a more realistic uncertainty of ∼2% on this measurement. This more conservative uncertainty value is consistent with the magnitude of the scatter observed between measurements across different days and bands.

The fractional width $\hat{f}_w$ of the crescent is considerably less well constrained than the diameter, with a scatter between data sets that is comparable to the magnitude of individual measurements. Furthermore, we see systematically larger fractional width measurements from the xs-ring model than from the xs-ringauss model (see Figure 7). Some of this offset is expected from differences in model specifications. A larger contributor to the discrepancy is likely to be the different data products being fit by the two models. For the data sets in which the xs-ring model prefers a significantly larger $\hat{f}_w$ than the xs-ringauss model, we find that the smoothing kernel (described by $\hat{s}$) for the xs-ring model is also systematically wider. This smoothing by a Gaussian has no effect on the modeled closure phases. The additional gain amplitude degrees of freedom permitted in the xs-ringauss model fits can thus compensate for the smoothing in a manner that is not possible for the xs-ring model, which is fit only to closure amplitudes. Such smoothing affects the inferred diameter in a correlated manner that is well understood (see Section 7 and Paper IV, their Appendix G).

In both models, and across all data sets, we consistently measure a value for $\hat{f}_w$ that is significantly smaller than unity. This rules out a filled-in disk structure at high confidence. We find instead that the emission must be concentrated in a relatively thin annulus, with a fractional width of $\lesssim$0.5, indicating the presence of a central flux depression. The brightness ratio $\hat{f}_c$ in this hole is also well constrained: we consistently measure $\hat{f}_c \lesssim 0.1$ (and often $\hat{f}_c \ll 0.1$). This value corresponds to a brightness contrast between the crescent and hole of at least a factor of 10.

We find a sharpness $\hat{s} \lesssim 0.2$, indicating that the smoothing kernel stays smaller than ∼20% of its diameter. The inner and outer edges of the crescent are therefore well defined, even if their locations are uncertain due to the large uncertainty in the width measurement.

We find that the crescent position angle $\hat{\phi}$ consistently confines the brightest portion of the crescent to be located in the southern half. We see some evidence for a net shift in orientation from ∼150°–160° (southeast) on April 5–6 to ∼180°–200° (south/southwest) on April 10–11, which

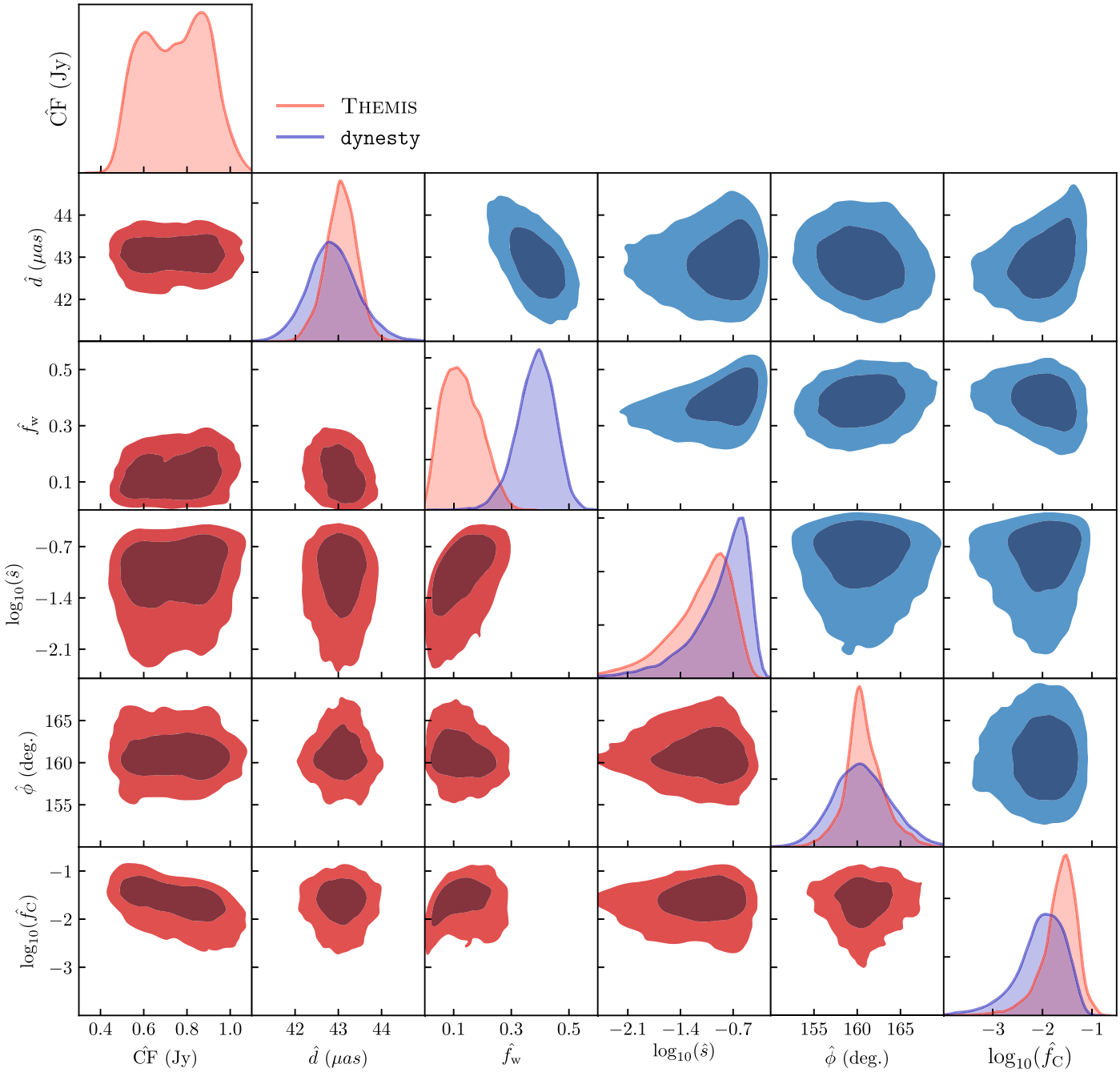

Figure 6. Joint posteriors for the key physical parameters derived from GC model fits to the April 5, high-band data set. Blue contours (upper-right triangle) show xs-ring posteriors obtained from the `dynesty`-based fitting scheme, while red contours (lower-left triangle) show xs-ringauss posteriors obtained using THEMIS. Contours enclose 68% and 95% of the posterior probability. Note that recovery of the total compact flux density $\hat{\mathrm{CF}}$ is not possible for the `dynesty`-based fits, which only make use of closure quantities.

amounts to a difference of ∼20–50 degrees between the two pairs of days. The direction of this shift is consistent with structural changes seen in the images from Paper IV, though the magnitude is a factor of ∼2 larger.

The xs-ringauss model fits find a typical compact flux density value of $\hat{\mathrm{CF}} \approx 0.75$ Jy. The inter-day measurement scatter is at the ∼50% level, which is consistent with the expected magnitude of the observational uncertainties as predicted by synthetic data in Appendix D.3. We find that the modeled $\hat{\mathrm{CF}}$ value is less well-constrained than, but in good agreement with, the $0.66^{+0.16}_{-0.10}$ Jy determined in Paper IV from consideration of both EHT and multi-wavelength constraints.

5.3. Calibrating the Crescent Diameter to a Physical Scale Using GRMHD Simulations

Though the GC models have been constructed to fit the M87 data well, the geometric parameters describing these models do not directly correspond to any physical quantities governing the underlying emission. Our primary physical parameter of interest is

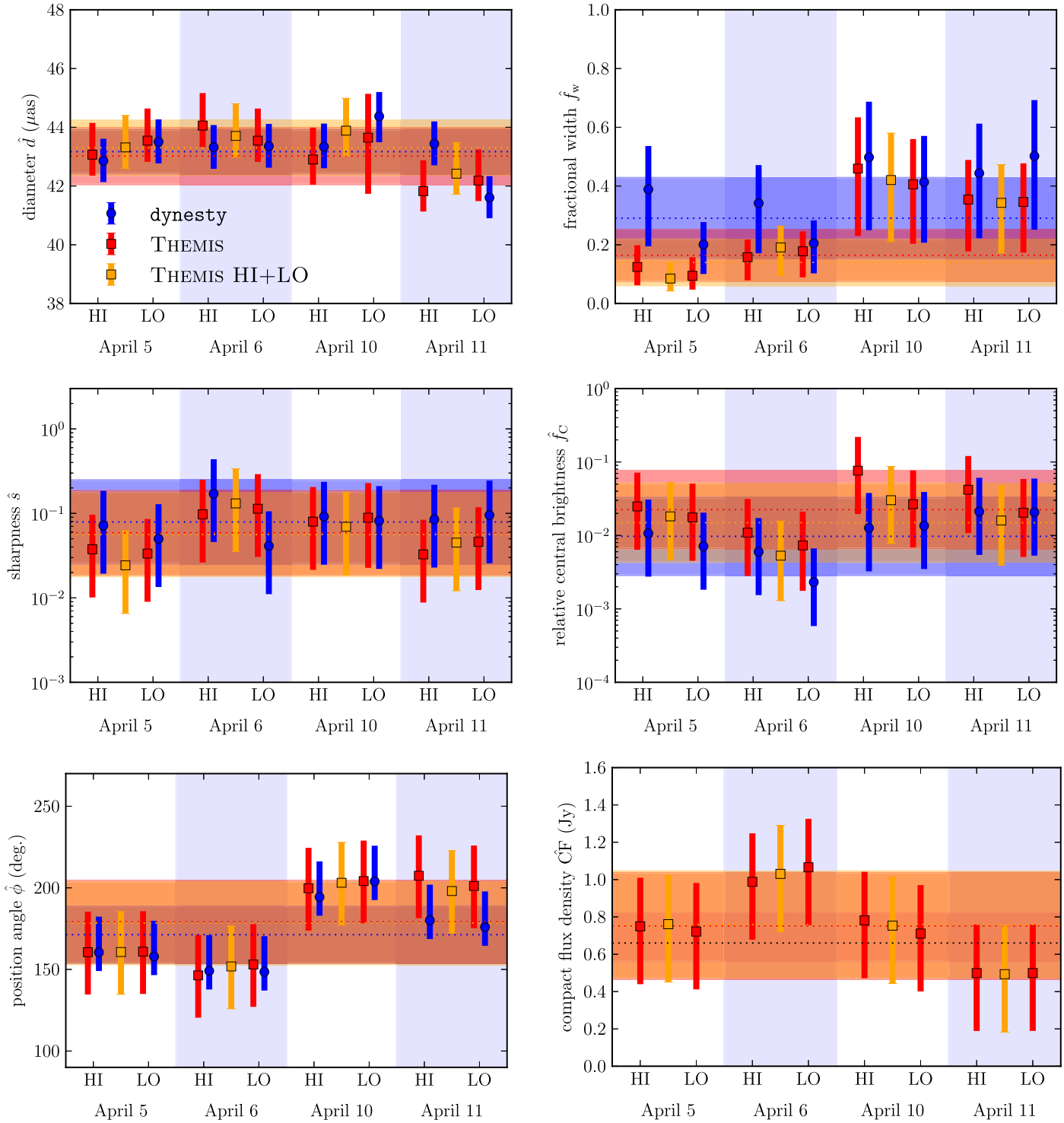

Figure 7. Posterior medians and 68% confidence intervals for selected parameters derived from GC model fitting for all observing days and bands. Blue circular points indicate xs-ring fits using the `dynesty`-based fitting scheme applied to individual data sets (i.e., a single band on a single day). Red square points indicate xs-ringauss fits using THEMIS applied to individual data sets, while orange square points show THEMIS-based xs-ringauss fits to data sets that have been band-combined. All plotted error bars include the systematic "observational uncertainties" estimated from simulated data in Appendix D; these uncertainties are listed in the bottom row of Table 3. Note that recovery of the total compact flux density $\hat{CF}$ is not possible for the `dynesty`-based fits, which use only closure quantities. The light purple band in the lower-right panel is the range inferred in Paper IV.

the angular size corresponding to one gravitational radius,

$$\theta_g = \frac{GM}{c^2 D}. \tag{26}$$

The gravitational radius sets the physical length scale of the emission region. Most of the observed 230 GHz emission is expected to originate near the photon ring (see, e.g., Dexter et al. 2012), whose scaling with θ_g is known for a given black hole mass and spin a_* (Bardeen 1973; Chandrasekhar 1983). The crescent component in the GC models does not necessarily correspond to the photon ring itself. If, however, the crescent component is formed by lensed emission near the horizon, then

Table 4
Calibrated Scaling Factors, α, and Corresponding θ_g Measurements

Model	$\hat{d}$ (μas)	Calibration	α	θ_g (μas)	$\sigma_{\rm stat}$ (μas)	$\sigma_{\rm obs}$ (μas)	$\sigma_{\rm thy}$ (μas)
xs-ring	43.2	MAD+SANE	11.56	3.74	(+0.064, −0.063)	(+0.064, −0.069)	(+0.42, −0.43)
		MAD only	11.13	3.88	(+0.057, −0.055)	(+0.050, −0.060)	(+0.32, −0.25)
		SANE only	12.06	3.58	(+0.073, −0.073)	(+0.089, −0.096)	(+0.44, −0.51)
xs-ringauss	43.4	MAD+SANE	11.35	3.82	(+0.038, −0.038)	(+0.078, −0.077)	(+0.44, −0.36)
		MAD only	11.01	3.94	(+0.040, −0.039)	(+0.092, −0.10)	(+0.25, −0.20)
		SANE only	11.93	3.64	(+0.036, −0.036)	(+0.061, −0.050)	(+0.54, −0.55)

Note. We use the angular diameter measurements ($\hat{d}$) from Section 5.2 and combine them with the calibrated scaling factors (α) from Section 5.3 to arrive at our measurements of θ_g. We list scaling factors calibrated using both magnetically arrested disks (MAD) and standard and normal evolution (SANE) GRMHD simulations (see Section 6.1), as well as ones calibrated using only MAD and only SANE simulations; for the final measurement presented in the text we have used the MAD +SANE calibration. The various uncertainty components are described in Appendix D.2. We quote median values for all measurements and the associated 68% confidence intervals for the different categories of uncertainty.

its size should obey a similar scaling with θ_g,

$$\hat{d} = \alpha\theta_g. \tag{27}$$

For emission at the photon ring, $\alpha \simeq 9.6$–10.4 depending on the black hole spin parameter. For a realistic source model, the emission is not restricted to lie exactly at the photon ring. The value of this scaling factor α and its uncertainty are therefore unknown a priori.

We have measured α and its uncertainty for both GC models using a suite of synthetic data sets generated from snapshots of GRMHD simulations from the GRMHD image library (Paper V). The full calibration procedure, including properties of the selected GRMHD simulations, the synthetic data generation process, and the calibration uncertainty quantification, is detailed in Appendix D. By fitting each calibration image with a GC model, and then comparing the corresponding $\hat{d}$ measurement to the input value of θ_g for the simulation that produced the image, we determine the value of α for that image. Combining the results of such fits from a large number of GRMHD simulations yields a calibration (and uncertainty) for α. For the xs-ring model we find a mean value of $\alpha = 11.55$, while for the xs-ringauss model we find a nearly identical $\alpha = 11.50$. Both of these values are somewhat larger than the $\alpha \approx 10$ expected for the photon ring itself, indicating that the GC models are accounting for emission in the GRMHD model images that preferentially falls outside of the photon ring.

Figure 8 shows the θ_g values obtained as a result of applying our calibrated scaling factor to the crescent diameter values measured for each day and band, and Table 4 lists the results from combining the measurements from all data sets. There is excellent agreement between the two GC models, resulting in an averaged value of $\theta_g = 3.77^{+0.45}_{-0.40}$ μas. We note that the 12% uncertainty in the θ_g measurement is dominated by the diversity of GRMHD models used in the primary calibration; the quantification of this "theoretical" uncertainty component from the GRMHD simulations is described in Appendix D.2.

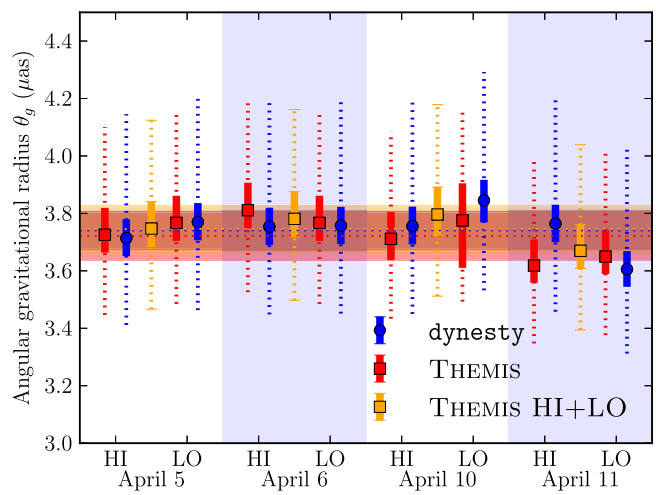

Figure 8. Constraints on θ_g arising from the GRMHD simulation calibrated GC model fits, by day and band. Solid error bars indicate 68% confidence intervals, while dashed error bars indicate the systematic uncertainty in the calibration procedure. Circular blue points indicate independent analyses for each band and on each day in the context of the xs-ring GC model fit using the `dynesty`-based method. Square points indicate independent analyses for each band (red) and band-combined analyses (orange) for each day using the xs-ringauss GC model with THEMIS. Colored bands around dashed lines (right) indicate the combined constraint across both bands and all days, neglecting the systematic uncertainty in the calibration procedure.

6. Direct Comparison with GRMHD Models

EHT data have the power to directly constrain GRMHD simulation based models of M87 and to estimate the physical properties of the black hole and emitting plasma. Such a direct comparison is challenging due to stochastic structure in the models.

The EHT 2017 data span a very short time frame for the M87 source structure. Its characteristic variability timescale at 230 GHz is $\simeq$50 days (Bower et al. 2015), much longer than our observing run. Thus, although the entire ensemble of model snapshots taken from a given simulation captures both the persistent structure as well as the statistics of the stochastic components, we do not yet have enough time coverage for M87 itself to measure its structural variations.

Model images from GRMHD simulations show a dominant, compact, asymmetric ring structure resulting from strong gravitational lensing and relativistic gas motions (Paper V). Hence, they capture the qualitative features found by image reconstructions in Paper IV and by geometric crescent models in Section 5. This motivates a direct comparison of the GRMHD model images with the EHT data.

In this section we summarize the GRMHD image library (Section 6.1) and fit individual simulation snapshot images (Sections 6.2 and 6.3) in a similar fashion to past work on

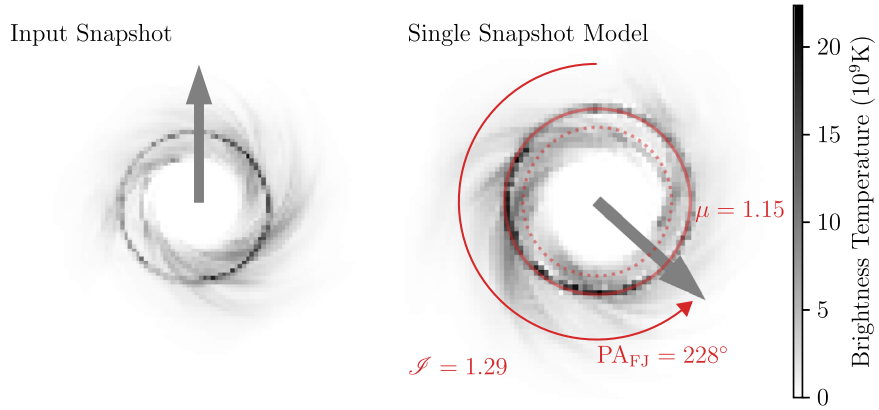

Figure 9. Illustration of the parameters of the SSM described in Section 6.2. Both the original GRMHD simulation (left) and the corresponding SSM for an arbitrary set of parameter values, (flux rescaling, stretching of the image, and rotation; right) are shown. In both panels, the gray arrow indicates the orientation of the forward jet.

GRMHD fitting to mm-VLBI data of Sgr A* (e.g., Dexter et al. 2010; Kim et al. 2016). We further develop and apply a method for testing the consistency of the M87 data with the simulation models (Section 6.4) and find that the majority of the simulation library models is consistent with the data. We use the results to estimate physical parameters, including the black hole angular radius GM/Dc^2 (Section 6.5). The implications of our results for the physical properties of the emission region are discussed in more detail in Paper V. From EHT data alone it is difficult to rule out many of the broad range of possible models for the black hole and plasma properties. However, in combination with other data (especially the observed jet power), ultimately more than half of the models can be excluded.

6.1. Summary of Simulations

As described in detail in Paper V, we have constructed a large image library of horizon-scale synchrotron emission images at 230 GHz computed from GRMHD simulations. We summarize the broad features of this library here and direct the reader to Paper V for more information. The GRMHD simulations cover a wide range of black hole spins as well as initial magnetic field geometries and fluxes. These result in images associated with a variety of accretion flow morphologies and degrees of variability. The magnetic flux controls the structure of the accretion flow near the black hole. Low magnetic fluxes produce the standard and normal evolution (SANE) disks characterized by low-efficiency jet production. In contrast, magnetically arrested disks (MAD) are characterized by large magnetic fluxes, set by the ram pressure of the confining accretion flow.

From these models, families of between 100 and 500 snapshot images were produced assuming synchrotron emission from an underlying thermal electron population (see Section 3.2 of Paper V). The snapshot image generation introduces additional astrophysical parameters associated with the intrinsic scales in the radiative transfer. These parameters include the black hole mass, the viewing inclination, i, and a model for the electron thermodynamics: $T_i/T_e \approx R_{\rm high}$ in gas-pressure dominated regions and is unity otherwise (Mościbrodzka et al. 2016), where T_i and T_e are the ion and electron temperatures.

The number density of emitting electrons is scaled independently for each simulation such that the typical 230 GHz flux density is ∼0.5 Jy. The temporal separation between snapshots is selected such that adjacent snapshots are weakly correlated.

6.2. Single Snapshot Model (SSM)

Each snapshot image generates a three-parameter SSM defined by the total compact flux (CF), angular scale (θ_g), and orientation (defined to be the position angle of the forward jet measured east of north, $\mathrm{PA_{FJ}}$). Variations in these parameters approximately correspond to variations in the accretion rate, black hole mass, and orientation of the black hole spin, respectively. Variations in mass are associated with changes in the diameter of the photon ring, a generic feature found across all of the images in the GRMHD image library.

Each snapshot image is characterized by a nominally scaled, normalized intensity map of the image, $\hat{I}(x, y)$, with a corresponding nominal total intensity $\hat{\mathrm{CF}}$, gravitational radius $\hat{\theta}_g$, and forward jet position angle $\mathrm{PA_{FJ}} = 0°$; associated with the intensity map are complex visibilities $\hat{V}(u, v)$. The SSM is then generated by rescaling, stretching, and rotating $\hat{V}(u, v)$:

$$V_{\rm SSM}(u, v; \mathscr{I}, \mu, \mathrm{PA_{FJ}}) = \mathscr{I}\hat{V}(\mu u', \mu v') \tag{28}$$

where $\mathscr{I} \equiv \mathrm{CF}/\hat{\mathrm{CF}}$, $\mu \equiv \theta_g/\hat{\theta}_g$, and (u', v') are counter-rotated from (u, v) by the angle $\mathrm{PA_{FJ}}$. This procedure is illustrated in Figure 9.

We show in Paper V that these approximations generally hold for flux and mass for rescalings by factors of $\lesssim 2$ from their fiducial values.

6.3. Fitting Single Snapshots to EHT Data

For both model selection and parameter estimation, the first step is fitting an SSM model to the EHT data set described in detail in Section 2.1. The only difference here is that intra-site baselines are excluded. These probe angular scales between $0\farcs1$ and $10''$, at which unmodeled large-scale features, e.g., *HST*-1, contribute substantially (see Section 4 of Paper IV). We verify after the fact that the reconstructed compact flux estimates are consistent with the upper limits necessarily implied by these baselines. The fitting process is complicated by large structural variations between snapshots resulting from turbulence in the simulations (see Section 6.4).

We employ two independent methods to fit SSMs to the EHT data sets. Both employ the likelihoods constructed as described in Section 4.1 for visibility amplitudes and closure phases. The two methods, THEMIS and GENA, are utilized as described in Section 4, producing posterior estimates or best-fit estimates, respectively, for CF, θ_g, and $\mathrm{PA_{FJ}}$.

We adopt a uniform prior on the total compact flux density between 0.1 and 10 Jy for THEMIS and between 0.1 Jy and 4 Jy for GENA; both of these priors cover ranges that substantially exceed the limits placed by Paper IV. While the position angle (PA) of the large-scale radio jet in M87 is well known, we permit the PA of the horizon-scale jet to be unconstrained, setting a uniform prior from [0°, 360°). Finally, we place a flat prior on θ_g ranging from 0.1 to 100 μas for THEMIS and between 0 and 10 μas for GENA, again substantially exceeding the physically relevant ranges.

6.4. Model Selection and Average Image Scoring (AIS)

Quantitatively assessing the quality of SSM fits presents unique challenges because of the presence of stochastic image features due to turbulence in the underlying GRMHD simulations that produce large variations in image structure. The structural variability leads to changes in EHT observables that are much larger than the observational errors. It is therefore not feasible to generate a sufficient number of images from existing GRMHD simulations to have a significant probability of finding a formally adequate (i.e., $\chi^2 \approx 1$) fit to the data (see the discussion in Paper V). Nevertheless, the ensemble of snapshots from a given simulation provides a natural way to characterize the impact of these stochastic features on the inferred SSM parameters.

We can thus assess individual GRMHD simulations, effectively comprised of many (100–500) snapshot images, by comparing the quality of SSM fits to a numerically constructed distribution of reduced χ^2 values. Note that this procedure is conceptually identical to the normal fitting procedure, in which a χ^2 is interpreted relative to the standard χ^2-distribution and thus a reduced $\chi^2 \approx 1$ is a "good" fit, with the exception that an additional source of noise has been effectively introduced as part of the underlying model, altering the anticipated distribution of χ^2 values. In practice, this comparison is executed via the AIS method described in Appendix F using the THEMIS SSM fitting pipeline.

We estimate the appropriate χ^2-distribution by performing multiple fits of an SSM constructed from the arithmetic average snapshot image to simulated data generated from each snapshot image within the underlying GRMHD model. Finally, the average snapshot image is compared to the EHT data, and the resulting χ^2 is assessed. Thus, THEMIS-AIS is effectively determining if the EHT data are consistent with being drawn from the GRMHD simulation. The result is characterized by a simulation p-value, which we call p_{AIS}. Because of the significant variations in data quality and baseline coverage across days, this procedure must be repeated independently for each day.

It is possible for a model to be ruled out by the AIS procedure both by the average image SSM having a χ^2 that is too high (the data is "further" from the average snapshot image than typical for the simulation) and by the average image SSM having a χ^2 that is too low (the data is "closer" to the average snapshot image than typical for the simulation, usually a consequence of too much variability in the GRMHD model). These are similar to finding a reduced χ^2 that is much larger and smaller than unity, respectively, in traditional fits. Both occur in practice.

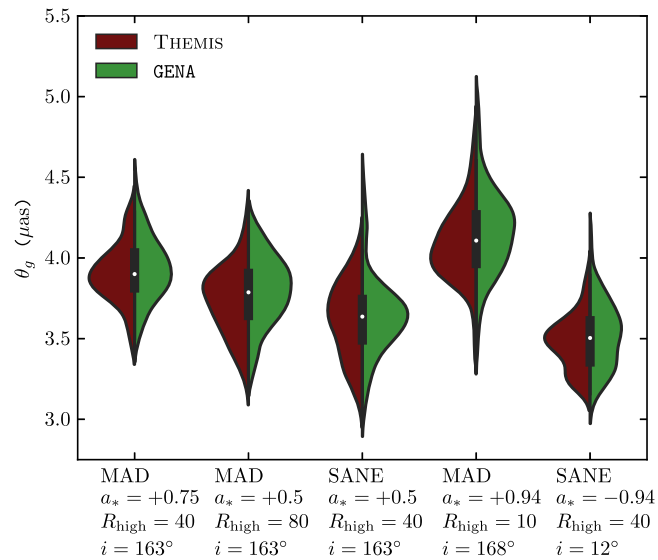

Figure 10. Distributions of recovered θ_g from five representative GRMHD simulations as measured by the THEMIS (left; maroon) and GENA (right; green) pipelines. Only those snapshots for which the likelihood is above the median (THEMIS), or for which the combined χ^2 statistic is below the median (GENA) are included. For a wide range of simulations, the recovered θ_g are consistent with each other. All of the simulations shown are deemed acceptable by AIS ($p_{\mathrm{AIS}} > 0.01$; see Section 6.4 for details).

The result of the THEMIS-AIS procedure is limited by the number of snapshots from each model, and thus is currently capable of excluding models only at the 99% level for a given day and band (i.e., $p_{\mathrm{AIS}} < 0.01$). Due to the long dynamical timescale of M87—GRMHD snapshots exhibit correlations extending up to $20GM/c^3 \approx 1$ week—this is not significantly improved by combining bands and/or days. Therefore, unless otherwise noted, we set a threshold of $p_{\mathrm{AIS}} > 0.01$, below which we deem a GRMHD model unacceptable and exclude it from consideration.

6.5. Ensemble-based Parameter Estimation

The posteriors for the SSM parameters for a given GRMHD model are estimated using both the observational errors in the EHT data and the stochastic fluctuations in the snapshot images themselves; among these "noise" terms, the latter significantly dominates. This is evidenced by the variations among SSM fit parameters from snapshots within a GRMHD model, which typically exceed the formal fit errors from the SSM fit alone (see Appendix G). Some care must be taken in extracting and interpreting parameter estimates from these.

Only SSM fits with likelihoods among the highest 10% within each model are used for parameter estimation. The results for θ_g are insensitive to the precise value of this fit-quality cut after it passes 50%. The measured values are consistent over the range of GRMHD models explored (see Figure 10 for five examples). The consistency is likely a result of the dominant strong lensing and relativistic motion that are common to all models.

The full posteriors are then obtained by marginalizing over all GRMHD models that are found to be acceptable via the THEMIS-AIS procedure. At this point we also include the ancillary priors on jet power, X-ray luminosity, and emission efficiency described in Paper V (see their Table 2). This procedure corresponds to

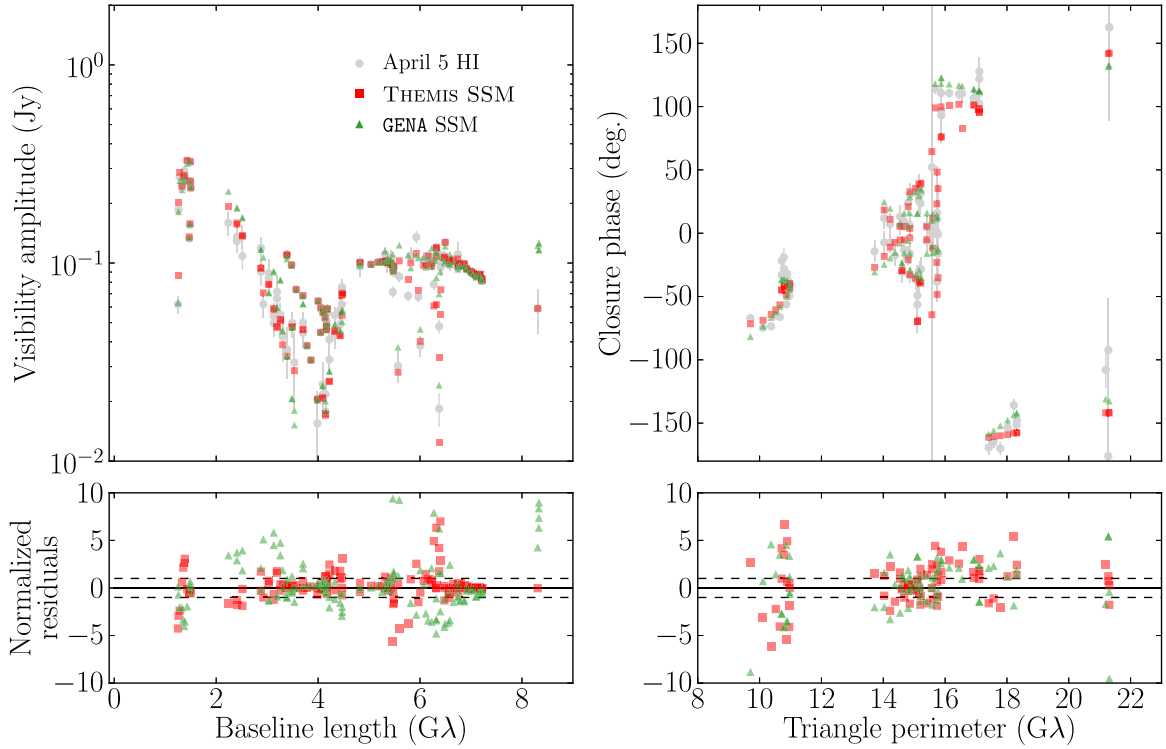

Figure 11. Visibility amplitude and closure phase residuals for an SSM fit to the April 5, high-band data for a "good" snapshot image frame from a MAD simulation with $a_* = 0$, $i = 167°$, and $R_{\rm high} = 160$. The reduced-χ^2 values for the fits are 5.9 (THEMIS) and 7.3 (GENA). All residuals are normalized by their corresponding estimated observational errors.

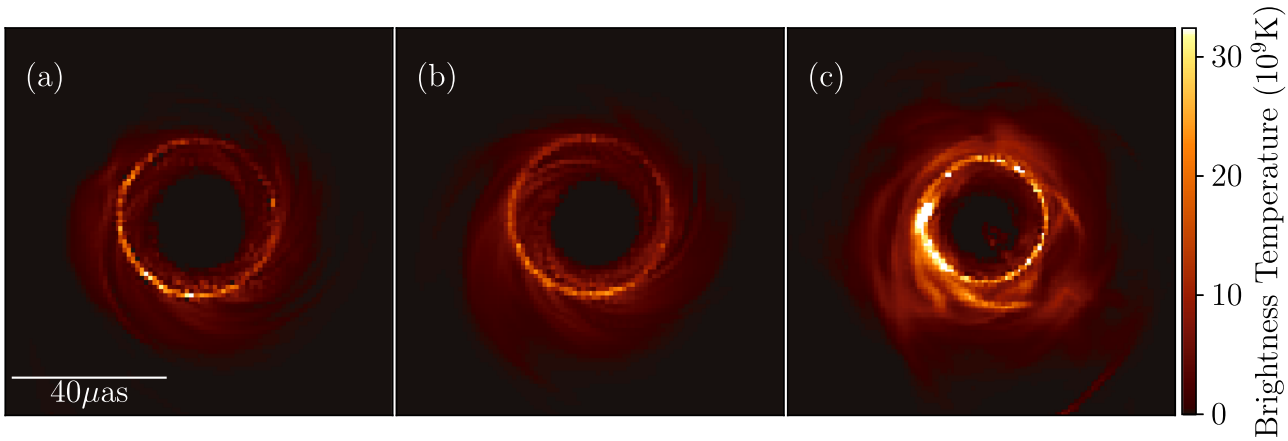

Figure 12. Three sample SSM fits to April 6 high-band data. All are from models with THEMIS-AIS $p_{\rm AIS} > 0.1$. In panels (a) and (b), the prominent photon ring places a strong constraint on θ_g. In panel (c), the extended disk emission results in a smaller θ_g estimate.

simply summing the posteriors obtained for each acceptable GRMHD model.

In principle, it is possible for the posteriors constructed in this fashion to suffer from biases induced by the treatment of the high values of χ^2 found when including only observational errors. We have attempted to estimate this bias using a large number of mock analyses. In those, simulated data were generated from a snapshot within a GRMHD model. Posteriors were then generated for that model given the simulated data and compared to their known SSM parameters; no significant biases were found. We have further conducted two posterior mock analyses for the full suite of GRMHD models, independently for the THEMIS and GENA pipelines. In these the impact of including "incorrect" GRMHD models was a key difference with the previous tests. See Appendix G for more details.

The results of both of these experiments only hold if the GRMHD models used as synthetic data provide a good description of M87. As multiple observation epochs become available, it will be possible to explicitly measure the statistics of the stochastic fluctuations, empirically addressing this assumption. It will also enable direct ensemble-to-ensemble comparison like that described in Kim et al. (2016). A promising, alternative approach would be to perform a principal component analysis (PCA) decomposition of the snapshots within each model

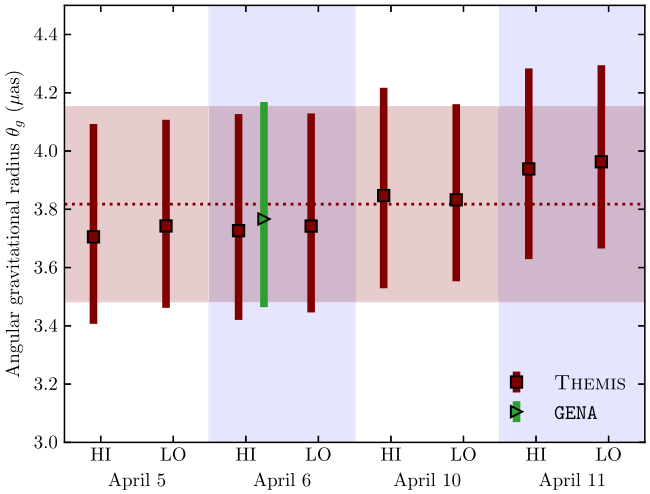

Figure 13. Constraints on θ_g arising from the GRMHD model fitting procedure, by day and band. The maroon squares and green triangles are the constraints arising form the THEMIS and GENA pipelines. Solid error bars indicate the 68% confidence levels about the median. The maroon colored band indicates the combined constraint across both bands and all days.

Table 5
Best-fit Parameters for All Data Sets from Direct GRMHD Simulation Fitting, as Defined in Section 6.2

Data Set			Parameter		
Day	Band	Code	θ_g (μas)	CF (Jy)	PA_{FJ} (deg.)
April 5	HI	THEMIS	$3.71^{+0.39}_{-0.30}$	$0.53^{+0.18}_{-0.11}$	233^{+35}_{-37}
	LO	THEMIS	$3.74^{+0.36}_{-0.28}$	$0.53^{+0.16}_{-0.10}$	228^{+33}_{-36}
April 6	HI	THEMIS	$3.73^{+0.40}_{-0.31}$	$0.52^{+0.16}_{-0.10}$	223^{+34}_{-35}
	HI	GENA	$3.77^{+0.40}_{-0.30}$	$0.42^{+0.08}_{-0.07}$	220^{+37}_{-40}
	LO	THEMIS	$3.74^{+0.39}_{-0.30}$	$0.56^{+0.16}_{-0.11}$	232^{+33}_{-35}
April 10	HI	THEMIS	$3.85^{+0.37}_{-0.32}$	$0.55^{+0.13}_{-0.10}$	232^{+52}_{-62}
	LO	THEMIS	$3.83^{+0.33}_{-0.28}$	$0.57^{+0.14}_{-0.10}$	238^{+49}_{-61}
April 11	HI	THEMIS	$3.93^{+0.35}_{-0.31}$	$0.58^{+0.14}_{-0.10}$	264^{+36}_{-52}
	LO	THEMIS	$3.96^{+0.33}_{-0.30}$	$0.60^{+0.14}_{-0.10}$	261^{+36}_{-50}

Note. Median posterior values are quoted with 68% confidence intervals.

(Medeiros et al. 2018), and fit images generated by varying the weights of the PCA components to the data to mimic the set of possible realizations of the turbulence.

6.6. M87 Fit Results

An example SSM fit is shown for both the THEMIS and GENA methods in Figure 11. As anticipated, the presence of stochastic features within the images results in a poor formal fit quality for all simulation snapshots, that is, reduced $\chi^2 \gtrsim 2$. Nevertheless, broad features of the visibilities and closure phases are accurately reproduced. These include the deep visibility amplitude minimum near 3.4 Gλ and amplitude of the following bump at 6.0 Gλ, both of which are key constraints on the image structure (see Section 3). Significant structure in the residuals, as seen in Figure 11, is a natural consequence of the presence of stochastic model components, but may also signify that the underlying model is insufficient to fully explain the EHT data. Representative fits obtained via this process are shown in Figure 12 for the best SSM from a selection of models that are not ruled out by THEMIS-AIS.

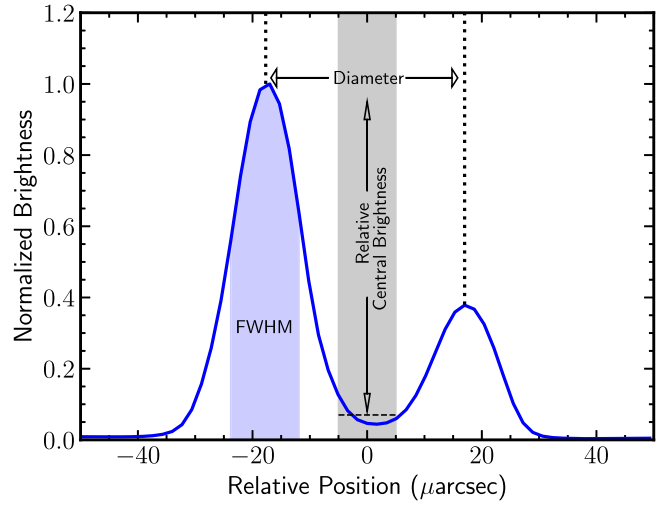

Figure 14. A sample image cross section showing the definitions of the image domain measures that we use in identifying and comparing features in the images (see Section 7).

Even aggressive model selection via THEMIS-AIS produces a very weak cut on the GRMHD models—upon choosing $p_{AIS} > 0.01$ and $p_{AIS} > 0.1$ only 9.7% and 28.5% of models are excluded. After applying the additional observational constraints, we discard 65.3% of the models (for details of the model selection, see Paper V). Here we focus on estimates of the compact flux density, θ_g and PA_{FJ}, after marginalizing over the acceptable models that remain.

The GRMHD-based SSM models produce compact flux estimates between 0.3 and 0.7 Jy. This is at the lower end of the range reported in Paper IV ($0.66^{+0.16}_{-0.10}$ Jy). The PA_{FJ} obtained via comparison of the GRMHD snapshots and the $\hat{\phi}$ found from fitting the GC models are generally consistent after accounting for the average 90° offset between the location of the forward jet in the GRMHD simulation and the location of the brightest region in the crescent image (Paper V). This appears marginally consistent with the mas-scale forward-jet PA measured at 3 and 7 mm of 288° (e.g., Walker et al. 2018), though see Paper V for further discussion on this point.

The posteriors for θ_g are broadly consistent among days and bands, as illustrated in Figure 13 and Table 5. The combined value for both the THEMIS and GENA analyses is $\theta_g = 3.77^{+0.51}_{-0.54}$ μas. Finally, note that the process by which this estimate is arrived at differs qualitatively from the analysis presented in Section 5. Here GRMHD snapshot images are fit directly to data, whereas in Section 5 GRMHD snapshots were used to calibrate the geometric models. These subsets are independent—the set of images used to calibrate the geometric models are not used in the GRMHD analyses. Nevertheless, a systematic correlation between these estimates may remain as a result of the use of the same set of underlying GRMHD simulations.

7. Image Domain Feature Extraction

In the previous sections, we fit geometric and numerical models in the visibility domain to measure the properties of features in the models that give rise to the observed interferometric data. In Paper IV, we performed direct image reconstruction using two RML methods (`eht-imaging` and

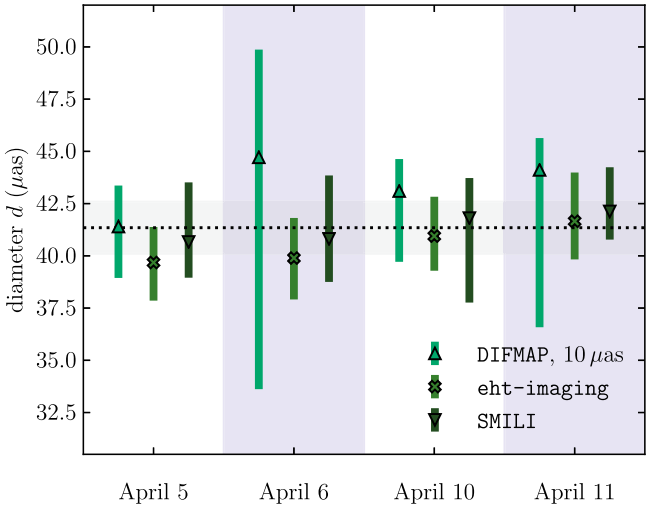

Figure 15. Image domain measurements of the ring diameter of M87 over all observing days comparing three image reconstruction methods. The error bars show the full range of results for the Top Set images using low-band data. The gray dashed line and band show the weighted average and uncertainty across methods and observing days.

SMILI; Akiyama et al. 2017a, 2017b) and one CLEAN method (DIFMAP; Shepherd 1997). Here we present a first analysis of ring properties seen in reconstructed M87 images. We describe the method used to extract parameters (Section 7.1). We then show that the extracted ring diameter is consistent across imaging methods and compare the ring diameter and width with that measured from geometric modeling (Section 7.2). We convert the diameter measurements to the physical scale around the black hole, θ_g, by calibrating with GRMHD simulations (Section 7.3). Finally, we measure the image circularity (Section 7.4).

7.1. Measuring the Parameters of Image Features

We describe the M87 image morphology using five quantities that are similar in spirit but not identical to those introduced in Equations (20)–(23) in Section 5.1: the diameter d of the ring/crescent, its fractional width f_w, the relative brightness f_c of its center with respect to its rim, and the PA ϕ. Figure 14 shows a schematic diagram of these parameters. Here we focus on the first two parameters. Measurements of the remaining parameters in the various image reconstructions and more details on the method can be found in Paper IV.

The reconstructions obtained in Paper IV use a pixel size of 2 μas ($\simeq 1/10$ of the EHT 2017 beam), but the GC image models considered below often show narrower structures. We interpolate both the GC models and image reconstructions onto a grid with pixel size of 0.5 μas before applying the feature extraction methods. When necessary, we use a 2D linear interpolation between adjacent pixels for finer sampling.

The radial brightness profile is characterized by a peaked distribution that declines toward the center. We first locate the (arbitrary) center of the ring. We measure the position of the radial brightness profile maximum along different azimuthal angles. For a trial center position, we calculate the dispersion of the radii defined by these maxima. The center is then chosen iteratively as the location that minimizes this dispersion. Once a center position is chosen, the mean diameter d of the image is defined as twice the distance to the peak, averaged over azimuth.

We define the ring width to be the FWHM of the bright region along each radial profile. The fractional width f_w of the image is the average of the FWHM over azimuthal directions divided by its mean diameter. In the following we first smooth the image with a 2 μas Gaussian. In Appendix H we show that variations on this method produce small (sub-pixel) differences in the results.

7.2. M87 Image Ring Diameters and Widths

Figure 15 shows the mean diameters of images reconstructed using the low-band data during all four days of M87 observations with three image reconstruction methods (eht-imaging, SMILI, DIFMAP; see Paper IV). Image samples are reconstructed for each data set and for a wide range of weights of the regularizers ($\sim$2000 images for eht-imaging and SMILI and $\sim$30 for DIFMAP, see Paper IV). Diameters measured from the full set of images that produce acceptable fits to the visibility data (the "Top Set") are shown here. The diameters of the ring features found across all methods and all days span the narrow range $\sim$38–44 μas.

Figure 16 shows the fractional width versus mean diameter for the Top Set images from eht-imaging and SMILI compared with those from geometric models for the low-band M87 data of April 6 (Section 5). For the two visibility domain methods, the points correspond to the diameters and widths obtained from a sample of 100 images from the xs-ring and xs-ringauss model, chosen randomly from their posteriors. Those model images have been analyzed in the same way as the reconstructed ones.

The fractional widths for the reconstructed images are $\lesssim$0.5, which are consistent with the results of geometric crescent models in Section 5. While both the image reconstructions and model fits show a large uncertainty in fractional width, the widths measured from the image reconstructions in the Top Sets are $\gtrsim$10 μas. Images of rings with narrower widths are consistent with the data and can be produced by the imaging algorithms; however, the parameters in the imaging algorithms (e.g., regularizer weights) that determine the Top Set images were trained on synthetic data from sources smoothed with a 10 μas beam (Paper IV, their Section 6.1). This may help explain the differences in the fractional widths measured with the different techniques.

An anti-correlation between diameter and fractional width for these image domain results is clearly present in three of the four days, but is less clear in the data of April 11. We consider two manifestations for this anti-correlation, based on the location of the first visibility amplitude minimum in simple ring models. First, we use the geometric crescent model of Kamruddin & Dexter (2013), and derive the following approximate fitting formula to the exact expression relating the mean ring diameter d and ψ:

$$d \simeq d_0 \frac{1 - \psi/2}{1 - 0.48\psi + 0.11\psi^5}, \tag{29}$$

where d_0 is the diameter of an infinitesimally thin ring that produces a null at baseline length b_1 (Equation (6)). The fractional width is $\hat{f}_w = \psi/(2 - \psi)$. The blue shaded region in Figure 16 shows the expected diameter and fractional width anti-correlation for a visibility minimum occurring at a range of baseline lengths 3.5–4.0 Gλ, similar to that seen in

Table 6
Measured Diameters, d, Calibrated Scaling Factors, α, and Corresponding Gravitational Radii, θ_g, for the Image Domain Analysis Presented in Section 7

Imaging Method	d (μas)	σ_d (μas)	α	θ_g (μas)	$\sigma_{\rm obs}$ (μas)	$\sigma_{\rm thy}$ (μas)
eht-imaging	40.5	0.5	10.67	3.79	(+0.06, −0.06)	(+0.42, −0.37)
SMILI	41.5	0.4	10.86	3.82	(+0.04, −0.05)	(+0.40, −0.38)
DIFMAP	42.5	0.8	11.01	3.84	(+0.09, −0.10)	(+0.42, −0.32)

Note. We quote median values and 68% confidence intervals. The angular diameters d are averages across the four observing days, weighted by the range within each day. Their uncertainties σ_d are the standard deviation of the mean over the four days. We combine the angular diameter measurements with the calibrated scaling factors (α) to arrive at measurements of θ_g. The various uncertainty components of θ_g are obtained using synthetic data, as described in Appendix E.

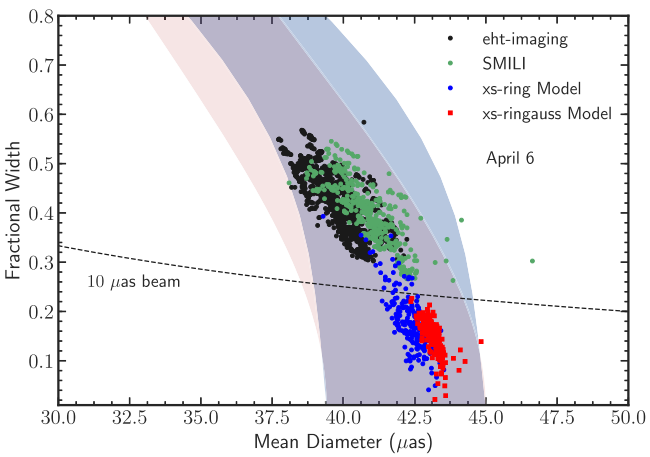

Figure 16. Diameters and fractional widths inferred from image (black and green) and visibility (red and blue) domain measurements on April 6. The visibility domain measurements are from GC model fitting (see Section 5), while the reconstructed images are from Paper IV. The filled regions show diameter and width anti-correlations expected in simple ring models (Section 7.2). The anti-correlation between mean diameter and width helps to explain the small (≃5%) offset in mean diameter found between methods.

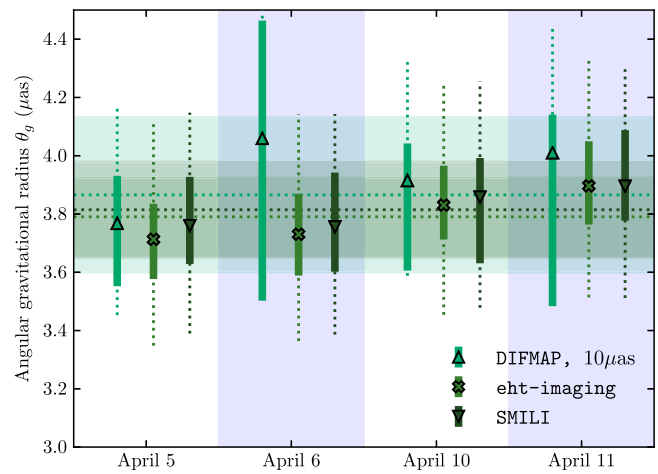

Figure 17. Constraints on θ_g from GRMHD simulation calibrated image domain feature extraction, by day and band. The solid lines show the full range of diameter measurements from the Top Set images. The dotted lines show the systematic calibration uncertainty. The shaded regions show the weighted average and uncertainty over observing days for each method.

the M87 data (Section 3, Paper III). This corresponds to $d_0 \simeq 39.5$–$45\ \mu$as.

We repeat this exercise for an infinitesimally thin ring convolved with a Gaussian. Here the mean diameter d can be approximated for FWHM $w \ll d$ as (Appendix G of Paper IV):

$$d \simeq d_0\left(1 - \frac{w^2}{4\ln 2 d_0^2}\right). \tag{30}$$

Here the fractional width $\hat{f}_{\rm w} = w/d$. The pink shaded area in Figure 16 shows the shaded region for this model, which follows a similar trend.

The measured properties of the images and source models inferred by all methods generally fall within the expected bands. At least part of the systematic differences in our diameter measurements may be attributed to the relatively large uncertainty in width, as a result of their weak anti-correlation.

7.3. From Image Diameter to Angular Gravitational Radius

We can convert the diameters measured from the reconstructed images to the black hole angular gravitational radius using a scaling factor, α (Equation (27)), following the same procedure used in the calibration of crescent model diameters to GRMHD images discussed in Section 5.3. We calculate a separate value of α for each image reconstruction method (eht-imaging, SMILI, DIFMAP) as described in Appendix E and listed in Table 6. The image domain methods do not report posteriors. We therefore estimate the statistical along with the observational component of the uncertainty in the calibration procedure using synthetic data. As found for the geometric crescent models, the theoretical uncertainty dominates the final error budget. The total observational uncertainty is similar to but slightly larger than the statistical spread of the median diameter measurement between days.

After applying the calibrated scaling factor to the image domain diameter measurements, we find consistent results across all observing days and reconstruction methods (Figure 17). This is further indication that the statistical component of the calibration error is sub-dominant. The combined value from all methods is $\theta_g = 3.82^{+0.42}_{-0.38}\ \mu$as. Despite small differences in the measured mean diameters, the physical scale θ_g is remarkably consistent with that found earlier from both geometric and GRMHD model fitting. This is because the corresponding calibration factors α obtained from synthetic data show the same trends as the measured diameters.

7.4. The Circular Shapes of the M87 Images

Our reconstructed M87 images appear circular. We quantify their circularity by measuring the fractional spread in the inferred diameters measured along different orientations for each of the reconstructed images. Here we define the fractional spread as the standard deviation of the diameters measured along different orientations divided by the mean diameter. For each image, the diameters along different orientations measure

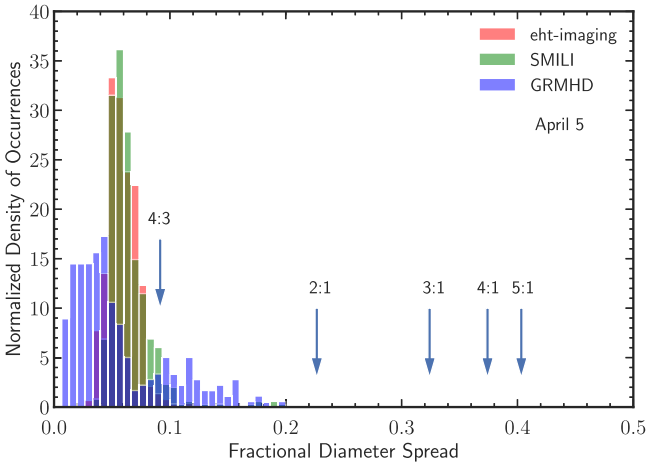

Figure 18. Distributions of fractional spreads in the inferred diameters of the M87 images measured along different orientations, for images reconstructed using two methods for the April 5 data set. The blue histogram is the distribution of fractional spreads for a subset of images from the GRMHD library. The values for elliptical shapes with different axes ratios are indicated with arrows (a value of 0 is an axis ratio of 1:1). The distribution for reconstructed images peaks at values ∼0.05–0.06, which is consistent with the range found from GRMHD model images.

the distance of the location of peak brightness from the center of the image along each orientation. A small fractional spread suggests that the locus of peak brightness on each image has a circular shape.

Figure 18 shows the distribution of the fractional spread in diameters for the Top Set images of M87 reconstructed using two image domain methods (`eht-imaging` and `SMILI`) for the April 5 low-band data set. The figure also shows the fractional spread in diameters of a subset of ∼300 images among those in the GRMHD image library discussed in Paper V that provide acceptable fits according to AIS. Note that these comparison images have a much higher intrinsic resolution than the reconstructed images of M87. The distributions of fractional spreads for the reconstructed images peak at a fractional spread of ∼0.05–0.06. This is within the range found in the GRMHD images. The GRMHD models mostly show circular image structure (peak $\lesssim$0.1 in blue distribution in Figure 18). This corresponds to the bulk of the images where the photon ring is the dominant feature (see Paper V). The tail to larger fractional diameter spread may in part be the result of occasional bright filaments that light up in a small azimuthal range and then quickly fade. During such snapshots, the locus of points with the brightest emission around the shadow becomes non-circular and the fractional spread increases. Arrows in Figure 18 indicate the expected fractional diameter spread for elliptical models. Our results suggest an image axial ratio of $\lesssim$4:3.

8. Prior Mass and Distance Estimates

In this section we briefly review prior estimates of the mass-to-distance ratio for M87's central black hole for comparison with our new EHT results. For a more detailed discussion, see Appendix I.

8.1. Distance

M87 is the central galaxy of the Virgo cluster, the closest galaxy cluster to the Milky Way. This proximity allows a high-precision measurement of its distance using primary or secondary standard candles available only for nearby galaxies within ∼20 Mpc. Among numerous distance estimators obtained for M87, we base the distance that we use here on two estimators of the absolute distance modulus (μ). The first uses as a primary candle the tip of the red giant branch (TRGB method). The second uses a well-calibrated secondary standard candle, the surface brightness fluctuations (SBF method) from resolved stellar distributions observed at high angular resolution.

We combine one TRGB measurement (Bird et al. 2010) with two SBF measurements (Blakeslee et al. 2009; Cantiello et al. 2018a) to arrive at a combined distance measurement. We consider the three distance measurements to be independent and calculate the combined posterior as their product. Based on these, we adopt a distance of $D = 16.8^{+0.8}_{-0.7}$ Mpc to M87. A more detailed description, together with the summary of each measurement, can be found in Appendix I.

8.2. Mass-to-distance Ratio and Related Quantities

For the mass of the central black hole in M87 we focus on the two latest dynamical measurements of the kinematic properties of surrounding stars and gas (Gebhardt et al. 2011; Walsh et al. 2013) that have high-quality data and state-of-the-art modeling approaches.

Stellar dynamical measurements. Gebhardt et al. (2011) used infrared spectroscopic observations of stellar absorption lines over the central 2″ (∼150 pc) of M87 and modeled the observed stellar kinematics to infer a mass of $(6.6 \pm 0.4) \times 10^9 M_\odot$, assuming a distance of 17.9 Mpc. They compared the full line-of-sight stellar velocity distributions at all points with the projected kinematics of axisymmetric models of the galaxy. The models allowed for adjustable but radially constant mass-to-light ratios of the central stellar population and the central effects of the M87 dark matter halo. The analysis demonstrates that kinematics cannot be fitted without the inclusion of a central compact non-luminous mass.

Gas dynamical measurements. Walsh et al. (2013) used *Hubble Space Telescope* (*HST*) Space Telescope Imaging Spectrograph observations of Hα and [N II] emission lines from the central gas-disk within the M87 nucleus to map its kinematic field within 40 pc of the black hole. The velocity field implies a compact mass of $(3.5^{+0.9}_{-0.7}) \times 10^9 M_\odot$, assuming a distance of 17.9 Mpc, on the assumption that the velocity field is Keplerian and is not subject to non-gravitational forces such as shocks and winds. Several factors could account for the lower mass inferred via this technique (see, e.g., Kormendy & Ho 2013; Jeter et al. 2018).

9. Inferred Black Hole Parameters and Discussion

9.1. Lensed Emission Around the Black Hole Shadow

The results of fitting analytic models (Section 5) and GRMHD image snapshots (Section 6) to visibility domain data, as well as image reconstructions (Paper IV, Section 7) strongly favor an asymmetric ring (crescent) source morphology with a deep central brightness depression. This morphology is robust among the different analysis methods and is consistent with characteristic features in the interferometric visibilities (Section 3).

Fitting geometric models to the data and extracting feature parameters in the image domain both allow us to quantify the following properties of the crescents: (i) a compact flux density

of ≃0.7 Jy, which is ≳50% of the total at arcsecond scale (see also Paper III and Paper IV); (ii) a mean emission diameter of ∼42 ± 3 μas; (iii) a fractional width of ≲0.5; (iv) a deep central brightness depression with a brightness contrast ratio of ≳10; and (v) a persistent asymmetry with the brightest region to the South (PA of 150°–200°).

All of these features support the interpretation that we are seeing emission from near the event horizon that is gravitationally lensed into a crescent shape near the photon ring. The central flux depression is the result of photons captured by the black hole: the black hole shadow (Falcke et al. 2000). The asymmetry is a result of Doppler beaming due to the rotation of plasma at relativistic speeds. The peak brightness location is expected to be oriented ≃90° away from the jet PA (Dexter et al. 2012; Mościbrodzka et al. 2016; Ryan et al. 2018; Chael et al. 2019b, see Paper V), roughly north–south as we find here.

In many active galactic nuclei, the radio VLBI jet core on parsecs and larger scales is inferred to be significantly offset from the black hole itself (e.g., Marscher et al. 2008). For M87, this is disfavored by past VLBI observations. The jet and counter-jet angular separation inferred by VLBA observations (Ly et al. 2004, 2007; Kovalev et al. 2007) locates the radio core close to the black hole. VLBA astrometric observations further tightly constrain the jet apex to be ≃41 ± 12 μas upstream of the VLBI core at 43 GHz (Hada et al. 2011, 2013; Nakamura & Asada 2013), suggesting that the mm emission originates very close to the black hole.

The observed EHT image morphology also disfavors an origin offset from the black hole. Models of M87 where the emission predominantly arises in the forward jet have found a larger size and blob-like Gaussian structure (e.g., Broderick & Loeb 2009) due to Doppler beaming resulting from the acceleration of the jet along the line of sight. Additionally, the stable source size over several years of mm-VLBI (Doeleman et al. 2012; Akiyama et al. 2015), despite changes in compact flux density by factors of ≃2–3 (Paper IV), favors the extreme gravitational lensing scenario. Future EHT observations will provide a sensitive additional test of this paradigm by measuring the source morphology on year timescales.

9.2. The Black Hole Mass and Comparison to Prior Dynamical Measurements

We have used several techniques to arrive at θ_g estimates from the EHT 2017 M87 data, and in Table 7 we list the result for each technique after averaging over observing days and bands (see also Figure 19). We find a striking level of consistency across all measurement methods, with GC modeling, direct GRMHD fitting, and image domain feature extraction procedures converging on a characteristic value of $\theta_g = 3.8 \pm 0.4$ μas as the angular size subtended by one gravitational radius. The measurement techniques themselves are entirely independent of one another. The mutual agreement that we see among the multiple measurements indicates that the θ_g value we have converged upon is robust to the many different choices that can be made regarding data products, model specifications, and parameter space exploration algorithms.

All of the individual θ_g estimates use the GRMHD simulation library, either through directly fitting GRMHD snapshots to the data (Section 6) or through calibration of diameters resulting from geometric models or reconstructed images (Sections 5 and 7). A degree of caution is therefore warranted. The measurements rely on images generated from GRMHD simulations and should be understood within that context (see also Paper V). We have also used only a small subset of 100 such randomly chosen frames (with randomly assigned SSM parameters) out of a much larger library. A simple (but poorly motivated) alternative to the full calibration presented here would be to assign the mean emission diameter to the size of the photon ring itself ($\alpha \simeq 9.6$–10.4 for all methods). That would give a nearly identical θ_g result for the image domain estimates and only a ≃10% increase for the geometric models, within its current systematic uncertainty.

The mass measurements that we have carried out with EHT data show a high level of consistency, converging to an average value of $M = 6.5 \times 10^9\, M_\odot$. All measurement techniques share a large source of systematic uncertainty arising from the GRMHD calibration, with an average value of $\sigma_{\rm sys} = 0.7 \times 10^9\, M_\odot$. The geometric crescent modeling and image domain measurements further enable an estimate of the systematic uncertainty associated

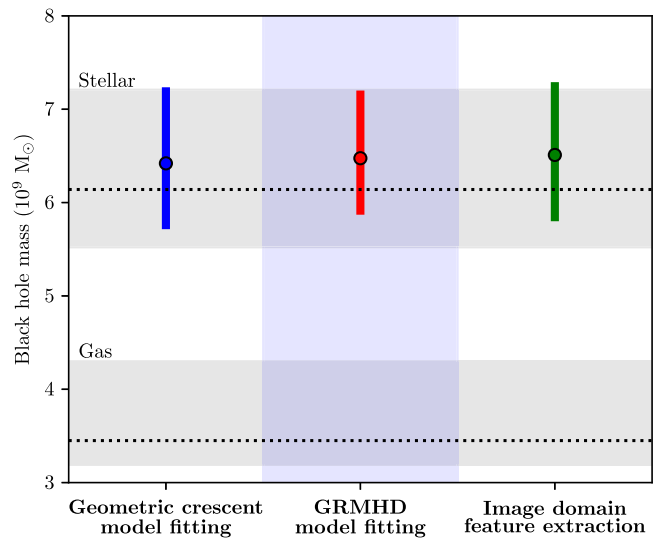

Figure 19. Estimates of the mass of the central black hole in M87 for the three different measurement techniques employed in this Letter (see also Table 7). Gray horizontal bands around dashed lines correspond to the 68% confidence levels for the stellar (top) and gas (bottom) dynamical mass measurements (see Table 9).

Table 7
Summary of θ_g and M Measurements

Measurement Method	θ_g (μas)	M ($10^9\, M_\odot$)
GC model fitting	$3.77^{+0.45}_{-0.40}$	$6.42^{+0.82}_{-0.71}$
GRMHD model fitting	$3.80^{+0.39}_{-0.31}$	$6.48^{+0.73}_{-0.61}$
Image domain feature extraction	$3.83^{+0.42}_{-0.36}$	$6.51^{+0.78}_{-0.71}$
Gas dynamics (Walsh et al. 2013)	$2.05^{+0.48}_{-0.16}$	$3.45^{+0.85}_{-0.26}$
Stellar dynamics (Gebhardt et al. 2011)	$3.62^{+0.60}_{-0.34}$	$6.14^{+1.07}_{-0.62}$
Combined measurements from this work	3.8 ± 0.4	6.5 ± 0.7

Note. Measurements made in this work (top) and from the literature (middle) are quoted as median values with 68% confidence intervals. The final combined measurements from this work are listed in bottom row of the table, rounded to two significant figures. The distance used to compute M from θ_g is 16.8±0.8 Mpc (see Section 8).

with the angular diameter measurement, which manifests in the mass measurement with an average, rounded value of $\sigma_{\rm stat} = 0.2 \times 10^9\, M_\odot$. As can be readily seen in Figure 19, our mass measurements are also in excellent agreement with those made by Gebhardt et al. (2011) using stellar dynamics (Section 8.2). Our mass measurement is inconsistent with the gas dynamics measurement of Walsh et al. (2013) at the ∼99% confidence level.

9.3. Implications for the Black Hole Environment

The measurement of a large black hole mass in M87 has a number of implications for the relationship between the black hole and its immediate environment. The observed line-of-sight velocities of atomic line emission produced within the gas flow at 10–100 pc place strong constraints on the dynamical state of gas on these scales and its relationship with the horizon-scale and milliarcsecond-scale features.

In combination with the stellar dynamics mass estimate, the mass M reported here provides an upper limit on the extended dark mass enclosed within the smallest scale probed by Gebhardt et al. (2011), 0.″25 or approximately 20 pc, set by the upper limit on the difference between the two masses: $M_{\rm G11} - M = -0.3^{+1.3}_{-0.9} \times 10^9 M_\odot$, where $M_{\rm G11}$ is the stellar dynamics mass in Table 7 and the 68% confidence intervals have simply been added in quadrature. Thus, at 95% confidence this comparison implies that inside 20 pc $\lesssim 2.3 \times 10^9\, M_\odot$, or $\lesssim$36% of the central black hole mass, can exist as a dark extended component. This limit is not yet sufficient to constrain the presence of a density "spike" of dark matter associated with the formation of the central black hole (see, e.g., Lacroix et al. 2015).

9.4. Evidence for a Horizon

The constraint on the size of the emission region, coupled with multi-wavelength limits on the emission from within the shadow region, provide evidence for the existence of event horizons. These limits arise from looking for the boundary-layer emission that should be present if a photosphere is visible, i.e., not hidden from view by an event horizon (Narayan & McClintock 2008; Broderick et al. 2015). The source of such emission is often called a "surface," though we note that it need not be so in practice.

The results reported in the previous section strengthen this argument. First, they provide an accurate reconstruction of the source structure, which now locates the central mass to within the photon orbit. Second, as discussed in Paper V, the observed image is broadly consistent with models of jet launching driven by electromagnetic processes. Jets are collimated by accreting material; thus a significant boundary-layer emission component would be expected if M87 is not a black hole (Broderick et al. 2015).

The spectrum of this additional boundary-layer emission component is generally thermal when the photon escape fraction is small, in which case this emission effectively couples the photosphere to itself on a timescale that depends only logarithmically on redshift (though see Lu et al. 2017 regarding the possibility of longer equilibrium times). The color temperature of the emission is set uniquely by the accretion power and *apparent* size of the emission region. The former can be related to within factors of a few to the total jet power, $\sim 10^{42}$ erg s^{-1} (see the discussion in Paper V). Note

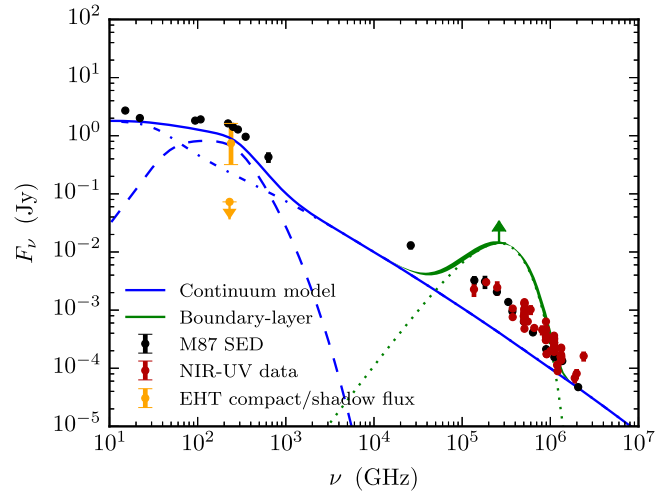

Figure 20. Spectral energy distribution of a putative photosphere in comparison to EHT and multi-wavelength data. The lower limit for the thermal bump associated with boundary-layer emission in the absence of a horizon is shown for a compact object with the size reported here (dark green band and arrow) and a jet power $\gtrsim 10^{42}$ erg s^{-1}. The photospheric component has been added to a jet synchrotron emission model (blue lines, M. Lucchini et al. 2019, in preparation). EHT compact flux densities and limits (orange points) are insensitive to a putative boundary-layer component. Its presence is ruled out by near-infrared, optical, and ultraviolet measurements (dark red and black points, see Broderick et al. 2015; Prieto et al. 2016).

that this lower limit is an order of magnitude smaller than the lower end of the range considered in Broderick et al. (2015). The resulting putative photospheric emission would have a color temperature of $T_C \lesssim 10^4$ K and peak in the near-infrared/optical.

While the EHT is not sensitive to this component, its existence can be excluded by near-infrared, optical, and ultraviolet flux measurements (see, e.g., Broderick et al. 2015; Prieto et al. 2016). We show this excess in Figure 20 for the mass measurement reported here.

9.5. Implications for the Kerr Nature of the Black Hole

The detection of a substantial central brightness depression in the image of M87 that we identify with the shadow of the black hole allows us, in principle, to perform two tests of the nature of the compact object and its spacetime. One is related to the size of the shadow, and the other to its shape.

There are two properties of spinning black holes that, depending on spin and observer inclination, could alter the size and shape of the black hole shadow. The spacetime quadrupole q tends to lend an oblate shape to the shadow, while frame dragging due to the spin a acts to compress the shadow in the direction perpendicular to its spin. When the spacetime quadrupole satisfies the Kerr condition $q = -a^2$, the two effects nearly cancel each other out, leaving a quasi-circular shadow with a mean diameter that lies in the very small range (9.6–10.4) GM/c^2. This shape is expected to be nearly circular for the low inclination of M87 (e.g., Takahashi 2004; Chan et al. 2013).

For a black hole of known mass-to-distance ratio, the angular size of the shadow on the sky is, therefore, fixed and can be used as a null-hypothesis test of the Kerr nature of the compact object (Psaltis et al. 2015). Alternatively, we can infer the mass-to-distance ratio of the black hole using the size of its shadow image, as we do here, and compare it to the

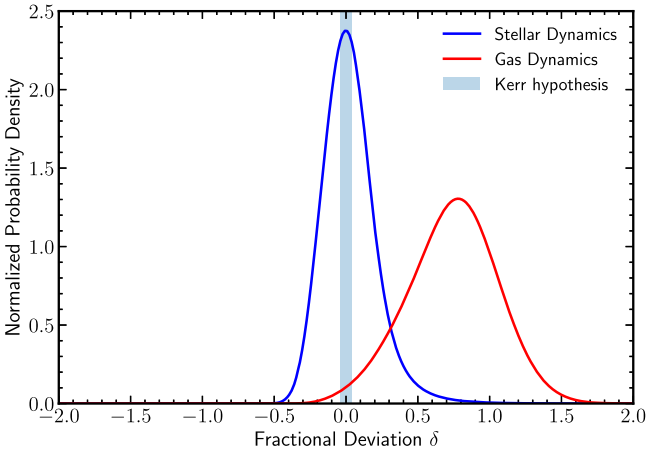

Figure 21. Posterior in the fractional difference δ between the inferred angular gravitational radius of the black hole in M87 based on the EHT data and the values measured using stellar and gas dynamics. The shaded region corresponds to the maximum $\pm 4\%$ discrepancy between the measurements that can be due to the weak dependence of the black hole shadow on the spin magnitude and orientation of a Kerr black hole. The fact that at least one prior mass measurement is consistent with the EHT measurement reported here provides a null hypothesis test of the Kerr nature of the central black hole.

mass-to-distance ratio measured dynamically at much larger distances. Demonstrating agreement between the two inferences results in an equivalent null-hypothesis test.

The null hypothesis in this case consists of three ingredients: that the dynamical measurements provide an accurate determination of the black hole mass, that the brightness depression we detect in the EHT image of M87 is indeed the black hole shadow, and that the spacetime of the black hole is described by the Kerr solution. Demonstrating a violation of this null hypothesis would imply that one or more of these assumptions is invalid.

We have used the 2017 EHT observations of M87 to infer the posterior probability $P_{\rm obs}(\theta_g)$ of the angular gravitational radius at the distance of M87. Earlier dynamical measurements also provide us with the prior probability $P_{\rm dyn}(\theta_{\rm dyn})$ for the same quantity. We can, therefore, measure the fractional difference δ between the predicted and measured mass-to-distance ratio for the black hole as

$$\delta \equiv \frac{\theta_g}{\theta_{\rm dyn}} - 1 \tag{31}$$

and its posterior as

$$P(\delta) = \int \theta_{\rm dyn} P_{\rm dyn}(\theta_{\rm dyn}) P_{\rm obs}(\theta_{\rm dyn}(\delta + 1)) d\theta_{\rm dyn}. \tag{32}$$

Figure 21 shows the posterior on the fractional deviation between the EHT and the dynamical inferences of the mass-to-distance ratio, when we assume the prior measurements based on stellar and gas dynamics. We find $\delta = -0.01 \pm 0.17$ (68% credible intervals) for the stellar and $\delta = 0.78 \pm 0.3$ for the gas dynamics priors. The fact that our measurement θ_g is consistent with one of the prior measurements $\theta_{\rm dyn}$ allows us to conclude that our null hypothesis has not been violated.

The second property of the black hole shadow that is affected by potential deviations of its spacetime from the Kerr metric is its shape. Shadows of Kerr black holes are nearly circular with a maximum asymmetry of $\lesssim 10\%$, as defined in Johannsen & Psaltis (2010). For the case of the $\sim 17^\circ$ inclination of M87 (and assuming that the large-scale jet points along the spin axis), the maximum asymmetry is $\lesssim 2\%$ for all values of black hole spin (e.g., Chan et al. 2013). Measuring a shadow shape that deviates from circular to a degree larger than this amount would require that the spacetime of the compact object is not described by the Kerr metric (Johannsen & Psaltis 2010).

Figure 18 shows that the circularity measured from reconstructed images of M87 is consistent with that found in model images from GRMHD simulations in the Kerr metric. The images used in our analysis in Section 7 measure the shape of the emitting region. In future work a similar analysis can be done using images from models that violate the no-hair theorem, where the photon ring/shadow shape can be highly prolate, oblate, or even amorphous (Broderick et al. 2014; Giddings & Psaltis 2018).

10. Conclusions

The horizon-scale emission of M87 at 1.3 mm exhibits a robust crescent-like structure. This is seen in image reconstructions (Paper IV) and supported by features in the visibility data from the 2017 EHT campaign (Paper III). Geometric crescent models are overwhelmingly preferred to similarly complex models that we have explored that do not have a central flux depression.

The crescent structure is well defined, with a rapid decline to a dark interior with a brightness $\gtrsim 10\times$ lower than the average of that in the annular region. The average diameter of the crescent is well constrained by multiple methods with a combined range of $42 \pm 3\,\mu$as. This is consistent among all observation days and bands.

Based on geometric models, GRMHD simulations, and image domain feature extraction, the angular size of the gravitational radius is $\theta_g = 3.8 \pm 0.4\,\mu$as. The uncertainty of this value is currently dominated by a systematic component associated with the location of the mean emission diameter in GRMHD simulations that is used to convert from an angular to physical scale. Accounting for this uncertainty explicitly, the resulting black hole mass is $M = 6.5 \pm 0.2|_{\rm stat} \pm 0.7|_{\rm sys} \times 10^9\,M_\odot$. This mass is consistent with that measured from stellar but not gas dynamics.

The crescent morphology, rapid drop to a deep interior flux depression, and broad consistency among days, methods, and the stellar dynamics measurement all point to the emission structure from M87 being due to strong gravitational lensing around a central black hole. The consistency between the 10 pc-scale stellar dynamics and EHT mass measurements provides a null test of the Kerr metric. The size constraint and qualitative support of the standard jet formation paradigm argues for the presence of a horizon. Together, our results strongly support the hypothesis that the central object in M87 is indeed a Kerr black hole, and provide new evidence for the long-believed connection between AGNs and SMBHs.

The authors of this Letter thank the following organizations and programs: the Academy of Finland (projects 274477, 284495, 312496); the Advanced European Network of E-infrastructures for Astronomy with the SKA (AENEAS) project, supported by the European Commission Framework Programme Horizon 2020 Research and Innovation action under grant agreement 731016; the Alexander von Humboldt

Stiftung; the Black Hole Initiative at Harvard University, through a grant (60477) from the John Templeton Foundation; the China Scholarship Council; Comisión Nacional de Investigación Científica y Tecnológica (CONICYT, Chile, via PIA ACT172033, Fondecyt 1171506, BASAL AFB-170002, ALMA-conicyt 31140007); Consejo Nacional de Ciencia y Tecnología (CONACYT, Mexico, projects 104497, 275201, 279006, 281692); the Delaney Family via the Delaney Family John A. Wheeler Chair at Perimeter Institute; Dirección General de Asuntos del Personal Académico–Universidad Nacional Autónoma de México (DGAPA–UNAM, project IN112417); the European Research Council Synergy Grant "BlackHoleCam: Imaging the Event Horizon of Black Holes" (grant 610058); the Generalitat Valenciana postdoctoral grant APOSTD/2018/177; the Gordon and Betty Moore Foundation (grants GBMF-3561, GBMF-5278); the Istituto Nazionale di Fisica Nucleare (INFN) sezione di Napoli, iniziative specifiche TEONGRAV; the International Max Planck Research School for Astronomy and Astrophysics at the Universities of Bonn and Cologne; the Jansky Fellowship program of the National Radio Astronomy Observatory (NRAO); the Japanese Government (Monbukagakusho: MEXT) Scholarship; the Japan Society for the Promotion of Science (JSPS) Grant-in-Aid for JSPS Research Fellowship (JP17J08829); JSPS Overseas Research Fellowships; the Key Research Program of Frontier Sciences, Chinese Academy of Sciences (CAS, grants QYZDJ-SSW-SLH057, QYZDJ-SSW-SYS008); the Leverhulme Trust Early Career Research Fellowship; the Max-Planck-Gesellschaft (MPG); the Max Planck Partner Group of the MPG and the CAS; the MEXT/JSPS KAKENHI (grants 18KK0090, JP18K13594, JP18K03656, JP18H03721, 18K03709, 18H01245, 25120007); the MIT International Science and Technology Initiatives (MISTI) Funds; the Ministry of Science and Technology (MOST) of Taiwan (105-2112-M-001-025-MY3, 106-2112-M-001-011, 106-2119-M-001-027, 107-2119-M-001-017, 107-2119-M-001-020, and 107-2119-M-110-005); the National Aeronautics and Space Administration (NASA, Fermi Guest Investigator grant 80NSSC17K0649); the National Institute of Natural Sciences (NINS) of Japan; the National Key Research and Development Program of China (grant 2016YFA0400704, 2016YFA0400702); the National Science Foundation (NSF, grants AST-0096454, AST-0352953, AST-0521233, AST-0705062, AST-0905844, AST-0922984, AST-1126433, AST-1140030, DGE-1144085, AST-1207704, AST-1207730, AST-1207752, MRI-1228509, OPP-1248097, AST-1310896, AST-1312651, AST-1337663, AST-1440254, AST-1555365, AST-1715061, AST-1614868, AST-1615796, AST-1716327, OISE-1743747, AST-1816420); the Natural Science Foundation of China (grants 11573051, 11633006, 11650110427, 10625314, 11721303, 11725312, 11873028, 11873073, U1531245, 11473010); the Natural Sciences and Engineering Research Council of Canada (NSERC, including a Discovery Grant and the NSERC Alexander Graham Bell Canada Graduate Scholarships-Doctoral Program); the National Youth Thousand Talents Program of China; the National Research Foundation of Korea (grant 2015-R1D1A1A01056807, the Global PhD Fellowship Grant: NRF-2015H1A2A1033752, and the Korea Research Fellowship Program: NRF-2015H1D3A1066561); the Netherlands Organization for Scientific Research (NWO) VICI award (grant 639.043.513) and Spinoza Prize SPI 78-409; the New Scientific Frontiers with Precision Radio Interferometry Fellowship awarded by the South African Radio Astronomy Observatory (SARAO), which is a facility of the National Research Foundation (NRF), an agency of the Department of Science and Technology (DST) of South Africa; the Onsala Space Observatory (OSO) national infrastructure, for the provisioning of its facilities/observational support (OSO receives funding through the Swedish Research Council under grant 2017-00648) the Perimeter Institute for Theoretical Physics (research at Perimeter Institute is supported by the Government of Canada through the Department of Innovation, Science and Economic Development Canada and by the Province of Ontario through the Ministry of Economic Development, Job Creation and Trade); the Russian Science Foundation (grant 17-12-01029); the Spanish Ministerio de Economía y Competitividad (grants AYA2015-63939-C2-1-P, AYA2016-80889-P); the State Agency for Research of the Spanish MCIU through the "Center of Excellence Severo Ochoa" award for the Instituto de Astrofísica de Andalucía (SEV-2017-0709); the Toray Science Foundation; the US Department of Energy (USDOE) through the Los Alamos National Laboratory (operated by Triad National Security, LLC, for the National Nuclear Security Administration of the USDOE (Contract 89233218CNA000001)); the Italian Ministero dell'Istruzione Università e Ricerca through the grant Progetti Premiali 2012-iALMA (CUP C52I13000140001); ALMA North America Development Fund; Chandra TM6-17006X. This work used the Extreme Science and Engineering Discovery Environment (XSEDE), supported by NSF grant ACI-1548562, and CyVerse, supported by NSF grants DBI-0735191, DBI-1265383, and DBI-1743442. XSEDE Stampede2 resource at TACC was allocated through TG-AST170024 and TG-AST080026N. XSEDE JetStream resource at PTI and TACC was allocated through AST170028. The simulations were performed in part on the SuperMUC cluster at the LRZ in Garching, on the LOEWE cluster in CSC in Frankfurt, and on the HazelHen cluster at the HLRS in Stuttgart. This research was enabled in part by support provided by Compute Ontario (http://computeontario.ca), Calcul Quebec (http://www.calculquebec.ca) and Compute Canada (http://www.computecanada.ca). We thank the staff at the participating observatories, correlation centers, and institutions for their enthusiastic support. This Letter makes use of the following ALMA data: JAO.ALMA#2016.1.01154.V. ALMA is a partnership of the European Southern Observatory (ESO; Europe, representing its member states), NSF, and National Institutes of Natural Sciences of Japan, together with National Research Council (Canada), Ministry of Science and Technology (MOST; Taiwan), Academia Sinica Institute of Astronomy and Astrophysics (ASIAA; Taiwan), and Korea Astronomy and Space Science Institute (KASI; Republic of Korea), in cooperation with the Republic of Chile. The Joint ALMA Observatory is operated by ESO, Associated Universities, Inc. (AUI)/NRAO, and the National Astronomical Observatory of Japan (NAOJ). The NRAO is a facility of the NSF operated under cooperative agreement by AUI. APEX is a collaboration between the Max-Planck-Institut für Radioastronomie (Germany), ESO, and the Onsala Space Observatory (Sweden). The SMA is a joint project between the SAO and ASIAA and is funded by the Smithsonian Institution and the Academia Sinica. The JCMT is operated by the East Asian Observatory on behalf of the NAOJ, ASIAA, and KASI, as well as the Ministry of Finance of China, Chinese Academy of Sciences, and the National Key R&D Program (No. 2017YFA0402700) of China. Additional funding support

for the JCMT is provided by the Science and Technologies Facility Council (UK) and participating universities in the UK and Canada. The LMT project is a joint effort of the Instituto Nacional de Astrófisica, Óptica, y Electrónica (Mexico) and the University of Massachusetts at Amherst (USA). The IRAM 30-m telescope on Pico Veleta, Spain is operated by IRAM and supported by CNRS (Centre National de la Recherche Scientifique, France), MPG (Max-Planck-Gesellschaft, Germany) and IGN (Instituto Geográfico Nacional, Spain). The SMT is operated by the Arizona Radio Observatory, a part of the Steward Observatory of the University of Arizona, with financial support of operations from the State of Arizona and financial support for instrumentation development from the NSF. Partial SPT support is provided by the NSF Physics Frontier Center award (PHY-0114422) to the Kavli Institute of Cosmological Physics at the University of Chicago (USA), the Kavli Foundation, and the GBMF (GBMF-947). The SPT hydrogen maser was provided on loan from the GLT, courtesy of ASIAA. The SPT is supported by the National Science Foundation through grant PLR-1248097. Partial support is also provided by the NSF Physics Frontier Center grant PHY-1125897 to the Kavli Institute of Cosmological Physics at the University of Chicago, the Kavli Foundation and the Gordon and Betty Moore Foundation grant GBMF 947. The EHTC has received generous donations of FPGA chips from Xilinx Inc., under the Xilinx University Program. The EHTC has benefited from technology shared under open-source license by the Collaboration for Astronomy Signal Processing and Electronics Research (CASPER). The EHT project is grateful to T4Science and Microsemi for their assistance with Hydrogen Masers. This research has made use of NASA's Astrophysics Data System. We gratefully acknowledge the support provided by the extended staff of the ALMA, both from the inception of the ALMA Phasing Project through the observational campaigns of 2017 and 2018. We would like to thank A. Deller and W. Brisken for EHT-specific support with the use of DiFX. We acknowledge the significance that Maunakea, where the SMA and JCMT EHT stations are located, has for the indigenous Hawaiian people.

Facility: EHT.

Software: THEMIS, `dynesty`, `eht-imaging`, `DIFMAP`, `SMILI`, `GENA`.

Appendix A
THEMIS Station Gain Amplitude Reconstruction

Both THEMIS and `eht-imaging` provide tools for analyzing EHT data within the visibility domain. Both address the reconstruction of individual station gains, though in substantially different ways. Here, we briefly describe the procedure employed by THEMIS and compare the reconstructed gains with the results reported in Paper IV.

We reconstruct gains on a scan-by-scan basis. Thus, for EHT 2017 data, the gain amplitudes constitute between 40 and 143 additional nuisance parameters per data set; more if sub-scan variations are necessary. For the GC models this represents a proliferation of parameters by 200%–700%.

Even with efficient sampling techniques, treating these identically with the other model parameters would result in a substantial (super-linear) increase in the computation expense needed to adequately sample the likelihood. Thus, in THEMIS, these are efficiently addressed instead by directly marginalizing the likelihood in Equation (9).

This is done by numerically maximizing $\mathcal{L}_{A,ij}$ over the $|g_i|$ (subject to Gaussian priors on the $|g_i|$) for each scan and then marginalizing over an expansion around this maximum (see A. E. Broderick et al. 2019, in preparation, for more details). Within this procedure it is assumed that gains from neighboring scans are independent. For all analyses presented here, the standard deviation of these priors for the LMT and all other stations are 100% and 20%, respectively. While the latter substantially exceeds the anticipated uncertainty stated in Table 3 of Paper III, the reconstructed station gains are typically very well constrained and close to unity.

Typically, the station gains on a given scan are significantly overdetermined. Thus, calibrating the station gains in this way produces model-independent patterns, driven primarily by the need for consistency among a given observation.

In Figure 22 we show the reconstructed LMT gains for the best-fit GC model model on each day (low-band only) in comparison to those obtained by image-domain methods for the LMT. This station was selected because it exhibits large gain excursions; the other reconstructed station gains are generally much closer to unity.

The two different procedures based on different intrinsic source models find remarkable agreement over all days. Importantly, there are no large gain offsets that would produce a significant impact on the reconstruction of the total compact flux.

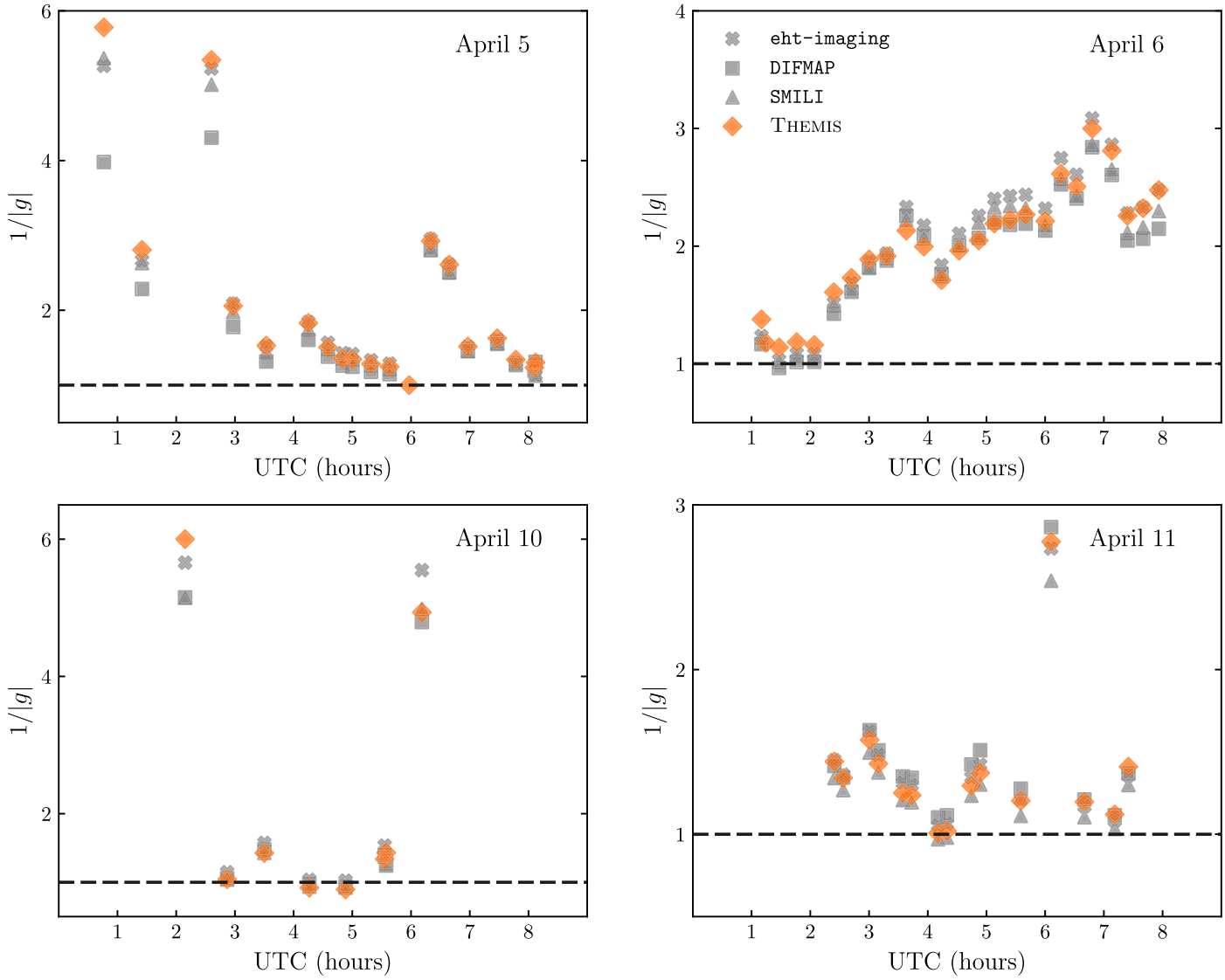

Figure 22. Reconstructed LMT station gains by THEMIS from GC model fits to the April 5, 6, 10, and 11 low-band data sets. All other station gains are very close to unity, and are consistent with those from image reconstruction. The inferred LMT gains are consistent with those found in Paper IV across all days.

Appendix B
Generalized Crescent Models

In this appendix we describe the GC models used in Section 5 to fit the M87 data. Descriptions of the model parameters and their associated priors are listed in Table 8.

B.1. Fourier-domain Construction of the GC models

Following Kamruddin & Dexter (2013), we start with a unit circular "top-hat" function circ(r), defined in the image domain to be

$$\mathrm{circ}(r) = \begin{cases} 1, & r \leqslant 1 \\ 0, & r > 1. \end{cases} \tag{33}$$

A disk of radius R can then be expressed as $\mathrm{D(r)} = \mathrm{circ}(r/R)$. The Fourier transform of such a disk is given by

$$\tilde{\mathrm{D}}(\rho) = \frac{\mathrm{R}}{\rho}\mathrm{J}_1(2\pi\rho R), \tag{34}$$

where $\rho = \sqrt{u^2 + v^2}$ is the Fourier-domain radial coordinate and $J_1(x)$ is the Bessel function of the first kind of order 1. We can construct a circular crescent C via the difference of two such disks after shifting the smaller, inner disk by r_0 in the negative x-direction prior to subtracting it from the outer disk. A spatial shift in the image domain corresponds to a frequency shift in the Fourier domain, such that

$$\begin{aligned}\tilde{\mathrm{C}}(u, v) &= \tilde{\mathrm{D}}_{\mathrm{out}} - e^{2\pi i r_0 u}\tilde{\mathrm{D}}_{\mathrm{in}} \\ &= \frac{R_{\mathrm{out}}}{\rho}J_1(2\pi\rho R_{\mathrm{out}}) - e^{2\pi i r_0 u}\frac{R_{\mathrm{in}}}{\rho}J_1(2\pi\rho R_{\mathrm{in}}),\end{aligned} \tag{35}$$

where R_{out} and R_{in} are the outer and inner disk radii, respectively.

Similar to Benkevitch et al. (2016), we define a "slash" operation s(x) that imposes a linear brightness gradient across the image. The slash operator can be expressed in the image

Table 8
Parameters and Priors for the GC Models

Parameter	Description	Prior: xs-ringauss	Prior: xs-ring	Units
V_0	Flux density of crescent component	⋯	$\mathscr{U}(0, 2)$	Jy
$V_0 + V_1$	Flux density of crescent component (including fixed Gaussian)	$\mathscr{U}(0, 2)$	⋯	Jy
$R_{\rm out}$	Outer radius of crescent	$\mathscr{U}(0, 100)$		μas
ϕ	PA	$\mathscr{U}(0, 360)$		degrees
ψ	Fractional thickness	$\mathscr{U}(0, 1)$		unitless
τ	Structural asymmetry parameter	$\mathscr{U}(0, 1)$		unitless
β	Flux asymmetry parameter	$\mathscr{U}(0, 1)$	$\mathscr{L}_e(-5, 5)$	unitless
σ	Width of Gaussian smoothing kernel	$\mathscr{U}(0, 100)$		μas
γ	Fractional amplitude of central emission floor	⋯	$\mathscr{U}(0, 1)$	unitless
V_F	Flux density of central Gaussian emission floor	$\mathscr{U}(0, 2)$	⋯	Jy
σ_F	Width of central Gaussian emission floor	$\mathscr{U}(0, 25)$	⋯	μas
V_G	Flux density of large-scale Gaussian	$\mathscr{U}(0, 10)$		Jy
σ_G	Width of large-scale Gaussian	$\mathscr{L}_{10}(-2, 1)$		arcsec
V_1/V_0	Ratio of fixed Gaussian flux density to crescent flux density	$\mathscr{U}(0, 1)$	⋯	unitless
$\sigma_x/R_{\rm out}$	Ratio of fixed Gaussian width to outer radius of crescent	$\mathscr{U}(0, 3)$	⋯	unitless
σ_y/σ_x	Axis ratio of fixed Gaussian	$\mathscr{U}(0, 100)$	⋯	unitless
V_g	Flux density of additional Gaussian component	$\mathscr{U}(0, 2)$		Jy
x_0	Central x-coordinate of additional Gaussian component	$\mathscr{U}(-200, 200)$	⋯	μas
y_0	Central y-coordinate of additional Gaussian component	$\mathscr{U}(-200, 200)$	⋯	μas
σ	Width of additional Gaussian component	$\mathscr{U}(0, 100)$	⋯	μas
A	Anisotropy of additional Gaussian component	$\mathscr{U}(0, 0.99)$	⋯	unitless
θ	PA of additional Gaussian component	$\mathscr{U}(0, 180)$	$\mathscr{U}(0, 90)$	degrees
$x_{0,0}$	Central x-coordinate of first additional Gaussian component	⋯	$\mathscr{U}(-100, 100)$	μas
Δx	Change in x-coordinates of adjacent Gaussian components	⋯	$\mathscr{U}(0, 100)$	μas
$y_{0,0}$	Central y-coordinate of first additional Gaussian component	⋯	$\mathscr{U}(-100, 100)$	μas
Δy	Change in y-coordinates of adjacent Gaussian components	⋯	$\mathscr{U}(-100, 100)$	μas
σ_x	Major axis width of additional Gaussian component	⋯	$\mathscr{U}(0, 100)$	μas
σ_y	Minor axis width of additional Gaussian component	⋯	$\mathscr{U}(0, 100)$	μas

Note. The top section of the table corresponds to crescent component parameters, and the bottom section corresponds to additional Gaussian component parameters (see Appendix B.2). $\mathscr{U}(a, b)$ denotes a uniform distribution spanning the range $[a, b]$, $\mathscr{L}_x(a, b)$ denotes a log-uniform distribution in base x spanning the range $[x^a, x^b]$.

domain as

$$s(x) = \frac{h_1 + h_2}{2} + \left(\frac{h_1 - h_2}{2R_{\rm out}}\right)x, \tag{36}$$

where h_1 and h_2 are the amplitudes of the function at $x = R_{\rm out}$ and $x = -R_{\rm out}$, respectively. We apply s(x) to the crescent via multiplication in the image domain, which corresponds to taking a derivative in the Fourier domain

$$\tilde{\rm s}(u) = \frac{h_1 + h_2}{2} + \frac{i}{2\pi}\left(\frac{h_1 - h_2}{2R_{\rm out}}\right)\frac{d}{du}. \tag{37}$$

Application of the slash is aided by the fact that the derivative of a Bessel function can be expressed in terms of other Bessel functions

$$\frac{d}{d\rho}J_1(2\pi\rho R) = \pi R[J_0(2\pi\rho R) - J_2(2\pi\rho R)], \tag{38}$$

and we denote the slashed crescent model as sC.

B.1.1. xs-ring Model

We now seek to add an emission "floor," F, to the center of sC to account for nonzero central emission. In the xs-ring construction, F takes the form of a circular disk with amplitude K and radius $R_{\rm in}$ that is shifted by r_0 along the x-axis,

$$\tilde{\rm F}(u, v) = \frac{KR_{\rm in}}{\rho}e^{2\pi i r_0 u}J_1(2\pi\rho R_{\rm in}). \tag{39}$$

In the image domain, we can express the slashed crescent plus emission floor [sC+F] as

$$[{\rm sC} + {\rm F}](x, y) = s(x)[D_{\rm out}(x, y) - D_{\rm in}(x - r_0, y)] + {\rm F}(x - r_0, y). \tag{40}$$

The model thus corresponds to the difference of two spatially offset circular disks having a linear brightness gradient across them, to which a central emission floor is then added. We then further allow the entire model to be rotated by some PA ϕ, which amounts to replacing $u \to u\cos(\phi) + v\sin(\phi)$ and $v \to -u\sin(\phi) + v\cos(\phi)$. Finally, we convolve the model in the image domain with a circular Gaussian kernel of width σ and then scale it to have a total flux density of V_0. The compact component of the xs-ring model can thus be written in the

Fourier domain as

$$\widetilde{\text{xs-ring}}(u, v) = \frac{V_0 e^{-2\pi^2\sigma^2\rho^2}\{\tilde{D}_{\text{out}} - e^{2\pi i\psi R(1-\tau)[u\cos(\phi)+v\sin(\phi)]}(\tilde{D}_{\text{in}} - \tilde{\text{F}})\}}{\frac{1}{2}\pi R_{\text{out}}^2\{(1+\beta) - (1-\psi)^2[(1+\beta) - \psi(1-\tau)(1-\beta) - 2\gamma\beta]\}}, \tag{41}$$

where

$$\tilde{\text{D}}_{\text{out}} = \frac{R_{\text{out}}(1+\beta)}{2\rho}J_1(X_{\text{out}}) - \frac{i(1-\beta)}{4\pi\rho^2} \times \left\{\pi R_{\text{out}}[J_0(X_{\text{out}}) - J_2(X_{\text{out}})] - \frac{1}{\rho}J_1(X_{\text{out}})\right\} \times [u\cos(\phi) + v\sin(\phi)], \tag{42}$$

$$\tilde{\text{D}}_{\text{in}} = \frac{R_{\text{out}}(1-\psi)}{2\rho}J_1(X_{\text{in}})[(1+\beta) + \psi(1-\tau)(1-\beta)] - \frac{i(1-\psi)(1-\beta)}{4\pi\rho^2} \times \left\{\pi R_{\text{out}}(1-\psi)[J_0(X_{\text{in}}) - J_2(X_{\text{in}})] - \frac{1}{\rho}J_1(X_{\text{in}})\right\} \times [u\cos(\phi) + v\sin(\phi)], \tag{43}$$

$$\tilde{\text{F}} = \frac{\gamma\beta R_{\text{out}}(1-\psi)}{\rho}J_1(X_{\text{in}}), \tag{44}$$

and we have followed Kamruddin & Dexter (2013) in defining the quantities

$$\begin{aligned}
\psi &\equiv 1 - \frac{R_{\text{in}}}{R_{\text{out}}}\\
\tau &\equiv 1 - \frac{r_0}{\psi R_{\text{out}}}\\
\gamma &\equiv \frac{K}{h_1}\\
\beta &\equiv \frac{h_1}{h_2}\\
h &\equiv h_2\\
V_0 &= \frac{1}{2}\pi h R_{\text{out}}^2\{(1+\beta) - (1-\psi)^2[(1+\beta) - \psi(1-\tau)(1-\beta) - 2\gamma\beta]\}\\
X_{\text{out}} &\equiv 2\pi\rho R_{\text{out}}\\
X_{\text{in}} &\equiv X_{\text{out}}(1-\psi).
\end{aligned}$$

The xs-ring model has eight free parameters describing the compact emission: V_0, R_{out}, ϕ, σ, ψ, τ, γ, and β. The ψ, τ, and γ parameters are restricted to lie between 0 and 1. The ψ parameter describes the typical fractional thickness of the crescent; as $\psi \to 1$ the crescent reduces to a filled disk, and as $\psi \to 0$ the crescent reduces to an infinitesimally thin ring (i.e., delta function in radius). The τ parameter is a measure of the crescent's structural symmetry; as $\tau \to 1$ the crescent reduces to a circular ring, and $\tau \to 0$ when the inner and outer disks meet at one edge. The γ parameter describes the amplitude of the emission floor, with $\gamma = 0$ indicating no central emission. The β parameter describes the strength of the emission gradient across the crescent, with $\beta = 1$ indicating no gradient.

In addition to the compact component, we add a large-scale circular Gaussian, G, to the model

$$\tilde{\text{G}}(\rho) = V_G e^{-2\pi^2\sigma_G^2\rho^2}. \tag{45}$$

This component is permitted to have very large widths, $\sigma_G \gg 1$ arcsec, to account for short-spacing flux that might be missed by the bulk of the array. The free parameters in G are its flux density (V_G) and width (σ_G), bringing the total number of parameters for the xs-ring model to 10. An example of the xs-ring model is shown in the left panel of Figure 3.

B.1.2. xs-ringauss Model

The xs-ringauss model differs from the xs-ring model in two key respects. The first difference is that the xs-ringauss model follows Benkevitch et al. (2016) and includes a fixed elliptical Gaussian component on top of the crescent. This component is centered at $(x, y) = (r_0 - R_{\text{in}}, 0)$ prior to applying the PA rotation, and its orientation is fixed to match that of the crescent. The additional free parameters provided by this Gaussian component are thus its widths (σ_x, σ_y) and flux density V_1. The second difference is that the emission floor F in the xs-ringauss model takes the form of a circular Gaussian rather than a disk,

$$\tilde{\text{F}}(\rho) = V_F e^{-2\pi^2\sigma_F^2\rho^2} = 2\pi\sigma_F^2 K e^{-2\pi^2\sigma_F^2\rho^2}. \tag{46}$$

In addition to the amplitude parameter K, this form of the emission floor has a width parameter σ_F that also enters into the model.

The remaining parameters in the xs-ringauss model match those in the xs-ring model, for a total of 14 free parameters: 10 of these parameters are shared with the xs-ring model, and the additional four are V_1, σ_x, σ_y, and σ_g. An example of the xs-ringauss model is shown in the right panel of Figure 3.

B.2. Nuisance Gaussian Components

In addition to the crescent components of the GC models, we also fit a small number (two to three) of additional "nuisance" Gaussian components (see Section 5.1). These additional components are intended primarily to capture extraneous amorphous emission surrounding the main ring (see, e.g., Figure 12) and secondarily to provide additional flexible degrees of freedom that allow the model to absorb systematic uncertainties.

B.2.1. Parameterization

We parameterize the Gaussian components in one of two ways. The first of these, used when fitting the xs-ring model, is given by

$$\tilde{G}_1(u, v) = V_{g,1} e^{2\pi i(ux_0 + vy_0)} e^{-4\pi^2\sigma_x^2\sigma_y^2(cu^2 - buv + av^2)}, \tag{47}$$

where

$$a = \frac{\cos^2(\theta)}{2\sigma_x^2} + \frac{\sin^2(\theta)}{2\sigma_y^2}, \tag{48}$$

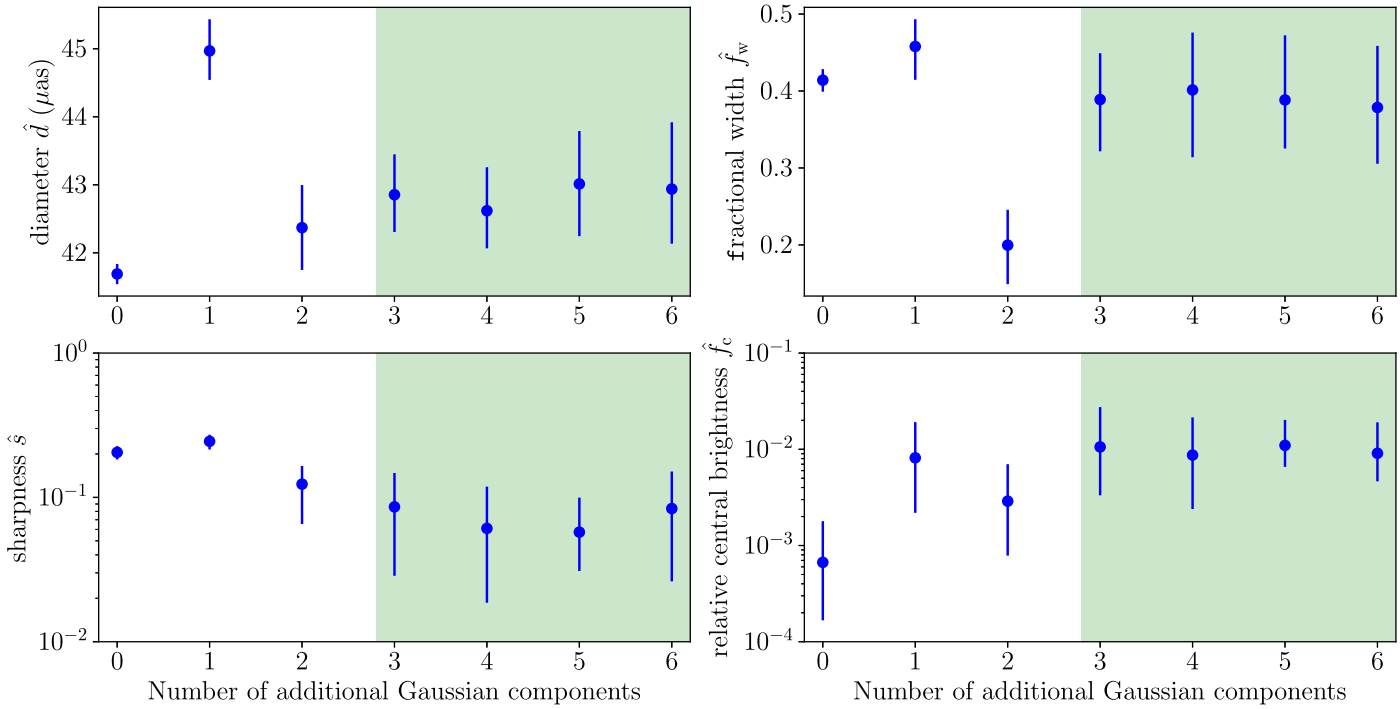

Figure 23. Measured crescent parameter values from fitting the xs-ring model with an increasing number of nuisance Gaussian components, shown for the April 5 high-band data set. We see that after a small number of components is reached (three for this data set, marked in green), adding additional components does not substantially modify the parameter posteriors.

$$b = \frac{\sin(2\theta)}{2\sigma_x^2} - \frac{\sin(2\theta)}{2\sigma_y^2}, \tag{49}$$

and

$$c = \frac{\sin^2(\theta)}{2\sigma_x^2} + \frac{\cos^2(\theta)}{2\sigma_y^2}. \tag{50}$$

Here, $V_{g,1}$ is the total flux density of the Gaussian, (x_0, y_0) are its central coordinates, (σ_x, σ_y) are the Gaussian widths along the two principal axes, and θ is the PA. A circular Gaussian model is constructed by setting $\sigma_x = \sigma_y$ and $\theta = 0$.

When fitting multiple Gaussian components in the context of the xs-ring model, we only parameterize the first component, as described above, with a central coordinate position of $(x_{0,0}, y_{0,0})$. All additional components have positions that are referenced to that of the previous component, such that $(x_i, y_i) = (x_{i-1} + \Delta x_i, y_{i-1} + \Delta y_i)$. Such a parameterization enables the imposition of a spatial ordering by treating the Δx or Δy parameters as slack variables, thereby breaking the multimodal labeling degeneracy otherwise caused by pairwise swaps of different Gaussian components.

The second Gaussian parameterization, used by the xs-ringauss model, follows the form described in Broderick et al. (2011). Specifically,

$$\tilde{G}_2(u, v) = V_{g,2} e^{2\pi i(ux_0 + vy_0)} e^{-\frac{\rho^2}{2\sigma^2}[1 - A\cos(\psi - \theta)]}, \tag{51}$$

where (ρ, ψ) are cylindrical polar coordinates in the (u, v)-plane. Here,

$$\sigma = \left(\frac{1}{\sigma_x^2} + \frac{1}{\sigma_y^2}\right)^{-1/2} \tag{52}$$

is a width parameter and

$$A = \frac{\sigma^2}{2}\left(\frac{1}{\sigma_x^2} - \frac{1}{\sigma_y^2}\right) \tag{53}$$

is an anisotropy parameter. For small numbers ($\lesssim 5$) of Gaussian components, tempering is sufficient to ensure that the MCMC exploration can navigate all posterior modes; because the xs-ringauss model never utilizes more than two additional Gaussian components, no mode collapsing is necessary.

B.2.2. Behavior in Fits to the M87 Data

In principle, it is possible to add a large number of nuisance Gaussian components to a model and thereby to fit the data arbitrarily well. However, our primary goal with model fitting is not to exactly reproduce all details of the emission structure, but rather to make robust measurements of the crescent component model parameters relevant for constraining the lensed part of the image. Once a sufficient number of Gaussian components have been added to the model, further additions do not substantially modify the derived crescent parameters (see Figure 23). We find that two nuisance Gaussians for the xs-ringauss GC model (for a total of 26 free parameters), and three for the xs-ring GC model (for a total of 28 free parameters), are the threshold values that most generally satisfy this criterion. These values are thus used for all GC model fits presented in this Letter.

When fit alongside the GC models to the M87 data, we find that the nuisance Gaussian components account for ∼10%–70% of the compact flux density. Assessing consistency in the best-fit parameter values for the nuisance Gaussian components across models is complicated by the differing model

specifications. In general we find less consistency in the properties of nuisance Gaussian components for a given day across models (within a single data set) than we do across bands (within a single model).

Within the context of a particular GC model, we find that the nuisance Gaussian components approximately fall into two categories: (1) components that reside near or on the crescent component and whose location and structure are consistent across bands within a single day, and (2) components that tend to reside far ($\gtrsim 40\,\mu$as) outside the crescent component and whose location and structure may vary across bands and days. We associate the first class of nuisance Gaussian components with attempts by the model to account for a real flux distribution that is too complex for the crescent component alone. The second class of nuisance Gaussians acts in a similar manner to the artifacts frequently seen in image reconstructions (see Paper IV). We thus associate this second class of components with the image-domain manifestation of systematic errors in the data products. We emphasize, however, that we have no mechanism for enforcing a categorization such as that described on the nuisance Gaussian components, and in general we expect that any single component will be influenced both by real source emission and by systematic uncertainties.

Appendix C
χ^2 Statistics

In this appendix we define the various χ^2 statistics used as diagnostics of model fit quality in Section 5. We note that the expressions presented here do not have any bearing on the fitting process itself; the likelihood functions used during fitting are described in Section 4.1.

The visibility amplitude reduced-χ^2 is given by

$$\chi^2_A = \frac{1}{N_A - N_\mathrm{p} - N_g}\sum\left(\frac{\hat{A} - A}{\sigma}\right)^2, \tag{54}$$

where N_A is the number of visibility amplitudes (see Table 1), N_p is the number of GC model parameters, N_g is the number of independent gain terms, σ is the uncertainty in visibility amplitude, and $\hat{A}$ and A are the modeled and measured visibility amplitudes, respectively. For the xs-ring GC model fits using `dynesty` we have $N_\mathrm{p} = 28$ model parameters, while for the xs-ringauss GC model fits using THEMIS we have $N_\mathrm{p} = 26$.

Analogous to Equation (54), the closure phase reduced-χ^2 is

$$\chi^2_{\psi_\mathrm{C}} = \frac{1}{N_{\psi_\mathrm{C}} - N_\mathrm{p}}\sum\left(\frac{\hat{\psi}_\mathrm{C} - \psi_\mathrm{C}}{\sigma_{\psi_\mathrm{C}}}\right)^2, \tag{55}$$

where N_{ψ_C} is the number of closure phases, σ_{ψ_C} is the closure phase uncertainty, and $\hat{\psi}_\mathrm{C}$ and ψ_C are the modeled and measured closure phases, respectively. As in Section 4.1, we avoid phase wrapping by selecting a branch of the closure phase space such that differences always fall between $-180°$ and $180°$.

For the logarithmic closure amplitude reduced-χ^2, we have

$$\chi^2_{\ln A_\mathrm{C}} = \frac{1}{N_{\ln A_\mathrm{C}} - N_\mathrm{p}}\sum\left(\frac{\ln\hat{A}_\mathrm{C} - \ln A_\mathrm{C}}{\sigma_{\ln A_\mathrm{C}}}\right)^2. \tag{56}$$

where $N_{\ln A_\mathrm{C}}$ is the number of logarithmic closure amplitudes, $\sigma_{\ln A_\mathrm{C}}$ is the logarithmic closure amplitude uncertainty, and $\ln\hat{A}_\mathrm{C}$ and $\ln A_\mathrm{C}$ are the modeled and measured logarithmic closure amplitudes, respectively.

For the THEMIS fits, we report the joint visibility amplitude and closure phase reduced-χ^2

$$\chi^2_{A+\psi_\mathrm{C}} = \frac{1}{N_A + N_{\psi_\mathrm{C}} - N_\mathrm{p} - N_g} \times\left[\sum\left(\frac{\hat{A} - A}{\sigma}\right)^2 + \sum\left(\frac{\hat{\psi}_\mathrm{C} - \psi_\mathrm{C}}{\sigma_{\psi_\mathrm{C}}}\right)^2\right]. \tag{57}$$

For the `dynesty` fits we have the joint closure phase and logarithmic closure amplitude reduced-χ^2

$$\chi^2_{\psi_\mathrm{C}+\ln A_\mathrm{C}} = \frac{1}{N_{\psi_\mathrm{C}} + N_{\ln A_\mathrm{C}} - N_\mathrm{p}} \times\left[\sum\left(\frac{\hat{\psi}_\mathrm{C} - \psi_\mathrm{C}}{\sigma_{\psi_\mathrm{C}}}\right)^2 + \sum\left(\frac{\ln\hat{A}_\mathrm{C} - \ln A_\mathrm{C}}{\sigma_{\ln A_\mathrm{C}}}\right)^2\right]. \tag{58}$$

The values for each of these statistics are reported in Table 2 for both fitting codes and for all data sets.

Appendix D
Using GRMHD Simulations to Calibrate the Generalized Crescent Model

To create a mapping between the GC model diameter and the angular gravitational radius θ_g, we require data sets for which we know both quantities. To this end, we take the GRMHD simulation library described in Paper V to provide our "ground truth" images. These simulations are necessarily limited in the range and resolution of physical parameter space that they probe, but they critically provide a large sample of plausible emission structures for which we know the underlying physical parameters. By treating these GRMHD simulations as "ground truth" images, generating synthetic data from them, and then fitting that data with the GC models, we aim to (1) determine a calibration of the measured crescent diameter $\hat{d}$ in terms of θ_g, and (2) estimate the magnitude of the uncertainty in this calibration.

D.1. GRMHD Image Selection and Synthetic Data Generation

For a given GRMHD simulation, individual "snapshots" are ray-traced to produce images of the 230 GHz emission as it would be seen from Earth. These images are then used as input for generating synthetic observational data with `eht-imaging`, which generates visibilities corresponding to the (u, v)-coverage from the 2017 EHT observations of M87 and corrupts this data with realistic levels of thermal noise and station-based systematics. A detailed description of the synthetic data generation pipeline is provided in Paper IV.

From the GRMHD simulation library we selected 103 separate snapshot images with which to generate synthetic data sets. These images were selected randomly from within the parameter space explored by the library, and thus included examples of emission structures that were incompatible with the M87 data. The images were split into two groups, from

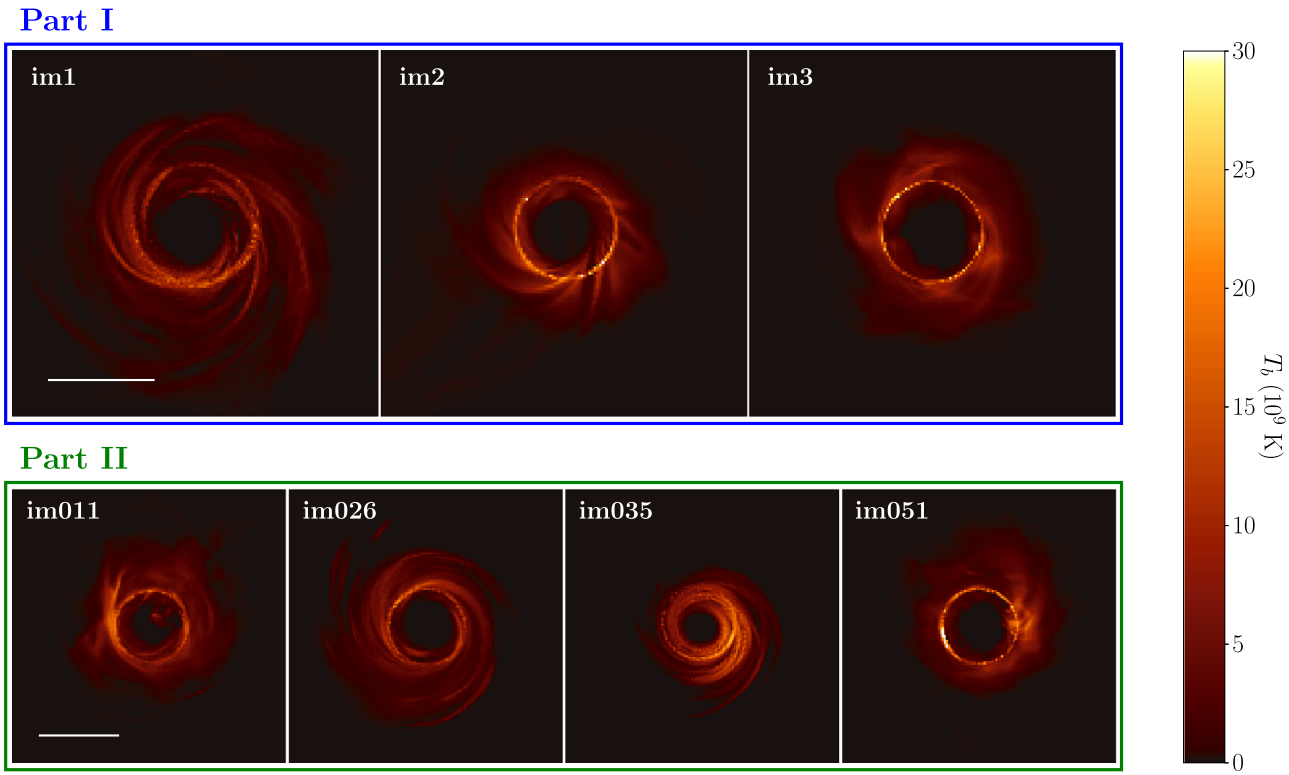

Figure 24. Examples of GRMHD snapshots used for calibration (see Appendix D). The top three panels show the images used to calibrate the "observational uncertainty" associated with changing (u, v)-sampling and systematics across days (Part I). The bottom four panels show example images taken from the pool of 100 that were used to calibrate the "theoretical uncertainty" caused by different physical parameters and turbulence realizations in the GRMHD simulations (Part II). 40 μas scale bars are shown in white.

which were generated two sets of synthetic data targeting different aspects of the calibration.

The first group of synthetic data sets, Part I, was created using only three simulated GRMHD images (shown in the top three panels of Figure 24). From each of these images 10 synthetic data sets were generated, corresponding to 10 different realizations of the observational noise (i.e., thermal noise and known systematics such as station gain fluctuations and polarization leakage) spanning the full range of (u, v)-coverage in the 2017 EHT M87 data and containing independent instances of thermal and systematic errors. The goal of the Part I data sets is to assess the impact of such observational corruptions on the recovered model parameters, which enters into the error budget for the calibration.

The second group of synthetic data sets, Part II, contains the remaining 100 GRMHD images (samples are shown in the bottom four panels of Figure 24). Only a single synthetic data set was generated for each of these images, using a randomly selected realization of the (u, v)-coverage from among the four days of 2017 M87 observations. The goal of the Part II data sets is to provide a sample of images for which we know both the underlying values of θ_g and the best-fit values of the diameter $\hat{d}$ from the GC model fits.

D.2. θ_g Calibration

We know the input value of the angular gravitational radius θ_g for each simulation in Parts I and II of the GRMHD calibration data set. The basic calibration task is then to fit each of the corresponding synthetic data sets with a GC model and determine the scaling factor α (see Equation (27)) relating the best-fit crescent diameter to θ_g for the underlying simulation. The value of this scaling factor is equal to the diameter measured in units of θ_g, which Figure 25 shows plotted for all simulations in the calibration data set. We obtain an estimate of the scaling factor from each individual fit in Parts I and II, and we use the mean of these fits as our final determination of α; the uncertainty in this mean value is roughly an order of magnitude smaller than any of the calibration uncertainties we consider below, and we thus neglect it in our error budget. Table 4 lists the calibrated α values, which we determine separately for THEMIS and `dynesty`.

We can see in Figure 25 that each set of 10 synthetic data sets corresponding to a single simulation from Part I shows excellent agreement across all measured d values. Comparing these to the measurements from Part II demonstrates that the inter-simulation scatter is substantially larger than the inter-observation scatter, and that the former will be the limiting factor in measuring θ_g from the M87 data.

D.3. Uncertainty Budgeting for All Parameters

In general, the error budget for any single measurement of θ_g will have three contributions: (1) a "statistical uncertainty" associated with the width of the posterior, (2) an "observational uncertainty" associated with incomplete (u, v)-coverage and unmodeled systematics that change from one observation to the next, and (3) a "theoretical uncertainty" associated with the data being a single sample from a dynamic system whose specific physical properties we are largely ignorant of. For other measured parameters that lack a counterpart input to the GRMHD simulations, we only consider the first two uncertainty components.

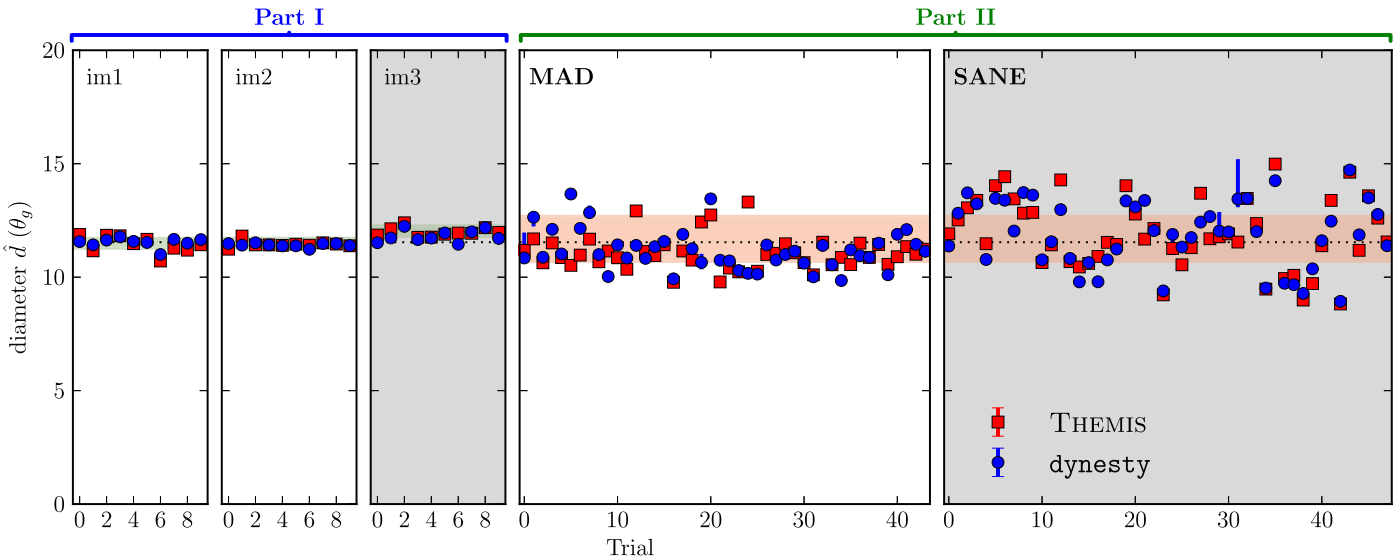

Figure 25. Reconstructed diameters using the GC models from synthetic data generated from GRMHD simulations. Green bands show the one-sided 68-percentile ranges within the Part I reconstructions (left). The red bands show the one-sided 68-percentile range of the combined Part I and II reconstructions (right). These are separated by GRMHD simulation type: MAD models are collected in white panels, while SANE models are collected in gray panels. The dotted lines indicate the MAD+SANE calibration factor, α for the xs-ringauss model (see Table 4).

To quantify the magnitude of these different uncertainty components, we employ a generalized lambda distribution (GλD). The GλD is an extension of the Tukey λ distribution (Tukey 1962) that provides a compact parameterization for representing a diverse family of probability densities. The GλD is also flexible and convenient, permitting highly asymmetric and heavy-tailed distributions to be analytically represented in terms of a function that depends only on their quantiles. We use the FMKL parameterization (Freimer et al. 1988), defined in terms of the inverse cumulative distribution function (CDF), which can be expressed using four parameters (λ_1, λ_2, λ_3, λ_4) as

$$Q_{\rm FMKL}(q) = \lambda_1 + \frac{1}{\lambda_2}\left[\frac{q^{\lambda_3}-1}{\lambda_3} - \frac{(1-q)^{\lambda_4}-1}{\lambda_4}\right], \quad (59)$$

where q is the quantile of the distribution. The fits were performed using the GLDEX package in R (Su 2007a, 2007b).

The GλD fits to all three components of the error budget are shown in Figure 26 for the θ_g measurements from each of the two fitting codes. We find that the theoretical uncertainty is dominant, being larger by a factor of $\sim$4–5 than either the statistical or observational components. However, the magnitude of this theoretical uncertainty depends strongly on the category of simulation being used for calibration. We find that SANE simulations show nearly a factor of $\sim$2 larger theoretical uncertainty than MAD simulations; the increased SANE scatter is visually apparent in Figure 25, and the effective decrease in calibration uncertainty that would result from using only MAD simulations is listed in Table 4. However, because such a preference for MAD over SANE is not well motivated from a theoretical standpoint (Paper V), we use the calibration factor determined from MAD+SANE for the measurements presented in this Letter.

The output of a MCMC or NS fitting run is a "chain" of samples from the posterior distribution. We determined the statistical uncertainty component for each parameter by fitting a single GλD to the ensemble of chains from all 130 Part I and II data sets simultaneously. Each chain was first mean-subtracted

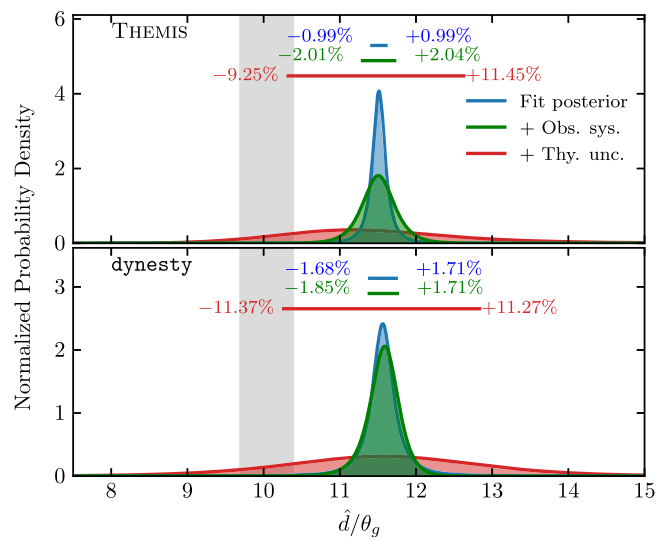

Figure 26. Sources and magnitudes of random and systematic uncertainty on the measurement of θ_g with GC models. These include the average posterior (blue), the impact of different realizations of unmodeled observational systematic errors (e.g., polarization leakage, (u, v)-coverage, etc.; green), and the impact of variations in the assumed underlying GRMHD simulation (red). (The latter two match the appropriately colored ranges shown in Figure 25.) These are similar for analyses that employ the xs-ringauss-based (THEMIS; top) and xs-ring-based (`dynesty`; bottom) GC models. The gray band shows the range of photon ring diameters for a Kerr black hole from spin 0 to 0.998 over all viewing inclination angles.

so that the GλD characterizes only the shape of the typical posterior distribution for a single GC model fit, rather than capturing variation in mean value between different fits.

The observational uncertainty component was determined using Part I data sets only. For each of the three simulations in Part I, we combined the 10 chains corresponding to the individual realizations of observational uncertainty for that simulation. We then subtracted out the mean of each combined chain before further combining all three chains and fitting a GλD to the resulting stack. This fitted distribution then

describes the typical variation in individual parameter measurements that we expect to see across multiple observations of the same underlying emission structure. The derived observational uncertainties are listed in Table 3 for each parameter.

The theoretical uncertainty component was determined using synthetic data sets from Parts I and II, and applies only to θ_g. We first made a fit-quality cut on the Part II data sets, removing all that had a measured diameter of $\hat{d} > 15\theta_g$; these outlying fits were deemed poor upon inspection, as they had arrived at large-diameter solutions by fitting the crescent portion of the model to extraneous emission while the Gaussian components were trying to form the ring. We found eight such fits out of 100. The chains for the remaining 92 data sets from Part II and three data sets from Part I (one randomly selected for each image) were then combined without performing any mean subtraction, and a GλD was fit to the entire set.

Note that this is by far the largest component of the calibration uncertainty. That is, the emission distribution can vary significantly in position and structure. This is reflected both in its net shift away from the photon ring size ($\alpha \simeq 11.5$ instead of $\simeq$10) and in its scatter between model images.

Appendix E
Using GRMHD Simulations to Calibrate Image Domain Feature Extraction

To create a mapping between image domain feature extraction methods and θ_g, we follow an analogous method to that described in Appendix D. For the same simulated data sets used in Appendix D, we generate reconstructed images using the RML methods as implemented in `eht-imaging` and `SMILI` and the CLEAN algorithm as implemented in `DIFMAP` (Paper IV). The images are generated with the fiducial hyper-parameters determined from the M87 Top Set. The spread in diameters from varying the hyper-parameters can be significant (Figure 15). Still, in the final error budget this term is significantly smaller than the full calibration error measured here (Table 6).

The reconstructed images frequently exhibit the dominant ring structures found in the underlying GRMHD model images. Occasionally, however, significant non-ring features are present, e.g., a single compact component or multiple rings. We discard images with such pathologies. For `DIFMAP`, `eht-imaging`, and `SMILI`, this leaves all 30 images from Part I, and 70, 86, and 96 of the 100 images from Part II. The acceptance rates for `eht-imaging` and `SMILI` are similar to those found for the geometric crescent models (92/100). The large number of rejected `DIFMAP` frames could lead to a bias in either the resulting calibration factor α or to an underestimate of the theoretical uncertainty component in the error bar on θ_g from this method.

The image domain feature extraction method described in Section 7 and Paper IV is then used to estimate the ring diameters of the Part I and Part II images. We find a qualitative similarity between the diameter measurements from the image reconstructions and those obtained in Figure 25: the Part II images exhibit substantially more scatter than the Part I images, and within Part II the SANE models are less tightly constrained than MAD.

We generate an error budget for the image domain diameter measurements in a fashion similar to that employed in Appendix D. The primary difference between the two budgets arises from the lack of posterior distributions reported using the image reconstructions. We estimate the combined statistical and observational systematic uncertainty components from the comparisons in Part I. The analysis of Part II retains the same meaning as in Appendix D, providing a measurement of the observational uncertainties (statistical and systematic) combined with the theoretical contribution to the systematic uncertainty associated with variations in the underlying intrinsic image structure. Both sets of uncertainties appear in Table 6.

Appendix F
Average Image Scoring

Assessing the consistency of a given GRMHD model with the EHT observations is complicated by stochastic features in the image, associated with turbulence in the underlying accretion flow. As a result of these, no single snapshot image from a simulation is expected to provide a high-quality fit directly to the EHT observations when only observational errors are included. However, the self-consistency of a model may be directly assessed by numerically constructing the anticipated distribution of χ^2 values using the ensemble of snapshot images from a GRMHD model.

Note that this procedure is identical in principle to that typically employed for assessing fit quality in the presence of Gaussian errors: the construction of a χ^2 and its comparison to the standard χ^2 distribution. In the case of interest here, the stochastic image fluctuations may be thought of as an additional noise term that is specified by the model. Apart from the need to numerically construct the appropriate χ^2 distribution, its interpretation is very similar to the normal procedure.

The AIS method formalizes this process and makes use of key efficiencies permitted by the small observational errors in comparison to the stochastic fluctuations. In order to both formulate a concrete method and ensure computational feasibility, the THEMIS-AIS method employs a SSM based on the arithmetic average image from the simulation. Therefore, the procedure for each GRMHD model and observation day is as follows.

1. Generate an SSM based on the average snapshot image.
2. Numerically construct a CDF of reduced χ^2 values by fitting this SSM to simulated data generated from each snapshot image associated with the GRMHD model of interest for the particular observation day of interest.
3. Finally, fit this SSM to the data, obtain the associated reduced χ^2 by fitting to the corresponding EHT observations, and assess in light of the previously constructed CDF.

The second step is the most onerous, requiring the generation of many additional simulated data sets. However, the dominance of the stochastic image features over the observational noise simplifies this process considerably. The CDF constructed from fitting the average image to the frames is similar to the CDF constructed from fitting the frames to the average image. This has been verified explicitly, and the resulting CDFs constructed both ways are indistinguishable. For each GRMHD model and observation day this procedure must be repeated, resulting in a family of more than 1200 CDFs generated by the THEMIS-AIS procedure.

The final step, interpreting the fit to the observations, is quantified by the two-sided quantile of the fit reduced χ^2:

$$p_{\rm AIS}(\mathcal{M}|\boldsymbol{D}) \approx \frac{N_{>|\chi^2-\chi^2_{\rm med}|}}{N}, \tag{60}$$

where N and $N_{>|\chi^2-\chi^2_{\rm med}|}$ are the number of frames for a given simulation, $\mathcal{M}$, and the number of those with a reduced χ^2 further from the median, $\chi^2_{\rm med}$ than that observed in the data. Note that this may be directly related to the likelihood of $\mathcal{M}$ via

$$\begin{aligned} P(\mathcal{M}|\boldsymbol{D}) &= \int d\chi^2 \frac{dp_{\rm AIS}}{d\chi^2} P(\chi^2|\boldsymbol{D}, \mathcal{M}) \\ &\approx p_{\rm AIS}(\mathcal{M}|\boldsymbol{D}) \end{aligned} \tag{61}$$

where $P(\chi^2|\boldsymbol{D}, \mathcal{M})$ is the distribution of fit reduced χ^2 and we have assumed that the distribution of χ^2 is broad and extends beyond the tails of the intrinsic χ^2 distribution in the relevant direction.

A qualitative illustration of this interpretation that uses only three closure phases as a proxy for the total reduced χ^2 is shown in Figure 27 for three GRMHD models that show the three potential outcomes. The direct comparisons to the full CDFs for each of these models are shown in Figure 28. For the first (top row), the typical deviation between the closure phases of the average image (red diamond) and those from the individual snapshot images (blue points) are similar to the deviation between the former and the EHT data (green triangle); this model has a $p_{\rm AIS}$ near unity.

In the second (middle row), the EHT data are further from the average image than the typical snapshot image; this model has a $p_{\rm AIS} < 0.01$. This is a model for which no snapshots are likely to be an adequate description of the data, regardless of computational limits. In the third (bottom row), the EHT data are *closer* to the average image than is typical; again the $p_{\rm AIS} = 0.01$, and this model is excluded. In this case it is likely that a snapshot could be found, given a sufficiently large number of images from this GRMHD model, that fits the EHT observations well. However, the fact that the reduced χ^2 is much less than that expected implies that the "noise" model, the distribution of stochastic image fluctuations, is wrong. That is, this GRMHD model is too variable. This is akin to finding a reduced χ^2 much less than unity in the standard fitting process.

Finally, note that the "true" model is necessarily accepted by the THEMIS-AIS procedure. That is, were a GRMHD simulation to produce the true image on the sky, the probability for it to be assigned a score of $p_{\rm AIS}$ is identically $p_{\rm AIS}$. Given a choice of the minimum acceptable $p_{\rm AIS}$, the probability of excluding the true model is then exactly that value (e.g., here 1%).

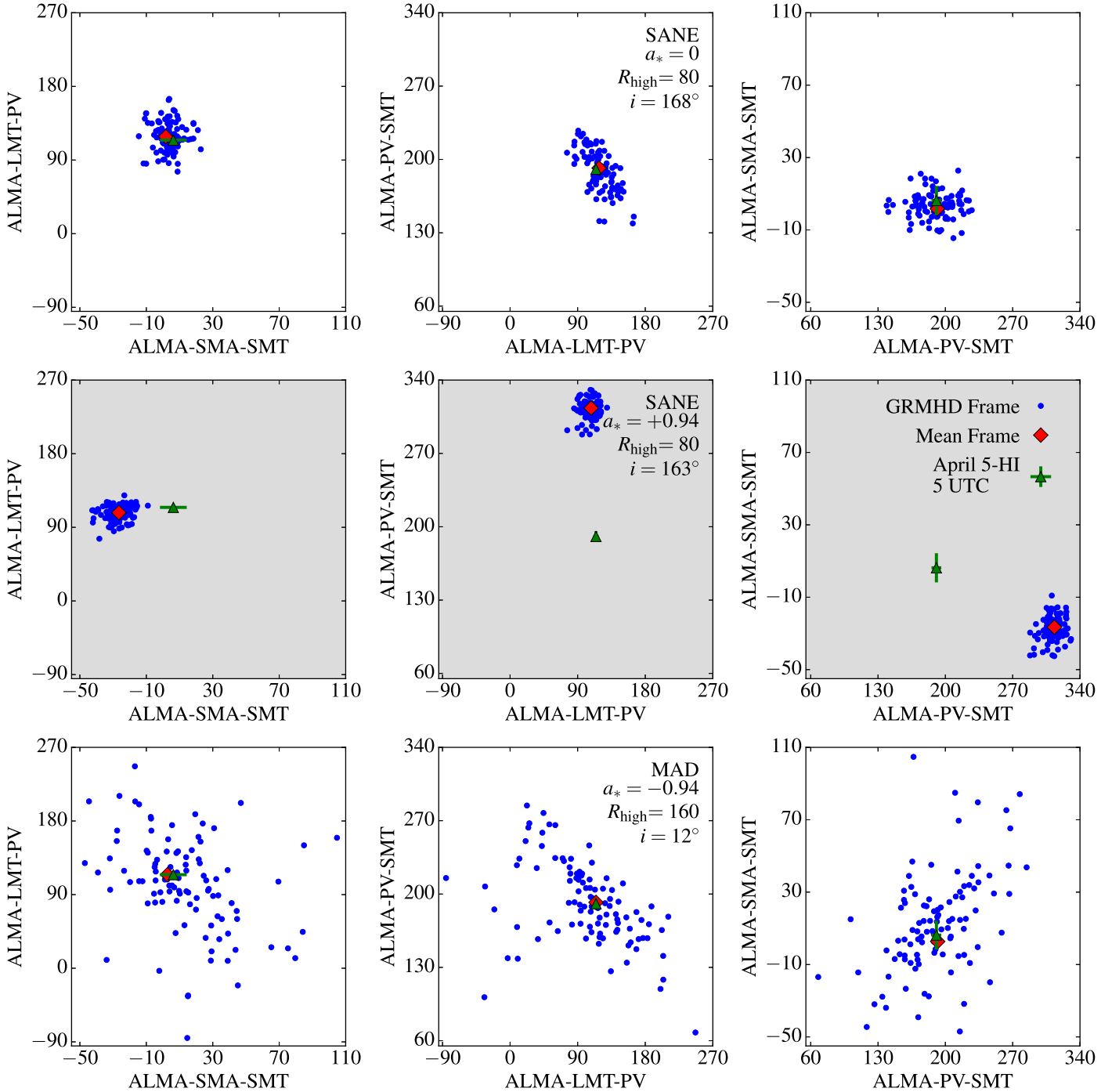

Figure 27. Illustration of "good" (top panels) and two "bad" (middle and bottom panels) models following the THEMIS-AIS procedure. Closure phases are shown for three triangles at 5 UTC for April 5 as proxies for the χ^2. Blue dots indicate the closure phases for the best-fit SSM associated with each simulation snapshot image. The red diamond shows the same for the average snapshot image. The green triangle shows the observed values on April 5, high-band, near 5 UTC. The manner in which the two models shown in the middle and bottom rows are excluded differs: in the middle case the reduced χ^2 is too large, while in the bottom case the χ^2 is too small to be consistent with that anticipated by the individual GRMHD model snapshots.

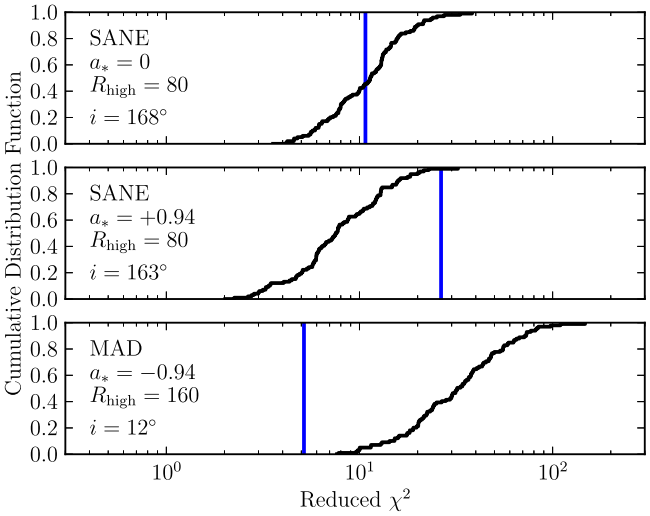

Figure 28. Anticipated cumulative distribution function of reduced χ^2 for the SSM for the same three representative models shown in Figure 27 for the April 5 high-band data. For comparison, the measured reduced χ^2 is indicated by the vertical blue line for each model.

Appendix G
GRMHD Model Parameter Estimation

The presence of a significant stochastic component in the snapshot images from GRMHD models complicates the interpretation of posterior distributions of the SSM parameters. This is exacerbated by the very incomplete coverage of the turbulent realizations by the simulation snapshots (relative to the observational noise) in a way similar to that found during model selection (Appendix F). Here we explicitly describe how we address this.

G.1. Ensemble-based Posterior Construction

The GRMHD models effectively comprise an ensemble of snapshot images, which simultaneously identify a "typical" image and the statistical distribution of the stochastic features within the image. In principle, this stochasticity can be addressed by introducing hyper-parameters associated with this additional image structure, subject to priors obtained from the statistics of the fluctuations within the snapshot ensemble, and subsequently marginalizing over them. In practice, we approximate this procedure by instead fitting and marginalizing over each snapshot image independently. Thus, we formally define the joint model-parameter posterior distributions for the SSM model, following Bayes' theorem, by

$$P(\boldsymbol{\Theta}, \mathcal{M}|\boldsymbol{D}) = \sum_{\mathcal{I}} \frac{P(\boldsymbol{D}|\boldsymbol{\Theta}, \mathcal{I}) P(\mathcal{I}|\mathcal{M}) \pi(\boldsymbol{\Theta}) \pi(\mathcal{M})}{P(\boldsymbol{D})}, \quad (62)$$

where $P(\boldsymbol{D}|\boldsymbol{\Theta}, \mathcal{I})$ is formally the likelihood, $\mathcal{I}$ refers to a particular snapshot image from $\mathcal{M}$ obtained with probability $P(\mathcal{I}|\mathcal{M})$, and $\pi(\boldsymbol{\Theta})$ and $\pi(\mathcal{M})$ are the priors on parameters $\boldsymbol{\Theta}$ and the model $\mathcal{M}$, respectively. We now discuss each of these terms separately.

The prior on a given model is obtained from the THEMIS-AIS procedure combined with theoretical priors based on X-ray luminosity, jet power, and radiative efficiency (see Table 2 of Paper V). Because the probability of finding a snapshot image within the ensemble generated for a particular GRMHD model that fits the EHT observations well when only observational errors are considered is small, we do not make significant distinctions between values of $p_{\rm AIS}(\mathcal{M}|\boldsymbol{D})$ above some threshold, $p_{\rm AIS,0}$ (see Appendix F). Thus, we set

$$\pi(\mathcal{M}) \approx \Theta[p_{\rm AIS}(\mathcal{M}|\boldsymbol{D}) - p_{\rm AIS,0}], \quad (63)$$

where $\Theta(x)$ is the Heaviside function. The priors on the SSM parameters, $\pi(\boldsymbol{\Theta})$, are described in Section 6.3.

The interpretation of the likelihood, $P(\boldsymbol{D}|\boldsymbol{\Theta}, \mathcal{I})$, is again complicated by the substantial stochastic image components. In the presence of only data-based uncertainties, this likelihood is formally no different from that described in Section 4.1. In practice, we find that the spread in "best-fit" $\boldsymbol{\Theta}_{p;\mathcal{I}}$ across different snapshots within a single GRMHD model is much larger than the distribution of the likelihood function for each individual snapshot (see Figure 29).

The value of $P(\boldsymbol{D}|\boldsymbol{\Theta}_{p;\mathcal{I}}, \mathcal{I})$ is misleading due to the sparse sampling of the stochastic image components within the snapshot ensembles. That is, for models deemed acceptable by the AIS procedure, even large reduced χ^2 (defined relative to the observational noise estimates) may be "high quality" in that they are well within the range anticipated by the stochastic variability. For the best of these, the expectation is that a realization of the turbulence close to that in the relevant snapshot image would constitute a "good" fit in the normal sense, i.e., a reduced χ^2 of unity; that such a fit was not found is a consequence only of the necessarily sparse nature of the snapshot image ensemble. Therefore, these "high-quality" fits are indicative of parameters for which a realization of the stochastic component could adequately explain the EHT observations.

We address this in two steps. First, by specifying "high quality" within a particular model by ranking the fits relative to the likelihood (THEMIS) or χ^2 (GENA) and placing a cut at some fractional level, e.g., for the THEMIS pipeline cutting on

$$q_{\mathcal{I},\mathcal{M}} = \frac{N_{>P(\boldsymbol{D}|\boldsymbol{\Theta},\mathcal{I})}}{N_{\mathcal{M}}}. \quad (64)$$

Fits with $q_{\mathcal{I},\mathcal{M}}$ above some cutoff q_0 are assumed to be sufficiently close to a formally acceptable fit in that a nearby realization of the stochastic image features could be found. Second, by making use of the comparatively narrow nature for the high-quality SSM posteriors

$$P(\boldsymbol{D}|\boldsymbol{\Theta}, \mathcal{I}) \approx \delta^3(\boldsymbol{\Theta} - \boldsymbol{\Theta}_{p;\mathcal{I}}) \Theta(q_{\mathcal{I},\mathcal{M}} - q_0). \quad (65)$$

Combining these, the estimated posteriors on the SSM parameters after marginalizing over all models and images is then

$$\begin{aligned} P(\boldsymbol{\Theta}|\boldsymbol{D}) &= \sum_{\mathcal{M}} P(\boldsymbol{\Theta}, \mathcal{M}|\boldsymbol{D}) \\ &= \frac{1}{P(\boldsymbol{D})} \sum_{\mathcal{M},\mathcal{I}} \delta^3(\boldsymbol{\Theta} - \boldsymbol{\Theta}_{p;\mathcal{I}}) \Theta(q_{\mathcal{I},\mathcal{M}} - q_0) \Theta \\ &\quad \times [p_{\rm AIS}(\mathcal{M}|\boldsymbol{D}) - p_{\rm AIS,0}] \pi(\boldsymbol{\Theta}). \end{aligned} \quad (66)$$

Key meta-parameters in this estimate are the quality cuts on models, $p_{\rm AIS,0}$, and on snapshot images within a model, q_0. In the following, we note that the posteriors are only weak functions of $p_{\rm AIS,0}$, and are converged for $q_0 < 0.5$, i.e., accepting snapshots with fit qualities above the median.

This procedure, while credible, does require a number of assumptions about the utility of what are ultimately low

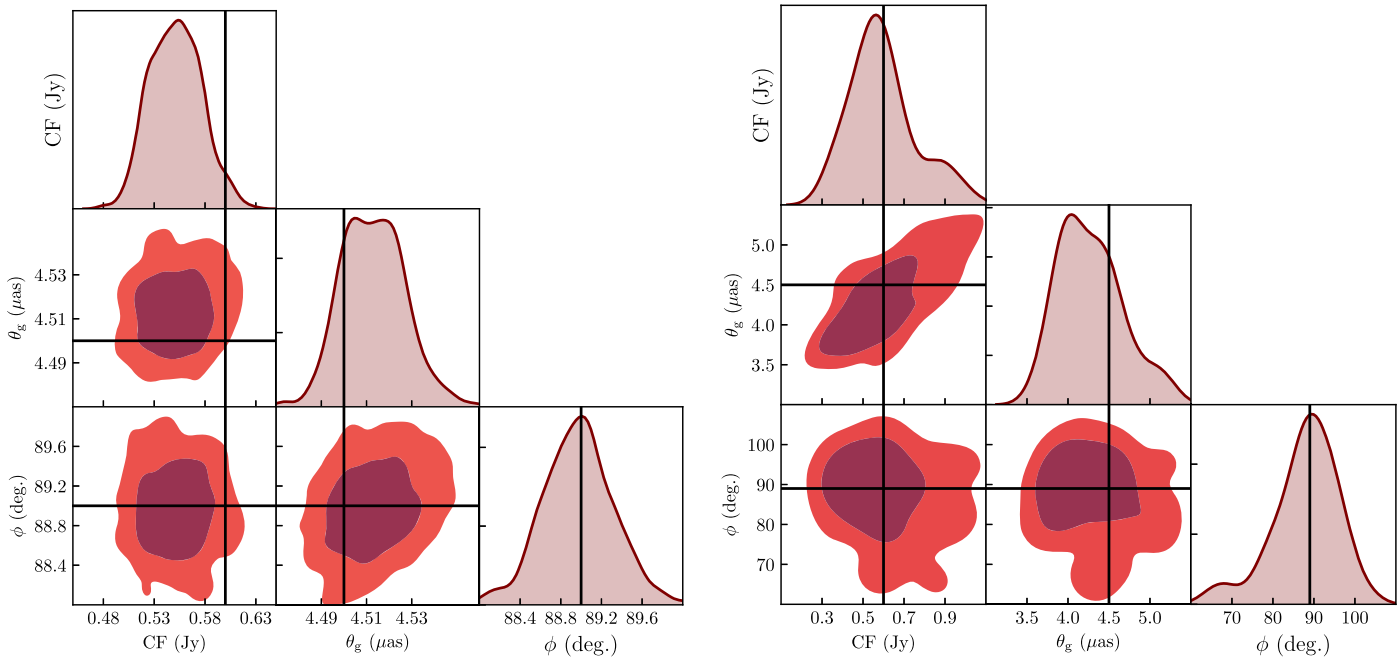

Figure 29. Example joint posterior plots for the SSM parameters from one of the many mock analyses performed as part of the ensemble-based posterior estimation validation. Shown are the distributions for compact flux density, θ_g, and PA from SSM analyses of simulated data sets using individual frame snapshots. Left panel: the posteriors from fitting *only* the frame from which the data was generated. Right panel: the stacked posteriors of snapshots with a likelihood larger than the median for the GRMHD simulation from which the simulated data was generated (i.e., $q < 0.5$). Note that the ranges on the right are much larger than those on the left. The underlying model was a SANE-type accretion flow with $a_* = 0.94$, $i = 163°$, $R_{\rm high} = 80$, and mass rescaled such that $\theta_g = 4.5$ μas. The data was generated for the April 5 (u, v)-coverage. Contours enclose 68% and 95% of the posterior.

likelihood fits when only observational noise is considered. While practically these comport with the expectation from the underlying GRMHD simulations (see Section 6.4), it may result in intrinsic biases. Therefore, we now turn to validating the method with mock analyses.

G.2. Validation with Mock Analyses

The first set of validation tests involves the construction of mock data from a GRMHD snapshot and subsequent analysis. In the creation of the mock data, the (u,v)-coverage from M87 observations was employed and realistic realizations of all known systematic errors were included (e.g., polarization leakage and gain fluctuations). In some cases, these tests have been repeated hundreds of times. See Appendix D.1 and Paper IV for descriptions of synthetic data generation.

Analyses using an SSM based on the snapshot from which the mock data was generated demonstrate the ability to reconstruct the SSM parameters, i.e., reconstruct $P(\boldsymbol{D}|\boldsymbol{\Theta}, \mathcal{I})$. An example, taken from the calibration data sets employed in Appendix D, is shown in the left panel of Figure 29. This analysis has been performed for all 130 of the sets described in Appendix D, and for more than 1200 additional data sets as part of the THEMIS-AIS scoring procedure and internal validation. Generally, we find that the input SSM parameters are recovered within the very narrow posterior distributions.

Ensemble-based posterior reconstruction was performed for all 130 simulated data sets described in Appendix D and the more than 1200 sets constructed as part of the THEMIS-AIS procedure using the "truth" model, i.e., for the GRMHD model from which a snapshot was selected from which to generate the data. This directly tests the ability to reconstruct $P(\boldsymbol{\Theta}|\boldsymbol{D})$ for a *single* GRMHD model, i.e., Equation (66). An example is shown in the right panel of Figure 29 for the same example data set shown in the left panel. As expected, the true parameters lie within the ensemble-based posterior distribution. Small net biases, defined by the difference of mean parameter value and the "truth" in units of the posterior width (measured by standard deviation, σ), have been identified: less than 0.3σ in the compact flux, less than 0.07σ in θ_g, and less than 0.02σ in $\mathrm{PA_{FJ}}$.

For two mock data sets, the ensemble-based posterior estimate, $P(\boldsymbol{\Theta}|\boldsymbol{D})$ in Equation (66), was reconstructed for the full GRMHD model library *without* model selection, i.e., $p_{\rm AIS,0} = 0$. Again, as expected, the true parameters lie within the ensemble-based posterior distribution.

G.3. Convergence Tests

There are a number of what might be deemed convergence tests, i.e., comparisons of the ensemble-based posteriors constructed in various ways that differ in the mechanics but not the underlying physical inputs.

Were the posteriors sensitive to outliers, we may have anticipated them to change with total number of snapshots used. A subset of GRMHD models had 500 snapshots generated from them, in comparison to the 100 snapshots that was standard. These do not show materially different ensemble-based posteriors when a subsample of 100 snapshots are used and when the full 500 snapshots are used.

The ensemble-based posteriors are typically generated from only a subset of the SSM analyses associated with a given GRMHD model, determined by a fit quality cut. This is characterized in terms of a likelihood or χ^2 percentile, with the expectation that particular bad fits are likely dominated by the peculiarities of the realization of the stochastic components. The ensemble-based posteriors cease to evolve after reducing the percentile cut below 50%; i.e., once the likelihoods (χ^2)

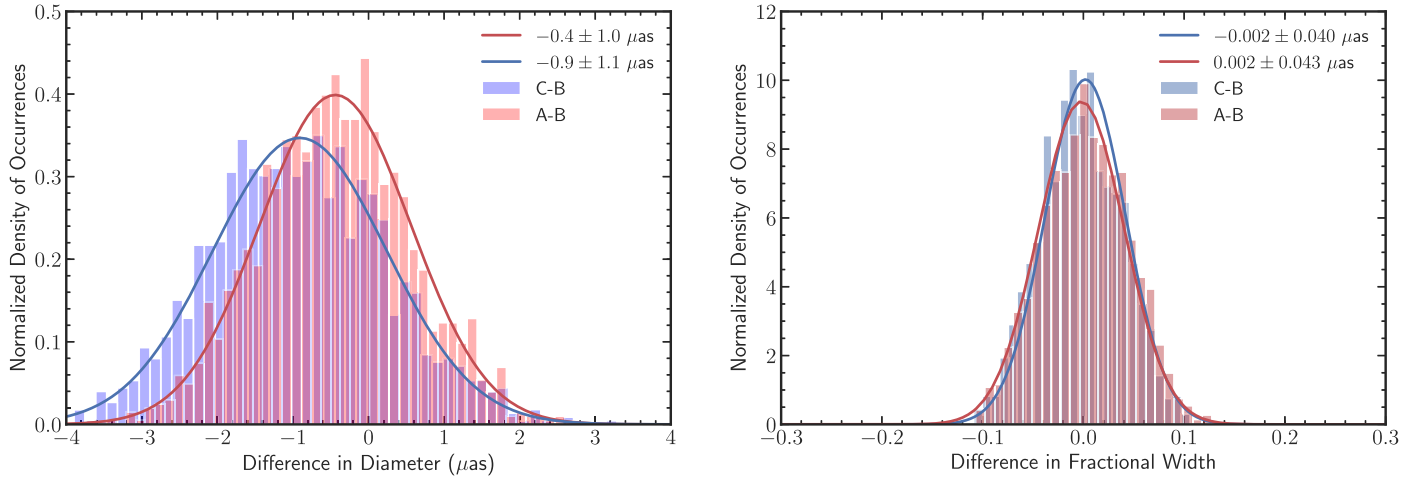

Figure 30. Differences in the measured (left panel) diameters and (right panel) fractional widths of the Top Set images reconstructed with `eht-imaging` using the April 5 M87 data when applying three different variants (A, B, and C; see the text for details) of the method for measuring these parameters. In both panels, the solid lines show Gaussian distributions with means and standard deviations equal to those of the histograms. The typical differences between the parameters measured with the three variants are smaller than the pixel size.

that are included are above (below) the median value. This suggests that these are not contaminated by particularly poor fits.

A subset of GRMHD models have been run with different GRMHD simulation codes and resolutions (and imaging resolutions); i.e., for the same black hole and initial accretion flow parameters, multiple GRMHD simulations have been performed. Individual SSM analyses do depend modestly on the GRMHD simulation resolution and the resolution of the snapshot image, though this is far smaller than the typical size of the ensemble-based posterior. Comparisons of the ensemble-based posteriors for identical simulation setups among GRMHD codes indicate that they are very consistent, implying that the number of frames is sufficient to adequately cover the posterior.

Appendix H
Image Domain Feature Extraction Method Tests

In order to explore and quantify the sensitivity of our measurement of the image parameters to the presence of noise in the images, the effect of pixelization, and the presence of outliers in the pixel brightness distribution, we performed a number of validation tests. We used the images reconstructed with `eht-imaging` data on April 5 and analyzed them using two different algorithmic implementations and three variants of the methods described above. Case A refers to the above definitions. Case B refers to using the same definitions but after having smoothed with a 2 μas Gaussian (Paper IV Section 9 uses this method to find the ring center before measuring the width and diameter from the unblurred image). Case C uses unsmoothed images but locates the centers by minimizing the difference between the 25th and the 75th percentile distances to the peak brightness over all azimuthal angles. It then calculates the image diameter using the median of the peak brightness distances from the center over all azimuthal angles. Case B tests the sensitivity of the measured parameters against the presence of noise in the image reconstruction. Case C tests against biases that might be introduced by outliers in the azimuthal cross sections.

Figure 30 shows the fractional differences in the measured diameters and fractional widths inferred using these three different variants. The differences in diameter between the three cases have means of 0.4–0.9 μas and comparable standard deviations, whereas the differences in fractional width have a mean of zero and a standard deviation of 0.04. These differences are smaller than the differences in the feature parameters inferred from the same data using different visibility- and image-domain techniques. In Section 7, we use Case B.

Appendix I
Prior Measurements of the Distance to M87 and the Dynamical Mass of Its Central Black Hole

I.1. Prior Distance Measurements

We provide the details of the methods and the uncertainties included in each distance measurement here.

TRGB method. The TRGB method leads to a direct distance measurement by utilizing the bright-end distributions of the red giant stars as a primary standard candle. Bird et al. (2010) reported the absolute distance modulus of $\mu = 31.12 \pm 0.14$, using data sets of the *HST* Advanced Camera Survey (ACS) Virgo Cluster Survey (VCS) that resolved the brightest red giant stars in M87 for the first time.

SBF method. The SBF method also utilizes red giant stars. It is often categorized as a secondary standard-candle method because it relies for its calibration on nearby galaxies for which distances are independently measured with resolved-star methods. Therefore, SBF measurements in Virgo Cluster surveys provide *relative* distances of Virgo galaxies to the calibrated mean distance of the entire Virgo Cluster. To date, there are two distinct measurements that fall into this category. The first one by Blakeslee et al. (2009) uses the *HST* ACS-VCS data and finds $\mu = 31.11 \pm 0.08$ (denoted hereafter as $\mu_{\rm SBF1}$; see also Mei et al. 2007). A second, more recent study by Cantiello et al. (2018a) reported $\mu = 31.15 \pm 0.04$ (denoted hereafter as $\mu_{\rm SBF2}$) based on data from the Next Generation Virgo Cluster Survey (NGVCS), obtained using ground-based adaptive-optics with the Canada French Hawaii Telescope.

There are a couple of other sources of systematic errors in SBF measurements. The first one is a systematic error of 0.1 mag on the distance zero-point (Cantiello et al. 2018b),

Table 9
Relevant Literature and Derived Quantities

Method	Measurement Type	Units	Value	References
TRGB	D	Mpc	$16.75^{+1.11}_{-1.04}$	Bird et al. (2010)
SBF	D	Mpc	$16.67^{+1.02}_{-0.96}$	Blakeslee et al. (2009)
SBF	D	Mpc	$16.98^{+0.96}_{-0.91}$	Cantiello et al. (2018a)
Gas dynamics	$\theta_{\rm dyn}$	μas	$2.05^{+0.48}_{-0.16}$	Walsh et al. (2013)
Stellar dynamics	$\theta_{\rm dyn}$	μas	$3.62^{+0.60}_{-0.34}$	Gebhardt et al. (2011)
Product of two SBF measurements	D	Mpc	$16.82^{+1.02}_{-0.86}$	This work
Product of three measurements	D	Mpc	$16.76^{+0.75}_{-0.66}$	This work
Gas dynamics	M	$10^9\,M_\odot$	$3.45^{+0.85}_{-0.26}$	Walsh et al. (2013); this work
Stellar dynamics	M	$10^9\,M_\odot$	$6.14^{+1.07}_{-0.62}$	Gebhardt et al. (2011); this work

Note. We report median values and 68% confidence intervals.

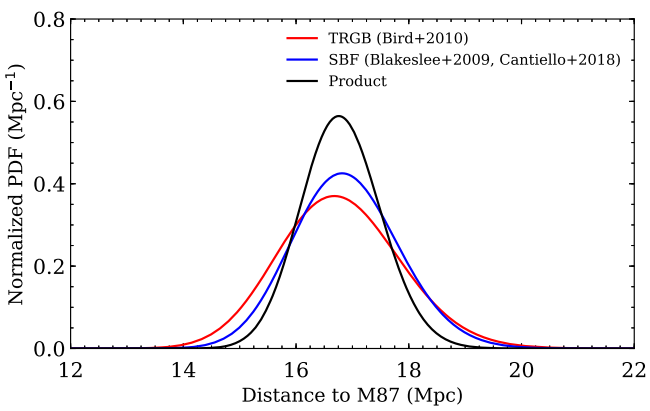

Figure 31. Normalized posteriors for the distance measurements to M87. Two colored lines show the posterior from the measurements using the TRGB method (Bird et al. 2010) and combined posterior from the SBF method (Blakeslee et al. 2009; Cantiello et al. 2018a). The black line shows the normalized product of three posteriors obtained by combining these measurements.

which was not accounted for in either of the two measurements. A second one, considered in Blakeslee et al. (2009) but not in Cantiello et al. (2018a), arise from the intrinsic scatter in the absolute fluctuation magnitude attributed to stellar populations (cosmic scatter; Tonry et al. 2000) and is estimated to be 0.06 mag (Blakeslee et al. 2009). Adding these in quadrature to the formal errors quoted above, we obtain for the absolute distant moduli $\mu_{\rm SBF1} = 31.11 \pm 0.13$ (Blakeslee et al. 2009) and $\mu_{\rm SBF2} = 31.15 \pm 0.12$ (Cantiello et al. 2018a). Finally, we average the two measurements weighted by their errors to get $\mu = 31.14 \pm 0.12$. We report these measurements in Table 9, together with the combined posterior as their product in Figure 31.

Assuming Gaussian posteriors $P(\mu)$ for the distance modulus measurements with the means and standard deviations given in Table 9, we calculate the posteriors for the distance $P(D)$ to M87 using the relation $\mu = 5\log_{10}(D) - 5$ as

$$P(D) = \frac{5}{\log 10}\frac{P(\mu)}{D}. \tag{67}$$

Finally, considering the three distance measurements to be independent, we calculate the combined posterior as their product. We show the posteriors in Figure 31 and quote their most likely values and uncertainties in Table 9.

I.2. Mass Determination

Both the stellar dynamical and the gas dynamical mass measurement techniques that we described in Section 8.2 measure, in reality, a mass-to-distance ratio rather than the mass of the central object directly. To convert these into posteriors over a mass, we first convert the measurements into posteriors over the mass-to-distance ratio $\mathcal{R}$ and then rescale them based on the posterior over distance that we described in the previous section.

We use the marginal χ^2 distributions for mass $M_{\rm BH}$ shown in Figure 6 of Gebhardt et al. (2011) and Figure 6 of Walsh et al. (2013) and set $M_{\rm BH} = \mathcal{R} \times (17.9\ {\rm Mpc})$. We denote the posteriors for the stellar and gas dynamical measurements as $P(\mathcal{R}_{\rm stars})$ and $P(\mathcal{R}_{\rm gas})$, respectively, and write

$$P(\mathcal{R}_i) \equiv \frac{\exp[-\chi^2(\mathcal{R}_i \times 17.9\ {\rm Mpc})/2]}{\int \exp[-\chi^2(\mathcal{R}_i \times 17.9\ {\rm Mpc})/2]\, d\mathcal{R}_i} \tag{68}$$

for each model (i = gas, stars). Table 9 summarizes the credible regions of these distributions.

We can also convert the mass-to-distance ratio from dynamical measurements directly to an angular size of one gravitational radius at the distance of M87, $\theta_{\rm dyn} \equiv G\mathcal{R}/c^2$. This posterior is given by

$$P(\theta_{\rm dyn}) = \frac{c^2}{G}P(\mathcal{R}). \tag{69}$$

We list the credible intervals for this quantity in Table 9.

We can now use the posterior over the mass-to-distance ratio and that over distance to calculate the posterior over the mass for the stellar and gas dynamics measurements as

$$P(M_i) = \int \frac{1}{D}P(D)P(\mathcal{R}_i)dD, \tag{70}$$

where $\mathcal{R}_i = M_i/D$.

ORCID iDs

Kazunori Akiyama https://orcid.org/0000-0002-9475-4254
Antxon Alberdi https://orcid.org/0000-0002-9371-1033
Rebecca Azulay https://orcid.org/0000-0002-2200-5393
Anne-Kathrin Baczko https://orcid.org/0000-0003-3090-3975

Mislav Baloković https://orcid.org/0000-0003-0476-6647
John Barrett https://orcid.org/0000-0002-9290-0764
Lindy Blackburn https://orcid.org/0000-0002-9030-642X
Katherine L. Bouman https://orcid.org/0000-0003-0077-4367
Geoffrey C. Bower https://orcid.org/0000-0003-4056-9982
Christiaan D. Brinkerink https://orcid.org/0000-0002-2322-0749
Roger Brissenden https://orcid.org/0000-0002-2556-0894
Silke Britzen https://orcid.org/0000-0001-9240-6734
Avery E. Broderick https://orcid.org/0000-0002-3351-760X
Do-Young Byun https://orcid.org/0000-0003-1157-4109
Andrew Chael https://orcid.org/0000-0003-2966-6220
Chi-kwan Chan https://orcid.org/0000-0001-6337-6126
Shami Chatterjee https://orcid.org/0000-0002-2878-1502
Ilje Cho https://orcid.org/0000-0001-6083-7521
Pierre Christian https://orcid.org/0000-0001-6820-9941
John E. Conway https://orcid.org/0000-0003-2448-9181
Geoffrey B. Crew https://orcid.org/0000-0002-2079-3189
Yuzhu Cui https://orcid.org/0000-0001-6311-4345
Jordy Davelaar https://orcid.org/0000-0002-2685-2434
Mariafelicia De Laurentis https://orcid.org/0000-0002-9945-682X
Roger Deane https://orcid.org/0000-0003-1027-5043
Jessica Dempsey https://orcid.org/0000-0003-1269-9667
Gregory Desvignes https://orcid.org/0000-0003-3922-4055
Jason Dexter https://orcid.org/0000-0003-3903-0373
Sheperd S. Doeleman https://orcid.org/0000-0002-9031-0904
Ralph P. Eatough https://orcid.org/0000-0001-6196-4135
Heino Falcke https://orcid.org/0000-0002-2526-6724
Vincent L. Fish https://orcid.org/0000-0002-7128-9345
Raquel Fraga-Encinas https://orcid.org/0000-0002-5222-1361
José L. Gómez https://orcid.org/0000-0003-4190-7613
Peter Galison https://orcid.org/0000-0002-6429-3872
Charles F. Gammie https://orcid.org/0000-0001-7451-8935
Boris Georgiev https://orcid.org/0000-0002-3586-6424
Roman Gold https://orcid.org/0000-0003-2492-1966
Minfeng Gu (顾敏峰) https://orcid.org/0000-0002-4455-6946
Mark Gurwell https://orcid.org/0000-0003-0685-3621
Kazuhiro Hada https://orcid.org/0000-0001-6906-772X
Ronald Hesper https://orcid.org/0000-0003-1918-6098
Luis C. Ho (何子山) https://orcid.org/0000-0001-6947-5846
Mareki Honma https://orcid.org/0000-0003-4058-9000
Chih-Wei L. Huang https://orcid.org/0000-0001-5641-3953
Shiro Ikeda https://orcid.org/0000-0002-2462-1448
Sara Issaoun https://orcid.org/0000-0002-5297-921X
David J. James https://orcid.org/0000-0001-5160-4486
Michael Janssen https://orcid.org/0000-0001-8685-6544
Britton Jeter https://orcid.org/0000-0003-2847-1712
Wu Jiang (江悟) https://orcid.org/0000-0001-7369-3539
Michael D. Johnson https://orcid.org/0000-0002-4120-3029
Svetlana Jorstad https://orcid.org/0000-0001-6158-1708
Taehyun Jung https://orcid.org/0000-0001-7003-8643
Mansour Karami https://orcid.org/0000-0001-7387-9333
Ramesh Karuppusamy https://orcid.org/0000-0002-5307-2919
Tomohisa Kawashima https://orcid.org/0000-0001-8527-0496
Garrett K. Keating https://orcid.org/0000-0002-3490-146X
Mark Kettenis https://orcid.org/0000-0002-6156-5617
Jae-Young Kim https://orcid.org/0000-0001-8229-7183
Junhan Kim https://orcid.org/0000-0002-4274-9373
Motoki Kino https://orcid.org/0000-0002-2709-7338
Jun Yi Koay https://orcid.org/0000-0002-7029-6658
Patrick M. Koch https://orcid.org/0000-0003-2777-5861
Shoko Koyama https://orcid.org/0000-0002-3723-3372
Michael Kramer https://orcid.org/0000-0002-4175-2271
Carsten Kramer https://orcid.org/0000-0002-4908-4925
Thomas P. Krichbaum https://orcid.org/0000-0002-4892-9586
Tod R. Lauer https://orcid.org/0000-0003-3234-7247
Sang-Sung Lee https://orcid.org/0000-0002-6269-594X
Yan-Rong Li (李彦荣) https://orcid.org/0000-0001-5841-9179
Zhiyuan Li (李志远) https://orcid.org/0000-0003-0355-6437
Michael Lindqvist https://orcid.org/0000-0002-3669-0715
Kuo Liu https://orcid.org/0000-0002-2953-7376
Elisabetta Liuzzo https://orcid.org/0000-0003-0995-5201
Laurent Loinard https://orcid.org/0000-0002-5635-3345
Ru-Sen Lu (路如森) https://orcid.org/0000-0002-7692-7967
Nicholas R. MacDonald https://orcid.org/0000-0002-6684-8691
Jirong Mao (毛基荣) https://orcid.org/0000-0002-7077-7195
Sera Markoff https://orcid.org/0000-0001-9564-0876
Daniel P. Marrone https://orcid.org/0000-0002-2367-1080
Alan P. Marscher https://orcid.org/0000-0001-7396-3332
Iván Martí-Vidal https://orcid.org/0000-0003-3708-9611
Lynn D. Matthews https://orcid.org/0000-0002-3728-8082
Lia Medeiros https://orcid.org/0000-0003-2342-6728
Karl M. Menten https://orcid.org/0000-0001-6459-0669
Yosuke Mizuno https://orcid.org/0000-0002-8131-6730
Izumi Mizuno https://orcid.org/0000-0002-7210-6264
James M. Moran https://orcid.org/0000-0002-3882-4414
Kotaro Moriyama https://orcid.org/0000-0003-1364-3761
Monika Moscibrodzka https://orcid.org/0000-0002-4661-6332
Cornelia Müller https://orcid.org/0000-0002-2739-2994
Hiroshi Nagai https://orcid.org/0000-0003-0292-3645
Neil M. Nagar https://orcid.org/0000-0001-6920-662X
Masanori Nakamura https://orcid.org/0000-0001-6081-2420
Ramesh Narayan https://orcid.org/0000-0002-1919-2730
Iniyan Natarajan https://orcid.org/0000-0001-8242-4373
Chunchong Ni https://orcid.org/0000-0003-1361-5699
Aristeidis Noutsos https://orcid.org/0000-0002-4151-3860
Héctor Olivares https://orcid.org/0000-0001-6833-7580
Daniel C. M. Palumbo https://orcid.org/0000-0002-7179-3816
Ue-Li Pen https://orcid.org/0000-0003-2155-9578
Dominic W. Pesce https://orcid.org/0000-0002-5278-9221
Oliver Porth https://orcid.org/0000-0002-4584-2557
Ben Prather https://orcid.org/0000-0002-0393-7734
Jorge A. Preciado-López https://orcid.org/0000-0002-4146-0113
Hung-Yi Pu https://orcid.org/0000-0001-9270-8812
Venkatessh Ramakrishnan https://orcid.org/0000-0002-9248-086X
Ramprasad Rao https://orcid.org/0000-0002-1407-7944
Alexander W. Raymond https://orcid.org/0000-0002-5779-4767
Luciano Rezzolla https://orcid.org/0000-0002-1330-7103
Bart Ripperda https://orcid.org/0000-0002-7301-3908
Freek Roelofs https://orcid.org/0000-0001-5461-3687
Eduardo Ros https://orcid.org/0000-0001-9503-4892
Mel Rose https://orcid.org/0000-0002-2016-8746
Alan L. Roy https://orcid.org/0000-0002-1931-0135
Chet Ruszczyk https://orcid.org/0000-0001-7278-9707
Benjamin R. Ryan https://orcid.org/0000-0001-8939-4461
Kazi L. J. Rygl https://orcid.org/0000-0003-4146-9043
David Sánchez-Arguelles https://orcid.org/0000-0002-7344-9920
Mahito Sasada https://orcid.org/0000-0001-5946-9960

Tuomas Savolainen https://orcid.org/0000-0001-6214-1085
Lijing Shao https://orcid.org/0000-0002-1334-8853
Zhiqiang Shen (沈志强) https://orcid.org/0000-0003-3540-8746
Des Small https://orcid.org/0000-0003-3723-5404
Bong Won Sohn https://orcid.org/0000-0002-4148-8378
Jason SooHoo https://orcid.org/0000-0003-1938-0720
Fumie Tazaki https://orcid.org/0000-0003-0236-0600
Paul Tiede https://orcid.org/0000-0003-3826-5648
Remo P. J. Tilanus https://orcid.org/0000-0002-6514-553X
Michael Titus https://orcid.org/0000-0002-3423-4505
Kenji Toma https://orcid.org/0000-0002-7114-6010
Pablo Torne https://orcid.org/0000-0001-8700-6058
Sascha Trippe https://orcid.org/0000-0003-0465-1559
Ilse van Bemmel https://orcid.org/0000-0001-5473-2950
Huib Jan van Langevelde https://orcid.org/0000-0002-0230-5946
Daniel R. van Rossum https://orcid.org/0000-0001-7772-6131
John Wardle https://orcid.org/0000-0002-8960-2942
Jonathan Weintroub https://orcid.org/0000-0002-4603-5204
Norbert Wex https://orcid.org/0000-0003-4058-2837
Robert Wharton https://orcid.org/0000-0002-7416-5209
Maciek Wielgus https://orcid.org/0000-0002-8635-4242
George N. Wong https://orcid.org/0000-0001-6952-2147
Qingwen Wu (吴庆文) https://orcid.org/0000-0003-4773-4987
André Young https://orcid.org/0000-0003-0000-2682
Ken Young https://orcid.org/0000-0002-3666-4920
Ziri Younsi https://orcid.org/0000-0001-9283-1191
Feng Yuan (袁峰) https://orcid.org/0000-0003-3564-6437
J. Anton Zensus https://orcid.org/0000-0001-7470-3321
Guangyao Zhao https://orcid.org/0000-0002-4417-1659
Shan-Shan Zhao https://orcid.org/0000-0002-9774-3606
Joseph R. Farah https://orcid.org/0000-0003-4914-5625
Daniel Michalik https://orcid.org/0000-0002-7618-6556
Andrew Nadolski https://orcid.org/0000-0001-9479-9957
Rurik A. Primiani https://orcid.org/0000-0003-3910-7529
Paul Yamaguchi https://orcid.org/0000-0002-6017-8199

References

Akiyama, K., Ikeda, S., Pleau, M., et al. 2017a, AJ, 153, 159
Akiyama, K., Kuramochi, K., Ikeda, S., et al. 2017b, ApJ, 838, 1
Akiyama, K., Lu, R.-S., Fish, V. L., et al. 2015, ApJ, 807, 150
Asada, K., & Nakamura, M. 2012, ApJL, 745, L28
Bambi, C., & Freese, K. 2009, PhRvD, 79, 043002
Bardeen, J. M. 1973, in Black Holes (Les Astres Occlus), ed. C. Dewitt & B. S. Dewitt (New York: Gordon and Breach), 215
Benkevitch, L., Akiyama, K., Lu, R., Doeleman, S., & Fish, V. 2016, arXiv:1609.00055
Bird, S., Harris, W. E., Blakeslee, J. P., & Flynn, C. 2010, A&A, 524, A71
Blackburn, L., Chan, C.-K., Crew, G. B., et al. 2019, arXiv:1903.08832
Blakeslee, J. P., Jordán, A., Mei, S., et al. 2009, ApJ, 694, 556
Blandford, R. D., & Königl, A. 1979, ApJ, 232, 34
Blandford, R. D., & Payne, D. G. 1982, MNRAS, 199, 883
Blandford, R. D., & Znajek, R. L. 1977, MNRAS, 179, 433
Bower, G. C., Dexter, J., Markoff, S., et al. 2015, ApJL, 811, L6
Braak, C. J. F. T. 2006, Statistics and Computing, 16, 239
Broderick, A. E., Fish, V. L., Doeleman, S. S., & Loeb, A. 2011, ApJ, 735, 110
Broderick, A. E., Johannsen, T., Loeb, A., & Psaltis, D. 2014, ApJ, 784, 7
Broderick, A. E., & Loeb, A. 2009, ApJ, 697, 1164
Broderick, A. E., Narayan, R., Kormendy, J., et al. 2015, ApJ, 805, 179
Cantiello, M., Blakeslee, J. P., Ferrarese, L., et al. 2018a, ApJ, 856, 126
Cantiello, M., Jensen, J. B., Blakeslee, J. P., et al. 2018b, ApJL, 854, L31
Chael, A., Bouman, K., Johnson, M., et al. 2019a, eht-imaging: v1.1.0: Imaging interferometric data with regularized maximum likelihood (Version v1.1.0), Zenodo, http://doi.org/10.5281/zenodo.2614016
Chael, A., Narayan, R., & Johnson, M. D. 2019b, MNRAS, submitted (arXiv:1810.01983)
Chael, A. A., Johnson, M. D., Bouman, K. L., et al. 2018, ApJ, 857, 23
Chael, A. A., Johnson, M. D., Narayan, R., et al. 2016, ApJ, 829, 11
Chan, C.-k., Psaltis, D., & Özel, F. 2013, ApJ, 777, 13
Chandrasekhar, S. 1983, The Mathematical Theory of Black Holes (Oxford: Clarendon), 672
Cohen, M. H., Moffet, A. T., Shaffer, D., et al. 1969, ApJL, 158, L83
Cunha, P. V. P., & Herdeiro, C. A. R. 2018, GReGr, 50, 42
Deb, K., Pratap, A., Agarwal, S., & Meyarivan, T. 2002, Trans. Evol. Comp., 6, 182
Dexter, J., Agol, E., Fragile, P. C., & McKinney, J. C. 2010, ApJ, 717, 1092
Dexter, J., McKinney, J. C., & Agol, E. 2012, MNRAS, 421, 1517
Di Matteo, T., Allen, S. W., Fabian, A. C., Wilson, A. S., & Young, A. J. 2003, ApJ, 582, 133
Doeleman, S. S., Fish, V. L., Schenck, D. E., et al. 2012, Sci, 338, 355
EHT Collaboration, et al. 2019a, ApJL, 875, L2 (Paper II)
EHT Collaboration et al. 2019b, ApJL, 875, L3 (Paper III)
EHT Collaboration et al. 2019c, ApJL, 875, L4 (Paper IV)
EHT Collaboration et al. 2019d, ApJL, 875, L5 (Paper V)
Falcke, H., & Markoff, S. B. 2013, CQGra, 30, 244003
Falcke, H., Melia, F., & Agol, E. 2000, ApJL, 528, L13
Freimer, M., Kollia, G., Mudholkar, G. S., & Lin, C. T. 1988, Communications in Statistics—Theory and Methods, 17, 3547
Fromm, C. M., Younsi, Z., Bazcko, A., et al. 2019, A&A, submitted (arXiv:1904.00106)
Gebhardt, K., Adams, J., Richstone, D., et al. 2011, ApJ, 729, 119
Giddings, S. B., & Psaltis, D. 2018, PhRvD, 97, 084035
Hada, K., Doi, A., Kino, M., et al. 2011, Natur, 477, 185
Hada, K., Kino, M., Doi, A., et al. 2013, ApJ, 775, 70
Hada, K., Kino, M., Doi, A., et al. 2016, ApJ, 817, 131
Ho, L. C. 1999, ApJ, 516, 672
Ho, L. C. 2008, ARA&A, 46, 475
Jeter, B., Broderick, A. E., & McNamara, B. R. 2018, arXiv:1810.05238
Johannsen, T., & Psaltis, D. 2010, ApJ, 718, 446
Kamruddin, A. B., & Dexter, J. 2013, MNRAS, 434, 765
Kim, J., Marrone, D. P., Chan, C.-K., et al. 2016, ApJ, 832, 156
Kim, J.-Y., Krichbaum, T. P., Lu, R.-S., et al. 2018, A&A, 616, A188
Kormendy, J., & Ho, L. C. 2013, ARA&A, 51, 511
Kovalev, Y. Y., Lister, M. L., Homan, D. C., & Kellermann, K. I. 2007, ApJL, 668, L27
Kulkarni, S. R. 1989, AJ, 98, 1112
Lacroix, T., Bœhm, C., & Silk, J. 2015, PhRvD, 92, 043510
Lannes, A. 1990a, Proc. SPIE, 1351, 38
Lannes, A. 1990b, JOSAA, 7, 500
Lu, W., Kumar, P., & Narayan, R. 2017, MNRAS, 468, 910
Luminet, J.-P. 1979, A&A, 75, 228
Ly, C., Walker, R. C., & Junor, W. 2007, ApJ, 660, 200
Ly, C., Walker, R. C., & Wrobel, J. M. 2004, AJ, 127, 119
Marscher, A. P., Jorstad, S. G., D'Arcangelo, F. D., et al. 2008, Natur, 452, 966
Medeiros, L., Lauer, T. R., Psaltis, D., & Özel, F. 2018, ApJ, 864, 7
Mei, S., Blakeslee, J. P., Côté, P., et al. 2007, ApJ, 655, 144
Mertens, F., Lobanov, A. P., Walker, R. C., & Hardee, P. E. 2016, A&A, 595, A54
Mościbrodzka, M., Falcke, H., & Shiokawa, H. 2016, A&A, 586, A38
Nakamura, M., & Asada, K. 2013, ApJ, 775, 118
Narayan, R., & McClintock, J. E. 2008, NewAR, 51, 733
Nelson, B., Ford, E. B., & Payne, M. J. 2014, ApJS, 210, 11
Özel, F., Psaltis, D., & Narayan, R. 2000, ApJ, 541, 234
Prieto, M. A., Fernández-Ontiveros, J. A., Markoff, S., Espada, D., & González-Martín, O. 2016, MNRAS, 457, 3801
Psaltis, D., Özel, F., Chan, C.-K., & Marrone, D. P. 2015, ApJ, 814, 115
Reynolds, C. S., Di Matteo, T., Fabian, A. C., Hwang, U., & Canizares, C. R. 1996, MNRAS, 283, L111
Rogers, A. E. E., Hinteregger, H. F., Whitney, A. R., et al. 1974, ApJ, 193, 293
Ryan, B. R., Ressler, S. M., Dolence, J. C., Gammie, C., & Quataert, E. 2018, ApJ, 864, 126
Sargent, W. L. W., Young, P. J., Boksenberg, A., et al. 1978, ApJ, 221, 731
Shepherd, M. C. 1997, in ASP Conf. Ser. 125, Astronomical Data Analysis Software and Systems VI, ed. G. Hunt & H. Payne (San Francisco, CA: ASP), 77
Skilling, J. 2006, BayAn, 1, 833
Speagle, J., & Barbary, K. 2018, dynesty: Dynamic Nested Sampling Package, Astrophysics Source Code Library, ascl:1809.013
Storn, R., & Price, K. 1997, Journal of Global Optimization, 11, 341
Su, S. 2007a, Journal of Statistical Software, 21, 1
Su, S. 2007b, Computational Statistics & Data Analysis, 51, 3983

Takahashi, R. 2004, ApJ, 611, 996
Thompson, A. R., Moran, J. M., & Swenson, G. W., Jr. 2017, Interferometry and Synthesis in Radio Astronomy (3rd ed.; Dordrecht: Springer)
Tonry, J. L., Blakeslee, J. P., Ajhar, E. A., & Dressler, A. 2000, ApJ, 530, 625
Tukey, J. W. 1962, Ann. Math. Statist., 33, 1
von Laue, M. 1921, Die Relativitätstheorie, Vol. 1. Das Relativitätsprinzip der Lorentztransformation—Vol. 2. Die allgemeine Relativitätstheorie und Einsteins Lehre von der Schwerkraft (Braunschweig: Vieweg)
Vousden, W. D., Farr, W. M., & Mandel, I. 2016, MNRAS, 455, 1919
Walker, R. C., Hardee, P. E., Davies, F. B., Ly, C., & Junor, W. 2018, ApJ, 855, 128
Walsh, J. L., Barth, A. J., Ho, L. C., & Sarzi, M. 2013, ApJ, 770, 86
Young, P. J., Westphal, J. A., Kristian, J., Wilson, C. P., & Landauer, F. P. 1978, ApJ, 221, 721
Yuan, F., & Narayan, R. 2014, ARA&A, 52, 529

The Event Horizon Telescope Collaboration

Kazunori Akiyama[1,2,3,4], Antxon Alberdi[5], Walter Alef[6], Keiichi Asada[7], Rebecca Azulay[8,9,6], Anne-Kathrin Baczko[6], David Ball[10], Mislav Baloković[4,11], John Barrett[2], Dan Bintley[12], Lindy Blackburn[4,11], Wilfred Boland[13], Katherine L. Bouman[4,11,14], Geoffrey C. Bower[15], Michael Bremer[16], Christiaan D. Brinkerink[17], Roger Brissenden[4,11], Silke Britzen[6], Avery E. Broderick[18,19,20], Dominique Broguiere[16], Thomas Bronzwaer[17], Do-Young Byun[21,22], John E. Carlstrom[23,24,25,26], Andrew Chael[4,11], Chi-kwan Chan[10,27], Shami Chatterjee[28], Koushik Chatterjee[29], Ming-Tang Chen[15], Yongjun Chen (陈永军)[30,31], Ilje Cho[21,22], Pierre Christian[10,11], John E. Conway[32], James M. Cordes[28], Geoffrey B. Crew[2], Yuzhu Cui[33,34], Jordy Davelaar[17], Mariafelicia De Laurentis[35,36,37], Roger Deane[38,39], Jessica Dempsey[12], Gregory Desvignes[6], Jason Dexter[40], Sheperd S. Doeleman[4,11], Ralph P. Eatough[6], Heino Falcke[17], Vincent L. Fish[2], Ed Fomalont[1], Raquel Fraga-Encinas[17], Per Friberg[12], Christian M. Fromm[36], José L. Gómez[5], Peter Galison[4,41,42], Charles F. Gammie[43,44], Roberto García[16], Olivier Gentaz[16], Boris Georgiev[19,20], Ciriaco Goddi[17,45], Roman Gold[36], Minfeng Gu (顾敏峰)[30,46], Mark Gurwell[11], Kazuhiro Hada[33,34], Michael H. Hecht[2], Ronald Hesper[47], Luis C. Ho (何子山)[48,49], Paul Ho[7], Mareki Honma[33,34], Chih-Wei L. Huang[7], Lei Huang (黄磊)[30,46], David H. Hughes[50], Shiro Ikeda[3,51,52,53], Makoto Inoue[7], Sara Issaoun[17], David J. James[4,11], Buell T. Jannuzi[10], Michael Janssen[17], Britton Jeter[19,20], Wu Jiang (江悟)[30], Michael D. Johnson[4,11], Svetlana Jorstad[54,55], Taehyun Jung[21,22], Mansour Karami[56,19], Ramesh Karuppusamy[6], Tomohisa Kawashima[3], Garrett K. Keating[11], Mark Kettenis[57], Jae-Young Kim[6], Junhan Kim[10], Jongsoo Kim[21], Motoki Kino[3,58], Jun Yi Koay[7], Patrick M. Koch[7], Shoko Koyama[7], Michael Kramer[6], Carsten Kramer[16], Thomas P. Krichbaum[6], Cheng-Yu Kuo[59], Tod R. Lauer[60], Sang-Sung Lee[21], Yan-Rong Li (李彦荣)[61], Zhiyuan Li (李志远)[62,63], Michael Lindqvist[32], Kuo Liu[6], Elisabetta Liuzzo[64], Wen-Ping Lo[7,65], Andrei P. Lobanov[6], Laurent Loinard[66,67], Colin Lonsdale[2], Ru-Sen Lu (路如森)[30,6], Nicholas R. MacDonald[6], Jirong Mao (毛基荣)[68,69,70], Sera Markoff[29,71], Daniel P. Marrone[10], Alan P. Marscher[54], Iván Martí-Vidal[72,73], Satoki Matsushita[7], Lynn D. Matthews[2], Lia Medeiros[10,74], Karl M. Menten[6], Yosuke Mizuno[36], Izumi Mizuno[12], James M. Moran[4,11], Kotaro Moriyama[33,2], Monika Moscibrodzka[17], Cornelia Müller[6,17], Hiroshi Nagai[3,35], Neil M. Nagar[75], Masanori Nakamura[7], Ramesh Narayan[4,11], Gopal Narayanan[76], Iniyan Natarajan[39], Roberto Neri[16], Chunchong Ni[19,20], Aristeidis Noutsos[6], Hiroki Okino[33,77], Héctor Olivares[36], Tomoaki Oyama[33], Feryal Özel[10], Daniel C. M. Palumbo[4,11], Nimesh Patel[11], Ue-Li Pen[78,79,80,81], Dominic W. Pesce[4,11], Vincent Piétu[16], Richard Plambeck[82], Aleksandar PopStefanija[76], Oliver Porth[29,36], Ben Prather[43], Jorge A. Preciado-López[18], Dimitrios Psaltis[10], Hung-Yi Pu[18], Venkatessh Ramakrishnan[75], Ramprasad Rao[15], Mark G. Rawlings[12], Alexander W. Raymond[4,11], Luciano Rezzolla[36], Bart Ripperda[36], Freek Roelofs[17], Alan Rogers[2], Eduardo Ros[6], Mel Rose[10], Arash Roshanineshat[10], Helge Rottmann[6], Alan L. Roy[6], Chet Ruszczyk[2], Benjamin R. Ryan[83,84], Kazi L. J. Rygl[64], Salvador Sánchez[85], David Sánchez-Arguelles[50,86], Mahito Sasada[33,87], Tuomas Savolainen[6,88,89], F. Peter Schloerb[76], Karl-Friedrich Schuster[16], Lijing Shao[6,49], Zhiqiang Shen (沈志强)[30,31], Des Small[57], Bong Won Sohn[21,22,90], Jason SooHoo[2], Fumie Tazaki[33], Paul Tiede[19,20], Remo P. J. Tilanus[17,45,91], Michael Titus[2], Kenji Toma[92,93], Pablo Torne[6,85], Tyler Trent[10], Sascha Trippe[94], Shuichiro Tsuda[95], Ilse van Bemmel[57], Huib Jan van Langevelde[57,96], Daniel R. van Rossum[17], Jan Wagner[6], John Wardle[97], Jonathan Weintroub[4,11], Norbert Wex[6], Robert Wharton[6], Maciek Wielgus[4,11], George N. Wong[43], Qingwen Wu (吴庆文)[98], André Young[17], Ken Young[11], Ziri Younsi[99,36], Feng Yuan (袁峰)[30,46,100], Ye-Fei Yuan (袁业飞)[101], J. Anton Zensus[6], Guangyao Zhao[21], Shan-Shan Zhao[17,62], Ziyan Zhu[42], Joseph R. Farah[11,102,4], Zheng Meyer-Zhao[7,103], Daniel Michalik[104,105], Andrew Nadolski[44], Hiroaki Nishioka[7], Nicolas Pradel[7], Rurik A. Primiani[106], Kamal Souccar[76], Laura Vertatschitsch[11,106], and Paul Yamaguchi[11]

[1] National Radio Astronomy Observatory, 520 Edgemont Rd, Charlottesville, VA 22903, USA
[2] Massachusetts Institute of Technology Haystack Observatory, 99 Millstone Road, Westford, MA 01886, USA
[3] National Astronomical Observatory of Japan, 2-21-1 Osawa, Mitaka, Tokyo 181-8588, Japan
[4] Black Hole Initiative at Harvard University, 20 Garden Street, Cambridge, MA 02138, USA
[5] Instituto de Astrofísica de Andalucía-CSIC, Glorieta de la Astronomía s/n, E-18008 Granada, Spain
[6] Max-Planck-Institut für Radioastronomie, Auf dem Hügel 69, D-53121 Bonn, Germany

[7] Institute of Astronomy and Astrophysics, Academia Sinica, 11F of Astronomy-Mathematics Building, AS/NTU No. 1, Section 4, Roosevelt Rd, Taipei 10617, Taiwan, R.O.C.
[8] Departament d'Astronomia i Astrofísica, Universitat de València, C. Dr. Moliner 50, E-46100 Burjassot, València, Spain
[9] Observatori Astronòmic, Universitat de València, C. Catedrático José Beltrán 2, E-46980 Paterna, València, Spain
[10] Steward Observatory and Department of Astronomy, University of Arizona, 933 N. Cherry Ave., Tucson, AZ 85721, USA
[11] Center for Astrophysics | Harvard & Smithsonian, 60 Garden Street, Cambridge, MA 02138, USA
[12] East Asian Observatory, 660 N. A'ohoku Pl., Hilo, HI 96720, USA
[13] Nederlandse Onderzoekschool voor Astronomie (NOVA), P.O. Box 9513, 2300 RA Leiden, The Netherlands
[14] California Institute of Technology, 1200 East California Boulevard, Pasadena, CA 91125, USA
[15] Institute of Astronomy and Astrophysics, Academia Sinica, 645 N. A'ohoku Place, Hilo, HI 96720, USA
[16] Institut de Radioastronomie Millimétrique, 300 rue de la Piscine, F-38406 Saint Martin d'Hères, France
[17] Department of Astrophysics, Institute for Mathematics, Astrophysics and Particle Physics (IMAPP), Radboud University, P.O. Box 9010, 6500 GL Nijmegen, The Netherlands
[18] Perimeter Institute for Theoretical Physics, 31 Caroline Street North, Waterloo, ON, N2L 2Y5, Canada
[19] Department of Physics and Astronomy, University of Waterloo, 200 University Avenue West, Waterloo, ON, N2L 3G1, Canada
[20] Waterloo Centre for Astrophysics, University of Waterloo, Waterloo, ON N2L 3G1 Canada
[21] Korea Astronomy and Space Science Institute, Daedeok-daero 776, Yuseong-gu, Daejeon 34055, Republic of Korea
[22] University of Science and Technology, Gajeong-ro 217, Yuseong-gu, Daejeon 34113, Republic of Korea
[23] Kavli Institute for Cosmological Physics, University of Chicago, 5640 South Ellis Avenue, Chicago, IL 60637, USA
[24] Department of Astronomy and Astrophysics, University of Chicago, 5640 South Ellis Avenue, Chicago, IL 60637, USA
[25] Department of Physics, University of Chicago, 5720 South Ellis Avenue, Chicago, IL 60637, USA
[26] Enrico Fermi Institute, University of Chicago, 5640 South Ellis Avenue, Chicago, IL 60637, USA
[27] Data Science Institute, University of Arizona, 1230 N. Cherry Ave., Tucson, AZ 85721, USA
[28] Cornell Center for Astrophysics and Planetary Science, Cornell University, Ithaca, NY 14853, USA
[29] Anton Pannekoek Institute for Astronomy, University of Amsterdam, Science Park 904, 1098 XH, Amsterdam, The Netherlands
[30] Shanghai Astronomical Observatory, Chinese Academy of Sciences, 80 Nandan Road, Shanghai 200030, People's Republic of China
[31] Key Laboratory of Radio Astronomy, Chinese Academy of Sciences, Nanjing 210008, People's Republic of China
[32] Department of Space, Earth and Environment, Chalmers University of Technology, Onsala Space Observatory, SE-439 92 Onsala, Sweden
[33] Mizusawa VLBI Observatory, National Astronomical Observatory of Japan, 2-12 Hoshigaoka, Mizusawa, Oshu, Iwate 023-0861, Japan
[34] Department of Astronomical Science, The Graduate University for Advanced Studies (SOKENDAI), 2-21-1 Osawa, Mitaka, Tokyo 181-8588, Japan
[35] Dipartimento di Fisica "E. Pancini," Universitá di Napoli "Federico II," Compl. Univ. di Monte S. Angelo, Edificio G, Via Cinthia, I-80126, Napoli, Italy
[36] Institut für Theoretische Physik, Goethe-Universität Frankfurt, Max-von-Laue-Straße 1, D-60438 Frankfurt am Main, Germany
[37] INFN Sez. di Napoli, Compl. Univ. di Monte S. Angelo, Edificio G, Via Cinthia, I-80126, Napoli, Italy
[38] Department of Physics, University of Pretoria, Lynnwood Road, Hatfield, Pretoria 0083, South Africa
[39] Centre for Radio Astronomy Techniques and Technologies, Department of Physics and Electronics, Rhodes University, Grahamstown 6140, South Africa
[40] Max-Planck-Institut für Extraterrestrische Physik, Giessenbachstr. 1, D-85748 Garching, Germany
[41] Department of History of Science, Harvard University, Cambridge, MA 02138, USA
[42] Department of Physics, Harvard University, Cambridge, MA 02138, USA
[43] Department of Physics, University of Illinois, 1110 West Green Street, Urbana, IL 61801, USA
[44] Department of Astronomy, University of Illinois at Urbana-Champaign, 1002 West Green Street, Urbana, IL 61801, USA
[45] Leiden Observatory—Allegro, Leiden University, P.O. Box 9513, 2300 RA Leiden, The Netherlands
[46] Key Laboratory for Research in Galaxies and Cosmology, Chinese Academy of Sciences, Shanghai 200030, People's Republic of China
[47] NOVA Sub-mm Instrumentation Group, Kapteyn Astronomical Institute, University of Groningen, Landleven 12, 9747 AD Groningen, The Netherlands
[48] Department of Astronomy, School of Physics, Peking University, Beijing 100871, People's Republic of China
[49] Kavli Institute for Astronomy and Astrophysics, Peking University, Beijing 100871, People's Republic of China
[50] Instituto Nacional de Astrofísica, Óptica y Electrónica. Apartado Postal 51 y 216, 72000. Puebla Pue., México
[51] The Institute of Statistical Mathematics, 10-3 Midori-cho, Tachikawa, Tokyo, 190-8562, Japan
[52] Department of Statistical Science, The Graduate University for Advanced Studies (SOKENDAI), 10-3 Midori-cho, Tachikawa, Tokyo 190-8562, Japan
[53] Kavli Institute for the Physics and Mathematics of the Universe, The University of Tokyo, 5-1-5 Kashiwanoha, Kashiwa, 277-8583, Japan
[54] Institute for Astrophysical Research, Boston University, 725 Commonwealth Ave., Boston, MA 02215, USA
[55] Astronomical Institute, St. Petersburg University, Universitetskij pr., 28, Petrodvorets, 198504 St. Petersburg, Russia
[56] Perimeter Institute for Theoretical Physics, 31 Caroline Street North, Waterloo, Ontario N2L 2Y5, Canada
[57] Joint Institute for VLBI ERIC (JIVE), Oude Hoogeveensedijk 4, 7991 PD Dwingeloo, The Netherlands
[58] Kogakuin University of Technology & Engineering, Academic Support Center, 2665-1 Nakano, Hachioji, Tokyo 192-0015, Japan
[59] Physics Department, National Sun Yat-Sen University, No. 70, Lien-Hai Rd, Kaosiung City 80424, Taiwan, R.O.C
[60] National Optical Astronomy Observatory, 950 North Cherry Ave., Tucson, AZ 85719, USA
[61] Key Laboratory for Particle Astrophysics, Institute of High Energy Physics, Chinese Academy of Sciences, 19B Yuquan Road, Shijingshan District, Beijing, People's Republic of China
[62] School of Astronomy and Space Science, Nanjing University, Nanjing 210023, People's Republic of China
[63] Key Laboratory of Modern Astronomy and Astrophysics, Nanjing University, Nanjing 210023, People's Republic of China
[64] Italian ALMA Regional Centre, INAF-Istituto di Radioastronomia, Via P. Gobetti 101, I-40129 Bologna, Italy
[65] Department of Physics, National Taiwan University, No.1, Sect.4, Roosevelt Rd., Taipei 10617, Taiwan, R.O.C
[66] Instituto de Radioastronomía y Astrofísica, Universidad Nacional Autónoma de México, Morelia 58089, México
[67] Instituto de Astronomía, Universidad Nacional Autónoma de México, CdMx 04510, México
[68] Yunnan Observatories, Chinese Academy of Sciences, 650011 Kunming, Yunnan Province, People's Republic of China
[69] Center for Astronomical Mega-Science, Chinese Academy of Sciences, 20A Datun Road, Chaoyang District, Beijing, 100012, People's Republic of China
[70] Key Laboratory for the Structure and Evolution of Celestial Objects, Chinese Academy of Sciences, 650011 Kunming, People's Republic of China
[71] Gravitation Astroparticle Physics Amsterdam (GRAPPA) Institute, University of Amsterdam, Science Park 904, 1098 XH Amsterdam, The Netherlands
[72] Department of Space, Earth and Environment, Chalmers University of Technology, Onsala Space Observatory, SE-43992 Onsala, Sweden
[73] Centro Astronómico de Yebes (IGN), Apartado 148, E-19180 Yebes, Spain
[74] Department of Physics, Broida Hall, University of California Santa Barbara, Santa Barbara, CA 93106, USA
[75] Astronomy Department, Universidad de Concepción, Casilla 160-C, Concepción, Chile
[76] Department of Astronomy, University of Massachusetts, 01003, Amherst, MA, USA
[77] Department of Astronomy, Graduate School of Science, The University of Tokyo, 7-3-1 Hongo, Bunkyo-ku, Tokyo 113-0033, Japan
[78] Canadian Institute for Theoretical Astrophysics, University of Toronto, 60 St. George Street, Toronto, ON M5S 3H8, Canada

[79] Dunlap Institute for Astronomy and Astrophysics, University of Toronto, 50 St. George Street, Toronto, ON M5S 3H4, Canada
[80] Canadian Institute for Advanced Research, 180 Dundas St West, Toronto, ON M5G 1Z8, Canada
[81] Perimeter Institute for Theoretical Physics, 31 Caroline Street North, Waterloo, ON N2L 2Y5, Canada
[82] Radio Astronomy Laboratory, University of California, Berkeley, CA 94720, USA
[83] CCS-2, Los Alamos National Laboratory, P.O. Box 1663, Los Alamos, NM 87545, USA
[84] Center for Theoretical Astrophysics, Los Alamos National Laboratory, Los Alamos, NM 87545, USA
[85] Instituto de Radioastronomía Milimétrica, IRAM, Avenida Divina Pastora 7, Local 20, E-18012, Granada, Spain
[86] Consejo Nacional de Ciencia y Tecnología, Av. Insurgentes Sur 1582, 03940, Ciudad de México, México
[87] Hiroshima Astrophysical Science Center, Hiroshima University, 1-3-1 Kagamiyama, Higashi-Hiroshima, Hiroshima 739-8526, Japan
[88] Aalto University Department of Electronics and Nanoengineering, PL 15500, FI-00076 Aalto, Finland
[89] Aalto University Metsähovi Radio Observatory, Metsähovintie 114, FI-02540 Kylmälä, Finland
[90] Department of Astronomy, Yonsei University, Yonsei-ro 50, Seodaemun-gu, 03722 Seoul, Republic of Korea
[91] Netherlands Organisation for Scientific Research (NWO), Postbus 93138, 2509 AC Den Haag , The Netherlands
[92] Frontier Research Institute for Interdisciplinary Sciences, Tohoku University, Sendai 980-8578, Japan
[93] Astronomical Institute, Tohoku University, Sendai 980-8578, Japan
[94] Department of Physics and Astronomy, Seoul National University, Gwanak-gu, Seoul 08826, Republic of Korea
[95] Mizusawa VLBI Observatory, National Astronomical Observatory of Japan, Hoshigaoka 2-12, Mizusawa-ku, Oshu-shi, Iwate 023-0861, Japan
[96] Leiden Observatory, Leiden University, Postbus 2300, 9513 RA Leiden, The Netherlands
[97] Physics Department, Brandeis University, 415 South Street, Waltham, MA 02453, USA
[98] School of Physics, Huazhong University of Science and Technology, Wuhan, Hubei, 430074, People's Republic of China
[99] Mullard Space Science Laboratory, University College London, Holmbury St. Mary, Dorking, Surrey, RH5 6NT, UK
[100] School of Astronomy and Space Sciences, University of Chinese Academy of Sciences, No. 19A Yuquan Road, Beijing 100049, People's Republic of China
[101] Astronomy Department, University of Science and Technology of China, Hefei 230026, People's Republic of China
[102] University of Massachusetts Boston, 100 William T, Morrissey Blvd, Boston, MA 02125, USA
[103] ASTRON, Oude Hoogeveensedijk 4, 7991 PD Dwingeloo, The Netherlands
[104] Science Support Office, Directorate of Science, European Space Research and Technology Centre (ESA/ESTEC), Keplerlaan 1, 2201 AZ Noordwijk, The Netherlands
[105] University of Chicago, 5640 South Ellis Avenue, Chicago, IL 60637, USA
[106] Systems & Technology Research, 600 West Cummings Park, Woburn, MA 01801, USA